

**River-bed sediment surface characterisation  
using wavelet transform-based methods**

A thesis submitted in partial fulfilment of the  
requirements of Napier University for the  
degree of Doctor of Philosophy

By  
Annie Nyander

October, 2004

School of the Built Environment,  
Napier University,  
Edinburgh, Scotland, U.K.

## ABSTRACT

The primary purpose of this work was to study the morphological change of river-bed sediment surfaces over time using wavelet transform analysis techniques. The wavelet transform is a rapidly developing area of applied mathematics in both science and engineering. As it allows for interrogation of the spectral made up of local signal features, it has superior performance compared to the traditionally used Fourier transform which provides only signal averaged spectral information. The main study of this thesis includes the analysis of both synthetically generated sediment surfaces and laboratory experimental sediment bed-surface data. This was undertaken using two-dimensional wavelet transform techniques based on both the discrete and the stationary wavelet transforms.

A comprehensive data-base of surface scans from experimental river-bed sediment surfaces topographies were included in the study. A novel wavelet-based characterisation measure - *the form size distribution (fsd)* - was developed to quantify the global characteristics of the sediment data. The *fsd* is based on the distribution of wavelet-based scale-dependent energies. It is argued that this measure will potentially be more useful than the traditionally used *particle size distribution (psd)*, as it is the morphology of the surface rather than the individual particle sizes that affects the near bed flow regime and hence bed friction characteristics.

Amplitude and scale dependent thresholding techniques were then studied. It was found that these thresholding techniques could be used to: (1) extract the overall surface structure, and (2) enhance dominant grains and formations of dominant grains within the surfaces. It is shown that assessment of the surface data-sets post-thresholding may allow for the detection of structural changes over time.

## ACKNOWLEDGEMENT

I would first like to express my particular thanks to my supervisor Professor Paul Addison for his helpful encouragement and detailed guidance throughout my PhD research.

I also would like to thank the people who shared data with me, without whom I would have had significantly less to analyse. These are Professor Gareth Pender of Heriot-Watt University, Dr Ian McEwan of University of Aberdeen, Dr John Heald of University of Aberdeen and Dr Lewis Dougan of Pavement Technology Ltd.

I am also grateful to the Royal Society of Edinburgh and the J M Lessells Travelling Scholarship Trust for their generous award which allowed me to attend the 15<sup>th</sup> annual ASCE Engineering Mechanics Conference in New York and visit researchers in the United States of America. A particular thanks is due to Professor Muhammad Hajj, (Virginia Polytechnic Institute and State University), Professor Nicholas P. Jones, (John Hopkins University), Professor Zhikun Hou, (Worcester Polytechnic Institute), Professor Kevin Amaratunga, (Massachusetts Institute of Technology) and Professor George Frantziskonis, (University of Arizona), for their time, consideration and generosity during this visit.

Special thanks to my friends and colleagues at Napier University with whom I have shared many memorable times and much laughter over the past years. I would also like to thank my very good friend Lynda for the many nights of “blethering” in front of the fire.

Finally, I would like to offer my thanks and love to my family for their undeviating encouragement and belief in me throughout my time at university and I would like to dedicate this work to my parents, Leif and Inger.

*- tack för allt.*

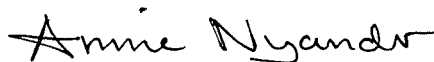
## DECLARATION

This thesis is submitted to Napier University for the degree of Doctor of Philosophy. The work described herein was carried out under the supervision of Professor Paul Addison. The work was undertaken within the School of Built Environment, Napier University. Except where stated otherwise, this thesis is the result of my own work and in accordance with the Napier University regulations governing the degree of Doctor of Philosophy. This thesis has not been submitted in whole or in part for any degree or diploma at this or any other university.

During the period of research the following papers have been published and/or presented at conference:

1. Nyander A, Addison P S, McEwan I and Pender G (2002) "River bed surface roughness analysis using 2-D wavelet transform-based methods", The 15<sup>th</sup> ASCE Engineering Mechanics Conference, June 2-5, New York , USA.
2. Nyander A, Addison P S, McEwan I and Pender G (2003) "Wavelet decomposition of sediment surface to characterise scale dependent properties and reveal individual feature", 16<sup>th</sup> Scottish Fluid Mechanics Meeting, May 28, University of Dundee, Dundee, U.K.
3. Nyander A, Addison P S, McEwan I and Pender G (2003) "Analysis of river bed surface roughness using 2D wavelet transform-based method" The Arabian Journal for Science and Engineering, Vol.28(1C), June, pp.107-121.
4. Nyander A, Addison P S, McEwan I and Pender G (2004) "Wavelet thresholding of simulated sediment to highlight pertinent bedform features", 17<sup>th</sup> Scottish Fluid Mechanics Meeting, May 19, University of Strathclyde, Glasgow, U.K.

These publications are reproduced in appendix B.



Annie Nyander

Napier University, Edinburgh.

## CONTENTS

<b>Abstract</b> .....	i
<b>Acknowledgement</b> .....	ii
<b>Declaration</b> .....	iii
<b>Contents</b> .....	iv
<b>List of tables</b> .....	viii
<b>List of figures</b> .....	ix
<b>Nomenclature</b> .....	xii
<b>Chapter 1 Introduction</b>	
1.1. Wavelet analysis and the characterisation of river bed surfaces .....	2
1.2. Scope of investigation .....	3
1.3. Outline of thesis.....	4
<b>Chapter 2 Literature review</b>	
2.1. Introduction and background.....	8
2.2. The history of wavelets.....	9
2.3. Other methods for data analysis .....	10
2.4. The continuous wavelet transform (CWT).....	11
2.4.1. Introduction .....	11
2.4.2. The wavelet function .....	12
2.4.3. The signal energy (CWT).....	13
2.4.4. The inverse continuous wavelet transform.....	13
2.5. The discrete wavelet transform (DWT).....	14
2.5.1. Introduction .....	14
2.5.2. Orthogonal wavelet bases.....	14
2.5.3. Dyadic grid scaling.....	15
2.5.4. The scaling function .....	15
2.5.5. Multiresolution .....	17
2.5.6. The Haar wavelet.....	18
2.5.7. Wavelet energy and wavelet statistics .....	20
2.6. The stationary wavelet transform (SWT).....	21
2.6.1. Introduction .....	21
2.6.2. Definition.....	22
2.7. The two-dimensional wavelet transform .....	24
2.7.1. The 2-D wavelet transform energy.....	25
2.8. Choice of wavelet bases .....	26

2.8.1. Introduction .....	26
2.8.2. Continuous or discrete transform .....	26
2.8.3. Analysing wavelet .....	27
2.8.3.1. General properties .....	28
2.8.3.2. Analysing wavelet similarity to test data .....	28
2.8.3.3. Vanishing moment .....	28
2.8.3.4. Selectivity in frequency .....	29
2.8.4. Wavelet mode .....	29
2.9. Wavelet tools .....	30
2.9.1. Introduction .....	30
2.9.2. Smoothing .....	31
2.9.3. Denoising .....	32
2.9.3.1. Denoising by hard or soft thresholding .....	32
2.9.3.2. Threshold value .....	33
2.9.3.3. Data analysis using amplitude thresholding .....	35
2.10. Application of the wavelet transform to the analysis of rough surfaces .....	37
2.10.1. Introduction .....	37
2.10.2. Engineering surface analysis .....	38
2.11. Sediment transportation .....	44
2.11.1. Introduction .....	44
2.11.2. River hydraulics .....	44
2.11.2.1. Fluid dynamics .....	44
2.11.2.2. Sediment motion .....	46
2.11.3. Bed armouring and cluster formation .....	48
2.11.4. Surface bed layer composition (sampling techniques) .....	51
2.12. Chapter summary .....	53
<b>Chapter 3 Algorithm development: Analysis of one-dimensional data</b>	
3.1. Introduction .....	78
3.2. Algorithm development .....	79
3.2.1. Software algorithm development and validation .....	79
3.2.2. Edge effects .....	79
3.2.3. Algorithm development for edge effects - Discrete wavelet transform .....	80
3.2.3. Algorithm development for edge effects - Stationary wavelet transform .....	81
3.3. Experimental data analysis - Fractals .....	82
3.3.1. Introduction fractional Brownian motion ( <i>fBm</i> ) .....	82
3.3.1.1. Fractal theory .....	83
3.3.2. Analysis of synthetic data using the DWT .....	85
3.3.3. Analysis of synthetic data using the SWT .....	85
3.4. Experimental data analysis - Cracked concrete profiles .....	86
3.4.1. Introduction and background .....	86
3.4.2. Analysis of experimental concrete crack profile data - DWT .....	87

3.4.3. Analysis of experimental concrete crack profile data – SWT .....	88
3.5. Analysis of medical signals using the discrete wavelet transform .....	89
3.5.1. Introduction .....	89
3.5.2. Smoothing and removal of signal drift in a pulse oximeter signal.....	89
3.5.3. Wavelet analysis of electrocardiogram (ECG) signals.....	90
3.6. Discussion and chapter summary .....	91
<b>Chapter 4    Global surface characterisation: Algorithm development and                   experimental results</b>	
4.1. Introduction .....	120
4.2. River bed sediment surface data.....	121
4.2.1. Introduction .....	121
4.2.2. Experimental procedure.....	122
4.2.3. Out of range values.....	124
4.2.4. Interpolation of rows and columns .....	124
4.2.5. Interpolation using triangulation .....	125
4.3. Sediment surface characterisation: particle and form size distributions .....	127
4.3.1. Surface topographies .....	127
4.3.2. Energy distribution: fBm test surfaces .....	128
4.3.3. 2-D edge effect .....	129
4.3.4. Discrete wavelet transform analysis of the river bed surfaces .....	132
4.3.5. Stationary wavelet transform analysis of river bed surfaces .....	133
4.3.6. Form size distribution: a new surface characteristic .....	134
4.3.7. Analysis of computer generated synthetic sediment surfaces .....	135
4.3.8. Comparison of DWT and SWT analysis .....	137
4.4. Discussion.....	137
4.5. Chapter summary.....	146
<b>Chapter 5    Local feature recognition: Algorithm development and                   experimental results</b>	
5.1. Introduction .....	218
5.2. Computer generated synthetic sediment surfaces.....	219
5.3. Analysis of the computer generated test surfaces with added features .....	221
5.3.1. Thresholding.....	221
5.3.2. Energy.....	222
5.3.3. Entropy .....	224
5.3.4. Entropy of the surfaces .....	226
5.3.5. Separation of entropy.....	226
5.4. Analysis of feature edge effects.....	228
5.4.1. Test surface data .....	228
5.4.2. The analysis .....	229

5.4.3. Analysis of test surface I .....	230
5.4.4. Analysis of test surface II .....	232
5.5. Discussion of results.....	233
5.6. Analysis of experimental river-bed sediment surfaces - thresholding .....	236
5.6.1. Data analysis.....	237
5.7. Discussion and chapter summary .....	240
<b>Chapter 6 Summary of conclusions, discussion and recommendations</b>	
6.1. Introduction .....	300
6.2. Achievement of the aims .....	300
6.3. Summary of completed work .....	301
6.3.1. Characterisation of profile traces.....	301
6.3.2. Global surface characterisation .....	302
6.3.3. Local feature recognition.....	304
6.4. Conclusions from this thesis.....	305
6.5. Recommendations for future research.....	306
<b>Appendices</b> .....	308
<b>References</b> .....	349



## LIST OF TABLES

### Chapter 3

Table 3.1	Number of edge coefficients for the DWT.....	94
Table 3.2	Number of edge coefficients for the SWT .....	95
Table 3.3	Determination of scaling properties of synthetic test profiles.....	96
Table 3.4	Scaling properties of the small sized cracked concrete profiles.....	97
Table 3.5	Scaling properties of the medium sized cracked concrete profiles .....	98
Table 3.6	Scaling properties of the large sized cracked concrete profiles .....	99

### Chapter 4

Table 4.1	Initial distribution of particle sizes in the three sediment mixtures .....	148
Table 4.2	Experimental program for river sediment surface bed experiments .....	149
Table 4.2	Experimental data-sets .....	150

### Chapter 5

Table 5.1	Proportion of energies within the synthetic surfaces, soft threshold.....	244
Table 5.2	Proportion of energies within the synthetic surfaces, hard threshold .....	244
Table 5.3	Synthetic surfaces with line features applying soft threshold .....	245
Table 5.4	Synthetic surfaces with circle features applying soft threshold. ....	246
Table 5.5	Synthetic surfaces with diamond features applying soft threshold .....	247
Table 5.6	Synthetic surfaces with square features applying soft threshold.....	248
Table 5.7	Synthetic surfaces with line features applying hard threshold.....	249
Table 5.8	Synthetic surfaces with circle features applying hard threshold .....	250
Table 5.9	Synthetic surfaces with diamond features applying hard threshold .....	251
Table 5.10	Synthetic surfaces with square features applying hard threshold .....	252
Table 5.11	Applying a hard threshold to the surface where the background equals 0 in height.....	253
Table 5.12	Applying a soft threshold to the surface where the background equals 0 in height.....	254
Table 5.13	Applying a hard threshold to the surface where the background is generated from uniform distribution .....	255
Table 5.14	Applying a soft threshold to the surface where the background is generated from uniform distribution .....	256

## LIST OF FIGURES

### Chapter 2

Figure 2.1	Decomposition of a fractional Brownian motion ( <i>fBm</i> ) signal .....	55
Figure 2.2	Examples of Daubechies wavelet and scaling functions.....	56
Figure 2.3	Haar decomposition of a sinusoidal signal.....	57
Figure 2.4	The difference between the DWT and the SWT decomposition .....	58
Figure 2.5	Examples of 2-D wavelets.....	59
Figure 2.6	Wavelet functions and scaling function of the 2-D Haar wavelet.....	60
Figure 2.7	Schematic diagram of the decomposition of data into two layers using the 2-D wavelet transform.....	61
Figure 2.8	Wavelet decomposition and reconstruction of shear layer velocity signal .....	62
Figure 2.9	Maximum frequency in Fourier space .....	63
Figure 2.10	Smoothing of test pulse oximeter signal .....	64
Figure 2.11	Schematic diagram of soft threshold and hard threshold .....	65
Figure 2.12	Test waveform with added noise.....	66
Figure 2.13	Hard thresholding of the test signal.....	67
Figure 2.14	Soft thresholding of the test signal.....	68
Figure 2.15	Characterisation of corrosion pit surface applying the WT .....	69
Figure 2.16	Wavelet analysis of fBm profiles .....	70
Figure 2.17	Analysis of cracked concrete profiles using the continuous wavelet transform .....	71
Figure 2.18	Multiscale decomposition of a metallic femoral head .....	72
Figure 2.19	The multiscale features and their location of the metallic femoral head .....	72
Figure 2.20	The raw measured surface and morphological surfaces of a worn ceramic head.....	73
Figure 2.21	Form, waviness and roughness decomposition of a surface texture .....	74
Figure 2.22	Sediment particle movement.....	75
Figure 2.23	Example of a particle size distribution.....	75
Figure 2.24	Cluster formation steps in mono-sized simulated sediment particles .....	76

### Chapter 3

Figure 3.1	Edge effects in the DWT for the Daubechies D6 wavelet .....	101
Figure 3.2	Compensating for edge effects in a test profile.....	102
Figure 3.3	Transaction of Daubechies wavelet filters to a signal using the DWT .....	103
Figure 3.4	The number of edge coefficients at each end of the transform .....	104
Figure 3.5	Fractal curve analysis using the discrete wavelet transform .....	105
Figure 3.6	Synthetic fBm-profile test data .....	106
Figure 3.7	Variance of the DWT coefficients for the test fBm profiles .....	108
Figure 3.8	Variance of the SWT coefficients for the test fBm profiles.....	111
Figure 3.9	Analysis of a cracked concrete profile .....	114
Figure 3.10	Smoothing of a pulse oximeter signal .....	115
Figure 3.11	Smoothing of a pulse oximeter signal where the blood flow has been stopped. ....	116
Figure 3.12	Examples of two pre-shock ECG heart signals.....	117
Figure 3.13	Energy in ECG signals during ventricular fibrillation (VF) .....	118

## Chapter 4

Figure 4.1	Experimental flume .....	154
Figure 4.2	Schematic evaluation and typical cross section of the flume.....	155
Figure 4.3	Close view of the laser displacement sensor used to scan the topography of the sediment surfaces .....	156
Figure 4.4	Linear interpolation replacing the drop-out values in the data.....	157
Figure 4.5	Removal of drop-out points using linear interpolation .....	158
Figure 4.6	Line and row interpolation of drop-out points .....	159
Figure 4.7	Estimating new values using barycentric co-ordinates .....	160
Figure 4.8	Interpolation using triangulation of the sediment surface to estimate new values for the drop-out points.....	161
Figure 4.9	Interpolation using triangulation to estimate new values replacing the drop-out points .....	162
Figure 4.10	Compensating for missing right corner in the modified sediment data ...	163
Figure 4.11	Examples of experimental sediment surface data-sets .....	164
Figure 4.12	Decomposition of sediment surface into wavelet details .....	166
Figure 4.13	River-bed sediment surface separated into different topographies .....	167
Figure 4.14	Fractional Brownian motion ( <i>fBm</i> ) test surfaces .....	168
Figure 4.15	Energy distribution of <i>fBm</i> surfaces .....	169
Figure 4.16	Energy distribution of a <i>fBm</i> surface compared to a sediment bed-surface .....	170
Figure 4.17	Performing a 3 level decomposition using the 2-D DWT on a synthetic <i>fBm</i> surface.....	171
Figure 4.18	Schematic diagram of modifying of the 2-D wavelet component details for edge effect coefficients.....	172
Figure 4.19	The DWT decomposition details of a sediment surface data-set .....	173
Figure 4.20	Form size distribution ( <i>fsd</i> ) established using the DWT method.....	175
Figure 4.21	The SWT decomposition details of a sediment surface data-set.....	192
Figure 4.22	Form size distribution ( <i>fsd</i> ) established using the SWT method .....	194
Figure 4.23	Groups of smaller particles can form a larger feature.....	211
Figure 4.24	River flow over two different sediment surface typographies .....	211
Figure 4.25	Results from synthetic surfaces analysis, DWT .....	212
Figure 4.26	Results from synthetic surfaces analysis, SWT .....	214
Figure 4.27	Form size distribution of synthetic surfaces, mixture 2mm and 3mm grains .....	216

## Chapter 5

Figure 5.1	Examples of synthetic background surfaces .....	258
Figure 5.2	Examples of the four different features shapes .....	259
Figure 5.3	Examples of different features sizes.....	260
Figure 5.4	Original surface and surface with synthetic diamond feature added .....	261
Figure 5.5	Reconstruction of details hard thresholded at $1.5\sigma$ at scales 1 to 4 .....	261
Figure 5.6	Synthetic diamond feature extraction through wavelet thresholding.....	262
Figure 5.7	Masks used to establish the amount of energy in surface and the diamond regions respectively.....	263
Figure 5.8	Plot of entropy for different surface features (hard threshold).....	264
Figure 5.9	Plot of entropy for different surface features (soft threshold).....	265
Figure 5.10	Reconstruction of a hard thresholded surface .....	266
Figure 5.11	Reconstruction of a soft thresholded surface .....	270

Figure 5.12	Dividing the coefficients of a profile into two parts .....	274
Figure 5.13	Separation of surface into two areas .....	275
Figure 5.14	Entropy measure through the thresholding process, underlying surface of grain size 2mm .....	276
Figure 5.15	Entropy measure through the thresholding process, underlying surface of grain size 3mm .....	277
Figure 5.16	Entropy measure through the thresholding process, underlying surface of mixture of grain sizes 2mm and 3mm.....	278
Figure 5.17	Examples of two synthetically generated test surfaces .....	279
Figure 5.18	Present the difference between not adding the approximation and adding the approximation in the reconstruction.....	280
Figure 5.19	The difference between zero and the reconstructed background surface will be picked up as information.....	280
Figure 5.20	Entropy values against hard threshold when the approximation at the largest scale has been excluded from the reconstruction .....	281
Figure 5.21	Entropy against hard threshold for the reconstructed surface with a flat background surface .....	281
Figure 5.22	Hard thresholded and reconstructed surface for different threshold values .....	284
Figure 5.23	Soft threshold, entropy for the reconstructed flat background surface .....	285
Figure 5.24	Hard threshold, entropy for the reconstructed background surface generated from a uniformly distributing .....	285
Figure 5.25	Example of hard thresholding and reconstruction of test surface .....	286
Figure 5.26	Entropy for the reconstructed soft thresholded background surface generated from a uniformly distributing .....	287
Figure 5.27	Example of soft thresholding and reconstruction of test surface .....	288
Figure 5.28	Measuring the entropy in the thresholded and reconstructed test surface .....	289
Figure 5.29	Reconstruction of sediment surface, threshold $2.5 \times \sigma$ and $3.0 \times \sigma$ . .....	290
Figure 5.30	Thresholding of experimental rived-bed sediment surface .....	291
Figure 5.31	Enhancement of possible coherent structure .....	292
Figure 5.32	Thresholding of experimental sediment surface, 2631h00m .....	293
Figure 5.33	Thresholding of experimental sediment surface, 2648h15m .....	294
Figure 5.34	Applying scale dependent thresholding to the sediment data .....	295
Figure 5.35	Reconstruction combining amplitude and scale threshold.....	296
Figure 5.35	Applying amplitude thresholding (experiment 7). .....	297
Figure 5.36	Applying scale dependent thresholding (experiment 7).....	298

## NOMENCLATURE

### Letters

$A$	area
$C_g$	admissibility constant
$E$	total energy
$F_D$	drag force
$F_L$	lift force
$H$	Hurst exponent
$K_f$	fractional diffusion coefficient
$L$	length
$M$	largest scale index
$N$	total number of points
$N_F$	wavelet filter length
$P$	wetted perimeter
$P_F$	Fourier power spectrum
$P_w$	wavelet power spectrum
$Q$	flow rate
$R$	hydraulic radius
$Re$	Reynolds number
$S_{m,n}$	scaling coefficients
$S_0$	original data
$S(p)$	Shannon entropy
$T$	period of the wavelet
$T_i^{hard}$	hard threshold
$T_i^{soft}$	soft threshold
$T_{m,n}^{scale}$	scale threshold
$T_{m,n}$	detail coefficients
$T_m^H$	horizontal component detail
$T_m^V$	vertical component detail
$T_m^D$	diagonal component detail
$W^p$	weight of a particle
$W_i$	vector with wavelet coefficients
$W_{i,j}$	2-D detail components
$a$	1) dilation parameter, measure of the width of the wavelet 2) amplitude
$b$	location parameter
$b_k$	reconfigured coefficients
$c_k$	scaling coefficient
$d$	1) detail component 2) surface roughness heights
$f$	frequency
$i$	row
$j$	column
$k$	moment
$l$	characteristic length
$m$	scale index
$n$	1) translation index 2) Manning's $n$
$p_i$	normalised energy of coefficients probability of occurrence

$t$	time
$u$	velocity

Greek symbols

$\Sigma$	sum
$\Phi(t_1, t_2)$	2-D scaling function
$\Psi^D(t_1, t_2)$	2-D diagonal wavelet function
$\Psi^H(t_1, t_2)$	2-D horizontal wavelet function
$\Psi^V(t_1, t_2)$	2-D vertical wavelet function
$\lambda$	threshold value
$\lambda_U$	universal threshold
$\sigma$	standard deviation
$\psi$	wavelet function, mother wavelet or analysing wavelet.
$\rho$	fluid density
$\mu$	dynamic viscosity
$\nu$	kinematic viscosity
$\phi$	scaling function, father wavelet
$\tau_0$	shear stress
$\theta$	channel slope

Acronyms

1-D	one-dimensional
2-D	two-dimensional
CWT	continuous wavelet transform
DWT	discrete wavelet transform
FT	Fourier transform
MAD	medium of absolute deviation of the wavelet coefficients
SWT	stationary wavelet transform.
WFT	windowed Fourier transform
WT	wavelet transform
$fBm$	fractional Brownian motion
$fsd$	form size distribution
$psd$	particle size distribution
$vb$	variable bandwidth

# **Chapter 1**

## **Introduction**

- 1.1 Wavelet analysis and the characterisation of river bed surfaces**
- 1.2 Scope of investigation**
- 1.3 Outline of thesis**

# CHAPTER 1

## INTRODUCTION

### **1.1. Wavelet analysis and the characterisation of river bed surfaces**

The wavelet transform (WT) was introduced in the early 1980's as a new signal processing technique (Goupillaud et al, 1984; Grossmann et al, 1984). Since then it has emerged to become a powerful analysing tool for the physical sciences. Over the past 15 years it has become increasingly widespread in its use and now covers many areas in both science and engineering. The WT has been found to be particularly useful for analysing signals which can best be described as noisy, discontinuous, transient and so on. Its ability to examine the signal simultaneously in both time and frequency in a distinctly different way to the traditional Fourier Transform (FT) has led to the generation of a number of new wavelet-based methods for signal analysis. Wavelet transform analysis has recently been applied as an analysis tool in a range of diverse areas including: crack surface characterisation, monitoring of crack propagation, climate analysis, financial indices, seismic signal denoising, heart monitoring, characterisation of turbulent intermittency, condition monitoring of rotating machinery, detection of air pressure changes, denoising of astronomical images, video image compression, compression of medical signal records, and so on (Addison, 2002). There is now an abundance of literature concerning the wavelet transform and its many applications.



The knowledge of sediment transport in open-channel flow is vital to river engineers. Most open channels have a constantly changing river bed-surface. Erosion and sediment transport are therefore common concerns. When a gravel surface is subjected to flood flow the topography of the bed-surface will change due to the movement and re-arrangement of the surface particles. This in turn affects the flow resistance in the channel, causing separation and re-circulation that influences the overall flow regime of the river. As the turbulence characteristics change which is likely to affect the rate of erosion of the bed-surface. It is therefore important to be able to characterise the bed-surface topography during and after the sedimentation process.

Recently, wavelet analysis has been employed in a variety of surface analysis tasks including the characterization of orthopedic joint prostheses (Jiang et al, 1999), fractional Brownian motions surfaces and cracked concrete surfaces (Dougan et al, 2000), pitting corrosions (Frantziskonis et al, 2000) and surface roughness of silicon (Moktadir and Sato, 2000), general surface roughness analysis (Lee et al, 1998) and the evaluation of engineering surfaces (Xiong et al, 2001). Motivated by this research concerning the application of the wavelet transform as a surface characterisation tool in such diverse fields, the author has investigated the utility of the wavelet transform in analysing experimental river-bed sediment surfaces data.

The project detailed herein concentrates on sediment surfaces characterisation using both the discrete wavelet transform (DWT) and the stationary wavelet transform (SWT). The study includes both real and synthetic surface data. The rest of this chapter introduces the aims and objectives underlying this thesis together with a brief summary of the content of subsequent chapters.

## **1.2. Scope of investigation**

The work detailed in this thesis has the following aims:

1. to characterise the topographical structural behaviour of experimental river-bed sediment surfaces over time using wavelet transform-based tools,
2. to separate bed form features within river bed sediment surfaces using the wavelet thresholding technique.

The aims were achieved through the following objectives:

1. to undertake a literature review to appraise current applications of the wavelet transform as a method for surface analysis,
2. to develop computer algorithms for overall characterisation of the sediment surface data,
3. to develop computer algorithms for the enhancement of local surface features in the data,
4. to apply the developed algorithms to analyse both synthetic and experimental sediment surfaces data.

### **1.3. Outline of thesis**

The remainder of this thesis is structured as follows:

Chapter 2 presents an introduction to the wavelet transform focusing on the mathematics of the discrete and stationary wavelet transforms. Wavelet transform tools and their applications are then discussed; specifically relating to the use of the wavelet transform in surface analysis. In addition, the chapter provides a general overview of sediment transport and the creation of coherent structures on sediment bed surfaces.

Chapter 3 describes the results of initial studies using the 1-dimensional wavelet transform as an analysis tool for the *characterisation of profile data*: both synthetic and real profile data were included in the analysis. In addition, the chapter also includes preliminary results from the analysis of medical data using the discrete wavelet transform.

Chapter 4 details work using a two-dimensional wavelet transform for *global surface characterisation*. The main work detailed in this chapter concerns the analysis of experimental river-bed sediment surface data. A new technique to characterise sediment surface data is introduced and its implementation as a computer algorithm is described.

Chapter 5 presents two-dimensional wavelet transform methods for the *identification of local surface features*. This study was carried out on computer generated synthetic test data and employed wavelet thresholding techniques to separate larger structures from the background surface topography.

Chapter 6 provides a summary of the conclusions presented throughout the thesis with recommendations for future research.

## Chapter 2

### Literature review

- 2.1 Introduction and background**
- 2.2 The history of wavelets**
- 2.3 Other methods for data analysis**
- 2.4 The continuous wavelet transform (CWT)**
  - 2.4.1 Introduction**
  - 2.4.2 The wavelet function**
  - 2.4.2 The signal energy (CWT)**
  - 2.4.4 The inverse continuous wavelet transform**
- 2.5 The discrete wavelet transform (DWT)**
  - 2.5.1 Introduction**
  - 2.5.2 Orthogonal wavelet bases**
  - 2.5.3 Dyadic grid scaling**
  - 2.5.4 The scaling function**
  - 2.5.5 Multiresolution**
  - 2.5.6 The Haar wavelet**
  - 2.5.7 Wavelet energy and wavelet statistics**
- 2.6 The stationary wavelet transform (SWT)**
  - 2.6.1 Introduction**
  - 2.6.2 Definition**
- 2.7 The two-dimensional wavelet transform**
  - 2.7.1 The 2-D wavelet transform energy**
- 2.8 Choice of wavelet bases**
  - 2.8.1 Introduction**
  - 2.8.2 Continuous or discrete transform**
  - 2.8.3 Analysing wavelet**
    - 2.8.3.1 General properties**
    - 2.8.3.2 Analysing wavelet similarity to test data**
    - 2.8.3.3 Vanishing moment**
    - 2.8.3.4 Selectivity in frequency**

- 2.8.4 Wavelet mode
- 2.9 Wavelet tools
  - 2.9.1 Introduction
  - 2.9.2 Smoothing
  - 2.9.3 Denoising
    - 2.9.3.1 Denoising by hard or soft thresholding
    - 2.9.3.2 Threshold value
    - 2.9.3.3 Data analysis using amplitude thresholding
- 2.10 Application of the wavelet transform to the analysis of rough surfaces
  - 2.10.1 Introduction
  - 2.10.2 Engineering surface analysis
- 2.11 Sediment transportation
  - 2.11.1 Introduction
  - 2.11.2 River hydraulics
    - 2.11.2.1 Fluid dynamics
    - 2.11.2.2 Sediment motion
  - 2.11.3 Bed armouring and cluster formation
  - 2.11.4 Surface bed layer composition (sampling techniques)
- 2.12 Chapter summary

# CHAPTER 2

## LITERATURE REVIEW

### 2.1. Introduction and background

According to Kim et al (2000) a wavelet is a small wave of short duration with finite energy, which integrates to zero. The wavelet transform (WT) is a mathematical tool to cut data, functions or operators into different frequency (or scale) components (Daubechies, 1992). Each frequency component may then be studied at its resolution. In this aspect the WT works in the same way as the Fourier transform, which extracts frequency content of a signal. However, the Fourier transform loses all the information about the time location of particular frequencies within the signal, whereas the WT is able to retain time location information of specific frequencies within a signal. This is achieved by moving the wavelet function to different locations and by stretching and squeezing it to different 'widths' along the signal. When analysing a signal with a narrow wavelet the high frequency components (usually noise) are sorted out from the signal. While a wider wavelet captures the low frequencies components (overall form) of the signal. This property allows for location of features in time (or space), which is the main advantage of the wavelet transform over other conventional techniques. In this chapter the wavelet transform method is reviewed with focus on the discrete wavelet transform (DWT) and the stationary wavelet transform (SWT) which are the methods the author has used in the analysis.

The chapter begins with section 2.2 where a short history of the wavelet transform is presented, followed by section 2.3 which describes alternative data analysis methods. The next two sections present the two main classes of wavelet transform: section 2.4 concerns the continuous wavelet transform (CWT) and section 2.5 the discrete wavelet transform (DWT). Thereafter follows a brief introduction of the redundant DWT, the stationary wavelet transform (SWT), in section 2.6. The two-dimensional wavelet transform is introduced in section 2.7. Section 2.8 discusses the choice of wavelet bases. Section 2.9 presents the application of the WT as a thresholding tool and section 2.10 presents the use of the wavelet transform in surface analysis. In section 2.11 a brief introduction to sediment transport and sediment surface sampling and analysis techniques are presented. Finally a summary of the findings of this chapter are given in section 2.12.

## **2.2. The history of wavelets**

The mathematical theory of wavelets can be traced all the way back to Joseph Fourier and his theories of frequency analysis at the beginning of the 19<sup>th</sup> century, (Alsberg et al, 1997). A century later Alfred Haar wrote a paper where he constructed the Haar wavelet (Haar, 1910). However, it was not until the 1980's that a general understanding of the wavelet concept was provided (Williams and Amaratunga, 1994). Strömberg (1982) introduced the first orthogonal wavelet at the beginning of the 1980's. Independently from Strömbergs' work, Lemarié and Meyer (1986) also constructed a new orthogonal wavelet expansion. Studies of the wavelet transform in its continuous form were undertaken by Grossmann and Morlet (1984, 1985). The most noticeable work in this field was carried out by Mallat (1989b, 1989c) and Meyer (1990) in the late 1980's. Coming from different directions Mallat (who was working with signal processing) and Meyer (a pure mathematician) created multiresolution theory. As a result of their work the fast wavelet transform and a mathematical theory of orthogonal wavelets were formed (Hubbard, 1996). Their work led to the construction of a set of wavelet orthogonal basis functions by Ingrid Daubechies, (Daubechies, 1988), which now is regarded as a cornerstone in wavelet theory.

Due to the good time-frequency localisation property of the wavelet transform (WT), fast algorithms and a simple form of analysis, it has proved to be a very useful (and

popular) analysing tool, (Ogden, 1997). Today the WT is found in a range of different areas in both science and engineering. In the late 1980's perhaps the most common use of wavelets were in the area of electrical and computational engineering. Particularly as a signal processing tool, where the WT have been used to extract the 'real' signal components from noisy data sets, i.e. denoising (Wickerhauser, 1994).

The application of the WT as a practical analysis tool for engineering data took off at the beginning of the 1990s. Background papers introducing the wavelet transform in engineering analysis include Williams and Amaratunga (1994), Lau and Weng (1995) and Torrence and Compo (1997). Over the past decade there has been an explosion in the quantity of research undertaken and the number of papers produced each year.

### **2.3. Other methods for data analysis**

A data series is a collection of observations made sequentially in space. Examples occur in a variety of fields, ranging from economics to engineering, and methods of analysing data series constitute an important area in statistics. A data series is said to be continuous when observations are made continuously in space. The term continuous is used for series of this type even when the measured variable can only take a discrete set of values. A data series is said to be discrete when observations are taken only at specific times, usually equally spaced. The term discrete is used for series of this type even when the measured variable is a continuous variable.

A signal can be represented in different ways but the most important ones are the time (or space for a spatial signal) and the frequency representations. The frequency content of a signal can be revealed by transforming the signal from its time domain to its frequency domain. A number of frequency methods to transform data are available.

One of the most prominent signal representation schemes is the *Fourier transform* (FT), which breaks a function up into its component frequencies. This frequency method transforms the data using smooth harmonic modes (sines and cosines), finding the instantaneous frequencies of the data. The Fourier transform finds the frequency content within a data but loses information about the location of specific frequencies (Mallat, 1999; Hubbard, 1996).



To overcome this, the *windowed Fourier transform* (WFT) was introduced which provides a degree of location of the time-frequency content of the data. The signal is studied segment by segment, where a window (which remains fixed in size through the transform) determines the size of the segment to be analysed. Once the frequency content of the analysed segment is determined the window slides along the data. The window allows for better detection of sudden changes in the data. However, due to its fixed window width signal components of duration longer than the window length are not picked up and those significantly smaller than the window length are lost due to averaging across the window.

Another common frequency analysis method is the quadric time-frequency method. The method transforms the data by comparing the data with itself. This avoids any loss of time-frequency resolution. The quadric time-frequency decomposition therefore possesses excellent time-frequency resolution and turns out to be ideal for the analysis of simple, monochromatic signals. However, these methods contain cross terms which makes analysis difficult for more complex signals. Examples of quadric time-frequency methods are *Wigner-Ville distribution* and *Cohen's class distribution*, (Mallat, 1999).

The above methods are good for analysing symmetric signals, however, they are unsuitable for studying data which contains localised or transient features. The wavelet transform, however, transforms a signal into time-frequency representation which reveals both the frequency content and the exact location of a specific frequency in the data.

The following section introduces the wavelet transform in more detail.

## **2.4. The continuous wavelet transform (CWT)**

### **2.4.1. Introduction**

This section introduces the basic theory for the continuous wavelet transform (CWT).

### 2.4.2. The wavelet function

A wavelet is, as the name suggests, a small wave or pulse that can be compressed and stretched to different scales over the length of the analysed data. The main advantage of wavelets are their varying window size: wide for low frequencies and narrow for high frequencies. This leads to an optimal time-frequency correlation in all frequency ranges. The basic wavelet function  $\psi(t)$  is known as the *mother wavelet*. This function should satisfy the condition:

$$\int_{-\infty}^{\infty} \psi(t) dt = 0 \quad (2.1)$$

A family of wavelets are generated by dilating the function using the scaling parameter  $a$  and translating it using the location parameter  $b$ . Thus the wavelet function can be rewritten as:

$$\psi_{(a,b)}(t) = \frac{1}{\sqrt{a}} \psi\left(\frac{t-b}{a}\right) \quad (2.2)$$

A large value of  $a$  stretches the function and allows analysis of low-frequency components while a small value of  $a$  squeezes the function and makes it possible to analyse high frequency components.

For a continuous signal  $x(t)$  the continuous wavelet transform is defined as:

$$T(a,b) = \int_{-\infty}^{\infty} \psi_{(a,b)}(t) x(t) dt \quad (2.3)$$

which, using equation 2.2, can be rewritten as:

$$T(a,b) = \int_{-\infty}^{\infty} \frac{1}{\sqrt{a}} \psi\left(\frac{t-b}{a}\right) x(t) dt \quad (2.4)$$

The signal  $x(t)$  may be any signal, e.g. an electrical, medical or mechanical signal. A wavelet must have finite energy, i.e. it must satisfy the following condition:

$$E = \int_{-\infty}^{\infty} |\psi(t)|^2 dt < \infty \quad (2.5)$$

If the Fourier transform of  $\psi(t)$  is defined as:

$$\hat{\psi}(f) = \int_{-\infty}^{\infty} \psi(t) e^{-i(2\pi f)t} dt \quad (2.6)$$

the wavelet function must satisfy the admissibility condition which is expressed as:

$$C_g = \int_{-\infty}^{\infty} \frac{|\hat{\psi}(f)|^2}{f} df < \infty \quad (2.7)$$

$C_g$  is known as the admissibility constant and its value depends on the wavelet chosen for the analysis. Wavelets which satisfy the condition in equation 2.7 are bandpass filters, hence only frequencies within a finite range are let through the filter.

### 2.4.3. The signal energy (CWT)

The energy of a signal  $x(t)$  is defined as the integral of squared signal components:

$$E = \int_{-\infty}^{\infty} |x(t)|^2 dt = \|x(t)\|^2 \quad (2.8)$$

where  $E$  is the total energy for the signal. Energy can also be defined in terms of the wavelet transform of the signal:

$$E = \frac{1}{C_g} \int_{-\infty}^{\infty} \int_0^{\infty} |T(a,b)|^2 \frac{da}{a^2} db \quad (2.9)$$

### 2.4.4. The inverse continuous wavelet transform

The inverse wavelet transform is defined as:

$$x(t) = \frac{1}{C_g} \int_{-\infty}^{\infty} \int_0^{\infty} T(a,b) \psi_{(a,b)}(t) \frac{dadb}{a^2} \quad (2.10)$$

This allows the original signal to be reconstructed from its wavelet transform, which is useful in the denoising and compression of data.

The CWT has proved to be very useful in data analysis in diverse fields in both science and engineering e.g. oceanography and meteorology (Meyers et al, 1993 and Liu, 2000),

engineering flow (Boniforti et al, 1997; Hajj et al, 1998; Addison, 1999), other engineering applications have been in non-destructive testing (Addison et al, 1997; Addison and Watson, 1997) and mechanical vibration (Hale and Adhami, 1998; Pislaru et al, 2003). The CWT is also widely used in the analysis of biosignals e.g. electrocardiogram (ECG) signals (Watson et al, 1999b; Addison et al, 2000), EEG signals (Schiff et al, 1994) and blood pressure (Bracic and Stefanovska, 1998).

This concludes a brief introduction to the CWT. The reader requiring more information of the CWT is referred to literature by, for example, Daubechies (1992), Bergh et al (1999) and Addison (2002).

## **2.5. The discrete wavelet transform (DWT)**

### **2.5.1. Introduction**

The continuous wavelet transform is a redundant transform, consequently computing overheads are high. The discrete wavelet transform (DWT) was developed, in part, to combat this. The DWT is constructed by choosing discrete values for the scaling parameter,  $a$ , and the location parameter,  $b$ . This provides for a fast computation of the transform and its inverse without redundancies.

### **2.5.2. Orthogonal wavelet bases**

The values of the scaling and translation parameters,  $a$  and  $b$  are usually determined from a logarithmic discretisation of the  $a$  scale. This is linked to the size of the steps between the  $b$  locations, where  $a$  is chosen greater than 1 and  $b$  has to be greater than 0. The wavelet's dilation and translation is controlled by integer indices  $m$  and  $n$  respectively, e.g.  $a = a_0^m$  and  $b = nb_0 a_0^m$ . Applying this discretisation to the continuous wavelet transform of equation 2.4 we get the DWT, written as:

$$T_{m,n} = \int_{-\infty}^{\infty} \frac{1}{a_0^{m/2}} \psi(a_0^{-m}t - nb_0) x(t) dt \quad (2.11)$$

The values of  $T_{m,n}$ , known as the wavelet coefficients, are located on a grid with indices  $m,n$ . The wavelet coefficient provides a measure of how well the wavelet (at scale index

$m$  and location index  $n$ ) fits locally (correlates) with the analysed signal. When the wavelet fits well with the signal the wavelet coefficient has a large positive value.

### 2.5.3. Dyadic grid scaling

For special choices of  $a_0$  and  $b_0$ ,  $\psi_{a,b}$  will constitute an orthonormal basis. For example an orthonormal basis can be constructed using  $a_0 = 2$  and  $b_0 = 1$ . For these values, equation 2.11 becomes:

$$T_{m,n} = \int_{-\infty}^{\infty} \frac{1}{2^{m/2}} \psi(2^{-m}t - n)x(t)dt \quad (2.12)$$

This choice of dilation and translation steps using integer powers of two is known as the dyadic grid arrangement. This is the simplest grid and it allows for the construction of an orthonormal wavelet basis. Where each wavelet is orthogonal to all others and is also normalised to have unit energy. In this case, all the information for the signal is stored in the wavelet coefficients without redundancy.

The wavelet coefficients are usually stored in a vector  $W_i$ ,  $i=0\dots N-1$ , where  $i = 2^{M-m} + n$  is the index of the wavelet coefficients and  $W_0$  is related to the signal mean. As an example, figure 2.1(a) shows a fractional Brownian motion (*fBm*) test signal and figure 2.1(b) the corresponding wavelet transform coefficients. It is clearly visible that the number of coefficients change with scale.

### 2.5.4. The scaling function

Associated with the orthonormal wavelet is the scaling function  $\phi(t)$  (or the father wavelet), which is defined as:

$$\phi_{m,n}(t) = 2^{-m/2} \phi(2^{-m}t - n) \quad (2.13)$$

Preferably the scaling function should have compact support, which means that it is zero outside a limited interval. Further we want the scaling function to have the following property:

$$\int_{-\infty}^{\infty} \phi(t) dt = 1 \quad (2.14)$$

The scaling function is used to smooth a signal by separating the approximations ( $S$ ), (the low frequency components) from the details ( $d$ ), (the high frequency components). Figure 2.2 shows a selection of wavelet functions with their associated scaling functions from the Daubechies family of wavelets. The approximation coefficients ( $S_{m,n}$ ) are found from a signal  $x(t)$  using the scaling function as follows:

$$S_{m,n} = \int_{-\infty}^{\infty} x(t) \phi_{m,n}(t) dt \quad (2.15)$$

The scaling function is set to a range of widths to generate the approximation coefficients at each scale. The approximation coefficients at a specific scale  $m$  are known collectively as the discrete approximation of the signal at that scale. It is possible to produce a continuous approximation of the signal at scale  $m$  as follows:

$$x_m(t) = \sum_{n=-\infty}^{\infty} S_{m,n} \phi_{m,n}(t) \quad (2.16)$$

where  $x_m(t)$  is the smooth version of the signal at scale  $m$ . The approximation is generated by placing a sequence of the scaling functions side by side. The approximation approaches the original signal as the scale decreases. The signal  $x(t)$  may be recovered by combining the approximation coefficients with the detail (wavelet) coefficients as follows:

$$x(t) = \sum_{n=-\infty}^{\infty} S_{m_0,n} \phi_{m_0,n}(t) + \sum_{m=-\infty}^{m_0} \sum_{n=-\infty}^{\infty} T_{m,n} \psi_{m,n}(t) \quad (2.17)$$

This equation shows that the signal  $x(t)$  is represented using the approximation at scale index  $m_0$  and the summation of the details at scales  $m_0$  to negative infinity. The signal detail at scale  $m$  can be rewritten as

$$d_m(t) = \sum_{n=-\infty}^{\infty} T_{m,n} \psi_{m,n}(t) \quad (2.18)$$

Using this expression, equation 2.17 can be rewritten as:

$$x(t) = x_{m_0}(t) + \sum_{m=-\infty}^{m_0} d_m(t) \quad (2.19)$$

Hence:

$$x_{m-1}(t) = x_m(t) + d_m(t) \quad (2.20)$$

This equation shows that if the approximation at scale index  $m$  is added to the detail at the same scale we get the signal representation at scale  $m-1$ , i.e. higher resolution. This is known as a multiresolution representation, described in more detail in the following section.

### 2.5.5. Multiresolution

The theory of multiresolution was developed by Mallat (1986) and Meyer (1986a, 1986b) and provided a framework for the construction of wavelets. The theory makes it possible to view a signal at different resolutions. The signal is studied at a coarse resolution to give the overall picture while the finer resolutions capture the details in the signal. For an orthogonal wavelet basis, the resolutions differ by a factor of two and the scaling function is used to go from one resolution to the next resolution.

It can be shown that approximation coefficients ( $S_{m,n}$ ) at scale ( $m$ ) can be used to generate both the approximation and the detail coefficients ( $T_{m,n}$ ) at the next scale using the formula:

$$S_{m+1,n} = \frac{1}{\sqrt{2}} \sum_k c_k S_{m,2n+k} = \frac{1}{\sqrt{2}} \sum_k c_{k-2n} S_{m,k} \quad (2.21)$$

for the approximation coefficients, where  $c_k$  is known as the scaling coefficient, and

$$T_{m+1,n} = \frac{1}{\sqrt{2}} \sum_k b_k S_{m,2n+k} = \frac{1}{\sqrt{2}} \sum_k b_{k-2n} S_{m,k} \quad (2.22)$$

for the detail coefficients, where  $b_k$  are the reconfigured coefficients. Equation 2.21 and equation 2.22 are known collectively as the multiresolution algorithm. These two equations can be used to generate the approximation and the detail coefficients at all scales. Equation 2.21 performs a lowpass filtering (letting through the low frequencies

in the signal) and equation 2.22 perform a highpass filtering (letting through the high frequencies in the signal).

The input signal is not continuous in practice but rather is sampled discretely. In practice the discrete input signal is set as  $S_{0,n}$  the approximation at scale  $m=0$ . From this  $S_{0,n}$  we can then use equation 2.21 and equation 2.22 to compute  $S_{m,n}$  and  $T_{m,n}$ , the approximation and the wavelet coefficients, at higher scales,  $m=1,2\dots M$ , where  $M$  is the scale index of the number of data points for the whole signal,  $N=2^M$ .

For a signal of finite length  $N$ , and  $N=2^M$ , the scales over which the signal can be analysed are in the range  $0 < m < M$ . The detail signal approximation for the signal  $N$  corresponding to the scale index  $m$  would be:

$$d_m(t) = \sum_{n=0}^{2^{M-m}-1} T_{m,n} \psi_{m,n}(t) \quad (2.23)$$

An approximation of the original signal at scale index 0 is generated by summing the details from scale 0 to  $M$  and adding the signal approximation at scale index  $M$ . The approximation of the signal at specific scale  $m$  consists of the approximations and the details of the signal at the lower scale, as shown in the equation:

$$x_m(t) = x_{m-1}(t) - d_m(t) \quad (2.24)$$

The difference between the approximations  $x_m(t)$  and  $x_{m-1}(t)$  is the detail component  $d_m(t)$ .

### 2.5.6. The Haar wavelet

A wavelet basis is orthogonal if each wavelet in the base is perpendicular to all the other wavelets in the base. The orthogonal wavelet transform is relatively easy to compute and the signal can be reconstructed perfectly using the scaled and translated wavelets. The simplest orthonormal wavelet basis is the Haar wavelet. The scaling coefficients for the Haar wavelet are  $c_0 = c_1 = 1$ , the scaling equation then becomes:

$$\phi(t) = \phi(2t) + \phi(2t-1) \quad (2.25)$$



where the scaling function is defined as:

$$\phi(t) = \begin{cases} 1 & 0 \leq t < 1 \\ 0 & \text{otherwise} \end{cases} \quad (2.26)$$

The corresponding wavelet function is defined in terms of its scaling function as:

$$\psi(t) = \phi(2t) - \phi(2t - 1) \quad (2.27)$$

from this the Haar wavelet is defined as:

$$\psi(t) = \begin{cases} 1 & 0 \leq t < \frac{1}{2} \\ -1 & \frac{1}{2} \leq t < 1 \\ 0 & \text{otherwise} \end{cases} \quad (2.28)$$

Using the wavelet function in equation 2.27 a Haar system of dyadic wavelets can be constructed.

The wavelet function and the scaling function associated with the Haar wavelet are shown in figure 2.2(a). The Haar wavelet transform only has two scaling coefficients  $c_0=c_1=1$  hence for equation 2.21 and equation 2.22 it can be seen that the approximation and the detail coefficients can be calculated through the equations:

$$S_{m+1,n} = \frac{1}{\sqrt{2}} [S_{m,2n} + S_{m,2n+1}] \quad (2.29)$$

for the approximation coefficients and

$$T_{m+1,n} = \frac{1}{\sqrt{2}} [S_{m,2n} - S_{m,2n+1}] \quad (2.30)$$

for the detail coefficients. To obtain the detail component  $d_m(t)$  of the signal the detail coefficients are simply multiplied by the wavelet at scale index  $m$  which, for the Haar wavelet, has an amplitude  $1/\sqrt{2^m}$ .

$$d_m(t) = \sum_{n=0}^{2^{M-m}-1} T_{m+1,n} \psi_{m,n}(t) \quad (2.31)$$

The signals approximation at the largest scale  $M$  is given by:

$$x_M(t) = S_{M,n} \phi_{M,n}(t) \quad (2.32)$$

The approximation of the signal at scale index  $m=0$  can be found by adding all the details together with the signal approximation at scale index  $M$ , i.e.

$$x_0(t) = x_M(t) + \sum_{m=1}^M d_m(t) \quad (2.33)$$

Using multiresolution analysis a signal can be transformed into details ( $d$ ), the high frequencies components, and approximations ( $S$ ), the low frequencies components.

Figure 2.3(a) shows a test waveform, the discrete sinusoid given by:

$$x_i = \sin\left(2\pi \frac{i}{128}\right) \quad (2.34)$$

A multiresolution decomposition was applied to this signal separating it into detail and approximation coefficients. At each scale, more and more information is stripped from the signal, finally ending up with a number of details and approximations for each scale. Figure 2.3(b) shows the details of the sinusoidal signal using the Haar wavelet. Figure 2.3(c) shows the associated approximations for the same signal. This shows the approximation tending towards the shape of the original signal as the resolution is increased towards the top of the figure.

### 2.5.7. Wavelet energy and wavelet statistics

After full decomposition of a signal is performed the energy (squared coefficient) contained within the wavelet coefficients at each scale  $m$  is given by:

$$E_m = \sum_{n=0}^{2^{M-m}-1} (T_{m,n})^2 \quad (2.35)$$

The total energy for the input signal is defined as:

$$E = \sum_{n=0}^{N-1} (S_{0,n})^2 \quad (2.36)$$

The sum of energies over all the scale indices and the energy in the approximation coefficient  $S_{M,0}$  gives the total energy i.e.:

$$E = \sum_{m=1}^M \sum_{n=0}^{2^{M-m}-1} (T_{m,n})^2 + (S_{M,0})^2 \quad (2.37)$$

The standard deviation, or the variance, ( $\sigma$ ) of the wavelet coefficients for each scale ( $m$ ) is defined as:

$$\sigma_m = \sqrt{\frac{\sum_{i=2^{M-m}}^{2^{M-m+1}-1} (T_{m,n})^2}{2^{M-m}}} \quad (2.38)$$

The variance is a useful property which may be related to the scaling laws exhibited by certain signals.

The discrete wavelet transform was introduced as a signal processing application in the early 1990's (Rioul and Vetterli, 1992). Since then it has found use in many different areas including: characterisation of engineering data (Simonsen et al, 1998), mechanical design (Tsai et al, 2000), damage detection (Wang and McFadden, 1995; Corbin et al, 2000; Lee and Tarng 2000), medical signal analysis (Thurner et al, 1998; Kalayci and Özdamar, 1995), geophysics (Moreau et al, 1995; Grubb and Walden, 1997; Fedorenko and Husebye, 1999), financial time series (Davidson et al, 1998; Shin and Han, 2000). One application where the DWT has proven to be particular useful is in data compression (Chen et al, 1993; Staszewski, 1998; Nygaard and Grue, 2000)

## 2.6. The stationary wavelet transform (SWT)

### 2.6.1. Introduction

As described earlier in this chapter the discrete wavelet transform (DWT) involves the translation of the wavelet along the signal in discrete dyadic steps, thus the analysis has limited resolution especially at larger scales. It is for this reason that the stationary wavelet transform (SWT) was introduced, where the wavelet translates along the signal continuously thus increasing the resolution of the analysis. The transform is known in the literature under a variety of names including: the *translation invariant*, *redundant*, *maximal overlap* and *non-decimated* wavelet transform.

### 2.6.2. Definition

The stationary wavelet transform (SWT) is a modified version of the basic discrete wavelet transform (DWT) algorithm. The idea is to ‘fill in the gaps’ caused by the discrete dyadic steps of the DWT. The wavelet scales remain as discrete steps, however, the wavelet translates continuously along the signal to be analysed. For practical implementation on discrete signals this corresponds to computing the transform at each time step. This increases the temporal resolution of the analysis. Similar to the DWT, two vectors of coefficients, the detail and the approximation, are produced at each scale. However, the SWT does not decimate the transform, therefore the resulting detail and approximation vectors have the same length as the original signal (i.e.  $N = 2^M$ ) at every scale (Nason and Silverman, 1995; Coifman and Donoho, 1995; Pesquet et al, 1996).

To constitute a SWT representation, the scale  $a$ , is sampled along a dyadic sequence  $a = 2^m$ . The translation parameter  $n$  is sampled at each time step. The SWT is defined as:

$$T_{m,n}^s = \int \frac{1}{\sqrt{2^m}} \psi\left(\frac{t-n}{2^m}\right) x(t) dt \quad (2.41)$$

The difference in resolution between the DWT and the SWT is shown in figure 2.4, where a typical signal has been decomposed into 8 levels. It can be seen that the DWT has a sampling rate which is too low to give a clear picture of signal whereas, due to its higher sampling rate, the SWT provide a much better representation of the signal.

In recent years the stationary wavelet transform has been applied in a number of different areas of data analysis.

Ngan et al (2000) applied the SWT to denoise medical data. The authors studied functional magnetic resonance imaging (fMRI), which is used to study brain functions. One difficulty in event-related fMRI data is the problem with the low signal-to-noise ratio (SNR) inherent in the data. Therefore filtering is generally applied to improve the SNR of the averaged data. To analyse the data using the SWT the authors applied a filter based on a cross-validation method, which has proven to give good estimations of the real signal component in simulated data contaminated with Gaussian white noise. The

normalised root mean square (NRMS) errors were found to be reduced by 35-38% due to the filtering. Subsequently the authors applied the filtering technique to real fMRI data and concluded that their filters were effective in improving the SNR of the raw data without oversmoothing.

Jung and Scharanski (2003) proposed a new method for image denoising and edge enhancement using the SWT. The authors wanted to retain edge-related coefficients while removing noise-related coefficients. They defined a shrinkage factor using a Gaussian distribution and found that the variance of the noise-related coefficients was smaller than the variance of the edge-related coefficients. The wavelet coefficients were assigned a probability of being either an edge or being noise. Compared to other denoising techniques they reported that their method produces both good quantitative and qualitative results.

Other studies applying the SWT for the noise reduction of data include those of Morris and Peravali (1999), Pan et al (1999), Berkner and Wells (2002) and Solbø and Eltoft (2002).

The SWT has also been used to characterise nonstationary behaviour of subtidal coastal sea level fluctuations by Percival and Mofjeld (1997). Their results indicated that the fluctuation in sea level was strongest during the winter (November to March) and occurred predominantly at scales of 4-16 days. The SWT provided a good basis for characterising these events. The authors concluded that a cycle statistical model of the fluctuations could be developed using SWT-based methods.

Lark and Webster (2001) used the SWT to analyse soil with non-stationary properties. The authors applied the transform to the measurement of pH and levels of clay and calcium carbonate on a 3km long transect in central England. The Daubechies wavelet was used in the analysis. By determining the changes in wavelet variance at each scale, places with significant difference in variance were identified. The result indicated that the SWT is useful in identifying the location of changes in soil properties very effectively.

## 2.7. The two-dimensional wavelet transform

For the analysis of two-dimensional (2-D) data, for example surfaces and images, 2-D wavelets are required. In figure 2.5 examples of 2-D wavelets from the Daubechies, Symmlet and Coiflet families of wavelets are shown.

The simplest way to construct a 2-D wavelet basis is by using three wavelet functions:

$$\Psi^H(t_1, t_2) = \phi(t_1)\psi(t_2) \quad (2.42a)$$

$$\Psi^V(t_1, t_2) = \psi(t_1)\phi(t_2) \quad (2.42b)$$

$$\Psi^D(t_1, t_2) = \psi(t_1)\psi(t_2) \quad (2.42c)$$

where  $H$ ,  $V$  and  $D$  stands for *horizontal*, *vertical* and *diagonal* respectively. The scaling function for the 2-D wavelet transform is defined as:

$$\Phi(t_1, t_2) = \phi(t_1)\phi(t_2) \quad (2.43)$$

Figure 2.6 show the wavelet functions and the scaling function for the 2-D Haar wavelet. When analysing 2-D data sets, horizontal edges are picked up by the horizontal ( $T_m^H$ ) component detail, the vertical edges by the vertical ( $T_m^V$ ) component detail and the diagonal edges by the diagonal ( $T_m^D$ ) component detail.

The two-dimensional multiresolution decomposition can be defined as:

$$S_{m+1, (n_1, n_2)} = \frac{1}{2} \sum_{k_1} \sum_{k_2} c_{k_1} c_{k_2} S_{m(2n_1+k_1, 2n_2+k_2)} \quad (2.44a)$$

$$T_{m+1, (n_1, n_2)}^H = \frac{1}{2} \sum_{k_1} \sum_{k_2} b_{k_1} c_{k_2} S_{m(2n_1+k_1, 2n_2+k_2)} \quad (2.44b)$$

$$T_{m+1, (n_1, n_2)}^V = \frac{1}{2} \sum_{k_1} \sum_{k_2} c_{k_1} b_{k_2} S_{m(2n_1+k_1, 2n_2+k_2)} \quad (2.44c)$$

$$T_{m+1,(n_1,n_2)}^D = \frac{1}{2} \sum_{k_1} \sum_{k_2} b_{k_1} b_{k_2} S_{m(2n_1+k_1, 2n_2+k_2)} \quad (2.44d)$$

For a data set ( $S_0$ ) with the original size  $N \cdot N$  at scale index 1, the next scale index 2 will consist of  $\frac{N}{2} \cdot \frac{N}{2}$  coefficients. The next scale index after that will contain  $\frac{N}{4} \cdot \frac{N}{4}$  coefficients of the original data set and so on. Figure 2.7 show a schematic of a 2-D data set  $S_0$  decomposed twice. Of course the decomposition can be performed further where each subsequent decomposition will contain one-quarter of the number of coefficients of the previous scale (Daubechies, 1992).

### 2.7.1. The 2-D wavelet transform energy

The energy of the 2-D data set and its transform is defined as:

$$E = \sum_{i=0}^{2^M-1} \sum_{j=0}^{2^M-1} (S_{0,i,j})^2 = \sum_{i=0}^{2^M-1} \sum_{j=0}^{2^M-1} (W_{i,j}^{(m)})^2 \quad (2.45)$$

where  $S_{0,i,j}$  and  $W_{i,j}^{(m)}$  are the elements of the input data and the wavelet decomposition matrices located on row  $i$  and column  $j$ . The energy in the original surface is equal to the energy in the transform.

The 2-D wavelet transform has been applied in a number of diverse areas including: simulated grain growth (Frantziskonis and Deymier, 2000a, 2000b), surfaces of orthopaedic joints (Jiang et al, 1999), mammographic images (Ferreia and Borges, 2003), magnetic resonance images (Xu et al, 1994; Wang and Huang, 1996), cosmic microwave background maps (Sanz et al, 1999a, 1999b) and texture classification (Li et al, 2003).

## **2.8. Choice of wavelet bases**

### **2.8.1. Introduction**

In general there are two choices to be made to determine which wavelet to apply in a particular analysis. The system of representation (e.g. continuous or discrete transform) and the properties of the wavelet base (i.e. the mother wavelet) itself, (Hubbard, 1996).

### **2.8.2. Continuous or discrete transform?**

As discussed previously, the two main classes of wavelet transforms are the continuous wavelet transform (CWT) and the discrete wavelet transform (DWT). Which one to choose depends primarily on the nature of the data to be analysed and the requirements of the analysis.

Because of the dyadic grid structure of the DWT no redundant information is generated in the transform and the multiresolution ensures perfect reconstruction, consequently this has a fast transform and less computer power is needed for the analysis. The CWT has superior resolution in both scale and location compared to the DWT, however it requires a much more computer intensive process. The increased computational expense of the CWT is due to the overlapping of the continuous wavelets, so most information encoded by one is also encoded by its neighbours. Murray (2000) compared the ability for the CWT and the DWT to construct a turbulent velocity signal from the inverse wavelet coefficient (see figure 2.8). The reconstruction of the data for the DWT shows that the signal was reconstructed without any loss of information. Whereas reconstruction for the CWT resulted in poorer representation of the signal. However, this is almost certainly due to the edge effects and frequency ranges used in the CWT. These are automatically taken care of by the DWT multiresolution algorithm. For further discussion on the subject the reader is referred to Teit and Kritikos (1992), who discusses the disadvantage and benefits of reconstructing signals using both the CWT and the DWT.

Due to the highly efficient algorithm used by the DWT to calculate the wavelet coefficients this transform is exclusively used in image processing which in general is a



computer intensive process. For image (or surface) analysis the DWT simply outperforms the CWT where the redundancy of the CWT makes it practically unusable.

### **2.8.3. Analysing wavelet**

There are no simple rules for the selection of the mother (or analysing) wavelet to use for a specific analysis task. There is a wide range of wavelet bases available e.g. Mexican hat, Morlet, Daubechies, Coiflet, Symmlet and many more. The most commonly applied mother wavelets for the CWT are the Mexican hat and Morlet wavelets. For the orthogonal DWT the Daubechies, Coiflet and Symmlet families of wavelets and the biorthogonal bases Biorthogonal Spline wavelets are commonly used. Biorthogonal wavelets have proven to be particularly useful in image compression. In fact a Biorthogonal wavelet is used by the Federal Bureau of Investigation (FBI) as the standard for compression of fingerprint images (Brislawn, 1995). For a more detailed description of the different wavelet bases available the reader is referred to the literature by Daubechies (1992) and Mallat (1999).

Research by Katul and Vidakovic (1996) showed that the choice of wavelet basis has, in general, only a minor influence on the results. Similarly Simonsen et al (1998) stated that the choice of wavelet is not crucial in any way. Moktadir and Sato (2000) investigated 4 different mother wavelets for the analysis of silicon surfaces. The authors found that the result from the analysis did not depend on the choice of wavelet. Hubbard (1996) suggested that 'one should spend more time on the actual analysis rather than the finding the 'ideal' wavelet for the analysis'. Tsai and Hsiao (2001) also concluded that the choice of the wavelet bases had only a small effect when they applied wavelets to detect abnormalities in structural textures. However the authors did conclude that in general orthogonal wavelets outperform biorthogonal wavelets. In addition, they stated that orthogonal wavelets with longer support provided poor detection of abnormalities within a surface as these wavelets oversmooth local anomalies. In addition, wavelets with compact support are more computer efficient which is an important feature in image and surface analysis as these are computer intensive processes.

From the above it can be seen that choosing an 'ideal' wavelet bases to use for a specific analysis is obviously not an easy task. However the following number of points

should be considered when choosing the mother wavelet: general properties of the wavelet function, the mother wavelets similarity to the test data, the number of vanishing moments and selectivity in frequency.

### 2.8.3.1. General properties

The scale decomposition of a signal should be obtained from the dilation and translation of only one mother wavelet. These wavelets should be mutually similar, namely scale covariant with each other, in particular they should have a constant number of oscillations. In addition the mother wavelet should be admissible (equation 2.7), i.e. the function's mean should be equal to zero. Finally, the mother wavelet should be invertible, that is, there should exist at least one reconstruction formula for recovering the signal from the wavelet coefficients and for allowing the computation of energy.

### 2.8.3.2. Analysing wavelet similarity to test data

Some investigations have shown that the results of the wavelet transform can be dependent on the similarity of the analysing wavelet to the test data (Grossmann et al, 1987; Qiu et al, 1995). The analysing wavelet should therefore be chosen in accordance with the structure of the test data. Interestingly, because of a lack of suitable wavelet bases available Qui et al (1995) used prominent features of the time series as the analysing function.

### 2.8.3.3. Vanishing moment

The vanishing moment determines '*what the wavelet cannot see*'. A wavelet with one vanishing moment cannot see linear functions; a wavelet with two vanishing moments can not see linear or quadric functions; and so on. The moment  $k$  of a general function  $f$  is given by:

$$m_k = \int_{-\infty}^{\infty} f(x)x^k dx \quad (2.46)$$

The moment 'vanishes' when  $m_k$  becomes equal to zero. The number of vanishing moments is weakly linked to the number of times the wavelet oscillates i.e. in general the more vanishing moments a wavelet has the more it oscillates. In practise, the

requirement is normally to concentrate the information of the data in a relatively small amount of wavelet coefficients; useful in, for example, data compression and the analysis of signals with discontinuities where the large coefficients would stand out against a background of smaller coefficients (Hubbard, 1996).

#### **2.8.3.4. Selectivity in frequency**

In Fourier analysis, the analysing function is a sinusoid of precise frequency. This gives a coefficient that corresponds to that frequency and no other. As the analysing wavelet is composed of a range of frequencies, each wavelet coefficient corresponds to this whole range of frequencies. The narrower the frequency range, the more selective the wavelet is in frequency. Therefore wavelet filters with fewer filter coefficients will be able to detect signal discontinuities better than wavelets with more filter coefficients. Ideally the wavelet should be localised in both frequency and time; i.e. very selective in frequency with compact temporal support. For example, it is generally understood that discrete wavelet filters with fewer coefficients are more compact in physical space but less in Fourier space. For example the Haar wavelet (with only two filter coefficients) is well localised in time but not in Fourier space. This is shown in figure 2.9 where the Haar wavelet and Daubechies D4 and D20 wavelets have been plotted with their respective Fourier transforms. Comparing the Haar wavelet with the D20 wavelet (i.e. 20 filter coefficients) it can be seen that the D20 wavelet is better localised in Fourier space whereas the Haar wavelet is better localised in time.

#### **2.8.4. Wavelet mode**

The wavelet transform considers all data to be of infinite length. In practice this is generally not the case, most data are in fact of finite extent. Analysis of the complete data-set is usually required. Consequently, as the wavelet approaches an edge of the signal (or surface) part of the wavelet will fall outwith the signal. This misrepresentation of the data at the signal borders has to be dealt with in the analysis. Various methods to cope with these edge conditions problems of the discrete wavelet transform have been developed. Some of which are listed below.

- (a) *Zero padding*, assumes the signal is zero outside the edges. The disadvantage with this method is that abrupt discontinuities are created at the signal borders.

- (b) *Value padding*, sets a constant value (equal to the first and the last value of the signal) to the beginning and the end of the signal.
- (c) *Decay padding*, adds some form of decay towards zero at both ends of the signal.
- (d) *Reflection*, reflects the signal at the edges, making up a mirror image of the signal at the edges.
- (e) *Smoothing windowing*, multiplies the signal with a window function that reduces the signal edge values to zero at the edges.
- (f) *Polynomial fitting*, applies a polynomial extrapolation of the signal at either ends.
- (g) *Signal following*, if focusing on a small part of the available signal the data points outside may be used if known.
- (h) *Periodization*, the end of the signal is followed by the beginning of the signal. The first point of the signal is continued by the last point hence, the end is put back on the beginning again.
- (i) *Wraparound*, similar to the periodization method. However, this methods wraps the part of the wavelet which falls off the edge at each side of the signal back to the other end again. Values are only represented within the length of the actual signal. Therefore there is no redundancy within this wavelet mode.

The author has applied the wavelet wraparound method to the data analysis reported in this thesis. This is the simplest and most common treatment for the edge effects where the number of decomposition coefficients equals the number of signal components. Whichever method is chosen to deal with the edges, has to take into account that features appearing close to the edges of a signal or data will contain information from outside the region of the data under investigation. Edge effects increase as the width of the wavelet increases (Addison, 2002).

## **2.9. Wavelet tools**

### **2.9.1. Introduction**

Novel uses of the wavelet transform in the area of signal analysis has primarily centred on the denoising and smoothing of data to recover the underlying function from noisy

data-sets, (Donoho and Johnstone, 1994,1995; Barclay et al, 1997; Krim et al, 1999; Abramovich et al, 2000). Smoothing employs a scale dependent threshold while denoising removes small-amplitude coefficients from the data regardless of their position. Smoothing and denoising has been applied to all sorts of signals, e.g. medical signals, engineering signals, geophysical data and financial data. The method has also been shown to be useful in many statistical applications.

### 2.9.2. Smoothing

Smoothing, or scale dependent thresholding, is performed by removing all the coefficients below a predetermined scale, regardless of their amplitude. By removing the smaller scales in the wavelet transform, e.g. scales that in general contains the unwanted high frequency signal noise, a new smoother signal is generated. In addition, often the signal drift also needs to be removed from the data. The removal of drift is achieved by removing the components at the largest scales.

The smoothing of the wavelet coefficients is expressed as:

$$T_{m,n}^{scale} = \begin{cases} 0 & m \leq m^* \\ T_{m,n} & m > m^* \end{cases} \quad (2.46)$$

where  $m^*$  is the index of the threshold scale. Figure 2.10 shows an example where the smoothing method have been applied to a medical test signal acquired from a pulse oximeter (pulse oximetry is explained in more detail in chapter 3, section 3.5.1). The original pulse oximeter signal shown in figure 2.10(a) is decomposed into the 11 scale details shown in figure 2.10(b). Scales  $m < 5$  can be regarded as noise and scales  $m > 8$  are related to the signal drift. The coefficients at these scales are therefore set to zero, reconstructing using only scale 5-8 produced the denoised, smooth pulse oximeter signal. This signal is shown in figure 2.10(c).

Scale dependent thresholding has been applied in a number of studies in other areas. For example Wang and Moon (1997) used wavelet transform smoothing to eliminate measurement noise in wheel surface measurement processes; Jiang et al (1999) separated and characterised the surface topography of orthopaedic joint prostheses; Tsai and Hsiao (2001) used smoothing to inspect local defects in texture surfaces, and Josso

et al (2001) applied scale dependent thresholding to separate engineering surfaces into different topographies.

### 2.9.3. Denoising

In all areas of research scientists face the problem of recovering a true signal from noisy and inaccurate data. Wavelet transform denoising is increasingly being used to undertake this task (Donoho, 1993). Denoising (or amplitude thresholding) can be divided into three basic steps (1) transforming the data into the wavelet domain; (2) applying a threshold method and (3) transforming the data back to its original domain using the inverse transform. This results in a new ‘estimate’ of the underlying signal.

#### 2.9.3.1. Denoising by hard or soft thresholding

Denoising is used to separate noise from a specific signal of interest. Denoising removes, or reduces, selected wavelet coefficients regardless of their position. Applying a hard or soft threshold is the most common way to denoise data. The threshold ( $\lambda$ ) value is generally related to the mean value of the wavelets coefficients. Soft thresholding is defined as:

$$T_i^{soft} = \begin{cases} \text{sign}(T_i)(|T_i| - \lambda) & |T_i| > \lambda \\ 0 & |T_i| \leq \lambda \end{cases} \quad (2.47)$$

Hard thresholding is defined as:

$$T_i^{hard} = \begin{cases} T_i & |T_i| > \lambda \\ 0 & |T_i| \leq \lambda \end{cases} \quad (2.48)$$

A schematic diagram of the two thresholds is shown in figure 2.11, where the threshold value ( $\lambda$ ) is set to equal unity. The soft threshold follows a scheme to keep or reduce wavelet coefficients. Coefficients smaller than  $\lambda$  are removed whilst coefficients larger than  $\lambda$  are reduced by the value of  $\lambda$ . The hard threshold applies a ‘keep or kill’ scheme, where wavelet coefficients smaller than  $\lambda$  are removed whilst the coefficients larger than  $\lambda$  are retained intact.

### 2.9.3.2. Threshold value

In the thresholding process we seek a scheme which differentiates between coefficients which belong to the reconstruction (i.e. those which significantly resemble the signal) and those coefficients which do not belong to the reconstruction (usually small coefficients that can be associated with noise). It is obvious that the choice of threshold value ( $\lambda$ ) will affect the performance of the thresholding process. If  $\lambda$  is chosen to be too small, unwanted noise will be retained in the reconstruction while if  $\lambda$  is set to too large a value this will cut off important information from the underlying signal.

As an example, hard and soft thresholding were applied to a test waveform with added random noise. The waveform consists of two sinusoidal signals of unit amplitude shown in figure 2.12(a) and (b). These were added together as shown in figure 2.12(c). Random Gaussian noise, figure 2.12(d), was added to the signal to give the final test signal shown in figure 2.12(e). This was then thresholded using  $\lambda=0.5, 1, 2, 3, 5$  and  $7$  applied respectively, using both the hard and the soft threshold. The results from reconstruction applying the hard thresholding method are shown in figure 2.13(a)-(f). It can be seen that when  $\lambda=0.5$ , (a), the thresholding method is unable to remove the noise from the signal. However for  $\lambda=7$  the reconstructed signal is oversmoothed. The best reconstruction appears to be achieved using  $\lambda=2$ . The results from applying the soft thresholding are shown in figure 2.14(a)-(f). Most of the noise is already removed at  $\lambda=0.5$ . At  $\lambda=7$  almost the complete signal have been removed. The soft threshold tends to remove more of the signal at lower threshold values than the hard thresholding method.

It is in general impossible to set a threshold that filters out all the noise without affecting the signal (Strang and Nguyen, 1996). However, a number of methods have been proposed to set the best threshold value ( $\lambda$ ) for the denoising of a signal. One of the most common and easiest ways to determine  $\lambda$  is using the universal threshold proposed by Donoho (1993). The universal threshold is defined as:

$$\lambda_U = (2 \ln N)^{1/2} \sigma \quad (2.49)$$

where  $(2 \ln N)^{1/2}$  is the expected maximum value of noise in a sequence of length  $N$  and  $\sigma$  is the standard deviation for the noise in the signal. Donoho (1993) showed that a near

optimal performance is achieved for denoising using this threshold, assuming that the noise is white. The universal threshold depends on the data characteristics only through  $\sigma$ . It has been shown that for large sample sizes the universal threshold has a high probability of removing all the noise in the signal. However, part of the underlying function might also be lost. Thus, the universal threshold tends to oversmooth a signal. To overcome this problem, it is common to keep the coefficients at the largest scales untouched even though they might not pass the threshold value, (Abramovich et al, 2000).

As mentioned above, the standard deviation,  $\sigma$ , of the noise in a signal is required to determine the threshold. In practise the value of  $\sigma$  is rarely known and must therefore be estimated from the data. We can do this by using a robust estimate of the standard deviation  $\hat{\sigma}$ , e.g. the medium of absolute deviation of the wavelet coefficients (MAD) at the smallest scale normalised by dividing it with 0.6745 (Abramovich et al, 2000). Equation 2.49 can be rewritten as:

$$\lambda_U = \frac{(2 \ln N)^{1/2} MAD}{0.6745} = (2 \ln N)^{1/2} \hat{\sigma} \quad (2.50)$$

Szilagyi et al (1999) used the universal threshold to calculate the time scale of coherent structures in atmospheric surface layers. They used the method proposed by Donoho and Johnstone (1994, 1995) for noise reduction in signals by applying the universal threshold could be used to detect coherent structures within surface layers of fluid flows.

A number of different methods to estimate the threshold value ( $\lambda$ ) are available: RiskShrink (Donoho and Johnstone, 1994), SURE and SureShrink (Donoho and Johnstone, 1995), WaveShrink (Donoho et al, 1995), Minimax, (Donoho and Johnstone, 1998), cross-validation (Weyrich and Warhola, 1995; Nason, 1996; Jansen et al, 1997), Bayesian approach (Abramovich et al, 1998) and Lorentz (Katul and Vidakovic, 1996; Visser, 2003). However these methods will not be discussed in detail in this thesis. The interested reader is instead referred to the literature by, e.g.: Odgen (1997) who evaluated a number of different methods to set the threshold values; Mallat (1999) who provides the mathematical background to thresholding techniques; Abramovich et al (2000) who provides a summary of different thresholding methods, and Addison (2002)



who presents an overview of thresholding techniques and cites many detailed papers concerning the use of wavelet thresholding (in statistical measurements, engineering flows, surface characterisation, data compression, medical and financial data).

### **2.9.3.3. Data analysis using amplitude thresholding**

Weiss and Dixon (1997) compared a high pass filtering method (*HPF*) with the wavelet denoising method for the removal of unwanted backscatter from high frequency acoustic underwater signals. Several signals were analysed and their results showed that both the HPF and the wavelet denoising removed unwanted backscatter from the data. However, the HPF proved to removed too much of the signal energy (62% of the energy retained) compare with the wavelet denoising (82% of the energy retained).

Both hard and soft thresholding methods were applied by Tikkanen (1999) to remove simulated noise in ECG signals. Four different rules for selecting the threshold values were applied, SURE, Heuristic SURE, Fixthres and Minimax methods. The results show that the most effective noise-removal soft-thresholding method was the Heuristic SURE which gave the lowest mean error for three different noise types. For the hard threshold, the Fixthres selection rule, gave the best performance with the lowest mean errors for noise types considered. The author concluded that soft thresholding tended to give a more acceptable overall denoising result compared to the hard thresholding.

Zahn et al (2000) apply wavelet thresholding to improve the computation time and reduce memory requirements for evaluating the scattered field statistics from synthetic rough surfaces. The authors demonstrated that by imposing a wavelet threshold on the data matrix only the significant elements of the matrix are preserved. This led to a sparser matrix and a requirement for less computing time.

Magnitude thresholding has not only been used for denoising (removal of noise) but also in the identification and separation of larger dominant features (characterised by larger coefficients) within a signal. Research by Wang (1995, 1999) has shown that the wavelet technique is ideal to detect jumps and sharp changes within signals. Struzik (2001) used the continuous wavelet transform to recognize abrupt changes in financial data series. Orthonormal wavelets were used by Hajj et al (2000) to identify pressure

peaks in time-varying of turbulence data where sharp changes were represented by larger wavelet coefficients. Thus, by applying a magnitude threshold the authors sorted the large amplitude coefficients, related to pressure peaks from the data.

Pettit et al (2000) used the wavelet method to detect changes of roof-corner pressure transients. The peaks (abrupt changes) in the signals were detected by retaining portions of the signal where the magnitude of the wavelet coefficients exceeded a certain pre-set threshold. The transients were sorted into classes dependent upon the number of peaks in the smooth version of the original signal. In a further study Pettit et al (2002) used a pattern classification scheme to investigate the underlying structure in pressure transients. The detected transients were removed from the signal where the underlying signal had the appearance of background noise and could be modelled reasonable as a Gaussian distribution.

Addison et al (2001a) used both the scale dependent threshold and magnitude thresholding (hard and soft) methods to separate a vortex shedding signal into strong and weak parts. The authors defined a scale dependent threshold at scale index  $m^*=6$ , where the strong signal is reconstructed using scales larger then  $m=6$ . Accordingly the weak signal is reconstructed using scales smaller then  $m=6$ . In addition, both a hard and a soft threshold were applied to the signal, where the threshold level was defined using the universal threshold. The results showed that scale thresholding leaves remnants in the weak signal part while the strong part smoothes much of the signal. Applying the hard threshold, much of the high frequency components of large amplitude were retained in the strong signal, however the vortex shedding fluctuations were removed from the weak signal leaving an even distribution of noise in the weak signal.

Amplitude thresholding of wavelet coefficients was applied by Teng and Qi (2003), who developed a freeway incident detection algorithm. The authors used the universal threshold to distinguish sharp changes in traffic behaviour, indicating possible accidents. The discrete wavelet coefficient at the finest level was thresholded where the largest coefficients exceeding the threshold value could be sorted. These coefficients represented an abrupt change in flow pattern. The performance was evaluated by comparing the detection rate and the false alarm rates. The authors results indicated that the wavelet transform performed better than other algorithms including a low-pass

filtering algorithm, multi-layer feed-forward (MLF) neural networks algorithm, the 'California' algorithm, the probabilistic neural network (PNN) algorithm and a fuzzy-wavelet RBFNN algorithm.

Wavelet thresholding has been applied to many other areas including: non-linear smoothing of Gaussian random processes (Moulin, 1994); reduction of ultrasonic grain noise (Lázaro et al, 2002); de-noising of 2-D signals (Hilton and Ogden, 1997); edge detection in images (Murtagh and Starck, 2003); improving surface simulation techniques (Lalonde and Fournier, 1997); data compression methods (Straszewski et al, 1997); mechanical vibration (Tanaka et al, 1997); detection of horizontal and vertical disparity ripples within random element patterns (Tyler and Kontsevich, 2001); edge detection in magnetic resonance (Xu et al, 1994), and edge detection in mammographic images (Laine et al, 1994; Ferreira and Borges, 2003).

## **2.10. Application of the wavelet transform to the analysis of rough surfaces**

### **2.10.1. Introduction**

In general the topography of a surface consists of a number of features of different length scales located at different positions. For engineering surfaces, the topography affects the functional behaviour of the surface through wear, friction, lubrication, corrosion, etc. Interest in methods to characterise the topography of surfaces is therefore increasing.

The use of the wavelet transform for texture analysis was pioneered by Mallat (1989a) who showed that a particular function of the wavelet orthonormal basis is equal to texture primitives with spatial orientation and narrow frequency tuning. Recently, wavelet analysis has been employed in a variety of surface analysis tasks including the characterization of fractional Brownian motion surfaces, cracked concrete surfaces, pitting corrosions, grain growth, orthopedic joint prostheses, general surface roughness analysis, the characterization of surface roughness of silicon and the evaluation of different engineering surfaces.

### 2.10.2. Engineering surface analysis

The surface topography of an engineering component is an important factor that affects its functional performance. The wavelet transform has been applied over a wide range of areas in both science and engineering to characterise and classify global surface features and to separate and identify individual features within surfaces.

Frantziskonis et al (2000) used wavelets to describe geometrical features of pitting corrosion damage in aluminium components. Several specimens of aerospace aluminium alloy were corroded in a controlled environment and the resulting corrosion pits analysed using a wavelet-based fractal analysis. An image of one of the corroded surfaces is shown in figure 2.15(a). Figure 2.15(b) displays a typical cross-section from the surface in figure 2.15(a). The specimens were interrogated using a wavelet-based method to establish the fractal scaling property characterised by the Hurst exponent ( $H$ ). Two perpendicular directions for each specimen were examined. The variance of the wavelet coefficients at each scale then plotted against the scale of the decomposition. The slope of the curve for a self-affine surface equals  $1/2+H$  from which roughness characteristics can be established. Two typical log plots of the variance plotted against the scale are shown in figure 2.15(c) and figure 2.15(d) for the respectively horizontal and the vertical profiles of a corrosion pit. It can be seen in these plots that a new relationship exists between variance and scale. This is a property of fractal scaling. Several specimens were analysed. Figure 2.15(e) shows the scaling properties from all the specimens for the vertical direction. The result from the analysis established that  $H$  was in the range  $0.63\pm 0.12$  for these corrosion pits. In addition, the ratio  $\omega$  of surface area of the corroded pit over the total area of its intersection with the plane at zero was established. This ratio, in combination with the  $H$  exponent, was sufficient to obtain 3-D information concerning the characterisation of the pit geometry from a 2-D image. The authors stated that the multiscale information obtained through the wavelet analysis could form the basis of a new approach for the characterisation of pitting corrosion.

In related work, Frantziskonis and Hansen (2000) also used the wavelet transform to establish the roughness, characterised by the Hurst exponent ( $H$ ), for self-affine random media. Frantziskonis and Deymier (2000a, 2000b) have demonstrated the analysis of simulated grain growth using a 2-D wavelet-based method. They showed that the wavelet energy provides useful statistical information about the material properties.

They established that the scale of the maximum wavelet energy corresponds with the mean grain radius. The wavelet method therefore proved useful as a tool to extract structural features in the microstructure of particle grain growth. Further research carried out by Frantziskonis and co-workers include the analysis of grain growth at different magnifications. This includes the work by Haynie and Frantziskonis (2001) who applied the wavelet transform to obtain quantitative information about the microstructures of material. In their method the dominant length scales at different resolution levels is identified using the peak of the scale-space energy of the wavelet transform. The method identifies which scales contain most information and therefore should be further investigated. In a later paper by Frantziskonis (2002) the effects on multiscale microstructures in porous material at different magnification was studied. The work showed how wavelet energy transfers to larger scales where the pores are dominant as the magnification increases. He found this to be an effective tool for studying the multiscale microstructure of material properties.

Wang et al (2003a) have also evaluated the performance of wavelet-based methods for studying the fractal characteristics of rough surfaces. In their study, synthetic curves with known fractal dimensions were generated and processed. The fractal curves generated using the Weierstrass-Mandelbrot function and Majumdar-Bhushan function are shown in figure 2.16(a)-(b). Fractals curves for three values of dimension (D) were analysed:  $D=1.2$ ,  $D=1.5$  and  $D=1.8$ . Eight algorithms for calculating the fractal dimensions were studied using a number of methods including a wavelet-based method. The other methods were: the box counting technique, the yardstick method, the co-validation method, the structure function method, the variation method, the power spectrum method and rescaled range analysis. The authors employed the Daubechies wavelet for the wavelet-based analysis and the fractal dimensions were obtained from the slope of the log plot of the modulus coefficients against the scale of the transform. Figure 2.16(c) show the log plots of the modulus of the wavelet coefficients plotted against the scale for the fBm profiles in figure 2.16(a)-(b). The fractal dimension determined using the wavelet method produced an error of  $1.2 \pm 0.7\%$ . The mean errors obtained using the other methods were: box counting method  $6.4 \pm 4.1\%$ ; the yardstick method  $9.4 \pm 9.2\%$ ; the co-validation method  $4.8 \pm 5.6\%$ ; the structure function method  $3.6 \pm 3.3\%$ ; the variation method  $4.5 \pm 2.9\%$ ; the power spectrum method  $13.3 \pm 11.6\%$  and the rescaled range analysis  $2.7 \pm 3.1\%$ . The results showed that the wavelet transform

provided the most accurate method for the determination of fractal dimension of the curves. The authors believe that this is a first step towards a new method to characterisation of machine surface topography. In a later related paper Wang et al (2003b) applied the wavelet transform to establish the fractal dimensions for rolled, hand and machined polished copper and stainless steel surfaces. In this work they found that the experimental surfaces had approximately the same fractal dimensions, established using the wavelet technique. Additionally the authors concluded that the wavelet transform is the most effective method to establish the fractal dimensions for these types of surfaces.

Both wavelets and fractals were applied by Dougan et al (2000) to characterise cracked concrete surfaces. Figure 2.17(a) illustrates typical concrete crack profiles and figure 2.17(b) shows the wavelet power spectrum (solid line) using the CWT for the concrete profiles. The Hurst exponent ( $H$ ) can be found from the slope of the spectrum. The authors established the scaling exponent of the cracked concrete to be in the range:  $H=0.57\pm 0.16$  (14 day test) and  $H=0.53\pm 0.09$  (28 day test) using Fourier analysis and  $H=0.64\pm 0.18$  (14 day test) and  $H=0.58\pm 0.09$  (28 day test) using the wavelet approach. Maktadir and Sato (2000) also used the CWT to characterize anisotropically etched silicon surfaces. The roughness exponent was established from the log-log plot of the scalogram versus the scale. The authors found the roughness exponent to be close to 0.5 for silicon. Simonsen et al (1998) applied both the wavelet transform and Fourier spectral analysis, to cracked concrete surfaces and economic index data in terms of  $H$ . The authors found that the wavelet transform outperformed the Fourier method for signals containing relatively few samples.

The wavelet transform has also proved to be useful in surface texture analysis. Jiang et al (1999) applied the wavelet transform to separate and characterise the surface topography of orthopaedic joint prostheses. Using 2-D biorthogonal wavelets they separated the surface into three topographies: *roughness*, *waviness* and *form*. The roughness was defined using the wavelet coefficients at the smallest scales; waviness was defined using the coefficients at the intermediate scales, and form was defined using the coefficients at the largest scales. A multiscale decomposition of a metallic femoral head and separation into roughness feature is shown in figure 2.18. A more important step for the surface characterisation is to identify and isolate pits, scratches and peaks within the surfaces. By applying a hard threshold these feature could be

located within the surfaces. This is shown in figure 2.19 where the multiscale features within the metallic femoral head surface are identified and located. Wavelet decomposition proved useful for topography separation as well as identifying and locating peaks, pits and scratches within orthopaedic joints surfaces. This information was used to evaluate bearing ratio, material volume and void volume. When applied to the manufacturing process this can be used to predict the wear mechanism of the joints.

The wavelet transform has also been applied by Jiang and Blunt (2001) to identify the morphology of the femoral counterface surface of artificial joints. It has been reported that defects or deep scratches present in a diamond like carbon coated head can cause an increase in the wear rate. Therefore the properties of the counterface of the joints has an important impact on the design of joints. The authors applied a hard thresholding technique where larger amplitude coefficients were kept and used in the reconstruction. The morphological features within the surface could then be identified. This is shown in figure 2.20(a) where shallow scratches have been removed (circled areas), revealing only the morphological surface figure 2.20(b). The wavelet analysis presented in their paper allows for a better understanding of the morphological surface of hip joints. Further work carried out by Jiang and co-workers in this area includes the application of lifting wavelet representations for separation and extraction of different components of both engineering and bioengineering surfaces (Jiang et al, 2000; Jiang et al, 2001a; Jiang et al, 2001b). In further research Xiao et al (2001) have evaluated the performance of biorthogonal B-spline and cubic spline wavelets to extract the rough surface from bioengineering surfaces. Xiong et al (2001) proposed a combined wavelet models and fractal theory to characterise engineering surfaces.

A number of other groups have applied the wavelet transform to engineering surfaces texture characterisation to separate the surfaces into three topographies. Josso et al (2002) separated texture surfaces into the three different scale components: roughness, waviness and form. The surfaces were transformed into a number of details using the Daubechies 20 wavelet. Details of the three different components were extracted from the original surface through selective summation of the wavelet scales. This is shown in figure 2.21(a) where the original surface profile and the three components are presented. The authors defined the form topography as scales 0 and 1, the waviness form was defined over scales 2 to 4 and the roughness topography over scales 5 and 6. The same

kind of decomposition and reconstruction was applied, using the 2-D wavelet transform, to a casting surface texture, as shown in figure 2.21(b). The wavelet proved to be a very useful tool for separation of surfaces into different topographies.

Separation of surface textures using wavelet methods has also been carried out by other groups. See for example papers by Chen et al (1995) who demonstrated the use of the wavelet transform for multi-scale feature location in electro-formed surfaces; Lee et al (1998) who analysed the local morphology characterisation of engineering surface; Chen et al (1999) who applied wavelet techniques to separated the roughness from surface profile, and Raja et al (2002) who reviewed different filters, including the wavelet transform, used to characterise engineering surfaces.

The wavelet transform has also proved to be useful as texture classification method in a range of areas ranging from fabric characterisation to the inspection and control of manufactured engineering surfaces.

In a study carried out by Jasper et al (1996), adaptive wavelet bases were applied to capture the texture information and detect and locate defects in woven fabrics. Manian and Vasquez (1998) classified invariant textures patterns using three different bases functions (Daubechies and Haar bases, biorthogonal Spline and non-orthogonal Gabor bases). They presented a method that recognises scaled and rotated textures, where inter-scale combination of coefficients gives invariant features within the texture. This was applied to classify 14 textures from the Brodatz album, where the textures were scaled and rotated. The results for texture patterns correctly classified was 80.4% for the Daubechies basis, 74.1% for the Haar basis, 72.2% for the biorthogonal basis and 60.1% for the Gabor basis. Comparing the four bases it was found that the Daubechies basis provides the best results for this type of classification. Recognition of translation-invariant features was later studied by Li et al (2003), using the discrete wavelet frame transform.

Multiresolution was applied by Tsai and Hsiao (2001) to extract and identify defects embedded in homogeneous texture surfaces. A simple threshold was applied to discriminate between defect regions and homogeneous regions on variety of real texture



surfaces including machined surfaces, natural wood, textile fabric, sandpaper and leather.

Podisadlo and Stachowiak (2002) compared different methods of analysis of tribological surface topography (e.g. Fourier transform, windowed Fourier transform, Cohen's class distribution, wavelet transform, fractal methods and a hybrid fractal method). The authors found that a hybrid fractal-wavelet method appeared to be the best method to determine the topography both scale-invariant manner and different scales. However, the wavelet transform was found to be the most suitable non-fractal method for the characterisation of surface topography. In a later paper by Stachowiak and Podisadlo (2004) a further evaluation of the performance of the hybrid fractal-wavelet (HFW) method to characterise tribological surfaces from images was carried out. Here the authors concluded that these types of surfaces can be successfully characterised and classified without any surface parameters using the HFW.

The wavelet transform has also been successfully applied as a surface denoising tool, to extracting the real surface data from a noisy data-set. Wang and Moon (1997) used the multiresolution method to study a grinding wheel surface. They found that the noise in the data could effectively be eliminated using the wavelet transform. The wheel surface could be reconstructed using a selected combination of wavelet scales according to the practical need. In addition, the ground surface roughness could be predicted as characteristic wavelengths can be associated with their characteristic grain sizes. They suggested that the method can be used to model grinding wheel surfaces and hence become a potentially useful tool for grinding process control.

Wavelet analysis was applied by Silva et al (2003) to ultrasonic signals for detection of corrosion at the back surface of an aircraft aluminium structure. Their method detects the changes in roughness due to corrosion rather than material loss or plate thinning and is therefore particularly useful in early corrosion detection.

Srinivasan and Wood (1997) applied fractals as a tolerance measure in mechanical design. The authors used the Daubechies 12 wavelet to calculate the relevant fractal parameters for mechanical products. As an example they applied the method to establish the roundness errors (main source of vibration) of rolling elements of ball bearings

supporting the trust load. The authors concluded that the wavelet transform can be used as a tool to compute relevant fractal parameters applied in design for manufacturing.

## **2.11. Sediment transportation**

### **2.11.1. Introduction**

The knowledge of sediment transport in open-channel flow is vital to river engineers. Most open channels have a constantly changing river bed-surface. Erosion and sediment transport is therefore a concern. The structure of a river bed-surface can take a variety of forms such as dunes, ripples, etc, creating obstacles and expansions in the river. These affect the flow resistance in the channel, causing separation and re-circulation that influences the overall flow of the river. This may increase the turbulence of the flow and it is likely to affect the rate of erosion of the bed-surface (and the river banks) thus, increasing the sediment transport rate (Graf, 1996). The understanding of transportation and deposition of solid particles in river flow represents an important issue within the field of hydraulics. Methods to analyse the structure and characteristics of the river-bed surface are therefore essential to river engineering work.

### **2.11.2. River hydraulics**

The shape of a natural channel depends on a number of variables. The most important factor is probably the discharge coefficient,  $Q$  (which may vary with time) geology, topography and the climate. The change in sediment transport rate along a river is noticeable, where material is eroded from one area and deposited somewhere downstream.

#### **2.11.2.1. Fluid dynamics**

River flow over a bed-surface is influenced by the friction (or resistance) of the surface. Traditionally Manning's  $n$ , (the coefficient of friction or the roughness coefficient), has been applied to measure the bed friction of a surface. Manning based his equation on the work carried out by Chézy concerning calculations of flow velocity over an average cross-section (McKay, 2002). Manning's equation for surface roughness is:

$$u = \frac{1}{n} R^{2/3} \sqrt{\sin \theta} \quad (2.51)$$

where  $u$  is the velocity,  $R$  is the hydraulic radius and  $\theta$  is the channel slope. This equation may also be rewritten in terms of flow rate  $Q$ :

$$Q = \frac{1}{n} \frac{A^{5/3}}{P^{2/3}} \sqrt{\sin \theta} \quad (2.52)$$

where  $A$  is the cross-sectional area and  $P$  is the wetted perimeter. Manning's  $n$  characterises the surface roughness as a value ranging from 0.009 (for smooth surfaces such as glass and plastic) to 0.15 (for very rough surfaces such as those including tree cover and flood plains). Manning's formula is today widely accepted because of its ability to be used within channels exhibiting a high degree roughness (Chow, 1959).

The Manning's  $n$  value can be estimated; using a tabulated  $n$  value or using empirical methods. A number of empirical methods have been suggested for the estimation of  $n$ . The Strickler equation is probably the most often used empirical method to compute  $n$ . The original Strickler equation is written as:

$$n = 0.047d^{1/6} \quad (2.53)$$

where  $d$  is the diameter in millimetres of uniform sand pasted on the sides and the bottom of a flume used by Strickler in his original experiments (French, 1994). Other forms of the Strickler equation have been proposed, with variations on both the multiplicative constant and the definition of the dimension  $d$ . For example the Strickler equation according to Raudkivi (1976) is defined as:

$$n = 0.013d_{65}^{1/6} \quad (2.54)$$

where the dimension,  $d$ , is measured in millimetres and  $d_{65}$  is the bed roughness such that 65% per cent of the roughness elements are smaller than this size. For bed material with significant proportions of coarse material Meyer-Peter and Muller (1948) suggested the following equation:

$$n = 0.038d_{90}^{1/6} \quad (2.55)$$

where  $d_{90}$  is the bed size in meters such that 90% of the material by weight is smaller than this size. In field experiments with cobble paved canals Lane and Calson (1953) determined that:

$$n = 0.026d_{75}^{1/6} \quad (2.56)$$

where  $d_{75}$  is the diameter of the bed material in inches.

The roughness of the bed surface is one of the factors that affects turbulent flow in an open channel. The effect of turbulence is the rapid and random motion of the fluid in form eddies that move downstream with the main river flow. There are three types of flow: *laminar or viscous flow*, where the fluid moves in discrete layers without mixing, *transitional flow*, where some unsteady motions occur within the flow layers and *turbulent flow*, where the flow consists of turbulent mixing eddies between the flow layers. All natural river flows are turbulent.

Flow regime is classified according to the dimensionless Reynolds number ( $R_e$ ), defined as:

$$R_e = \frac{\rho ul}{\mu} = \frac{ul}{\nu} \quad (2.57)$$

where  $\rho$  is the fluid density,  $u$  is the average velocity,  $l$  is the characteristic length,  $\mu$  is the dynamic viscosity and  $\nu$  is the kinematic viscosity (Rott, 1990). Viscous forces dominate the laminar flow where the particles move in a smooth and coherent manner. While turbulent flows are dominated by the inertial forces and particles within the flow move in a random path, (Chow, 1959 and McKay, 2002). The irregular motion of the turbulent flow affects the particles of bed-surface material to a greater degree than the laminar flow where the bed particles are set in motion by the flow, transported and allowed to settle again on the bed-surface further down the river.

#### **2.11.2.2. Sediment motion**

There are three different modes of sediment transport that can be identified:

1. *Bedload transportation*, (or contact load) where the sediment particles move by rolling and sliding in direct contact with the other particles in the surface bed. The particles move, remain stationary for some time, then move again.
2. *Saltation transportation*, where the particles move in a bouncing or hopping motion. This is due to uplifting force by the fluid or by collision with other particles.
3. *Suspended sediment*, where finer particles (this usually applied to fine silt) are swept up by the flow and held in suspension by turbulent fluctuations in the fluid.

The moving fluid transfers energy to the particles which induces particle movement. The energy required to move a particle has to overcome the natural resistance to motion by the particle, which is known as the 'threshold of movement'. For a perfectly round object placed on a smooth horizontal surface, only a very small horizontal force applied to the object is required to make it roll. However, the natural sediment particles on a bed-surface are unlikely to be perfectly round. Additionally, they will sit on a rough surface, which itself is not flat or horizontal. The force applied to a particle will only cause motion if it overcomes the natural resistance to motion of the particle, figure 2.22(a). For a flow over a gravel-bed sediment surface, the contact surface between water and sediment will be subjected to shear stresses ( $\tau_0$ ) due to the flowing fluid. If the shear forces are gradually increased, a point will be reached where the particles start to move this is the 'threshold of movement'. The shear force for a gravel-bed surface is shown schematically shown in figure 2.22(b), (Chadwick and Morfett, 1986).

As shear forces increase, the particles starts to move and roll over their neighbours. The moving particles collide with each other and other stationary particles causing the sediment movement to spread. This starts a further and more complex pattern of forces that enhance particle movements. The movement of particles go through a cycle of four steps: (1) *no particle movement*, the shear stress ( $\tau_0$ ) is not large enough to move the particles, then, (2) *localised movement*, with an increase in shear stress particle movement is noticed at a number of small locations across the surface. This is followed by, (3) *general sediment motion*, where a small increase of shear stress is generally sufficient to cause a widespread sediment motion, before, (4) *suspended load*, which

occurs after a further increase in the shear stress whereby the fine particles are swept up into the flow.

### **2.11.3. Bed armouring and cluster formation**

The bed armouring process occurs when the bed-sediment progressively re-arranges and re-organises itself so that it becomes more stable and resistant to further erosion. Three different conditions of armouring may be considered: static armour, mobile armour and full motion (Hunziker and Jaeggi, 2002). For shear stresses slightly above the critical shear stress the somewhat higher mobility of finer material will produce slightly higher sediment transport rates and a coarsening of the bed-surface will occur. This is called the static armouring condition. Also, coarser grains will move from less stable positions in the surface to a more stable arrangement against each other. If no sediment is supplied the bed load transport rate will reduce significantly and a stable armour layer may form which will prevent further erosion. For higher shear stresses a stable armour cannot form because all the grain sizes are in motion (Church et al, 1998). Grain sorting processes for this condition will lead to a top layer which is slightly coarser than the subsurface. This layer is known as mobile armour layer. For even higher shear stresses the coarse grain are more easily transported on the bed of finer grains. This is because the shear stresses now far exceed the critical shear stress causing all the grains to be equally mobile. The bed is now said to be in full motion. (Church et al, 1998; Hunziker and Jaeggi, 2002).

The traditional measure of the characteristic ‘sizes’ of a sediment bed surface is the *particle size distribution (psd)*. This measures the cumulative percentage by weight of particles within different size ranges (Craig, 1987). The most common method to determine the *psd* is using the sieve analysis method. A representative sample of the soil is oven-dried. The dried sample is shaken through a set of standard test sieves arranged in a descending order of mesh sizes. The weight of the sample retained at each sieve is recorded and the cumulative percentage of the sample passing each sieve size calculated. From this, the particle size distribution can be plotted on a semi-logarithmic scale that is known as the grading curve of the sample (Whitlow, 1995). Full details of the sieving analysis method used for determination of the *psd* is given in BS 1377 (1990). The soil is then classified according to the distribution of sizes. The

classification system used by the British Standard Institute is the MIT (Massachusetts Institute of Technology) system. Figure 2.23 show an example of a particle distribution sheet for a well graded gravely SAND with the boundaries as defined in the system. The particle sizes are plotted on the horizontal axis and the cumulative percentage of sediment on the vertical axis (Smith and Smith, 1998).

However, in research by Gessler (1990) it is stated that the '*psd*' is rather independent of the friction factor of the surface bed. He stated that it is the arrangement of the bed surface material rather than the '*psd*' that determines the flow environment and the hydraulic resistance of an armoured bed. The re-arrangement of the surface grains may constitute interlocking of the sediment particles where larger more stable grains group together to form coherent, more stable bed-surface structures, i.e. clusters. These clusters will affect the near bed flow environment of the bed-surface. Additionally, the clusters will work as a sheltering mechanism to smaller less stable grains in the structure. Retention of sediment material will cause a rapid decrease in the sediment transport rate. However, larger grains will lose their stability when the finer material is washed away from around them. As these larger, more stable, grains are transported away the unprotected finer material becomes exposed to the flow and is incorporated into the bedload. This results in a bedload fluctuation in the sediment transport rate. Sediment bedload transportation and fluctuations due to the bed armouring processes have been studied both in the laboratory and in the field. See for example the work by the following authors: Tait et al (1992), Lisle and Madej (1992), Willets et al (1998), Carling et al (2000a), Carling et al (2000b), Kneller and Buckee (2000), Pender et al (2001) and Niño et al (2003).

The need to further understand the mechanisms behind sediment cluster formation and their influence on the river-bed stability was highlighted by Brayshaw et al (1983). The clusters are believed to congregate into certain shapes during the armouring process. According to Papanicolaou et al (2003) clusters undergo changes in size and shape depending on the sediment rate and the flow condition. The clusters are formed in a cycle as follows: (1) two particles collide and form a two particle cluster, (2) further particles attach themselves to the cluster forming a comet shape, (3) as the shear stress increases on the comet, triangular clusters forms, (4) the final shape is a rhomboid and (5) when the flow conditions reach twice the critical shear stress the cluster will break-

up. The cluster formation cycle is shown in figure 2.24. In a later paper by Papanicolaou and co-workers (Strom et al, 2004) the authors found that cluster formations in the bed surface effect the bedload transport rate. During unsteady flow the effect of clusters on bedload was classified into three different phases: (1) sink phase (the cluster absorbs incoming sediment particles), (2) neutral phase (the cluster does not effect the bedload) and (3) source phase (particles are released from the cluster). The formations of clusters will also, naturally, be influenced by the supply of sediment material. Church et al (1998) studied the development of surface structures in experimental gravel-bed stream channels during low bed material transport rates. They observed that the surface congregated into a complex grain structure. Larger more stable particles on the surface rolled into contact with each other forming a cluster. As more particles attach themselves, the cluster grows into a line of particles. Eventually these lines join up and formed rectangular structures which the authors refer to as stone cells. These structures will reduce the sediment transport rate as they effectively protect smaller material from the flow. In the presence of sediment supply, the surface structures will adjust themselves in a manner which is dependent upon the proportion to feed material. These types of sediment structure patterns in mobile gravel-bed surfaces during flow conditions have also been observed by for example Barndroff-Nielsen (1989) and Tait and Willetts (1991). Development of surface structure during material feed has been studied by e.g. Dietrich et al (1989). The authors studied surface structures at different sediment feed rates in an experimental flume, where the water discharge and the bedload grain size distribution were held constant. The results showed that the degradation of grain sizes into zones varied with the supply. For the initial high sediment supply the surface consisted of bedload sheets of coarse, fine and transitional zones travelling downstream in the channel. This caused fluctuations in the bedload at the end of the channel. As the sediment supply decreased these sheets became both less frequent and less distinct. Instead, zones with coarse inactive material could be observed, which increased to a progressive narrower zone of fine material as the sediment supply reduced further. For this condition the bedload travelled in long-wavelength pulses.

It has been argued that clusters are formed in the presence of well-graded sediment, therefore the strongest clusters are formed in rivers with uniform sediment sorting (Reid et al, 1992). However, laboratory experiments by Papanicolaou et al (2003) has shown



that simulated mono-sized sediment particles can form clusters. The architectural shape of the clusters are dependent on the sediment availability and, for twice the incipient shear stress flow condition, the clusters disintegrate. Recent research has also suggested that sediment availability and specific gravity have a strong influence on the formation of clusters where heavier particles will create a stabilising obstacle trapping finer particles with less mass (Best et al, 2001; Ryan, 2001).

#### **2.11.4. Surface bed layer composition (sampling techniques)**

It is generally assumed that the composition of the surface is the dominant factor in determining its behaviour. However, as stated earlier, recent research has suggested that, in addition to the surface composition, the stability of a sediment surface is dependent of the arrangement and location of the surface grains. Krichener et al (1990) show that there is considerable variability in the critical entrainment shear stresses for particles of similar size on a graded sediment surface. The sampling techniques for the determination of the particle size distribution (*psd*) using the sieve analysing method will unavoidably destroy the bed structures. As a bulk test sample is removed from the surface all the information about the structure characteristics of the surface, i.e. location and orientation of the particles as well as coherent structures within the surface are destroyed. It would therefore be advantageous to use non-destructive methods to analyse the structure of the sediment bed surface layer. A number of methods to collect information about the composition of the bed-surface layer have been proposed, there are: wax sampling (Marion, 1997; Pender et al, 2001), photography and digital images (Adams, 1979; Tait et al, 1992; Butler et al, 2001a; Butler et al, 2001b), 3-D-laser-scanning (Willets et al, 1999; McEwan et al, 2000) and video recordings (Niño et al, 2003; Papanicolaou et al, 2003).

The grain size distribution as well as the location of specific grains can be determined from the above mentioned surface sampling techniques. Pender et al (2001) compared wax sample of initial bed compositions with the final bed composition. It was shown that the final sample showed a greater percentage of coarser fractions compared with the initial sample. Hence the wax sample technique was able to identify trends in the bed composition during the armouring process. Kellerhals and Bray (1971) applied a grid-by-number measurement, which they assumed equivalent to the sieve-by-weight

measurements. Tait et al (1992) used a size-to-number basis where a square grid was superimposed onto plan-view photographs. The grain under each grid point was measured. From this the bulk mass-size distribution was determined.

A parallel edge detector was used by Butler et al (2001a) to identify sediment particle boundaries in digital images (edge detection is a standard function in most image processing packages). Grain-size information was automatically extracted from the image by fitting and measuring an ellipse for each feature. From this a particle-size distribution of the sediment surface was constructed.

Willems et al (1999) studied 3-D laser scans of sediment bed-surfaces. Each scan produced an array of x-y-z co-ordinates, from which a model of the sediment surface topography, or any transect of it, could be constructed. The authors suggest that the contour plots of the surface scans can be used to obtain information regarding surface decomposition as well as the arrangement of the surface particles.

An image-processing technique was developed by McEwan et al (2000) to extract grain size information from laser scans of water-worked sediment beds. Using the 'Canny algorithm' particle edges were detected and image segmentation used to convert the grain edges into closed regions from which the surface grain sizes and location could be determined. Hence the size composition of the surface was obtained. This technique was tested for three surfaces with different sediment distributions. The results were compared with the traditional surface composition measure of volumetric sieving. The authors concluded that the two size compositions produce similar values for the surfaces composition and the image processing method provide a reliable means of determining the surface composition as well as providing information of grain location and orientation. In related work, Marion et al (2003) employed a 2-D structure function to identify different grain scale features in the sediment bed-surface data. Two classes of grain scale bed features developed over time: (1) a slow forming features with strong lateral and streamwise coherence associated with stable beds, formed under stationary armouring condition and (2) a quick forming features with strong streamwise coherence associated with phases of dynamic armouring.

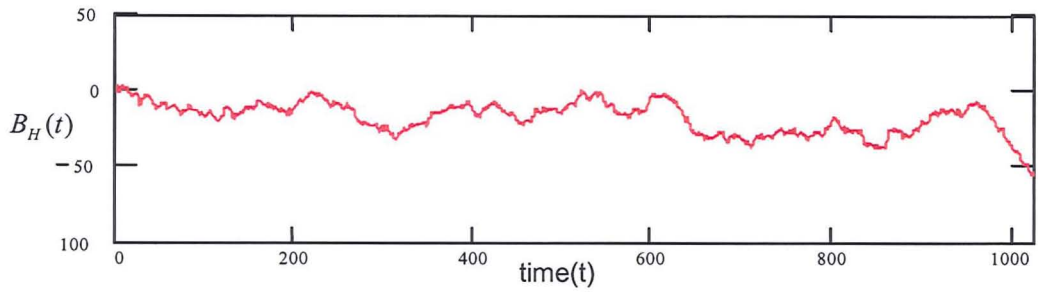
## **2.12. Chapter summary**

The work detailed in this thesis is based upon previous work from a variety of sources, the background details of which have been presented in this chapter. The basic concept of wavelet transform has been described, including both the CWT and DWT and the special case of redundant DWT known as the SWT. In addition the 2-D wavelet transform has been introduced, followed by the factors to consider when choosing the wavelet transform to use and the analysing wavelet itself.

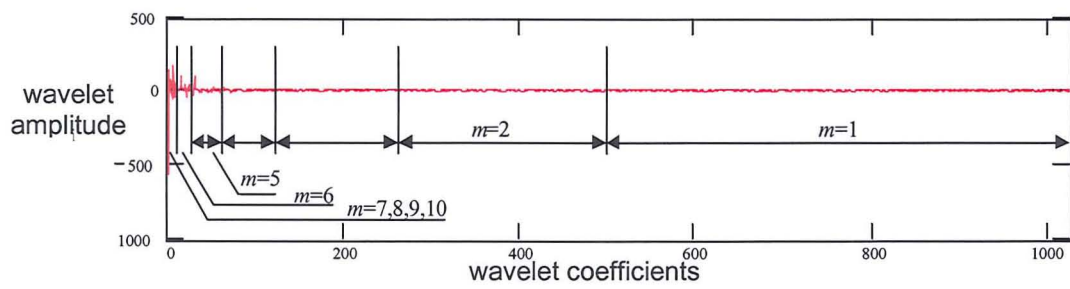
In the later sections of this chapter the application of the wavelet transform as a tool for signal smoothing and denoising using scale (smoothing) and amplitude (denoising) thresholding was presented. A review of the wavelet transform's role in surface analysis revealed that the wavelet transform has proven to be a powerful method for surface characterisation, both globally and locally. Finally a brief review of channel sedimentation processes was presented and current sediment bed-surface sampling and analysing techniques were described.

## **CHAPTER 2**

Figures

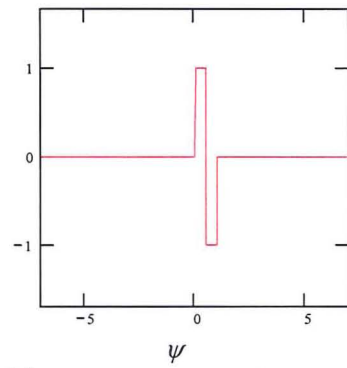


(a) A fractional Brownian motion ( $fBm$ ) signal.

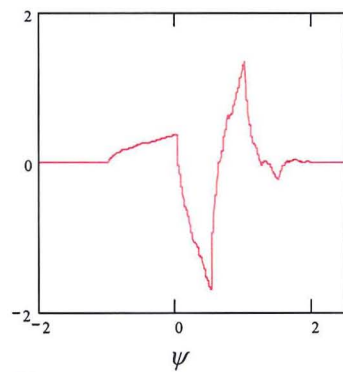
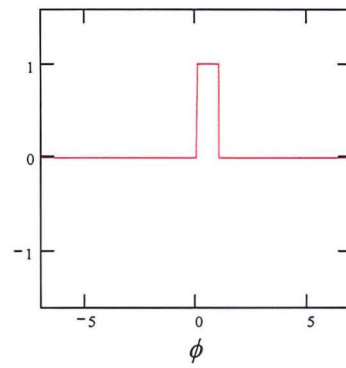


(b) The wavelet transform coefficients corresponding to the  $fBm$  signal. (The location of the coefficients corresponding to each scale  $m$  are shown.)

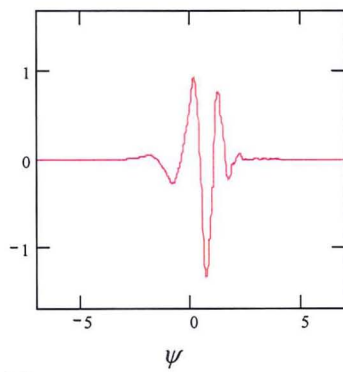
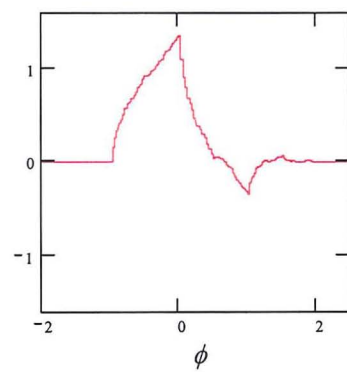
**Figure 2.1** Decomposition of a fractional Brownian motion ( $fBm$ ) signal.



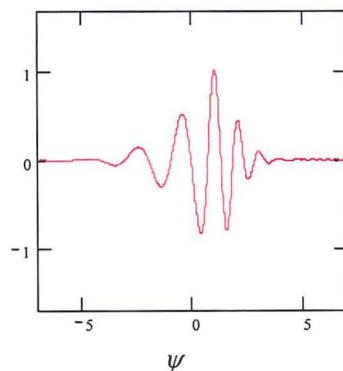
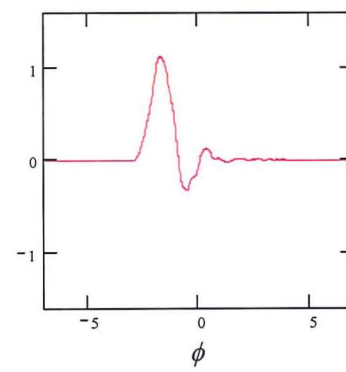
(a) Daubechies 2 wavelet



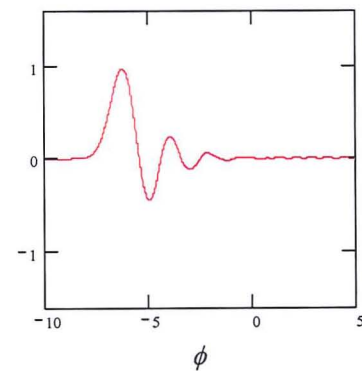
(b) Daubechies 2 wavelet



(c) Daubechies 8 wavelet

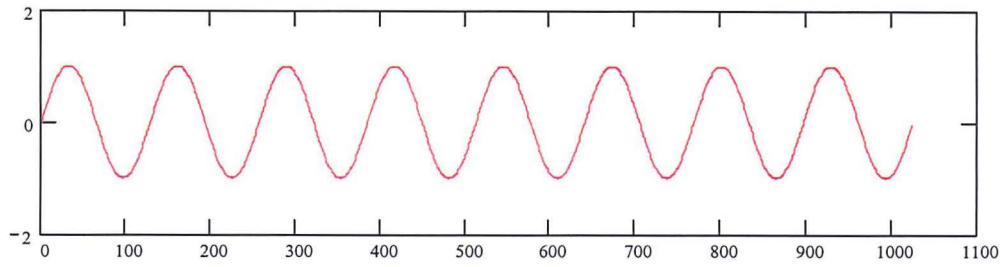


(d) Daubechies 20 wavelet

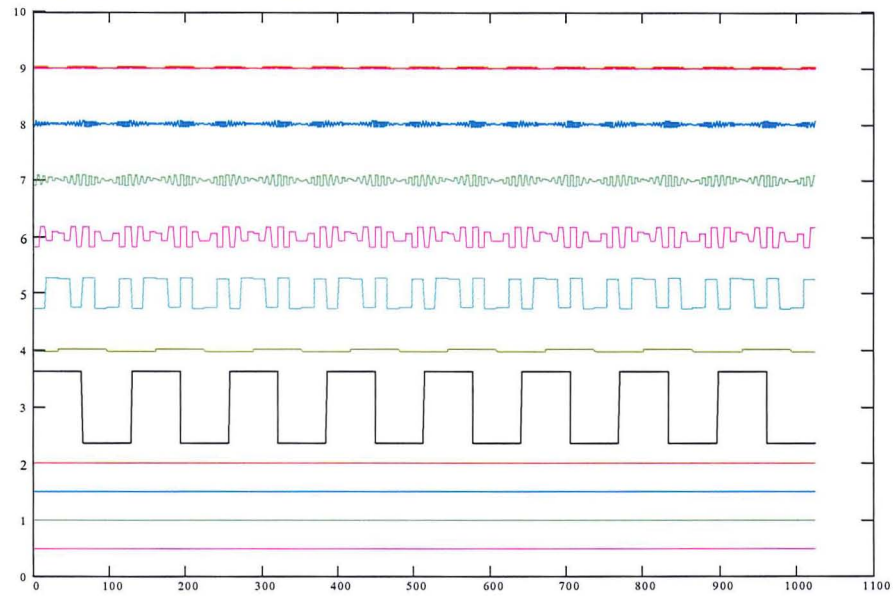


Selected wavelet functions, ( $\psi$ ) (left) and their associated scaling functions, ( $\phi$ ) (right).

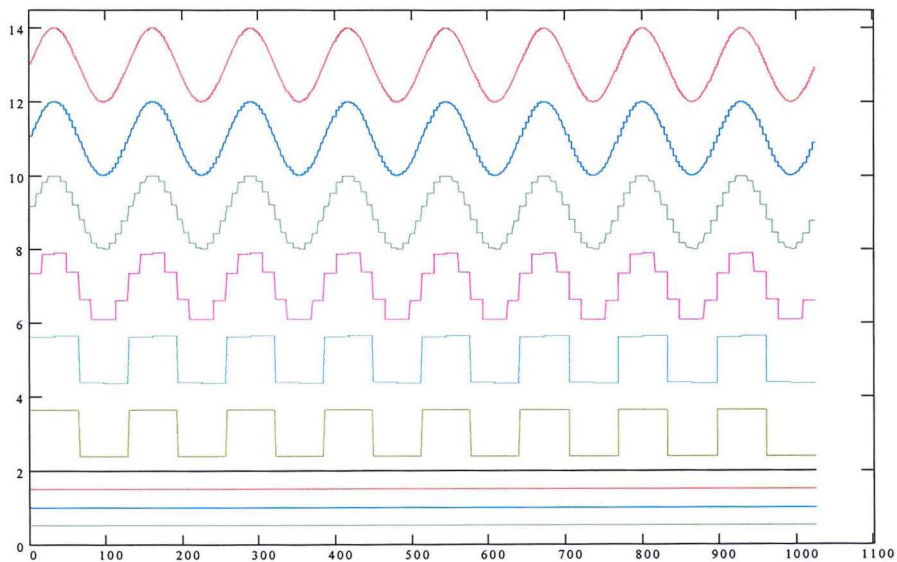
**Figure 2.2** Examples of Daubechies wavelet and scaling functions.



(a) Original sinusoidal signal.

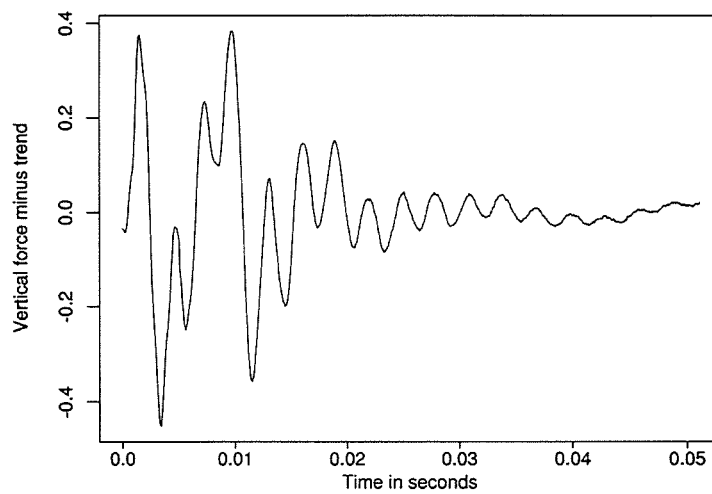


(b) The wavelet details of the signal.

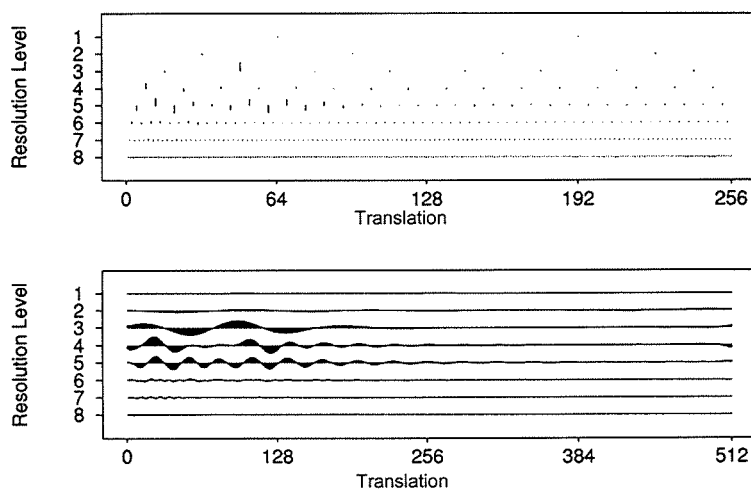


(c) The approximation of the signal

**Figure 2.3** Haar decomposition of a sinusoidal signal.



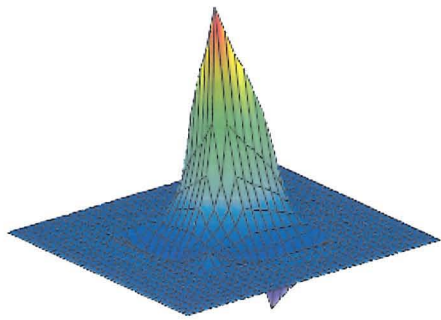
(a) Original signal



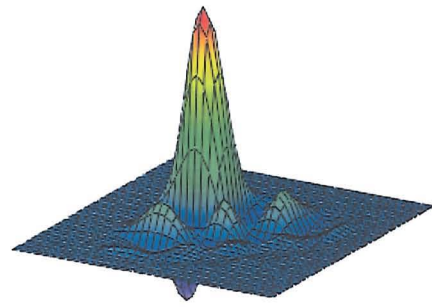
(b) Decomposition using the DWT (top) and the SWT (bottom).

**Figure 2.4** The difference between the DWT and the SWT decomposition (from Nason and Silverman, 1995).

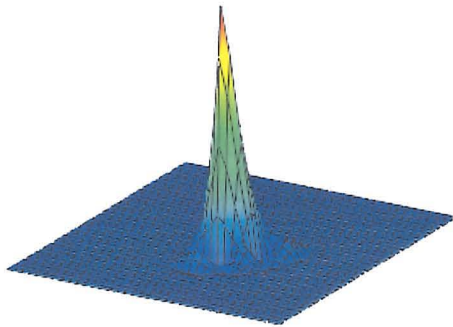




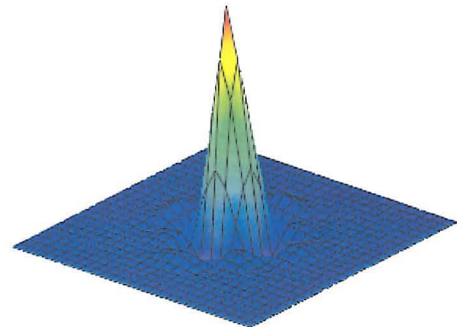
(a) Daubechies (4) wavelet



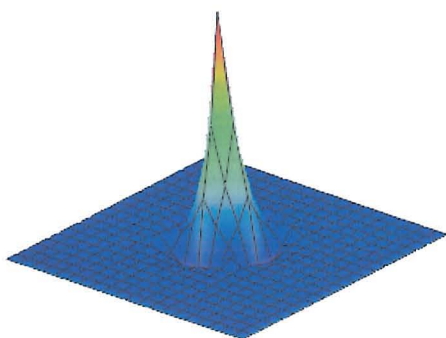
(b) Daubechies (12) wavelet



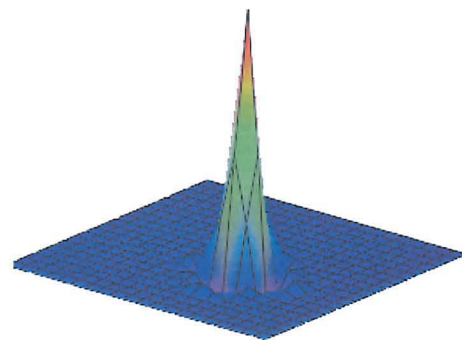
(c) Symmlet (6) wavelet



(d) Symmlet (12) wavelet

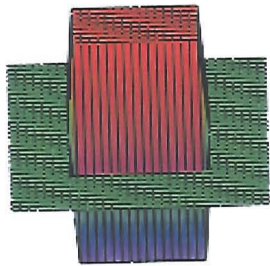


(e) Coiflet (6) wavelet

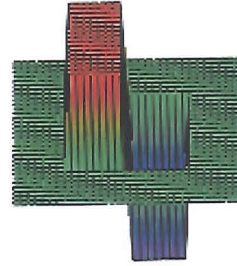


(f) Coiflet (12) wavelet

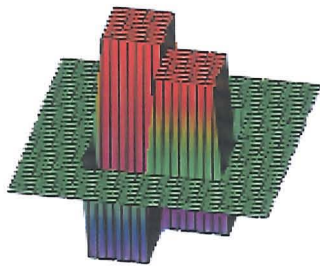
**Figure 2.5** Examples of 2-D wavelets, from the Daubechies, Symmlet and Coiflet families of wavelets.



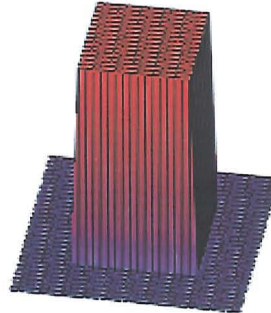
(a) Horizontal wavelet



(b) Vertical wavelet

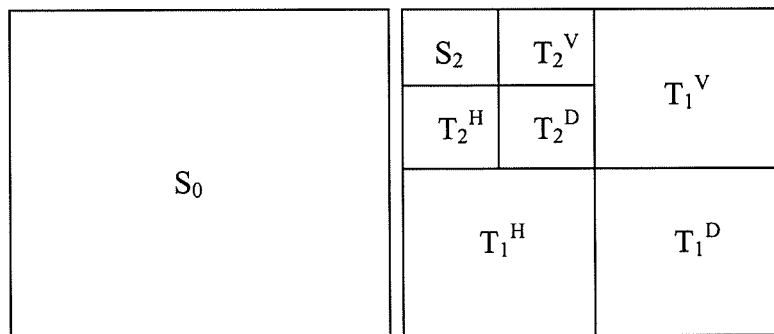


(c) Diagonal wavelet



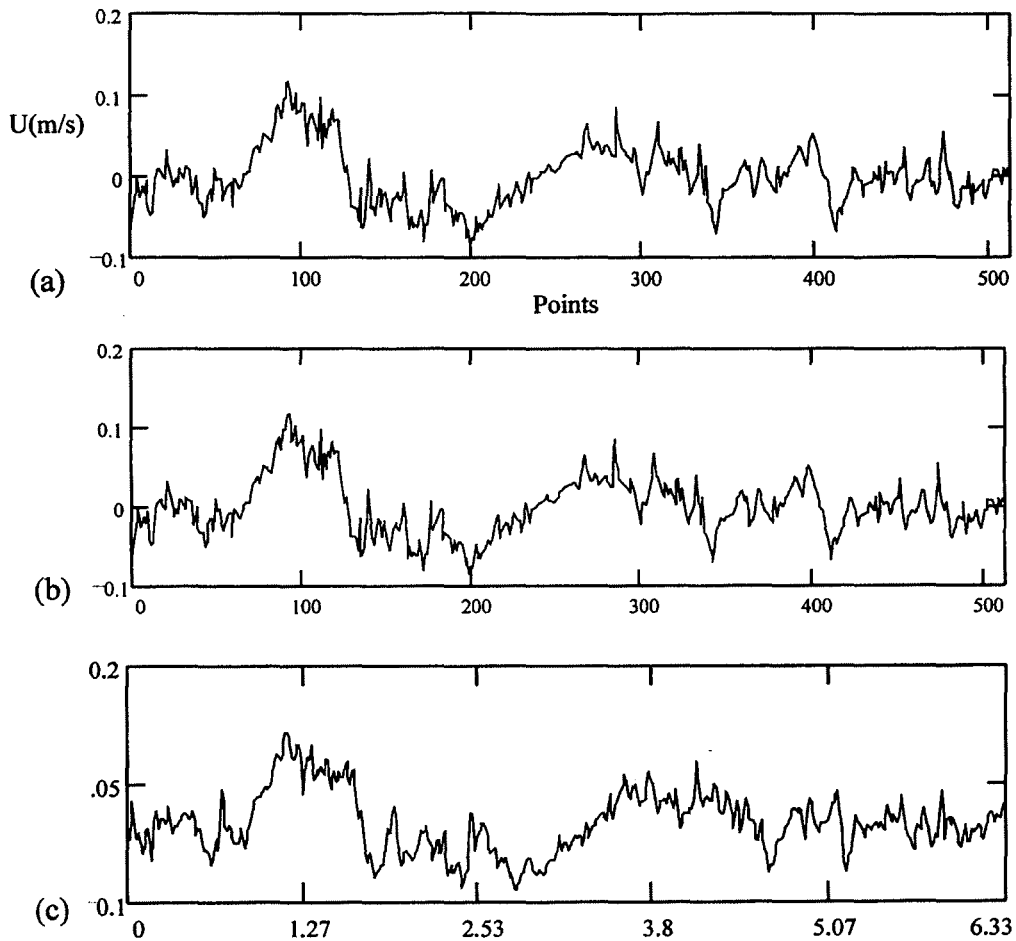
(d) Scaling function

**Figure 2.6** The wavelet functions and the scaling function for the 2-D Haar wavelet.



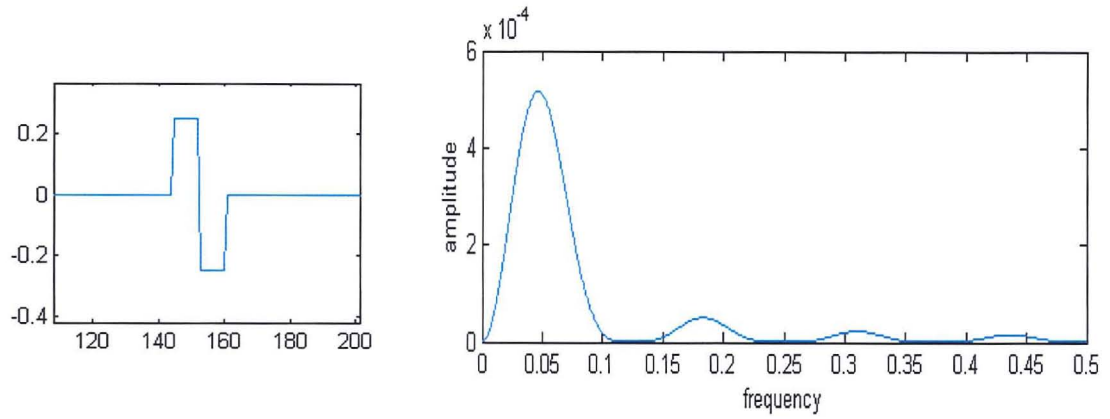
H, V and D represents the horizontal, vertical and diagonal detail respectively.

**Figure 2.7** Schematic diagram of the decomposition of data ( $S_0$ ) into two levels using the 2-D wavelet transform.

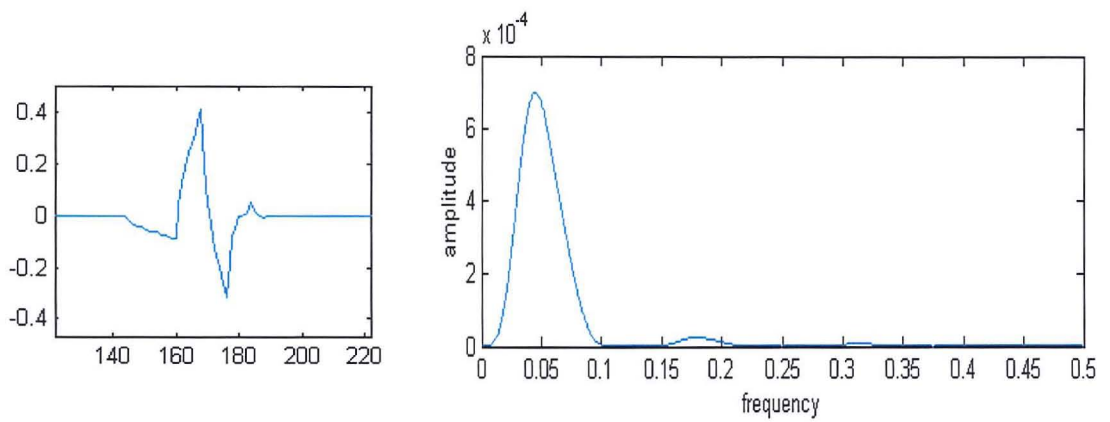


(a) The velocity signal from a shear layer in a flume, length of 512 points (6.33 sec), (b) the reconstructed signal using the DWT and (c) the reconstructed signal using the CWT.

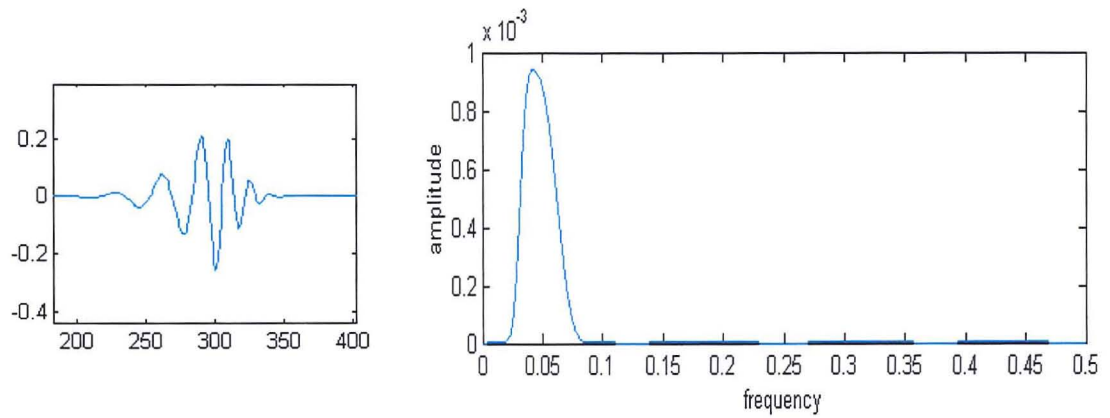
**Figure 2.8** Wavelet decomposition and reconstruction of shear layer velocity signal (from Murray, 2000)



(a) Haar wavelet (Daubechies D2 wavelet)



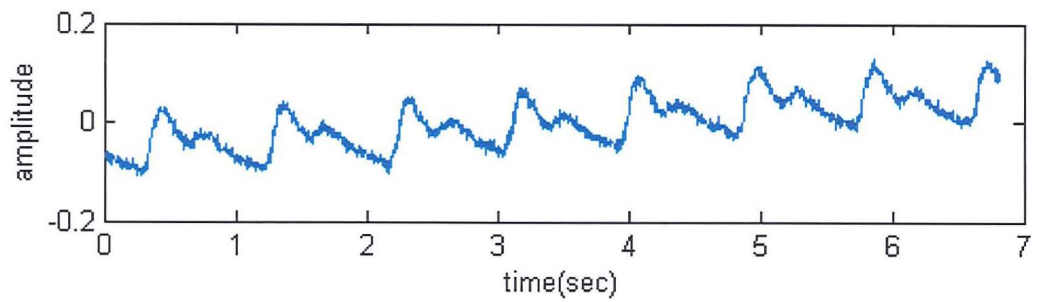
(b) Daubechies D4 wavelet



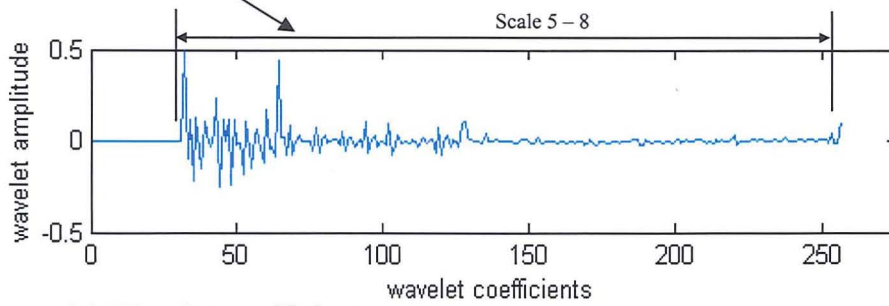
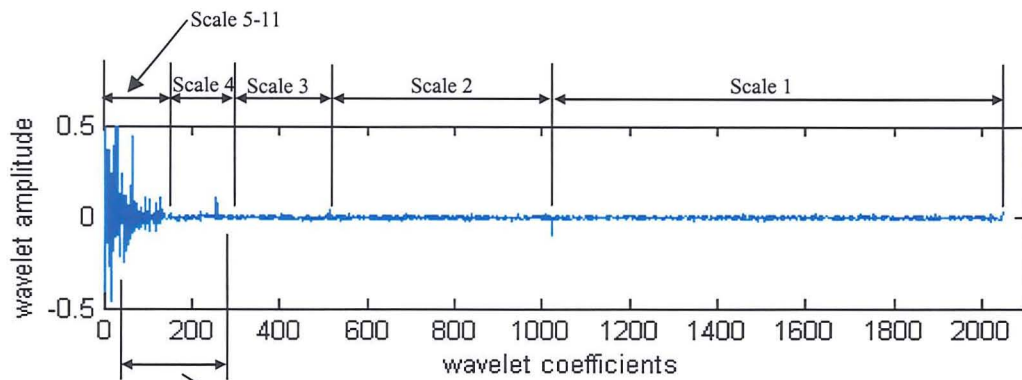
(c) Daubechies D20 wavelet

The wavelet at scale 4 (left) and its respective Fourier transform (right).

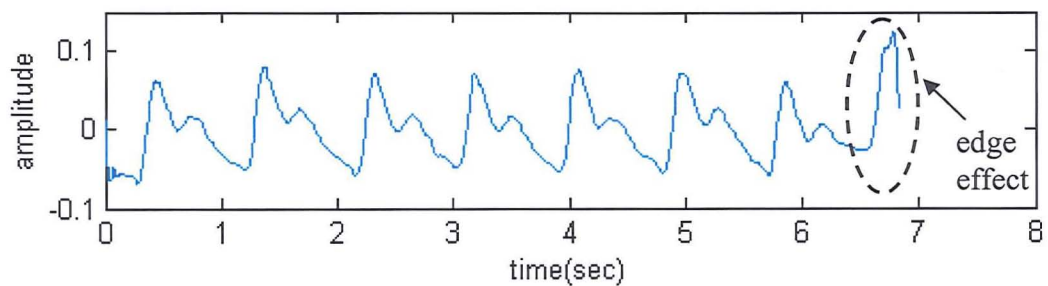
**Figure 2.9** The maximum frequency in Fourier space for the Haar wavelet and Daubechies wavelets, D4 and D20.



(a) Original signal



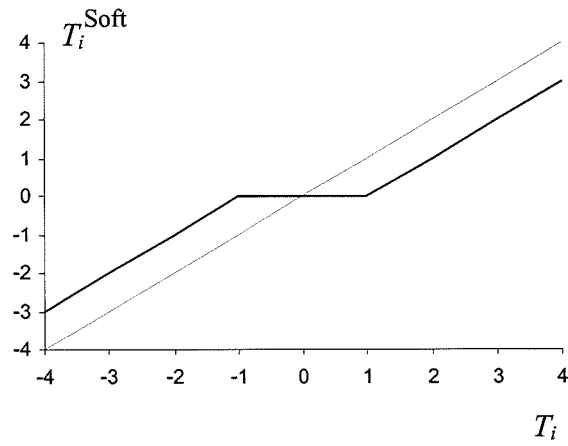
(b) Wavelet coefficients.



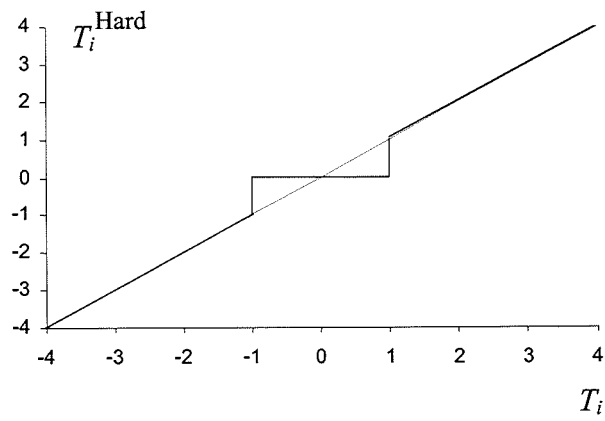
(c) Smoothed and reconstructed signal.

Scale-dependent smoothing of an oximeter signal. Removing noisy coefficients scale 1-4 and signal drift coefficients scale 9-12. (a) original signal, (b) extraction of wavelet coefficients scale 5-8 and (c) Reconstructed signal using scale 5-8.

**Figure 2.10** Smoothing of test pulse oximeter signal.

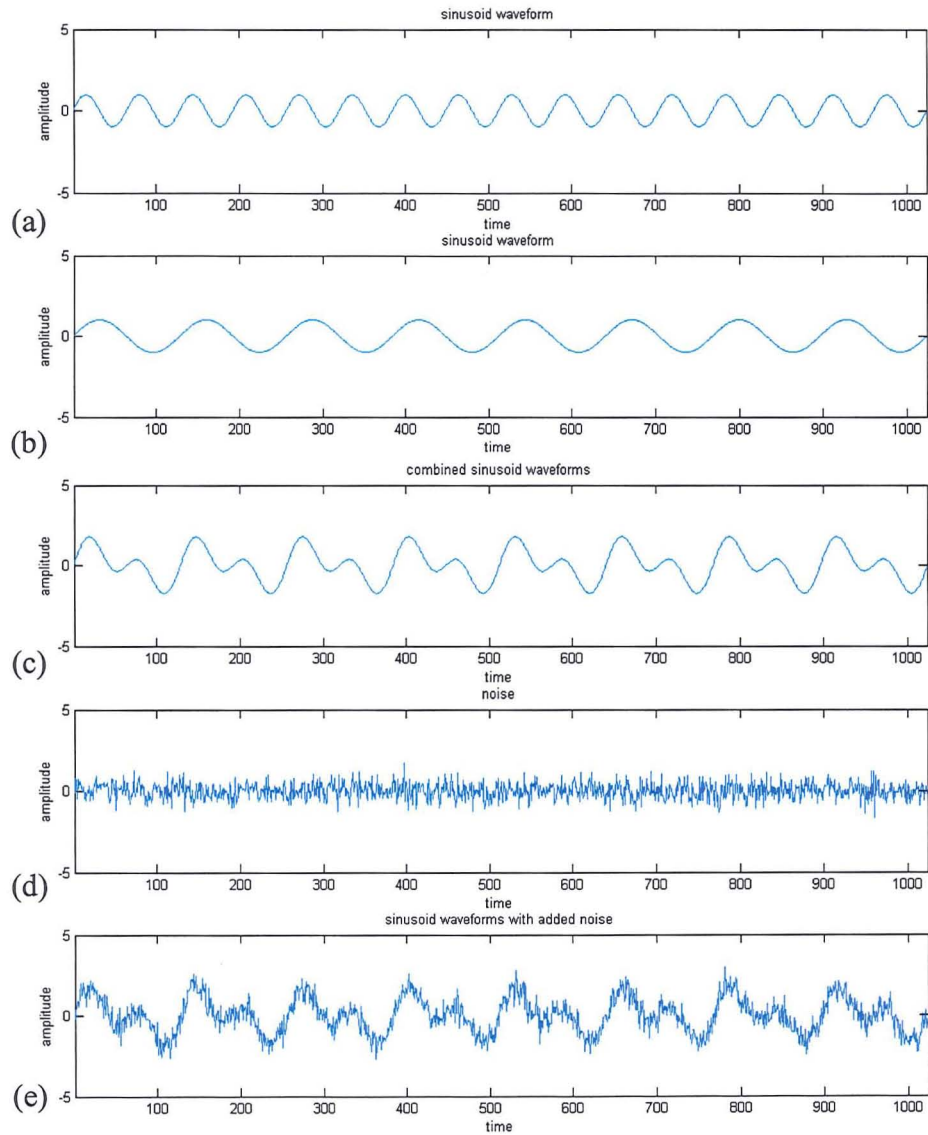


(a) Soft threshold



(b) Hard threshold

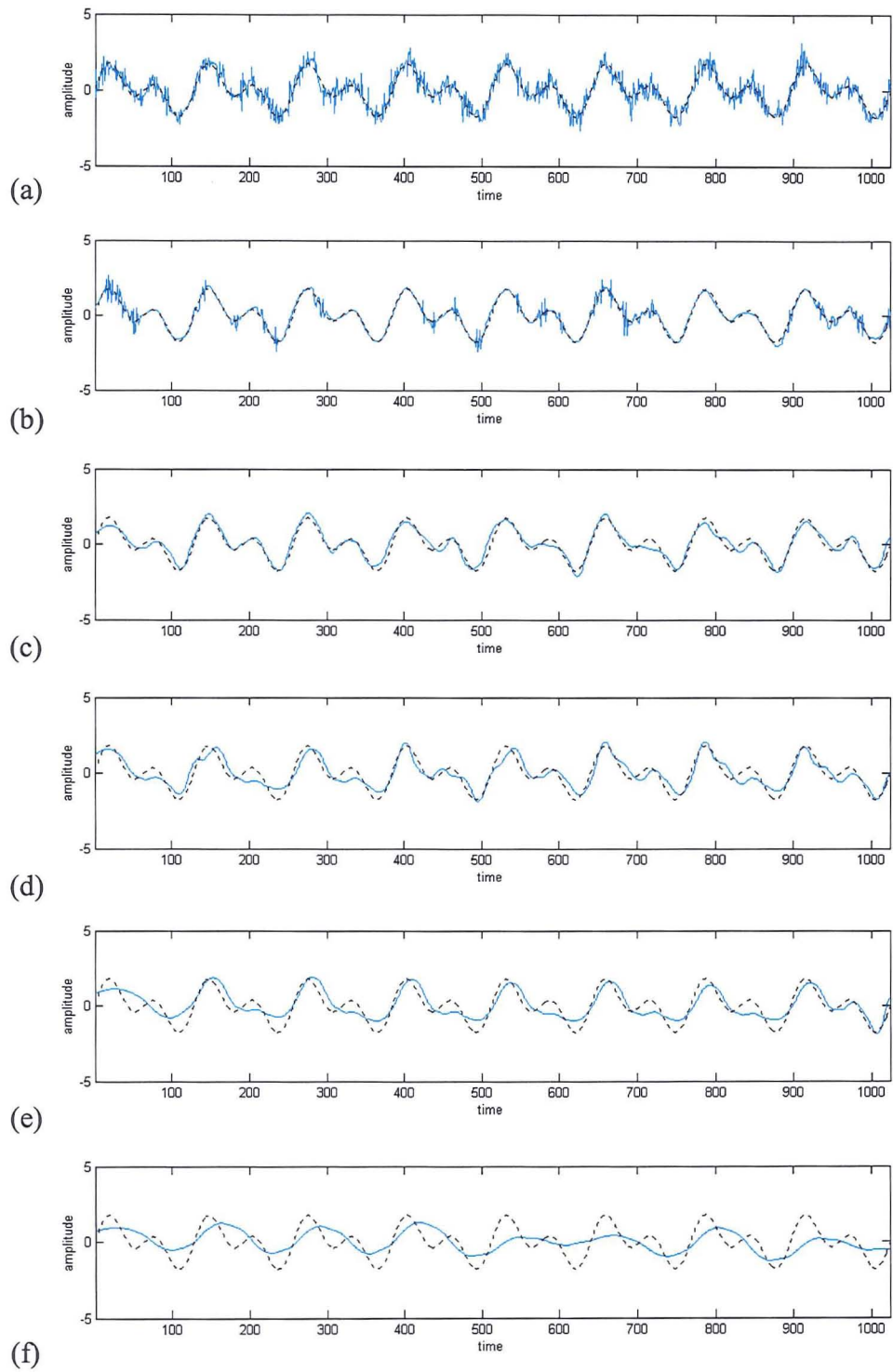
**Figure 2.11** Schematic diagram of soft threshold and hard threshold with the threshold ( $\lambda$ ) set equal to unity.



(a) The first sinusoidal waveform, (b) the second sinusoidal waveform, (c) the combination of the two waveforms in (a) and (b), (d) random noise and (e) the combined test waveform with added noise.

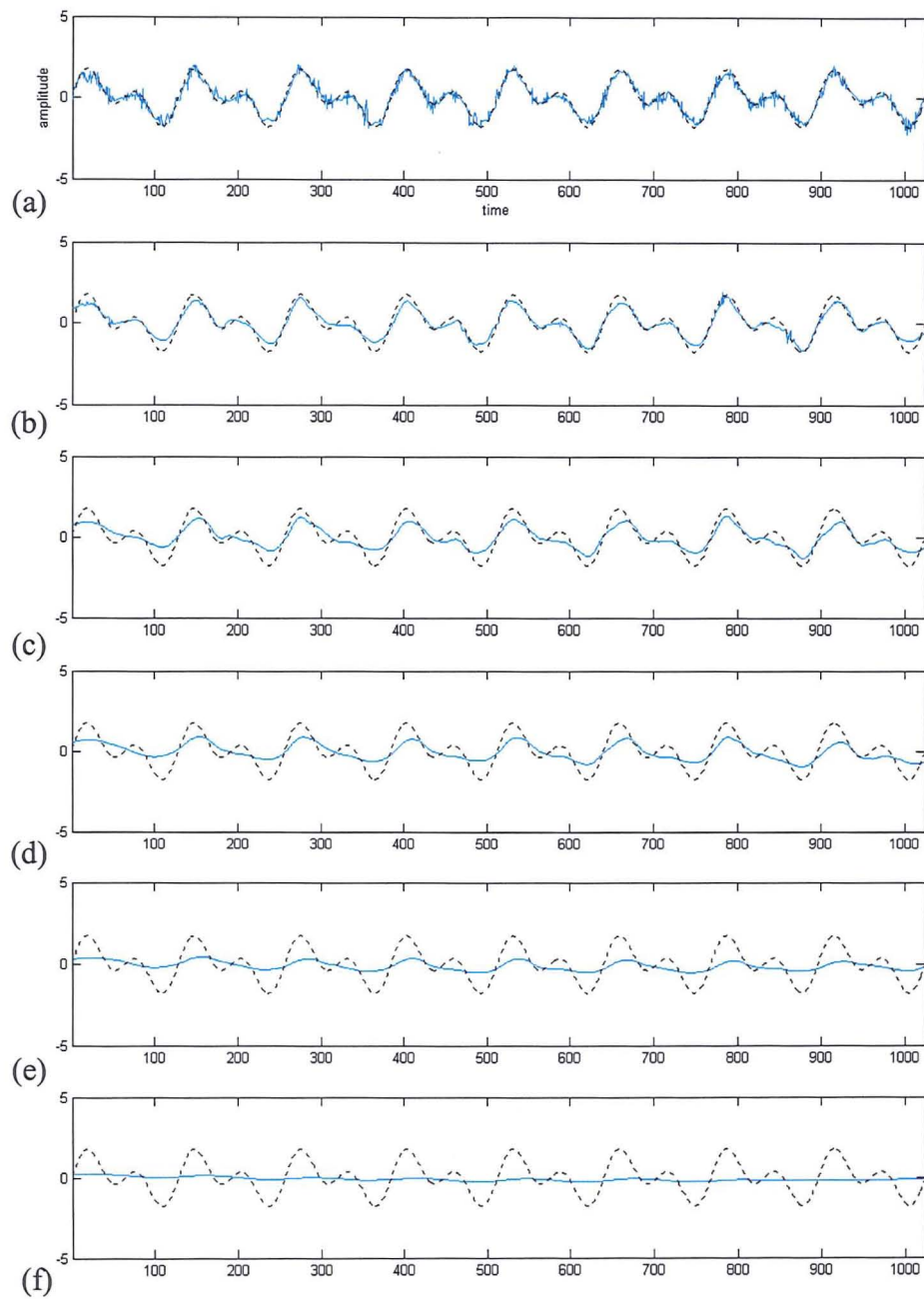
**Figure 2.12** Test waveform with added noise.





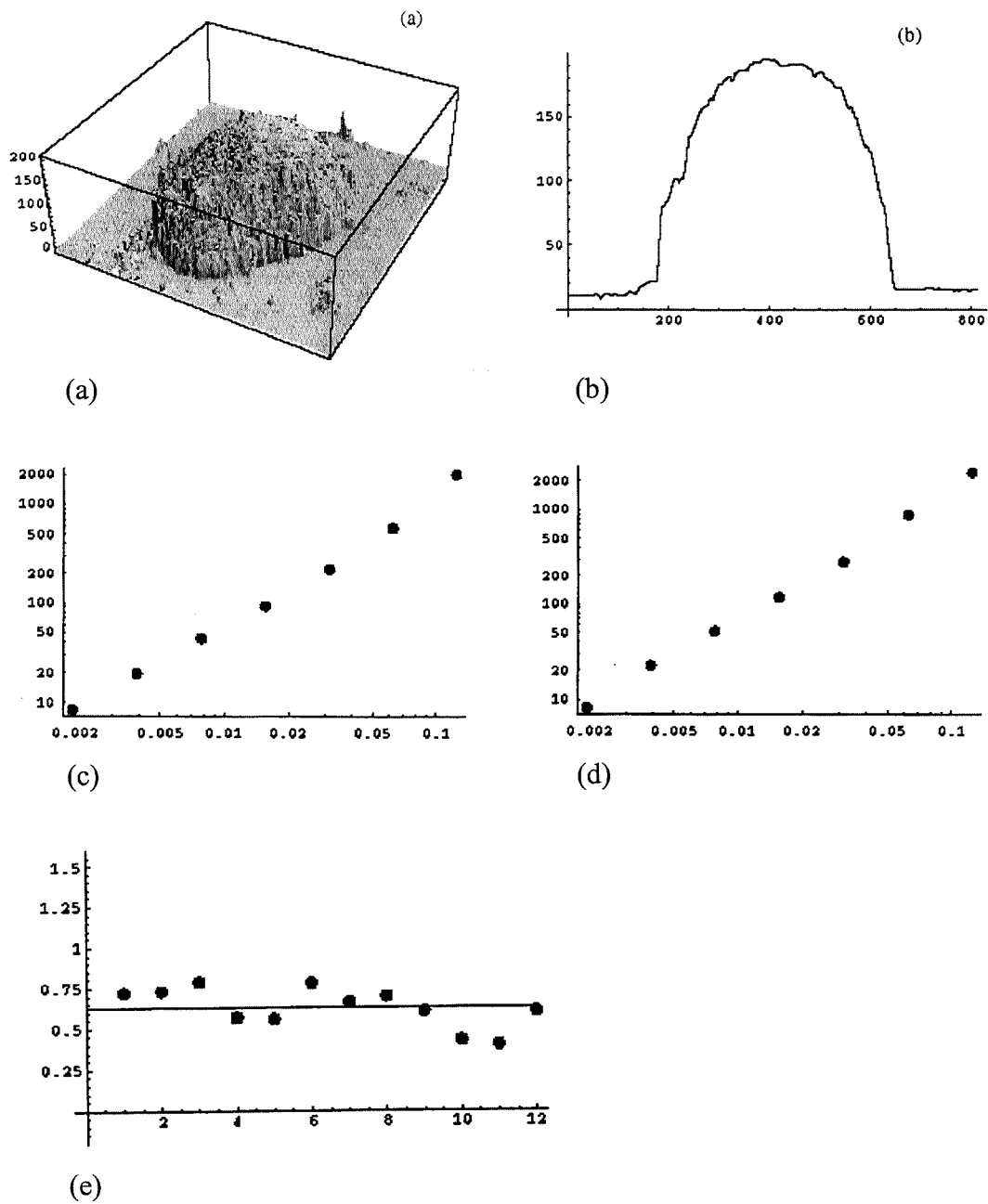
Hard threshold applied to the wavelet coefficients of the test waveform in figure 2.11. Solid line: reconstructed thresholded signal. Dotted line: original signal. Hard threshold were set to equal (a) 0.5, (b) 1, (c) 2, (d) 3, (e) 5 and (f) 7.

**Figure 2.13** Hard thresholding of the test signal.



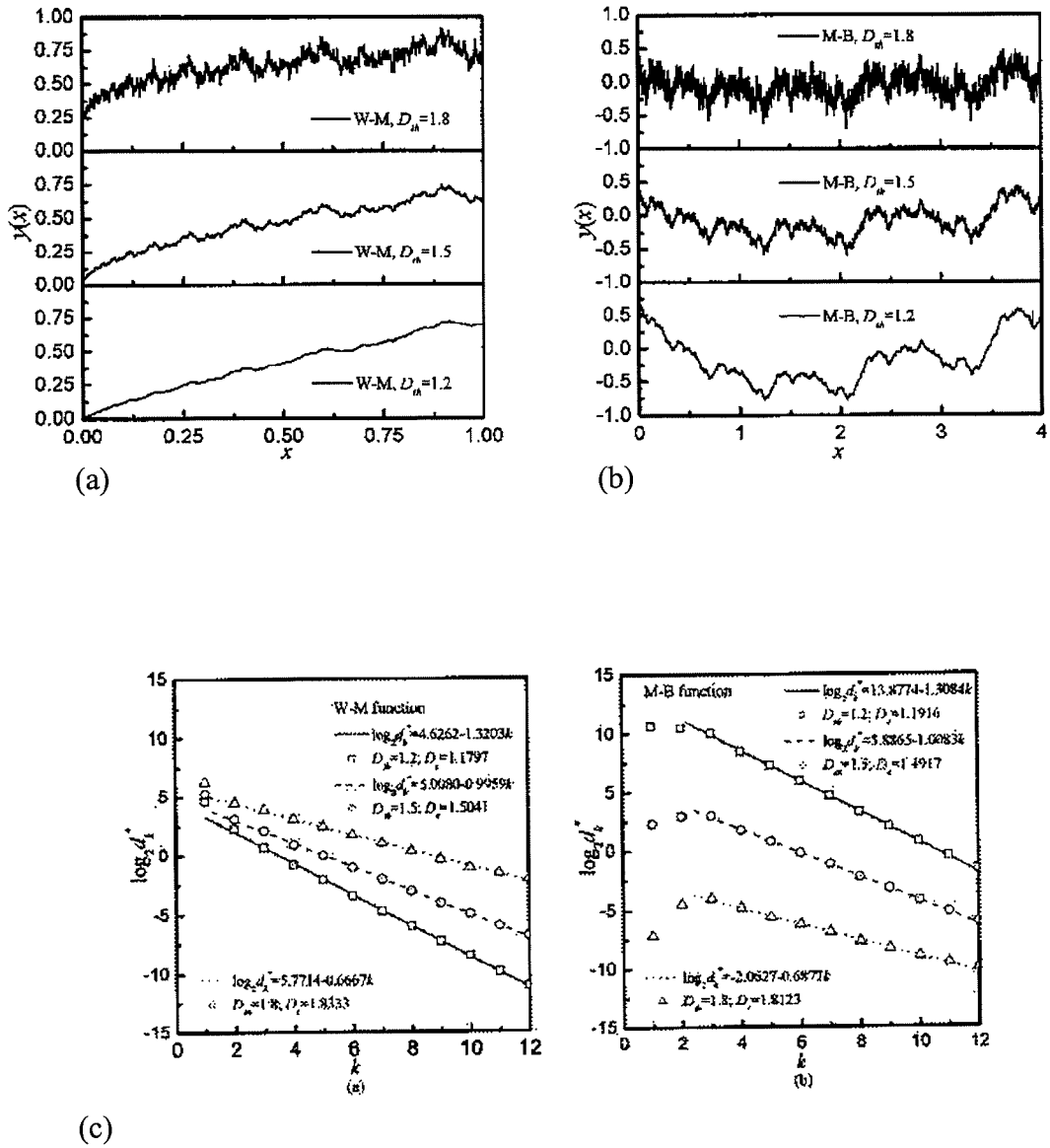
Soft threshold applied to the wavelet coefficients of the test waveform in figure 2.11. Solid line: reconstructed thresholded signal. Dotted line: original signal. Soft threshold were set to equal (a) 0.5, (b) 1, (c) 2, (d) 3, (e) 5 and (f) 7.

**Figure 2.14** Soft thresholding of the test signal.



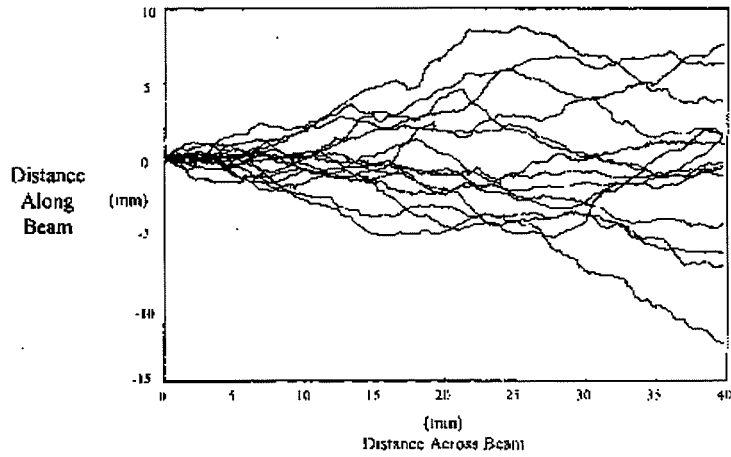
(a) An image of the corrosion pit, (b) a profile taken from the corrosion pit, (c) the log plot of the horizontal direction, (d) log plot of the vertical direction and (e) show the results of the  $H$  from analysis of several specimens in the vertical direction.

**Figure 2.15** Characterisation of corrosion pit surface applying the wavelet transform (from Frantziskonis et al, 2000).

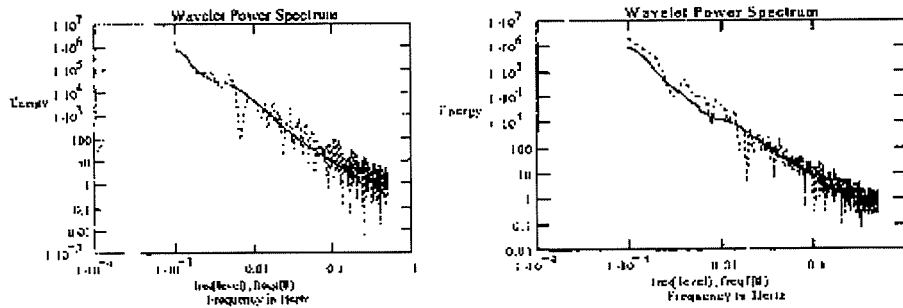


Generated fBm profiles using (a) the Weierstrass-Mandelbrot function, (b) Majumdar-Bhushan function and (c) the modulus of the wavelet coefficient plotted against the wavelet scale.

**Figure 2.16** Wavelet analysis of fBm profiles (from Wang et al, 2003).



(a) The profiles of cracked concrete.



Crack profiles 14-5 (left) and 28-6 (right)

(b) The wavelet power spectrum (solid line) for cracked concrete profiles.

**Figure 2.17** Analysis of cracked concrete profiles using the continuous wavelet transform (from Dougan et al, 2000).

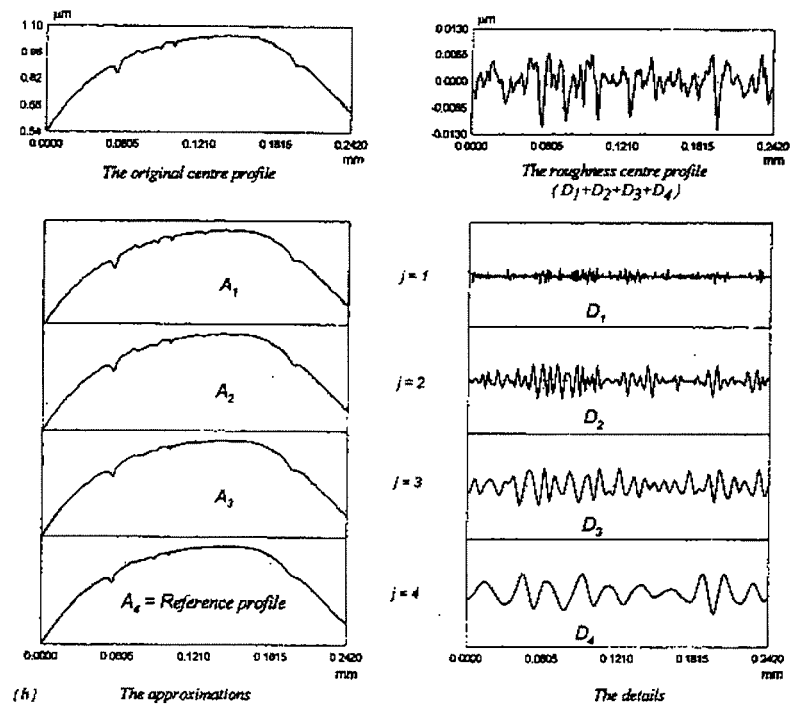


**Figure 2.18** Multiscale decomposition of a metallic femoral head (from Jiang et al, 1999).

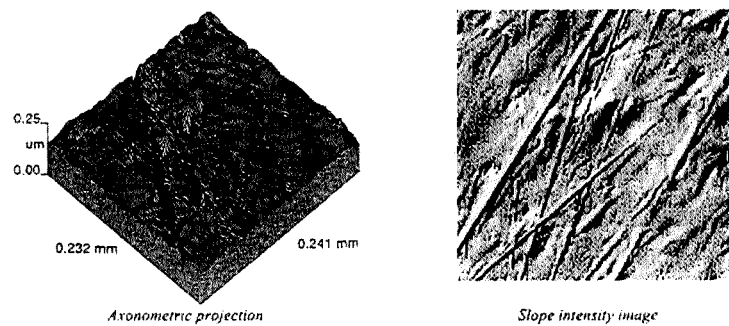


**Figure 2.19** The multiscalar features and their location of the metallic femoral head (from Jiang et al, 1999).

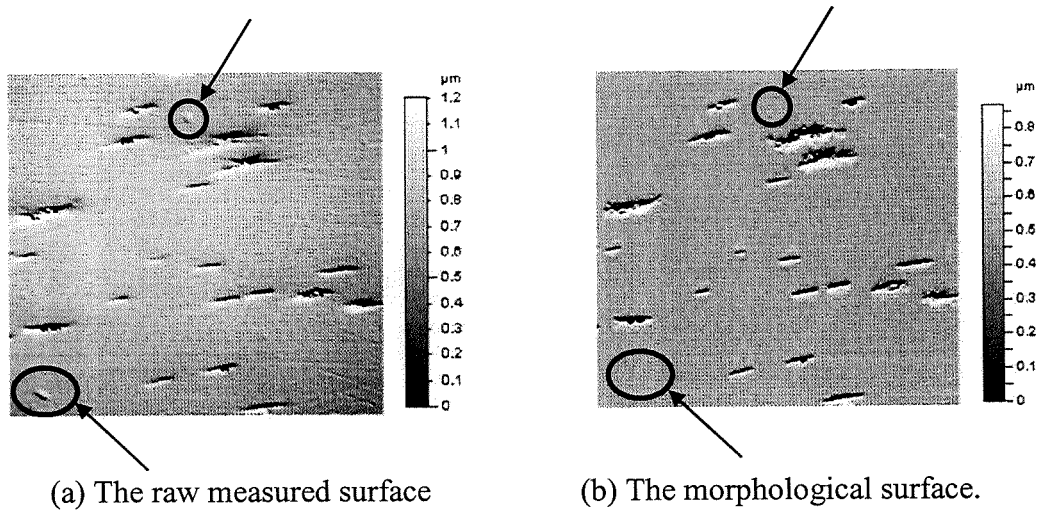
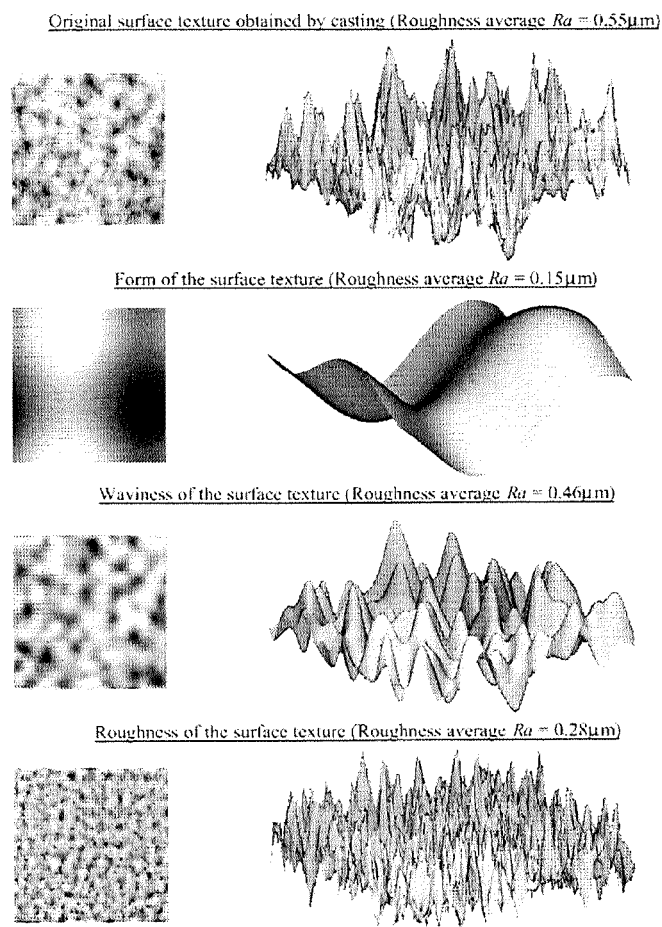
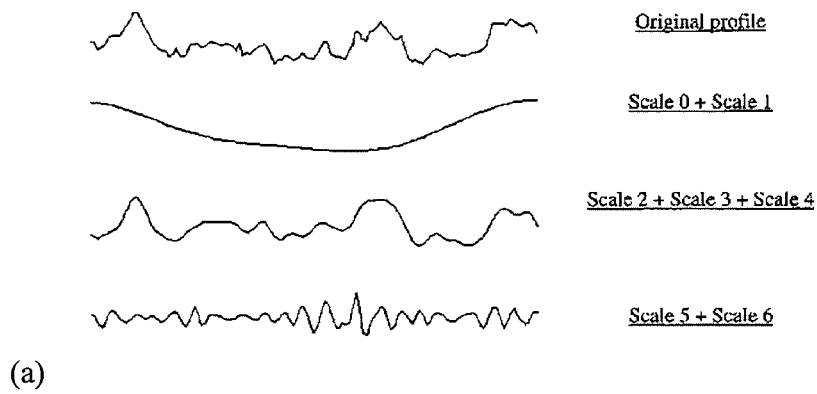


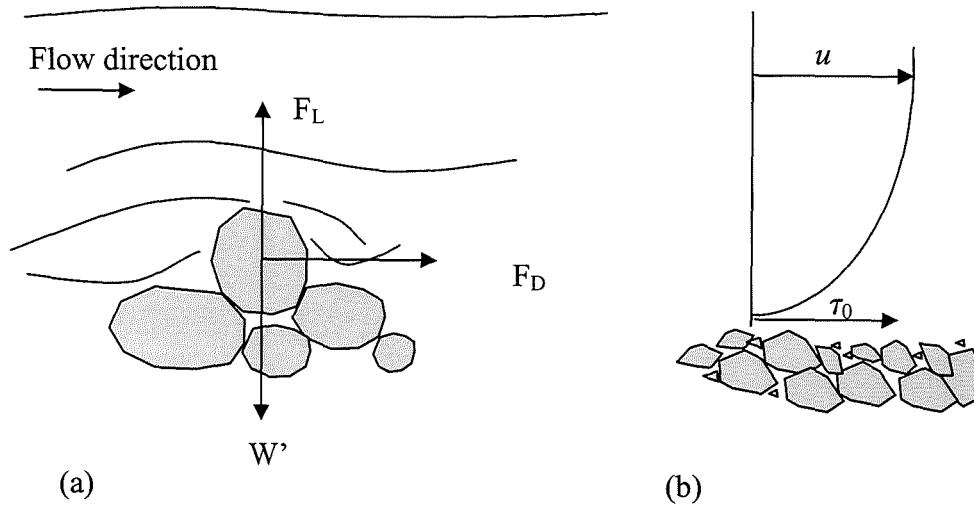
**Figure 2.20** The raw measured surface and morphological surfaces of a worn ceramic head (from Jiang and Blunt, 2001).



(a) The multiscale decomposition of surface texture profiles. (b) the decomposition of the surface into three different topographies.

**Figure 2.21** Form, waviness and roughness decomposition of a surface texture (from Jasso et al, 2002).





(a) The natural resistance to motion of the particle where  $F_L$  is the lift force,  $F_D$  is the drag force and  $W'$  is the weight of a particle. (b) the shear stress on a sediment bed surface where  $u$  is the velocity and  $\tau_0$  is the shear stress at the solid surface.

**Figure 2.22** Sediment particle movement.

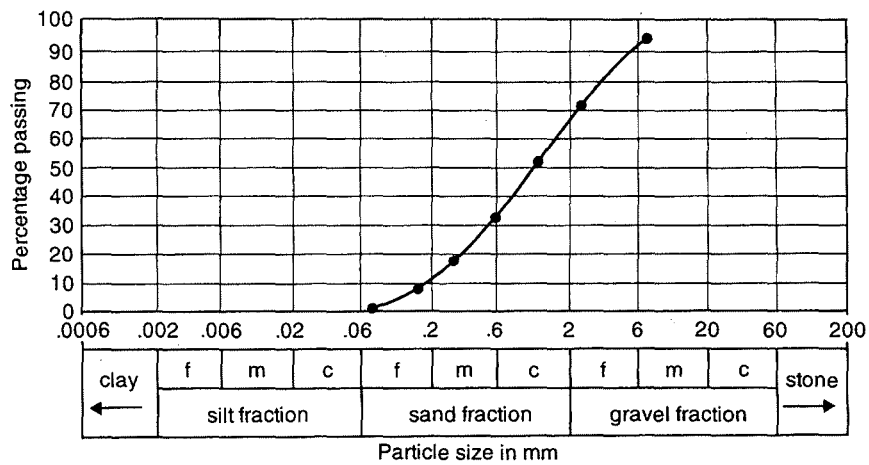
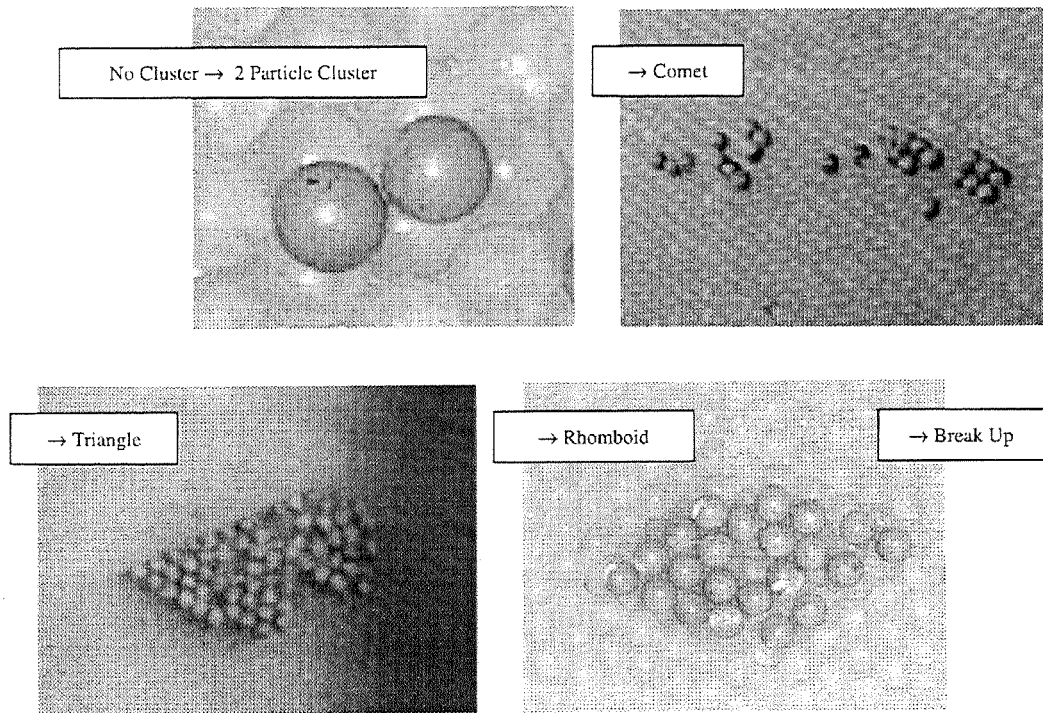


**Figure 2.23** Example of a particle size distribution (from Smith and Smith, 1998)



The clusters structures go through a formation cycle of five steps.

**Figure 2.24** Cluster formation steps in mono-sized simulated sediment particles (from Papanicolaou et al, 2003).

## **Chapter 3**

### **Algorithm development and experimental results: Characterisation of profile data**

- 3.1 Introduction**
- 3.2 Algorithm development**
  - 3.2.1 Software algorithm development and validation**
  - 3.2.2 Edge effects**
  - 3.2.3 Algorithm development edge effects – Discrete wavelet transform**
  - 3.2.4 Algorithm for edge effects – Stationary wavelet transform**
- 3.3 Experimental data analysis - fractals**
  - 3.3.1 Introduction fractional Brownian motions (*fBm*)**
    - 3.3.1.1 Fractal theory**
  - 3.3.2 Analysis of synthetic data using the DWT**
  - 3.3.3 Analysis of synthetic data using the SWT**
- 3.4 Experimental data analysis - Cracked concrete profiles**
  - 3.4.1 Introduction and background**
  - 3.4.2 Analysis of experimental concrete crack profile data - DWT**
  - 3.4.3 Analysis of experimental concrete crack profile data – SWT**
- 3.5 Analysis of medical signals using the discrete wavelet transform**
  - 3.5.1 Smoothing and removal of signal drift in a pulse oximeter signal**
  - 3.5.2 Wavelet analysis of electrocardiogram (ECG) signals**
- 3.6 Discussion and chapter summary**

# CHAPTER 3

## ALGORITHM DEVELOPMENT: ANALYSIS OF ONE-DIMENSIONAL DATA

### 3.1. Introduction

This chapter describes the analysis of experimental one-dimensional (1-D) data using both the discrete wavelet transform (DWT) and the stationary wavelet transform (SWT). The analysis was carried out primarily for the author to familiarise herself with the wavelet transform technique. It was necessary to know the basics of the 1-D wavelet transform method before undertaking the analysis of two-dimensional (2-D) data using the 2-D wavelet transform which comprises the main research work detailed in subsequent chapters of this thesis.

This chapter is structured as follows: section 3.2 describes the development of new algorithms to compensate for edge effects caused by large edge coefficients. Section 3.3 describes the analysis of synthetically generated test profiles (fractional Brownian motions ( $fBm$ ) profiles); section 3.4 contains the analysis of the experimental data obtained from cracked concrete profiles; section 3.5 includes preliminary work carried out on medical data, and the final section, 3.6, provides a discussion and a summary of the work contained in the chapter.

## **3.2. Algorithm development**

### **3.2.1. Software algorithm development and validation**

This section contains a brief description of the development of algorithms used in the analysis in this and subsequent chapters. The analysis presented in this thesis has been undertaken using the computer software package MATLAB R12, version 6.0. This is a powerful data analysis tool integrating both computation and visualisation of data. With the software a range of toolboxes are available in areas of for example; mathematics, financial modelling, control system design, neural network, signal and image processing. The author employed the wavelet toolbox in her analysis. All the algorithms were developed using command line functions. This allowed for easy extraction of the transformed data components (i.e. the wavelet coefficients) for further processing, including calculation of standard deviation, energy content and the application of wavelet thresholding methods. To validate the code prior to the analysis of the experimental data, simple test data were run through the developed algorithms. These contained only one, or a few, non-zero coefficient(s) set to unit values that allowed the author to compute the expected results. These were then compared with the result obtained from analysis. Further, synthetic data, including both fBm data and synthetic sediment surface data, with known properties were analysed and again the computed results could be compared with those expected. In addition, computer intensive processes, such as the SWT analysis, with long execution times were run as batch files. This allowed several data files to be analysed in overnight runs.

### **3.2.2. Edge effects**

In engineering practice experimental data is not infinite but is both limited in extent and discretely sampled in time. When the wavelet transform is applied to data of finite length, edge effects will unavoidably occur at the beginning and the end of the transformation. As explained in section 2.8.4, there are ways to compensate for these edge effects. In this, and subsequent chapters, the wrap-around method has been applied, where the section of the wavelet that ‘hangs off’ one end of the time series is placed back onto the other end of the data. However, due to misalignment between the two edges of the data, erroneous edge coefficients are often created in this region. This is shown schematically in figure 3.1 where the Daubechies D6 wavelet has been applied

to a signal vector using a DWT. Where the wavelet moves along the signal in discrete steps. The wavelet filter coefficients outside the signal at the beginning and end of the signal produce edge coefficients. The edge effect is carried through the transform process. The first and the last approximation coefficients for scale  $2^{m+1}$  shown in figure 3.1(b) are the edge coefficients. This is shown schematically where the 'X' symbolises the edge coefficient carried through from the previous level of the transform. For the next level,  $2^{m+2}$ , figure 3.1(c), the first two and the last two approximation coefficients are now edge coefficients, carried through from the previous level.

In general, the edge coefficients are significantly larger than the rest of the transform coefficients (as a significant discontinuity often exists between both ends of the signal), hence these erroneous coefficients will dominate the analysis. Large edge coefficients are visible in figure 3.2 where a synthetic fBm profile has been analysed using the SWT. Figure 3.2(a) shows the original synthetic (*fBm*) test profile, while figure 3.2(b) shows the original wavelet coefficients from the second scale of the transform and figure 3.2(c) shows the same coefficients but with the edge coefficients removed, i.e. only those wavelet transform coefficients unaffected by the edge are left.

This chapter presents the results from the analysis of a number of synthetic (*fBm*) and real (cracked concrete) profiles. The author was primarily interested in the amount of energy preserved at each scale of the transform. The erroneous coefficients created at the edges, cause incorrect values of scale dependent energies. This markedly affects the total energy computed at each scale. The author has, therefore, developed new algorithms to compensate for these edge effects. The algorithms for extracting pertinent coefficients at each scale of the wavelet transform are described in the following two sub-sections. Section 3.2.3 considers the removal for the edge coefficients for the discrete wavelet transform and section 3.2.4 for the stationary wavelet transform.

### **3.2.3. Algorithm development for edge effects - Discrete wavelet transform**

As described in section 2.5 the translation and scaling of the discrete wavelet transform (DWT) takes place on a dyadic grid i.e. the wavelet both moves along the signal and dilates in steps which are discrete power of two. The size of the edge effect depends on the length of the applied wavelet filter.

The filter is first placed at an initial location on the signal. In the work presented herein for the Daubechies family of wavelets, the wavelet filter is initially placed on the signal at the location given by:

$$Filter = \frac{N_F}{2} - 1 \quad (3.1)$$

where  $N_F$  is the length of the wavelet filter. This is shown in figure 3.3, where the first three mother wavelets from the Daubechies family of wavelets are shown at the first two locations at the beginning of the signal. The location of the first signal value ( $=S_{0,0}$ ) is matched with coefficient  $\left(\frac{N_F}{2} - 1\right)$  of each wavelet filter. Using this relationship the author has established the number of edge coefficients produced at each side of the discrete wavelet transform corresponding to each scale of the transform. The number of edge coefficients for the Daubechies family of wavelets at each scale are given in table 3.1.

Once the number of edge coefficients for each end was determined, an algorithm to remove these coefficients from the transform was developed. Results from the analysis of synthetic and real data using the author's modified DWT algorithm are presented in sections 3.3.2 and 3.4.2.

#### **3.2.4. Algorithm development for edge effects - Stationary wavelet transform**

The sampling procedures of the stationary wavelet transform (SWT) vary from the DWT as the wavelet translates along the data 'continuously', i.e. for discrete data in steps equal to the sampling interval. Consequently, a larger number of edge coefficients are created at the beginning and end of the transformed data. The number of erroneous coefficients increases for iteration of the transform process.

To develop an algorithm for the removal of edge coefficients for the SWT, the number of edge coefficients for each level of the transform had first to be determined. This was initially done numerically using a test vector consisting of zeros, with the values at either end alternately made equal to unity or zero, depending on which edge coefficients were being computed. This is shown schematically for the Daubechies D4 wavelet in figure 3.4. Running this test signal through the SWT algorithm, the edge coefficient at

each scale were established. These are given in table 3.2. However, subsequent to studying the results shown in the table, two equations were derived to determine the number of edge coefficients at each end of the transform for the Daubechies family of wavelets. The equations are defined as follows for numbers of left and right edge coefficients respectively:

$$N_{Leftedge} = (2^m - 1) \times \left( \frac{N_F}{2} - 1 \right) \quad (3.2)$$

$$N_{Rightedge} = (2^m - 1) \times \left( \frac{N_F}{2} \right) \quad (3.3)$$

where  $N_F$  is the wavelet filter length. As with the DWT, for useful analysis the author requires only those coefficients at each scale that are unaffected by the edges. Therefore, the above relationships are used in the modified SWT algorithm to remove the edge coefficients at the beginning and the end of the transformed data. Results from the analysis of synthetic and real data using the modified SWT are presented in sections 3.3.3 and 3.4.3.

### 3.3. Experimental data analysis - Fractals

#### 3.3.1. Introduction fractional Brownian motion (*fBm*)

Fractals were brought to the forefront of data analysis by Mandelbrot in the 1960s (Mandelbrot and Van Ness, 1968; Mandelbrot and Wallis, 1969). Fractals have very simple scaling laws and Mandelbrot proposed that they could be used to describe many real objects and processes (Mandelbrot et al, 1984). Fractals have since been applied to model a large variety of physical phenomena, including for example; DNA sequences, the structure of clouds, radar imagery, risk analysis, landscape surfaces, financial data, image textures, fluid turbulence, ocean waves and cracked concrete profiles. See for example the paper by Addison and Ndumu (1999), which discusses the connection between fractional Brownian motion (*fBm*) and a variety of diffusive processes. The authors showed that fractal *fBm*'s could be used to describe many engineering applications and included both synthetic and experimental data.



### 3.3.1.1. Fractal theory

Fractional Brownian motion (*fBm*) is a random fractal function. It is classified according to the Hurst exponent ( $H$ ) which describes how rough the fBm is. As a time-series becomes smoother the Hurst exponent tends towards unity. FBm traces are classified as anti-persistent if  $0 < H < 0.5$  and persistent if  $0.5 < H < 1.0$ . If  $H$  is equal to 0.5 it is known as neutrally persistent and this special case relates to ordinary Brownian motion (Einstein, 1905).

As the fBm diffuses through time, the standard deviation,  $\sigma_c$ , scales with time as  $\sigma_c \propto t^H$ . Hence, if  $(\sigma_c)^{1/H}$  is plotted against time, a linear relationship is obtained where the slope is equal to twice the fractional diffusion coefficient,  $K_f$ : a measure of fBm spreading.  $K_f$  is defined as:

$$K_f = \frac{(\sigma_c)^{1/H}}{2t} \quad (3.4)$$

In engineering practice, neither  $K_f$  nor  $H$  may be known, in which case they can both be determined from the logarithmic plot of  $\sigma_c$  against time. The best fit line through the data has a slope equal to  $H$  and the point where the line crosses the vertical axis is equal to  $H \log(2K_f)$ , (Addison, 1997). A common method to determine  $H$  for an fBm profile is using the Fourier power spectrum, as the spectrum is a function of the frequency dependent  $H$ :

$$P_F(f) \propto f^{-(2H+1)} \quad (3.5)$$

From this relationship we can see that  $H$  can be determined from the slope of the logarithmic plot of the power against the frequency. The discrete wavelet transform can be used to determine  $H$  by plotting the variance of the wavelet coefficients at each scale against the scale,  $m$ . The variance is defined as:

$$\langle T_{m,n}^2 \rangle = \frac{\sum_{n=0}^{2^M-m-1} (T_{m,n})^2}{2^{M-m}} \quad (3.6)$$

Addison (2002, chapter 4) derives the relationship between equation 3.6 and the wavelet power spectra as  $P_W(f_m) \propto \langle T_{m,n}^2 \rangle_m$ . Combining these expression we obtain:

$$\langle T_{m,n}^2 \rangle_m \propto a_m^{(2H+1)} \quad (3.7)$$

where  $a$  is the wavelet scale. In the literature, the variance is often written as  $\sigma_m^2$  therefore:

$$\sigma_m^2 \propto a_m^{(2H+1)} \quad (3.8)$$

The discrete wavelets used here scale in proportion to  $2^m$ , hence taking the base 2 logarithm on each side of the expression gives the following equation:

$$\log_2(\sigma_m^2) = (2H + 1) + \text{constant} \quad (3.9)$$

where the constant depends on both the wavelet used and the Hurst exponent. Plotting the variance at each scale against the scale, the Hurst exponent can be determined from the best-fit line through the data. Figure 3.5 shows the analysis of an fBm profile with a known  $H$  of 0.55. The fBm profile plotted in figure 3.5(a) was analysed using the DWT, employing the Haar wavelet as the analysing wavelet and transforming the profile into 10 detail levels. The variance  $(\sigma_m)^2$  for each of the detail levels of the transform was computed and plotted against the scale index,  $m$ . This is shown in figure 3.5(b). The expected slope for this fractal curve is  $(2H + 1) = 2.10$  and the slope obtained from the plot was 2.13. The difference in the computed slope and the actual slope of the profile may be due to the way the best-fit line is fitted through the data. For this profile the author fitted the line by eye. At large scales, due to the correspondingly large size of the discrete wavelets, only a few transform coefficients are produced. Thus, these scales (having only a few coefficients) may not be representative of the actual scaling property of the analysed data. Therefore, the larger scales were ignored and the best-fit line was fitted through the remaining values (scale  $m=1-6$ ) of the data.

In a further study, fBm-profiles with known Hurst exponents ranging from  $H=0.1$  to  $H=1.0$  were analysed. One hundred fBms of each value of  $H$  were analysed. The profiles are shown in figure 3.6. Each of the 100-trace sets, were generated using 1024 points. The code for generating the fBm profiles is found in appendix A program *fBmgen.m*. The analysis of the data is described below in section 3.3.2 (DWT) and 3.3.3 (SWT).

### 3.3.2. Analysis of synthetic data using the DWT

The calibration of the analytical techniques using the discrete wavelet transform was conducted using the generated fBm profiles in figure 3.6. The analysis was performed using the Daubechies D4 mother wavelet, which has 4 filter coefficients. Table 3.1 shows that the D4 wavelet produces one edge coefficient at both the beginning and the end of the data at each scale of the transform. The coefficients causing the edge effects are removed from the transform, leaving the ‘true’ profile components. Program *fBm\_dwt.m* in appendix A contains the algorithm for the DWT analysis of the fBm profiles.

The wavelet transform was modified to account for edge coefficients as described in section 3.2.3. The variance of the scale related wavelet coefficients were plotted against the scale for each profile, as shown in figure 3.7. The mean curve is then calculated from these plots from which the scaling properties can be determined using equation 3.9 to find the Hurst exponent ( $H$ ). The slope of the best-fit line was then calculated using the ‘least squares’ method. The equation for the best-fit line provides the slope from which  $H$  was determined. The results of the analysis are tabulated in table 3.3(a). The results are discussed at the end of the next section.

### 3.3.3. Analysis of synthetic data using the SWT

As stated in section 2.6 the DWT provides poor resolution to the analysis due to its sampling procedure using a dyadic grid. To increase the resolution, the stationary wavelet transform (SWT) was applied to the analysis of the data. The SWT keeps the scaling of the wavelet in discrete steps but moves along the data continuously, therefore the spatial resolution of the data increases.

To investigate the accuracy of the results using the SWT the fBm profiles in figure 3.6 were analysed using the SWT. The 100 fBm profiles were interrogated using the same mother wavelet used for the DWT: the D4 wavelet. The wavelet transform coefficients were modified to remove edge coefficients as described in section 3.2.4. Program *fBm\_swt.m* in appendix A contains the algorithm for the SWT analysis of the fBm profiles. Using equation 3.6 the variance for the modified wavelet coefficients were

determined and are plotted against the scale,  $m$ . These plots are shown in figure 3.8. The scaling properties,  $H$ , were determined from the best-fit line slope of the data. The results from the analysis are presented in table 3.3(b).

The wavelet transform proved useful in determining the scaling properties characterised by the Hurst exponent ( $H$ ) for fBm-profiles. The results from the analysis of the profiles are close to the actual value of  $H$  for both the DWT and the SWT methods for profiles in the range  $H=0.3$  to  $0.8$ . However, for  $H$  values less than  $0.2$  and  $H$  values larger than  $0.9$ , the accuracy of the results decreases significantly. For  $H=0.1$  the difference between actual  $H$  and the calculated  $H$ , 50% for the DWT and 73% for the SWT. Similar for  $H=1.0$  are -34% for the DWT and -34% for the SWT. In the research carried out here, the wavelet transform methods do not produce accurate results for these regions. This has also been concluded by Qu (1999), who, through her work on fractional Brownian motions determined that  $H$  can only be established with any reliable accuracy for  $H$  values within the range  $0.2-0.9$ .

### **3.4. Experimental data analysis - Cracked concrete profiles**

#### **3.4.1. Introduction and background**

The cracked concrete profiles analysed in this part of the preliminary study were generated by Dougan (2002), who applied fractals to describe the geometry of concrete fractures.

The concrete beam specimens were made with “Ordinary Portland Cement CEM I 42,5N” (OPC) defined in BS EN 197-1 (2000), with both fine aggregate and crushed rock aggregate no larger than 20mm in size which comply to the grading envelopes defined in BS 882 (1983). The beams were cast in blockboard moulds to give a smooth finish to the beam surface, hence, it was possible to generate clearly defined fracture profiles. Three different sizes of beams were studied:

small size - 80mm across  $\times$  60mm deep  $\times$  165mm long,

medium size - 80mm across  $\times$  120mm deep  $\times$  330mm long, and

large size - 80mm across × 240mm deep × 660mm long

The concrete specimens were subjected to 3 point bending until failure in flexure where a tension crack appears on the bottom face of the beam. The fracture was perpendicular to the longitudinal bending force on the specimen. The fracture profiles on each side of the specimen were photographed using a digital camera. The digital image was transferred to a computer where erroneous image-data could be removed. A specially developed algorithm, differentiating between light and dark pixels within the image was used. This program enables the separation of the crack profile from its surroundings as a number of pixel co-ordinates. Further information concerning the gathering of the experimental data can be found in Dougan (2002).

The profiles analysed in this study included 25 profiles from the small beams, 24 profiles from the medium beams and 20 profiles from the large beams.

#### **3.4.2. Analysis of experimental concrete crack profile data - DWT**

The same analysis method calibrated using the  $fBm$  profiles, was applied to the cracked concrete profile data. DWT analysis was carried out to determine the scaling properties as characterised by the Hurst exponent,  $H$ . The cracked concrete profile data was transformed into 10 detail levels using a Daubechies D4 wavelet. The transform was modified as described in section 3.2.3 in order to remove the large edge coefficients at each scale. The algorithm for the analysis of the concrete profiles using the DWT can be found in appendix A (program *prof\_dwt.m*). The variance of the modified wavelet coefficients at each scale was plotted against the scale. An example of one of the cracked concrete profiles is shown in figure 3.9. The scale dependent variance is plotted against the scale for each profile, producing a curve close to a straight line. The Hurst exponent is determined from the best-fit line through the plot. The results from the analysis using the modified DWT are presented in table 3.4, table 3.5 and table 3.6. These compare well with the results obtained using the variable bandwidth ( $vb$ ) method of fractal analysis carried out by Dougan et al (2000).

The results indicate that using the DWT produces slightly higher values of  $H$  compared to those produced using the  $vb$  method. The mean Hurst exponent value using DWT is

$H=0.84\pm0.08$  for the small sized beams,  $H=0.84\pm0.10$  for the medium sized beams and  $H=0.87\pm0.08$  for the large sized beams. This can be compared with the  $vb$  method where the mean  $H$  for the beams were determined to be  $H=0.80\pm0.06$  (small sized beams),  $H=0.79\pm0.04$  (medium sized beams) and  $H=0.80\pm0.03$  (large sized beams). This produces a mean difference between the two methods of 5, 7 and 9% for the small, medium and large sized beams respectively. There is, however, no 'gold standard' measurement technique for real data and hence comment cannot be made on the relative accuracy of the methods.

### 3.4.3. Analysis of experimental concrete crack profile data – SWT

The analysis described in the previous section was repeated using SWT analysis carried out using the Daubechies D4 as the mother wavelet. The edge coefficients created by the transform process were removed as described in section 3.2.4. The variance for the  $O$ modified coefficients were then plotted against the scale and  $H$  was established from the slope of the variance-scale plot. The algorithm used in the analysis using the SWT can be found in appendix A (program *prof\_swt.m*). The results from the analysis are tabulated in table 3.4, table 3.5 and table 3.6.

It can be seen from the tables that the SWT produces higher values of  $H$  compared with the variable bandwidth ( $vb$ ) method. The mean value of Hurst exponent using SWT is  $H=0.83\pm0.06$  for the small beams,  $H=0.84\pm0.10$  for the medium beams and  $H=0.88\pm0.07$  for the large beams. Comparing these results with the  $vb$  method it can be seen that the mean difference between the two methods are 4% for the small beams, 7% for the medium beams and 9% for the large beams.

The results from analysis of the concrete profiles using the DWT and the SWT exhibit a close resemblance. The mean  $H$ 's were found to be; 0.84, 0.84 and 0.87 for the small, medium and large sized beams respectively using the DWT and 0.83, 0.84 and 0.88 for the small, medium and large sized beams respectively using the SWT. These are close to the expected Hurst exponent values which for a crack concrete profile would be around  $H=0.8$ , (Issa and Hammad, 1993, 1994; Chiaia et al, 1998; Addison et al, 1999; Dougan et al, 2000)

### **3.5. Analysis of medical signals using the discrete wavelet transform**

#### **3.5.1. Introduction**

This section outlines research undertaken by the author to analyse two different types of medical signals. In particular it details the smoothing of pulse oximeter signals and the analysis of ECG (Electrocardiogram) signals. These were two convenient in-house signals with which to test the author's wavelet analysis methods.

#### **3.5.2. Smoothing and removal of signal drift in a pulse oximeter signal**

The method of scale dependent thresholding described in section 2.9.2 was used to smooth and remove drift from pulse oximeter signals (photoplethysmograms). Pulse oximetry estimates the arterial oxygen saturation by measuring the light absorbed in human tissue beds. When light passes through human tissue (bones, skin, blood vessels, fluids, venous and arterial blood including haemoglobin) it is absorbed. As the amount of oxygenated blood in tissue changes, the amount of absorbed light changes. Different haemoglobin absorbs light of different wavelength. Oxygenated haemoglobin ( $HbO_2$ ) absorbs light in the red spectrum and deoxygenated haemoglobin ( $RHb$ ) absorbs light in the near-infrared spectrum. The content of the two different haemoglobins in blood can be measured by passing red and infrared light through a blood vessel. In addition, the heart rate can be determined from the cyclical changes of light absorption, (Salyer, 2003).

Several pulse oximeter signals were recorded by the author, using a sampling rate of 300 Hz. The acquisition was performed using a finger probe placed on one finger. From the set of collected traces, two traces were selected for the analysis. The two signals are plotted in figures 3.10(a) and figure 3.11(a). The first of the signals is a typical oximeter signal and the second was taken as the pulse amplitude was gradually decreased by applying pressure to the finger. The first signal consists of  $2^{14}$  (i.e. 16384) data points and the second consists of  $2^{13}$  (i.e. 8192) data points. Hence, the first signal could be divided into 14 wavelet details and the second signal could be divided into 13 wavelet details as shown in figure 3.10(b) and figure 3.11(b). The wavelet transform was

performed using Daubechies D8 wavelet (i.e. 8 wavelet filter coefficients), for both oximeter signals. Figure 3.10(b) shows that it is only detail in D5, D6, D7 and D8 that contributes significantly towards the true signal and the rest can be regarded as noise (detail D1-D4) or drift (detail D9-D14). The heart signal can therefore be reconstructed using detail D5, D6, D7 and D8. Figure 3.10(c) shows the smoothed and detrended reconstructed oximeter signal. The same method was applied to the second oximeter trace 3.11(a). Similar conclusion as for the previous signal can be drawn for this data, figure 3.11(b), i.e. the true oximeter signal, is to be found in the wavelet transform details D5 to D8. Figure 3.11(c) shows the reconstructed signal when the details containing noise and signal drift are removed. This example provides a simple illustration of a wavelet-based method for the removal of both noise and signal-drift from a signal.

### **3.5.3. Wavelet analysis of electrocardiogram (ECG) signals**

The electrocardiogram (ECG) is a measure of the electrical activity associated with the heart. Most patients who present with sudden cardiac death exhibit the arrhythmia known as ventricular fibrillation (VF). These rhythms have, up until recently, been assumed to be disorganised electrical activity in the heart. However, recent research carried out by Addison et al (2001b) has shown that analysis of these signals using the continuous wavelet transform (CWT) can reveal a rich underlying structure. This section describes work, carried out by the author, which applied the discrete wavelet transform (DWT) to the ECG signals used in the research by Addison et al (2001b) to determine whether a DWT-based analysis could provide more information on these signals. The analysis of the ECG data was carried out to determine the dominant frequency of the ventricular fibrillation signals and whether it is possible to predict the outcome of defibrillation shock using the DWT.

The pre-shock heart signals analysed here were classified as either ROSC (return of spontaneous circulation) signals, (70 data sets) or asystole (no pulse) signals (80 data sets). Two typical ECG signals are shown in figure 3.12. The signals are 20 seconds in length and the data points were collected at a sampling frequency of 100 Hz.



The DWT was performed by the author using a Daubechies D8 wavelet. The scale dependent energies were determined for each signal. Because of differences when measuring the heartbeat due to the probe location on the patients chest, the signals also had to be normalised in order to compare them accurately. The coefficient energy plot for the ROSC signals is shown in figure 3.13(a) and for the asystole signal in figure 3.13(b). From the plot for the ROSC signal one can see that most of the signals have an energy peak at scale  $m=4$ . This can be translated into a frequency measure using the following equation:

$$f = \frac{1}{T} \quad (3.10)$$

where  $T$  is the period of the wavelet. The maximum energy is found at scale  $m=4$  i.e. for this scale  $2^4=16$  which corresponds to a time period  $T=16 \times 0.01=0.16$  seconds using a sampling rate equal to 100 Hz. Using equation 3.10 the frequency at scale  $m=4$  equals 6.25 Hz.

For the asystole signals two major peaks are visible one at scale  $m=4$  and one at scale  $m=5$ , these peaks corresponds to 6.25 Hz and 3.13 Hz respectively. Thus, many of these signals possess low frequency waveforms. This is consistent with the outcome as it is known that negative shock outcomes are correlated with reduction in fibrillation frequency (Addison et al, 2001b).

### **3.6. Discussion and chapter summary**

This chapter has presented results of the application of 1-D discrete wavelet transforms (DWT) and the 1-D stationary wavelet transforms (SWT) to the analysis of a variety of synthetic and experimentally acquired data-sets. The wavelet transform has proven to be useful in deriving the global Hurst roughness exponent for different engineering data, (Flandrin, 1992; Fischer and Akay, 1996; Simonsen et al, 1998; Dougan et al 2000; Frantziskonis et al, 2000; Zunino et al, 2004). In study carried out by the author the wavelet transform was used to determine scaling properties characterised by the Hurst exponent ( $H$ ) for fBm-profiles and cracked concrete profiles.

Due to misalignment that generally occurs between the two ends of the data, significant edge effects are present at the transform edges. As the edge coefficients in general are significantly larger than the rest of the transform coefficients, these erroneous coefficients will dominate the results. Algorithms were therefore developed by the author where the number of erroneous coefficients were determined and removed prior to the main analysis.

The results from the analysis of the fBm profiles using the DWT and the SWT showed small differences between the actual  $H$  and  $H$  determined using the wavelet transform, (table 3.3). The analysis provided an accurate determination of the scaling properties of fBm's. The scaling properties for the cracked concrete profiles were determined using the same method as for the fBm profiles and the results obtained were similar to previously published work using the variable bandwidth method (Dogan et al, 2000).

An analysis of medical data using the DWT was also included in this chapter. A smoothing method was applied to noisy pulse oximeter signals to extract the true pulse oximeter signal. The analysis showed that both noise and signal drift can be removed successfully from the signal using a basic smoothing method. The medical data analysis also included an attempt to develop a predictor of defibrillation success in ECG signals. However, due to the dyadic nature of the discrete wavelet transform, only a crude frequency resolution could be achieved and hence the technique is unable to determine shock outcome with the accuracy necessary for implementation within a medical device.

In summary, the work described in this chapter illustrates the usefulness of the wavelet transform method and allowed the author to develop her skills in employing the DWT and SWT methods.

## **CHAPTER 3**

### Tables

Wavelet	Scale									
	1	2	3	4	5	6	7	8	9	10
Daubechies 2 (Haar)	0	0	0	0	0	0	0	0	0	0
Daubechies 4	1	1	1	1	1	1	1	1	1	1
Daubechies 6	1	2	2	2	2	2	2	2	2	2
Daubechies 8	2	3	3	3	3	3	3	3	3	3
Daubechies 10	2	3	4	4	4	4	4	4	4	4
Daubechies 12	3	4	5	5	5	5	5	5	5	5
Daubechies 14	3	5	6	6	6	6	6	6	6	6
Daubechies 16	4	6	7	7	7	7	7	7	7	7
Daubechies 18	4	6	7	8	8	8	8	8	8	8
Daubechies 20	5	7	8	9	9	9	9	9	9	9

The number of edge coefficients at each end of the signal for each scale of the transform. The Daubechies family of wavelets, applying the DWT.

**Table 3.1** Number of edge coefficients for the DWT.

Wavelet	Scale									
	1	2	3	4	5	6	7	8	9	10
Daubechies 2 (Haar)										
<i>left</i>	1	1	1	1	1	1	1	1	1	512
<i>right</i>	1	3	7	15	31	63	127	255	511	512
Daubechies 4										
<i>left</i>	1	3	7	15	31	63	127	255	512	512
<i>right</i>	2	6	14	30	62	126	254	510	512	512
Daubechies 6										
<i>left</i>	2	6	14	30	62	126	254	512	512	512
<i>right</i>	3	9	21	45	93	189	381	512	512	512
Daubechies 8										
<i>left</i>	3	9	21	45	93	189	381	512	512	512
<i>right</i>	4	12	28	60	124	252	508	512	512	512
Daubechies 10										
<i>left</i>	4	12	28	60	124	252	512	512	512	512
<i>right</i>	5	15	35	75	155	315	512	512	512	512
Daubechies 12										
<i>left</i>	5	15	35	75	155	315	512	512	512	512
<i>right</i>	6	18	42	90	186	378	512	512	512	512
Daubechies 14										
<i>left</i>	6	18	42	90	186	378	512	512	512	512
<i>right</i>	7	21	49	105	217	441	512	512	512	512
Daubechies 16										
<i>left</i>	7	21	49	105	217	441	512	512	512	512
<i>right</i>	8	24	56	120	248	504	512	512	512	512
Daubechies 18										
<i>left</i>	8	24	56	120	248	512	512	512	512	512
<i>right</i>	9	27	63	135	279	512	512	512	512	512
Daubechies 20										
<i>left</i>	9	27	63	135	279	512	512	512	512	512
<i>right</i>	10	30	70	150	310	512	512	512	512	512

The number of edge coefficients at each side for each scale of the transform. The Daubechies family of wavelets, using the stationary wavelet transform (SWT).

**Table 3.2** Number of edge coefficients for the SWT.

$fBm$	slope	H (DWT)	Difference
0.1	1.300	0.15	50%
0.2	1.450	0.23	13%
0.3	1.600	0.30	0%
0.4	1.786	0.39	-2%
0.5	1.964	0.48	-4%
0.6	2.129	0.56	-6%
0.7	2.371	0.69	-2%
0.8	2.471	0.74	-8%
0.9	2.500	0.75	-17%
1.0	2.329	0.66	-34%

(a) Determine  $H$  using the DWT.

$fBm$	slope	H (SWT)	Difference
0.1	1.345	0.17	73%
0.2	1.479	0.24	20%
0.3	1.636	0.32	6%
0.4	1.793	0.40	-1%
0.5	1.957	0.48	-4%
0.6	2.136	0.57	-5%
0.7	2.357	0.68	-3%
0.8	2.514	0.76	-5%
0.9	2.483	0.74	-18%
1.0	2.314	0.66	-34%

(b) Determine  $H$  using the SWT.

**Table 3.3** Determination of the scaling properties characterised by the Hurst exponent ( $H$ ) of synthetic test profiles with known  $H$  values.

Profile	H(vb)	H(dwt)	H(swt)
s1r	0.71	0.69	0.67
s1l	0.74	0.88	0.73
s1l	0.88	0.96	0.93
s2r	0.76	0.78	0.76
s2r	0.80	0.75	0.70
s2l	0.82	0.82	0.81
s2l	0.94	0.96	0.90
s3r	0.84	0.84	0.87
s3l	0.82	0.80	0.80
s4r	0.75	0.76	0.81
s4l	0.91	0.76	0.77
s5r	0.74	0.82	0.79
s5l	0.80	0.85	0.80
s6r	0.74	0.77	0.79
s6l	0.86	0.86	0.83
s7l	0.82	0.82	0.84
s8r	0.69	0.75	0.72
s8l	0.75	0.73	0.70
s9r	0.81	0.84	0.80
s9l	0.80	0.74	0.83
s10r	0.79	0.69	0.79
s10l	0.79	0.71	0.74
<i>mean</i>	0.80	0.84	0.83
<i>std</i>	0.06	0.08	0.06
<i>diff.</i>		5%	4%

Characterising of the small sized cracked concrete profiles using the discrete wavelet transform (DWT) and the stationary wavelet transform (SWT) methods comparing the results with the variable bandwidth (vb) method of Dougan et al (2000). Additionally the mean  $H$  value (*mean*), the standard deviation of the results (*std*) and the percentage difference (*diff.*) between the *vb* method and the wavelet transform method are determined.

**Table 3.4** Determination of the scaling properties of the small sized cracked concrete profiles characterised by the Hurst exponent ( $H$ ).

Profile	H (vb)	H (dwt)	H(swt)
<i>m1r</i>	0.74	0.85	0.86
<i>m1l</i>	0.77	0.76	0.83
<i>m2r</i>	0.82	0.93	0.94
<i>m2r-</i>	0.76	0.83	0.82
<i>m2l</i>	0.76	0.91	0.93
<i>m2l-</i>	0.74	0.77	0.75
<i>m3r</i>	0.82	1.01	0.98
<i>m3l</i>	0.77	1.01	0.94
<i>m4r</i>	0.83	0.82	0.81
<i>m4l</i>	0.78	0.88	0.86
<i>m5r</i>	0.75	0.70	0.68
<i>m5r-</i>	0.76	0.76	0.76
<i>m5l</i>	0.75	0.58	0.57
<i>m5l-</i>	0.77	0.82	0.79
<i>m6r</i>	0.77	0.93	0.88
<i>m6l</i>	0.84	0.94	0.93
<i>m7r</i>	0.77	0.75	0.74
<i>m7l</i>	0.81	0.88	0.91
<i>m8r</i>	0.83	0.74	0.73
<i>m8l</i>	0.77	0.88	0.90
<i>m9r</i>	0.88	0.96	0.93
<i>m9l</i>	0.77	0.82	0.89
<i>m10r</i>	0.81	0.93	0.93
<i>m10l</i>	0.81	0.75	0.79
<i>mean</i>	0.79	0.84	0.84
<i>std</i>	0.04	0.10	0.10
<i>diff.</i>		7%	7%

Characterising of the medium sized cracked concrete profiles using the discrete wavelet transform (DWT) and the stationary wavelet transform (SWT) methods comparing the results with the variable bandwidth (vb) method of Dougan et al (2000). Additionally the mean  $H$  value (*mean*), the standard deviation of the results (*std*) and the percentage difference (*diff.*) between the *vb* method and the wavelet transform method are determined.

**Table 3.5** Determination of the scaling properties of the medium sized cracked concrete profiles characterised by the Hurst exponent ( $H$ ). Comparing the wavelet transform with the variable bandwidth (*vb*) method.



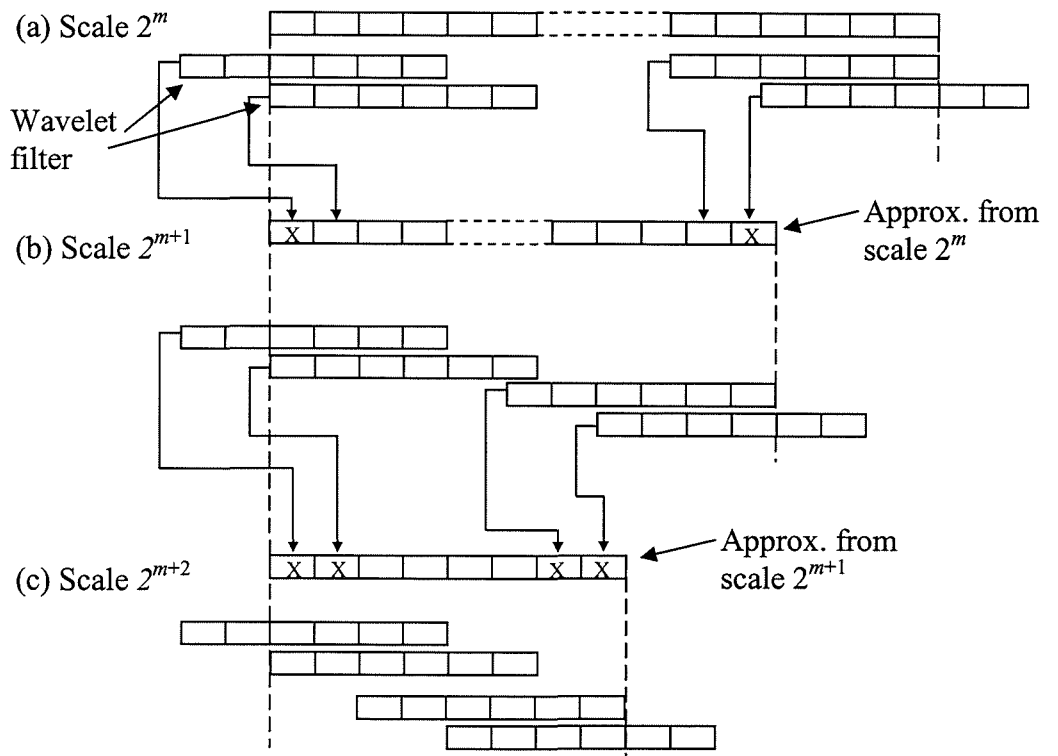
Profile	H (vb)	H (dwt)	H (swt)
L1r	0.83	0.90	0.91
L1l	0.78	0.66	0.76
L2r	0.85	0.95	0.95
L2l	0.75	1.02	1.00
L3r	0.79	0.86	0.91
L3l	0.84	0.92	0.88
L4r	0.78	0.96	0.90
L4l	0.80	0.93	0.93
L5r	0.83	0.75	0.70
L5l	0.85	0.84	0.83
L6r	0.81	0.85	0.89
L6l	0.80	0.87	0.91
L7r	0.73	0.92	0.89
L7l	0.80	0.93	0.92
L8r	0.80	0.87	0.81
L8l	0.78	0.89	0.88
L9r	0.77	0.84	0.86
L9l	0.82	0.91	0.95
L10r	0.83	0.87	0.88
L10l	0.84	0.77	0.78
<i>mean</i>	0.80	0.87	0.88
<i>std</i>	0.03	0.08	0.07
<i>diff.</i>		9%	9%

Characterising of the large sized cracked concrete profiles using the discrete wavelet transform (DWT) and the stationary wavelet transform (SWT) methods comparing the results with the variable bandwidth (vb) method of Dougan et al (2000). Additionally the mean  $H$  value (*mean*), the standard deviation of the results (*std*) and the percentage difference (*diff.*) between the *vb* method and the wavelet transform method are determined.

**Table 3.6** Determination of the scaling properties of the large sized cracked concrete profiles characterised by the Hurst exponent ( $H$ ). Comparing the wavelet transform with the variable bandwidth (*vb*) method.

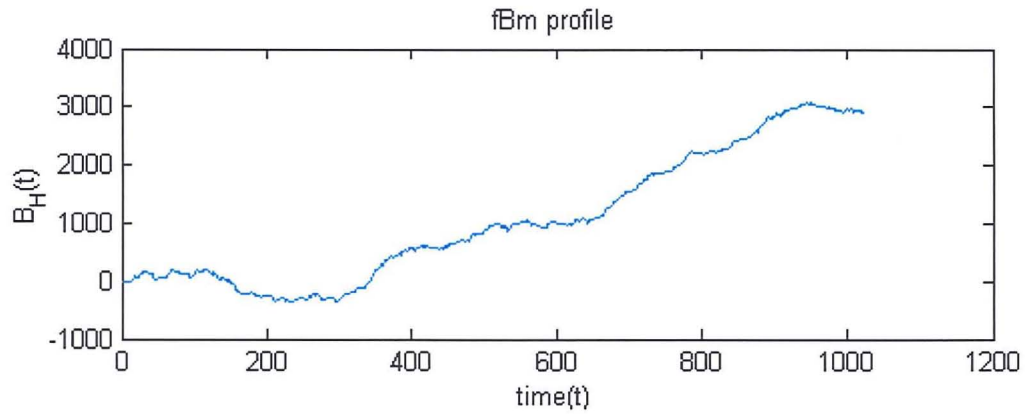
## **CHAPTER 3**

Figures

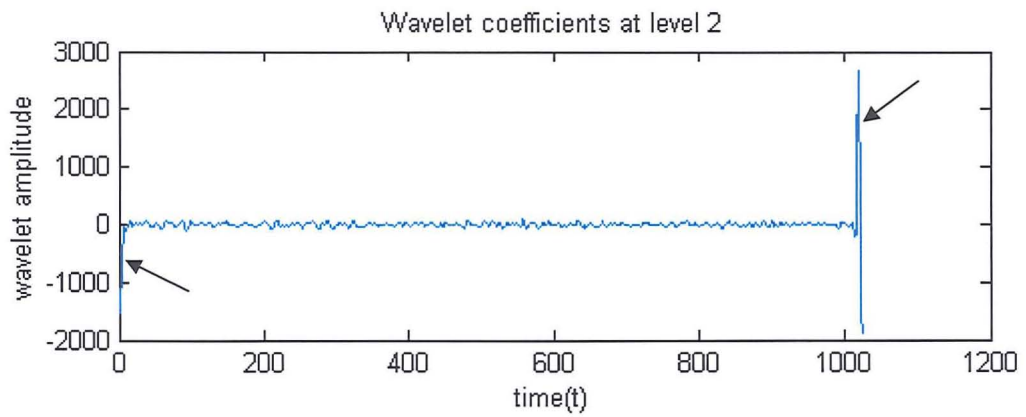


The edge effect coefficients (marked as  $X$ ) are carried through the multiresolution process. (a) at the first iteration from  $2^m$  to scale  $2^{m+1}$  one edge coefficient is created at each end of the transform, (b) at the second iteration from  $2^{m+1}$  to the next scale  $2^{m+2}$  two edge coefficients are created at each end of the transformed signal and, (c) for the following iterations from  $2^{m+2}$  to  $2^M$  two edge coefficients are created at each end of the transform at each iteration.

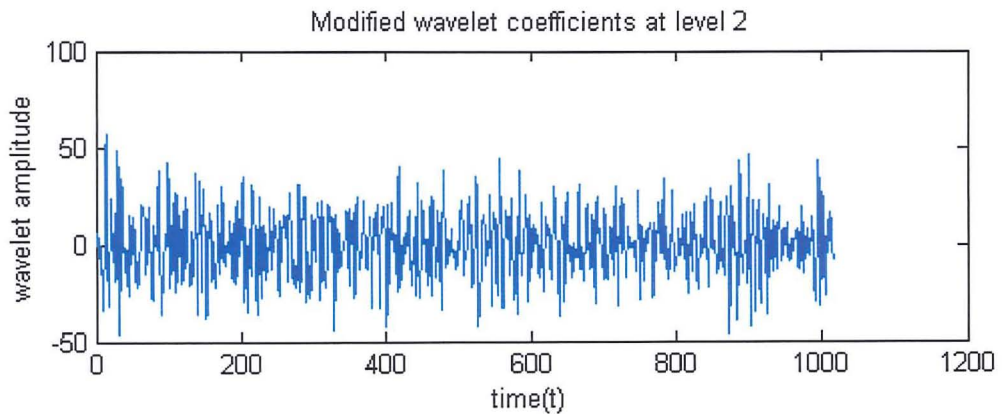
**Figure 3.1** Edge effects in the DWT for the Daubechies D6 wavelet.



(a) A synthetic fractional Brownian motion profile.

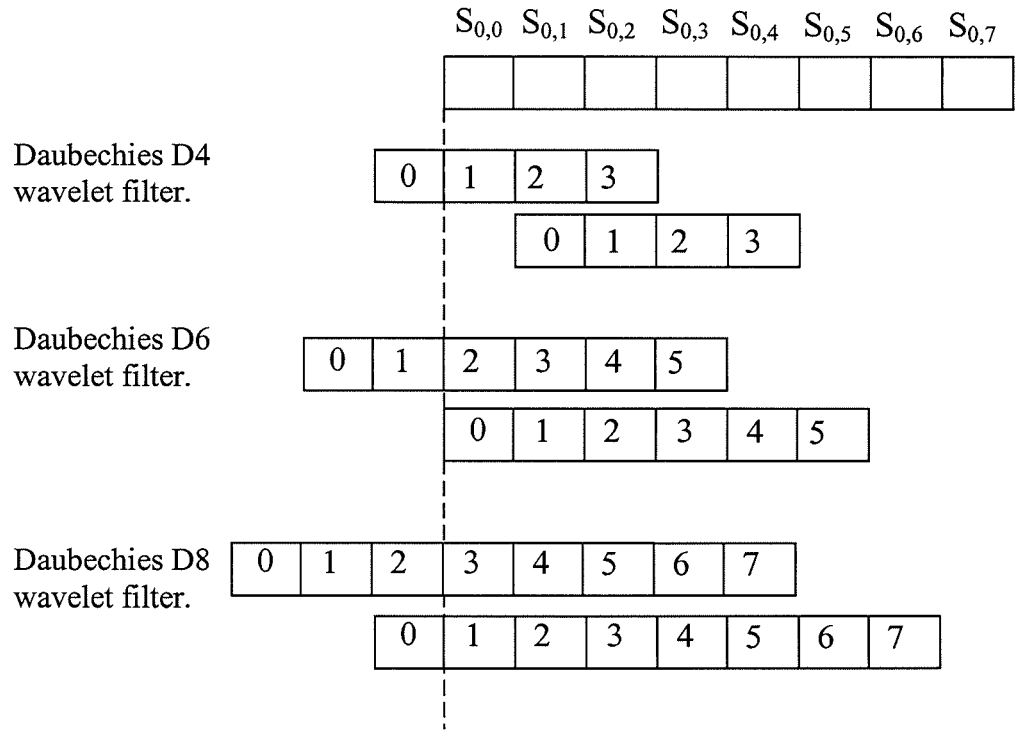


(b) Level 2 of the decomposition of the signal in (a) with unmodified coefficients. The large 'edge' coefficients are marked by arrows.



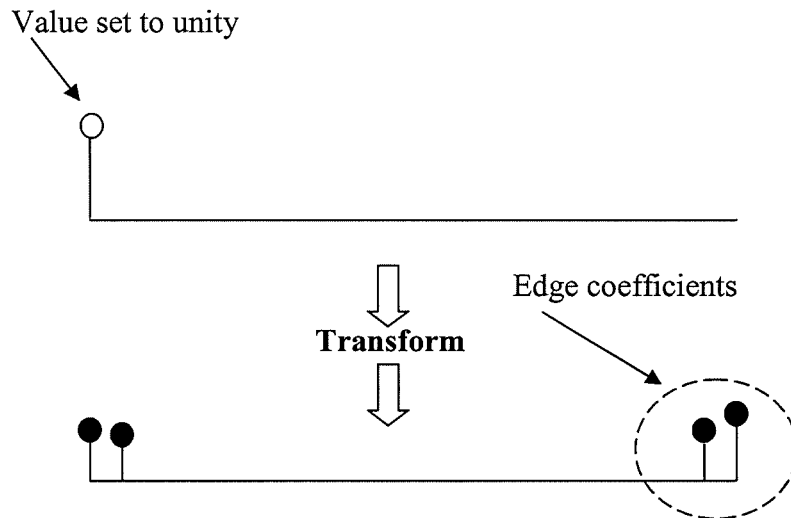
(c) As plot (b) but with the large 'edge' coefficients at the beginning and end removed.

**Figure 3.2** Compensating for edge effects in a test profile.

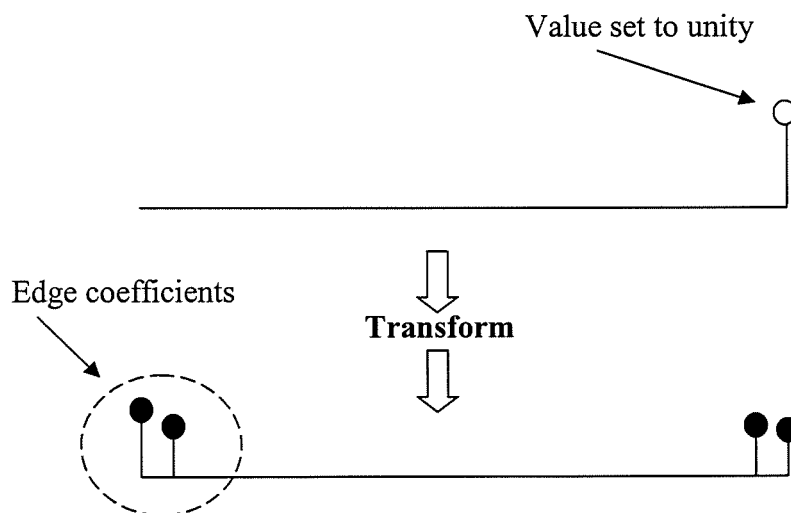


The Daubechies wavelet filters are located  $\frac{N_F}{2} - 1$  where it transects a signal, where  $N_F$  is the length of the wavelet filter.

**Figure 3.3** Transaction of Daubechies wavelet filters (D4, D6 and D8) to a signal using the DWT.

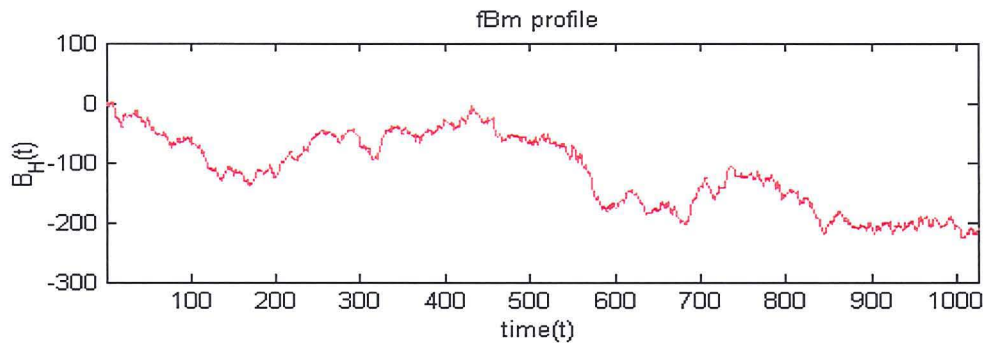


(a) Number of edge coefficients for the right side of the transform are determined when the first value (on the left side) is set to unity.

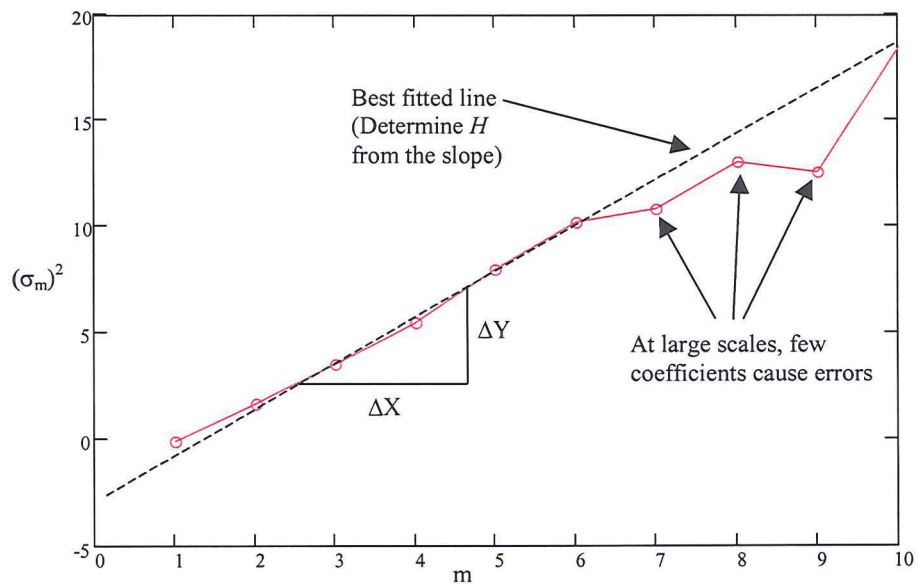


(b) Number of edge coefficients for the left side of the transform are determined when the first value (on the right side) is set to unity.

**Figure 3.4** The number of edge coefficients at each end of the transform for the Daubechies D4 wavelet are calculated by setting the opposite end values to unity, in tern.

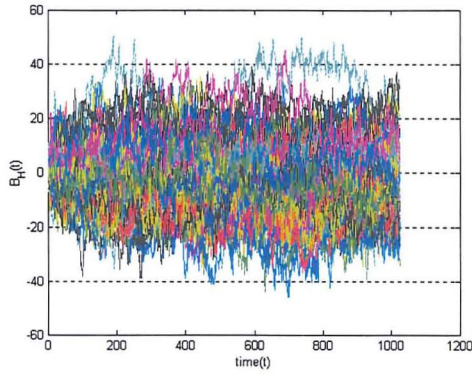


(a) The original fBm profile.

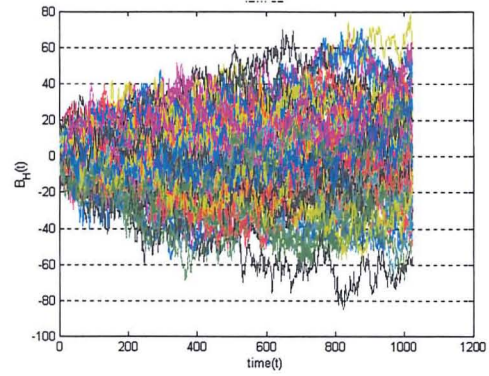


(b) Variance of the coefficients  $(\sigma_m)^2$  plotted against scale ( $m$ ) with the best fitted line.

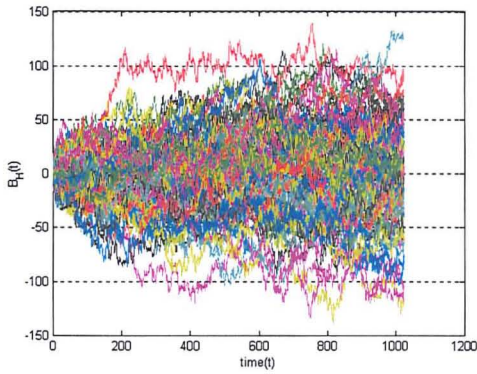
**Figure 3.5** Fractal curve analysis using the discrete wavelet transform.



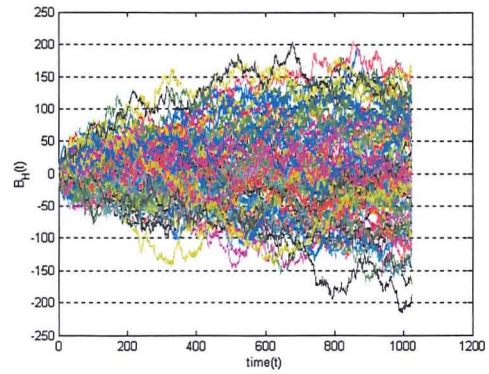
(a) fBm traces,  $H=0.1$ .



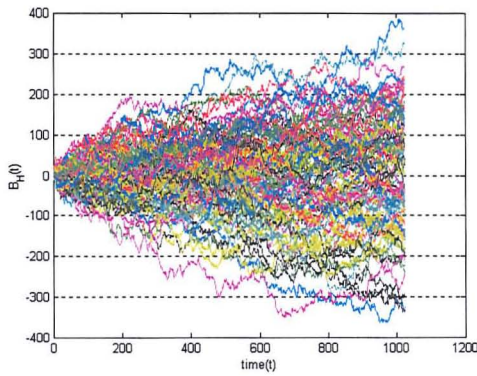
(b) fBm traces,  $H=0.2$ .



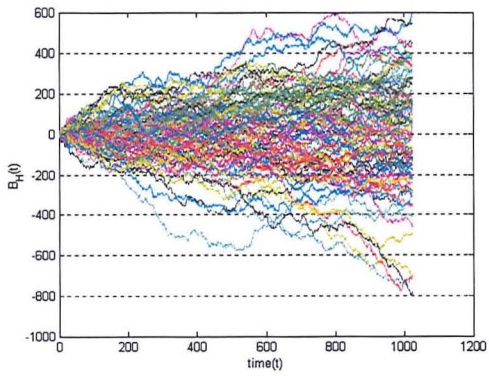
(c) fBm traces,  $H=0.3$ .



(d) fBm traces,  $H=0.4$ .



(e) fBm traces,  $H=0.5$ .

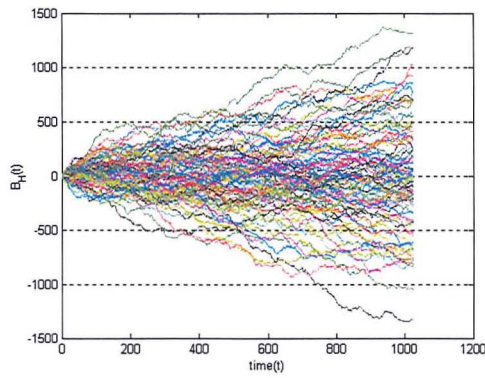


(f) fBm traces,  $H=0.6$ .

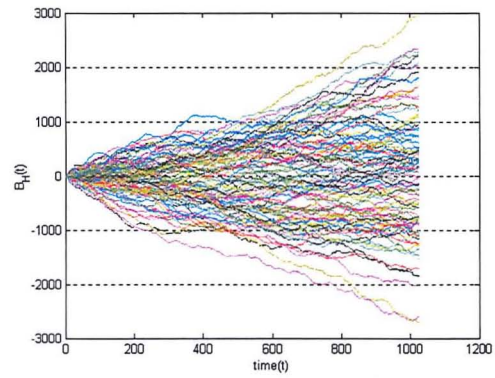
One hundred generated fBm-profiles for ten different Hurst exponent ( $H$ ) values. The  $H$  values range between 0.1 (a) to 0.6 (f).

**Figure 3.6** Synthetic fBm-profile test data.

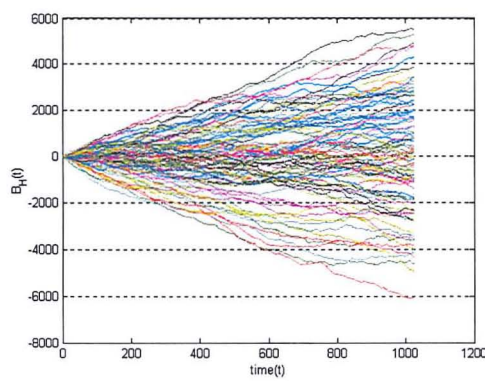




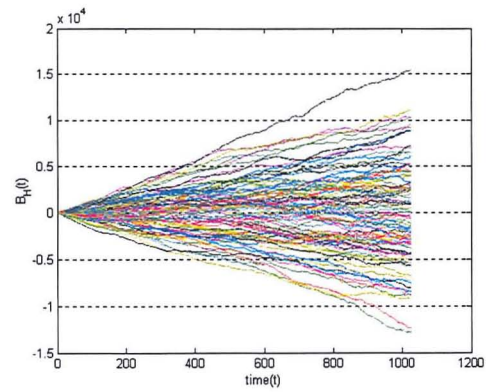
(g) fBm traces,  $H=0.7$ .



(h) fBm traces,  $H=0.8$ .



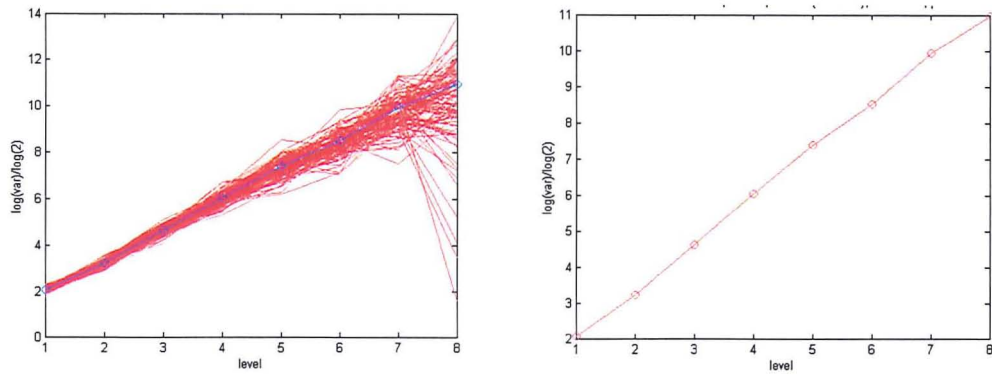
(i) fBm trace  $H=0.9$ .



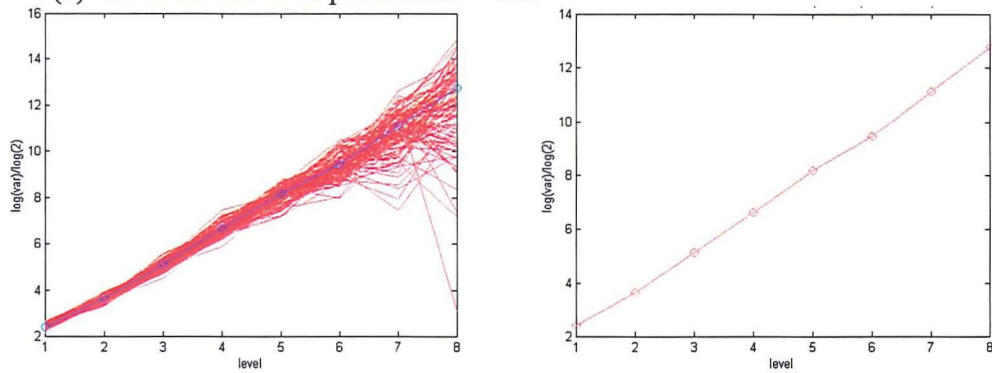
(j) fBm trace  $H=1.0$ .

One hundred generated fBm-profiles for ten different Hurst exponent ( $H$ ) values. The  $H$  values range between 0.7 (g) to 1.0 (j).

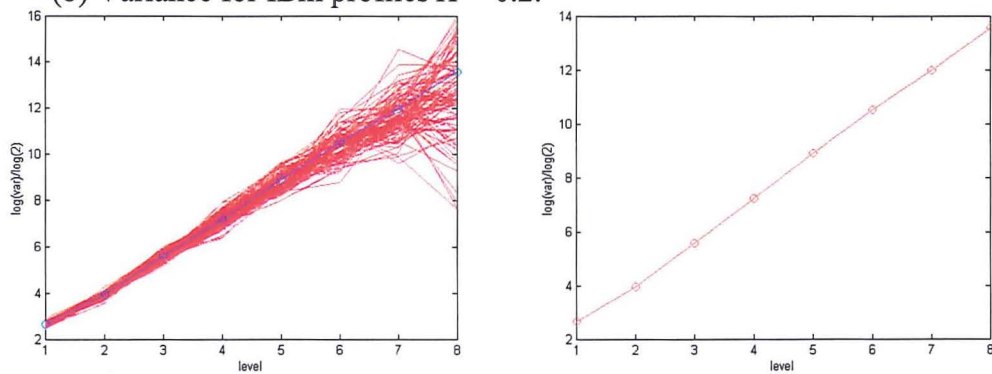
**Figure 3.6 (continued)** Synthetic fBm-profile test data.



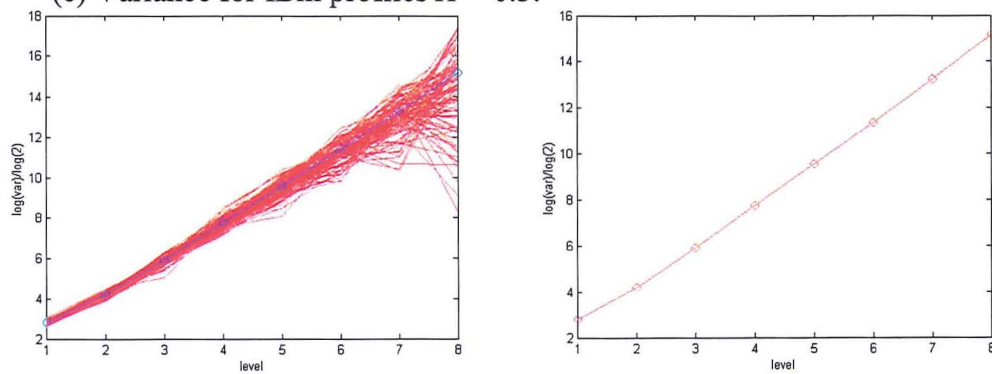
(a) Variance for fBm profiles  $H = 0.1$ .



(b) Variance for fBm profiles  $H = 0.2$ .



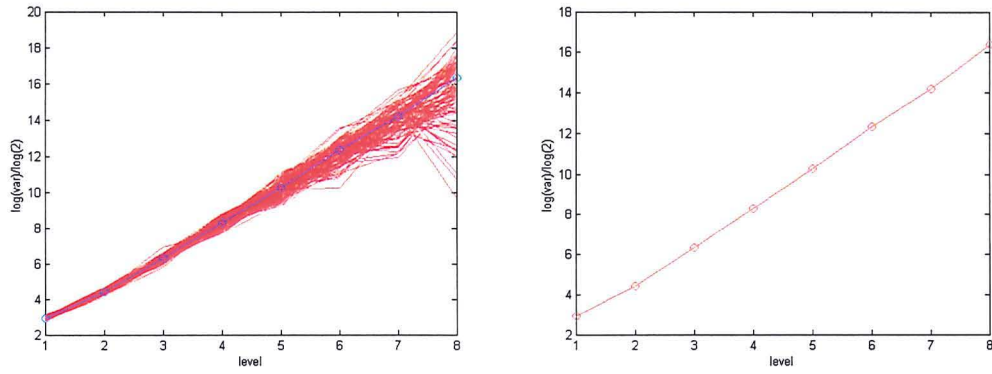
(c) Variance for fBm profiles  $H = 0.3$ .



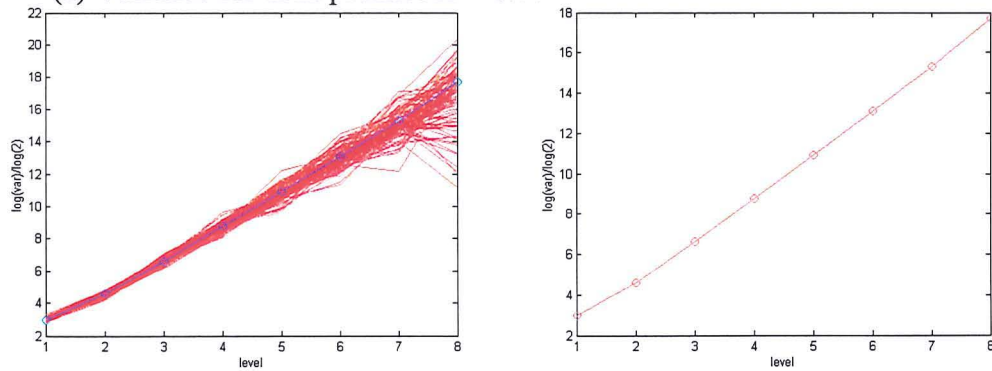
(d) Variance for fBm profiles  $H = 0.4$ .

The wavelet coefficients of the DWT plotted against the scale for the hundred synthetic fBm profiles (left) and the average variance for the profiles (right).

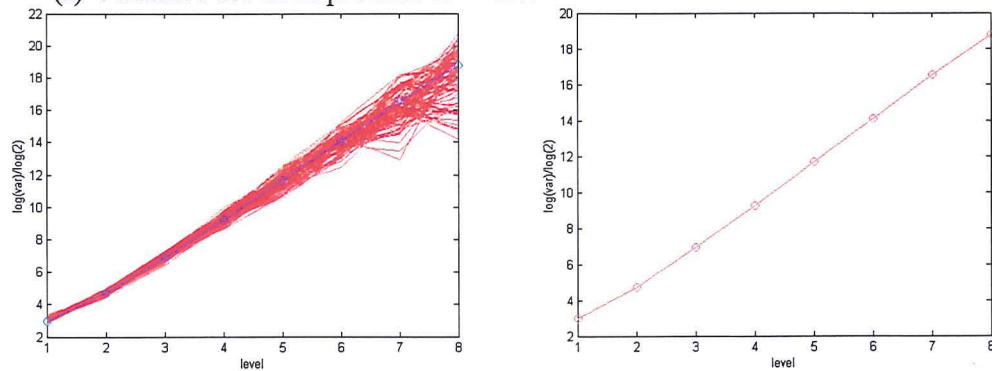
**Figure 3.7** Variance of the discrete wavelet transform coefficients for the test fBm profiles.



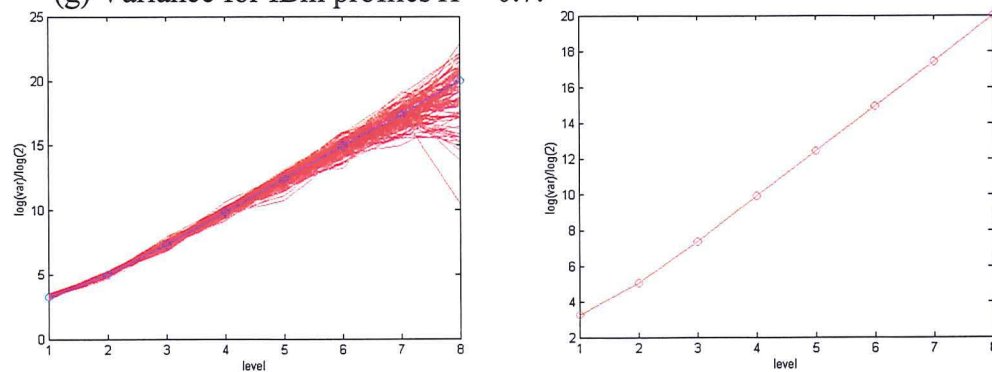
(e) Variance for fBm profiles  $H = 0.5$ .



(f) Variance for fBm profiles  $H = 0.6$ .



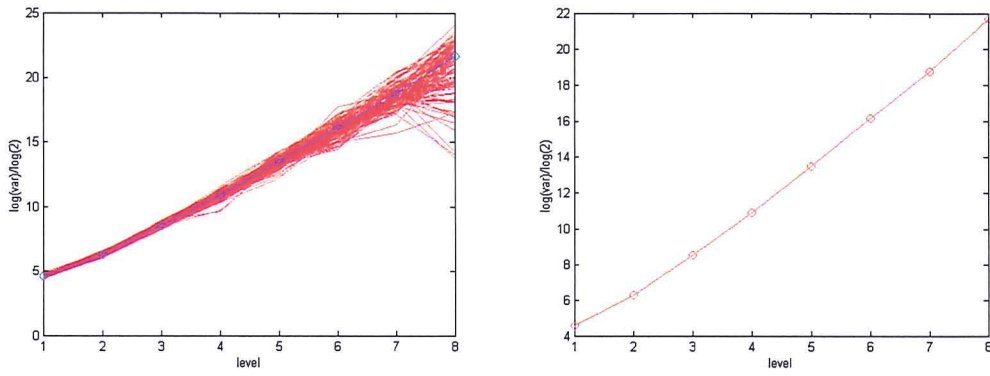
(g) Variance for fBm profiles  $H = 0.7$ .



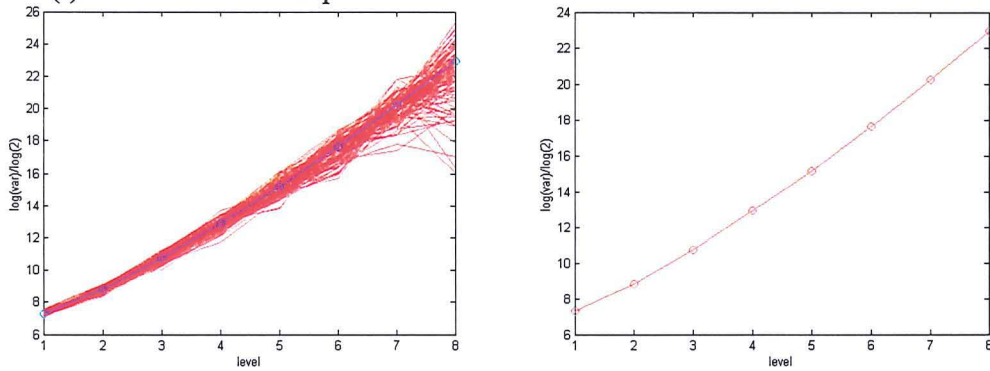
(h) Variance for fBm profiles  $H = 0.8$ .

The wavelet coefficients of the DWT plotted against the scale for the hundred synthetic fBm profiles (left) and the average variance for the profiles (right).

**Figure 3.7 (continued)** Variance of the discrete wavelet transform coefficients for the test fBm profiles.



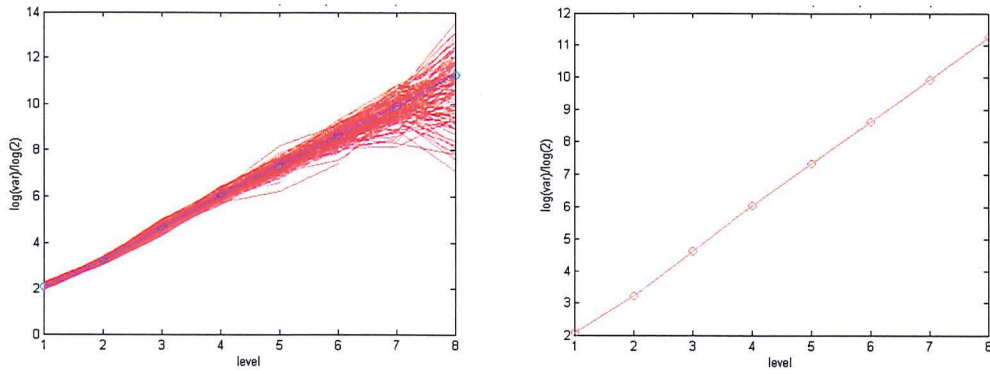
(i) Variance for fBm profiles  $H = 0.9$ .



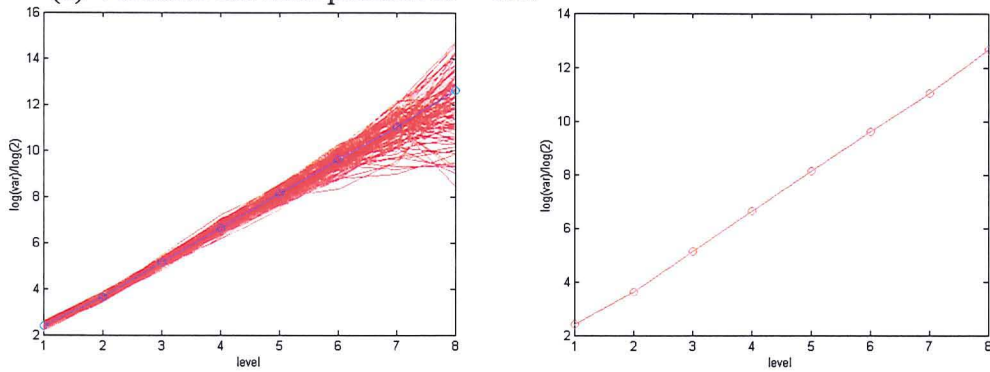
(j) Variance for fBm profiles  $H = 1.0$ .

The wavelet coefficients of the DWT plotted against the scale for the hundred synthetic fBm profiles (left) and the average variance for the profiles (right).

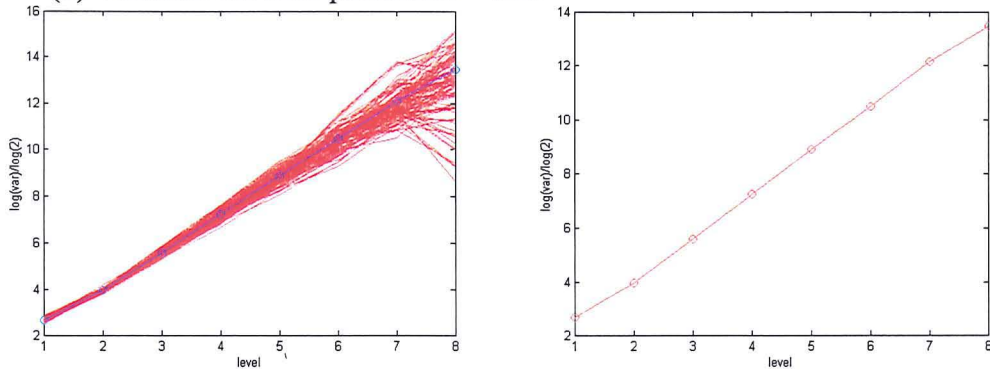
**Figure 3.7 (continued)** Variance of the discrete wavelet transform coefficients for the test fBm profiles.



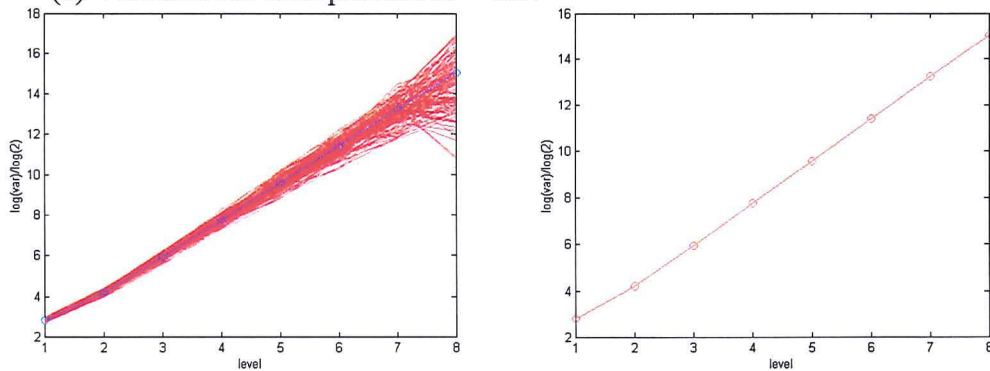
(a) Variance for fBm profiles  $H = 0.1$ .



(b) Variance for fBm profiles  $H = 0.2$ .



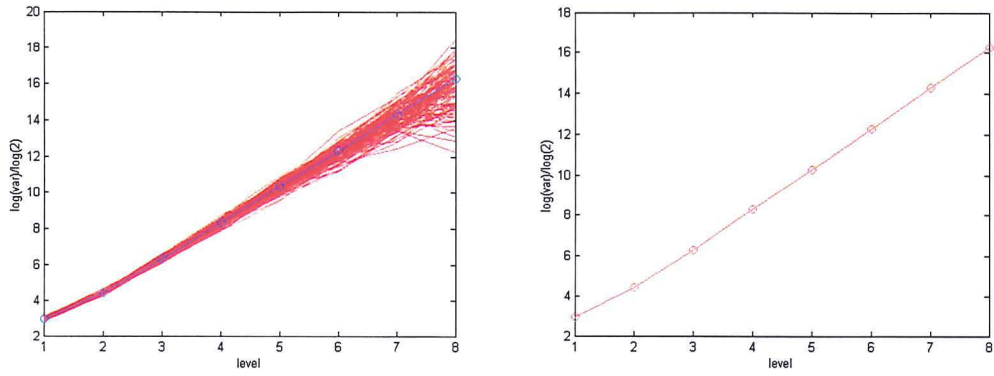
(c) Variance for fBm profiles  $H = 0.3$ .



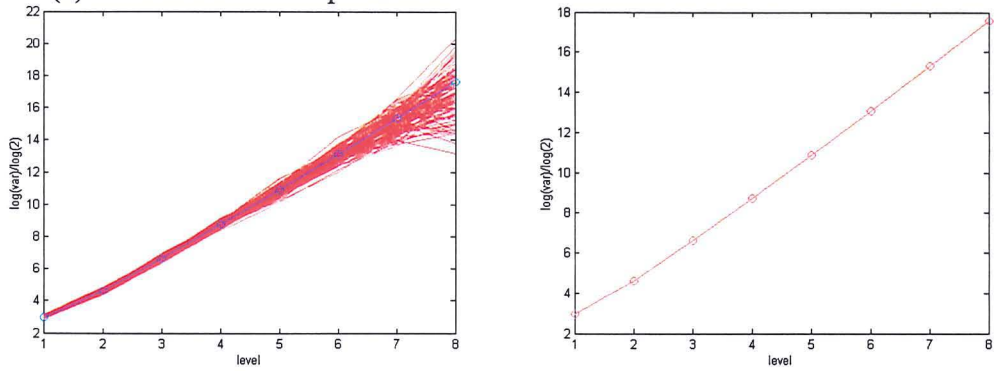
(d) Variance for fBm profiles  $H = 0.4$ .

The wavelet coefficients of the SWT plotted against the scale for the hundred synthetic fBm profiles (left) and the average variance for the profiles (right).

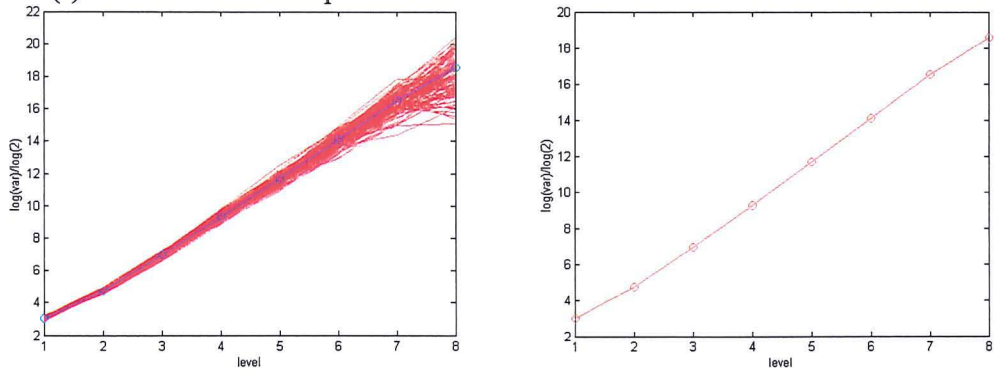
**Figure 3.8** Variance of the stationary wavelet transform coefficients for the test fBm profiles.



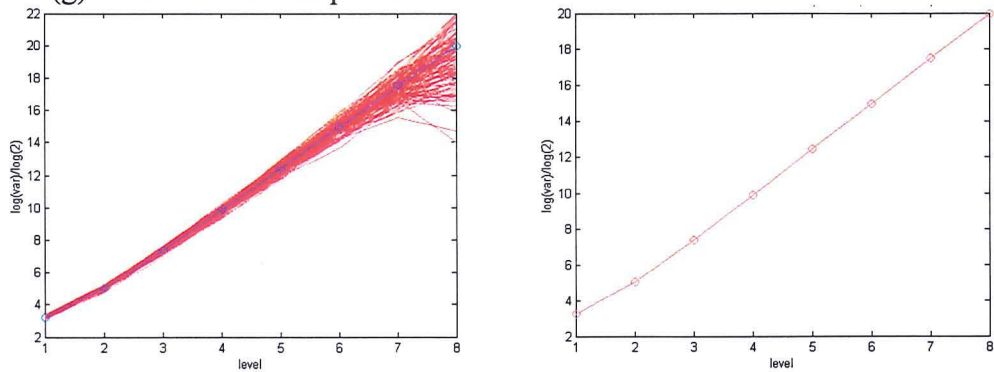
(e) Variance for fBm profiles  $H = 0.5$ .



(f) Variance for fBm profiles  $H = 0.6$ .



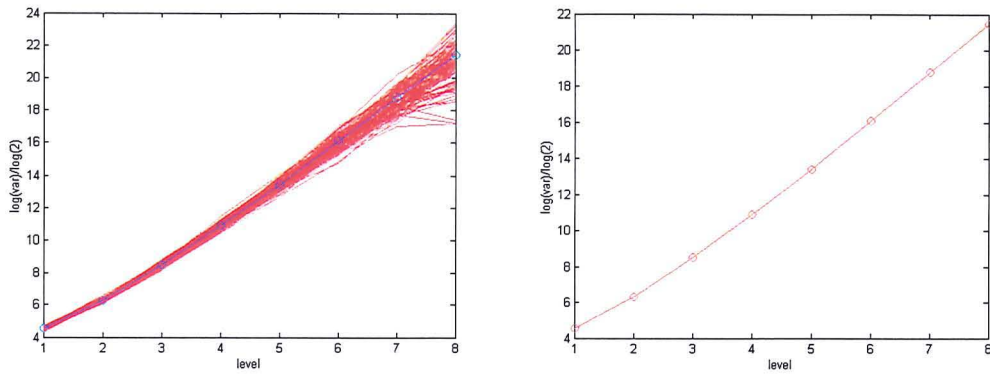
(g) Variance for fBm profiles  $H = 0.7$ .



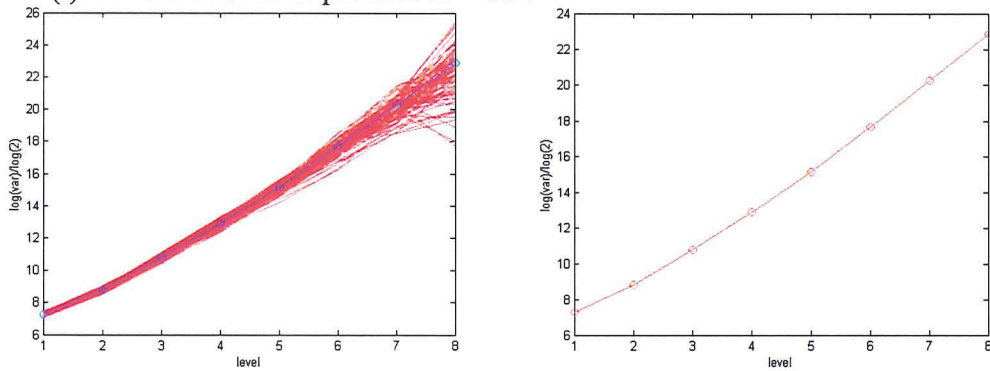
(h) Variance for fBm profiles  $H = 0.8$ .

The wavelet coefficients of the SWT plotted against the scale for the hundred synthetic fBm profiles (left) and the average variance for the profiles (right).

**Figure 3.8 (continued)** Variance of the stationary wavelet transform coefficients for the test fBm profiles.



(i) Variance for fBm profiles  $H = 0.9$ .



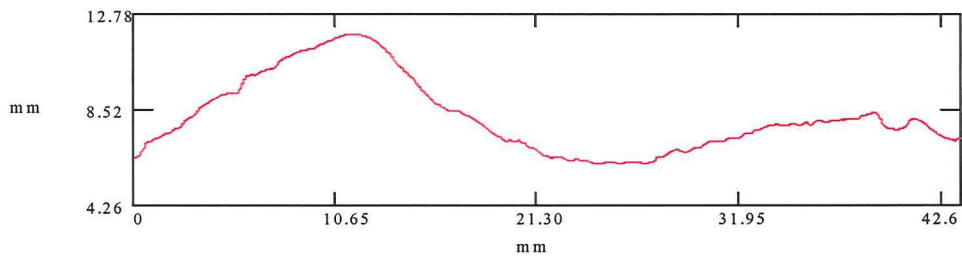
(j) Variance for fBm profiles  $H = 1.0$ .

The wavelet coefficients of the SWT plotted against the scale for the hundred synthetic fBm profiles (left) and the average variance for the profiles (right).

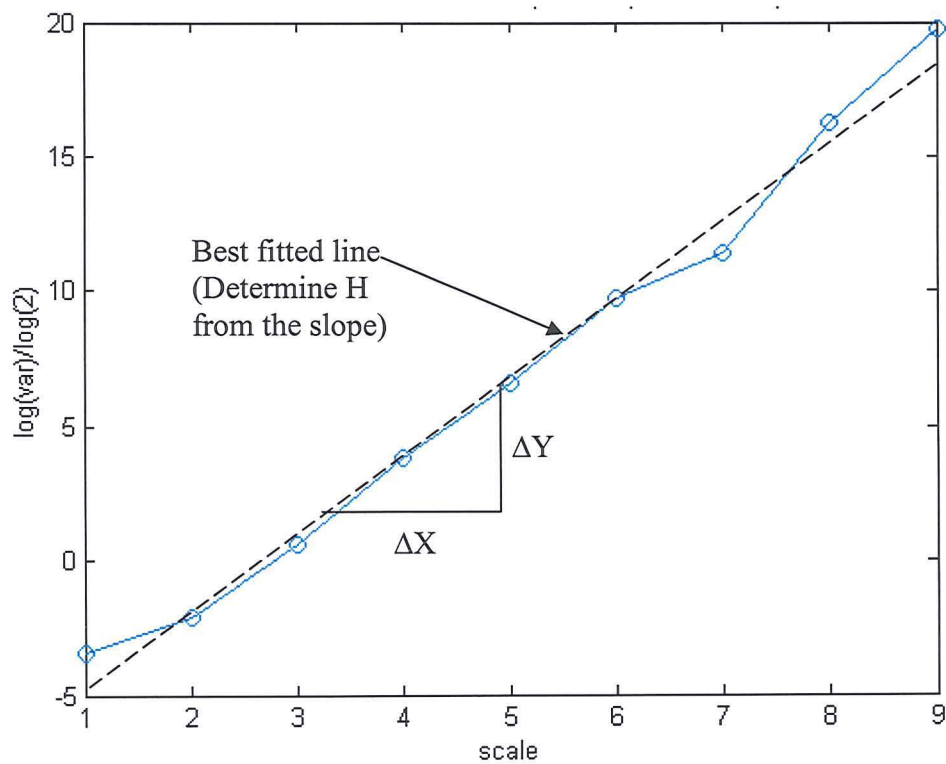
**Figure 3.8 (continued)** Variance of the stationary wavelet transform coefficients for the test fBm profiles.



(a) Image of cracked concrete profile.



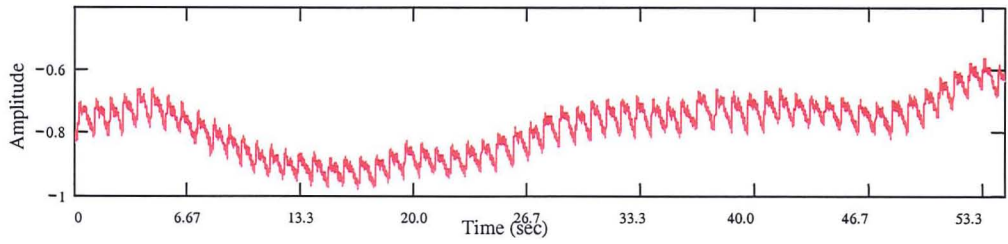
(b) Cracked concrete profile.



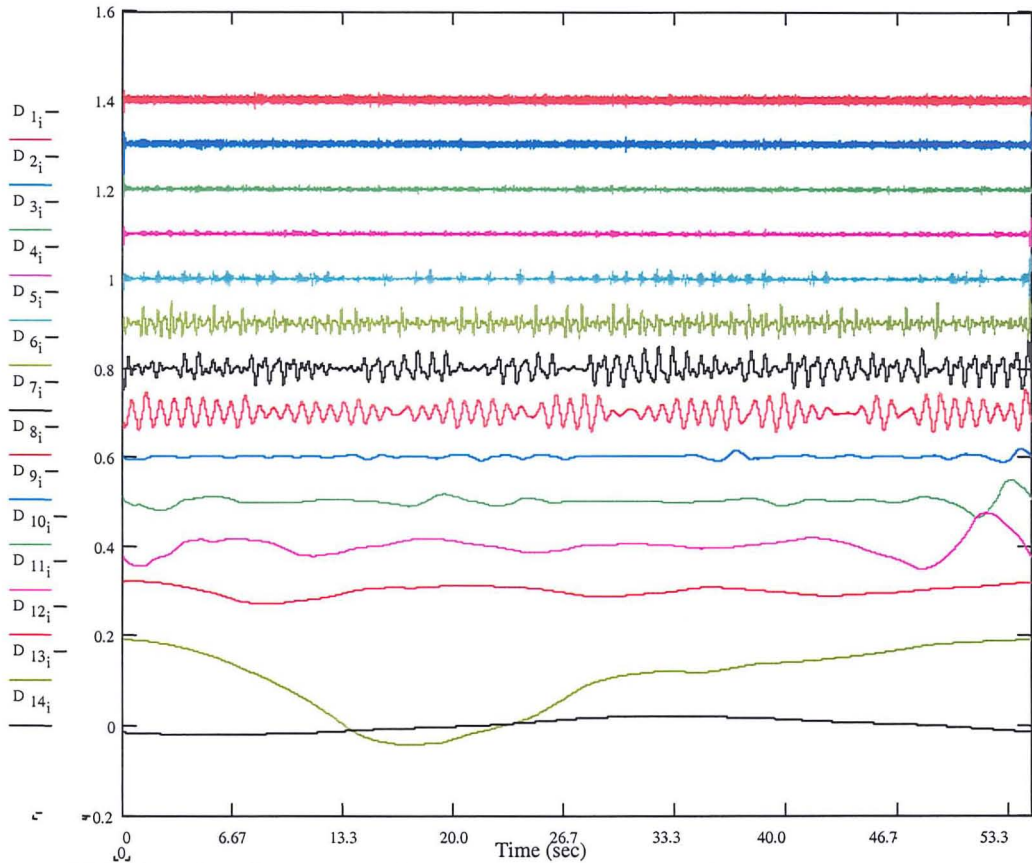
(c) Variance ( $\sigma_m^2$ ) plotted against the scale ( $m$ ) for the crack profile and the best fitted line through the data.

**Figure 3.9** Analysis of a cracked concrete profile.

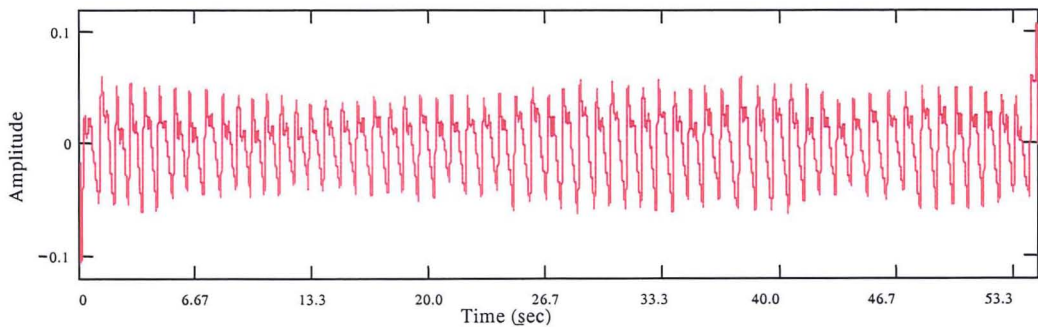




(a) Original pulse oximeter signal.

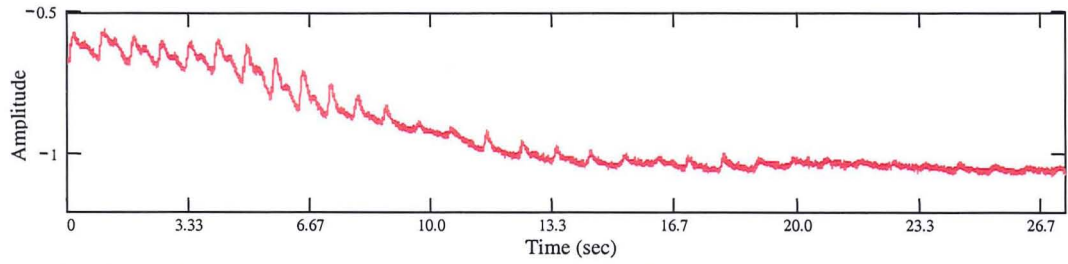


(b) Pulse signal separated into wavelet transform details.

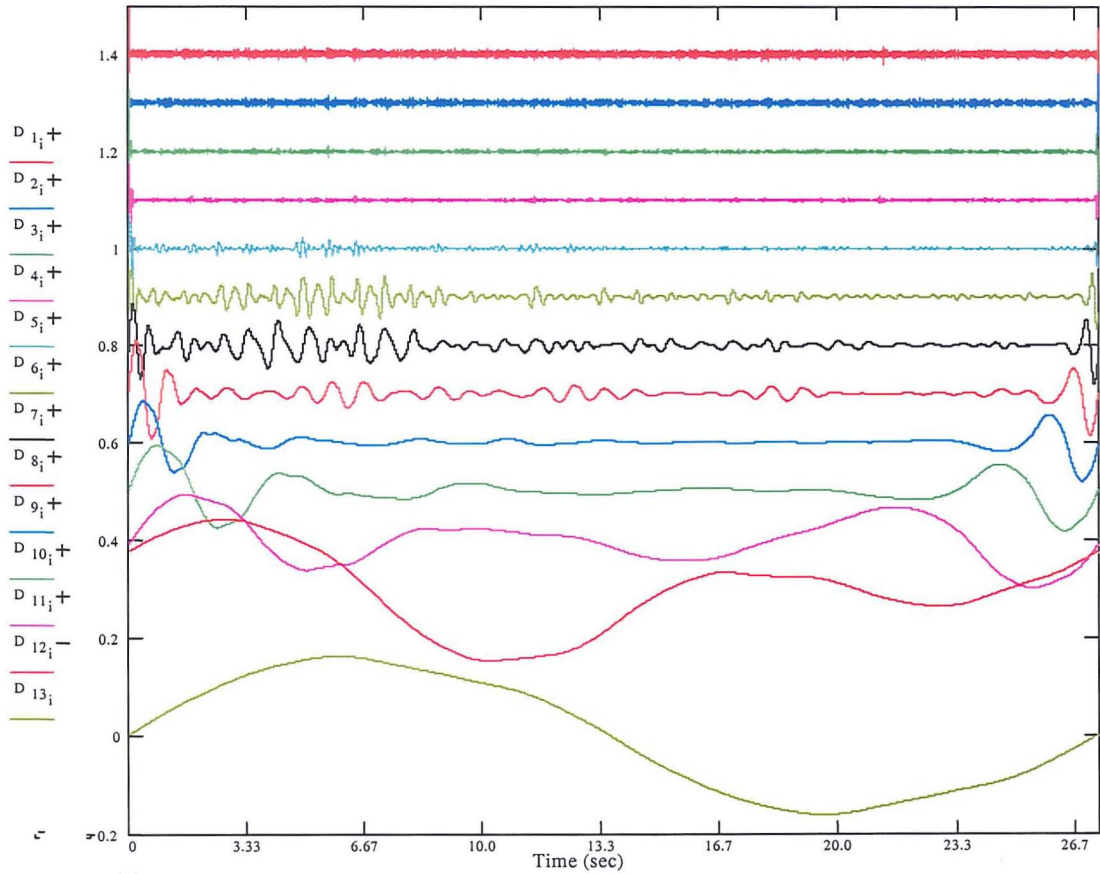


(c) Reconstructed smoothed and detrended signal using detail D5 to D8.

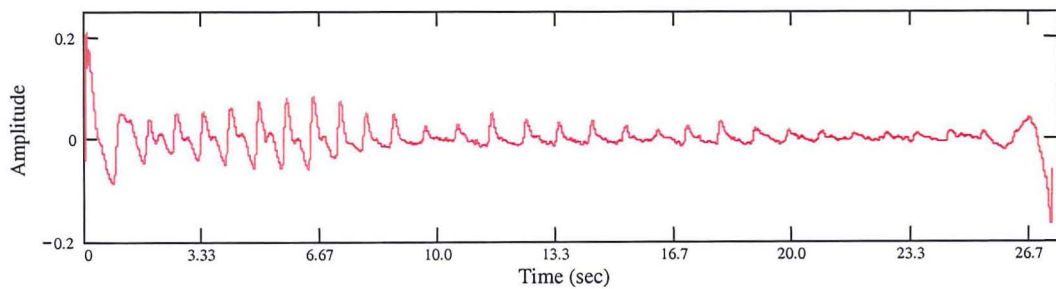
**Figure 3.10** Smoothing of a pulse oximeter signal.



(a) Original pulse oximeter signal, pulse gradually stopped.

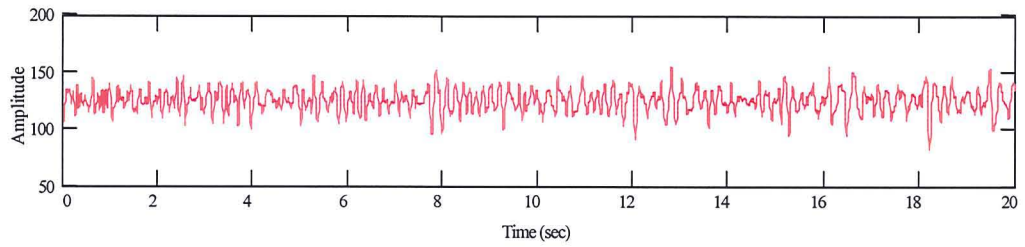


(b) Pulse signal separated into wavelet transform details.

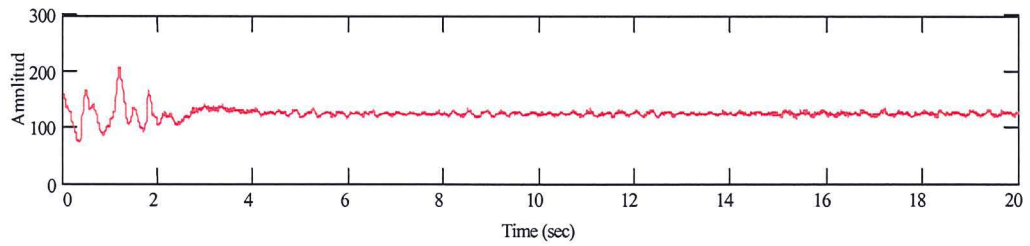


(c) Reconstructed smoothed and detrended signal using detail D5 to D8.

**Figure 3.11** Smoothing of a pulse oximeter signal where the blood flow has been stopped.

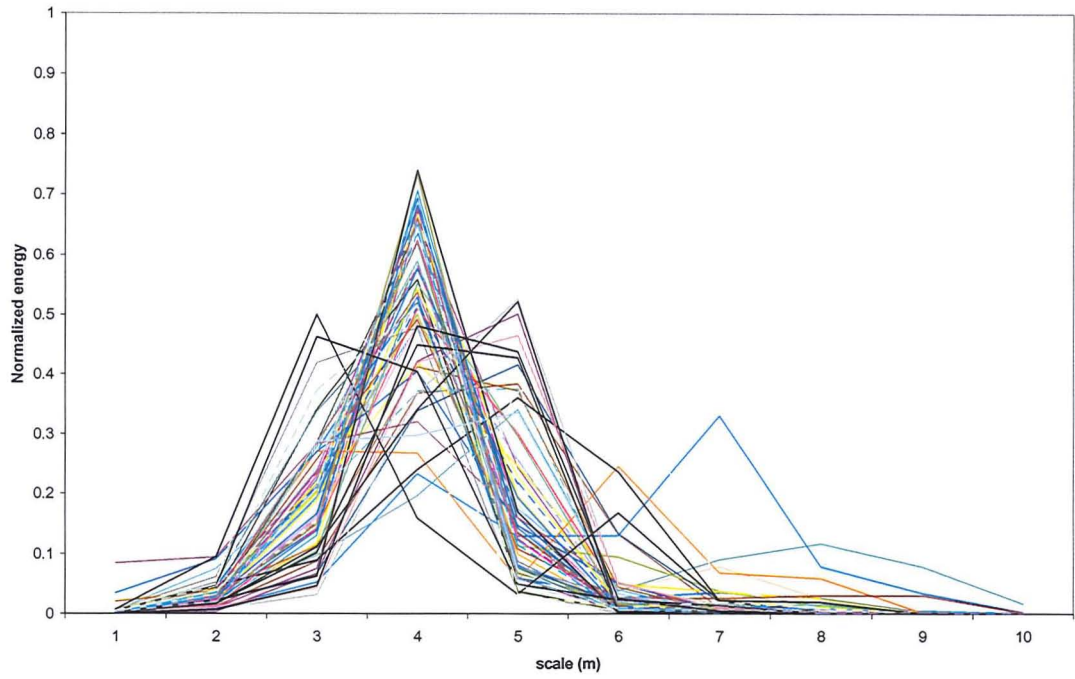


(a) Example of a pre-shock trace which corresponds to a ROSC (return of spontaneous circulation) heart signal.

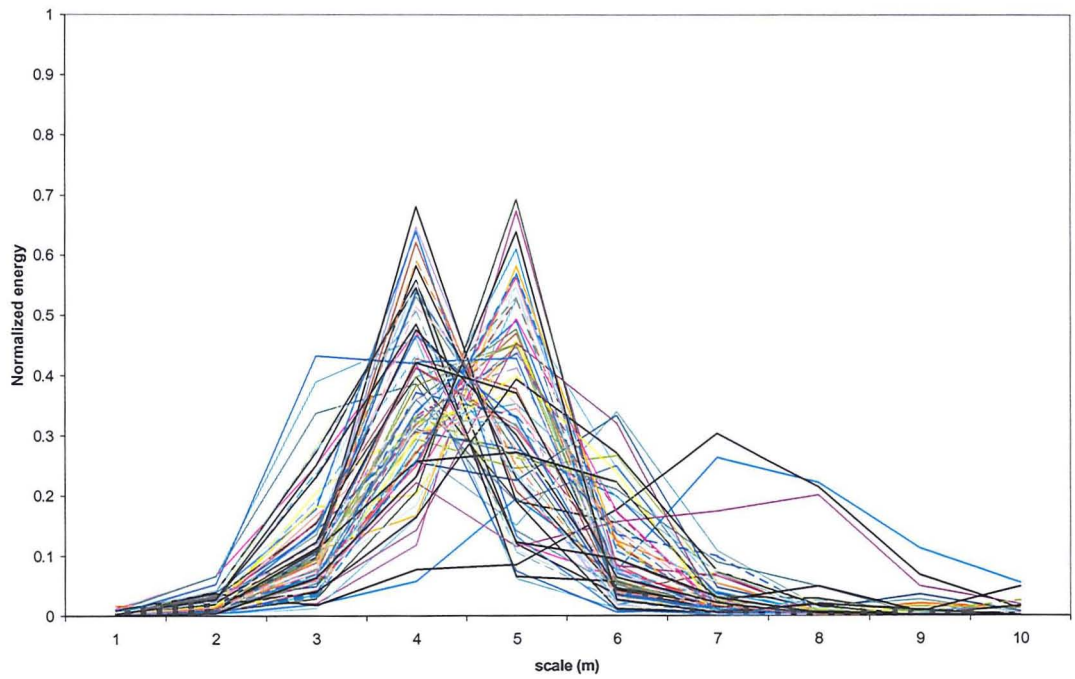


(b) Example of a pre-shock trace which corresponds to an asystole signal.

**Figure 3.12** Examples of two pre-shock ECG heart signals.



(a) The energy at each scale for the ROSC signals.



(b) The energy at each scale for the asystole signals.

**Figure 3.13** Energy in ECG signals during ventricular fibrillation (VF).

## **Chapter 4**

### **Global surface characterisation: Algorithm development and experimental results**

- 4.1 Introduction**
- 4.2 River bed sediment surface data**
  - 4.2.1 Introduction**
  - 4.2.2 Experimental procedure**
  - 4.2.3 Out of range values**
  - 2.2.4 Linear interpolation of rows and columns**
  - 2.2.5 Linear interpolation using triangulation**
- 4.3 Sediment surface characterisation: particle and form size distributions**
  - 4.3.1 Surface topographies**
  - 4.3.2 Energy distribution: fBm test surfaces**
  - 4.3.3 2-D edge effect**
  - 4.3.4 Discrete wavelet transform analysis of the river bed surfaces**
  - 4.3.5 Stationary wavelet transform analysis of river bed surfaces**
  - 4.3.6 Form size distribution: a new surface characteristic**
  - 4.3.7 Analysis of computer generated synthetic sediment surfaces**
  - 4.3.8 Comparison of DWT and SWT analysis**
- 4.4 Discussion**
- 4.5 Chapter summary**

# CHAPTER 4

## GLOBAL SURFACE CHARACTERISATION: ALGORITHM DEVELOPMENT AND EXPERIMENTAL RESULTS

### 4.1. Introduction

This chapter describes the results of the analysis dealing with *global surface characterisation*. This concerns the statistics of the complete surface whereby a number of river-bed sediment surfaces were studied using 2-D wavelet transform-based methods (DWT and SWT) developed by the author.

As described in section 2.10, the wavelet transform has proven to be a useful tool for the characterisation of a variety of surfaces. In the study described in this chapter the wavelet transform has been applied to characterise experimental sediment surfaces from 3-D laser scans of the river bed-surface topography. It is shown that, through wavelet transform decomposition the separation between different sized features making up the surface can be established. This is then used to provide a wavelet-based characterisation measure of the river-bed surface structures. This characterisation was employed to characterise the river-bed topography in order to detect changes of the bed-surface structure over time.

This chapter is structured as follows: section 4.2 introduces the sediment surface data-sets used in the main study including a description of the algorithms developed by

the author for the removal of out-of range values within these data-sets; section 4.3 presents the results from the analysis of the data, which also includes program development and explanations of the algorithms used in the study of the surface properties; section 4.4 contains a discussion of results; finally, section 4.5. summarises the main results of the work described in the chapter.

## **4.2. River bed sediment surface data**

### **4.2.1. Introduction**

The bed-surface roughness of rivers and channels has traditionally been characterised by the *particle size distribution (psd)*. However, this method is limited in that it only provides information on the distribution of the different particle sizes within the surface material. Information regarding the arrangement of the particles or the morphological structure of the surface is not accounted for in the *psd*. Research by Gessler (1990) has shown that the *psd* is independent of the actual friction factor of the bed surface. A number of alternative techniques have been developed to establish the surface bed layer composition. These were introduced in section 2.11, e.g. wax sampling, photographs and digital image processing, 3-D-laser-scanning analysis and video recordings. Although, these methods do not disturb the bed-surface topography they are primarily employed to determine the distribution of particle sizes of the surface material, rather than provide a morphological measure of the actual surface structure.

The experimental river-bed sediment data-sets analysed in this study were provided by Dr Ian McEwan at the Department of Engineering at Aberdeen University. The data was acquired during an earlier study which sought to better understand the physical processes of grain transportation by water; specifically the near-bed sedimentation process (Willets et al, 1998; Pender et al, 2001). This earlier study involved assessment of laboratory sediment degradation experiments carried out at HR Wallingford Ltd in a tilted flume. The financial support for the experiments was provided by the Engineering and Physical Sciences Research Council (EPSRC) and the European Union through a Human Capital Mobility grant to HR Wallinford Ltd. With the help of the EU funding, a Graded Sediment Transport Group was formed with researchers from the University of Aberdeen, Glasgow, Padua and Sheffield and the State Institute of Hydrology, St

Petersburg, Russia and the experimental data was freely shared between the participants (EPSRC Grant References: GR/L22058, GR/L22065 and GR/J67567). Further information concerning the work undertaken by the group can be found in Willets et al (1998), McEwan et al (1999b), Pender et al (2001), Nikora et al (2001a), and McEwan (2002).

The bed surface heights over a preselected region of the flume bed were measured using a laser profilometer. The data acquired using the laser scanning equipment was used by the Graded Sediment Transport Group to develop a tool for grain identification through image edge detection (Willets et al, 1998; McEwan et al, 2000, as described earlier in chapter 2 section 2.11). It is these 3-D topographical data-sets that were reanalysed by the author using wavelet transform methods to provide an alternative characterisation of the sediment bed-surface structure.

#### **4.2.2. Experimental procedure**

The sediment transport experiments were conducted in the 2.46m wide flume containing a main channel flanked by flood plains. The working length of the flume was 16.7m and the slope equal to 1:400 (0.25%). The main channel had a top width of 1.1m, bed width of 0.8m and with side slopes inclined at 45°. The banks and the flood plains were made from mortar and the bed of the inner channel comprised a surface of mobile sediment material. The sediment degradation experiments were conducted in the inner channel of the flume and the bankfull water depth was 0.15m for the experiments. The depth of the bed changed slightly during the experiment due to non-uniformities caused by the sediment activities. Figure 4.1(a) and 4.1(b) contains photographs of the flume and the transverse carriage holding the laser scanning equipment for measuring the bed surface topography and figure 4.2 contains schematic diagrams of the flume and its cross-section.

Graded dry sediment was placed in the central section of the flume. The experiments began with a fully mixed bed of one of three sediment composition types: B, C or B-remix. Full details of these composition types are given in table 4.1. The initial bed slope of the sediment was set to 0.25%, i.e. equal to the slope of the flume. After placement, the sediment was slowly and carefully subjected to water flow. The sediment



was first exposed to gentle water flow for a few hours to remove air bubbles and finer grains. The sediment was then subjected to a flood flow regime during the main phase of the experiment. Over time the sediment degraded as finer material washed away. Thus during the sedimentation process the bed surface layer rearranged itself. Data-sets from 17 of the sediment surface degradation experiments were used in the work described in this thesis. Table 4.2 shows a record of the laboratory experimental program for these experiments (EPSRC Grant Reference: GR/L22058). The table provides information for each experiment concerning: start and completion dates, sediment composition type, time of initial degradation, feed rates and duration of material feeding, total duration of experiment and the number of laser profilometer surface scans obtained. In all experiments, except number 7, sediment material was fed into the flume during the course of the experiment. The material was fed in at the top of the channel. The feed conveyor belt feeding the sediment material into the flume is shown in the schematic diagram in figure 4.2, (EPSRC Grant References: GR/L22058).

The bed surface was monitored during each experimental run and measurements of sediment transport rate and grain size composition were taken using three transversely placed traps across the flume. Longitudinal profiles of the bed surface were recorded at intervals of approximately 1 hour. In addition, plan black and white photographic documentation of the bed surface was carried out. At the end of each working day, after approximately 6-9 hours, a number of pictures were taken at cross sections along the channel. The bed surface topography was surveyed during the subsequent 6-12 hours when the flow was reduced. This was done by scanning a square region of the sediment surface bed near the trap of the channel using a laser profilometer. The laser profilometer, shown in figure 4.3, was moved within a fine grid structure collecting height measurements of the surface at each grid point. Each scan produced an array of  $x$ - $y$ - $z$  co-ordinates. Each data set consisted of a  $512 \times 512$  array of surface heights with spacing of 0.5mm, hence the physical size of the scanned surface was 256mm $\times$ 256mm. From this array a 3-D representation of the sediment surface topography can be constructed. For three of the experiments (numbers 19, 20 and 21) the laser profilometer spacing was set to 0.25mm to obtain better resolution of the digital data and identify smaller grains. Although a  $512 \times 512$  array of co-ordinates was still used, hence the

physical size of these surfaces were 128mm×128mm (Willettts et al, 1998; McEwan et al, 2000; Pender et al, 2001).

#### **4.2.3. Out of range values**

Due to the nature of the data acquisition techniques, ‘out-of-range’ values (or drop-out points) were included in data-sets where the laser profilometer had failed to take a reading. These points take the form of outliers from the valid surface height values (set to a numeric value of -999) within the data-sets. Most data-sets contained at least a few drop-out points and it was necessary to take account of these prior to the analysis of the surfaces. Table 4.3 lists the experimental sediment data-sets and the number of drop-out points contained in each. The filename identifying each data-set in the table provides information concerning the experiment number and the time when the surface was scanned. For example, data-set number ‘1050h56m’ corresponds to experiment number 10 where the surface scan which was performed 50 hours and 56 minutes after the start of this experiment.

Methods to compute new values for the erroneous drop-out points were developed by the author. Two different interpolation techniques were developed and tested. These are described in the following two sections.

#### **4.2.4. Interpolation of rows and columns**

Using an ‘averaged interpolation method’ an algorithm was developed by the author to locate the drop-out points within the surface data array and estimate new values which lie in-between known, or ‘valid’, values. Linear interpolation was chosen to estimate these new values at the locations of the drop-out points. The method developed by the author fits a linear function between each pair of valid values containing a drop-out point or collection of points between them. The true values at the location of the drop-out point(s) is then determined from the interpolated function. The method is shown schematically in figure 4.4.

This interpolation technique was applied to each row and each column of the surface independently. Thus, the drop-out points were removed and replaced with new

estimated values. This produced two ‘new’ matrices of the data, one where the data had been interpolated over the rows and one where data had been interpolated over the columns. The mean value of the data at each grid point was then computed from these two matrices. The algorithm for this *averaged interpolation method*, program *interp1.m* can be found in appendix A. This was a relatively fast process with a computer execution time of approximately 90 seconds for each surface 512×512 array. As an example figure 4.5 illustrates the method applied to one of the sediment data-set from experiment 22. Figure 4.5(a) shows the original surface with drop-out points (123 out of 262144 points for this particular surface). Figure 4.5(b) shows the surface after the drop-out points have been removed using the method.

However, for cases where several drop-out points were located together at one of the edges, this technique was unable to produce estimated data values as there are no second valid value to use to define the interpolation function. To solve this problem an edge extrapolation method was applied to the drop-out points located at the edges, whereby the values at the drop-out point locations were computed from a linear extrapolation based on the gradient of the last two valid points.

This averaged linear interpolation method proved to be a fast method for the removal and interpolation of new surface values. However, for data-sets with excessive amounts of drop-out points located together (in both rows and columns), the method did not produce acceptable interpolation, as show in figure 4.6. This surface had a large number of drop-out points, as shown in figure 4.6(a). Using the average linear interpolation method the new surface still contained a large number of erroneous values as the method produces a row of increasing or decreasing values as it extrapolates the data to the edges, as shown in figure 4.6(b). Therefore a more refined interpolation technique to compensate for drop-out points was developed and tested. This is described in the following section.

#### **4.2.5. Interpolation using triangulation**

An improved method for estimating the missing surface values was developed based on Delaunay triangulation. As the name suggests this method requires the triangulation of the existing data points which involves connecting each data point to its nearest

neighbour points, forming a mesh of triangles. The nearest enclosing triangle was found for each of the co-ordinates of drop-out points on the original 512×512 grid. Using the specified triangles, new values replacing the removed drop-out points could be estimated, the simplest method to do this was using triangular-based linear interpolation of the known data values at the vertices of the triangles. Thus, the missing values are estimated using a method based on the geometry of the barycentric coordinates of the triangulated data. This is described as follows.

Interpolation of the values at a point ( $P$ ) within a triangle at specified co-ordinates ( $x_i, y_i$ ) was performed by determining its barycentric co-ordinates. These are a triple of numbers ( $t_1, t_2, t_3$ ) corresponding to the masses placed at the vertices of the triangle where  $t_1 + t_2 + t_3 = 1$ ,  $0 \leq t_1, t_2, t_3 \leq 1$  and  $P$  is strictly located within the triangle. Thus, the new value at point  $P$  is determined as a weighted mean of the three known values associated with the triangle vertices. Figure 4.7 shows a schematic illustration of the interpolation of known values given at the vertices of the triangle vertices to determine the value at point  $P$  shown in the figure. The known values are located at the vertices ( $A_1, A_2, A_3$ ) of the triangle shown in the figure. In figure 4.7(a), point  $P$  is located within the triangle. Its value is determined as  $P = t_1 \times A_1 + t_2 \times A_2 + t_3 \times A_3$ , where  $t_1, t_2$  and  $t_3$  are the distances between the known vertices and  $P$ . If any of the  $t$ 's are equal to zero then  $P$  is located on one of the lines joining the vertices of the triangle. This is shown in figure 4.7(b) where point  $P$  is located on the line segment joining  $A_1$  and  $A_2$ , therefore  $t_3$  will equal zero and  $P$  can be determined as  $P = t_1 \times A_1 + t_2 \times A_2$ . Figure 4.8 shows an example of the method used to estimate the values of the drop-out points for one of the sediment surface data-sets. The heights at the 224 drop-out points on the original surface grid were interpolated using the technique. The algorithm for estimating the surface height at the drop-out points is contained in program *interp2.m* and can be found in appendix A.

This interpolation algorithm based on triangulation of the data was computationally more intensive compared with the previously described technique of linear interpolation of rows and columns described in section 4.2.4. The computing execution time increased to approximately 240 minutes per data-set. However, it produced a more realistic estimate of the true values at the locations of the edges of the data, which can

be seen by comparing figures 4.6 and 4.9. However, for one of the data-sets this method could not produce interpolated data values at the bottom right corner of the surface-bed. Following the interpolation a small amount of drop-out points had not been accounted for, see figures 4.10(a) and (b). In the surface matrix these values appeared as NaNs (Not-a-Number), which have an undefined numerical value. Performing the wavelet transform on this matrix will not produce a result and therefore these points had to be removed from the matrix. This was done by manually locating the NaN values and replacing them with the last valid value in that row, (see program *modcorn.m* in appendix A). This region only contains a small amount of NaN surface data values and therefore the method produces a relatively realistic estimation of the surface values. Although this method was not effective in removing larger amount of drop-out points as discussed above in section 4.2.4. The reconstructed bottom right corner is shown in figures 4.10(c) and (d).

The interpolation method for estimating the values at the drop-out points, based on Delaunay triangulation was applied to all the experimental data-sets. These modified sets were used in all subsequent analysis. As an example the complete set of modified experimental data from laboratory experiment number 25 is shown in figure 4.11.

### **4.3. Sediment surface characterisation: particle and form size distributions**

#### **4.3.1. Surface topographies**

There are a number of different methods for the global characterisation of surfaces including the determination of scaling properties, energy distribution and surface topographical information. It has been shown by a number of groups that by selectively combining wavelet details together surfaces can be separated into different topographies; usually known in terms of *roughness*, *waviness* and *form* (Chen et al, 1995; Jiang et al, 1999; Lee et al, 1998; Josso et al, 2002; Raja et al, 2002). This work has been reviewed in chapter 2, section 2.10.

In an initial study, the author followed the work of Jiang et al (1999) and used the wavelet transform in this way to separate the river-bed sediment surface into three

distinct topographies or form distributions. These were named *small forms*, *medium forms* and *large forms* respectively. The 2-D DWT was computed using the Daubechies D12 wavelet. As an example figure 4.12(a) show the original surface of data-set '2276h50d'. This was decomposed into 9 wavelet details. These are shown in figures 4.12(b)-(j). By selective combination of the details the three topographies were generated. The 'small form' surface for the river-bed was defined as details 1-5. This is shown in figure 4.13(a). These details were chosen to represent the 'small form' since the maximum grain size of the sediment was 20mm (see table 4.1), which falls between details 5 and 6. Therefore scales smaller than scale 6 must primarily be related to the particle sizes. The 'medium form' was constructed using details 6-8 as shown in figure 4.13(b). These details correspond to scales larger than the maximum measured grain size, these therefore must relate specifically to bed-form and be made from multiple grain aggregation. The 'largest form' surface of the bed-surface contains only the largest detail 9 and shows the overall form (largest scale) of the surface shown in figure 4.13(c). Even though this appears at first to be flat when plotted to the same vertical scale as figure 4.13(a) and figure 4.13(b), the topographic nature of this largest form surface can be seen in the exaggerated vertical scale plot of figure 4.13(d).

The method of separation of forms in this way proves to be an effective qualitative visual tool to separate the different form sizes within the surface. However it does not provide quantitative information about the actual surface structure. The following sections detail work carried out to provide such a measure.

#### **4.3.2. Energy distribution: fBm test surfaces**

To determine a quantitative measure of the surface topography it was decided to investigate the energy distribution of wavelet coefficients across scales. It was hypothesised that by comparing the energy distribution over time, information regarding the change of the surface structure could be extracted.

To develop the methodology the wavelet transform energies of synthetic fractal surfaces, fractional Brownian motions (*fBm*), were computed. These fractals have well known scaling behaviour across scales (Addison, 1997). It has been shown in previous work that both wavelet and Fourier spectral methods are superior to traditional fractal

methods, including the box counting and variable bandwidth methods, for analysing engineering surfaces which possess fractal properties (Dougan et al, 2000). This is particularly evident when analysing a single data realisation rather than an ensemble average.

Several fBm surfaces were generated with known characteristic scaling coefficients ranging from  $H=0.5$  to  $H=0.9$  (typical values for engineering surfaces). These are shown in figure 4.14. The surfaces were created using an existing *in-house* FORTRAN code for generating fBm surfaces, (Ndumu, 2000). The surfaces were decomposed into scale details using the 2-D Haar wavelet. A linear increase in coefficient energies with scale is expected for an fBm signal, (Addison, 2002). For the DWT this relationship is defined as:

$$\log_2 E_m = 2Hm + \text{constant} \quad (4.1)$$

where  $E_m$  is the wavelet scale dependent energy. For the fBm surfaces in figure 4.14,  $E_m$  was determined and plotted against scale in figure 4.15. It can be clearly seen that the scale dependent energy of the wavelet coefficients scales expected for these fractal surfaces (i.e. as given by equation 4.1). Thus the surfaces show fractal behaviour. Figure 4.16 contains a plot of the scale dependent energy against scales for one of the sediment surfaces compared with a synthesised fBm surface with Hurst exponent  $H=0.6$ . The relatively linear increase in coefficient energies with scale for the fBm surface contrasts with the reduction in coefficient energy for the sediment surface at large scales indicating that the sediment surface is not (mono) fractal in its behaviour across scales. At the largest scales (scale 8 and 9) the curve appear to loose its linearity. As discussed earlier in section 3.6, chapter 3, concerning the analysis of surface profile data, this is because of the larger step width of the wavelet which produces fewer coefficients at these scales. This part of the curve may therefore not be representative of the scaling properties of the fBm surface. The analysis of the fBm surfaces provides a useful validation of the author's algorithm for determining surface scale-dependent energy.

### 4.3.3. 2-D edge effect

Prior to the main analysis, edge effects caused at the boundaries of the data arrays had to be considered. Effects similar to the 1-D wavelet transform edge effects (chapter 3,

sections 3.2.1) will occur at the boundaries for the 2-D wavelet transform. These persist throughout the multiresolution analysis. The number of edge coefficients causing the edge effects for the 2-D wavelet transform can be derived from the number of the edge coefficients in the 1-D wavelet transform (see table 3.1 for the DWT and table 3.2 for the SWT in chapter 3). For the 2-D analysis there are edge coefficients present at all four boundaries of the transformed data.

The edge effect for an fBm surface of size  $128 \times 128$  can be clearly seen in the example given in figure 4.17(a). This example is the results of performing a 2-D DWT using a Daubechies D4 wavelet decomposition of the fBm surface. The first three levels of the wavelet coefficients are shown in figures 4.17(b)-(d). The edge effects are clearly visible at the boundaries of the surface. As described in chapter 3, if the edge coefficients are not taken account of in the transform process they will lead to erroneous results in the analysis. Algorithms to remove edge effect coefficients therefore had to be developed by the author. This was done for both the DWT and the SWT.

In the analysis described within this section the author was only interested in valid detail coefficients at each level: defined as those coefficients not corrupted by edge effects. The edge coefficients were therefore removed from the detail coefficients at each level, leaving only the valid coefficients. For the DWT the number of edge coefficients at each level was determined automatically for the selected wavelet used within the algorithm. The coefficients representing edge effects at the boundaries of each detail component ( $T_{m,n}$ ) could then be established. The modified detail component can be defined as:

$$T_{m,((edtop(m)+1):(2^m-edbottom(m)),(edleft(m)+1):(2^m-edright(m)))} \quad (4.2)$$

where  $edtop$ ,  $edbottom$ ,  $edleft$  and  $edright$  represent the limits of the edge effects at the boundaries of the transform and  $m$  is the scale index. Figure 4.18 shows a schematic of the original detail component ( $T_{m,n}$ ) and the detail component after the modification of the edges according to equation 4.2. At each level the three wavelet details component (vertical, horizontal and diagonal) were extracted and the edge coefficients were removed prior to combining them. Therefore after modifying the details only the valid



wavelet coefficients remain. The energy content of the modified wavelet detail is defined as:

$$E_m = \sum_{i=edtop(m)+1}^{2^m - edbottom(m)} \sum_{j=edleft(m)+1}^{2^m - edright(m)} (W_{i,j}^{(m)})^2 \quad (4.3)$$

where  $W_{i,j}^{(m)}$  is the combined wavelet detail components (vertical, horizontal and diagonal) at scale index  $m$ . However, as can be seen from equation 4.3 the edges are discarded from the energy computation, hence there is an apparent energy reduction as the scale  $m$  increases due to the encroaching edges. To account for this, the energy ( $E_m$ ) is rescaled using the ratio of the number of original coefficients to modified coefficients. This assures that the energy in the computation is representative of the whole detail surface. The original number of coefficients in the detail component ( $N_1$ ) at scale index  $m$  is given by:

$$N_1^{(m)} = (2^{M-m})^2 \quad (4.4)$$

and the number of coefficients in the modifying the detail component ( $N_2$ ) is given by:

$$N_2^{(m)} = (2^{M-m} - edtop(m) - edbottom(m)) \times (2^{M-m} - edleft(m) - edright(m)) \quad (4.5)$$

hence equation 4.3 is modified to become:

$$E_m = \sum_{i=edtop(m)+1}^{2^m - edbottom(m)} \sum_{j=edleft(m)+1}^{2^m - edright(m)} (W_{i,j}^{(m)})^2 \times \left( \frac{N_1^{(m)}}{N_2^{(m)}} \right) \quad (4.6)$$

which gives the representative scale dependent energy. Using this equation, the scale dependent energy content of the DWT details were determined for each data-set.

As for the DWT an algorithm was developed by the author to modify the details component in the SWT analysis. All four edges had to be modified in order to remove the edge effects from the valid data coefficients. For the SWT the number of edge coefficients at the boundaries are derived using equations 3.2 (top and left edges) and 3.3 (bottom and right edges). Once the size of the edge effect had been established the detail component could be modified and the edge coefficient removed. The SWT does not involve the down-sampling of the details through the transform, i.e. the size of the detail at each scale is equal to the size of the original input data. Thus, for the SWT equation 4.2 can be rewritten as:

$$T_{m,((edtop(m)+1):(2^M - edbottom(m)),(edleft(m)+1):(2^M - edright(m)))} \quad (4.7)$$

In addition, the SWT had to be modified for redundancy in the transform to ensure accurate energy content for each detail component. This was done prior to modifying the detail component for edge effect by dividing each detail component by  $4^{(lev/2)}$ , hence  $T_{m,(n1,n2)}/4^{(lev/2)}$ . The number of coefficients in the original detail component at each scale index ( $m$ ) is for the SWT defined as:

$$N_1^{(m)} = (2^M)^2 \quad (4.8)$$

and the number of coefficients for the modified detail component is defined as:

$$N_2^{(m)} = (2^M - edtop(m) - edbottom(m)) \times (2^M - edleft(m) - edright(m)) \quad (4.9)$$

For the SWT, equation 4.6 is therefore rewritten as:

$$E_m = \sum_{i=edtop(m)+1}^{2^M - edbottom(m)} \sum_{j=edleft(m)+1}^{2^M - edright(m)} (W_{i,j}^{(m)})^2 \times \left( \frac{N_1^{(m)}}{N_2^{(m)}} \right) \quad (4.10)$$

Using this equation the scale dependent energy content of the SWT details was determined.

#### 4.3.4. Discrete wavelet transform analysis of the river bed surfaces

As discussed in section 2.8, an ideal wavelet base would be well localised in both location (space or time depending on the type of signal) and frequency. The Haar wavelet is well localised in space but not in frequency. To improve the frequency localisation it is advantageous to use a wavelet with longer support. However, due to the oscillation of the wavelet with longer support the analysis may oversmooth the analysed data, thus it will be less effective to detect discontinuities. Further, wavelets with compact support are more computer efficient and because surface analysis are computer intensive processes wavelets with shorter support are advantageous (Tsai and Hsiao, 2001). The author therefore used the Daubechies D4 wavelet (i.e. four filter coefficients) as the main analysing wavelet. This wavelet is better localised in frequency compared to the Haar wavelet but still effective in detecting local discontinuities in the data compared to wavelets with longer support.

The 2-D DWT using D4 wavelet was employed to analyse the sediment surface data-sets introduced in section 4.2. The experimental sediment surface data-sets to be analysed contained an array of  $512 \times 512$  points, thus each data-set could be transformed into 9 levels of wavelet detail coefficients. An example of a discrete transform of a typical experimental sediment surface (data-set '2310h00m') is shown in figure 4.19. The original sediment surface is shown in figure 4.19(a) and the 9 level decompositions are shown in figures 4.19(b) (detail coefficients at the smallest level), to 4.19(i) (detail coefficients at the largest level). Each of these detail levels can be related to a specific physical size, as the measurement increments for the laser profilometer were set to 0.5mm (or 0.25mm for some cases). The scales of the DWT are set to powers of two, therefore the physical dimension associated with scale  $m$  is equal to  $0.5 \times 2^m$ .

The energy from each of the detail levels can therefore be associated with the contribution of surface forms at each scale to the overall topography. The sum of all scale dependent wavelet-based energies is equal to the energy of the original surface. Therefore, the wavelet-based energy at each scale provides information on the relative contribution to the overall surface topography attributed to each form size. The energy at each of the modified details was determined according to equation 4.6. The cumulative energy for each of the detail levels was plotted against the scale. This produced a distribution of scale forms related to the form of the sediment surface. The algorithm developed for the DWT analysis is contained in program *fsddwt.m* listed in appendix A. The results from the analysis of each of the sediment surface data-sets using the 2-D DWT are presented in figures 4.20(a)-(q). In each plot, the energy distributions are plotted for the sediment surfaces at each data collection time during the experiment. In addition, the corresponding particle size distribution (*psd*) is plotted on each graph for comparison.

#### **4.3.5. Stationary wavelet transform analysis of river bed surfaces**

As stated earlier, the DWT provides poor resolution in the analysis because of its translational invariance. The stationary wavelet transform (SWT) was therefore applied to increase the resolution of the analysis. Again the Daubechies D4 wavelet was employed. The SWT decomposition of the experimental sediment surface shown in figure 4.21(a) is shown in figures 4.21(b)-(j). This is the same surface used for

illustration of the DWT decomposition as that described in the previous section. The enhanced resolution of the SWT details is obvious when comparing figure 4.21 with 4.19. The edges were modified as described in section 4.3.3 where only the valid wavelet coefficients were extracted from the transform. The energy of the SWT coefficients for each of the detail level was determined according to equation 4.10 and plotted against scale. The algorithm developed for the SWT analysis of the sediment surface is contained in the program *fsdswt.m* found in appendix A. The results of the energy determination from the analysis of the sediment surfaces data using the 2-D SWT are presented in figures 4.22(a)-(q). Again the particle size distribution (*psd*) is plotted on each graph for clarity.

#### **4.3.6. Form size distribution: a new surface characteristic**

As described in the preceding two sections the sediment surfaces were each decomposed into a range of scale details using both the DWT and the SWT. Each detail of the wavelet transformed surfaces can be associated with a real physical surface 'form' within a range of scales. The results from the analysis shows the cumulative sum of the energy of the wavelet coefficients at each scale expressed as a percentage of the total sum of all wavelet coefficient energy at all scales. These curves are therefore representative of the distribution of surface form scales. This '*form size distribution*' (*fsd*) is suggested as a more appropriate measure of surface morphology than the commonly used *psd*.

The traditional measure of the characteristic 'sizes' of a sediment bed surface is the *particle size distribution (psd)*, as described in chapter 2, section 2.11.3. This measures the cumulative percentage by weight of particles within different size ranges; where the distribution of weights is determined using a series of standard sieves of successively smaller mesh sizes (Craig, 1987).

From the plots contained in figures 4.20 and 4.22 it can be seen that the wavelet-based *fsd* does not follow the distribution of the individual particle sizes of the bed material. The scales corresponding to the largest form size cannot correspond to individual sediment grain sizes because none of the grains were larger than approximately 20 mm (between scales  $m=5$  and 6 – the maximum of the *psd*). At scales larger than these, the

wavelet decomposition picks up specific surface formations, or ‘forms’, rather than individual particles. In fact, it can also be concluded that some of the *forms* at physical scales less than 20mm may also be related to the overall structure. This is because coherent masses of small particles can be picked up as larger forms at larger scales. This is shown schematically in figure 4.23.

Hence it is proposed that the *fsd* of a surface is potentially a more useful measure for characterising river bed surfaces than the *psd*, as it is the aggregate topographical nature of the surface which affects the flow characteristics and not the constituent bed surface grain size distribution. This point is shown schematically in figures 4.24(a) and 4.24(b), which shows the flow over two surfaces with similar *particle size distribution* but different *form size distributions*. The surface in figure 4.24(a) contains a higher degree of large scale forms than that of figure 4.24(b), which is much flatter. The two surfaces will affect the flow differently depending on their surface topology. The rougher surface (figure 4.24(a)) will cause a greater disturbance to the flow increasing its bed friction characteristics and altering flow depths and velocity distributions within the channel.

#### **4.3.7. Analysis of computer generated synthetic sediment surfaces**

As an extension to the study of energy distribution of sediment surfaces, the above described analysis was also used to investigate the nature of computer generated synthetic sediment surfaces. (These are described in more detail in section 5.2, where methods for the optimal thresholding of surface features located on these background surfaces is described in detail.) The surfaces are composed of grain sizes 2mm and 3mm respectively. The original surface data, supplied to the author by Dr John Heald at the University of Aberdeen, were in the form of a 1024×1024 point array. However, due to the computer intensive process of the SWT the data had to be down-sampled by two to perform a complete SWT decomposition, thus the surfaces analysed were 512×512 point arrays. For these surfaces 10 points in the array is equal to a 1mm physical scale, i.e. the surfaces had physical dimensions of 51.2mm×51.2mm. Again the Daubechies D4 wavelet was used and the wavelet transform details were modified for edge effects at the boundaries as described previously. The energy content for each of the scale details was established for the DWT using equation 4.6 and for the SWT using equation 4.10. The results are presented in figure 4.25 for the DWT and figure 4.26 for the SWT.

In figures 4.25(a) and 4.26(a) the cumulative scale energy have been plotted against the scale producing a distribution of surface energy, i.e. the *fsds*. These graphs show a clear difference in the size distributions between the surfaces containing grains of size 2mm and surface with grains of size 3mm. Since the 2mm surfaces are made up from smaller particle sizes a relatively higher amount of scale energy is expected for these curves at lower scales. It can be observed from the figures that the curves for the 2mm surfaces do exhibit a higher percentage of cumulative energy at each scale compared to the curves generated from the 3mm surfaces. This is observed for both the DWT and the SWT analysis.

Note that the real physical width of wavelet is in fact not equal to  $2^m$ . A representative period of the wavelet at each scale can be determined from its Fourier spectrum, i.e.  $p=1/f$ , where  $p$  is the period and  $f$  is a representative frequency of the wavelet often taken to be the maximum frequency of the power spectrum of the wavelet. Figure 2.9 shows the D4 wavelet at scale 4 and its Fourier transform, where the maximum frequency occurs at 0.045Hz. This is actually the frequency of the wavelet at scale 4, to get a representative period of the wavelet  $p$  therefore has to be divided by the size of the wavelet at this scale, (i.e.  $2^4$ ). As stated earlier, each point in the synthetic surface is equal to 0.1mm in physical scale, thus the ‘period’ of the wavelet at each scale can therefore be determined as  $0.1 \times p \times 2^m$ , where  $p$  is the period of the mother wavelet ( $p$  is 1.39 for the D4).

The two different grain sizes are marked by dotted lines in figures 4.25(a) and 4.26(a). For the DWT analysis it can be seen that the *fsd* curves reach the size of the surface grains at approximately 60% for both the 2mm and 3mm surfaces. Similarly for the SWT analysis the *fsd* curves reach the grain sizes at approximately 70% for both the 2mm and 3mm surfaces, respectively. Thus, information picked up after this point must solely be related to the form of the surface rather than the constituent particles. In figures 4.25(b) and 4.26(b) the normalised energy at each scale has been plotted against scale. A possible best fit line was fitted to the data by eye for the 2mm and 3mm surfaces. It can be seen from the graphs that the maximum energy occurs at approximately 2mm and 3mm, which is the respective grain size for the two different surfaces.

Comparing the results of the DWT and the SWT analysis (figures 4.25 and figure 4.26), we observe that the *fsd* curves produced using the SWT, essentially lie on top of each other for the two particle sizes. However, the *fsd* curves produced using the DWT are more spread out, particularly at larger scales. This is also shown in figure 4.27 where results of the DWT and the SWT for synthetic surfaces made up from a mixture of grains of sizes 2mm and 3mm analysis have been plotted on the same graph. The *fsd* curves are more spread out for the DWT when compared to the SWT curves. This shows that the DWT has poorer reproducibility compared to the SWT. This is because the DWT downsamples the data at each level, hence at the larger scales only a few wavelet coefficients are produced. As the SWT does not involve downsampling it is more consistent over all scales and especially at larger scales.

#### **4.3.8. Comparison of DWT and SWT analysis**

The DWT is a fast transform with an execution time of less than 10 seconds when computing the scale related energy distribution within a surface. This is due to the dyadic grid structure of the transform. For the SWT however, the execution time increases to approximately 1 hour and 30 minutes per data-set, due to the higher resolution of the analysing transform. The noticeable difference in resolution can be seen when comparing the plots of the wavelet details in figures 4.19 (DWT) and 4.21 (SWT). In addition it has been shown that the DWT has poorer reproducibility when compared to the SWT especially at larger scales. In the analysis of the computer generated sediment surfaces, the *fsd* curves produced using the DWT (figure 4.25) are more spread out than those produced using the SWT (figure 4.26).

#### **4.4. Discussion**

The work presented in this chapter describes the use of the wavelet transform as an analysis tool for studying the characteristics of river-bed sediment surfaces. The work showed that the 2-D wavelet transform can be used to effectively separate a surface into different details or size ranges. The cumulative sum of the energy of the coefficients at each scale expressed as a percentage of the total sum of all wavelet coefficient energy was plotted against the scale, i.e. at different sizes. These curves are representative of

the distribution of surface forms. Thus, instead of determining the *particle size distribution (psd)* of the sediment surfaces, the wavelet-based method outlined here provides a quantitative measure of the distribution of forms on the sediment surface across physical scales i.e. a *form size distribution (fsd)*.

Both the discrete wavelet transform and the stationary wavelet transform have been used to create *fsd* curves for the river-bed data. Similar results were found for the two different transforms, which would be expected as the SWT is, in effect, a redundant DWT. However, as mentioned earlier higher resolution is provided using the SWT, which results in an improved reproducibility of the *fsd* curves when compared to the DWT. This could be seen when observing the results of computer generated surface analysis presented in section 4.3.7. Therefore, the following discussion of the results of the wavelet transform analysis of the laboratory experimental sediment surface data is limited to the SWT analysis. First, each bed will be considered separately in turn. In addition, the *fsd* curves produced for experiment 7 to 12 have also been compared with the measured mobility of the surface bed, i.e. feeding rates at the upstream and observed sediment transport rates at the downstream end of the flume as reported in Marion et al (2003).

### **Experiment 7**

The results from the analysis of data-sets in experiment 7 is shown in figure 4.22(a). No sediment material was fed into the flume during this experiment. Therefore, undisturbed degradation of the sediment surface over time can be evaluated. Observing the distribution of the *fsd* curves it can be seen that most curves are in close proximity to each other. However, the *fsd* of the initial data-set, '0700h00m', is located at the top of the distribution curves, visibly separated from the *fsd* curves obtained from subsequent scans. Also notice that data-set '0718h02m' located at the bottom of the *fsd* curves is quite separate from the others. This indicates that at this point in time the surface in the scan region contains a higher amount of larger forms compared to the other data-sets. Further, the two data-sets '0740h02m' and '0772h25m' have similar *fsds* indicating that the surface topographic has remained stable during the period between these two consecutive surface scans. Because no sediment material was fed into the flume for this experiment the bedload transport rate decreased significantly after about 5 hours of the experimental run. This is because as the surface developed towards a static armour and



bedload transport rates reduced. Hence, after initial degradation only small amount of surface material was removed. The highest bedload transport rate was found at the time for data-set '0702h34m' with approximately 7g/s, however the *fsd* curve for this data-set is located in the middle of the other curves, hence compared with the other *fsd* curves, with lower bedload transport rates, no significant difference can be seen.

For the remaining 16 experiments, sediment material was fed continuously into the flume at the top of the channel. Information concerning the feed rates and duration of material feeds can be found in table 4.2.

### **Experiment 8**

Figure 4.22(b) shows the results from the analysis of data-sets in experiment 8. In this experiment sediment material was fed into the flume for 67 hours at a feed rate of 2.5g/s. Because of problems with the laser profilometer, an initial surface scan (at time zero) could not be obtained. The first scan of the surface was therefore taken 28 hours and 10 minutes from the start of the experiment. The *fsd* curves from this experiment are located relatively close to each other with the exceptions of data-sets '0828h10m' and '0836h00c'. These are separated from the subsequent *fsd*'s indicating that they exhibit a relatively higher amount of larger forms. Further, studying the results after the feeding of material had stopped, data-set '0883h00m' exhibits a higher amount of smaller surface forms comparing with the following data-set, '0887h00m', indicating that degradation of the surface-bed occur between these two scans. Comparing the results with the variations in bedload transport rate, high sediment transport rate was observed at the time for data-sets '0842h00m' and '0883h00m', with an approximate transport rate of 4.0g/s. These two curves were located towards the top of the *fsd* curves. The same comparison at the lowest sediment transport rate, 1.5g/s, is found at the time of data-set '0828h10m', this is located at the bottom of the *fsd* curves.

### **Experiment 9**

The results from the analysis of the data-sets in experiment 9 are presented in figure 4.22(c). Material was fed into flume for 49hours and 13 minutes with a feed rate of 5g/s. Comparing with the results of previous two experiments the *fsd* curves in this experiment are more spread out over the scales. The initial data-set, '0900h00m', shows the highest percentage of smaller surface forms. As material is fed into the flume

through the experiment no distinctive change towards a coarser surface form can be observed. In addition, there appears to be little change in the form distribution for the last 13hours (i.e. after the cessation of sediment feeding) as data-sets '0956h16m' to '0969h32m' have similar *fsds*. For this experiment the highest bedload transport rate, about 8.0g/s, is observed for data-set '0949h13m' for which the *fsd* curve is located at the bottom of the distribution curves while the lowest transport rate, 0.5g/s, is found for data-set '0906h00m' located at the top of the *fsd* curves.

### **Experiment 10**

Figure 4.22(d) shows the results from the analysis of surfaces in experiment 10. In this experiment sediment was fed into the flume at a feed rate of 5g/s for 42hours and 55minutes. Due to problems with the laser profilometer a surface scan at time zero could not be obtained. These *fsd* curves appear more spread out than those for the previous experiment. Comparing two surface scans following the end of material feeding, it can be seen that data-set '1050h34m' exhibits a higher percentage of smaller forms (for size 1mm to 10mm) compared to the final surface scan '1059h34m'. Studying the bedload mobility data-set '1027h18m' has the highest bedload transport rate, with approximately 7.0g/s, while the lowest bedload transport rate, about 1.0g/s, is observed 17hours after material feeding has stopped, data-set '1059h34m'. Observing the location of the *fsd* for these data-sets '1027h18m' is located at the bottom and '1059h34' is located in the middle of the distribution curves.

### **Experiment 11**

The results from the analysis of surfaces in experiment 11 are shown in figure 4.22(e). Material was fed into the flume for 32hours at a feed rate of 5g/s for this experiment. The *fsd* curves in this experiment are again relatively well spread out over scales. Further, the initial data-set, '1100h00m', exhibits the highest amount of smaller forms. The highest amount of smaller surface forms is found in data-set '1148h99m' as the material feeding ends. The available data-sets for this experiment were only in the regions of low bedload transport rates, i.e. at the start and the end of the experiment. The highest amount bedload transport is found at the time of data-set '1101h51m' with a transport rate of 2.5g/s located in the middle of the *fsd* curves. The lowest level of sediment transport is found for the last data-set '1160h33m' with a transport rate of 0.5g/s located towards the bottom of the *fsd* curves.

### Experiment 12

In experiment 12 the material feed rate was 5g/s and the duration of the feeding was 32hours and 34minutes. The results from the analysis of the surfaces in this experiment are presented in figure 4.22(f). Observing these distribution curves it can be seen that the curves are located over a relatively narrow band, with the exception of data-sets '1207h12m' and '1207h13m' which are located separate from the other data-sets. The initial *fsd* curve (data-set '120h00mc') is located close to the top of the distribution curves. Because of the material fed into the flume during the experiment no clear pattern of degradation could be seen in the following *fsds*. However, after the material feeding had stopped the surface appears to degrade as data-set '1240h00c' has a higher percentage of smaller forms compared to the final data-set '1273hdry'. For this experiment the highest bedload was found at the time of data-set '1223h51m' with an approximate transport rate of 5g/s. The corresponding *fsd* curve is located in the middle of the *fsd* curves. The lowest bedload transport rate, 0.5g/s, was found for data-sets '1207h12m' and '1207h13', which are the surface scans during material feeding. A transport rate of 0.5g/s was also found for the final surface scan, data-set '1273hdry', 40 hours after material feeding has stopped. The corresponding *fsd* curves are all located towards the bottom of the *fsd* curves plot.

### Experiment 18

Figure 4.22(g) shows the results from the analysis of sediment surfaces in experiment 18. Sediment material was fed for 29hours at a feed rate of 5g/s into the flume during this experiment. These *fsd* curves are located relatively close to one another. However a separation of the *fsd* curves can be seen at larger scales. This is marked with dotted lines in the figure where one group of *fsd* curves exhibit a higher amount of larger forms (marked with an arrow) compared to the other group of *fsd* curves. Interrogation of the results indicates that this is not related to the end of material feeding. The difference is therefore probably related to the movement of material over the surface through time. Further, the *fsd* for the initial data-set, '1800h00d', is positioned at the bottom of the distribution curves, hence the following data-sets appear to have a higher amount of smaller forms. This is probably due to material being fed during the experiment and therefore no obvious degradation of the surface is clearly visible. However, the final data-set, '18phase3', have a high amount of larger forms at larger sizes, i.e. it has coarser surface structure.

### **Experiment 19a**

During experiment 19a material was fed for 27hours at a feed rate of 5g/s. Figure 4.22(h) shows the results from the analysis of data-sets from this experiment. These *fsd* curves are positioned close to one another. However, the initial data-set, '1900h00m', is positioned at the top of the distribution curves. No distinct pattern of the relatively position of the *fsds* can be observed in the plot.

### **Experiment 19**

The *fsd* curves produced for experiment 19 are shown in figure 4.22(i). In this experiment, sediment material was fed for 29hours at a feed rate of 5g/s. The laser profilometer was set to have a spacing of 0.25mm for this experiment. These curves are, similar to the previous experiment, positioned close to one another. However, the initial *fsd*, for data-set '1900h00m', is positioned at the top of the distribution curves, a clear difference can be observed particularly at the smaller sizes (0.5mm to approximately 7mm). However, no clear pattern could be seen for the subsequent data-sets.

### **Experiment 20**

The results from the analysis of data-sets in experiment 20 are shown in figure 4.22(j). In this experiment sediment was fed into the fume for 32hours at a feed rate of 5g/s. Again these data-sets were scanned with a laser spacing of 0.25mm. These *fsd* curves for this experiment are positioned close together. Still, observing the results a difference can be seen at smaller scales (i.e. size 0.5mm to 4mm) between data-set '2000h00m' and the following data-sets. The final surface scan was taken at 32hours, thus the surface was not allowed to degrade in the absence of added material

### **Experiment 21**

Figure 4.22(k) show the results of the analysis of surfaces in experiment 21. This surface was also scanned with a laser spacing setting of 0.25mm for data-sets '2114h40s' to '2137h50s and a laser spacing setting of 0.5mm for data-sets '2142h10m' to '2154h30m'. Sediment was fed into the flume for 52hours and 45minutes at a feed rate of 5g/s. These *fsd* distributions are positioned close together with the exception of data-sets '2137h50s' and '2148h00m'. The data-set '2137h50s' has the highest amount of smaller surface forms. This may suggest that a larger amount of smaller sediment

material have settled in surface at the time of this surface scan. Further, the *fsd* curve of data-set '2148h00m' has a much higher amount of larger forms when compared with the other data-sets in this experiment.

### **Experiment 22**

The results from the analysis of data-sets in experiment 22 are presented in figure 4.22(l). In this experiment sediment material was fed for 30hours and 55minutes at a feed rate of 5g/s. It can be seen that three data-sets ('2215h00m', '2268h00m' and '2276h50m') are separated from the other curves. It is noticeable that these surface scans are not sequential and therefore highlight the variability of the topography of the mobile surface bed in the scan region. At the smallest sizes 1mm and 2mm the initial data-set '2200h00d' has the highest percentage of surface forms when compared to the other data-sets.

### **Experiment 23**

Sediment was fed into the flume for 31hours and 50minutes at a feed rate of 5g/s in this experiment. Figure 4.22(m) shows the results from the analysis of the surfaces in this experiment. These *fsd* curves are more spread out over the scale sizes, compared to the results of some of the previous experiments. The initial distribution curve for data-set '2320h00m' appears to contain a higher amount of larger form sizes as the *fsd* is located at the bottom of the distribution curves. Further, after the feeding of material has ended it can be seen that the data-set '2334h20m' has a higher amount of smaller form sizes comparing with the final data-set '2367h00m'.

### **Experiment 24**

The results from the analysis of surfaces in experiment 24 are shown in figure 4.22(n). For this experiment material was fed into the flume for 45hours at a feed rate of 5g/s. The *fsd* curves for this experiment are relatively spread out. The initial data-set, '2400h00m', is located in the middle of the distribution curves. No clear degradation pattern can be seen in the location of the *fsd* curves.

### **Experiment 25**

During experiment 25 material was fed into the flume for 42hours and 30minutes at a feed rate of 5g/s. Studying the results, shown in figure 4.22(o), it can be seen that the

curves are relatively spread out, similar to those of the previous experiment. Studying the results further, it can be seen that the initial data-set '2500h00m' is positioned at the top of the distribution curves. For the following curves no clear pattern can be seen. The final *fsd* '2564h30m' is actually located in the middle of the distribution curves. Further, data-sets '2523h30'm and '2547h30m' appear to have a similar distribution of form sizes.

### **Experiment 26**

In this experiment material was fed into the flume for 21hours and 15minutes at a feed rate of 5g/s. The results from the analysis of the data-sets from this experiment are shown in figure 4.22(p). The distribution curves are located close together, showing similar *fsd* curves. As with the previous experiment, no clear degradation pattern can be seen. However, the last surface scan, data-set '2648h15m', is located towards the bottom of the distribution curves especially at larger scales. This indicates that the surface has a relatively coarser surface structure.

### **Experiment 27**

Figure 4.22(q) shows the results from the analysis of surfaces in experiment 27. This experiment was fed with material for 16 hours at a feed rate of 5g/s. Only two data-sets could be obtained from this experiment. By observing the *fsd* curves it can be seen that the final data-set, '2708h30m', appears to have a greater amount of smaller surface forms compared with the initial data-set, '2700h00m'. This higher amount of smaller forms in the later data-set may be because material is being fed into the flume.

### **General observations**

Studying the results as a whole it can be seen that some of the *fsds* show a higher quantity of proportional energy at larger scale forms. It is suggested this indicates the presence of large topographical differences in the surface while a smaller amount of large scale energy represent a rather flat surface topography. The results show that, in general, the initial *fsd* has a smaller amount of relative large scale energy compared to subsequent surfaces. As this is before the surface is subjected to water flow the surface is expected to have a rather flat topography, which is exhibited in the *fsd* curves. However, from the above results it is clear that it is difficult to distinguish an obvious degradation pattern within each experiment. The results will be affected by the feeding

of sediment material into the flume which will increase the quantity of sediment material in the surface over time. Also the formation and breaking-up of coherent structures of particles during the armouring of the surface (as describe in section 2.11.3) produces local variations in the surface topography over time. Larger coherent structures will be regarded as larger forms in the wavelet transform analysis. Consequently the *fsds* will have a higher amount of larger surface forms during periods when a local surface feature is present. As these structures break up or move away the *fsd* will change significantly. Because the scanned area is relatively small, this process causes large variability in the *fsds* over time. This explains why a general trend was not observed in the *fsd* curves for the experiments. The large variability of the *fsds* is evident when studying the *fsds* for data-sets '1207h12m' and '1207h13m' in experiment 12. Although these two surface scans are only separated by one minute in time a clear difference can be seen between the produced *fsd* curves. Further, in experiment 18, it was noticed that the three surfaces ('1800h00d', '1820h00m' and '18phase3') exhibited a relatively higher amount of large surface forms. As these surfaces were not sequential, this indicates the variability of the topography of the mobile surface bed in the scan region. This was also seen in experiment 22 where the *fsd* curves for surfaces '2215h00m', '2268h00m' and '2276h50m', again not sequential in time, are located separately from the remaining *fsds*. In addition, for experiment 7 to 12 the *fsd* curves were also compared with material feeding and bedload transport rates for each individual experiment. The location of the *fsd* curves was compared with the amount of bedload transport rate at specific times. Studying the *fsd* during low bedload transport rates, three of the experiments (number 8,11 and 12) had *fsd* curves located at the bottom of the distribution curves. Similarly comparing the *fsd* curves at high bedload transport rates two experiments (number 8 and 10) had *fsd* curves located towards the top of the distribution curves. As a higher amount of sediment material is expected to move through the scanned area at high transport rates a larger amount of smaller forms would be expected, i.e. the *fsd* would be located towards the top of the distribution curves. However, for one of the experiments (number 9) the *fsd* curve was located at the top of the curves for the low bedload transport rate while the *fsd* for the high transport rate was located at the bottom. Therefore, for the observed data-sets in this study, no general conclusion could be drawn between mobility data of the sediment surfaces and the location of specific *fsd* curves. However, this could be an interesting topic for future

research where more comprehensive data sets could be probed to determine whether a link exists between the changes in the *fsd* and the mobility of the surface material.

#### **4.5. Chapter summary**

This chapter has presented the results from the 2-D wavelet transform analysis of experimental river-bed sediment surfaces. The chapter dealt with *global surface characterisation*, which concerns the global characterisation of the complete surface.

Due to the nature of the data-acquisition techniques, the original river-bed experimental sediment surface data contained a number of drop-out points. An algorithm therefore had to be developed by the author to estimate new values replacing drop-out points, which otherwise would have produced erroneous results of the analysis. Evaluating two different interpolation methods it was found that interpolation using Delaunay triangulation produced a more realistic estimation of the true values at the locations of the drop-out points, especially at the edges of the data. Therefore this method was applied to all the experimental data-sets to estimate values replacing the drop-out points and these modified data-sets were used in all subsequent analysis.



## **CHAPTER 4**

### Tables

Sieve size (mm)	Sediment mixtures Mass retained at each sieve size in percent		
	B %	C %	B-remix %
20	0.9	0	0
14	5.5	0	3.3
10	7.2	6.0	4.7
6.3	10.2	40.1	11.6
5	14.2	13.9	18.5
3.35	29.4	5.7	27.6
2	12.6	4.7	11.3
1.18	4.7	10.6	3.5
0.6	3.8	9.1	3.6
0.425	3.2	2.3	2.9
<0.425	8.4	7.9	13.1

**Table 4.1** Initial distribution of particle sizes in the three sediment mixtures.

### Graded Sediment Experimental Program in the Tilted Flume

Experiment Number*	Start date	Sediment	Initial degradation (min)	Feed min/rate(g/s)	Total duration (min)	Completion Date	Number of data sets (512x512)
7/OB	2.10.95	B	4810	NA	4810	12.10.95	9
8/IB	23.10.95	B	NA	4020/2.5	5220	8.11.95	8
9/IB	13.11.95	B	NA	2953/5.0	4172	21.11.95	12
10/OB	4.12.95	B	NA	2575/5.0	3775	14.12.95	5
11/IB	15.1.96	B	NA	1920/5.0	3633	26.1.96	6
12/OB	9.2.96	B	NA	1954/5.0	4380	22.2.96	13
18/IB	25.2.98	C	NA	1740/5.0	3480	7.3.98	9
19a/IB	19.3.98	C	NA	1620/5.0	2321	31.3.98	6
19/IB	8.4.98	C	NA	1740/5.0	4530	28.4.98	7
20/I&OB	6.5.98	C	NA	1920/5.0	4800	23.5.98	5
21/I&OB	4.6.98	B-remix	NA	3165/5.0	3720	26.5.98	8
22/I&OB	13.7.98	B-remix	NA	1855/5.0	4610	2.7.98	9
23/OB	2.9.98	B-remix	NA	1910/5.0	4620	28.8.98	7
24/OB	30.9.98	B-remix	NA	2700/5.0	5040	27.10.98	14
25/OB	30.10.98	B-remix	NA	2550/5.0	4170	20.11.98	10
26/OB	27.11.98	B-remix	NA	1275/5.0	2895	2.12.98	6
27/IB	8.12.98	B-remix	NA	960/5.0	960	10.12.98	2

\*IB=inbank, OB=overbank

**Table 4.2** Experimental program for river sediment surface bed experiments (EPSRC Grant Reference: GR/L22058).

<i>filename</i>	<i>No. drop-out points</i>	<i>length</i>	<i>percent drop-out</i>
<b>Ex07</b>			
0700h00c	32	0.5mm	0.01%
0702h34m	65	"	0.02%
0710h37m	256	"	0.10%
0718h02m	127	"	0.05%
0725h38m	123	"	0.05%
0733h11c	47	"	0.02%
0740h02m	71	"	0.03%
0772h25m	235	"	0.09%
0780h10m	5	"	0.00%
		<i>mean</i>	0.03%

<i>filename</i>	<i>No. drop-out points</i>	<i>length</i>	<i>percent drop-out</i>
<b>Ex08</b>			
0828h10m	135	0.5mm	0.05%
0836h00c	73	"	0.03%
0842h00m	40	"	0.02%
0850h45m	18	"	0.01%
0859h00m	118	"	0.05%
0867h00c	28	"	0.01%
0883h00m	52	"	0.02%
0887h00m	310	"	0.12%
		<i>mean</i>	0.04%

<i>filename</i>	<i>No. drop-out points</i>	<i>length</i>	<i>percent drop-out</i>
<b>Ex09</b>			
0900h00m	22	0.5mm	0.01%
0906h00m	22	"	0.01%
090hdryc	25	"	0.01%
0913h56m	111	"	0.04%
0920h51m	29	"	0.01%
0928h21m	27	"	0.01%
0934h36c	1499	"	0.57%
0941h18m	278	"	0.11%
0949h13m	62	"	0.02%
0956h16m	64	"	0.02%
0965h27m	90	"	0.03%

0969h32m	220	"	0.08%
		<i>mean</i>	0.19%

<i>filename</i>	<i>No. drop-out points</i>	<i>length</i>	<i>percent drop-out</i>
<b>Ex10</b>			
1027h18m	45	0.5mm	0.02%
1035h03m	2	"	0.00%
1042h55m	262	"	0.10%
1050h56m	16	"	0.01%
1059h34m	68	"	0.03%
		<i>mean</i>	0.04%

<i>filename</i>	<i>No. drop-out points</i>	<i>length</i>	<i>percent drop-out</i>
<b>Ex11</b>			
1100h00m	171	0.5mm	0.07%
1101h51m	26	"	0.01%
110hdryc	89	"	0.03%
1148h00m	76	"	0.03%
1156h05m	79	"	0.03%
1160h33m	236	"	0.09%
		<i>mean</i>	0.04%

<i>filename</i>	<i>No. drop-out points</i>	<i>length</i>	<i>percent drop-out</i>
<b>Ex12</b>			
1207h12m	20	0.5mm	0.01%
1207h13m	284	"	0.11%
120h00mc	96	"	0.04%
120hdryc	101	"	0.04%
1215h04m	39	"	0.01%
1223h51m	57	"	0.02%
1232h34c	409	"	0.16%
1240h00c	1536	"	0.59%
1248h13m	51	"	0.02%
1256h02m	29	"	0.01%
1264h38m	7	"	0.00%
1273h00m	21	"	0.01%
1273hdry	108	"	0.04%
		<i>mean</i>	0.21%

**Table 4.3** Experimental data-sets.

<i>filename</i>	<i>No. drop-out points</i>	<i>length</i>	<i>percent drop-out</i>
<b>Ex18</b>			
1800h00d	1059	0.5mm	0.40%
1812h44m	2295	"	0.88%
1820h00m	34711	"	13.24%
1826h51m	10682	"	4.07%
1832h15m	8378	"	3.20%
1858h00m	6662	"	2.54%
1858hdr1	2786	"	1.06%
18endwet	6662	"	2.54%
18phase3	4274	"	1.63%
	<i>mean</i>		3.92%

<i>filename</i>	<i>No. drop-out points</i>	<i>length</i>	<i>percent drop-out</i>
<b>Ex19A</b>			
19a00h00	1315	0.5mm	0.50%
19a07h45	1697	"	0.65%
19a13h34	5201	"	1.98%
19a20h00	55514	"	21.18%
19a26h40	15367	"	5.86%
19a34h00	29665	"	11.32%
	<i>mean</i>		8.11%

<i>filename</i>	<i>No. drop-out points</i>	<i>length</i>	<i>percent drop-out</i>
<b>Ex19</b>			
1900h00m	162	0.25mm	0.06%
1905h30m	154072	"	58.77%
1913h30m	100798	"	38.45%
1919h20m	480	"	0.18%
1922h20m	676	"	0.26%
1945h00m	348	"	0.13%
1970h30m	202	"	0.08%
	<i>mean</i>		24.37%

<i>filename</i>	<i>No. drop-out points</i>	<i>length</i>	<i>percent drop-out</i>
<b>Ex20</b>			
2000h00m	33958	0.25mm	12.95%
2012h37m	4634	"	1.77%
2017h34s	1924	"	0.73%

2021h00m	3850	"	1.47%
2032h00m	176	"	0.07%
	<i>mean</i>		5.38%

<i>filename</i>	<i>No. drop-out points</i>	<i>length</i>	<i>percent drop-out</i>
<b>Ex21</b>			
2114h40s	60	0.25mm	0.02%
2121h00m	9	"	0.00%
2137h50s	47	"	0.02%
2142h10m	947	0.5mm	0.36%
2144h30a	13729	"	5.24%
2144h30m	68	"	0.03%
2148h00m	151	"	0.06%
2154h30m	77	"	0.03%
	<i>mean</i>		0.72%

<i>filename</i>	<i>No. drop-out points</i>	<i>length</i>	<i>percent drop-out</i>
<b>Ex22</b>			
2200h00d	0	0.5mm	0.00%
2207h00m	1	"	0.00%
2215h00m	7	"	0.00%
2225h00a	0	"	0.00%
2228h00m	17	"	0.01%
2237h30m	123	"	0.05%
2268h00m	1	"	0.00%
2276h50d	2779	"	1.06%
2276h50m	9	"	0.00%
	<i>mean</i>		0.12%

<i>filename</i>	<i>No. drop-out points</i>	<i>length</i>	<i>percent drop-out</i>
<b>Ex23</b>			
2300h00m	1	0.5mm	0.00%
2310h00m	13	"	0.00%
2320h00m	289	"	0.11%
2327h00b	38	"	0.01%
2334h20m	173	"	0.07%
2342h00m	75	"	0.03%
2367h00m	50	"	0.02%
	<i>mean</i>		0.03%

**Table 4.3** (continued) Experimental data-sets.

<i>Filename</i>	<i>No. drop-out points</i>	<i>length</i>	<i>percent drop-out</i>
<b>Ex24</b>			
2400h00m	32	0.5mm	0.01%
2409h00m	19	"	0.01%
2416h30m	1550	"	0.59%
2421h00m	1773	"	0.68%
2425h10m	29	"	0.01%
2431h10m	660	"	0.25%
2435h30m	0	"	0.00%
2438h30m	0	"	0.00%
2445h00m	1179	"	0.45%
2451h30m	0	"	0.00%
2463h00m	15880	"	6.06%
2472h30m	0	"	0.00%
2482h00m	2403	"	0.92%
2484h00d	2	"	0.00%
		<i>mean</i>	<i>0.69%</i>

<i>Filename</i>	<i>No. drop-out points</i>	<i>length</i>	<i>percent drop-out</i>
<b>Ex25</b>			
2500h00m	4617	0.5mm	1.76%
2510h30m	74	"	0.03%
2516h30m	0	"	0.00%
2523h30m	1	"	0.00%
2539h00m	1	"	0.00%

2542h30m	10	"	0.00%
2547h30m	529	"	0.20%
2550h30m	24	"	0.01%
2556h30m	53	"	0.02%
2564h30m	215	"	0.08%
		<i>mean</i>	<i>0.21%</i>

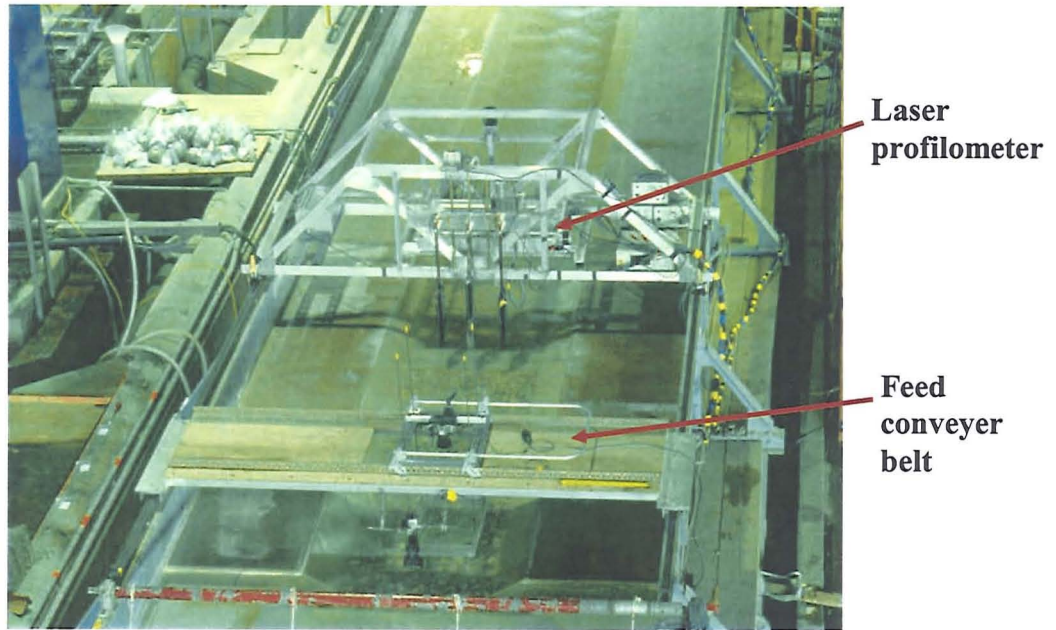
<i>filename</i>	<i>No. drop-out points</i>	<i>length</i>	<i>percent drop-out</i>
<b>Ex26</b>			
2604h00m	37	0.5mm	0.01%
2613h00m	251	"	0.10%
2622h00m	16345	"	6.24%
2631h00m	81	"	0.03%
2644h55m	0	"	0.00%
2648h15m	58	"	0.02%
		<i>mean</i>	<i>0.92%</i>

<i>filename</i>	<i>No. drop-out points</i>	<i>length</i>	<i>percent drop-out</i>
<b>Ex27</b>			
2700h00m	10	0.5mm	0.00%
2708h30m	10	"	0.00%
		<i>mean</i>	<i>0.00%</i>

**Table 4.3 (continued)** Experimental data-sets.

## CHAPTER 4

Figures



(a)



(b)

(a) The flume and (b) a close up showing the transverse system and laser sensor used to measure the bed surface texture.

Figure 4.1 Experimental flume.



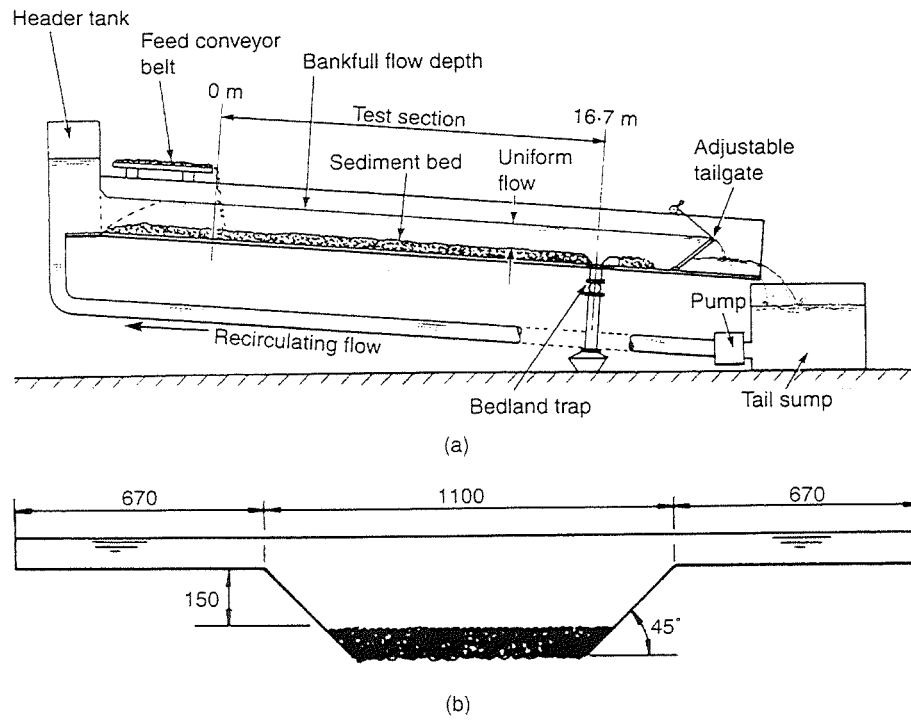


**Figure 4.2** Schematic evaluation and typical cross section of the flume (from Willetts et al, 1998).

**Laser  
displacement  
sensor**

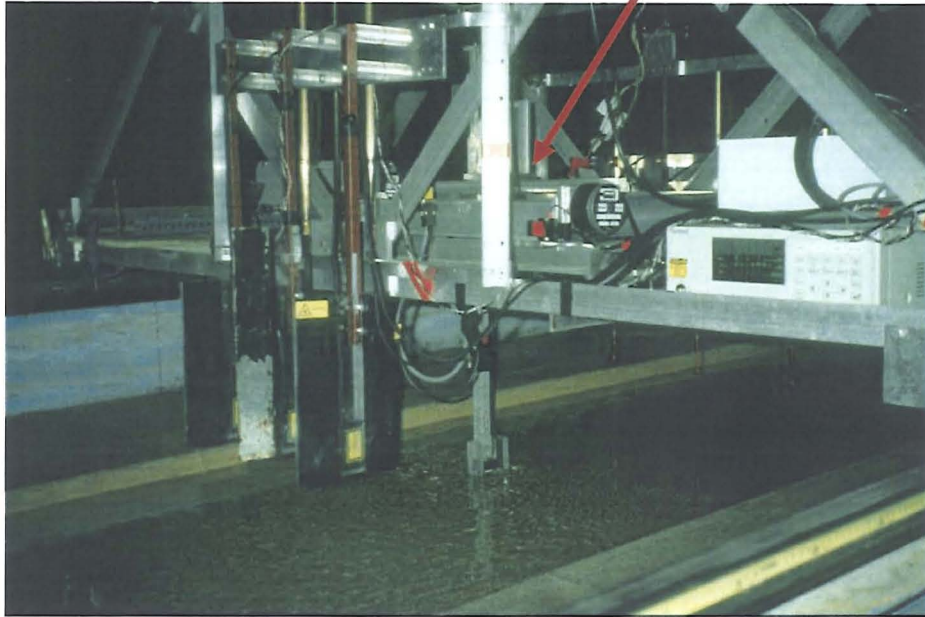
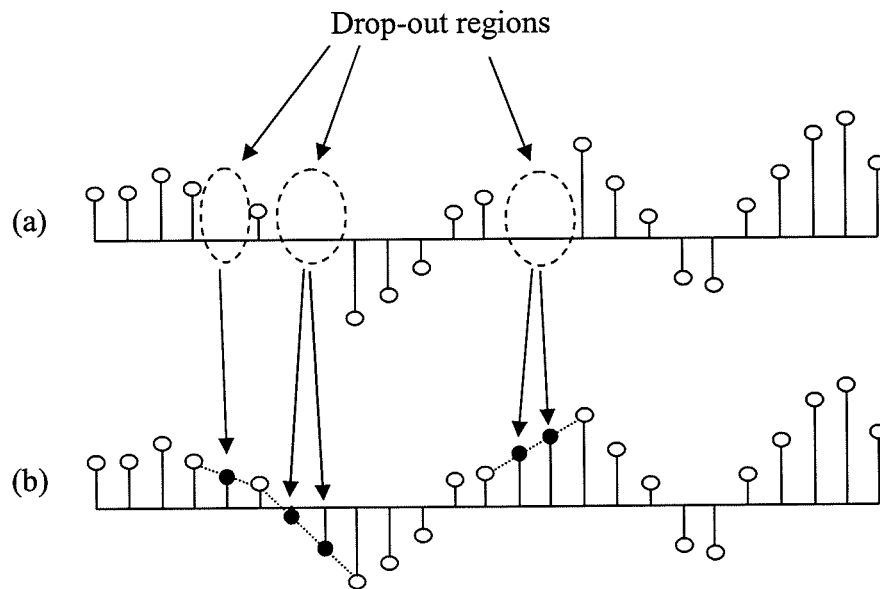
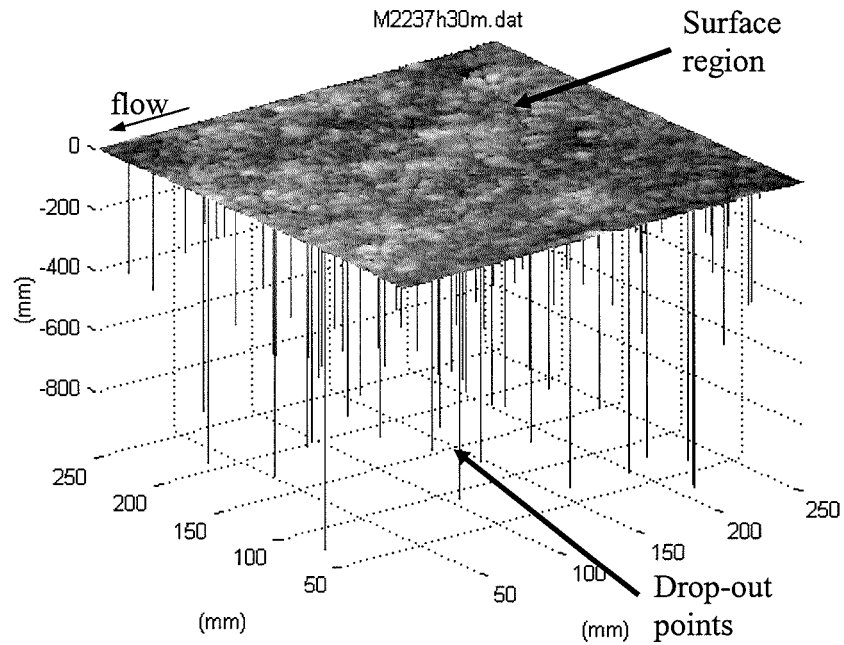


**Figure 4.3** Close view of the laser displacement sensor (marked with arrow) used to scan the topography of the sediment surfaces.

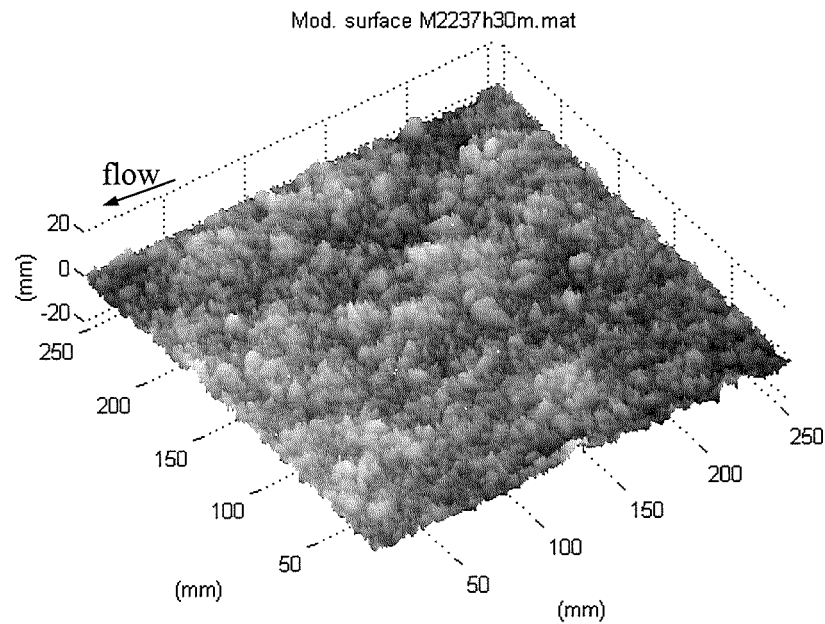


(a) Original data and (b) new data using *averaged interpolation method*.

**Figure 4.4** Linear interpolation replacing the drop-out values in the data.



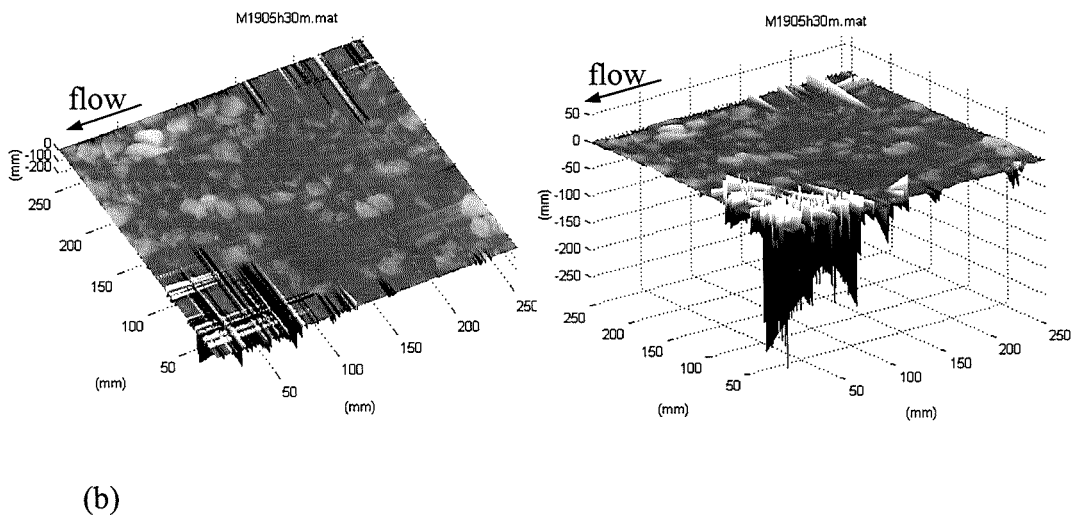
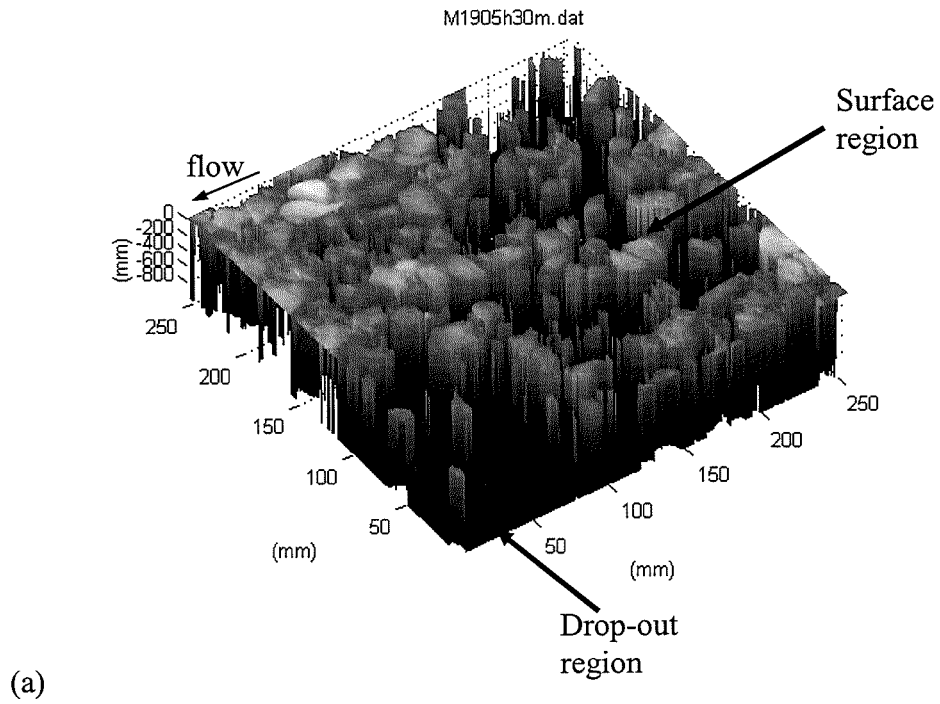
(a)



(b)

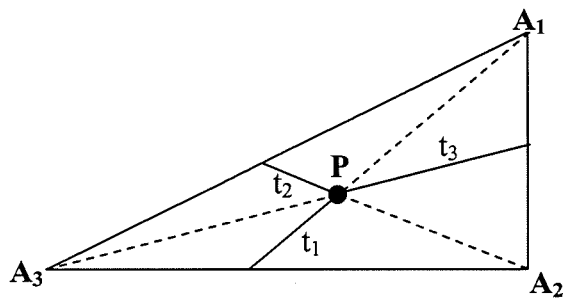
(a) One of the sediment surfaces where the drop-out points are clearly visible and (b) the same surface as (a) where the drop-out points have been removed using linear interpolation.

**Figure 4.5** Removal of drop-out points using linear interpolation.

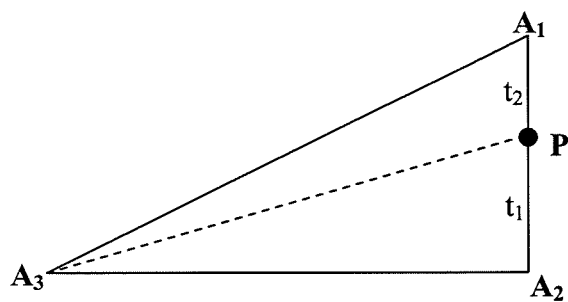


(a) One of the original sediment data sets and (b) show how the drop-out points at the edges produce erroneous very high or very low surface values.

**Figure 4.6** Line and row interpolation of drop-out points.

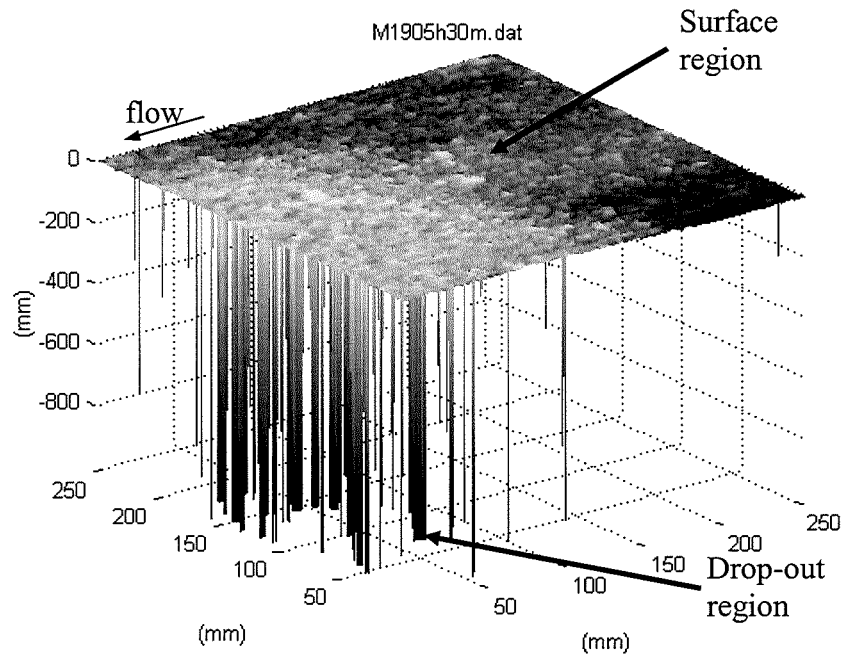


(a)

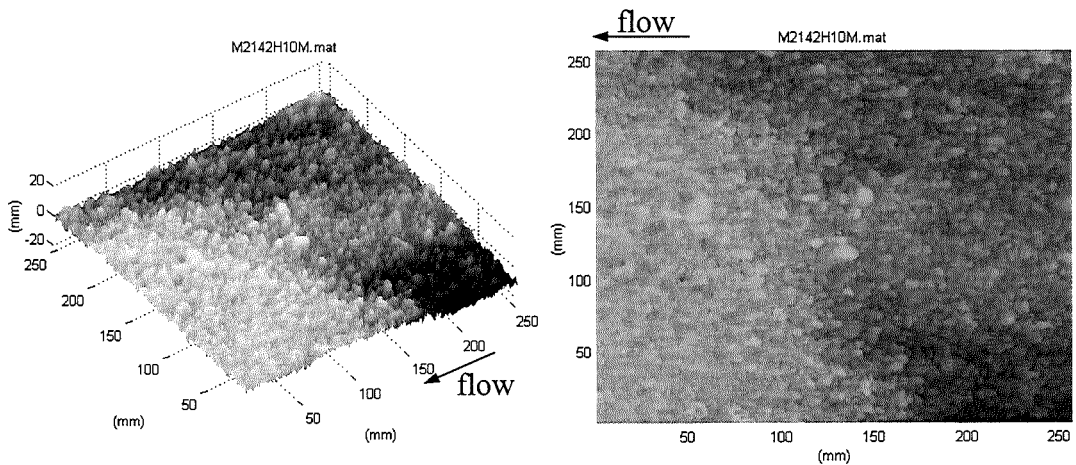


(b)

**Figure 4.7** Estimating new values replacing the drop-out points using barycentric co-ordinates.



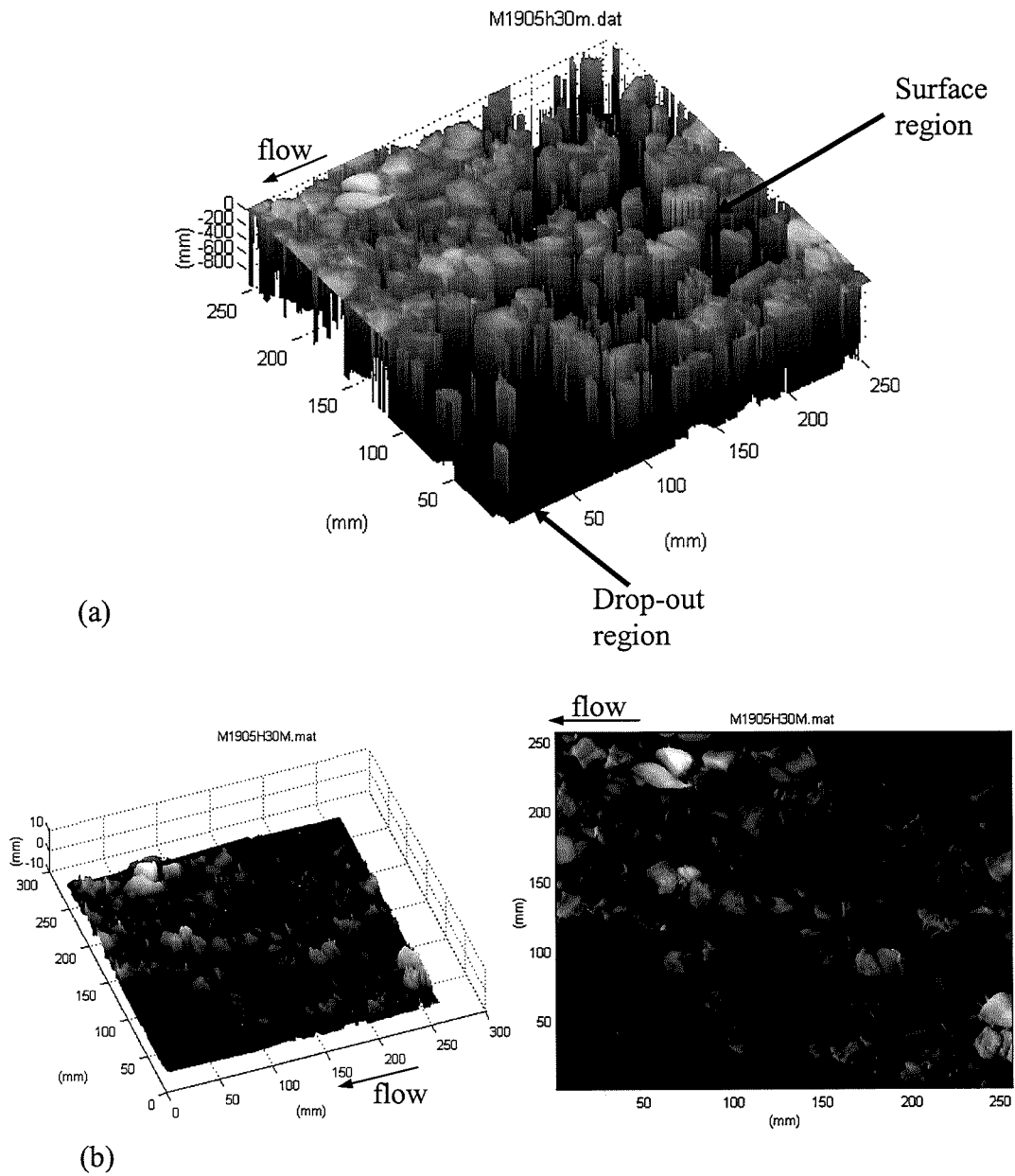
(a)



(b)

(a) The original sediment data set and (b) show the same surface once the drop-out points have been removed.

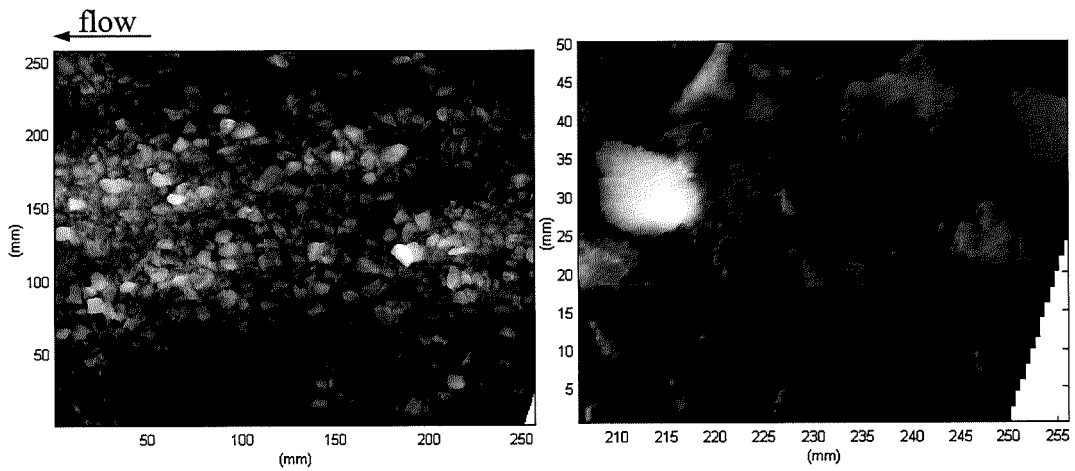
**Figure 4.8** Interpolation using triangulation of the sediment surface to estimate new values for the drop-out points.



(a) The original sediment data set and (b) show the same surface once the drop-out points have been removed.

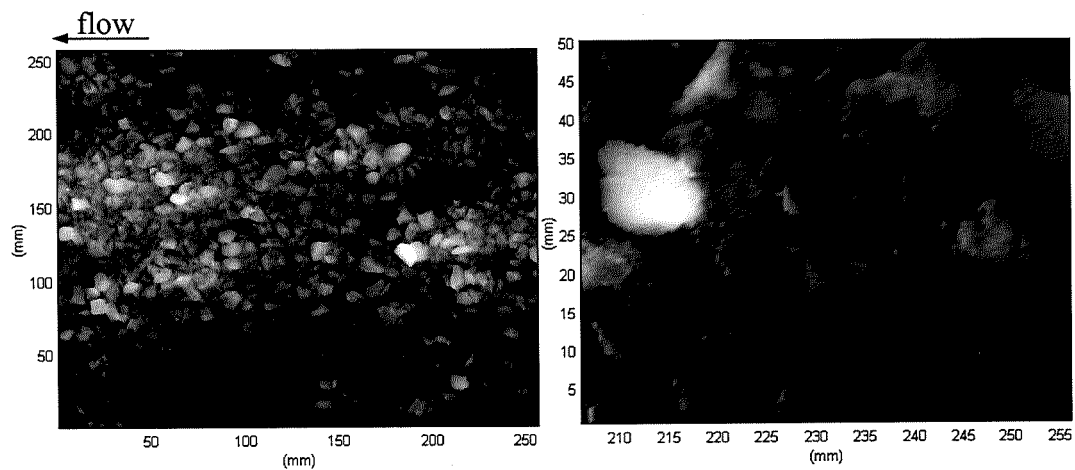
**Figure 4.9** Interpolation using triangulation to estimate new values replacing the drop-out points.





(a) Modified sediment data.

(b) Close up view of right hand bottom corner.

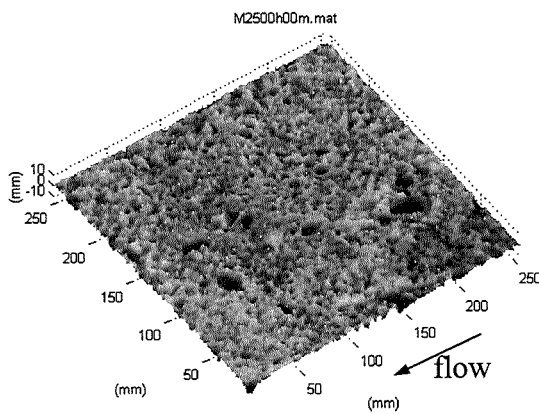


(c) Modified right hand bottom corner.

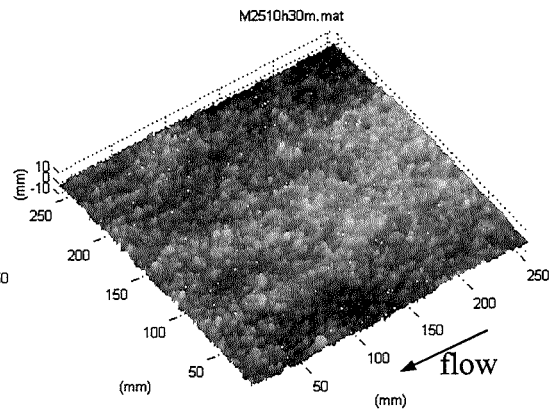
(d) Close up view of modified right hand bottom corner.

(a), (b) Is the sediment surface data modified for drop-out points, (b) however, left in the bottom right corner a patch of NaN values and (c) and (d) using linear interpolation and extrapolation to modify for the 'missing' values of the right corner.

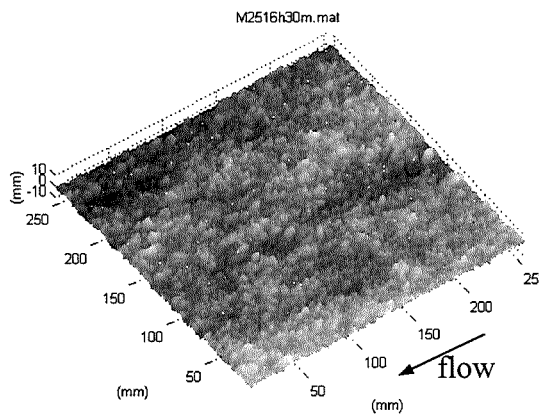
**Figure 4.10** Compensating for the missing right corner in the modified sediment data.



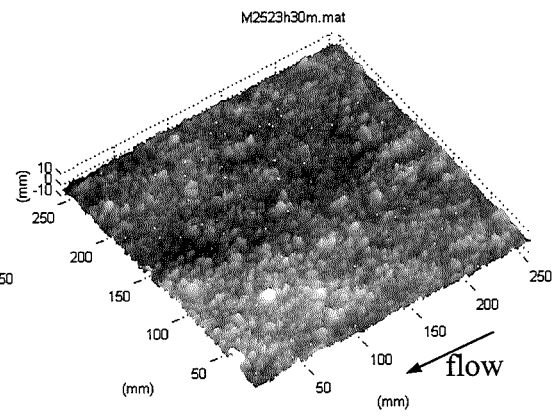
(a) Initial surface at time = 0.



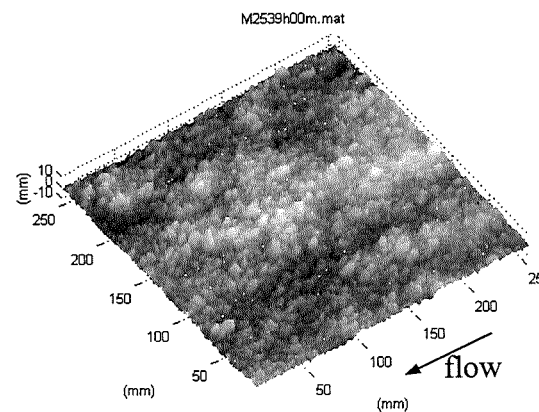
(b) Surface at time = 10h30min.



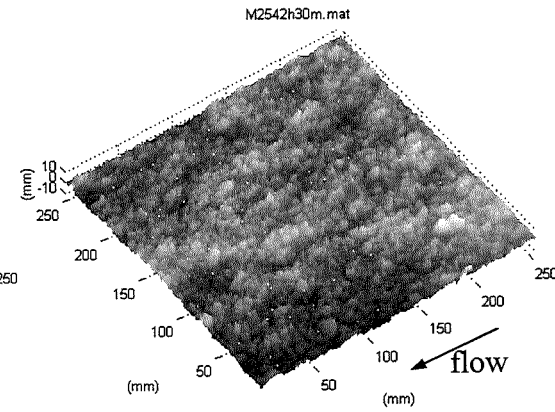
(c) Surface at time = 16h30min.



(d) Surface at time = 23h20min.

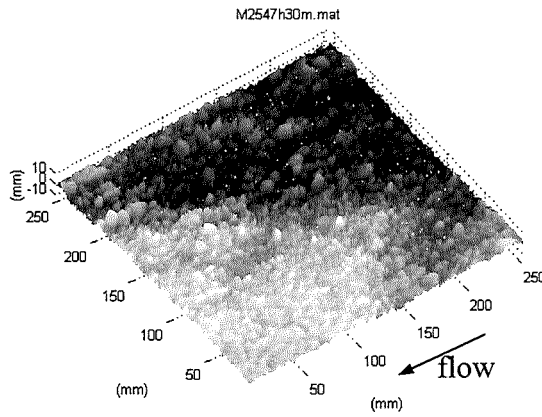


(e) Surface at time = 39h00min.

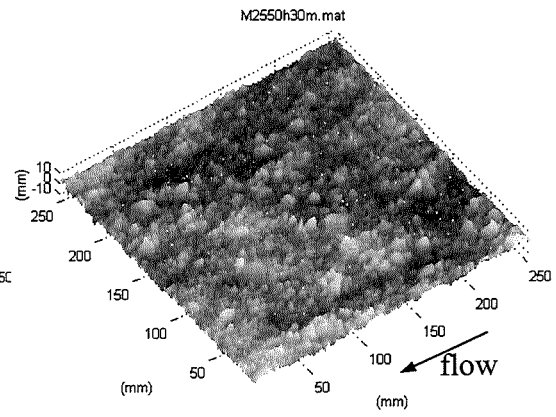


(f) Surface at time = 42h30min.

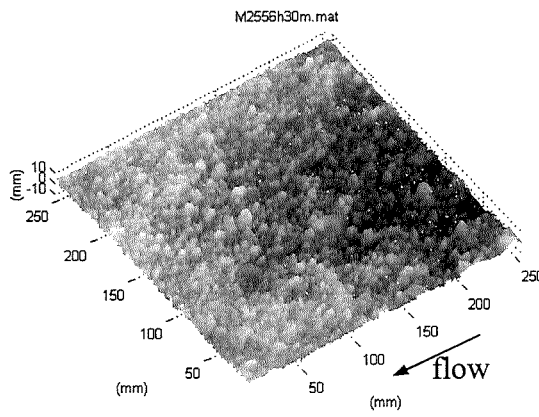
**Figure 4.11** Examples of experimental sediment surface data-sets from experiment number 25.



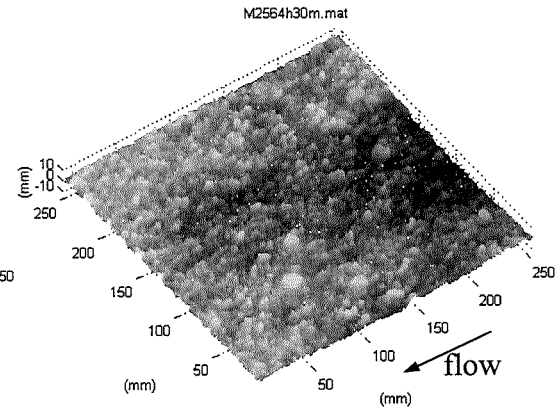
(g) Surface at time = 47h30min.



(h) Surface at time = 50h30min.

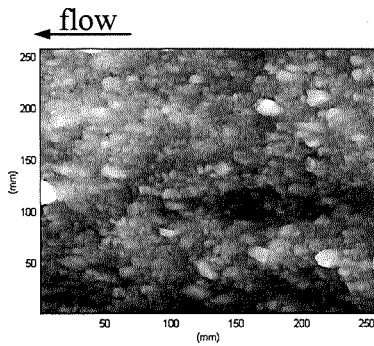


(i) Surface at time = 56h30min.

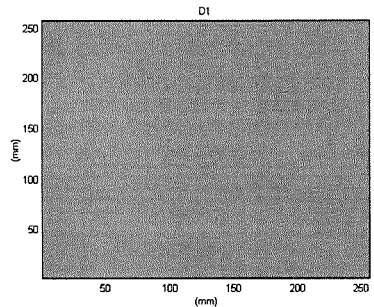
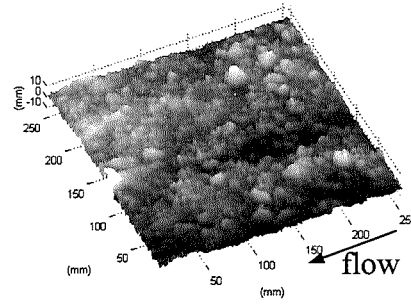


(j) Surface at time = 64h30min.

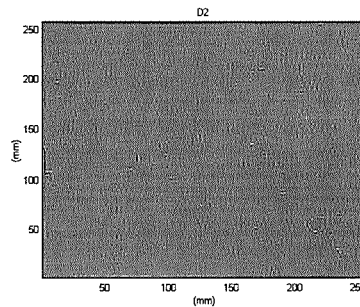
**Figure 4.11 (continued)** Examples of experimental sediment surface data-sets from experiment number 25.



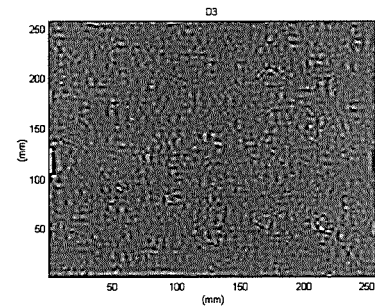
(a) Original surface.



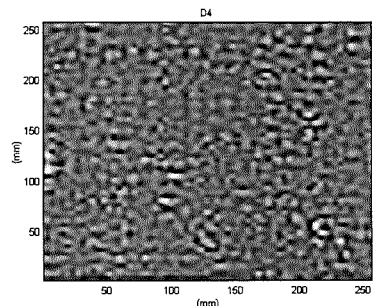
(b) Detail 1.



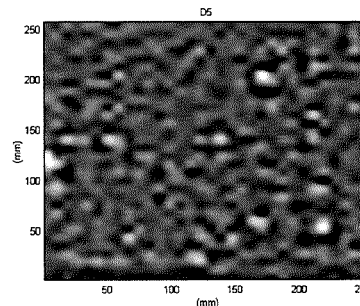
(c) Detail 2.



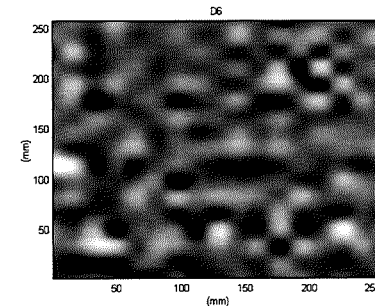
(d) Detail 3.



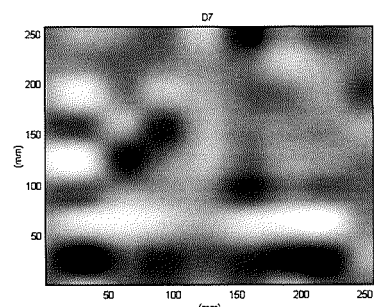
(e) Detail 4.



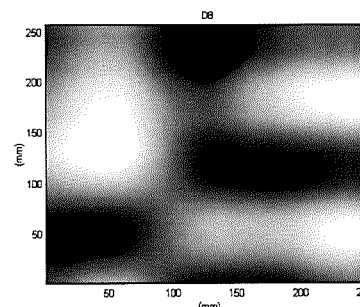
(f) Detail 5.



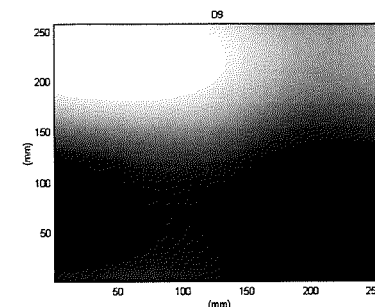
(g) Detail 6.



(h) Detail 7.



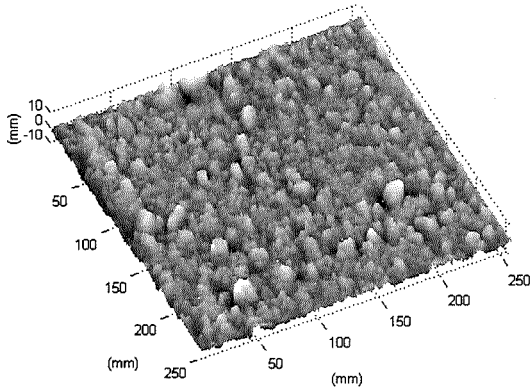
(i) Detail 8.



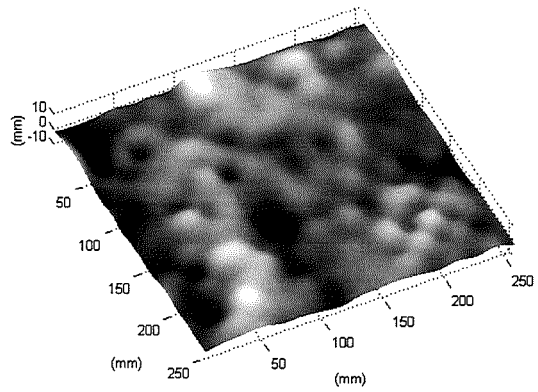
(j) Detail 9.

(a) Show the original river-bed sediment surface and (b)-(j) show the wavelet scale details, where (b) is the smallest scale and (j) is the largest scale.

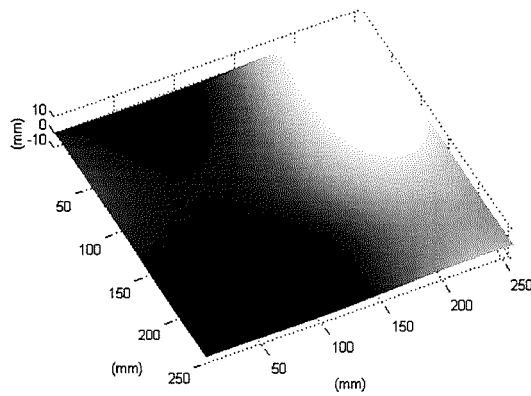
**Figure 4.12** Decomposition of sediment surface into wavelet details.



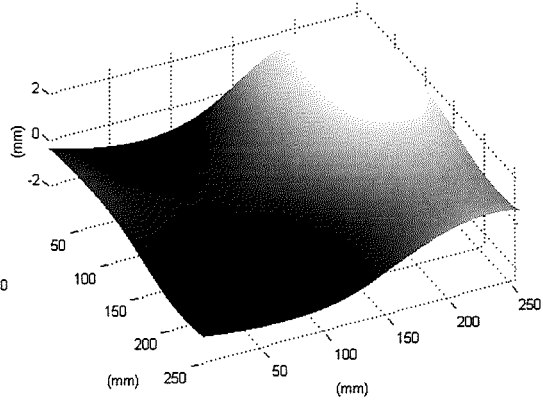
(a) Small forms.



(b) Medium forms.

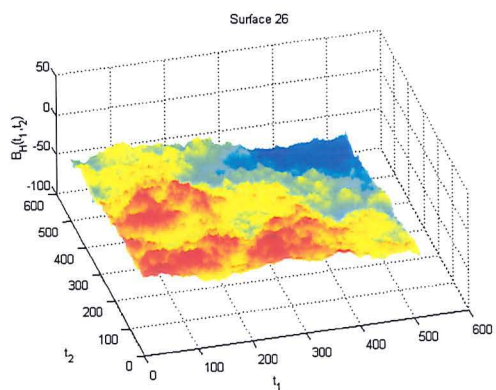


(c) Large forms.

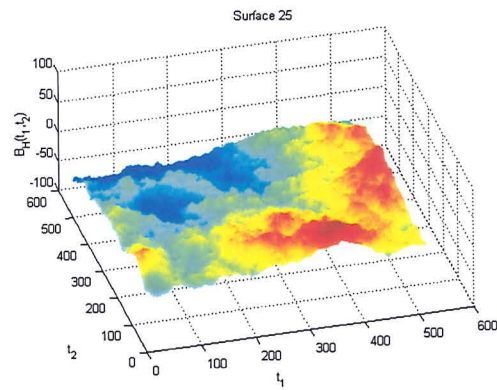


(d) Large forms (exaggerated vertical scale).

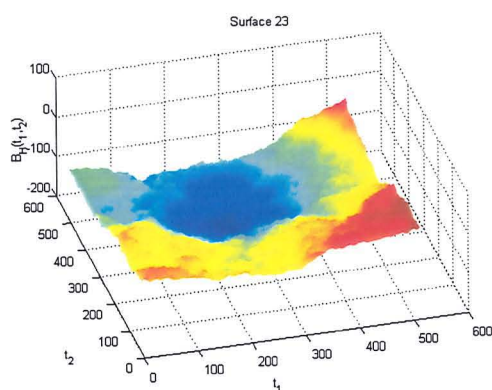
**Figure 4.13** River-bed sediment surface separated into different topographies.



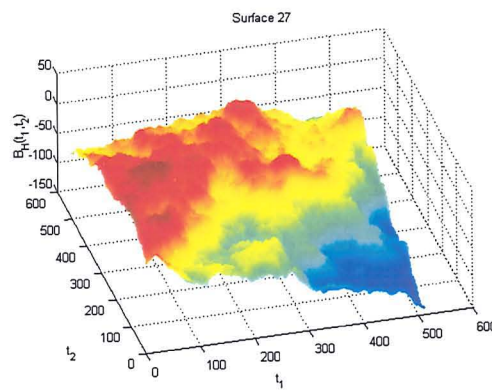
(a)  $H=0.5$



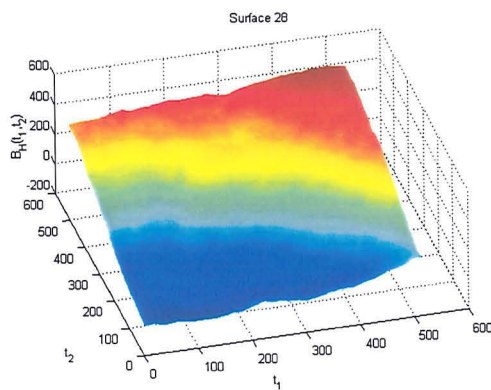
(b)  $H=0.6$



(c)  $H=0.7$



(d)  $H=0.8$

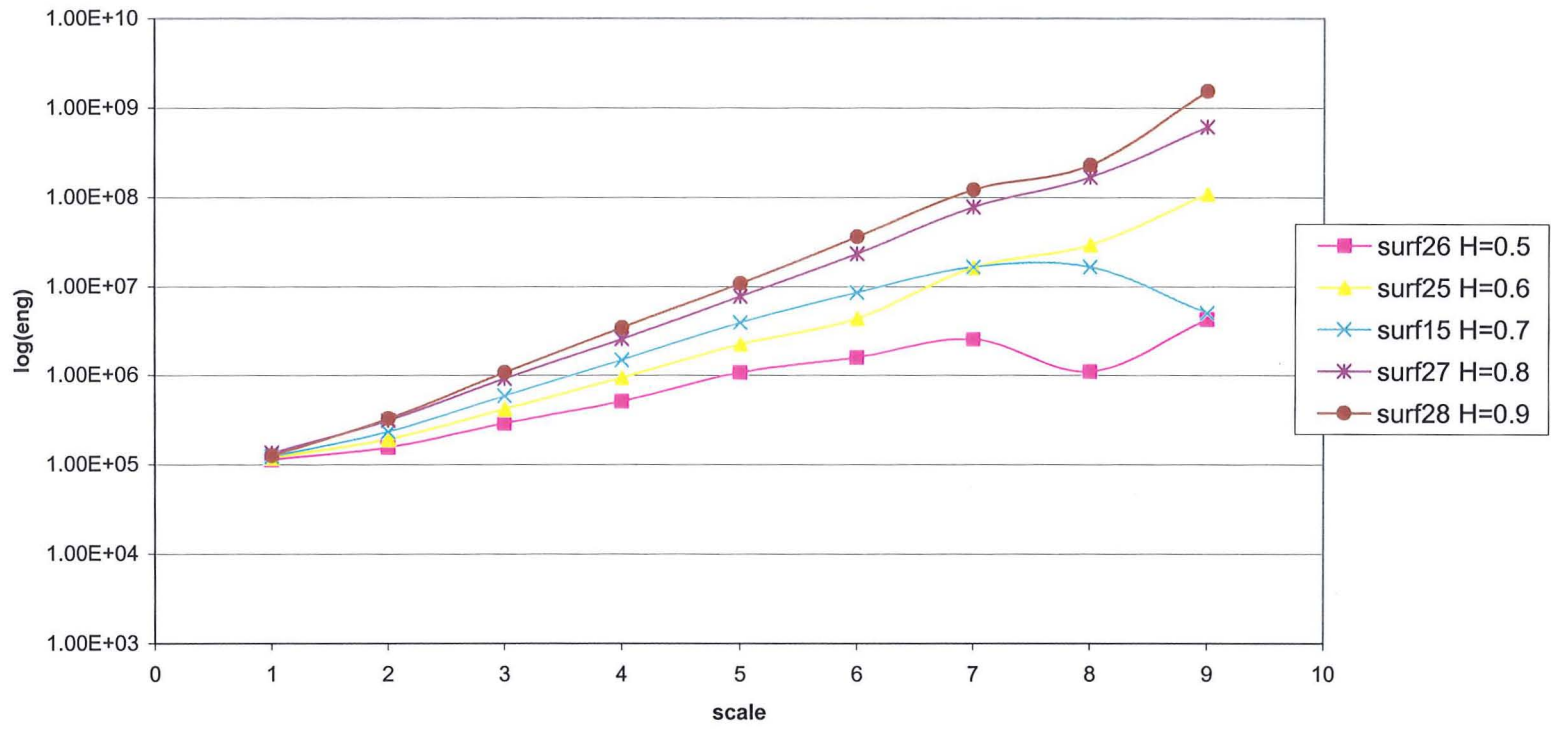


(e)  $H=0.9$

Scaling property of fBm surfaces characterised by Hurst exponent ( $H$ ) are ranging from  $H=0.5$  to  $H=0.9$ .

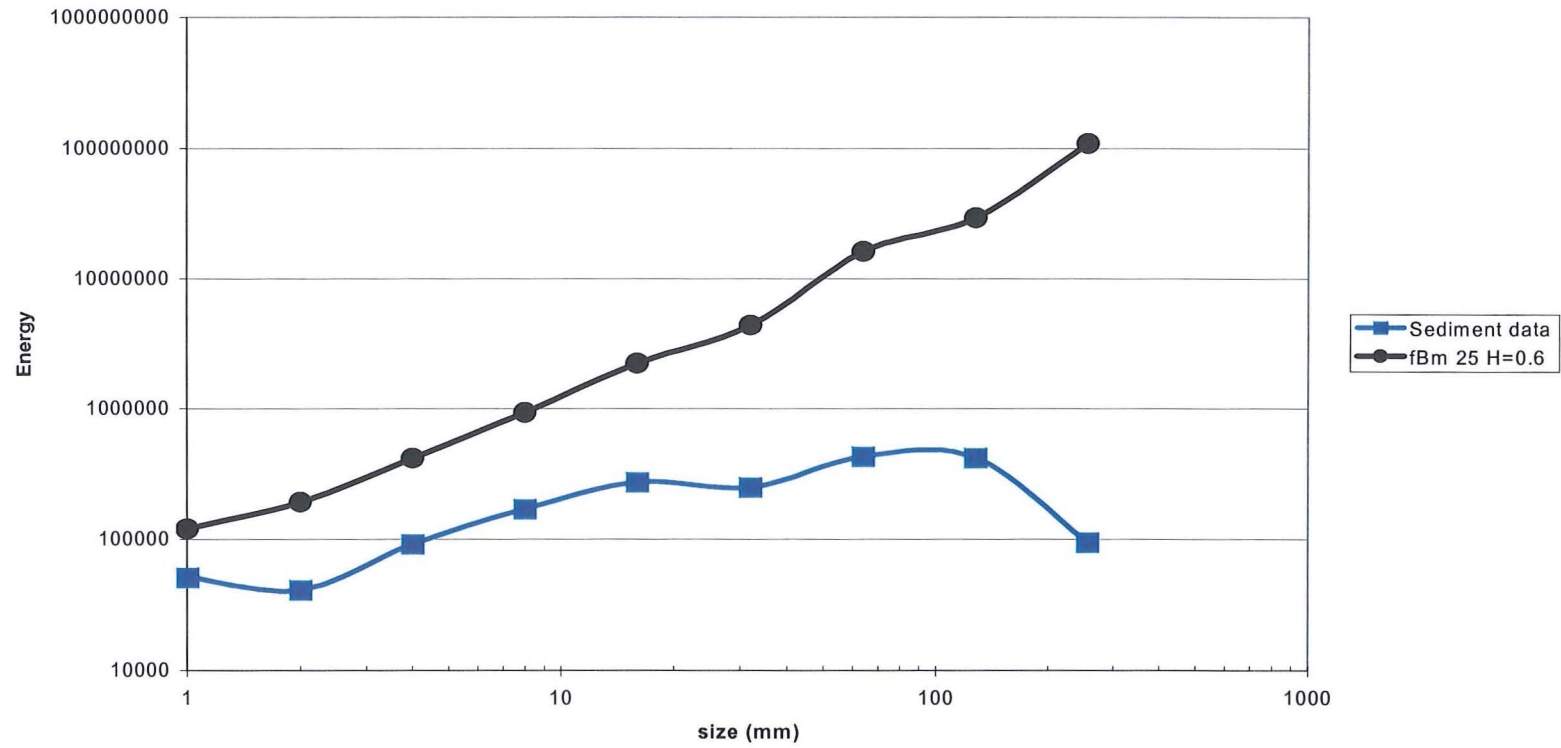
Figure 4.14 Fractional Brownian motion (*fBm*) test surfaces.

Energy distribution of fBm surfaces



Logarithmic plot of wavelet coefficient energy against scale for the fBm surfaces shown in figure 4.14.

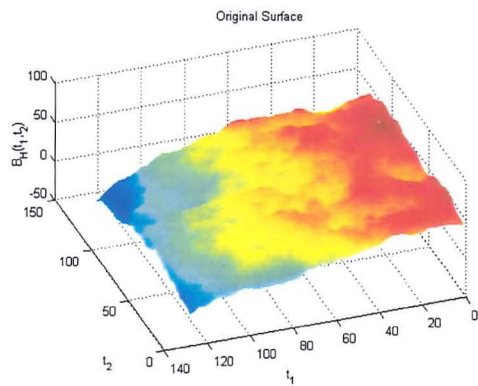
Figure 4.15 Energy distribution of fBm surfaces.



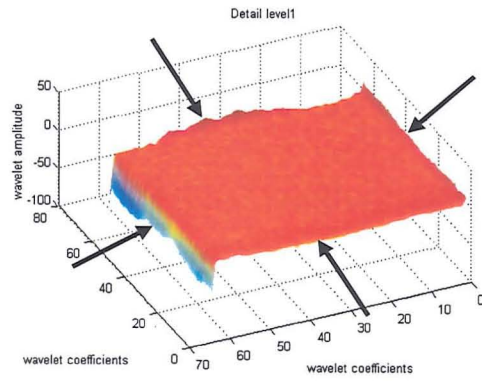
Logarithmic plot of wavelet coefficient energy against scale for a sediment surface and a synthesised fBm (Hurst exponent  $H=0.6$ ).

**Figure 4.16** Energy distribution of a fBm surface compared to a sediment bed-surface.

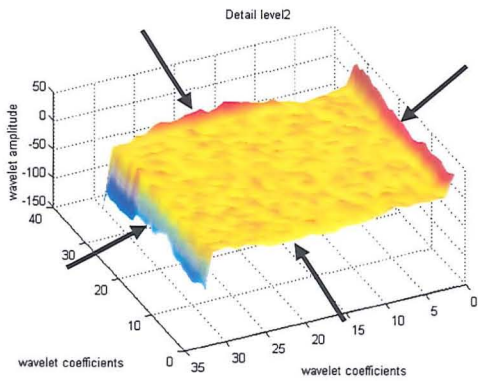




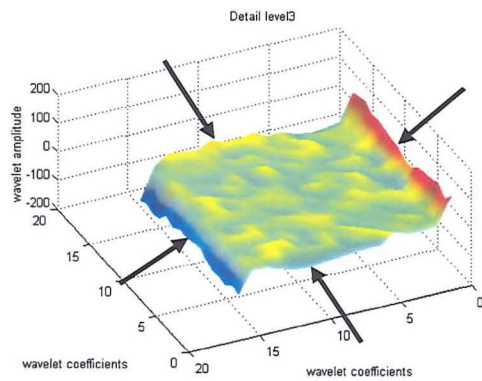
(a) Original *fBm* surface.



(b) 1<sup>st</sup> level of detail coefficients.



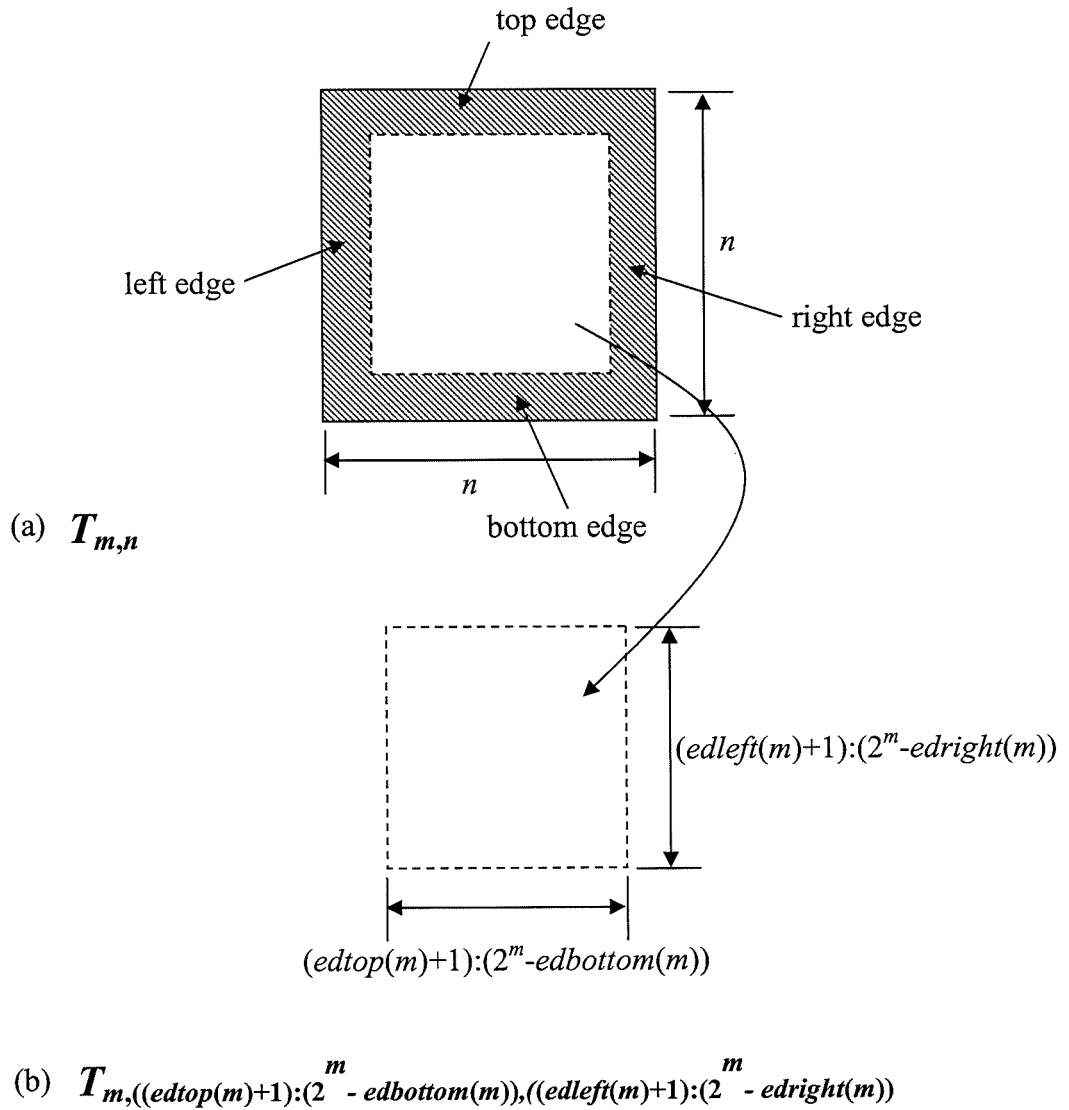
(c) 2<sup>nd</sup> level of detail coefficients.



(d) 3<sup>rd</sup> level of detail coefficients.

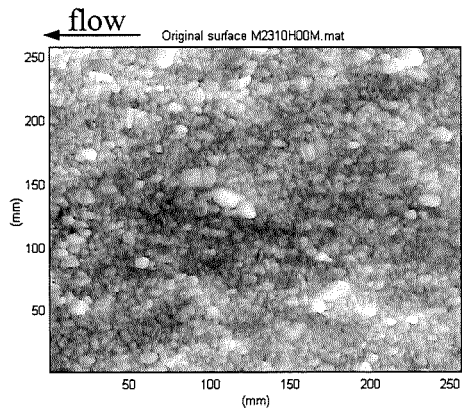
The edge effect of the transform are located by the arrows. The larger edge effects are due to greater discontinuities between opposite edges of the surface.

**Figure 4.17** Performing a 3 level decomposition using the 2-D DWT on a synthetic *fBm* surface the edge effect are clearly visible through the transform.

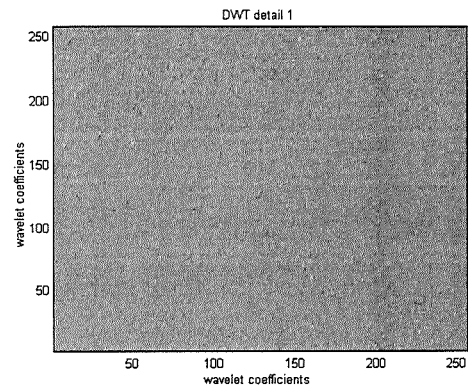


(a) The original component detail defined as  $T_{m,n}$  those coefficient corrupted by edge effects are shown shaded (b) the modified component detail where the edge effect coefficients have been removed.

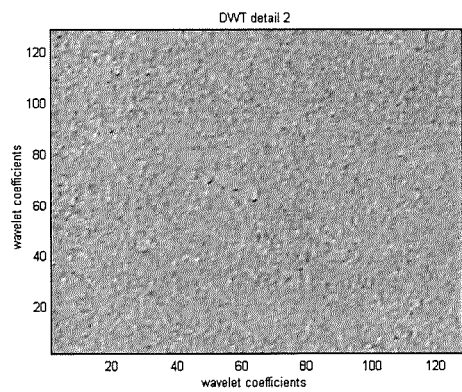
**Figure 4.18** Schematic diagram of modifying of the 2-D wavelet component details for edge effect coefficients.



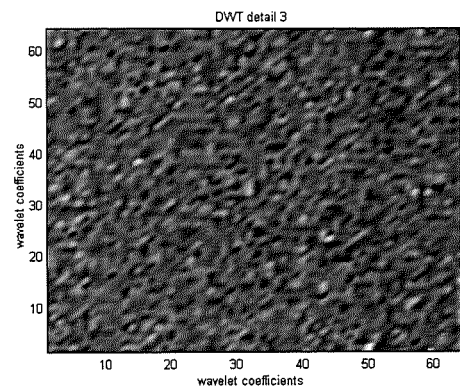
(a) Original sediment surface.



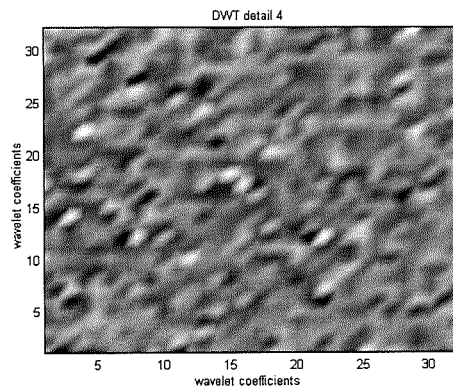
(b) Detail scale 1.



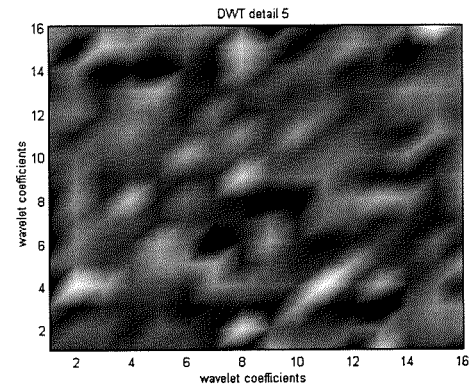
(c) Detail scale 2.



(d) Detail scale 3.



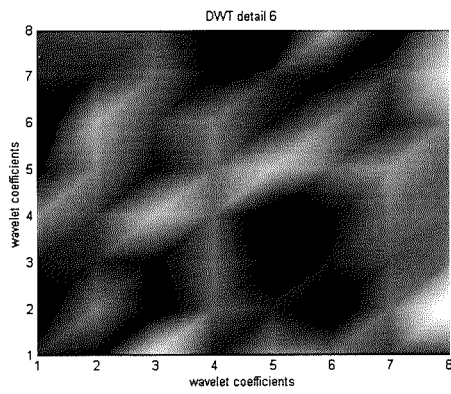
(e) Detail scale 4.



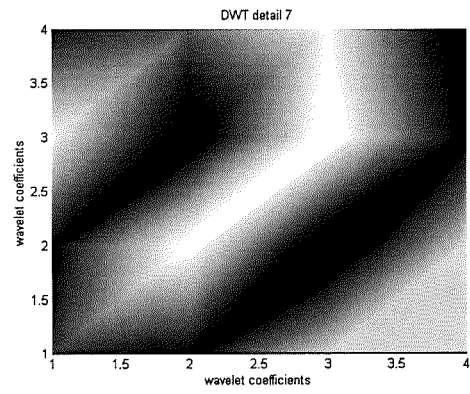
(f) Detail scale 5.

(a) Detail 1 is the smallest scale detail and (f) detail 8 is the largest scale detail.

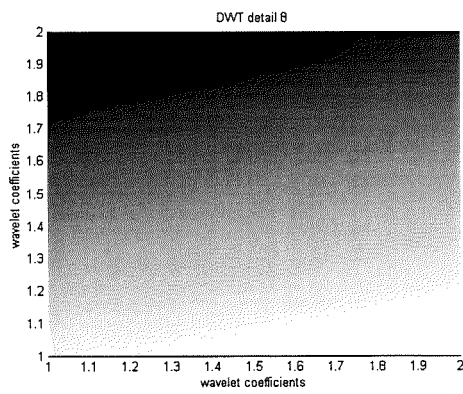
**Figure 4.19** The DWT decomposition details of sediment surface data-set '2310h00m' in experiment 23.



(g) Detail scale 6.



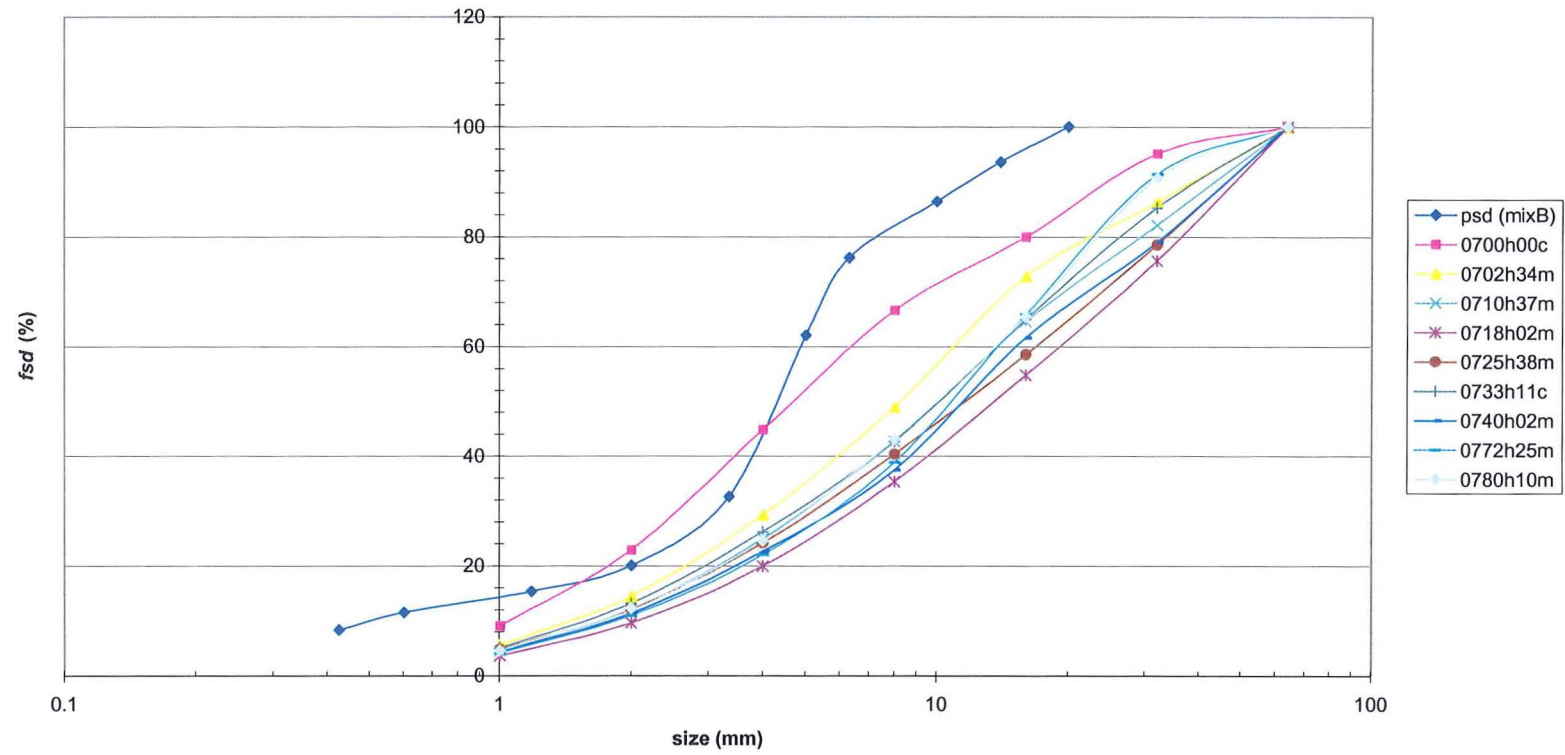
(h) Detail scale 7.



(i) Detail scale 8.

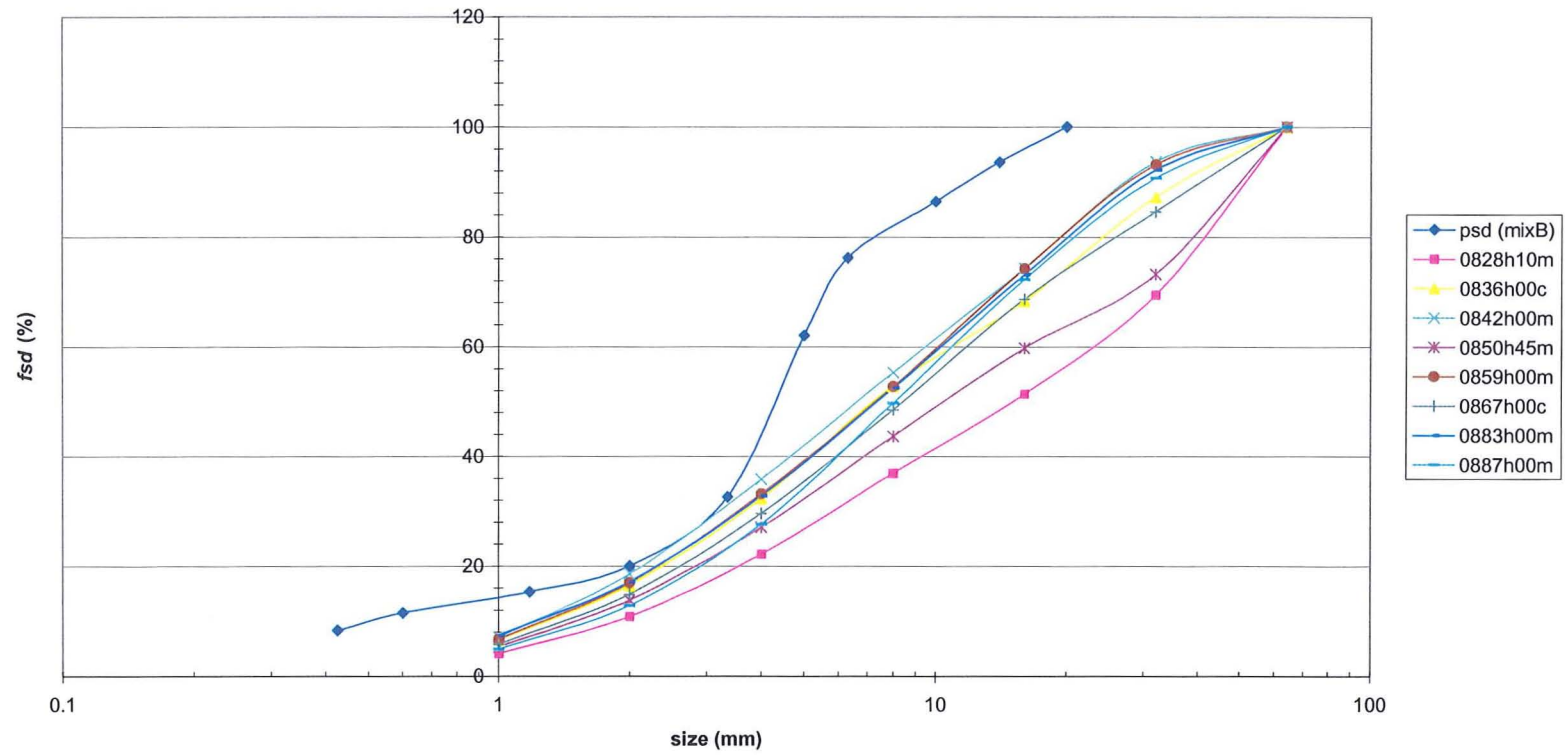
(a) Detail 1 is the smallest scale detail and (i) detail 8 is the largest scale detail.

**Figure 4.19 (continued)** The DWT decomposition details of sediment surface data-set '2310h00m' in experiment 23.



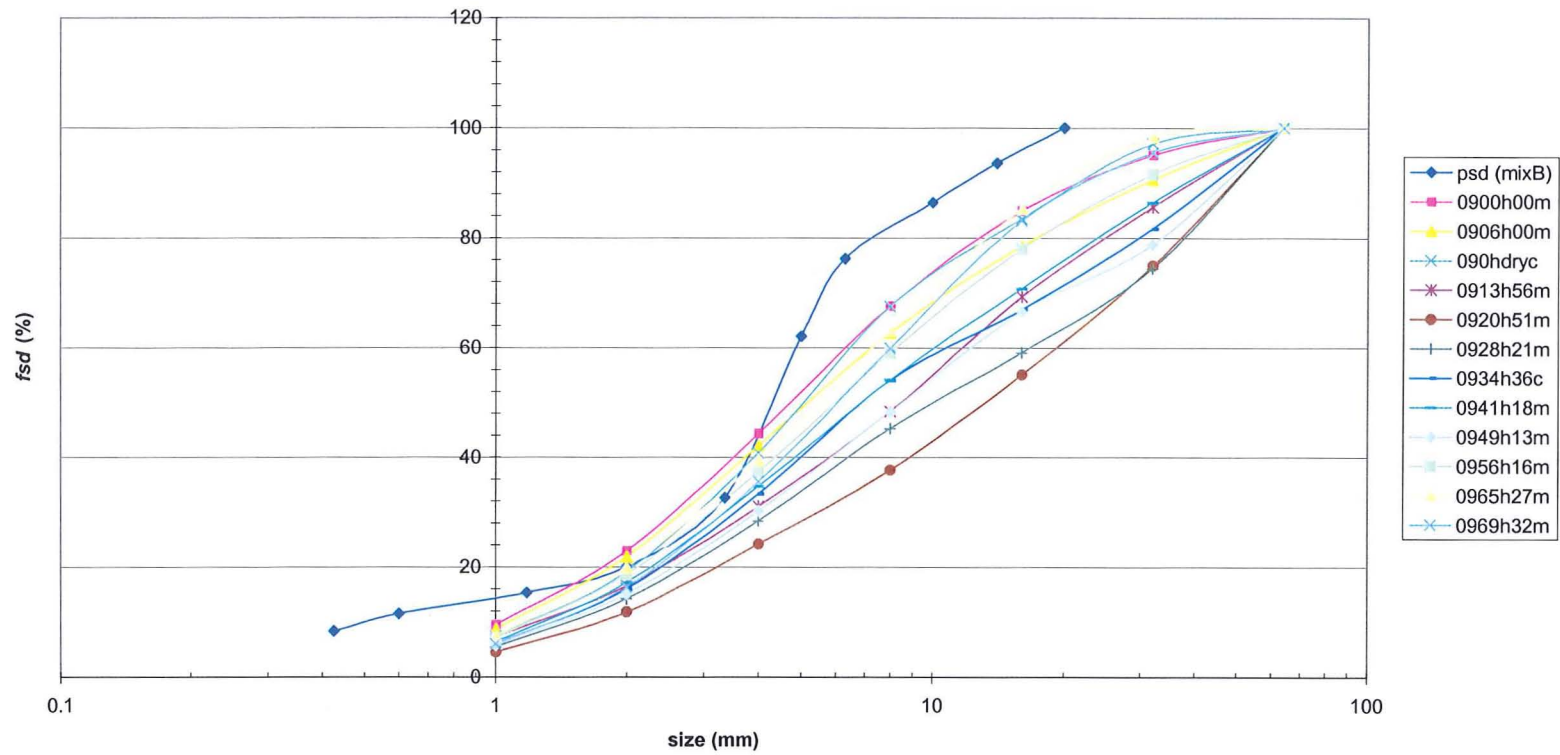
(a) Experiment 07.

**Figure 4.20** Form size distribution ( $fsd$ ) established using the DWT method.



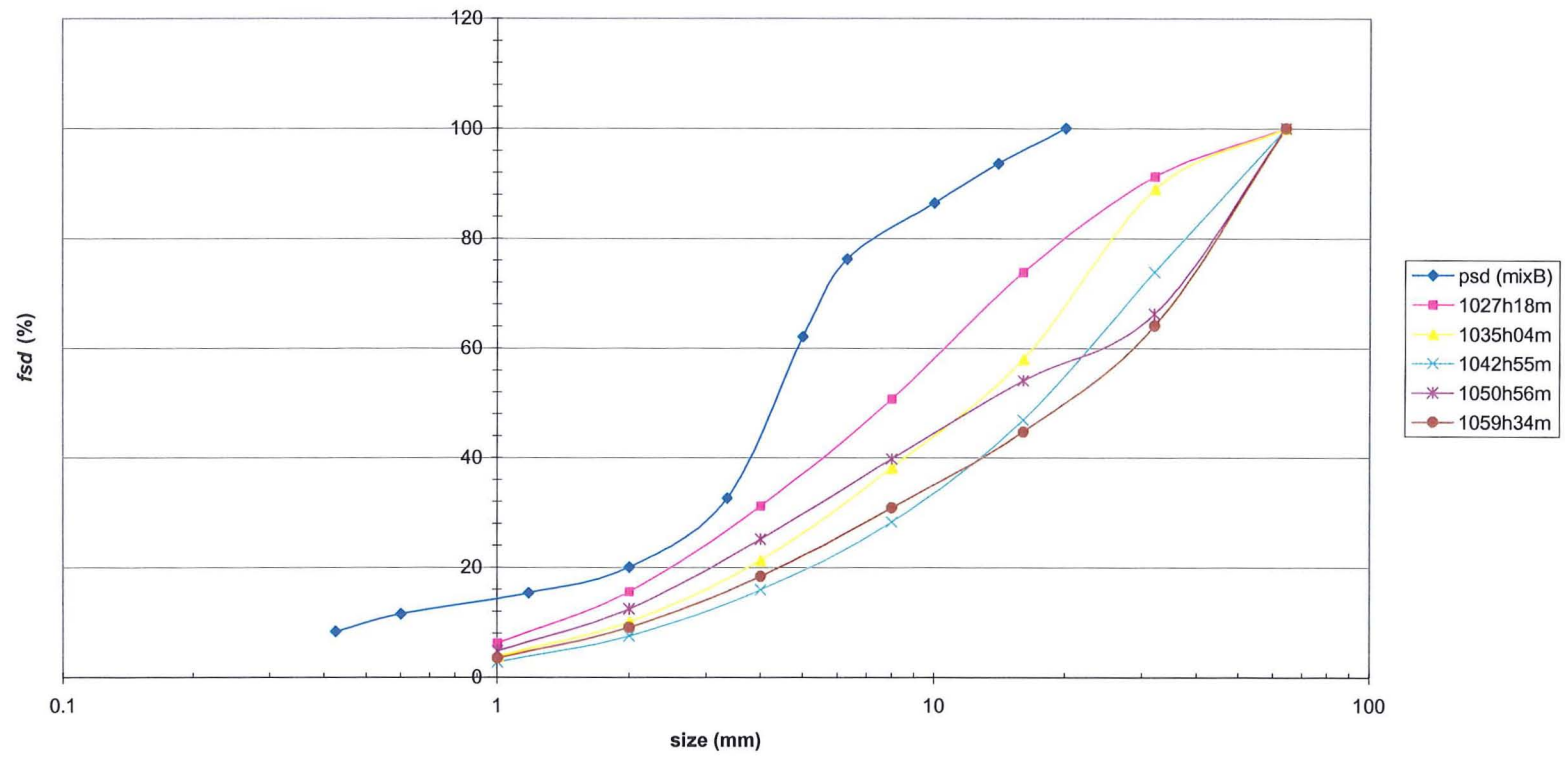
(b) Experiment 08.

**Figure 4.20 (continued)** Form size distribution (*fsd*) established using the DWT method.



(c) Experiment 09.

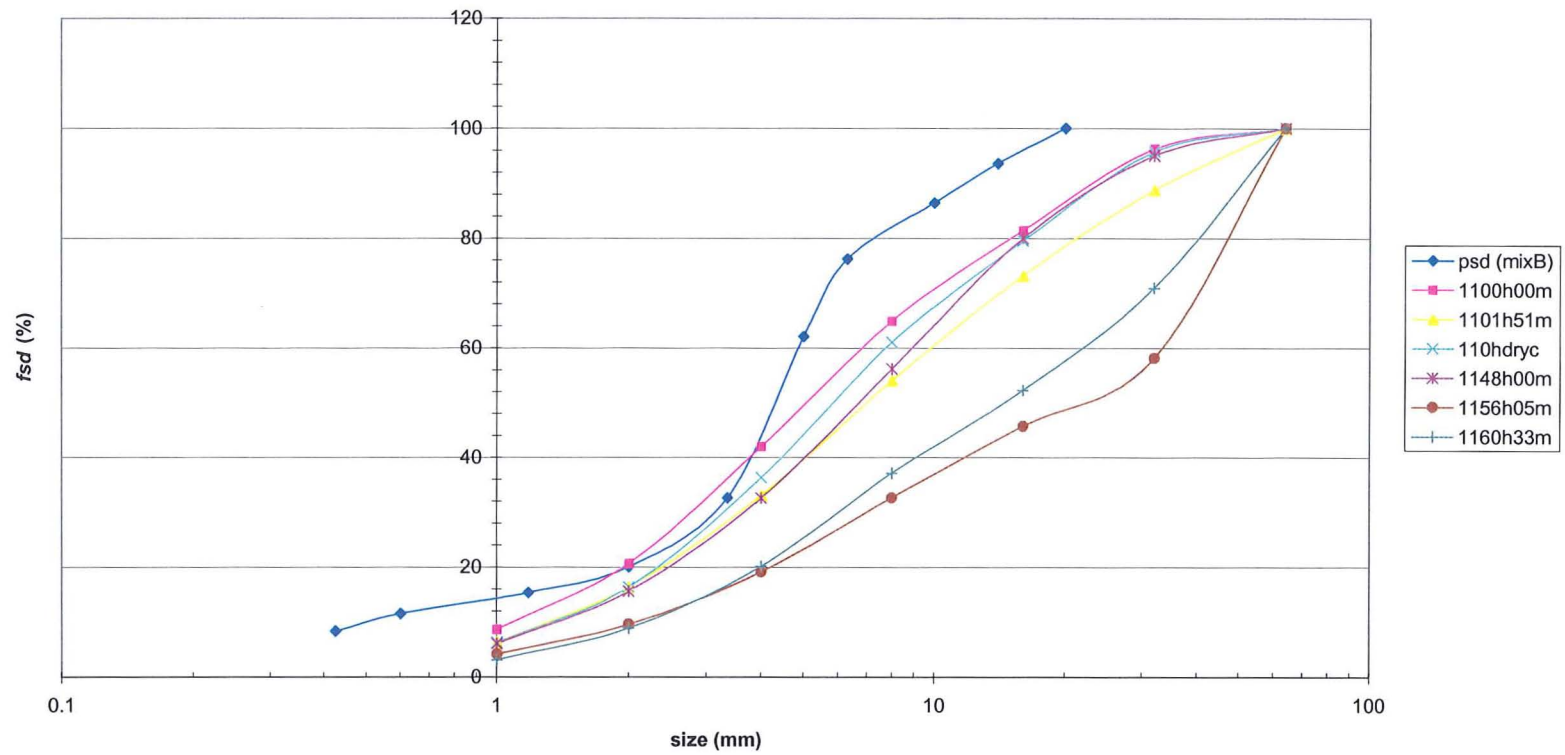
**Figure 4.20 (continued)** Form size distribution (*fsd*) established using the DWT method.



(d) Experiment 10.

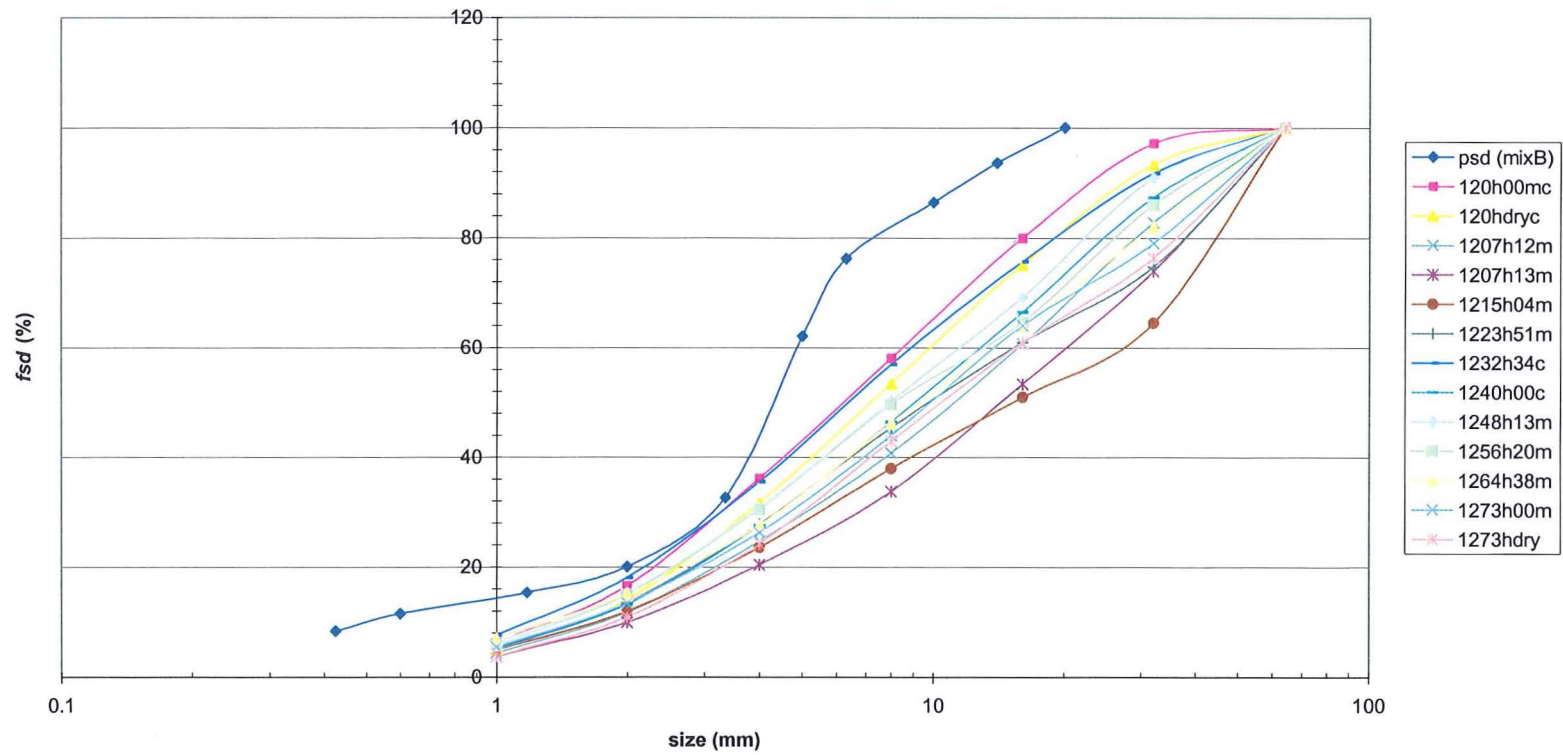
Figure 4.20 (continued) Form size distribution (*fsd*) established using the DWT method.





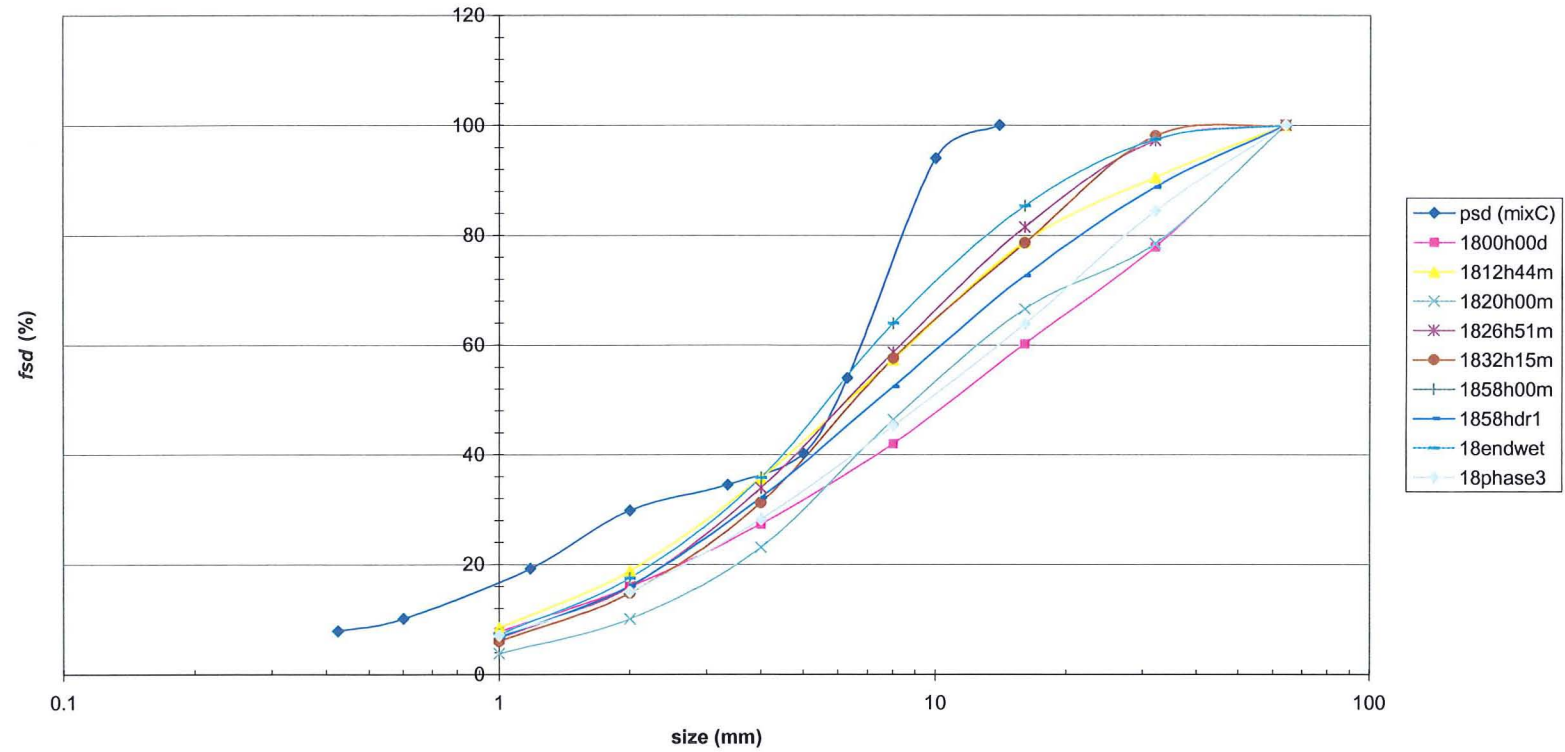
(e) Experiment 11.

Figure 4.20 (continued) Form size distribution (*fsd*) established using the DWT method.



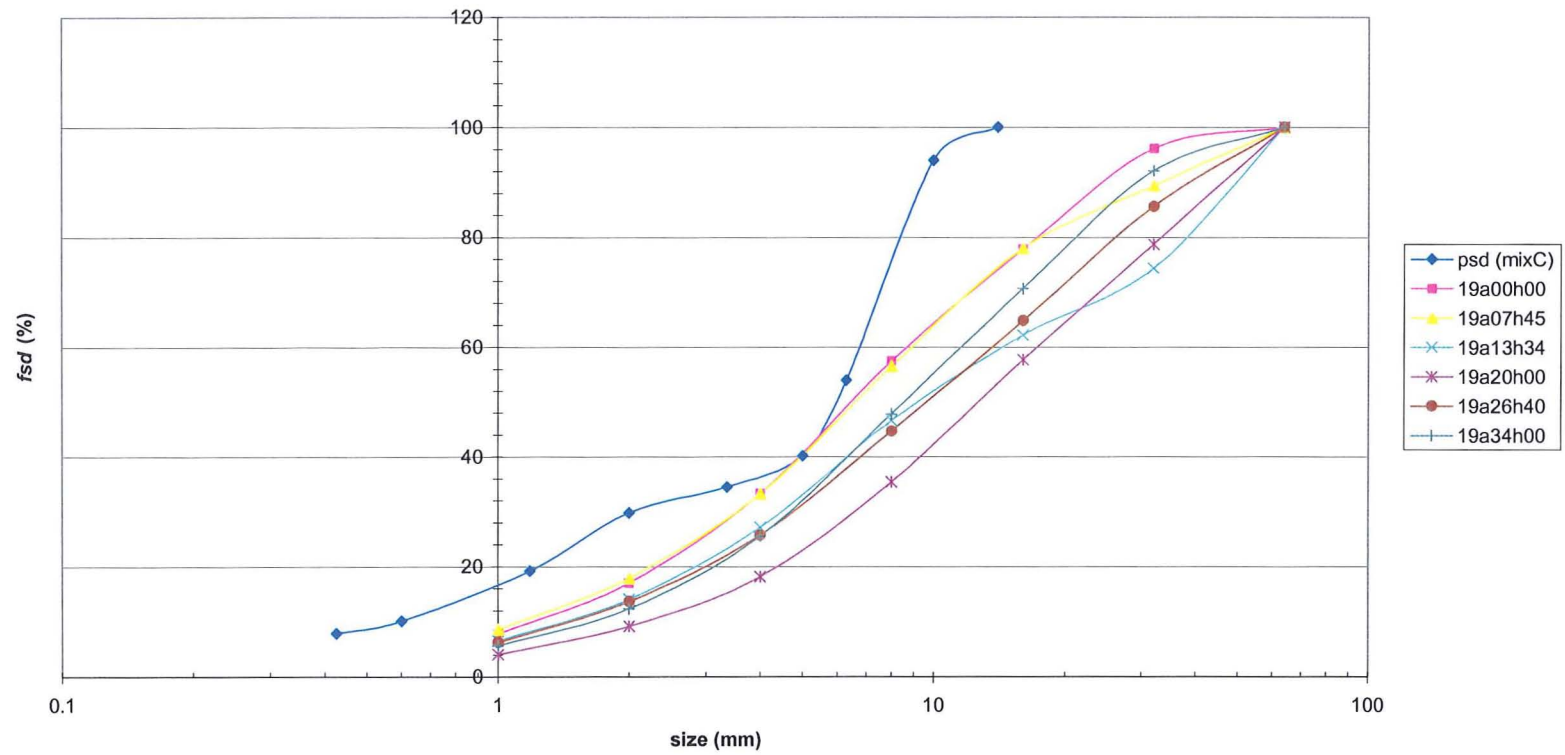
(f) Experiment 12.

Figure 4.20 (continued) Form size distribution (*fsd*) established using the DWT method.



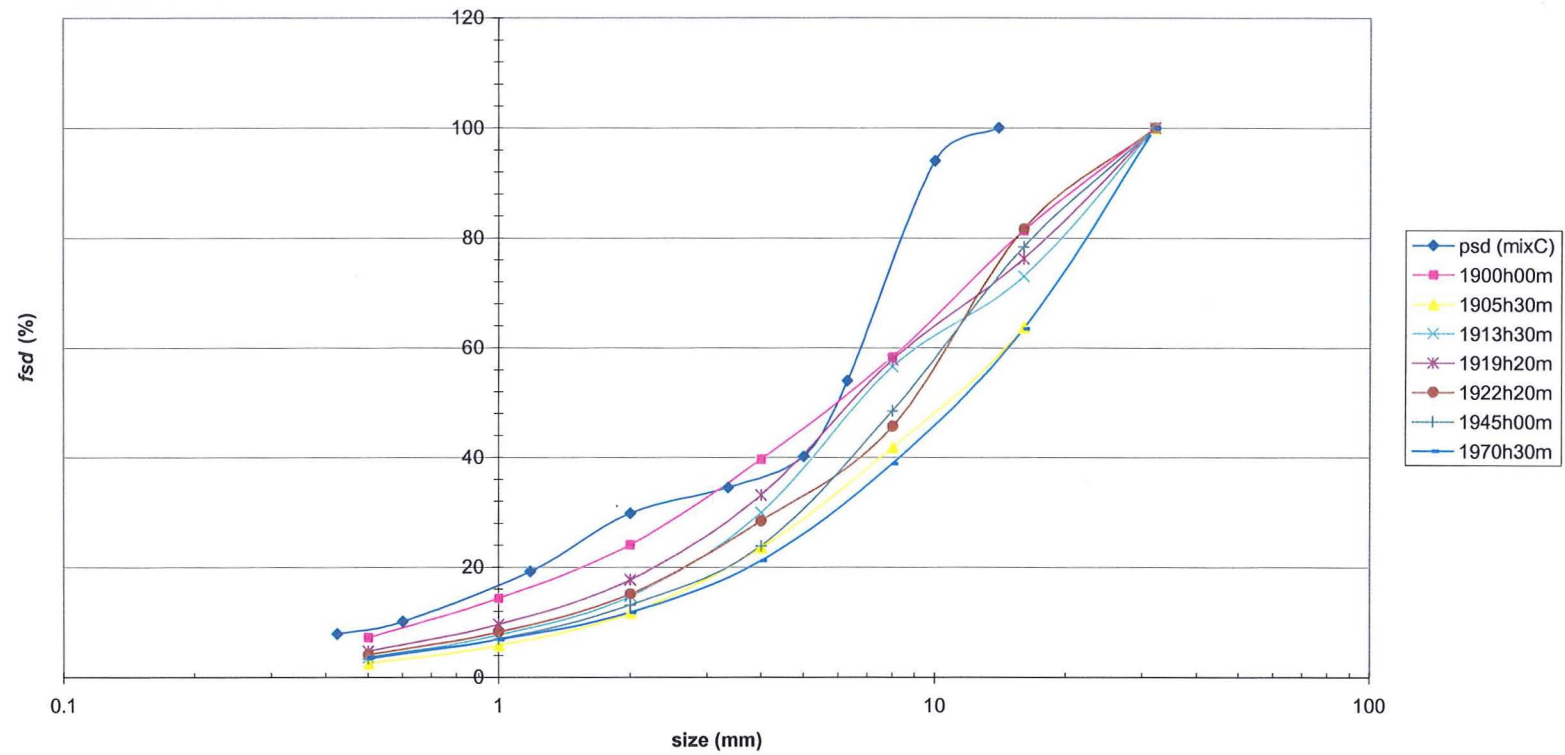
(g) Experiment 18.

Figure 4.20 (continued) Form size distribution (*fsd*) established using the DWT method.



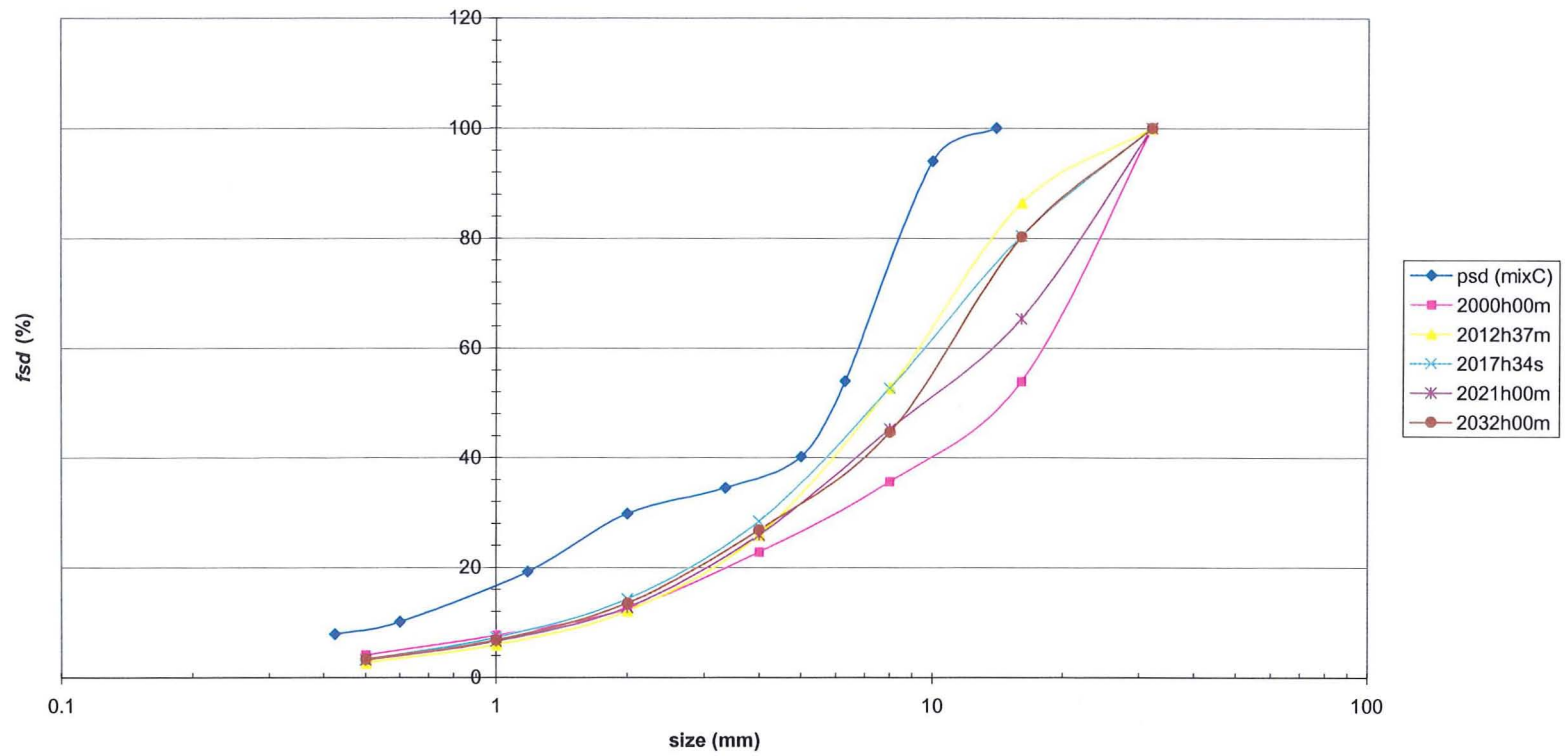
(h) Experiment 19A.

**Figure 4.20 (continued)** Form size distribution (*fsd*) established using the DWT method.



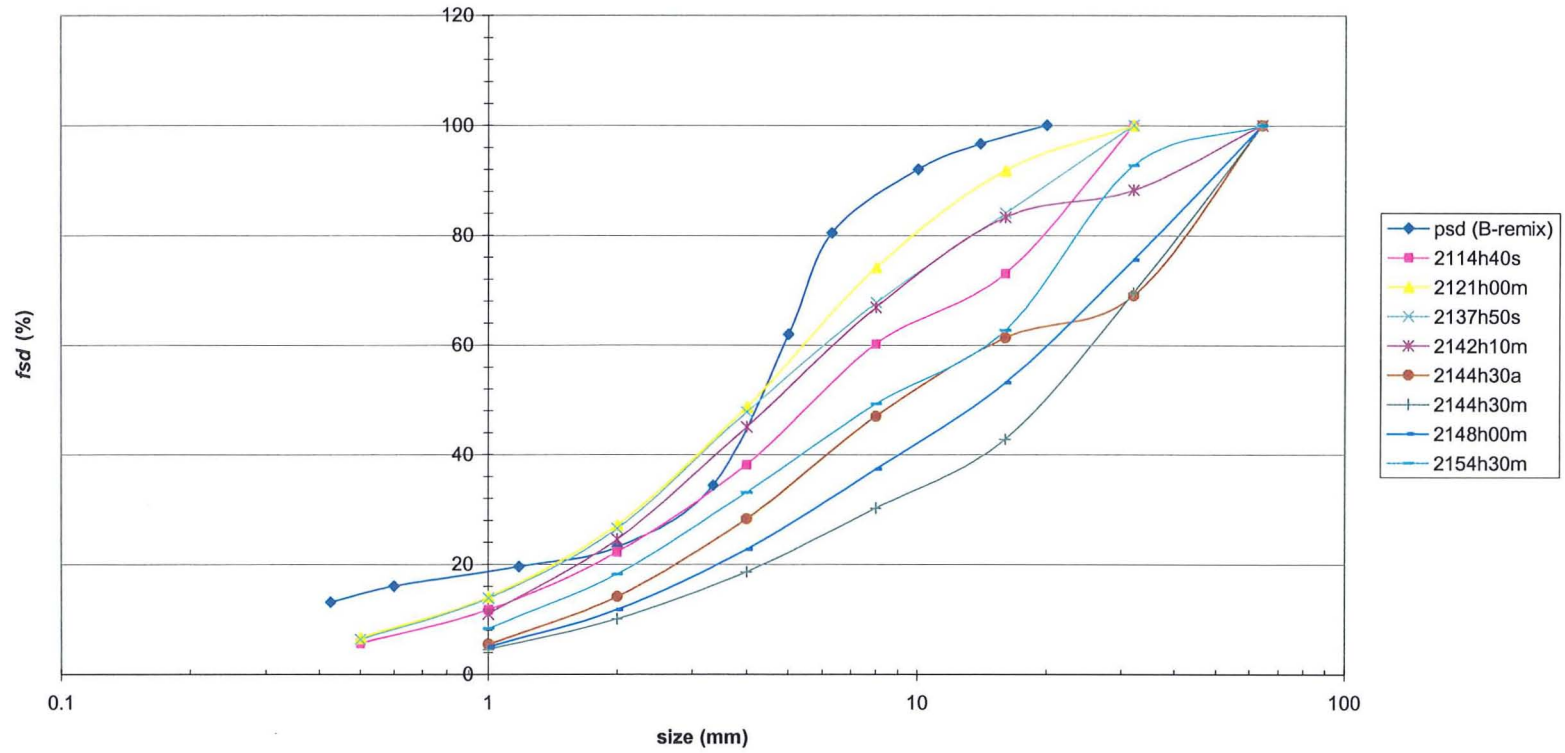
(i) Experiment 19.

**Figure 4.20 (continued)** Form size distribution (*fsd*) established using the DWT method.



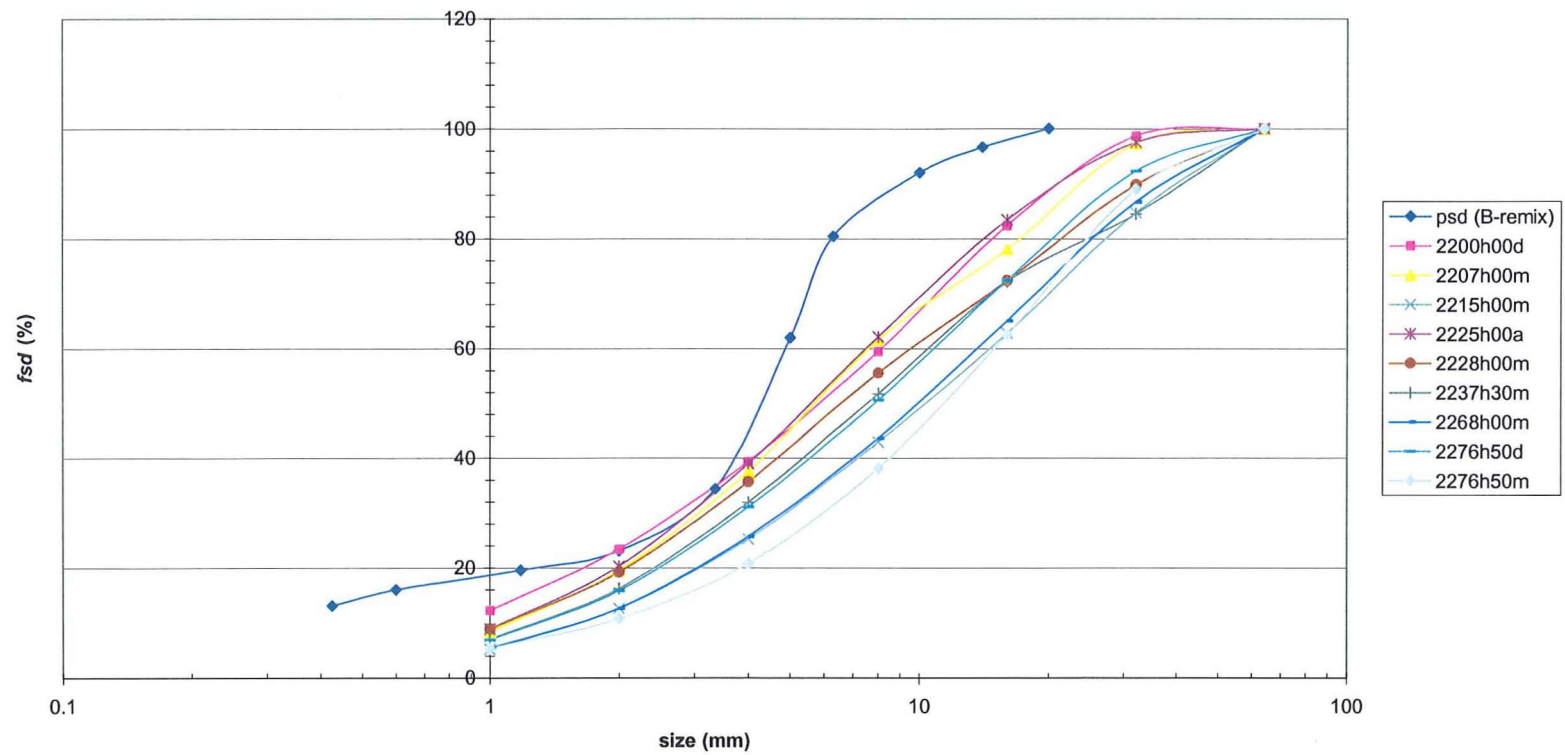
(j) Experiment 20.

**Figure 4.20 (continued)** Form size distribution ( $fsd$ ) established using the DWT method.



(k) Experiment 21.

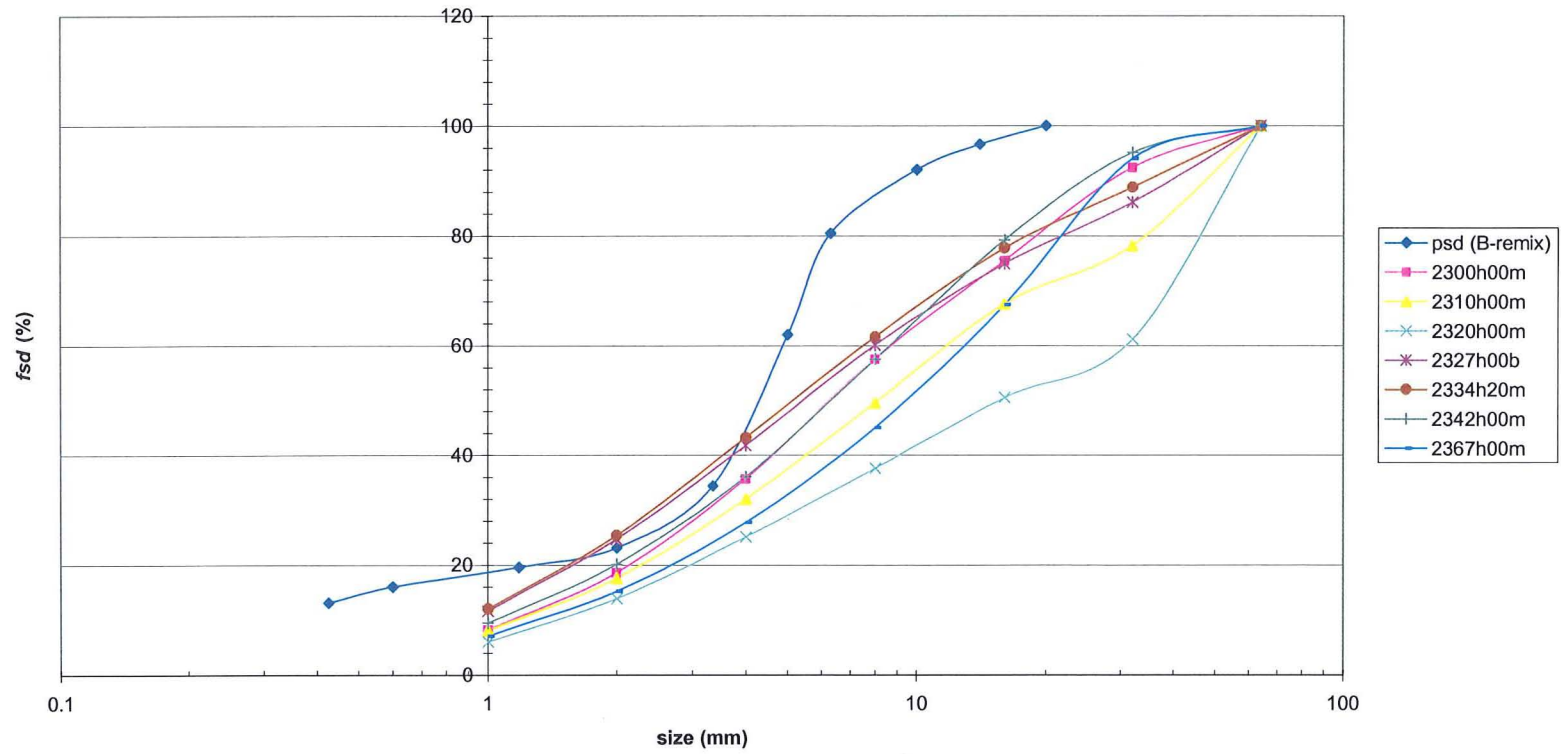
Figure 4.20 (continued) Form size distribution ( $f_{sd}$ ) established using the DWT method.



(l) Experiment 22.

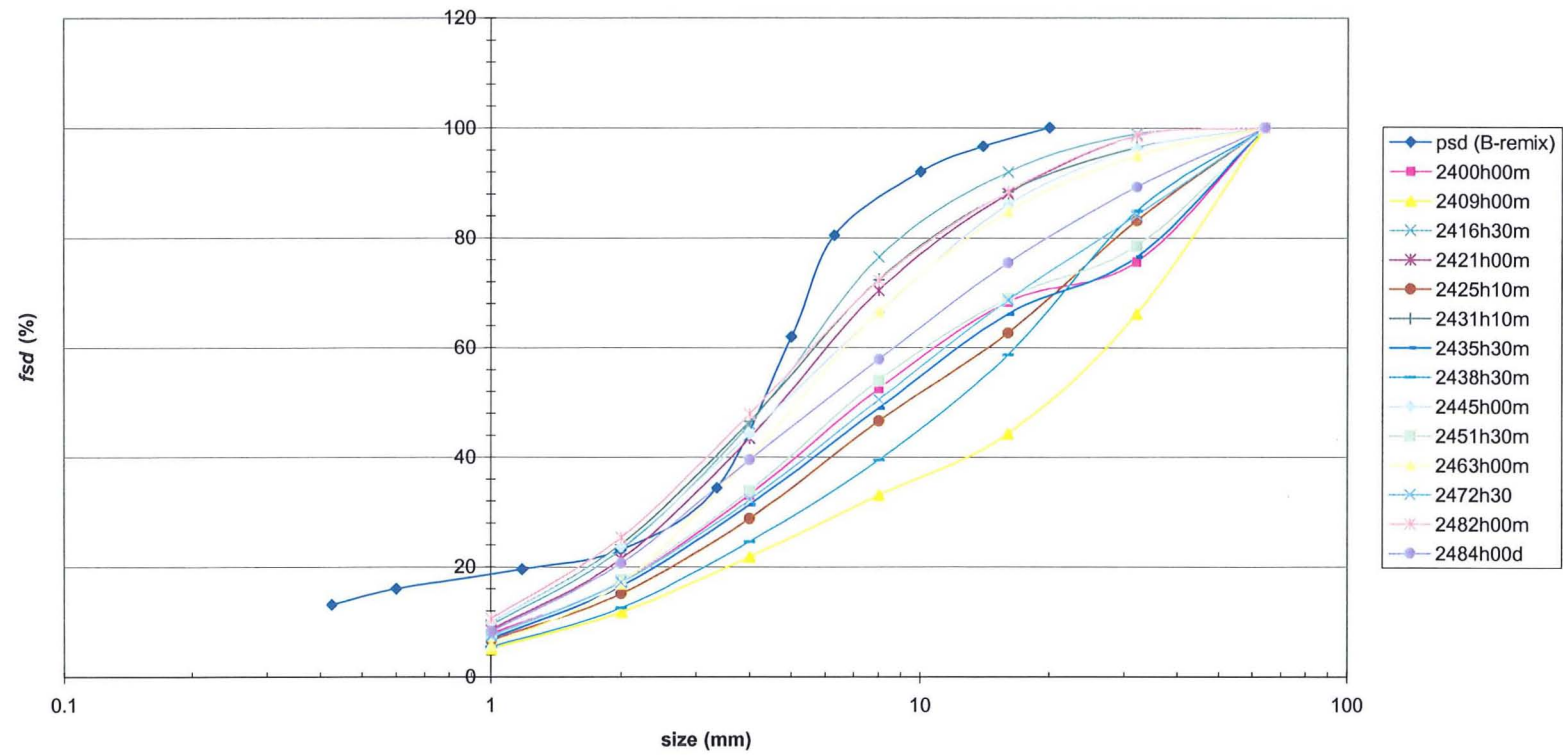
Figure 4.20 (continued) Form size distribution ( $f_{sd}$ ) established using the DWT method.





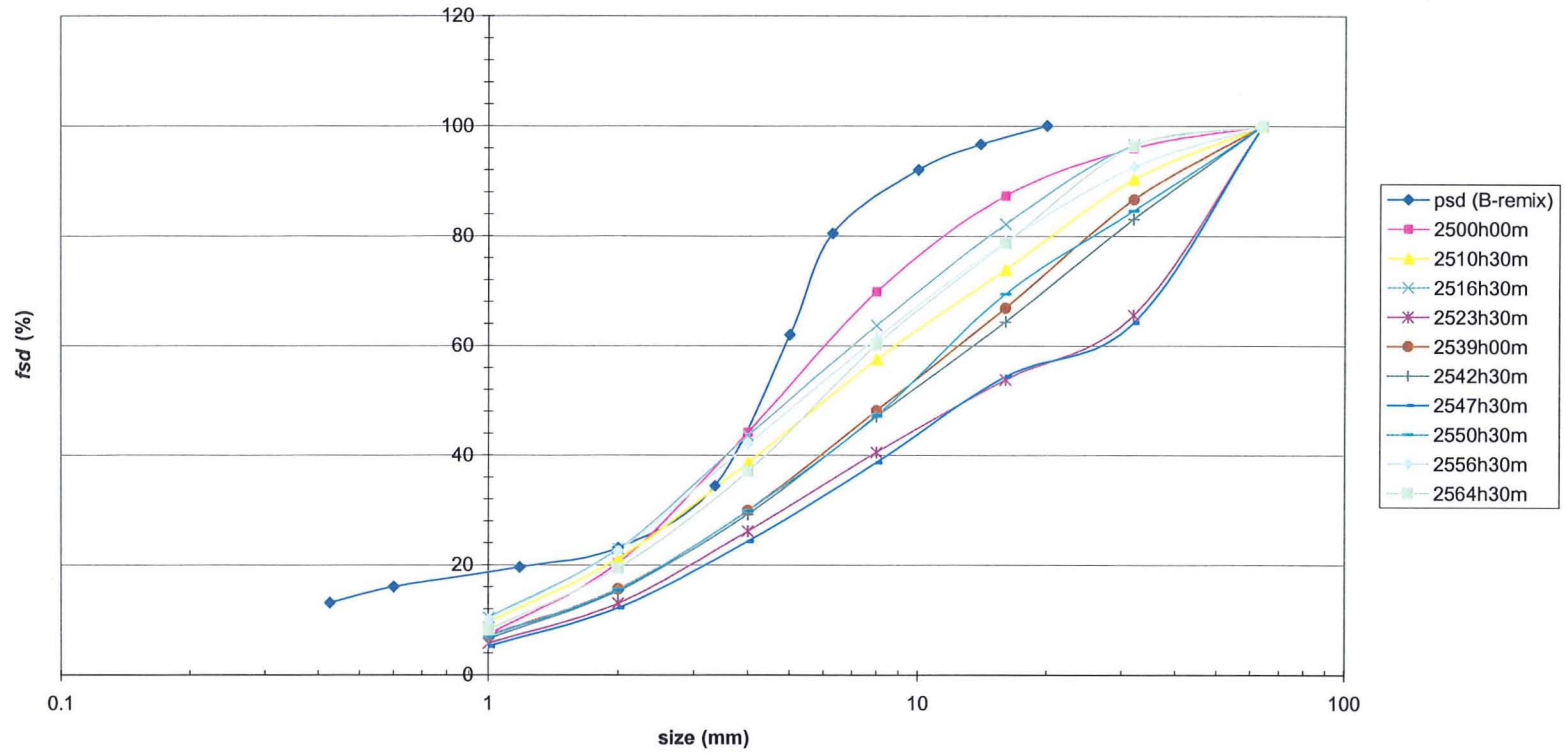
(m) Experiment 23.

Figure 4.20 (continued) Form size distribution (*fsd*) established using the DWT method.



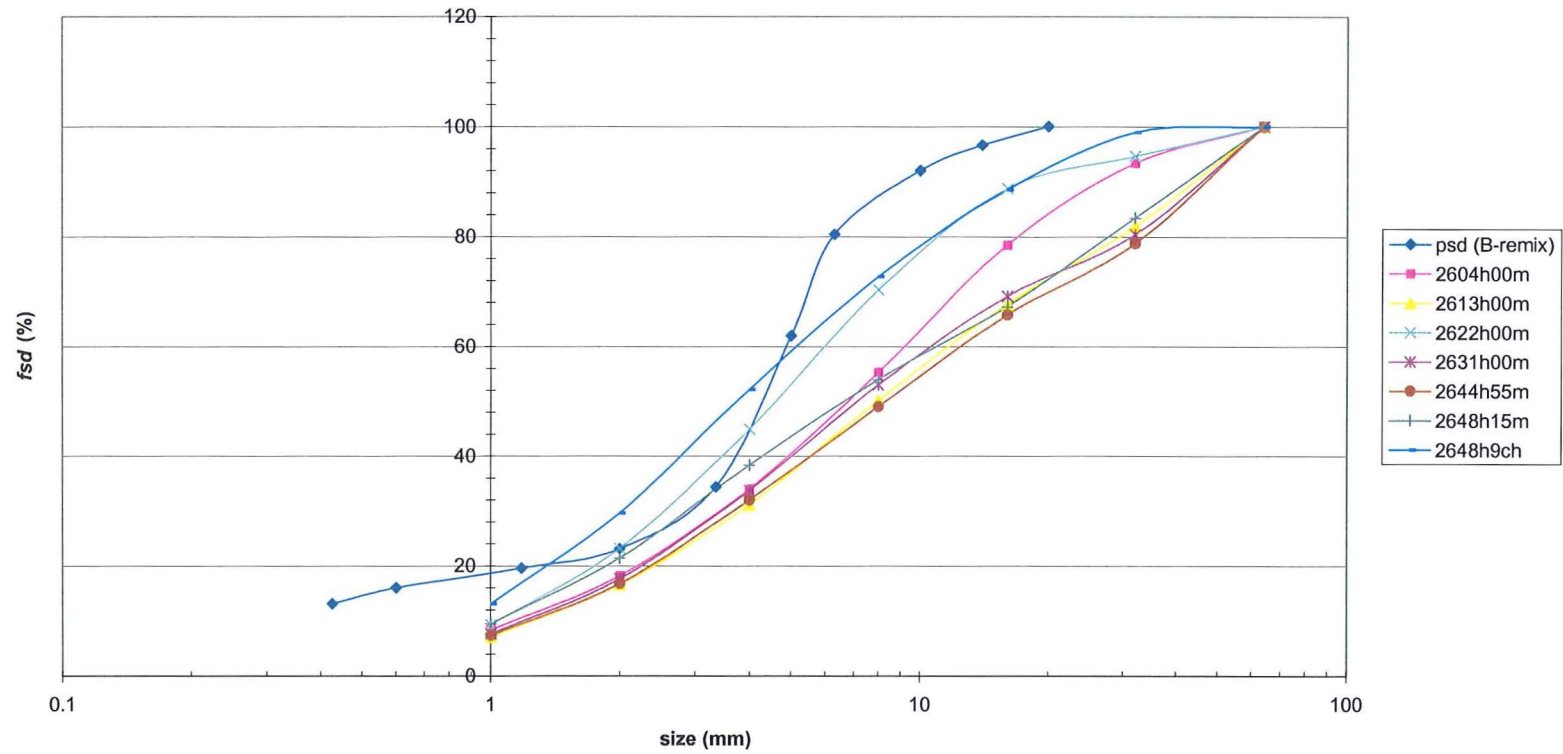
(n) Experiment 24.

Figure 4.20 (continued) Form size distribution (*fsd*) established using the DWT method.



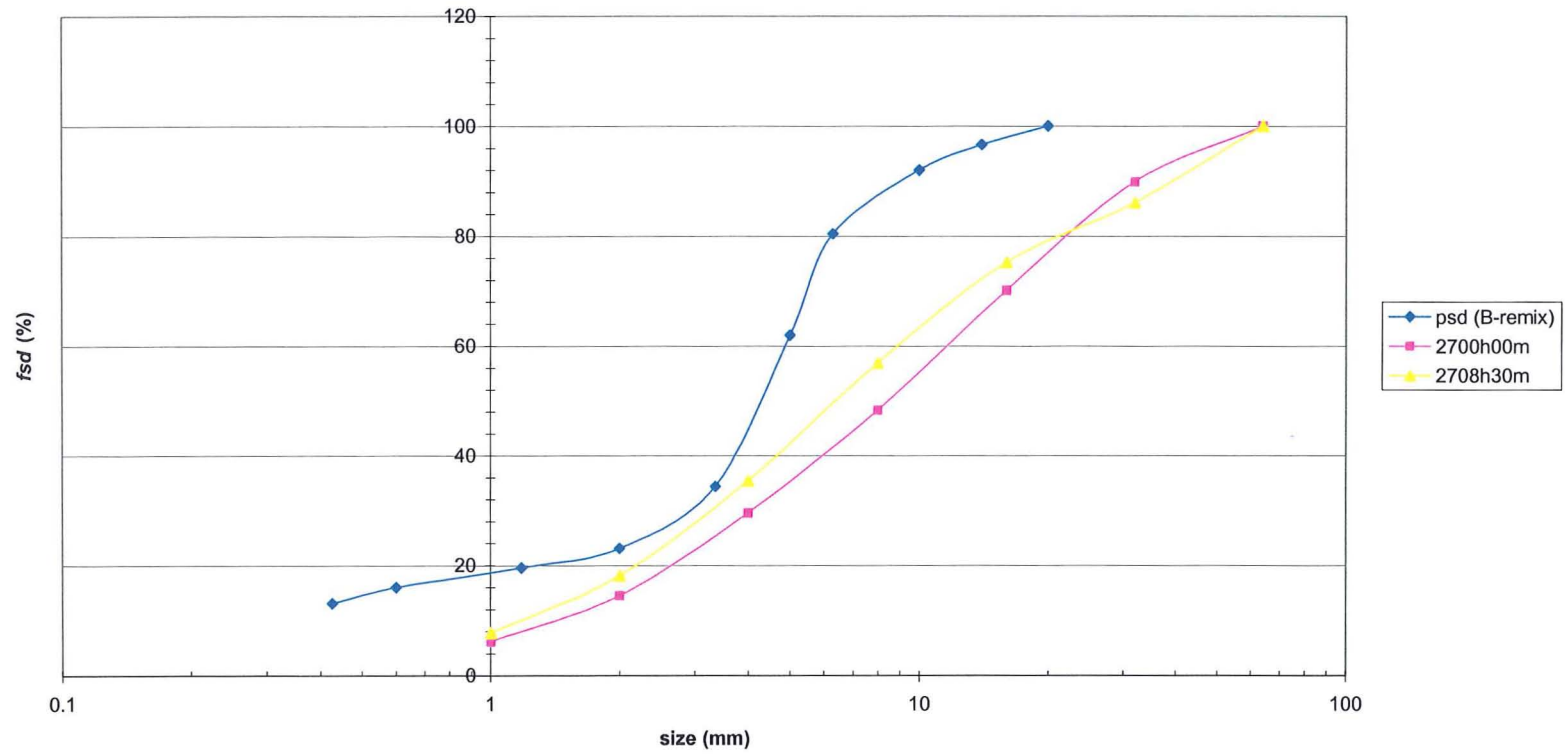
(o) Experiment 25.

**Figure 4.20 (continued)** Form size distribution (*fsd*) established using the DWT method.



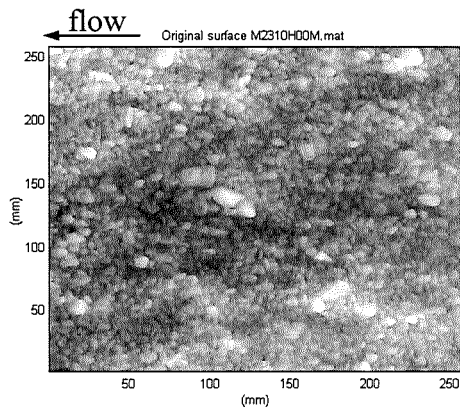
(p) Experiment 26.

Figure 4.20 (continued) Form size distribution (*fsd*) established using the DWT method.

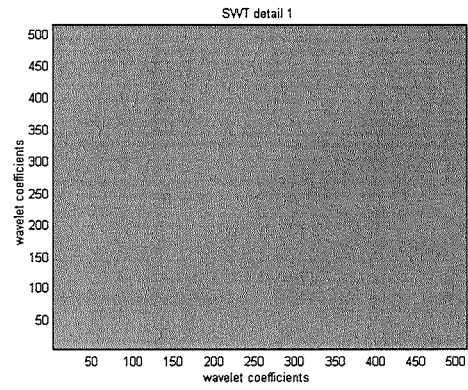


(q) Experiment 27.

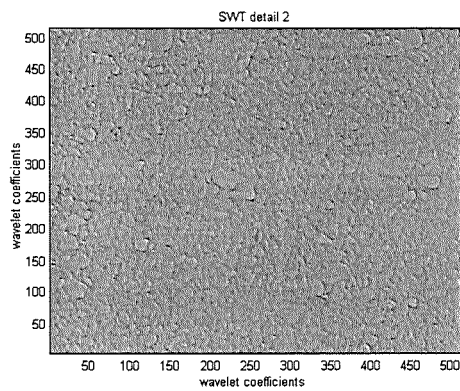
**Figure 4.20 (continued)** Form size distribution ( $f_{sd}$ ) established using the DWT method.



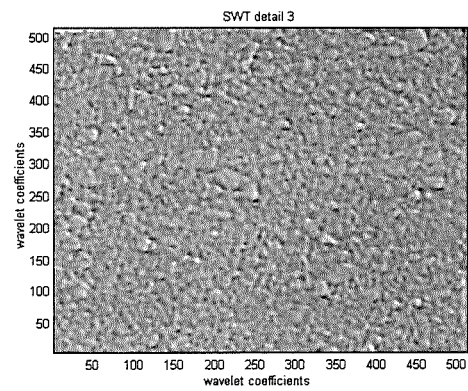
(a) Original sediment surface.



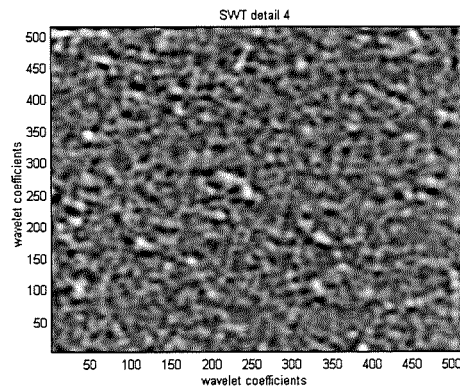
(b) Detail scale 1.



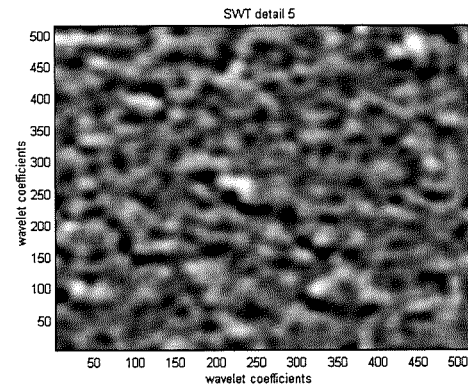
(c) Detail scale 2.



(d) Detail scale 3.



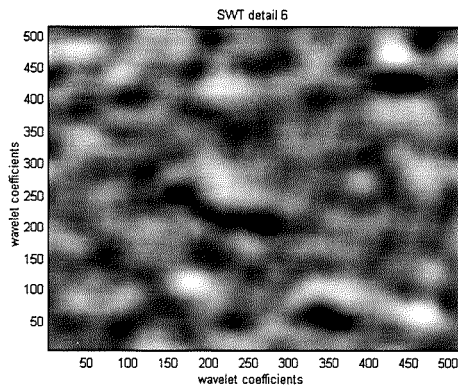
(e) Detail scale 4.



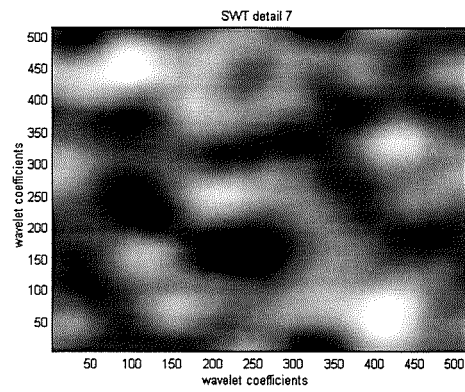
(f) Detail scale 5.

(a) Detail 1 is the smallest scale detail and (f) detail 9 is the largest scale detail.

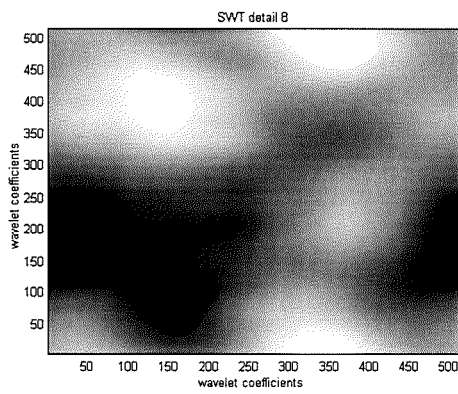
**Figure 4.21** The SWT decomposition details of sediment surface data-set '2310h00m' in experiment 23.



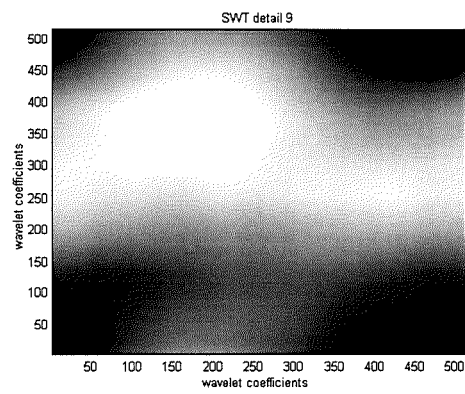
(g) Detail scale 6.



(h) Detail scale 7.



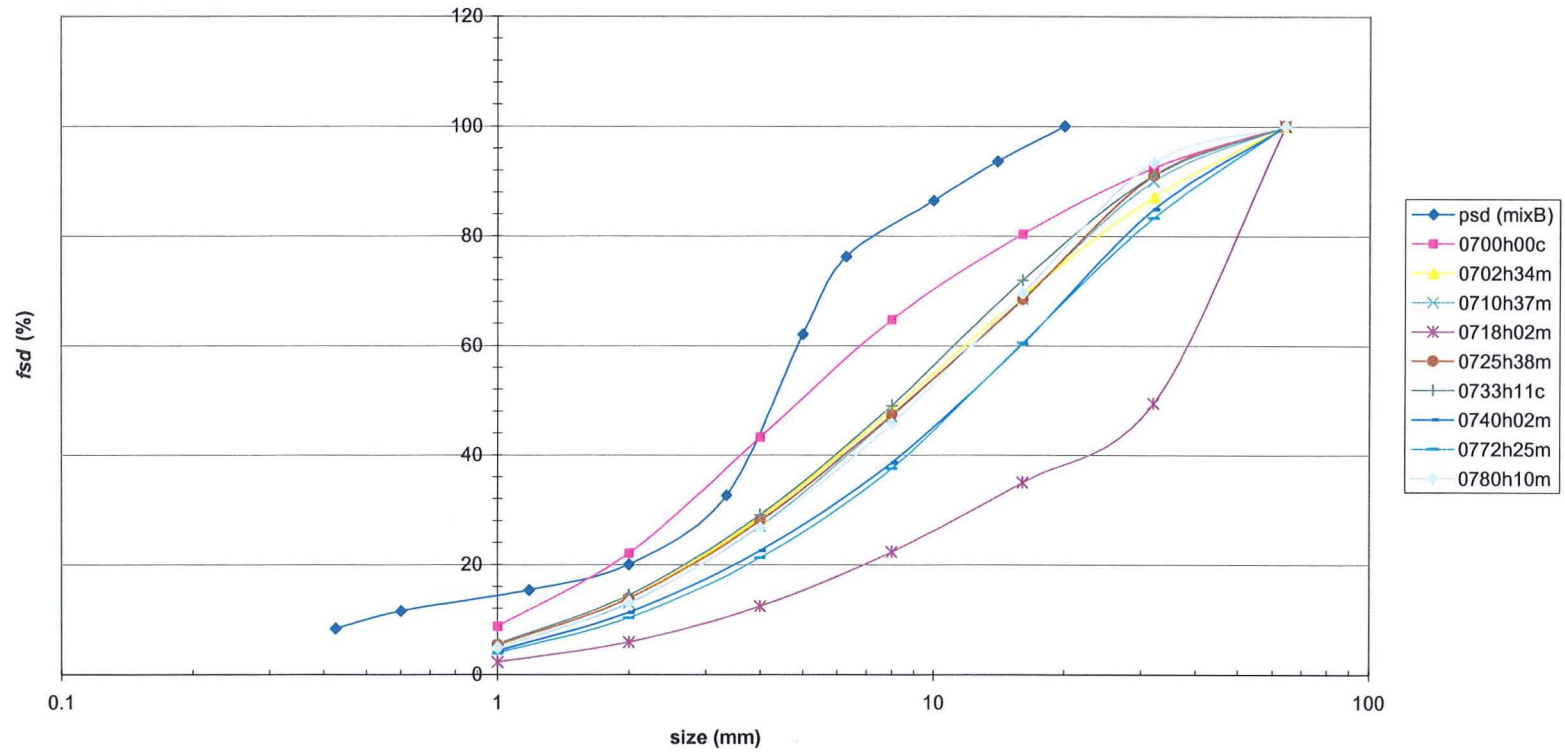
(i) Detail scale 8.



(j) Detail scale 9.

(a) Detail 1 is the smallest scale detail and (f) detail 9 is the largest scale detail.

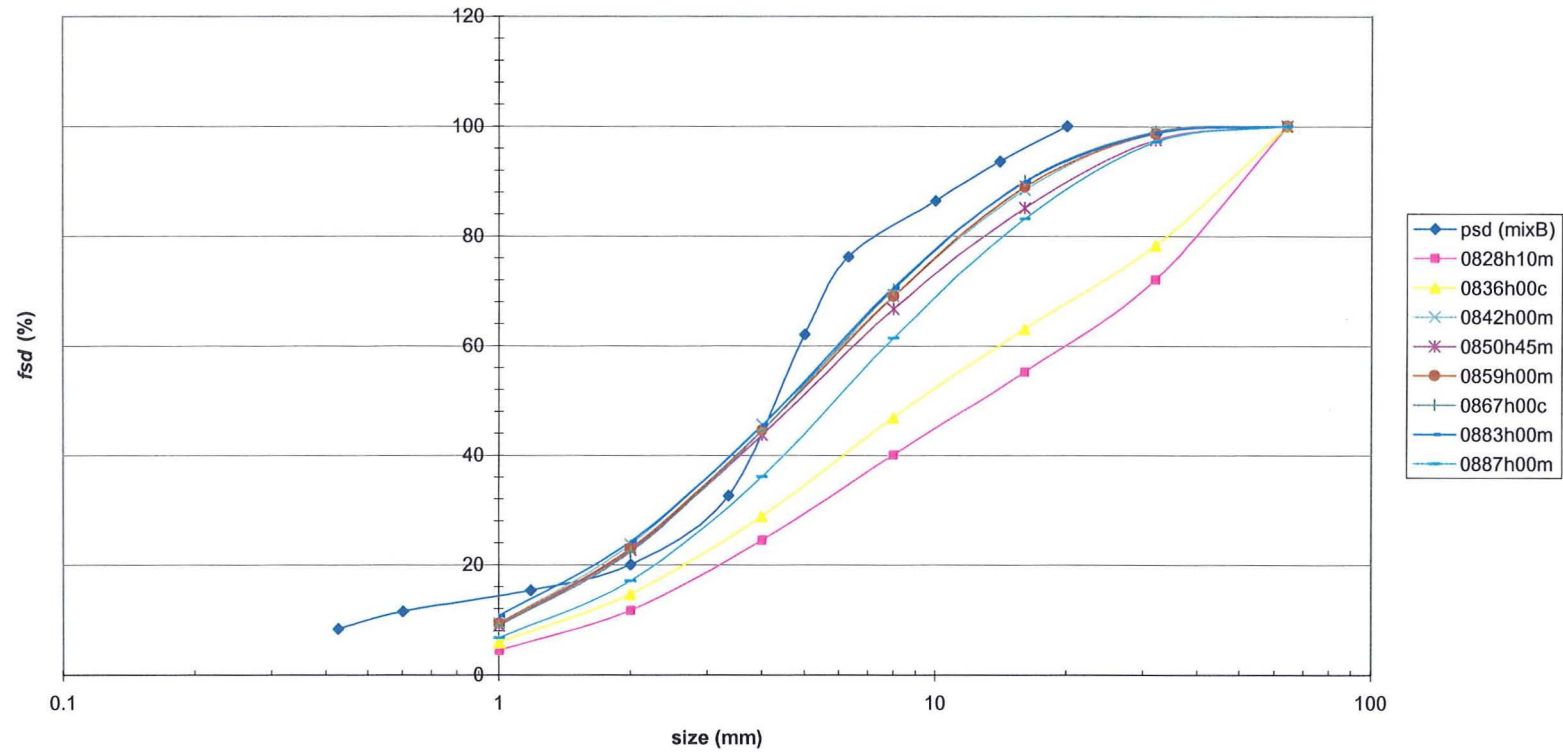
**Figure 4.21 (continued)** The SWT decomposition details of sediment surface data-set '2310h00m' in experiment 23.



(a) Experiment 07.

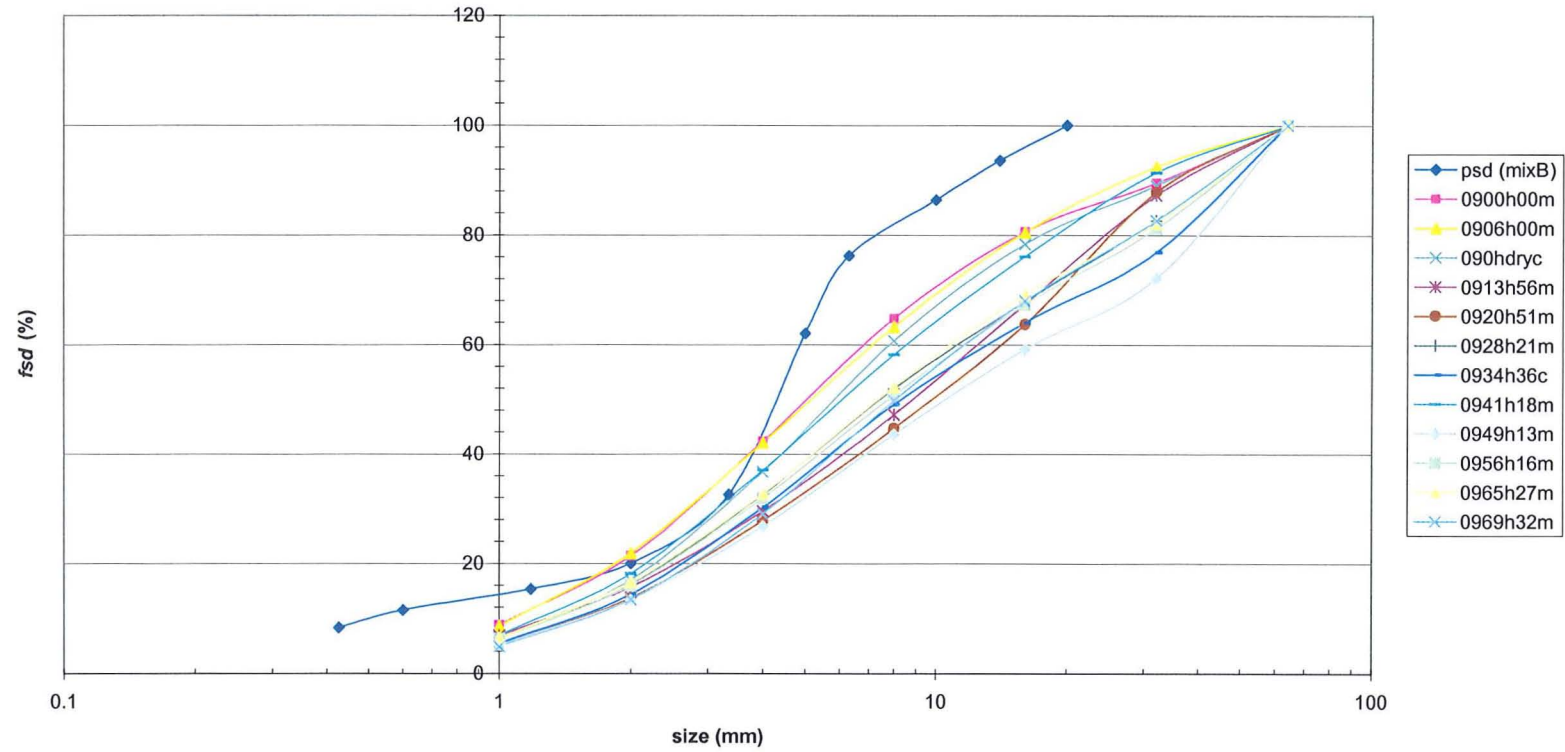
**Figure 4.22** Form size distribution (*fsd*) established using the SWT method.





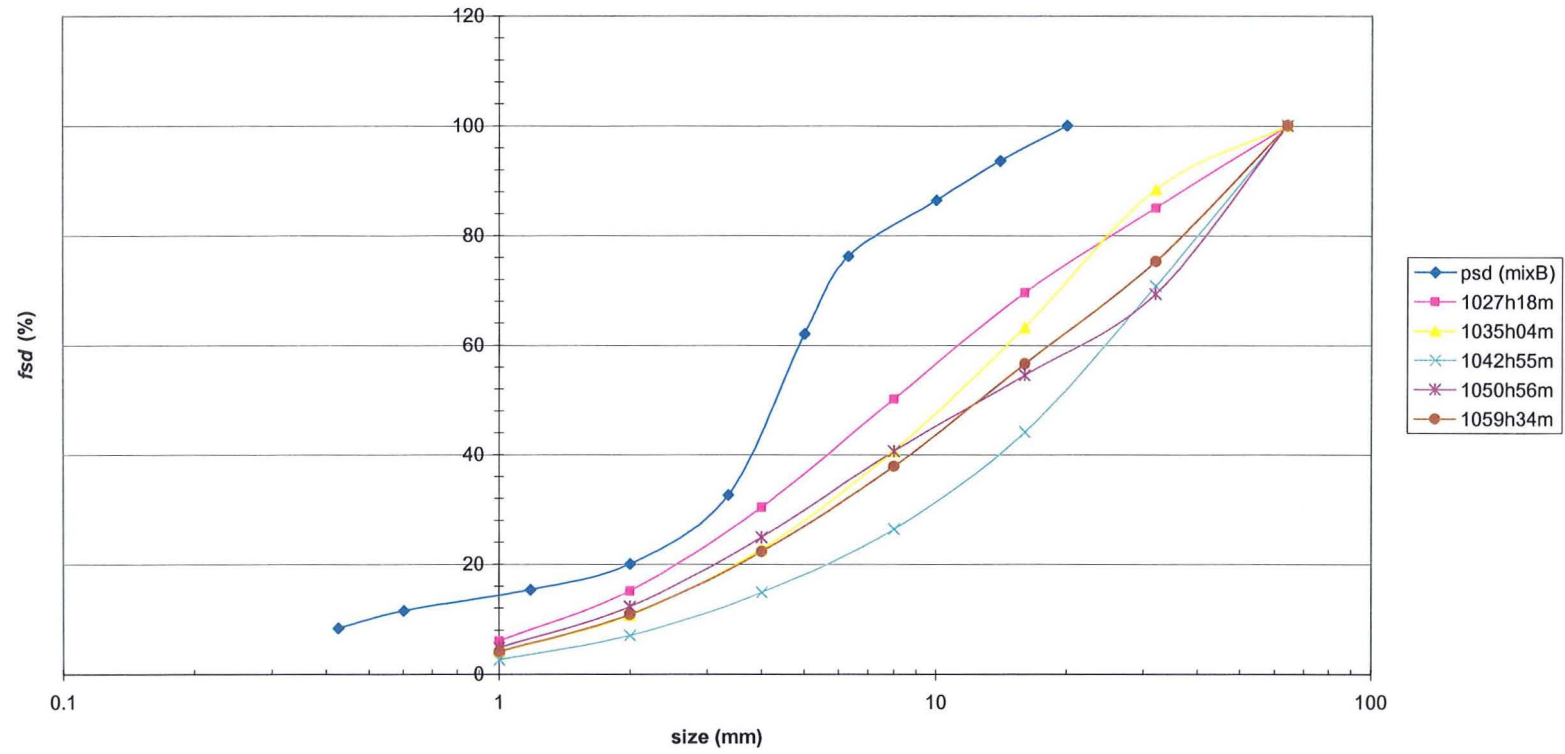
(b) Experiment 08.

**Figure 4.22 (continued)** Form size distribution (*fsd*) established using the SWT method.



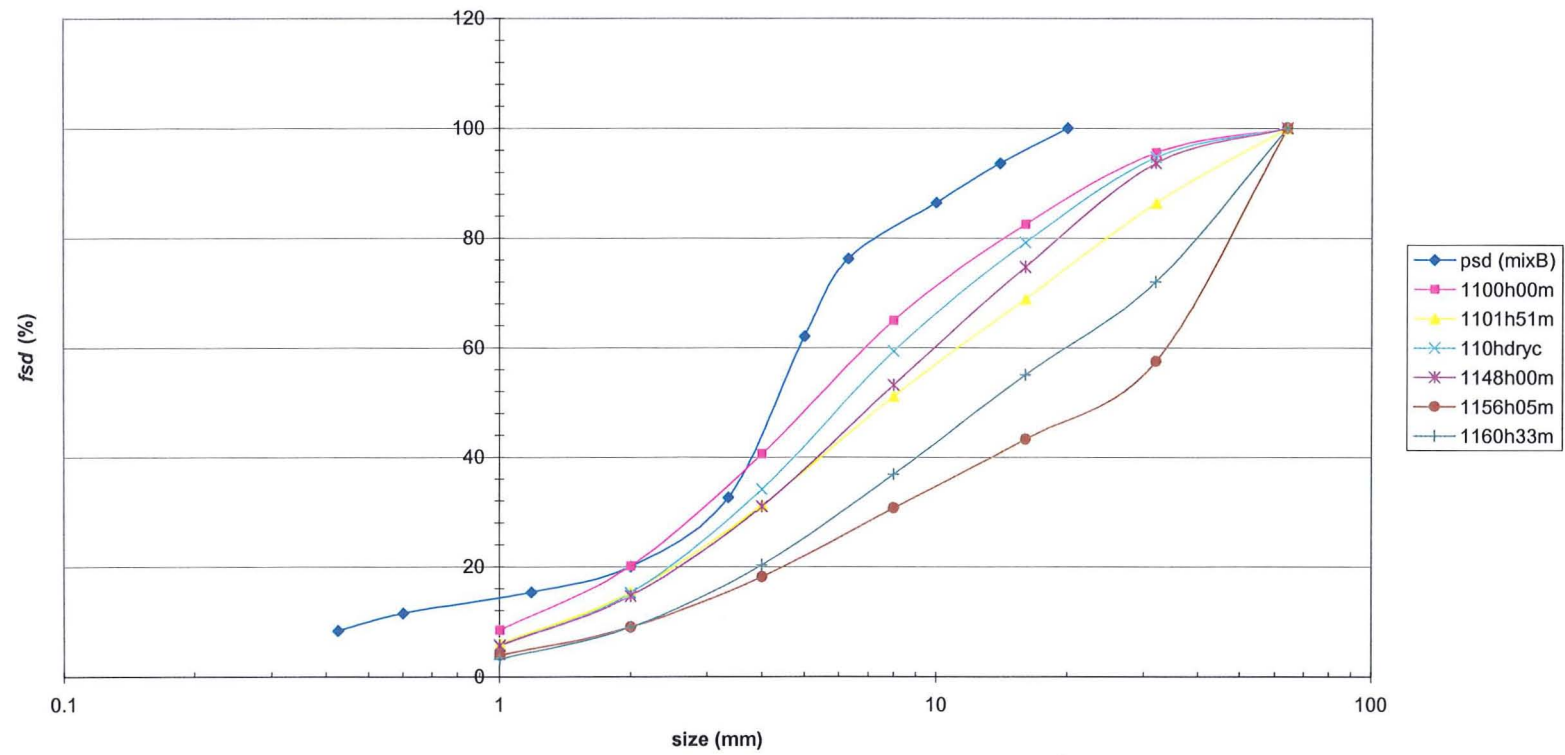
(c) Experiment 09.

Figure 4.22 (continued) Form size distribution (*fsd*) established using the SWT method.



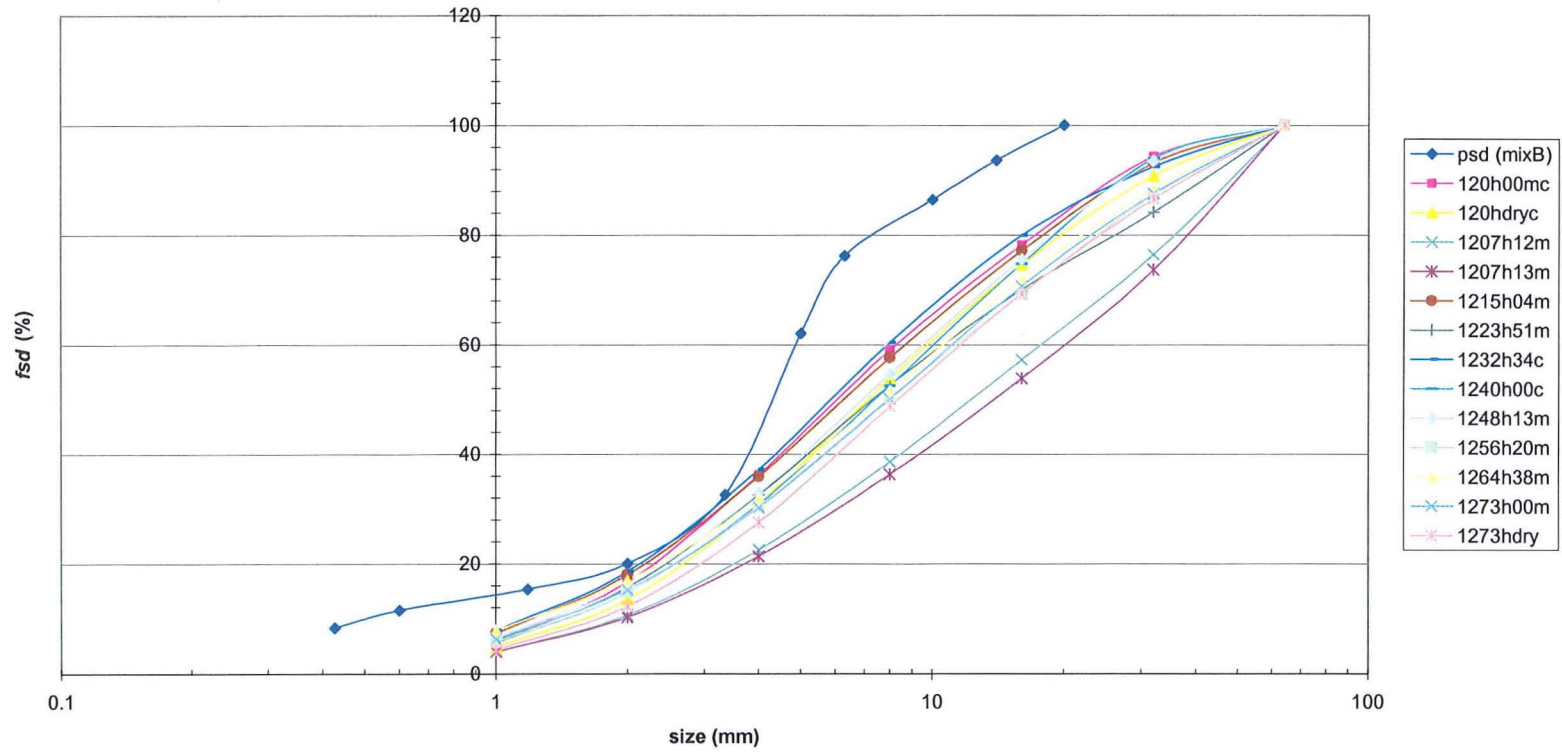
(d) Experiment 10.

Figure 4.22 (continued) Form size distribution (*fsd*) established using the SWT method.



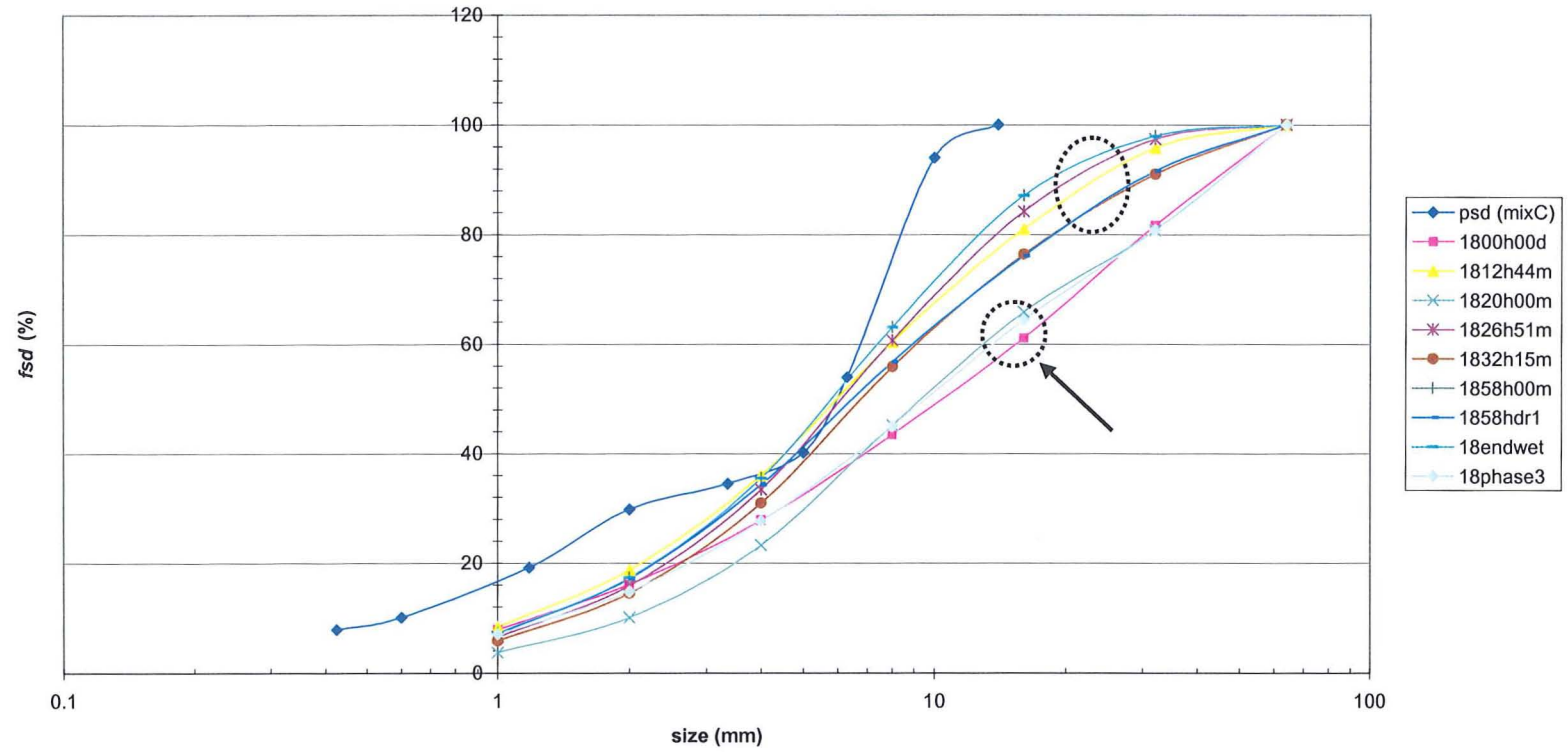
(e) Experiment 11.

Figure 4.22 (continued) Form size distribution (*fsd*) established using the SWT method.



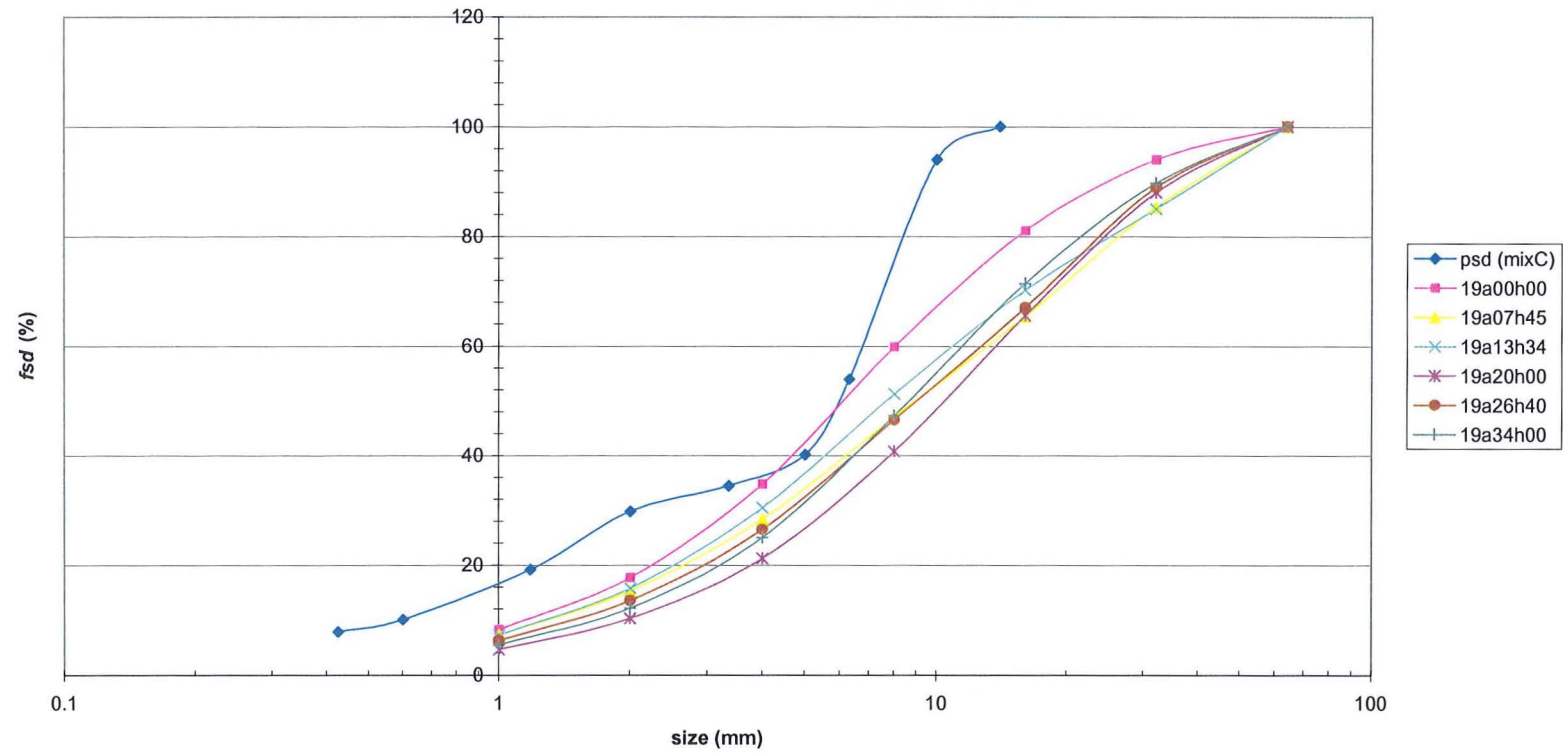
(f) Experiment 12.

**Figure 4.22 (continued)** Form size distribution (*fsd*) established using the SWT method.



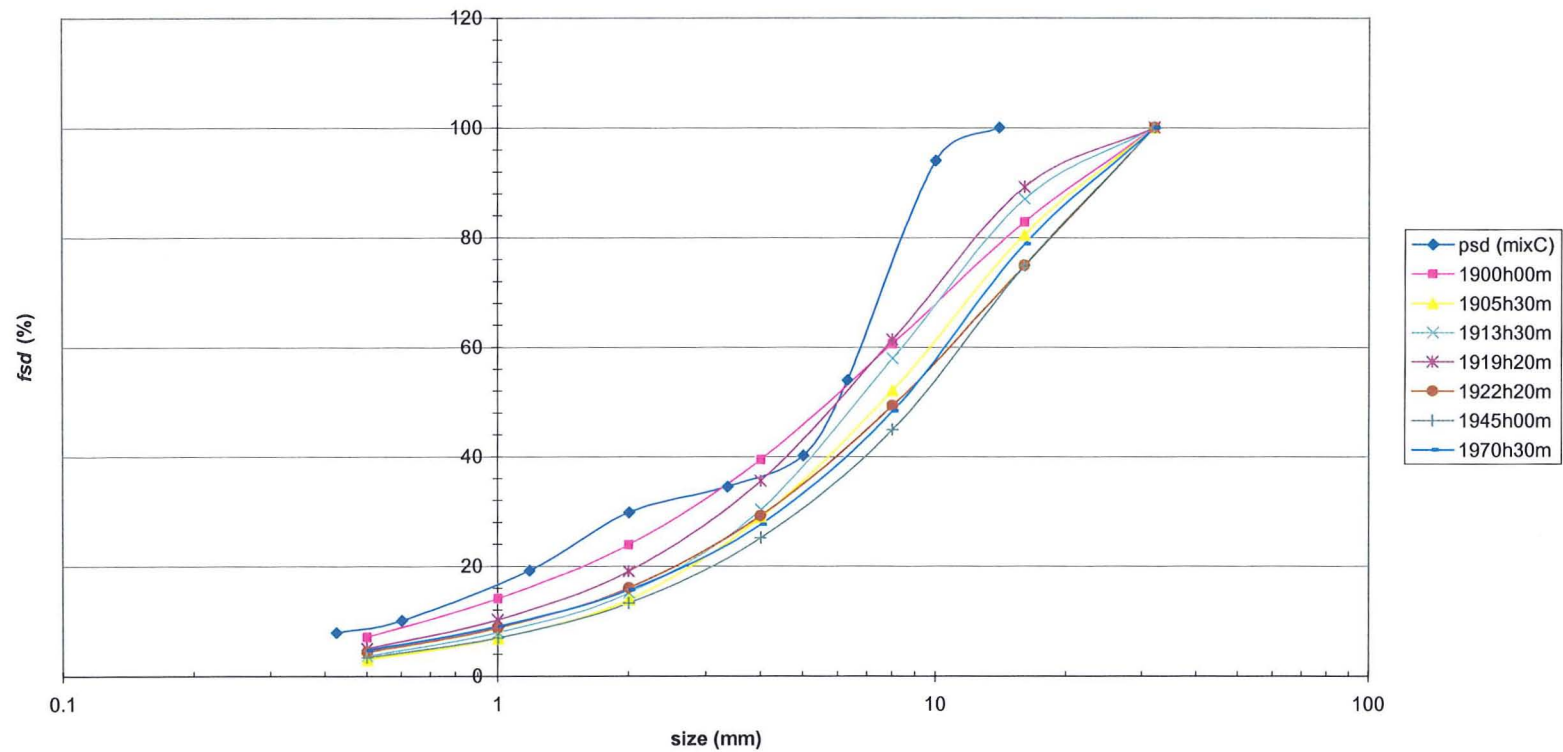
(g) Experiment 18.

Figure 4.22 (continued) Form size distribution (*fsd*) established using the SWT method.



(h) Experiment 19A.

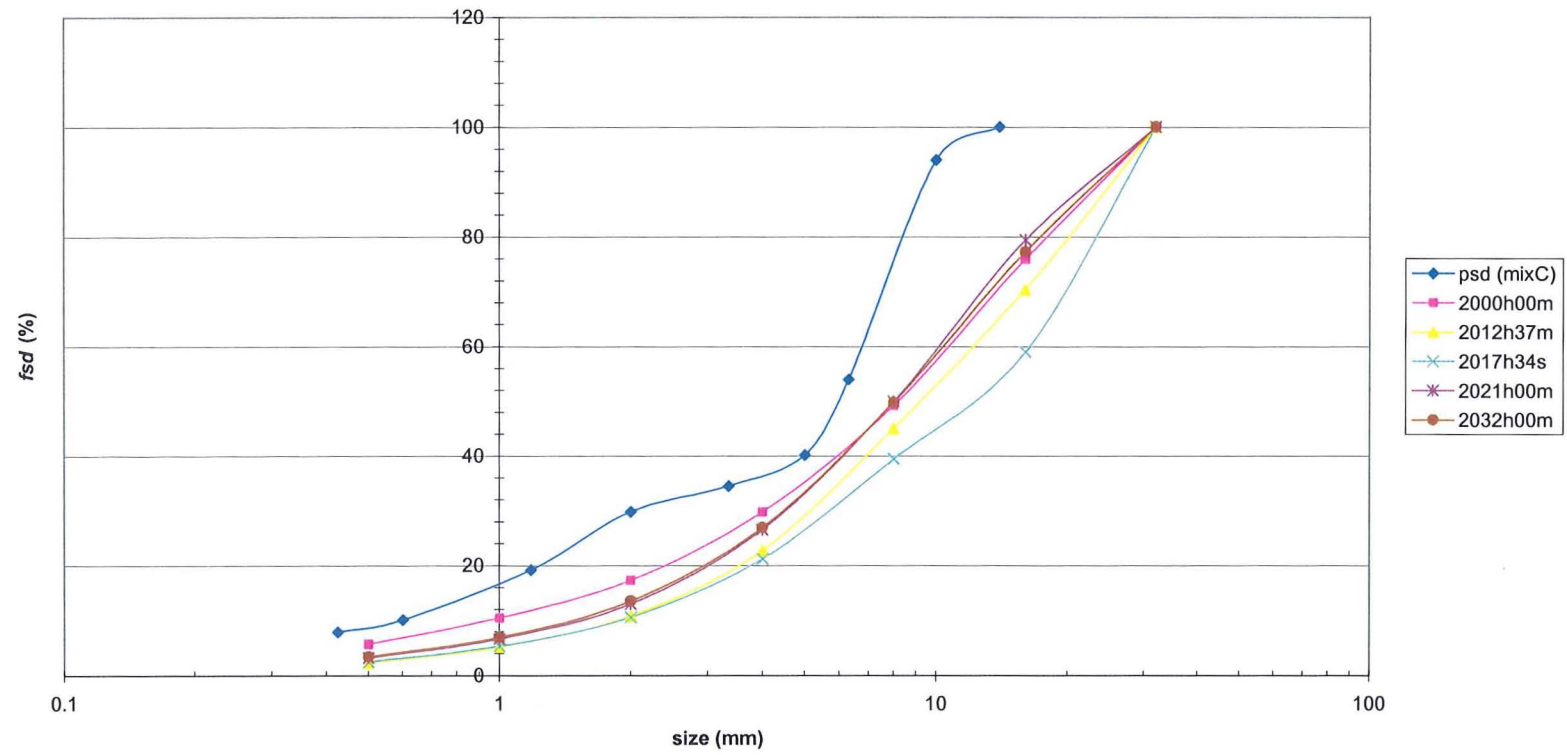
Figure 4.22 (continued) Form size distribution (*fsd*) established using the SWT method.



(i) Experiment 19.

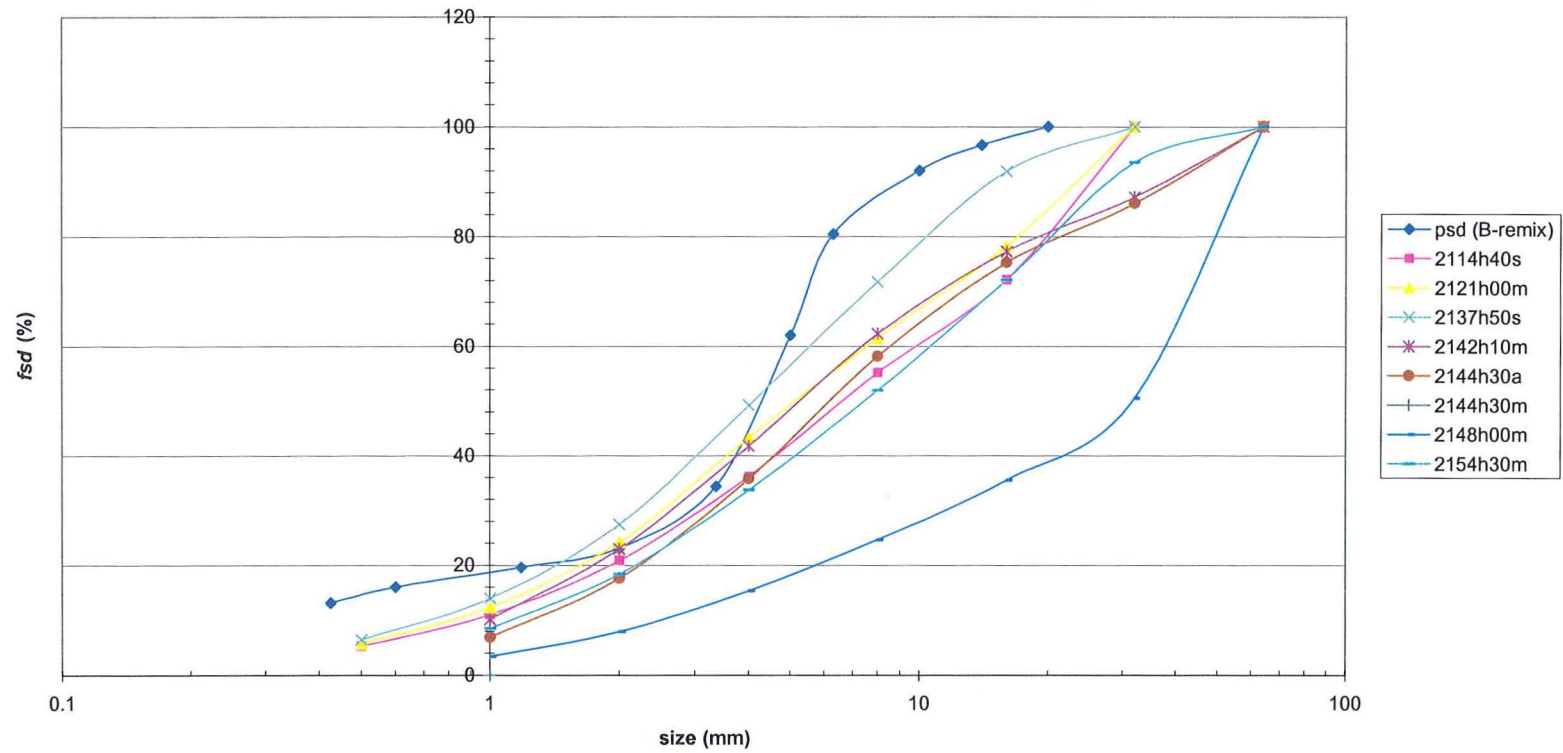
**Figure 4.22 (continued)** Form size distribution (*fsd*) established using the SWT method.





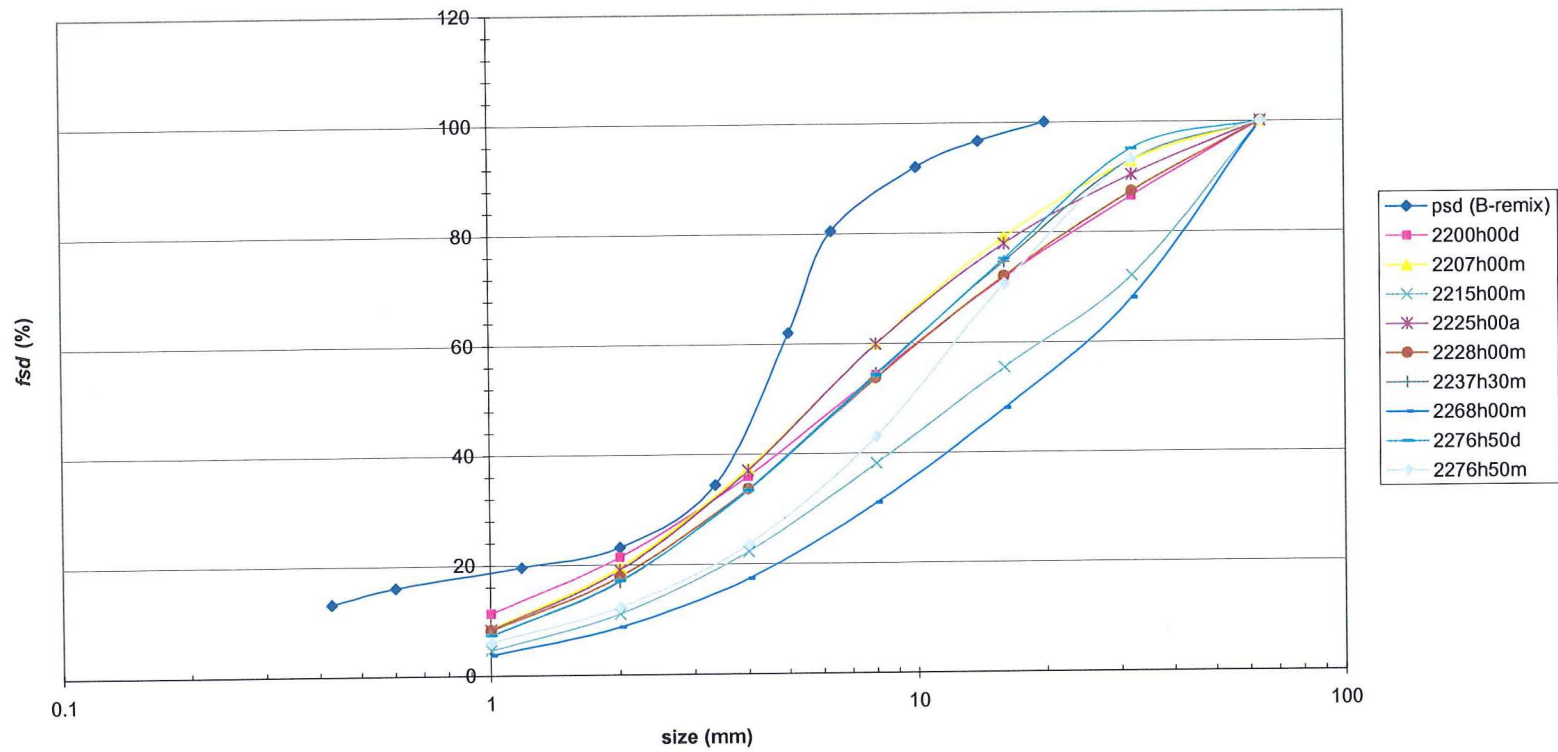
(j) Experiment 20.

**Figure 4.22 (continued)** Form size distribution (*fsd*) established using the SWT method.



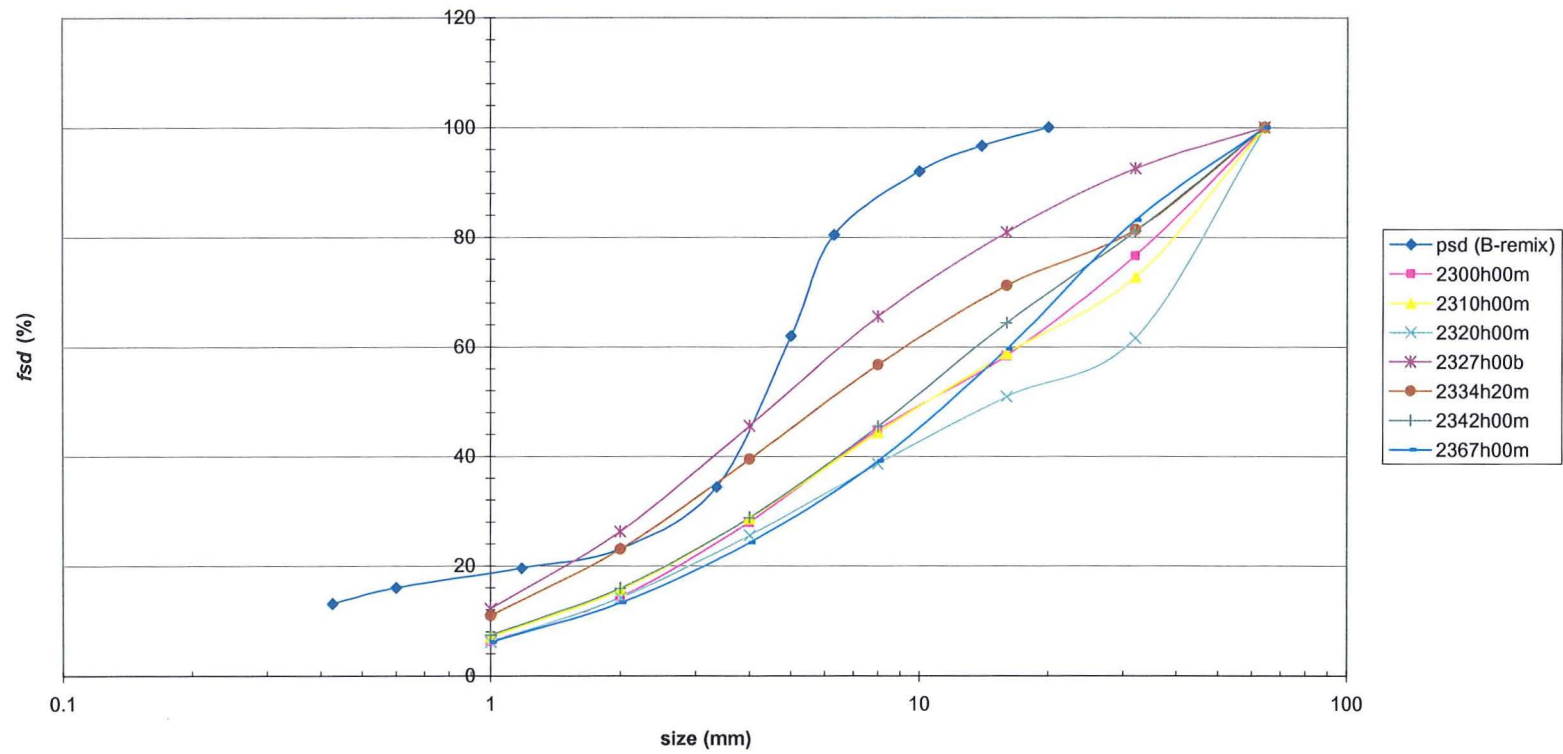
(k) Experiment 21.

**Figure 4.22 (continued)** Form size distribution (*fsd*) established using the SWT method.



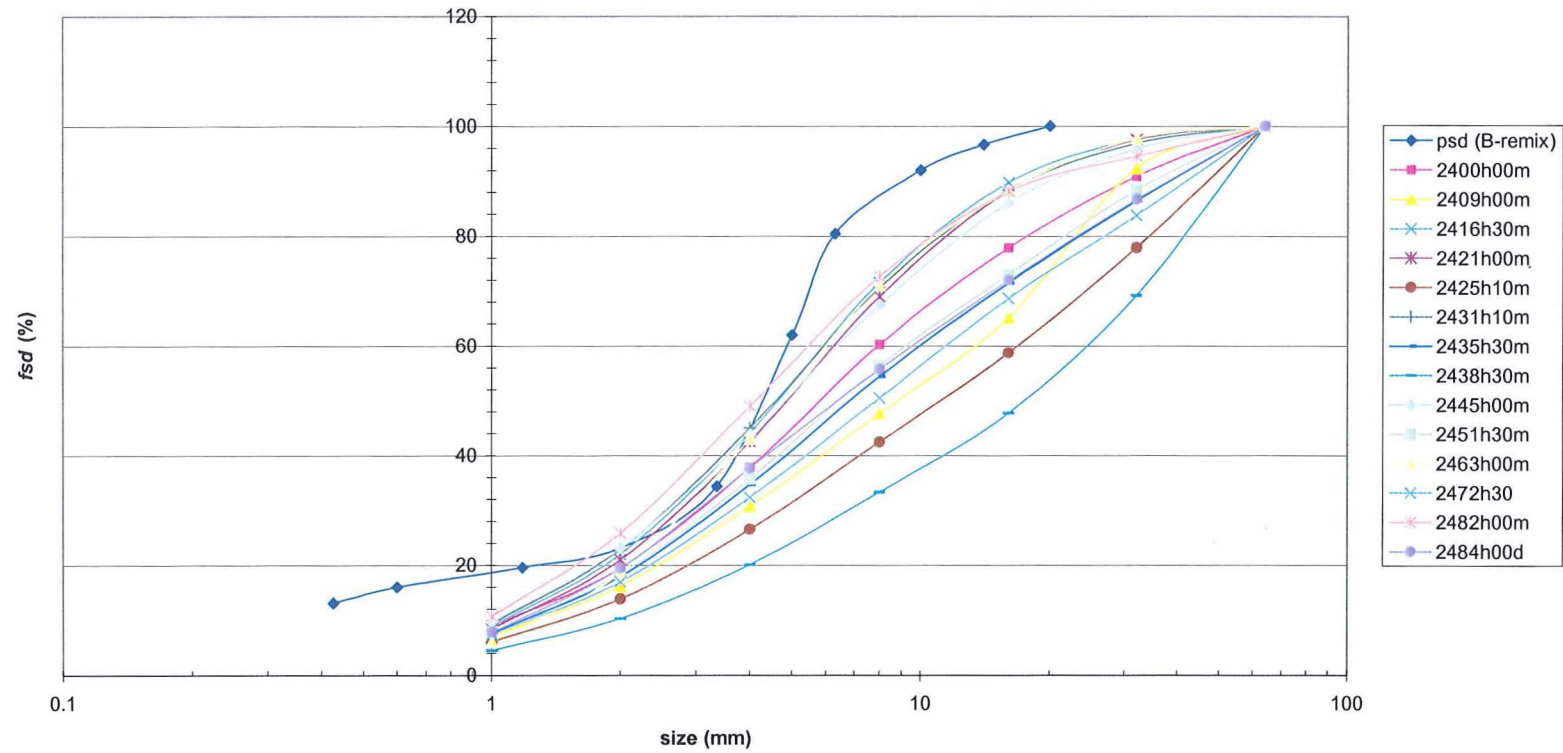
(l) Experiment 22.

Figure 4.22 (continued) Form size distribution (*f<sub>sd</sub>*) established using the SWT method.



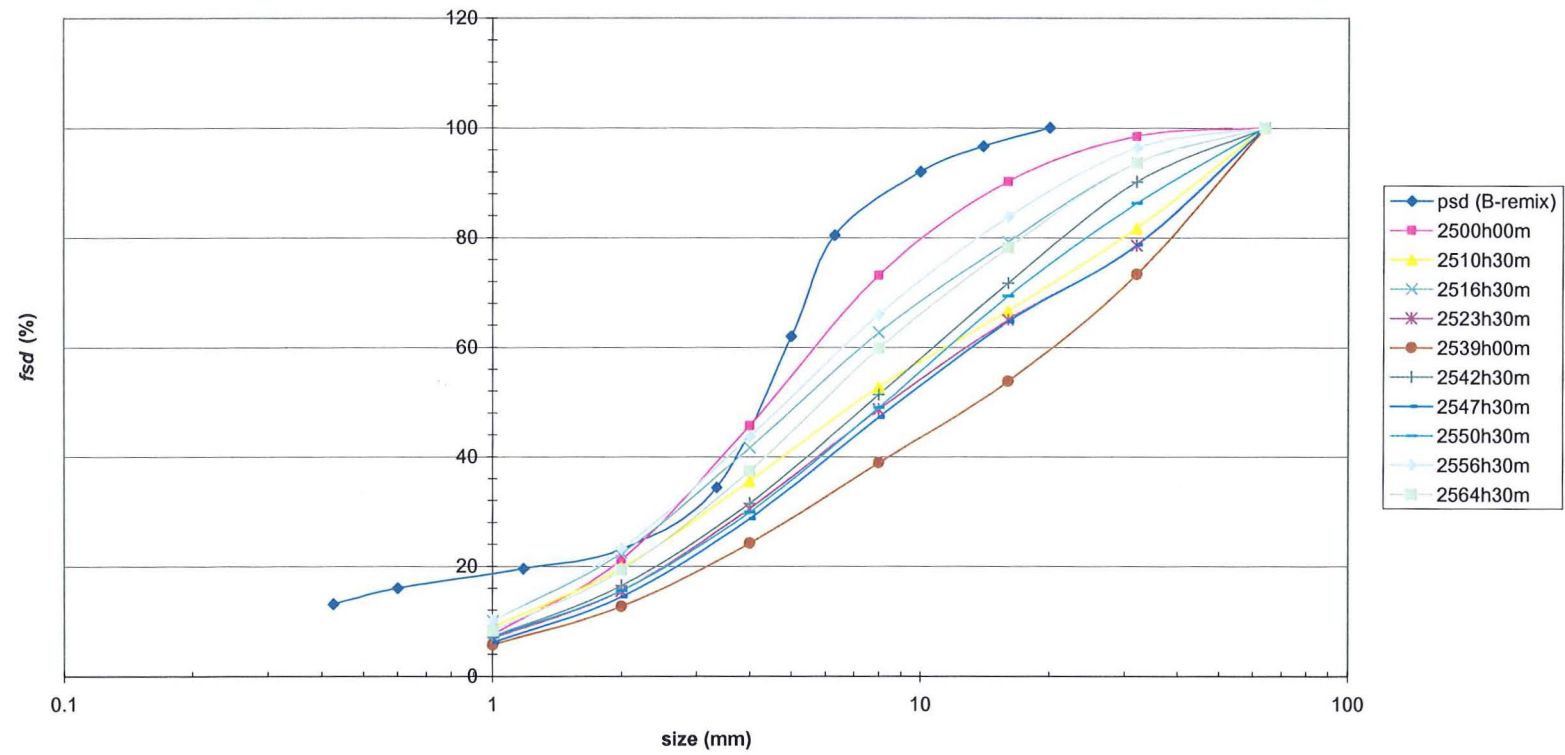
(m) Experiment 23.

**Figure 4.22 (continued)** Form size distribution (*f<sub>sd</sub>*) established using the SWT method.



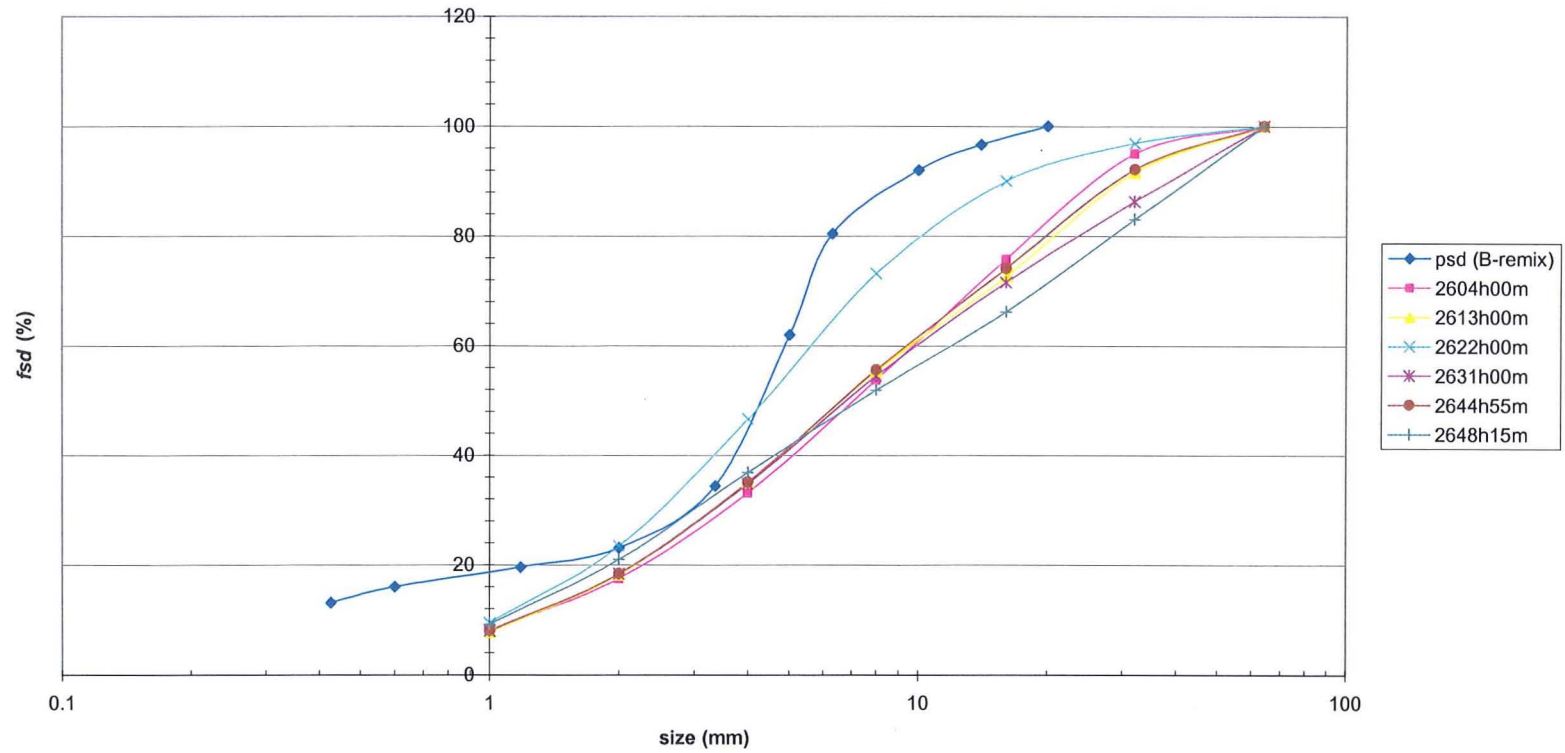
(n) Experiment 24.

Figure 4.22 (continued) Form size distribution (*fsd*) established using the SWT method.



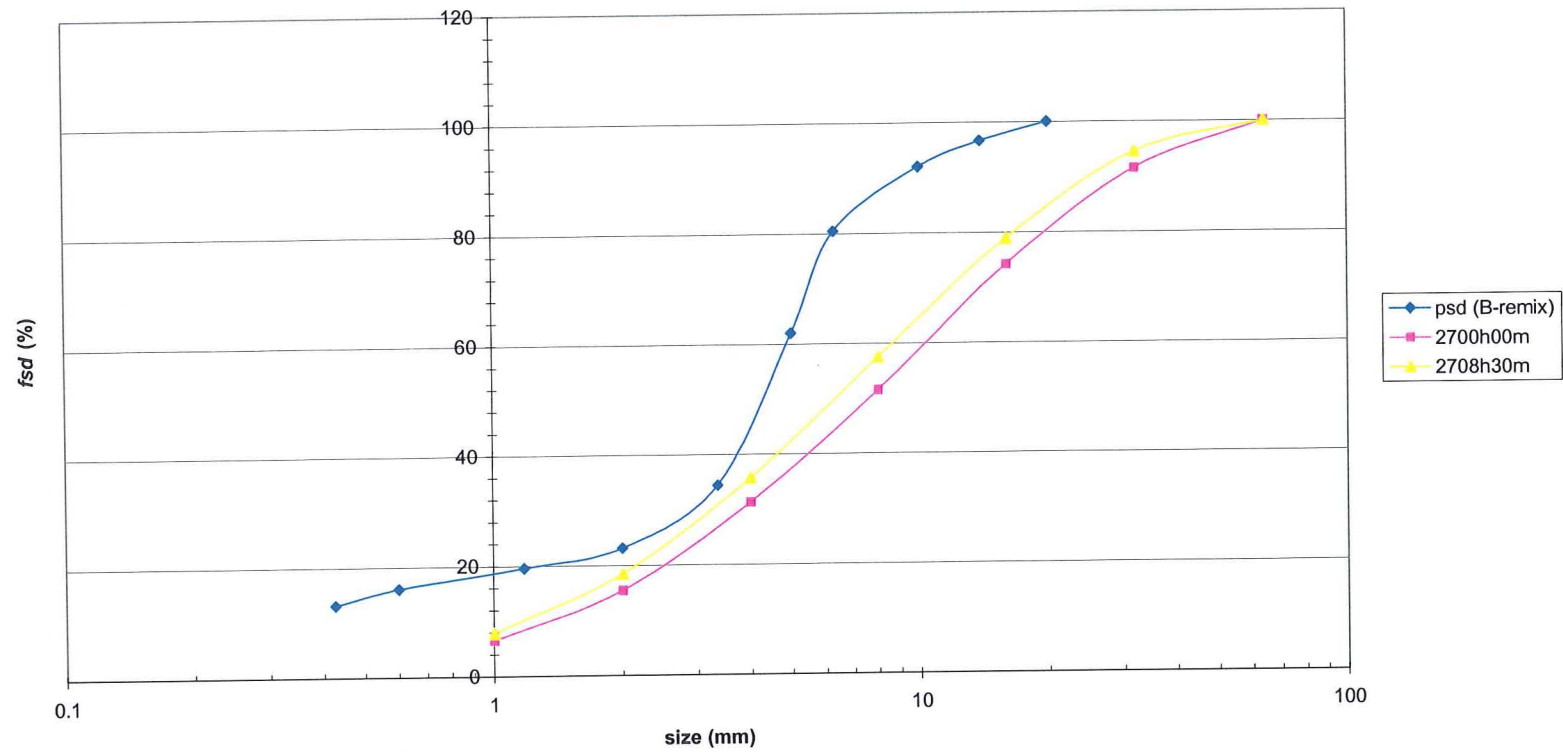
(o) Experiment 25.

Figure 4.22 (continued), Form size distribution (*fsd*) established using the SWT method.



(p) Experiment 26.

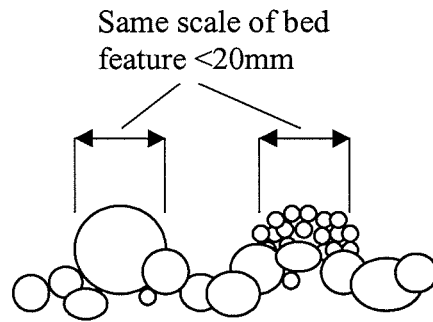
Figure 4.22 (continued), Form size distribution (*fsd*) established using the SWT method.



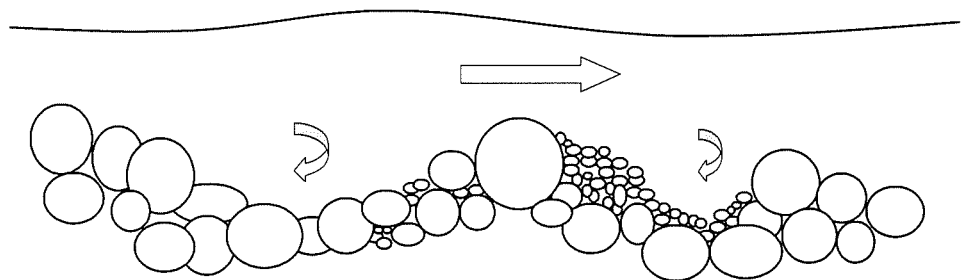
(q) Experiment 27.

Figure 4.22 (continued) Form size distribution (*fsd*) established using the SWT method.

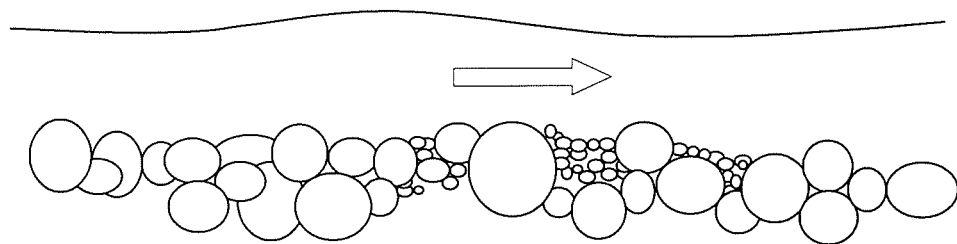




**Figure 4.23** Groups of smaller particles can form a larger feature (i.e. at a larger scale).



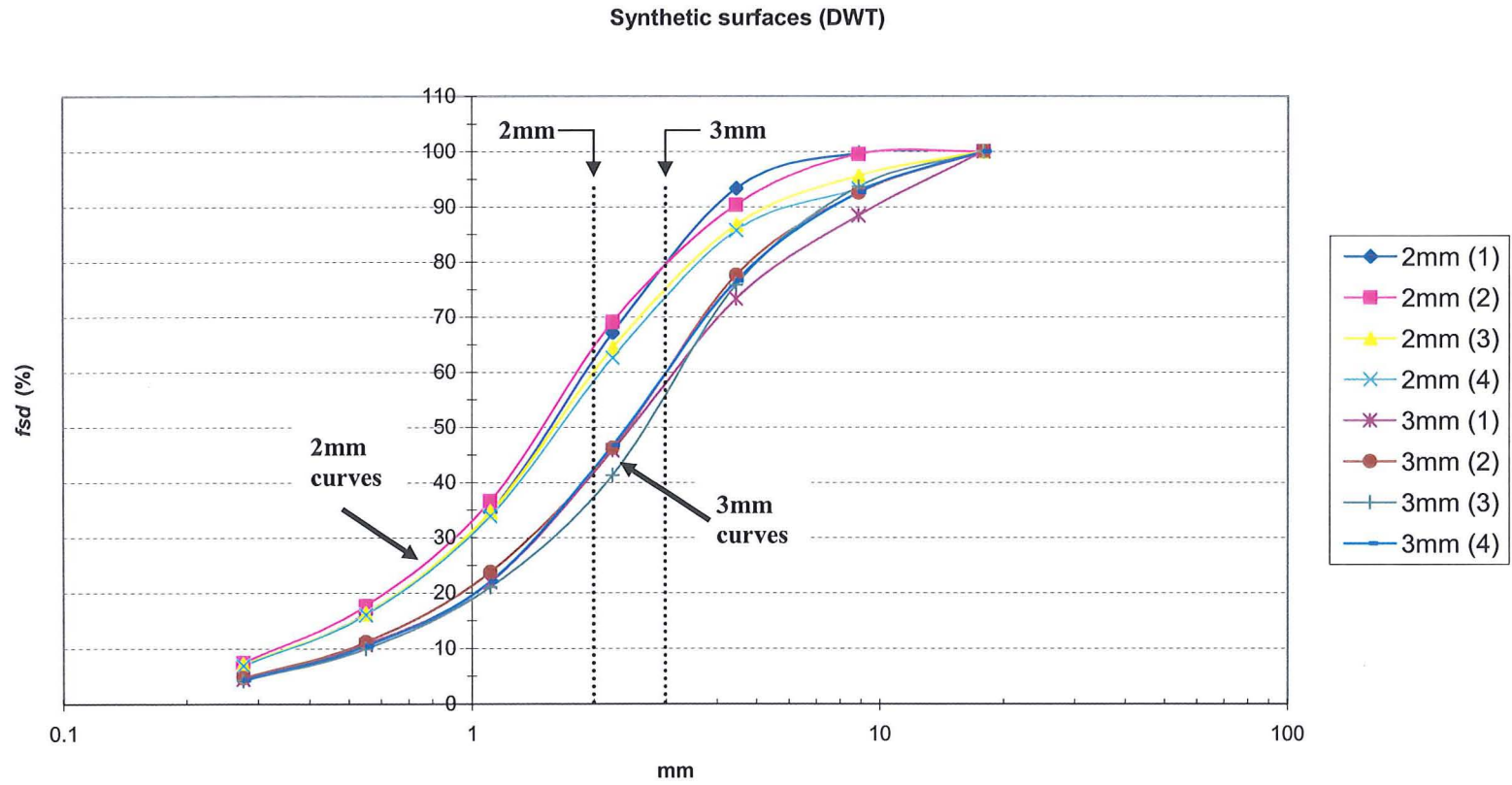
(a) Flow over a rough surface.



(b) Flow over flat surface.

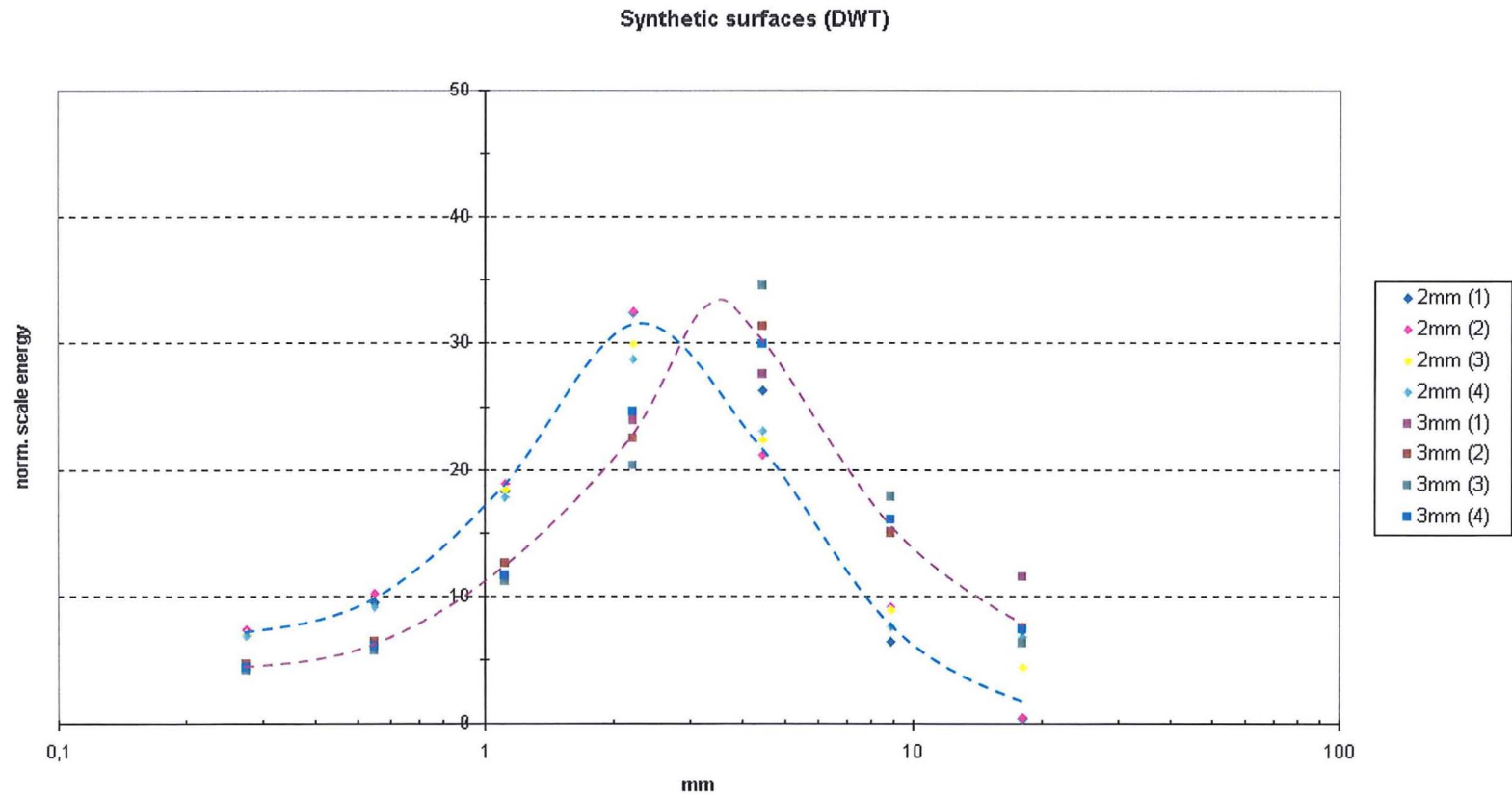
Even though the two surface have similar particle size distribution the typographies shape of the bed-surface will affect the river flow differently for the two surfaces.

**Figure 4.24** River flow over two different sediment surface typographies.



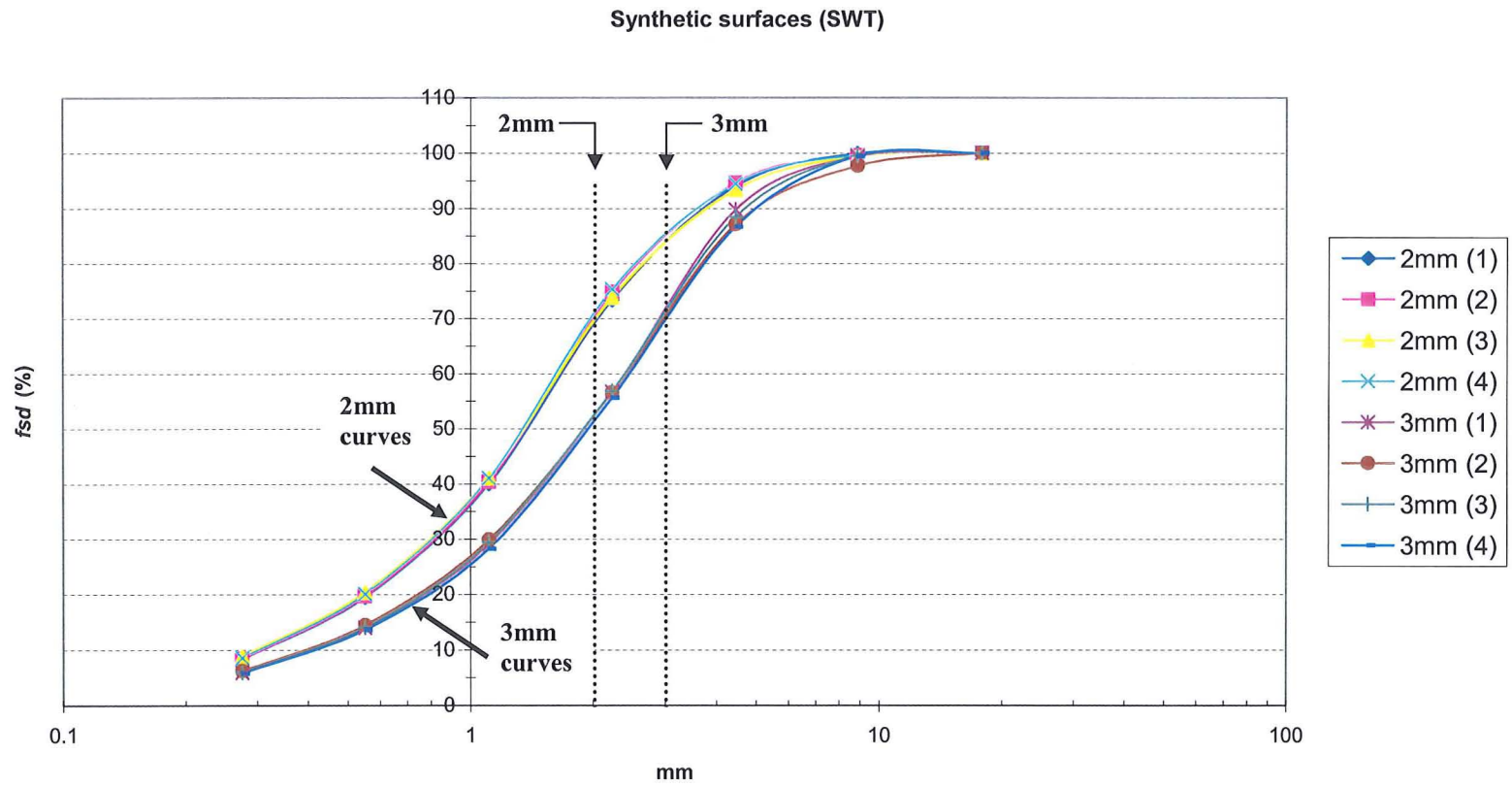
(a) Form size distribution.

Figure 4.25 Results from synthetic surface analysis, DWT.



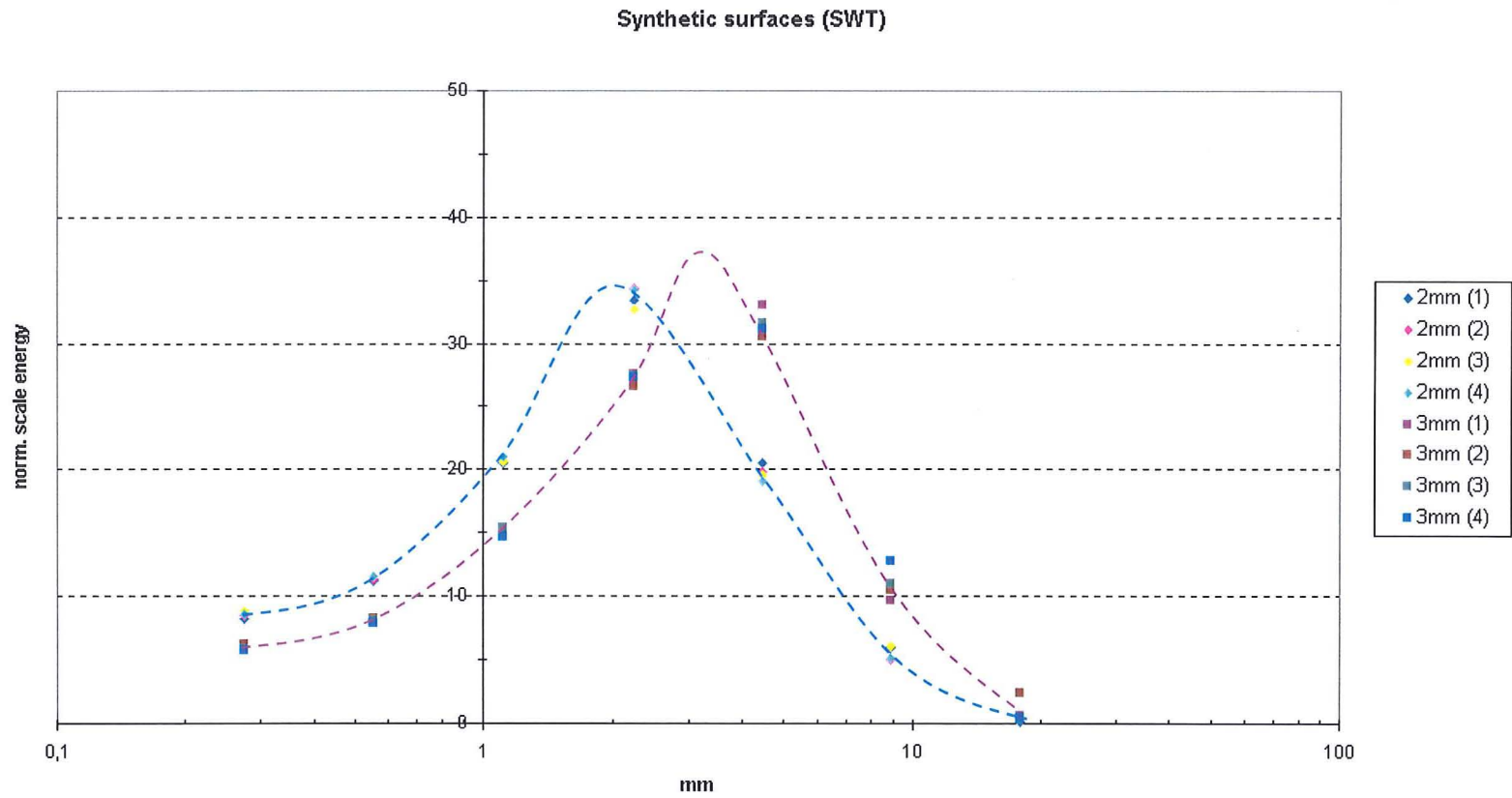
(b) Distribution of normalised scale energy. Blue line: 2mm surfaces, and purple line: 3mm surfaces.

**Figure 4.25(continued)** Results from synthetic surface analysis, DWT.



(a) Form size distribution.

**Figure 4.26** Results from synthetic surface analysis, SWT.



(b) Distribution of normalised scale energy. Blue line: 2mm surfaces, and purple line: 3mm surfaces.

**Figure 4.26(continued)** Results from synthetic surface analysis, SWT.

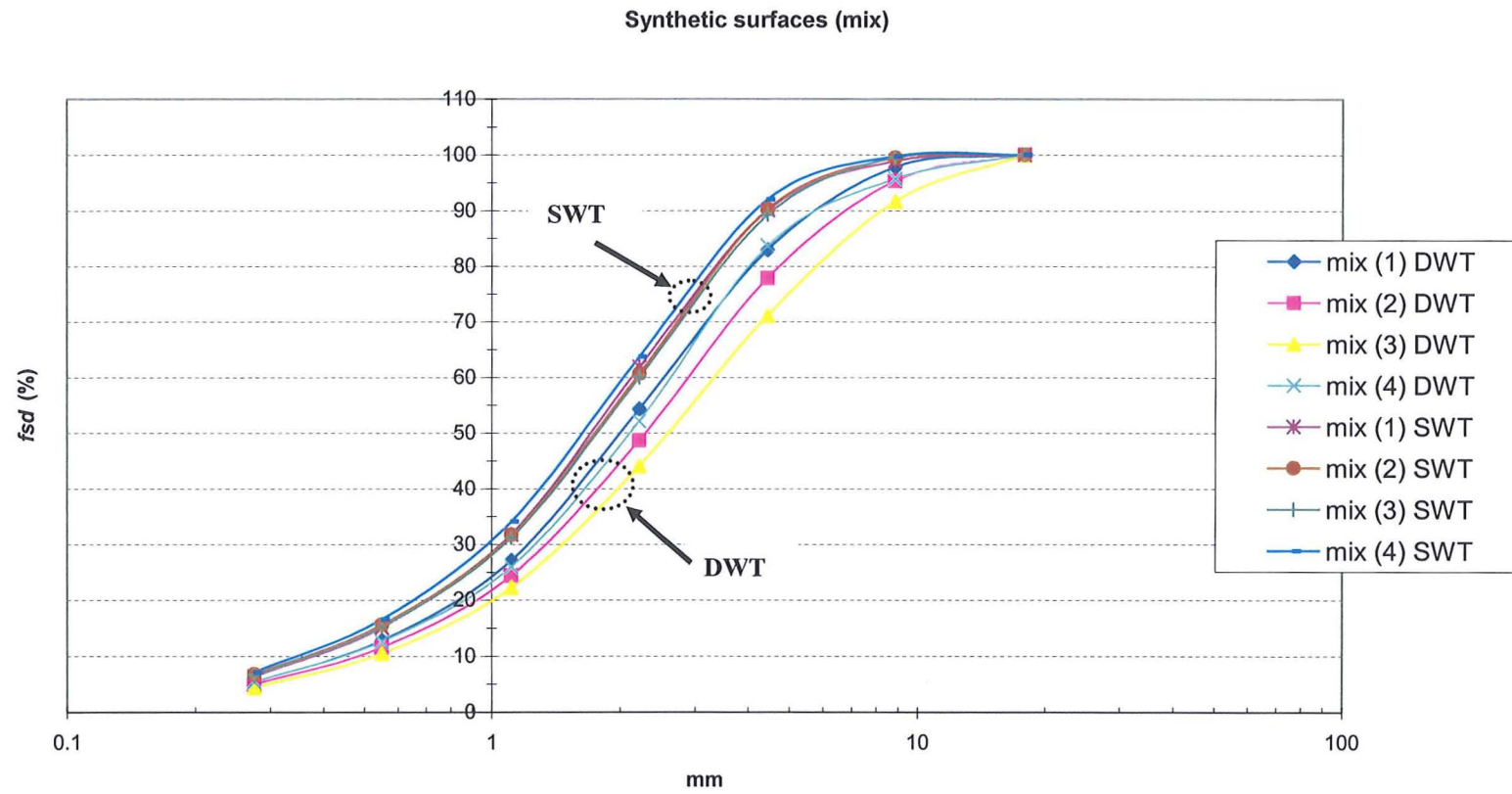


**Figure 4.27** Form size distribution of synthetic surfaces, mixture of 2mm and 3mm grains.

## **Chapter 5**

### **Local feature recognition:**

#### **Algorithm development and experimental results**

- 5.1 Introduction**
- 5.2 Computer generated synthetic sediment surfaces**
- 5.3 Analysis of the computer generated test surfaces with added features**
  - 5.3.1 Thresholding**
  - 5.3.2 Energy**
  - 5.3.3 Entropy**
  - 5.3.4 Entropy of the surfaces**
  - 3.3.5 Separation of entropy**
- 5.4 Analysis of feature edge effects**
  - 5.4.1 Test surface data**
  - 5.4.2 The analysis**
  - 5.4.3 Analysis of test surface I**
  - 5.4.4 Analysis of test surface II**
- 5.5 Discussion of results**
- 5.6 Analysis of experimental river-bed sediment surfaces - thresholding**
  - 5.6.1 Data analysis**
- 5.7 Discussion and chapter summary**

# **CHAPTER 5**

## **LOCAL FEATURE RECOGNITION: ALGORITHM DEVELOPMENT AND EXPERIMENTAL RESULTS**

### **5.1. Introduction**

It is known that distinct grain formations may appear during the armouring process of river-beds (Barndroff-Nielsen, 1989; Tait and Willetts, 1991; Church et al, 1998). Thresholds can be applied to the wavelet coefficients prior to using them in the reconstruction to detect and extract larger coefficients corresponding to significant features within data (Pettit et al, 2000; Teng and Qi, 2003; Murtagh and Starck, 2003; Ferreira and Borges, 2003). It was therefore proposed to use a wavelet-based thresholding method to identify predominant formations of grains (or features) in sediment surfaces which could prove useful in locating and following the spatio-temporal behaviour of such features. The aim of this study was to evaluate wavelet thresholding methods to extract coherent structures within the surfaces. These coherent structures were categorised as (1) dominant grains and (2) large scale surface formations.

In the study, computer generated sediment surfaces with superimposed coherent structures were analysed using a wavelet thresholding method. The aim was to identify an 'ideal' threshold value which provide an optimal extraction of coherent structures within the surfaces. Amplitude thresholding was employed for the task, where



small-amplitude wavelet coefficients are removed regardless of their position. In addition, both hard and soft thresholding methods were considered. The thresholding technique applied for feature extraction in the synthetic surfaces was intended to be used in the analysis of river-bed sediment surface data. Features elucidated by the thresholding process in this way could be used to indicate where sediment has gathered on the surface in distinct formations.

This chapter is divided into the following sub-sections: section 5.2 introduces the computer generated synthetic sediment surfaces used in the main study; section 5.3 presents the results from the wavelet thresholding of these surface; section 5.4 describes the development of edge effects in the reconstruction due to the thresholding process using two simple synthetic test surfaces, and section 5.5 provides a discussion of the results in section 5.3 and 5.4. Section 5.6 presents the results from applying the thresholding method to experimental river-bed sediment surface data. Finally a summary of the results is given in section 5.7.

## **5.2. Computer generated synthetic sediment surfaces**

Prediction of turbulent flow and granular material behaviour has proven to be a difficult problem (McEwan et al, 1999a). There are still many uncertainties concerning the basic mechanics that determine the transport of sediment in open channels. Current research seeks to understand the processes controlling these variables. Models and simulations of sedimentation processes using computers have proven to be helpful tools and are gaining an increasing interest from the scientific community. Investigations of sediment processes using computer models have been developed by a number of research groups including Kondolf (1994), Rivenæs (1997), McEwan et al (1999a) and Bitzer and Salas (2002).

A number of computer generated surfaces containing a variety of added bed-form features were supplied to the author by Dr John Heald at the University of Aberdeen. These were simulated sediment grain surfaces generated using a discrete particle model, called the *Aberdeen Discrete Particle Model* (AbdnDPM). This model uses spheres to represent the individual grains within a sediment mixture. Synthetic surfaces are formed from the aggregation of particles dropped onto a horizontal reference plane. Each

particle is dropped from a random position above the plane, from where it then falls under gravity and undergoes a series of collisions before coming to rest in a stable position. Once the grain has stopped moving it is fixed in place and the next grain is dropped. This process is repeated a number of times until the synthetic bed is created. An in-depth description of the AbdnDPM is to be found in Heald (2001). Modelling of particle entrainment using this computer simulation has been applied by McEwan et al (1999), Nikora et al (2001b) and McEwan et al (2004), who used it to reproduce the mechanisms of sediment grain movement over simulated bed surfaces.

The synthetic background bed-surfaces constructed using the AbdaDPM were composed of three different grain sizes, these were:

*Background surface:* Underlying bed of 2mm grains.  
Underlying bed of 3mm grains.  
Underlying bed of uniform mixture of 2-3mm grains.

Four different surface structures were generated for each of the grain size mixtures. Thus, a total of 12 different background test surfaces with superimposed structures were constructed. Figures 5.1 (a)-(c) shows examples of three background surfaces containing the three different grain mixtures.

Synthetic clusters of particles were then superimposed on top of the background surfaces. These specially arranged grain clusters were placed onto an already settled bed surface. They were moved into and held in position in a regular pattern. The clusters (or features) were of the shape of a line, a circle, a diamond and a square. Three different cluster sizes (small, standard and expanded) were used in the study, these were:

*Line:* Standard: 2mm grains in a line of length 8mm.  
Small: 1.5mm grains in a line of length 8mm.  
Expanded: 2mm grains in a line of length 12mm.

*Circle:* Standard: 2mm grains in a circle of radius 5mm.  
Small: 1.5mm grains in a circle of radius 5mm.  
Expanded: 2mm grains in a circle of radius 7mm

<i>Diamond:</i>	Standard:	2mm grains in a diamond of 6 by 6mm.
	Small:	1.5mm grains in a diamond of 6 by 6mm.
	Expanded:	2mm grains in a diamond of 12 by 12mm.
<i>Square:</i>	Standard:	2mm grains in a square of width 8mm.
	Small:	1.5mm grains in a square of width 8mm.
	Expanded:	2mm grains in a square of width 12mm.

Four examples of synthetic test surfaces with the added feature shapes are shown in figure 5.2. Figure 5.3 illustrates the different feature clusters generated for the circular shape features.

### **5.3. Analysis of the computer generated test surfaces with added features**

This section describes the results from the analysis of the synthetically constructed sediment surfaces applying amplitude thresholding methods. The purpose was to investigate whether an ideal threshold value could be found which when applied to the test surfaces resulted in an optimal extraction of the superimposed features.

#### **5.3.1. Thresholding**

As shown in the previous chapter, although computationally more intensive, the SWT provides higher resolution, especially at larger scales, and ensures translation invariance in the decomposition. Therefore the analysis presented in this chapter is restricted to the SWT. This study aims to extract coherent structures i.e. changes in the surface topographies. The Haar wavelet is well localised in space and therefore well suited to detect discontinuities (i.e. sharp changes) in data. Thus, the Haar wavelet was therefore applied as the analysing wavelet in subsequent analysis of this chapter.

Initial analysis was undertaken using one of the synthetic surfaces together with the addition of the standard diamond feature as shown in figure 5.5. This surface had a underlying surface mixture of grain-size 2mm and 3mm and a standard size diamond

feature shape. In order to extract the diamond shape from the surface both hard and soft thresholding were applied using the Haar wavelet. A range of threshold values were employed ranging from  $0.1\sigma$  to  $10\sigma$ , where  $\sigma$  is the standard deviation of the wavelet coefficients at each scale. Thus, this is an amplitude threshold where a scale related threshold value is applied to each individual scale of the transform. This threshold method will, from here on, be referred to as amplitude thresholding by the author.

Performing the 2-D inverse wavelet transform and adding selected details together allowed features and patterns in the surface to be detected. Figure 5.5 shows the reconstruction for each individual detail from scale 1 to 4 for the coefficients thresholded at  $1.5\sigma$ , where  $\sigma$  is the standard deviation of the coefficients at each scale. Figure 5.6 shows the combined reconstructions for details 1 to 4 for both soft and hard thresholding at various threshold values. The reconstructions for thresholds set to  $1\times\sigma$ ,  $2\times\sigma$  and  $3\times\sigma$  are plotted in figures 5.6(a) to (c) respectively for soft thresholding and figures 5.6(d) to (f) respectively for hard thresholding. Performing the 2-D inverse wavelet transform and adding selected details together in this way allows features and patterns in the surface to be made more visible. Thus enhancement allows for manual detection. However, a means was sought to provide a quantitative method to determine the optimum thresholding to enhance the feature relative to its background.

### 5.3.2. Energy

To evaluate the performance of the thresholding process quantitatively, the amount of energy left in the feature region and the background surface region were determined separately. To extract the respective energy contents two masks were constructed. One mask where the feature region was set to 1 and background region was set to 0, (figure 5.7(a)) and a second mask where the feature region was set to 0 and background region was set to 1, (figure 5.7(b)). The masks were used to separate the feature from the underlying surface to compare their respective energy contents. Thus, the amount of energy remaining in each part after thresholding and reconstruction could be determined. The algorithm to determine the energy content of the reconstructed surface can be found in appendix A (program *file\_energy.m*).

Tables 5.1 and 5.2 show the proportion of energies left in the regions where the added feature lies and the background surface region after thresholding for each of the thresholds employed. For example from table 5.1 it can be seen that for the soft threshold of  $1 \times \sigma$ , 18.7% of the original energy remains in the feature region whereas only 5.3% of the original background surface energy remains. As the threshold value increases, the energies in both the feature and background regions reduce, but the background energy reduces much more rapidly. Comparing tables 5.1 and 5.2 it can be seen that the hard threshold follows a similar pattern of the relative decrease of energies in the background and foreground, although it retains more energy at each stage than the soft thresholding. However, with either threshold method there is a trade off between the enhancement of the feature (compared with the background) and the accuracy of reconstruction due to reduction in coefficient values obtained at the higher thresholds.

To evaluate the relative energy differences between different shapes of features the above analysis was extended to several synthetic sediment surfaces consisting of background surface of grain size 2mm with different superimposed features (line, circle, diamond and square). A range of threshold values in terms of standard deviation were applied to the surfaces and the energy remaining after thresholding determined. Only wavelet details 1 to 4 were used for the thresholding and reconstruction procedures. This range of details was chosen because the maximum grain size in the surface (2mm) corresponds approximately to wavelet detail 4 in the transform. It is assumed that most information concerning the dominant grains within the surface is therefore contained within this range of details. The results from this analysis are presented in tables 5.3-5.6 for the soft threshold method and tables 5.7-5.10 for the hard threshold method.

Comparing the remaining energies throughout the thresholding process, a proportional decrease in energy in both the feature and the background parts can be observed. A distinct difference is shown in the respective proportions of the remaining energy for the feature and the background parts throughout the thresholding process. For the first threshold value ( $0.5 \times \sigma$ ), using the soft thresholding method, the mean remaining energy (over all data-sets) in the features is  $66.6\% \pm 1.6\%$  whilst only  $37\% \pm 0.6\%$  for the background energy remains. For the same threshold value applying a hard threshold the mean energy decreases to  $94.7\% \pm 2.4\%$  for the features and  $78.0\% \pm 6.7\%$  for the backgrounds. The same comparison at  $5 \times \sigma$  showed that the mean energy had reduced in

the feature part to  $3.3\% \pm 1\%$  and in the background part to  $0.7\% \pm 0.1\%$  for the soft threshold. At the same threshold value using the hard threshold the remaining energy in the feature part were  $26.7\% \pm 4.9\%$  and in the background to  $6.5\% \pm 0.8\%$  of the initial energy.

From this investigation it can be seen that the energy in the background surface reduces much faster than the energy in the feature part. This is because the feature part consists of proportionally larger coefficients compared to the background surface coefficients. The coefficients in the feature part will therefore remain longer in the reconstruction. Also noticeable from the tabulated results is the increase in the hard thresholded energies as compared to the soft thresholding energies. This is to be expected as the retained coefficients in the soft thresholding method are reduced by the value of the threshold, hence reduced in energy, whereas the retained coefficients in the hard thresholding method are left unaltered.

However, based on these results no conclusion on what would be an 'ideal' threshold value to apply could be established. Therefore a further investigation was carried out which applied an entropy measure in an attempt to evaluate the optimal threshold with which to measure the ability of the reconstruction to highlight pertinent features. This is described in the following sections.

### **5.3.3. Entropy**

In many applications we want to extract the 'relevant' information from a signal using as few coefficients as possible. A common way to measure this property is by using the Shannon entropy measure. Entropy has been applied in a number of different scientific areas as a method to measure information, for example: turbulence analysis (Toh, 1995), classifying system complexity (Pincus, 1990), signal restoration (Starck et al, 1998), as a project control tool (Bushuyev and Sochnev, 1999) and medical data analysis (Pincus and Goldberger, 1994; Richman and Moorman, 2000).

The Shannon entropy measure for a 1-D data set is defined as:

$$S(p) = -\sum_{i=1}^N p_i \log(p_i) \quad (5.1)$$

where  $N$  is the total number of discrete coefficients making up the signal and  $p_i$  is the probability of occurrence of the measured variable. In this study the energy of the coefficients is the target variable, i.e.:

$$p_i = \frac{x_i^2}{\sum_{i=1}^N x_i^2} \quad (5.2)$$

For a 2-D data set, with grid values defined at locations  $i,j$ , the entropy is defined as:

$$S(p) = -\sum_{i=1}^N \sum_{j=1}^N p_{i,j} \log(p_{i,j}) \quad (5.3)$$

In this study the  $p_{i,j}$  values are the squared and normalised wavelet coefficients and hence

$$\sum_{i=1}^N \sum_{j=1}^N p_{i,j} = 1 \quad (5.4)$$

where  $p_{i,j}$  is defined as:

$$p_{i,j} = \frac{x_{i,j}^2}{\sum_{i=1}^N \sum_{j=1}^N x_{i,j}^2} \quad (5.5)$$

where  $x_{i,j}$  are the wavelet transform coefficient values. In addition, for the Shannon entropy measure the definition is made:  $p_{i,j} = 0 \Rightarrow p_{i,j} \log p_{i,j} = 0$ . It is easily seen from the above that the maximum entropy value occurs when the data has an even distribution of information, i.e. when all the wavelet coefficients have the same value. Consequently the lowest value of entropy occurs when all the information is concentrated in a single discrete coefficient.

In the following section the information retained in the synthetic surfaces after each threshold level was quantified using the Shannon entropy measure.

#### 5.3.4. Entropy of the surfaces

The entropy of the thresholded and reconstructed surfaces was determined according to equation 5.5 for all features studied. The algorithm for computing the entropy is contained in appendix A: program *file\_entrl.m*. The results from this analysis are presented in figure 5.8 (hard threshold) and figure 5.9 (soft threshold). From the figures one can see that the initial entropy (at a threshold equal to zero) is at its maximum for all the surfaces, i.e. the surfaces values are widely distributed. The entropy then decreases as increasing levels of the thresholds are applied. This is expected as more and more coefficients are set to zero on the surface through the thresholding process. It is interesting, however, that a distinct change in slope of the entropy curves can be identified: from an initial slope to a less steep slope. This occurs for both the soft and the hard threshold curves. A transition point between the two slopes can be identified. These are indicated by the arrows in the plots and are located between  $2.5 \times \sigma$  and  $3.0 \times \sigma$  for the hard threshold and between  $2.0 \times \sigma$  and  $2.5 \times \sigma$  for the soft threshold. The question is, what does this change in slope mean in physical terms?

After analysis of the surfaces it was found that the slope change indicates a point where almost all of the information located within the background surface had been removed by the thresholding process. This can be seen by observing the reconstructed surfaces in figure 5.10 (hard threshold) and figure 5.11 (soft threshold) with thresholds ranging from  $0 \times \sigma$  to  $20.0 \times \sigma$ . In the reconstructed surfaces the background surface is being removed through the thresholding process. Only the feature part remains in the reconstructed surface from threshold value  $3.0 \times \sigma$  for the hard threshold and from  $2.5 \times \sigma$  for the soft threshold. It is therefore clear through this visual inspection that all information is located only within the feature region at subsequently higher threshold levels. It was therefore decided to conduct a further study to calculate the entropy for the feature area and the background surface area independently.

#### 5.3.5. Separation of entropy

In this study the entropy measure was applied to establish the distribution of information on the surface during the thresholding process. Therefore, following each threshold and reconstruction of the surface, the contribution to total entropy for the



regions containing the original feature and the original background surface were determined separately. The total entropy was also determined.

To measure the relative contribution to the entropy, the entropy measure was split into background and feature parts as shown schematically in figure 5.12, where  $N_1$  is the number of coefficients making up the feature and  $N_2$  is the number of coefficients forming the background. This can be written as:

$$S(p) = -\sum_{i=1}^{N_1} p_i \log(p_i) - \sum_{i=1}^{N_2} p_i \log(p_i) \quad (5.6)$$

where

$$p_i = \frac{x_i^2}{\sum_{i=1}^{N_1+N_2} x_i^2} \quad (5.7)$$

The study was conducted using surfaces with superimposed line features (small, standard and expanded) alone. These features were superimposed on top of three different background surface structures: of 2mm grains, 3mm grains and a mixture between 2mm and 3mm grains. The entropies for the feature area and the background area were computed separately. The algorithm to compute the separate entropies is contained in appendix A program *file\_entr2.m*. The area corresponding to the feature and the background were partitioned as shown in figure 5.13. To be able to compare the analysis the same size of feature area was used for all three features; small, standard and expanded. The entropy was examined for threshold values in terms of standard deviation in the range of  $0 \times \sigma$  to  $20 \times \sigma$ . As the soft thresholding method provided the most distinct difference in slope this method was applied to the analysis. The results from the analysis are presented in figures 5.14 to 5.16.

When evaluating the results presented in figures 5.14-5.16, it was shown that the total entropy, as well as the background surface entropy contribution, decreases as the threshold values increase. In contrast, an initial increase in entropy for the feature area is observed, i.e. the information content of this area actually increases. Since information is removed from the feature through the thresholding process an increase in entropy is

not expected. This initial increase is observed for all three background surface structures, hence it is independent of the background surface structure. The increase in the feature entropy was therefore thought to be related to the edge effects appearing in the reconstruction of the surface due to thresholds technique.

Further, it can be seen that after initial increase of the feature entropy, the rate of increase decreases slightly after threshold values of approximately  $4 \times \sigma$ , after which point the curves become erratic. It is suggested that this erratic behaviour is due to the reduction of information in the entire reconstructed surface. It can be seen from equation 5.7 that the separated coefficient energies are divided by the total amount of components in the whole surface. Studying the reconstructed surfaces in figures 5.10 and 5.11 it can be seen that most of the surface components have, in fact, been removed at a threshold value of approximately  $10 \times \sigma$ . Thus, as components are removed from the surface the entropy curve values are dominated by a decreasingly smaller denominator whose value is dictated by the few (arbitrary) remaining coefficients. Hence, the erratic nature of the curve at large threshold values.

A further in-depth study of the entropy increase in the feature area through the thresholding process was therefore carried out as described below.

#### **5.4. Analysis of feature edge effects**

To evaluate the possible influence of the edge effects in the entropy contribution of the background and the feature region simple test surfaces were constructed and analysed using the two-dimensional stationary wavelet transform. The results from the analysis of two test surfaces are presented in this section.

##### **5.4.1. Test surface data**

The synthetic test surfaces were constructed by combining a background surface with a square block feature superimposed at its centre. The analysis was undertaken using the two different test surfaces shown in figure 5.17(a) and (b). Both surfaces contain  $64 \times 64$  ( $=2^6$ ) data points. In the surface shown in figure 5.17(a) the background surface values were set to 0 and in the surface shown in figure 5.17(b) the background surface values

were generated using a uniform probability distribution in the interval (0,0.1). For both surfaces the superimposed feature was  $7 \times 7$  grid-points in dimension and had a height of 0.4. The mean was taken off the background surface in figure 5.17(c), prior to the feature being added.

#### **5.4.2. The analysis**

The test surfaces were analysed using the Haar-based two-dimensional stationary wavelet transform (2-D SWT). The author investigated the amount of information retained within the surface after thresholding and reconstruction. For this purpose the entropy measure described in section 5.3.5 was applied. The  $64 \times 64$  surface array was transformed into 6 levels of details containing the wavelet transform coefficients, where scale 1 contains the smallest-amplitude coefficients and scale 6 contains the largest-amplitude coefficients. As before, an amplitude threshold was applied and each level was thresholded using a separate threshold value which was a function of the standard deviation ( $\sigma$ ) of that level. Following each threshold and each reconstruction of the surface the entropy for the regions containing the original feature and the original background surface were determined (equation 5.6). In addition, the total entropy was also determined.

Threshold values were set at multiples of the standard deviation ( $\sigma$ ) of the coefficients at each level of the transform. These multiples were set in the range of 0 to 14.0, increasing in steps of 0.5. The author applied both hard and soft thresholding methods in the analysis. The inverse 2-D SWT transformed the thresholded data back into a new thresholded reconstructed form. In addition, when reconstructing, the last approximation at level 6 was also thresholded, reconstructed and added to the new surface. This was done to preserve the mean of the background surface equal to zero. It was realised during the early experimentation that if the approximation was not added the height difference between zero and the reconstructed background surface would be regarded as additional information when applying the entropy measure algorithm. This is shown in figure 5.18 where a surface, with the background set to equal zero, has been decomposed and reconstructed (no threshold was applied). Figure 5.18(a) shows the reconstructed surface where the last approximation was not added and figure 5.18(b) the reconstructed surface where the last approximation has been added to the

reconstruction. The difference (size of the mean  $-0.0048$ ) between zero and the reconstructed background surface in figure 5.18(a) is clearly illustrated in the close up view in figure 5.19. The entropy measure assumes this height difference is a uniform distribution of information, hence a high entropy value is obtained even though in reality nothing has been added to this part of the surface. This is shown in the results of the entropy measure in figure 5.20 where hard thresholds have been applied to the surface in figure 5.18(a). The computed entropy has a value approaching 2 for the background at threshold factor  $0 \times \sigma$  although it should be equal to zero. Hence, to establish reliable results of the entropy measure the last approximation has to be included in the reconstruction.

### 5.4.3. Analysis of test surface I

This section presents the results from the analysis of the test surface with a flat background (i.e. background surface values set to zero) shown in figure 5.17(a). The analysis was carried out initially applying the hard thresholding method at increasing threshold values as described above. The entropy of the surface was calculated at each threshold level and the results are presented in table 5.11. In addition, the entropy is plotted against the threshold standard deviation factors in figure 5.21.

The entropy for the background surface is zero at the first threshold value ( $0 \times \sigma$ ). Because the original surface had the background uniformly set equal to zero there is no information in the background surface, consequently the measured entropy is zero. However, there is a high entropy value in the feature, which equals the total entropy for the reconstructed surface. Hence, the whole contribution to the total entropy is located within the feature region.

For threshold value  $0.5 \times \sigma$  the entropy curve has a value of 0.75 for the background surface area. Since there was no information here originally, it was concluded that this increase in the entropy within the background area of the surface must be related to an edge effect from the feature occurring due to the thresholding process. This is confirmed when observing the surface and profile plots of the reconstructed surface shown in figure 5.22, for thresholds ranging from  $0 \times \sigma$  (original surface) to  $12.5 \times \sigma$ , where the increase in edge effects can be clearly seen from the plots of threshold values between

$0.5 \times \sigma$  to  $12.0 \times \sigma$ . This edge effect is due to the removal of wavelet coefficients through the thresholding process and occurs in both the region of the background surface and the region of the feature. When coefficients are removed or reduced, local information regarding the surface structure is 'missing' from the transform. The multiresolution property of perfect reconstruction can therefore no longer be achieved, hence edge effects will appear in the reconstruction. The increase in entropy in the background is simply due to edge effects occurring in this region of the reconstruction. However, at a threshold level of  $0.5 \times \sigma$  there is still more information kept within the feature with a higher entropy value compared to the background entropy.

However, when the threshold value increases to  $1.0 \times \sigma$ , the entropy values change accordingly and the entropy for the background surface is higher compared to the feature part. This can also be seen in figure 5.22(c) where edge effect spreads further into the background surface region. The higher entropy for the background surface implies that this part contains a relatively larger spread of components compared with the feature part. The subsequent entropy values from thresholding factors show a slow decrease within the background surface. The entropy values for the feature, at the same threshold factor range, remains close to a straight line until  $12.5 \times \sigma$ . At which point all the information within the surface has been removed through the thresholding process.

The results of the analysis using soft thresholding are presented in figure 5.23 and table 5.12. The same test surface data-set (figure 5.17(a)) was used and similar results to those obtained from the hard thresholding method were found. The entropy curve is smoother given that the soft threshold smooths the data through the reduction of the remaining coefficient by the size of the threshold. It is interesting to note that at threshold value  $0.5 \times \sigma$  the entropy for the background is already higher than the entropy for the feature. This may be due to the reduction of coefficient heights carried out in the soft thresholding technique. The information in the background surface increases rapidly and then reduces gradually as the threshold values increase. While the entropy for the feature decreases slowly from a threshold value equal to  $0.5 \times \sigma$ . At a threshold of  $12.5 \times \sigma$  all information has been removed from the surface. This examination of the relative distribution of entropy for the test feature with a plane background surface has therefore allowed the observation of the edge effects which contaminate the

thresholding process. In the next section the analysis is repeated for the same feature superimposed on a random background surface.

#### **5.4.4. Analysis of test surface II**

The same analysis as that described in the previous section was carried out using a second surface consisting of the same foreground block sitting on a background surface generated from a uniform random distribution (figure 5.17(b)). Prior to applying the middle block feature the mean was removed from the data. The background surface therefore varied in the interval  $(-0.05, 0.05)$  with a mean equal to 0. The middle feature was again set to equal 0.4 in height. As before, the surface was analysed using the Haar-based 2-D SWT method and both hard and soft amplitude thresholding was used.

For the hard threshold, the entropy calculations now exhibit a different pattern compared to the previous surface (which had a uniform background set to zero). The entropy curves for the feature, background surface and the total entropy for the reconstructed surface are shown in figure 5.24 and the results are also tabulated in table 5.13. For the first threshold value,  $0 \times \sigma$ , the background surface contains a higher entropy value and a lower entropy value for the feature part. Since the background has evenly distributed randomness throughout the surface, i.e. all the coefficients have unit values, higher entropy would be expected in this part. The feature part shows a lower entropy value as the contribution from the feature is contained within fewer coefficients.

When a threshold value  $0.5 \times \sigma$  is applied to the surface, the entropy for the background decreases and the entropy for the feature increases. The reduction of entropy in the background indicates that information is removed through the thresholding process. This is also visible in figure 5.25 where the reconstructed surfaces for the first 4 thresholded values (between  $0 \times \sigma - 1.5 \times \sigma$ ) are shown. The figure reveals how the background surface is removed through the thresholding process as the threshold value increases. It can be seen from figure 5.24 that the total entropy changes from a less steep (negative) slope to a steeper slope at  $0.5 \times \sigma$  and again to a less steep slope at a threshold value of  $1.5 \times \sigma$ . Changes of slope at these specific threshold values can also be seen in the entropy of the background and the feature regions. The background entropy follows the behaviour of the total entropy curve and decreases with increasing threshold values,

while the entropy curve of the feature region increases rapidly until a threshold value of  $1.5 \times \sigma$ . In fact it can be seen that, at the threshold value of  $1.5 \times \sigma$ , the complete background surface has been removed and the entropy contribution from the background region is mainly due to the edge effects.

The soft thresholding method produces similar results as the hard thresholding method. The results of the entropy measure of the soft thresholding are presented in figure 5.26 and table 5.14. The first change in slope of the entropies occurs at  $0.5 \times \sigma$ , this is particularly evident in the total and the background entropies. The total entropy and the entropy for the background region then decreases as the entropy in the feature region increases until  $1.5 \times \sigma$ . At this point the background surface has been removed by the thresholding process, hence after reconstruction only the remaining feature and the edge effect occurring in the background region are left. This is shown in figure 5.27 where the reconstruction at threshold value  $1.5 \times \sigma$ , (d), only consists of the feature part and edge effects.

## 5.5. Discussion of results

The occurrence of edge effects is evident in the results of the analysis of the test surface containing the plane background region shown in figure 5.17(a). In the plot of the entropy curves in figures 5.21 (hard threshold) and 5.23 (soft threshold) it can be observed that the entropy contains components in the background surface area as the threshold value increases. Since there was no information in the background surface to begin with, this increase in the entropy contribution must be associated with the edge effects appearing through the thresholding process. This enhancement of the edge effects due to thresholding is visible in the surface and profile plots of figure 5.22. The occurrence of edge effects results in an increase of the measured entropy in the background surface region and consequently an increase in the total entropy.

The appearance of edge effect is also found when visually inspecting the results from the analysis of the test surface with a random background surface form, as shown in figure 5.17(b). For this surface the edge effects are clearly seen in the reconstruction of the surface for both the hard threshold shown in figure 5.25 and the soft threshold shown in figure 5.27. In fact almost the whole background surface region has been removed at a threshold of  $1.5 \times \sigma$  and therefore the entropy of the background area (see

figures 5.24 and 5.26) must primarily be related to the edge effects occurring in this region. Comparing the entropies, a decrease in the total and the background region entropies with increasing threshold values can be observed. While the entropy in the feature region increases. It is also noticed that there are distinct changes in the slope of the curves through the thresholding process. The slope changes from an initial slope to a steeper slope and then back to a less steep slope. Visually inspecting the surface plots in figures 5.25 and 5.27, it can be seen the second change of the slope is at a point where most of the background surface has been removed by the thresholding process, hence only the feature region and corresponding edge effects remain in the reconstruction.

As information is removed from the test surface the entropy in the background region will decrease. However, an increase of entropy for the feature region can be observed. It is believed that this is related to the overall decrease of information in the whole surface. As shown in equation 5.7 the separated entropies are relative to the information of the complete surface. The feature region consists of larger wavelet coefficients compared with the background surface coefficients. Thus, the background coefficients will be removed by the thresholding before the coefficients in the feature. Therefore as the overall information is reduced, the entropy in the feature region relative to the information in the complete surface will increase. In addition, the increase reaches a maximum at the same threshold value as the total entropy curve changes slope to a less steep slope. It was previously noted above, through visual inspection, that this was at a point where the complete background surface has been removed. Hence remaining information is located in the feature region and the occurring edge effects. It can therefore be concluded that the increase in feature entropy for the synthetic sediment surfaces (figures 5.14(c) to 5.16(c)) are due to the overall reduction of surface components through the thresholding process and the occurring edge effects in this region.

The change of the slope of the total entropy was previously found in the analysis of the simulated sediment surfaces, figures 5.8 to 5.9, where the distinct change of the slope occurred at a threshold value between  $2.5 \times \sigma$  and  $3.0 \times \sigma$  for the hard threshold and between  $2.0 \times \sigma$  and  $2.5 \times \sigma$  for the soft threshold. Inspecting the results of the analysis of the sediment surfaces with added line features, the change in the slope of the background surface entropies (figures 5.14(b) to 5.16(b)) as well as the total entropy



(figures 5.14(a) to 5.16(a)) can be seen. Based on the results from the simple test surface analysis in section 5.4, it can therefore be concluded that the change in the slope of entropies in fact occur at a threshold value where the synthetic background surface region has been removed completely by the thresholding process.

Further, in the results from the simple test surfaces (figures 5.24 and 5.26) an initial change in the slope of the entropy curve can be observed at a threshold value of  $0.5 \times \sigma$ . This change in slope at a threshold value of  $0.5 \times \sigma$  can also be seen in the entropy curves in figures 5.8 and 5.9 (synthetic sediment surfaces). This is particularly evident when using a hard threshold. This can also be seen when observing the results in figures 5.14 to 5.16, which correspond to the sediment surfaces with added line features. It can therefore be concluded that the major components of the information contributing to the background surface are removed between threshold values of  $0 \times \sigma$  to  $1.5 \times \sigma$ . This is shown when applying threshold values in steps of  $0.1 \times \sigma$  to the test surfaces in 5.17(b). The results of the entropy measure are shown in figure 5.28(a) for the hard threshold and figure 5.28(b) for the soft threshold. For the hard threshold the total entropy changes to a steeper slope at threshold value of  $0.7 \times \sigma$  and again to a less steep slope at  $1.5 \times \sigma$ . Similar results are found for the soft threshold, however the change in slope is less obvious.

It was concluded earlier, that the second transition point for slope change at the entropy curve is at a threshold value where the complete background surface has been removed. It is therefore suggested that the first transition point between the slopes on the entropy curve represents the threshold value to apply to retain the larger background coefficients and remove smaller background coefficients. It is assumed that, after this transition point, the steeper slope of the entropy curve indicates that a larger quantity of information is removed from the background surface at each incremental increase in threshold value. Thus, this is the threshold value to apply to filter out less significant background forms and hence extract dominant grains in the background surface.

The following points can be concluded from this section:

The entropy curve of the thresholded and reconstructed surfaces changes slope at different threshold values. This is due to the removal of information from the surface through the thresholding process combined with the occurrence of edge effects in the reconstruction.

Separation of the entropy measure into the feature and background regions indicated an increase of entropy in the feature region with increasing threshold values. It was concluded that the increase in feature entropy was related to the overall reduction of information in the thresholded surface combined with the occurrence of edge effects in this region.

Further, by visually inspecting the entropy curve slope two transition points could be identified. It was concluded that the first transition point was largely related to the removal of a significant amount of information in the background surface region. It was therefore hypothesised that this point identifies the threshold value to apply to filter out less significant information and therefore enhance larger features (i.e. dominant grains) in the surface. It was shown that the second transition point occurs where the complete background surface has been removed by the thresholding process. Hence, the entropy in the background after the second transient point is solely due to the edge effects in this region.

Comparing the soft and hard thresholding methods it can be seen that the hard thresholding method provides a more marked change in the slope of each entropy curve at the two transition points. This would be expected as the soft threshold method smooths the data. It is therefore recommended to use *hard thresholding* method, where the retained coefficients remain untouched in the reconstruction, thus causing a further enhancement of larger coherent structures.

## **5.6. Analysis of experimental river-bed sediment surfaces - thresholding**

As highlighted earlier in chapter 2, section 2.11.3, distinct grain formations may appear during the armouring process of river beds (Barndroff-Nielsen, 1989; Tait and Willetts 1991; Church et al, 1998). This section describes work undertaken by the author to

apply the wavelet thresholding technique to the experimental river-bed sediment surfaces to extract dominant grains and reveal large formations of grains within the surfaces for manual detection. The analysis described in this section follows on from the work on the synthetic surface analysis described in sections 5.3 and 5.4.

### **5.6.1. Data analysis**

In the previous section (5.5) it was concluded that the total entropy for the thresholded and reconstructed synthetic surfaces changed slope as increasing threshold values were applied. A distinct difference in the slope was found at a threshold value between  $2.5 \times \sigma$  and  $3.0 \times \sigma$ . However, when this threshold value is applied to the experimental river-bed sediment surfaces too much of the surface structure is removed and no coherent structures can be seen. This can be observed in figure 5.29, where the reconstructed surfaces (data-set '2644h55m') using threshold values of  $2.5 \times \sigma$  and  $3.0 \times \sigma$  are shown. This confirms the results from the synthetic data analysis where the complete background surface was removed (figures 5.10 and 5.11) at thresholds beyond these values.

Therefore the analysis of the experimental sediment surfaces will concentrate on the initial change in slope of the entropy curve. It was hypothesised in the previous section that this change in the slope was related to the reduction of smaller coefficients in the background surface. It is therefore suggested that the best threshold value to apply for enhancement of dominant grains within the surfaces can be found by identifying an initial transition point in the slope of the entropy curve.

Amplitude wavelet thresholding was applied to threshold and reconstruct one of the experimental river-bed sediment surfaces (data-set '2644h55m'), shown in figure 5.30(a). The levels to threshold and reconstruct were chosen as the wavelet details which could be primarily associated with the grain size of the original sediment mixture. Thus details 1 to 5 were included in the thresholding and reconstruction, where detail 5 (i.e. size 16mm) is approximately the size of the maximum particle size. The entropy for the thresholded and reconstructed surface was plotted against the standard deviation multiple values shown in figure 5.30(b). By visually inspecting the entropy a change in the slope of the curve can be identified (from an initial slope to a steeper

slope). The curve was inspected manually and the range of values contributing to each slope were selected. The best-fit lines over the selected values representative of each slope were determined using the 'least squares' method. The slope transition point was chosen as the cross section of the two best fit lines. For this particular surface a threshold value of approximately  $0.75 \times \sigma$  is found, marked with an arrow in figure 5.30(b). Thus, this threshold value was applied to remove smaller coefficients from the surface and enhance larger structures. The thresholded and reconstructed surface is shown in figures 5.30(c) and 5.30(d). When observing the reconstructed surface it can be seen that the thresholding process has enhanced possible coherent structures. In figure 5.31(a) these coherent structures have been marked with dotted lines. These are generated from the local agglomeration of particles on the surface. The original surface is shown in figure 5.31(b) for comparison.

This method is applied to two further experimental data-sets: '2631h00m' and '2648h15m', the surface scans directly before and after the data-set shown in figure 5.31. The results from the analysis of these two sediment surfaces are shown in figures 5.32 (data-set '2631h00m') and 5.33 (data-set '2648h15m'). Comparing the reconstructed surfaces, data-set '2644h55m' appears to have more visible coherent structures than the earlier surface scan, '2631h00m'. Further, surface '2648h15m' show more visible coherent structures compared with data-set '2644h55m'. This may indicate that the surface grains have been rearranged to become more stable over time, hence the more visible structures in the later surface scan.

To extract the general form of the surface a scale dependent threshold (described in section 2.9.2) was also applied to the data-sets. This method was previously used to separate a sediment surface into different topographies (section 4.3.1). Using this method, smaller scale details associated with the grain size could be excluded from the reconstruction and the overall general form of the sediment surface extracted. Initially the reconstruction was performed using detail 6 alone (32mm) as shown in figure 5.34(a), (c) and (e). This detail was chosen as it was the immediate detail larger than the maximum grain size. Some possible ridges (marked with arrows) could be seen, however, the general structure is not obvious using this detail alone. Therefore details 6 to 8 were reconstructed, which was previously thought to hold the medium forms of the surface. Figure 5.34(b), (d) and (f) show this reconstruction. Here the change of the

general surface structure over time can be observed. In figure 5.34(d) a larger amount of sediment has gathered on the surface, marked with an arrow. This structure is not visible in the following data-set, figure 5.34(f). This method in combination with the amplitude thresholding could be used to manually detect changes in the sediment surface structure over time.

The surface was also reconstructed combining the amplitude thresholded and the scale thresholded surfaces shown in figure 5.35(a) and (b). However, observing the reconstructed surface shown in figure 5.35(c) it can be seen that dominant grains become less obvious when combining the two thresholding methods. It is therefore suggested that the most distinct formations and general structure can be detected visually by using the two thresholding methods separately.

The above described analysis was also applied to three of the data-sets in experiment 7, i.e. where no sediment material was added in the flume through the experiment. The selected surfaces were; the initial surface (data-set '0700h00c'), the surface scan 40hours into the experiment (data-set '0740h00m') and the final surface scan after 80hours running (data-set '0780h00m'). Figure 5.36 show the result of the amplitude thresholding of the surface data. Observing the results, more features can be seen in the two later surface scans in figure 5.36(b) and (c) comparing with the earlier surface scan in figure 5.36(a). The thresholding method has isolated larger grains and potential coherent structures of dominant grains in the surfaces. Comparing (b) and (c) it can be seen that some larger grains have stayed relatively stable (marked with arrows in the plot) while smaller material has been restructured in the surface. Figure 5.37 show the results from wavelet scale thresholding using details 6 to 8 for the reconstruction. Again the later surface scans, i.e. figure 5.37(b) and (c), appear to have larger structural variations within the surface in comparison to the initial surface, figure 5.37(a), which has a relatively flat surface structure. This would be expected as the surface has not yet been exposed to water. These results show that the surface changes from a flat to a rougher topography through the course of the experimental run. It appears that there are smaller topographical differences between the surfaces in figure 5.37(b) and (c). This would suggest that, for these experiments, the major degradation of the sediment surface bed appear in the early stages of the sedimentation process. However, what appears to be movement of sediment material has been marked with arrows in the

figure. Observing the reconstructions in figure 5.36(b) and (c), it appears that smaller sediment material has been moved towards the left at the top of the figures, i.e. in the direction of the flow.

## 5.7. Discussion and chapter summary

This chapter has dealt with *identification of local surface features*. Research has shown that by thresholding the wavelet transform coefficients large predominant coefficients can be extracted from the transform (Tikkanen, 1999; Pettit et al, 2000, 2002; Addison et al, 2001a; Teng and Qi, 2003). An attempt has been made to identify an ideal threshold value which to apply to extract dominant grains within a surface. To extract these larger features an amplitude threshold was applied using both hard and soft wavelet thresholding techniques. The threshold values were established as multiples of the standard deviation for each level of the wavelet transform.

The main analysis was conducted using computer generated synthetic sediment surfaces with superimposed features. To evaluate the thresholding performance the thresholded energy content within the feature and the background parts of the reconstructed synthetic sediment surfaces were determined separately. Observing the energy content (table 5.3 to table 5.10) it was found that there is a much faster reduction in energy content for the background surface region compared to the reduction in energy for the feature region. In addition, there is a slower reduction in the hard thresholded energies compared to the soft thresholded energies with increasing threshold values. However, an 'ideal' threshold value could not be established through the comparison of the energy contents.

Therefore the Shannon entropy measure was applied to calculate the amount of information kept in the reconstructed surface after each threshold. The entropy was plotted against threshold value (figure 5.8 and 5.9) it was noticed that a marked change of slope occurred in the entropy curves and a transition point between the two slopes could be identified. This was located between  $2 \times \sigma$  and  $2.5 \times \sigma$  for the soft threshold and between  $2.5 \times \sigma$  and  $3.0 \times \sigma$  for the hard threshold. It became apparent that the transition point could identify the threshold value at which the background surface had been removed completely by the thresholding process.

To compare the entropy in different areas of the surface, the entropy was divided into a background and a feature region. Comparing the separated entropy components it was found that the entropy in the background decreases during the thresholding process. However, the entropy for the feature increases initially. Since information is removed through the thresholding process an increase in the feature is not expected. It was hypothesised that the increase in feature entropy was related to edge effect occurring in the reconstruction through the thresholding process.

An in-depth investigation of the occurrence of edge effects due to the thresholding process confirmed this. The analysis of two simple test surfaces revealed the presence of edge effects in the reconstruction. This study also determined that as the information in the whole surface decreases the relative amount of information in the feature region increases compared to the background region. This and the occurrence of edge effects in the feature region produces an increase in entropy.

Further, the analysis showed that the total entropy changed slope at a point where the background surface has been removed by the thresholding process. Hence, the threshold value at the transient point would be the threshold value which to apply to extract the feature and remove the background. However, in this study it was sought to find a threshold value which did not remove the surface completely but only the smaller coefficients while retaining the more significant dominant grains.

Studying the entropies of the test surface it became apparent that an initial change in the slope of entropy curves occurred between threshold values  $0 \times \sigma$  and  $1.0 \times \sigma$ . This initial change in slope can also be observed in the results from the synthetic sediment surface data analysis. It was assumed that this was related to reduction of smaller coefficients in the background surface. As increasingly larger threshold values are applied larger amount of information is removed at each threshold step and therefore the steeper slope. It was thought, because of the clear difference in the slope of the entropy curve, that this would be the 'ideal' threshold value to apply to remove the smaller coefficients and retain larger coefficients to enhance features in the surface. Hence, by identifying the transient point between the two slopes a threshold value, in terms of a multiple value of the standard deviation, could be found. Further, it was determined that the total entropy

for the thresholded and reconstructed surfaces could be used to find the 'ideal' threshold value.

Applying this analysis to the experimental river-bed sediment surfaces, it was found that dominant grains and potential larger coherent structures could be identified in the surfaces by applying wavelet thresholding techniques. By evaluating the thresholded and reconstructed surfaces over time it could be seen that the later surface scans (figure 5.33) contained more 'structures' compared to the earlier surface scans (figures 5.30 and 5.32). This may indicate that the surface topography is restructured to become more stable to the shear stresses of the flow. Further it was shown that the overall surface structure could be extracted by applying a scale dependent wavelet threshold. By evaluating the surface using these two thresholding methods this allowed for structural changes over time to be detected.

Sediment material was fed into the flume throughout the experiment. This had to be considered as it made it more difficult to identify coherent structures and detect movement of these structures within the surface over time. Particularly if the structural changes were due to sediment feeding or rearrangement of the sediment material.

Therefore, the analysis was also applied to three of the data-sets in the unfed experiment (number 7). The results of the amplitude thresholding indicated that the two later surface scans had more visible structures in comparison with the initial surface scan. Further, by applying a scale dependent threshold the two later surfaces appeared to have a more similar topographical structure compared to the initial surface. This would suggest that for these experiments the major degradation of the surface occurs in the early stages of the sedimentation process.

In summary, this chapter has presented an investigation into the use of (1) amplitude thresholding for extracting dominant grains and (2) scale dependent thresholding to extract the general form of the surface. Both synthetic and real sediment surface data was included in the study. The results have demonstrated the potential of the wavelet thresholding technique as a method for sediment surface analysis.



## **CHAPTER 5**

Tables

<b>Threshold Value in Terms of Coefficient Standard Deviation</b>	<b>Proportion of reconstructed energy for synthetic feature</b>	<b>Proportion of reconstructed energy for background surface</b>
0.0	1.000	1.000
0.1	0.862	0.766
0.2	0.739	0.580
0.3	0.631	0.436
0.4	0.537	0.325
0.5	0.455	0.241
1.0	0.187	0.053
1.5	0.070	0.012
2.0	0.025	0.003
2.5	0.009	0.001
3.0	0.003	0.000
3.5	0.001	0.000
5.0	0.000	0.000
5.2	0.000	0.000
6.0	0.000	0.000
10.0	0.000	0.000

**Table 5.1** Proportion of energies within the synthetic feature and background regions remaining after thresholding at various threshold values for *Soft Thresholding*.

<b>Threshold Value in Terms of Coefficient Standard Deviation</b>	<b>Proportion of reconstructed energy for synthetic feature</b>	<b>Proportion of reconstructed energy for background surface</b>
0.0	1.000	1.000
0.1	0.999	0.998
0.2	0.994	0.987
0.3	0.983	0.958
0.4	0.964	0.915
0.5	0.947	0.857
1.0	0.773	0.450
1.5	0.556	0.182
2.0	0.311	0.070
2.5	0.174	0.025
3.0	0.083	0.007
3.5	0.036	0.001
5.0	0.008	0.000
5.2	0.008	0.000
6.0	0.000	0.000
10.0	0.000	0.000

**Table 5.2** Proportion of energies within the synthetic feature and background regions remaining after thresholding at various threshold values for *Hard Thresholding*.

## Superimposed line features

Threshold Value*	Proportion of reconstructed energy					
	small		standard		expanded	
	<i>background</i>	<i>feature</i>	<i>background</i>	<i>feature</i>	<i>background</i>	<i>feature</i>
0.0	1.000	1.000	1.000	1.000	1.000	1.000
0.5	0.358	0.699	0.360	0.675	0.361	0.678
1.0	0.166	0.496	0.168	0.471	0.171	0.480
1.5	0.090	0.355	0.091	0.330	0.095	0.344
2.0	0.054	0.261	0.055	0.234	0.059	0.251
2.5	0.034	0.194	0.036	0.167	0.039	0.185
3.0	0.023	0.146	0.024	0.119	0.027	0.137
3.5	0.015	0.110	0.016	0.086	0.018	0.102
4.0	0.011	0.083	0.012	0.063	0.013	0.076
4.5	0.007	0.062	0.008	0.047	0.009	0.057
5.0	0.005	0.047	0.006	0.036	0.007	0.043
5.5	0.004	0.037	0.004	0.028	0.005	0.033
6.0	0.003	0.028	0.003	0.022	0.004	0.026
7.0	0.001	0.018	0.002	0.014	0.002	0.016
8.0	0.001	0.012	0.001	0.009	0.001	0.011
9.0	0.000	0.008	0.001	0.006	0.001	0.007
10.0	0.000	0.005	0.000	0.004	0.000	0.005
12.0	0.000	0.003	0.000	0.002	0.000	0.002
15.0	0.000	0.001	0.000	0.001	0.000	0.001
17.0	0.000	0.000	0.000	0.000	0.000	0.000
20.0	0.000	0.000	0.000	0.000	0.000	0.000

\*in terms of coefficient standard deviation

Underlying surface composed of 2mm grain and with superimposed line features.

**Table 5.3** Results from analysis of synthetic surfaces with line features applying soft threshold.

## Superimposed circle features

Threshold Value*	Proportion of reconstructed energy					
	small		standard		expanded	
	<i>background</i>	<i>feature</i>	<i>background</i>	<i>feature</i>	<i>background</i>	<i>feature</i>
0.0	1.000	1.000	1.000	1.000	1.000	1.000
0.5	0.366	0.654	0.369	0.646	0.375	0.653
1.0	0.180	0.434	0.181	0.433	0.194	0.443
1.5	0.104	0.289	0.103	0.291	0.117	0.304
2.0	0.065	0.195	0.065	0.197	0.076	0.213
2.5	0.043	0.133	0.042	0.134	0.050	0.150
3.0	0.025	0.061	0.028	0.092	0.034	0.106
3.5	0.019	0.063	0.019	0.063	0.023	0.075
4.0	0.013	0.043	0.013	0.044	0.016	0.053
4.5	0.009	0.030	0.009	0.031	0.011	0.038
5.0	0.006	0.022	0.006	0.022	0.008	0.028
5.5	0.005	0.016	0.005	0.016	0.005	0.021
6.0	0.003	0.012	0.003	0.012	0.004	0.016
7.0	0.002	0.007	0.002	0.007	0.002	0.009
8.0	0.001	0.004	0.001	0.004	0.001	0.006
9.0	0.001	0.002	0.001	0.002	0.001	0.004
10.0	0.000	0.001	0.000	0.001	0.000	0.002
12.0	0.000	0.000	0.000	0.000	0.000	0.001
15.0	0.000	0.000	0.000	0.000	0.000	0.000
17.0	0.000	0.000	0.000	0.000	0.000	0.000
20.0	0.000	0.000	0.000	0.000	0.000	0.000

\*in terms of coefficient standard deviation

Underlying surface composed of 2mm grain and with superimposed circle features.

**Table 5.4** Results from analysis of synthetic surfaces with circle features applying soft threshold.

## Superimposed diamond features

Threshold Value*	Proportion of reconstructed energy					
	small		standard		expanded	
	<i>background</i>	<i>feature</i>	<i>background</i>	<i>feature</i>	<i>background</i>	<i>feature</i>
0.0	1.000	1.000	1.000	1.000	1.000	1.000
0.5	0.362	0.681	0.363	0.675	0.374	0.659
1.0	0.175	0.472	0.173	0.481	0.190	0.447
1.5	0.099	0.328	0.097	0.350	0.114	0.304
2.0	0.062	0.230	0.060	0.258	0.074	0.209
2.5	0.040	0.162	0.039	0.192	0.050	0.144
3.0	0.027	0.115	0.026	0.143	0.034	0.100
3.5	0.018	0.082	0.018	0.106	0.024	0.070
4.0	0.013	0.059	0.012	0.078	0.016	0.049
4.5	0.013	0.059	0.009	0.058	0.012	0.034
5.0	0.006	0.030	0.006	0.043	0.008	0.025
5.5	0.004	0.022	0.004	0.033	0.006	0.018
6.0	0.003	0.016	0.009	0.058	0.004	0.013
7.0	0.002	0.009	0.002	0.015	0.003	0.008
8.0	0.001	0.006	0.001	0.006	0.002	0.005
9.0	0.001	0.003	0.001	0.006	0.001	0.003
10.0	0.000	0.002	0.000	0.004	0.001	0.002
12.0	0.000	0.001	0.000	0.001	0.000	0.001
15.0	0.000	0.000	0.000	0.000	0.000	0.000
17.0	0.000	0.000	0.000	0.000	0.000	0.000
20.0	0.000	0.000	0.000	0.000	0.000	0.000

\*in terms of coefficient standard deviation

Underlying surface composed of 2mm grain and with superimposed diamond features.

**Table 5.5** Results from analysis of synthetic surfaces with diamond features applying soft threshold.

## Superimposed square features

Threshold Value*	Proportion of reconstructed energy					
	small		standard		expanded	
	<i>background</i>	<i>feature</i>	<i>background</i>	<i>feature</i>	<i>background</i>	<i>feature</i>
0.0	1.000	1.000	1.000	1.000	1.000	1.000
0.5	0.364	0.655	0.367	0.652	0.373	0.659
1.0	0.178	0.433	0.180	0.445	0.191	0.453
1.5	0.102	0.288	0.103	0.304	0.115	0.315
2.0	0.064	0.196	0.065	0.208	0.074	0.222
2.5	0.042	0.135	0.043	0.144	0.049	0.158
3.0	0.028	0.093	0.029	0.100	0.032	0.113
3.5	0.019	0.064	0.020	0.070	0.022	0.081
4.0	0.013	0.045	0.014	0.050	0.015	0.058
4.5	0.009	0.031	0.009	0.035	0.010	0.042
5.0	0.006	0.022	0.007	0.049	0.007	0.031
5.5	0.004	0.016	0.005	0.019	0.005	0.023
6.0	0.002	0.007	0.003	0.014	0.004	0.017
7.0	0.001	0.004	0.002	0.008	0.002	0.010
8.0	0.001	0.004	0.001	0.005	0.001	0.006
9.0	0.001	0.002	0.001	0.003	0.001	0.004
10.0	0.000	0.001	0.000	0.001	0.000	0.002
12.0	0.000	0.000	0.000	0.000	0.000	0.001
15.0	0.000	0.000	0.000	0.000	0.000	0.000
17.0	0.000	0.000	0.000	0.000	0.000	0.000
20.0	0.000	0.000	0.000	0.000	0.000	0.000

\*in terms of coefficient standard deviation

Underlying surface composed of 2mm grain and with superimposed square features.

**Table 5.6** Results from analysis of synthetic surfaces with square features applying soft threshold.

## Superimposed line features

Threshold Value*	Proportion of reconstructed energy					
	small		standard		expanded	
	<i>background</i>	<i>feature</i>	<i>background</i>	<i>feature</i>	<i>background</i>	<i>feature</i>
0.0	1.000	1.000	1.000	1.000	1.000	1.000
0.5	0.800	0.966	0.801	0.949	0.800	0.944
1.0	0.565	0.913	0.567	0.903	0.565	0.888
1.5	0.379	0.825	0.382	0.818	0.381	0.803
2.0	0.261	0.724	0.264	0.736	0.268	0.711
2.5	0.188	0.636	0.191	0.655	0.198	0.631
3.0	0.142	0.565	0.144	0.564	0.152	0.558
3.5	0.110	0.504	0.111	0.485	0.121	0.501
4.0	0.086	0.454	0.087	0.408	0.096	0.439
4.5	0.068	0.399	0.070	0.336	0.078	0.377
5.0	0.054	0.340	0.055	0.278	0.063	0.326
5.5	0.042	0.291	0.043	0.225	0.049	0.273
6.0	0.033	0.239	0.034	0.181	0.039	0.222
7.0	0.020	0.162	0.022	0.118	0.024	0.142
8.0	0.012	0.109	0.014	0.089	0.016	0.101
9.0	0.008	0.080	0.010	0.064	0.011	0.075
10.0	0.005	0.063	0.007	0.054	0.007	0.063
12.0	0.004	0.050	0.005	0.042	0.005	0.048
15.0	0.001	0.018	0.001	0.015	0.001	0.015
17.0	0.000	0.012	0.001	0.009	0.001	0.010
20.0	0.000	0.006	0.000	0.004	0.000	0.003

\*in terms of coefficient standard deviation

Underlying surface composed of 2mm grain and with superimposed line features.

**Table 5.7** Results from analysis of synthetic surfaces with line features applying hard threshold.

## Superimposed circle features

Threshold Value*	Proportion of reconstructed energy					
	small		standard		expanded	
	<i>background</i>	<i>feature</i>	<i>background</i>	<i>feature</i>	<i>background</i>	<i>feature</i>
0.0	1.000	1.000	1.000	1.000	1.000	1.000
0.5	0.798	0.955	0.568	0.879	0.798	0.978
1.0	0.564	0.887	0.568	0.879	0.567	0.877
1.5	0.390	0.784	0.392	0.785	0.405	0.774
2.0	0.285	0.671	0.283	0.688	0.309	0.673
2.5	0.217	0.564	0.214	0.587	0.246	0.584
3.0	0.171	0.479	0.168	0.496	0.198	0.511
3.5	0.136	0.405	0.133	0.414	0.159	0.440
4.0	0.107	0.337	0.104	0.341	0.126	0.369
4.5	0.084	0.272	0.082	0.275	0.098	0.305
5.0	0.065	0.213	0.064	0.217	0.076	0.244
5.5	0.050	0.160	0.049	0.167	0.058	0.194
6.0	0.039	0.123	0.037	0.130	0.044	0.150
7.0	0.024	0.077	0.024	0.080	0.028	0.097
8.0	0.016	0.051	0.013	0.033	0.014	0.030
9.0	0.010	0.038	0.009	0.024	0.010	0.022
10.0	0.008	0.029	0.007	0.031	0.009	0.037
12.0	0.005	0.020	0.005	0.022	0.006	0.028
15.0	0.001	0.003	0.001	0.002	0.001	0.006
17.0	0.000	0.001	0.000	0.000	0.001	0.004
20.0	0.000	0.000	0.000	0.000	0.000	0.001

\*in terms of coefficient standard deviation

Underlying surface composed of 2mm grain and with superimposed circle features.

**Table 5.8** Results from analysis of synthetic surfaces with circle features applying hard threshold.



## Superimposed diamond features

Threshold Value*	Proportion of reconstructed energy					
	small		standard		expanded	
	<i>background</i>	<i>feature</i>	<i>background</i>	<i>feature</i>	<i>background</i>	<i>feature</i>
0.0	1.000	1.000	1.000	1.000	1.000	1.000
0.5	0.798	0.961	0.800	0.943	0.800	0.948
1.0	0.563	0.905	0.565	0.889	0.568	0.886
1.5	0.385	0.820	0.384	0.808	0.399	0.790
2.0	0.276	0.723	0.272	0.730	0.298	0.683
2.5	0.208	0.623	0.201	0.657	0.234	0.589
3.0	0.162	0.534	0.155	0.597	0.190	0.504
3.5	0.128	0.463	0.122	0.534	0.155	0.431
4.0	0.101	0.399	0.096	0.476	0.124	0.362
4.5	0.080	0.336	0.075	0.409	0.099	0.294
5.0	0.062	0.281	0.058	0.348	0.079	0.234
5.5	0.049	0.226	0.045	0.288	0.060	0.180
6.0	0.038	0.173	0.035	0.233	0.047	0.140
7.0	0.024	0.108	0.022	0.149	0.030	0.085
8.0	0.015	0.070	0.015	0.106	0.020	0.058
9.0	0.010	0.052	0.010	0.079	0.013	0.041
10.0	0.007	0.038	0.007	0.063	0.010	0.031
12.0	0.005	0.028	0.005	0.045	0.002	0.006
15.0	0.001	0.004	0.001	0.011	0.002	0.006
17.0	0.000	0.002	0.001	0.004	0.001	0.002
20.0	0.000	0.000	0.000	0.002	0.000	0.001

\*in terms of coefficient standard deviation

Underlying surface composed of 2mm grain and with superimposed diamond features.

**Table 5.9** Results from analysis of synthetic surfaces with diamond features applying hard threshold.

## Superimposed square features

Threshold Value*	Proportion of reconstructed energy					
	small		standard		expanded	
	<i>background</i>	<i>feature</i>	<i>background</i>	<i>feature</i>	<i>background</i>	<i>feature</i>
0.0	1.000	1.000	1.000	1.000	1.000	1.000
0.5	0.798	0.957	0.800	0.943	0.797	0.944
1.0	0.563	0.893	0.566	0.891	0.565	0.878
1.5	0.389	0.776	0.391	0.815	0.401	0.783
2.0	0.284	0.659	0.282	0.723	0.305	0.686
2.5	0.216	0.562	0.215	0.619	0.240	0.598
3.0	0.169	0.477	0.169	0.522	0.194	0.522
3.5	0.134	0.410	0.135	0.432	0.155	0.451
4.0	0.106	0.344	0.107	0.358	0.124	0.386
4.5	0.083	0.275	0.062	0.228	0.096	0.323
5.0	0.064	0.216	0.066	0.239	0.074	0.261
5.5	0.049	0.170	0.052	0.189	0.056	0.210
6.0	0.038	0.130	0.040	0.146	0.042	0.167
7.0	0.023	0.075	0.025	0.091	0.027	0.107
8.0	0.014	0.053	0.016	0.060	0.017	0.070
9.0	0.009	0.039	0.010	0.044	0.012	0.052
10.0	0.007	0.029	0.007	0.032	0.009	0.039
12.0	0.005	0.019	0.005	0.023	0.006	0.030
15.0	0.001	0.004	0.001	0.005	0.001	0.008
17.0	0.000	0.002	0.000	0.002	0.000	0.003
20.0	0.000	0.000	0.000	0.000	0.000	0.001

\*in terms of coefficient standard deviation

Underlying surface composed of 2mm grain and with superimposed square features.

**Table 5.10** Results from analysis of synthetic surfaces with square features applying hard threshold.

Threshold (*std)	<i>std</i> (total)	Check	Entropy (total)	Entropy (feature)	Entropy (background)
0.0	0.479	1.0	1.69	1.69	0.00
0.5	0.48	1.0	2.16	1.41	0.75
1.0	0.48	1.0	2.61	0.96	1.65
1.5	0.48	1.0	2.33	0.99	1.34
2.0	0.48	1.0	2.29	0.99	1.31
2.5	0.48	1.0	2.23	0.97	1.26
3.0	0.48	1.0	2.18	0.96	1.22
3.5	0.48	1.0	2.09	0.95	1.14
4.0	0.48	1.0	2.02	0.94	1.08
4.5	0.48	1.0	1.97	0.95	1.03
5.0	0.48	1.0	1.94	0.93	1.01
5.5	0.48	1.0	1.84	0.89	0.95
6.0	0.48	1.0	1.77	0.86	0.90
6.5	0.48	1.0	1.70	0.84	0.86
7.0	0.48	1.0	1.70	0.84	0.86
7.5	0.48	1.0	1.70	0.84	0.86
8.0	0.48	1.0	1.60	0.80	0.80
8.5	0.48	1.0	1.60	0.80	0.80
9.0	0.48	1.0	1.60	0.80	0.80
9.5	0.48	1.0	1.60	0.80	0.80
10.0	0.48	1.0	1.60	0.80	0.80
10.5	0.48	1.0	1.60	0.80	0.80
11.0	0.48	1.0	1.38	0.69	0.69
11.5	0.48	1.0	1.38	0.69	0.69
12.0	0.48	1.0	1.38	0.69	0.69
12.5	0.48	NaN	NaN	NaN	NaN
13.0	0.48	NaN	NaN	NaN	NaN

**Table 5.11** Applying a hard threshold to the surface where the background equals 0 in height.

Threshold (*std)	<i>std</i> (total)	Check	Entropy (total)	Entropy (feature)	Entropy (background)
0.0	0.48	1.0	1.69	1.69	0.00
0.5	0.48	1.0	2.55	1.08	1.47
1.0	0.48	1.0	2.49	0.98	1.51
1.5	0.48	1.0	2.28	0.99	1.29
2.0	0.48	1.0	2.23	0.98	1.25
2.5	0.48	1.0	2.15	0.96	1.19
3.0	0.48	1.0	2.07	0.96	1.11
3.5	0.48	1.0	1.98	0.94	1.04
4.0	0.48	1.0	1.94	0.93	1.01
4.5	0.48	1.0	1.90	0.91	0.99
5.0	0.48	1.0	1.83	0.89	0.95
5.5	0.48	1.0	1.75	0.85	0.90
6.0	0.48	1.0	1.72	0.84	0.88
6.5	0.48	1.0	1.68	0.83	0.85
7.0	0.48	1.0	1.66	0.82	0.84
7.5	0.48	1.0	1.62	0.81	0.81
8.0	0.48	1.0	1.60	0.80	0.80
8.5	0.48	1.0	1.59	0.80	0.80
9.0	0.48	1.0	1.59	0.79	0.79
9.5	0.48	1.0	1.57	0.79	0.79
10.0	0.48	1.0	1.54	0.77	0.77
10.5	0.48	1.0	1.43	0.71	0.71
11.0	0.48	1.0	1.38	0.69	0.69
11.5	0.48	1.0	1.38	0.69	0.69
12.0	0.48	1.0	1.38	0.69	0.69
12.5	0.48	NaN	NaN	NaN	NaN
13.0	0.48	NaN	NaN	NaN	NaN

**Table 5.12** Applying a soft threshold to the surface where the background equals 0 in height.

Threshold (*std)	std (total)	Check	Entropy (total)	Entropy (feature)	Entropy (background)
0.0	0.48	1.0	3.42	0.40	3.02
0.5	0.48	1.0	3.37	0.45	2.91
1.0	0.48	1.0	2.87	0.73	2.14
1.5	0.48	1.0	2.42	0.93	1.49
2.0	0.48	1.0	2.30	0.97	1.33
2.5	0.48	1.0	2.25	0.94	1.31
3.0	0.48	1.0	2.19	0.92	1.27
3.5	0.48	1.0	2.06	0.93	1.14
4.0	0.48	1.0	1.97	0.94	1.03
4.5	0.48	1.0	1.92	0.91	1.01
5.0	0.48	1.0	1.86	0.86	1.00
5.5	0.48	1.0	1.75	0.92	0.83
6.0	0.48	1.0	1.72	0.85	0.87
6.5	0.48	1.0	1.63	0.74	0.89
7.0	0.48	1.0	1.45	0.58	0.87
7.5	0.48	1.0	1.20	0.60	0.60
8.0	0.48	1.0	1.20	0.60	0.60
8.5	0.48	1.0	1.15	0.57	0.57
9.0	0.48	1.0	0.30	0.15	0.15
9.5	0.48	NaN	NaN	NaN	NaN

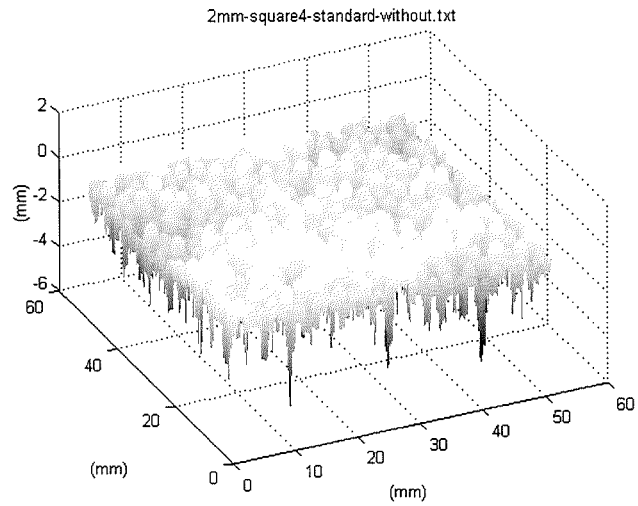
**Table 5.13** Applying a hard threshold to the surface where the background is generated from uniform distribution.

Threshold (*std)	<i>std</i> (total)	Check	Entropy (total)	Entropy (feature)	Entropy (background)
0.0	0.48	1.0	3.42	0.40	3.02
0.5	0.48	1.0	3.18	0.65	2.54
1.0	0.48	1.0	2.61	0.91	1.70
1.5	0.48	1.0	2.30	0.97	1.33
2.0	0.48	1.0	2.24	0.96	1.28
2.5	0.48	1.0	2.17	0.94	1.23
3.0	0.48	1.0	2.09	0.92	1.17
3.5	0.48	1.0	1.99	0.91	1.08
4.0	0.48	1.0	1.92	0.89	1.03
4.5	0.48	1.0	1.85	0.86	0.99
5.0	0.48	1.0	1.78	0.84	0.95
5.5	0.48	1.0	1.71	0.80	0.90
6.0	0.48	1.0	1.64	0.75	0.88
6.5	0.48	1.0	1.47	0.64	0.83
7.0	0.48	1.0	1.32	0.60	0.72
7.5	0.48	1.0	1.20	0.58	0.62
8.0	0.48	1.0	1.19	0.56	0.63
8.5	0.48	1.0	1.11	0.45	0.66
9.0	0.48	NaN	NaN	NaN	NaN
9.5	0.48	NaN	NaN	NaN	NaN

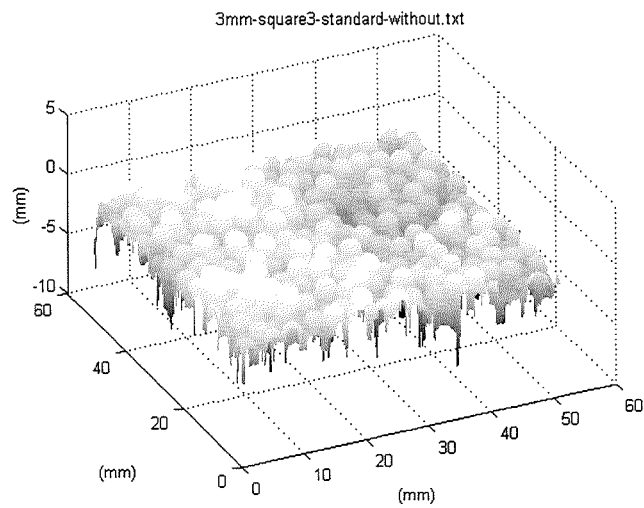
**Table 5.14** Applying a soft threshold to the surface where the background is generated from uniform distribution.

## CHAPTER 5

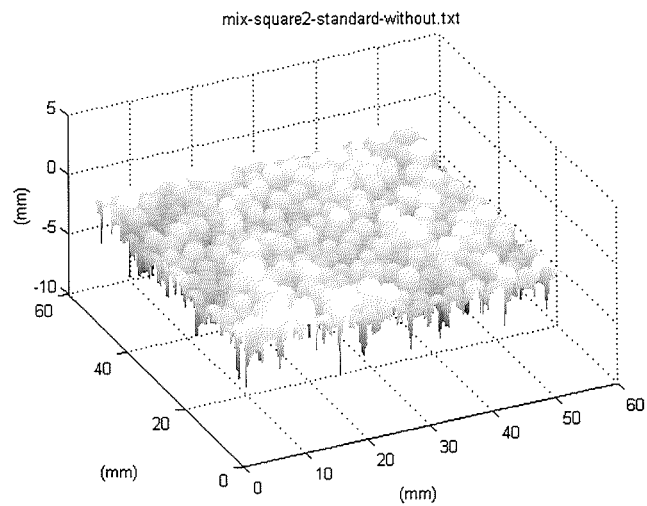
Figures



(a) 2mm surface grains.



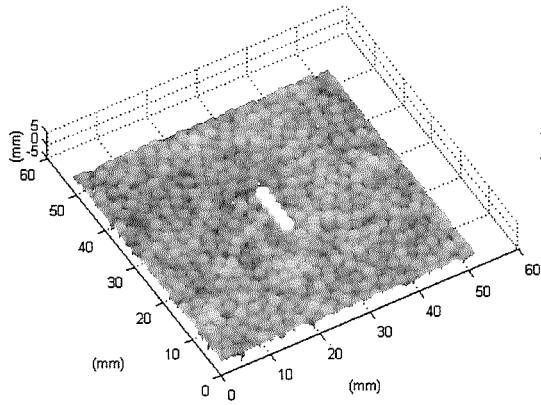
(b) 3mm surface grains.



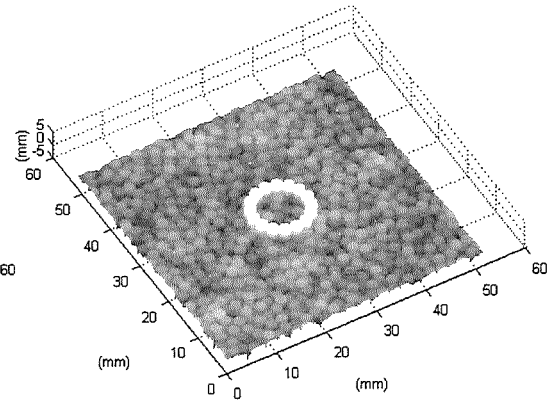
(c) Mix between 2mm and 3mm surface grains.

**Figure 5.1** Examples of synthetic background surfaces.

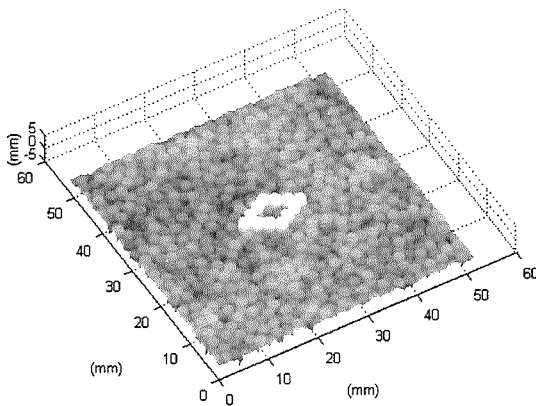




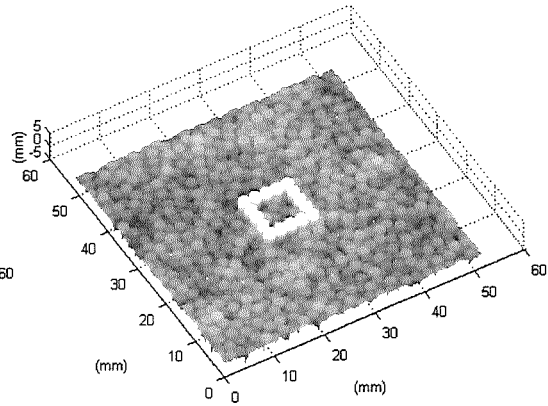
(a) Line, standard size.



(b) Circle, standard size.

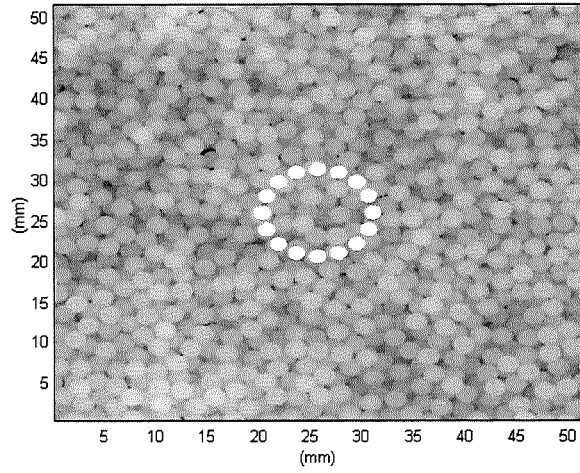


(d) Diamond, standard size.

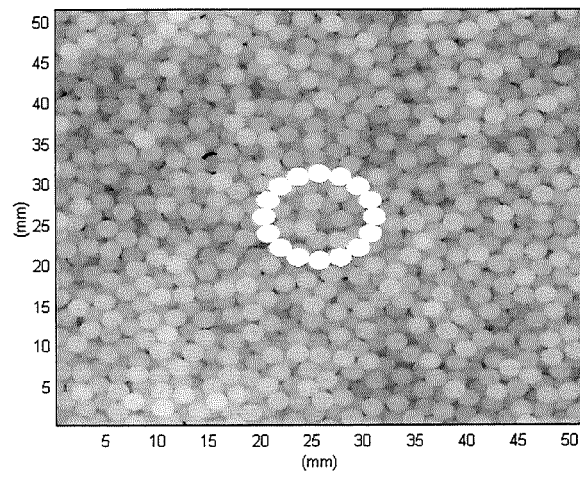


(e) Square, standard size.

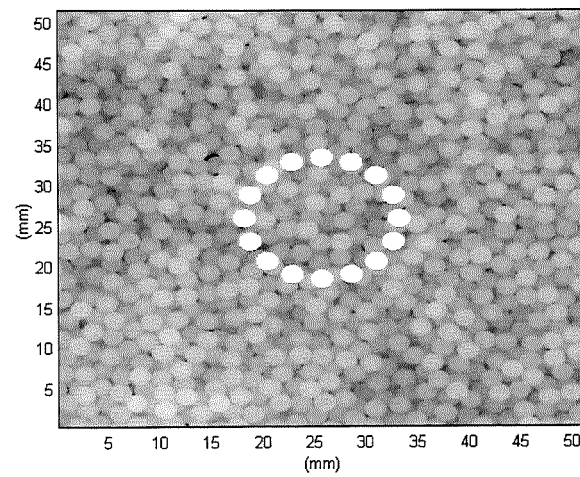
**Figure 5.2** Examples of the four different features shapes.



(a) Small size.



(b) Standard size.



(c) Expanded size.

Circular feature shape.

**Figure 5.3** Example of different features sizes.

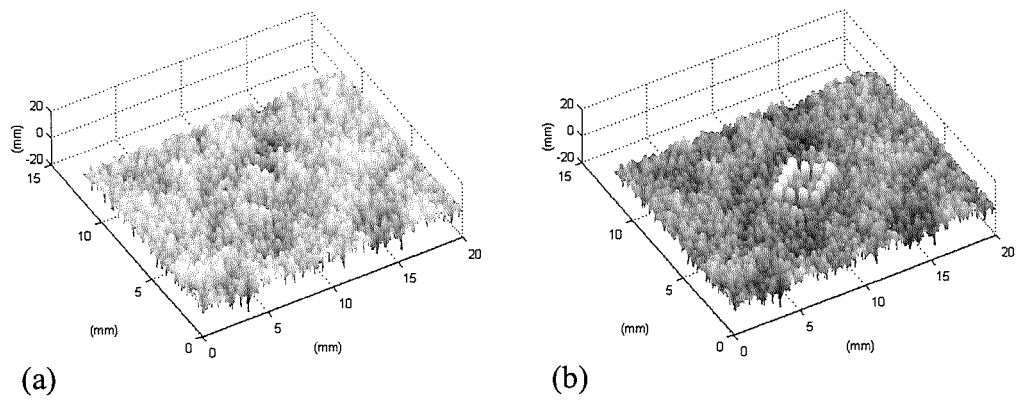


**Figure 5.4** (a) Original surface and (b) surface with synthetic diamond feature added.

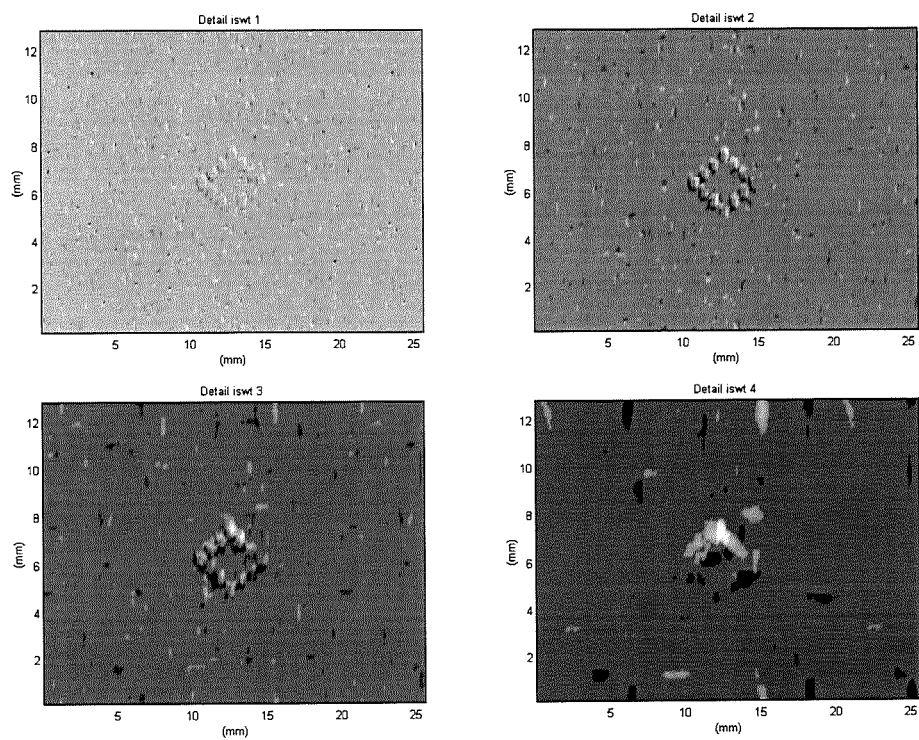
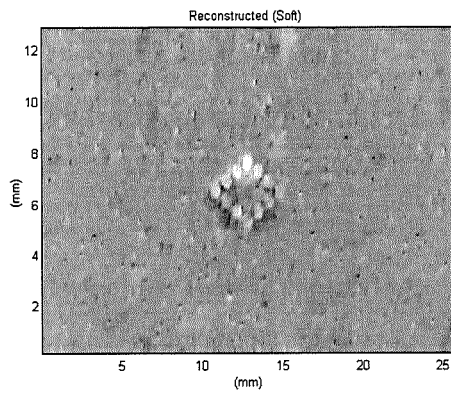
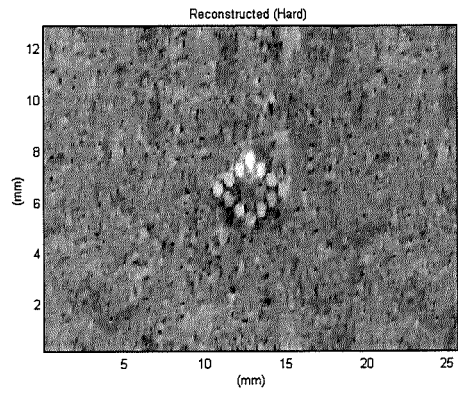


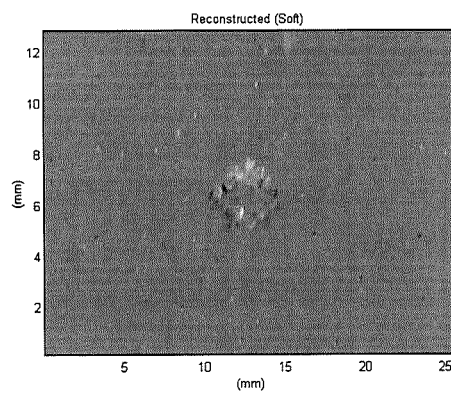
**Figure 5.5** Reconstruction of details hard thresholded at  $1.5\sigma$  at scales 1 to 4.



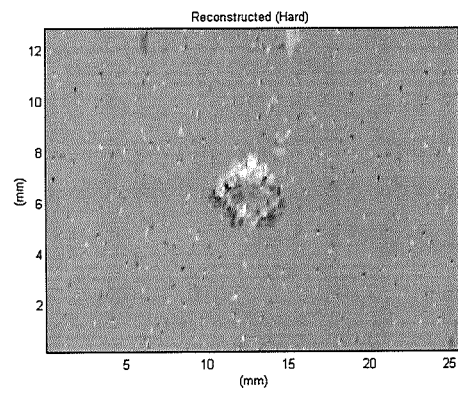
(a) Soft threshold =  $1\sigma$ .



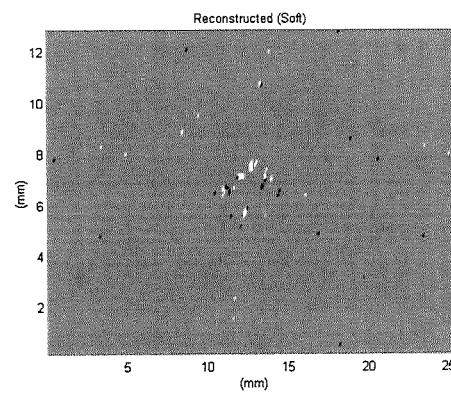
(d) Hard threshold =  $1\sigma$ .



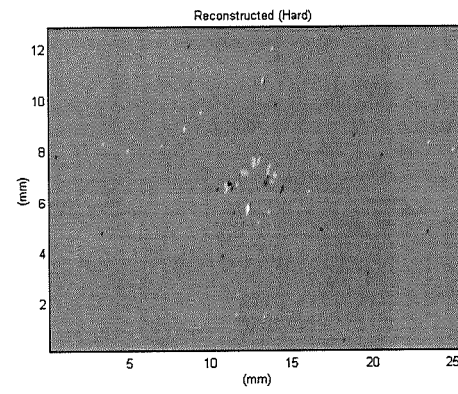
(b) Soft threshold =  $2\sigma$ .



(e) Hard threshold =  $2\sigma$ .

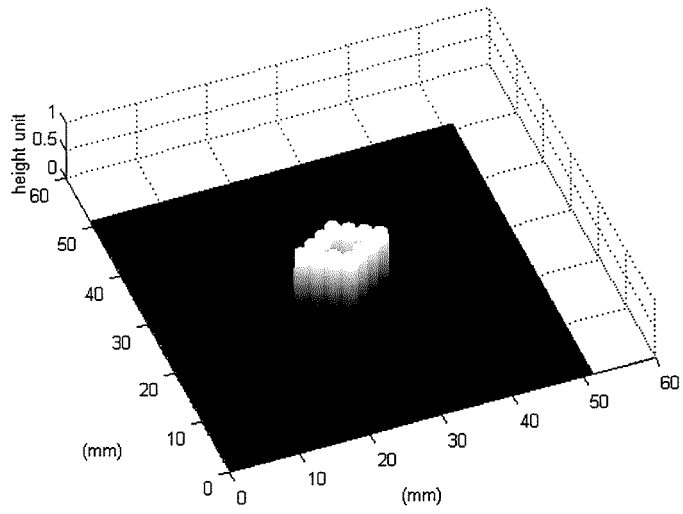


(c) Soft threshold =  $3\sigma$ .

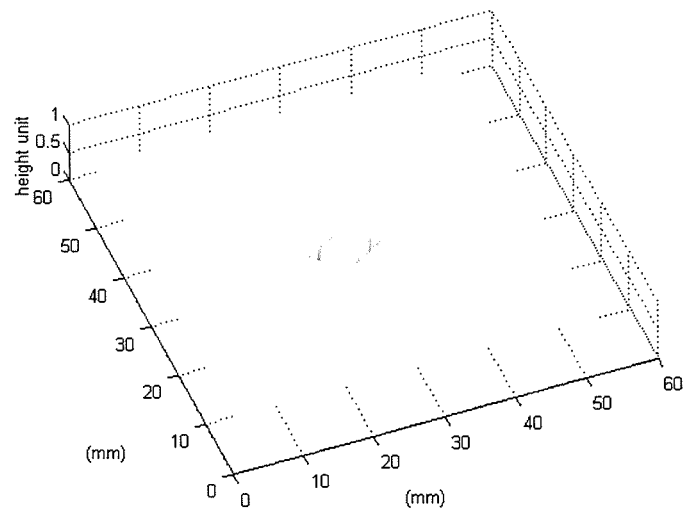


(f) Hard threshold =  $3\sigma$ .

**Figure 5.6** Synthetic diamond feature extraction through wavelet thresholding.



(a)



(b)

(a) The mask for the feature region and (b) the mask for the background region.

**Figure 5.7** Masks used to establish the amount of energy in surface and the diamond regions respectively.

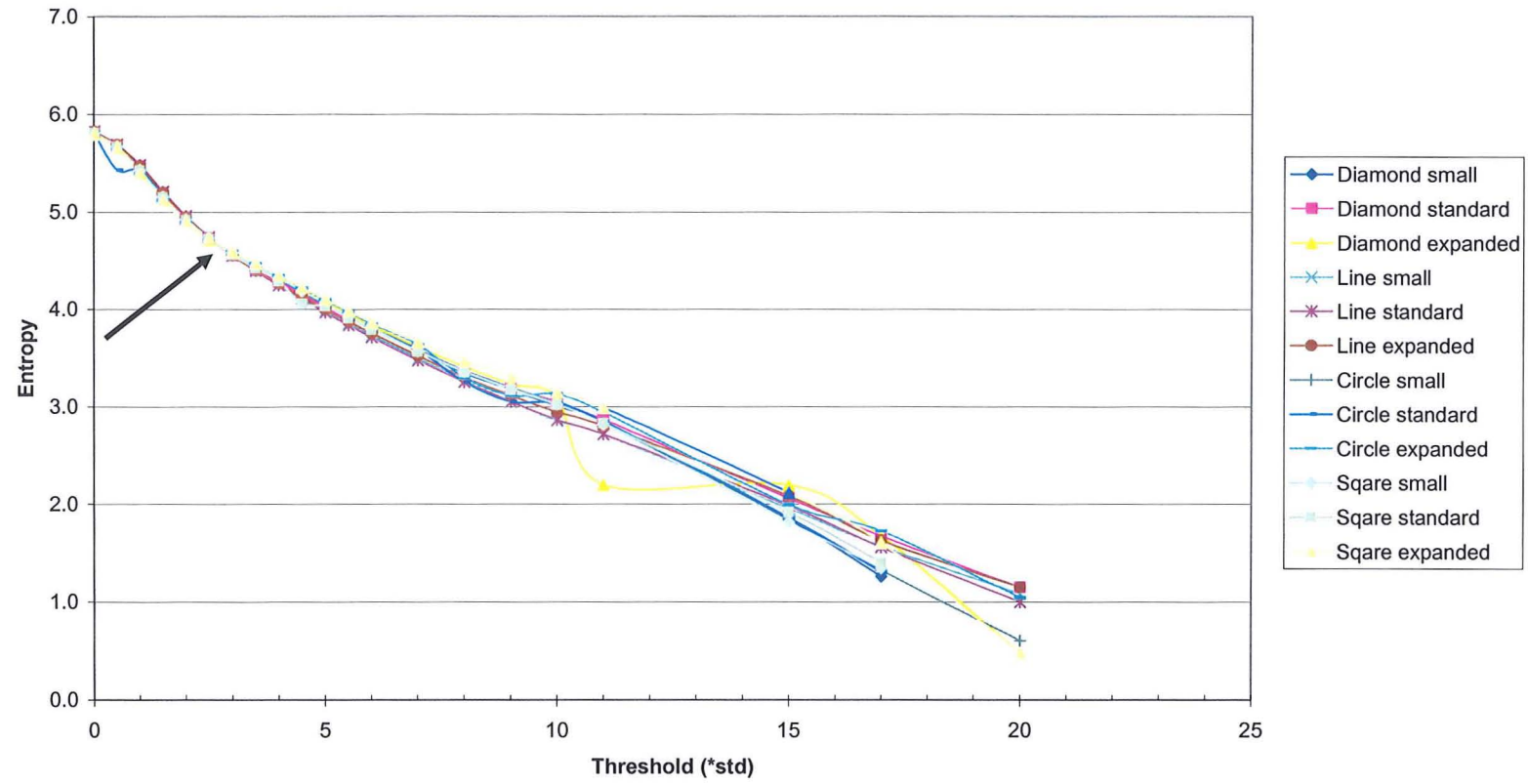


Figure 5.8 Plot of entropy for different surface features (hard threshold).

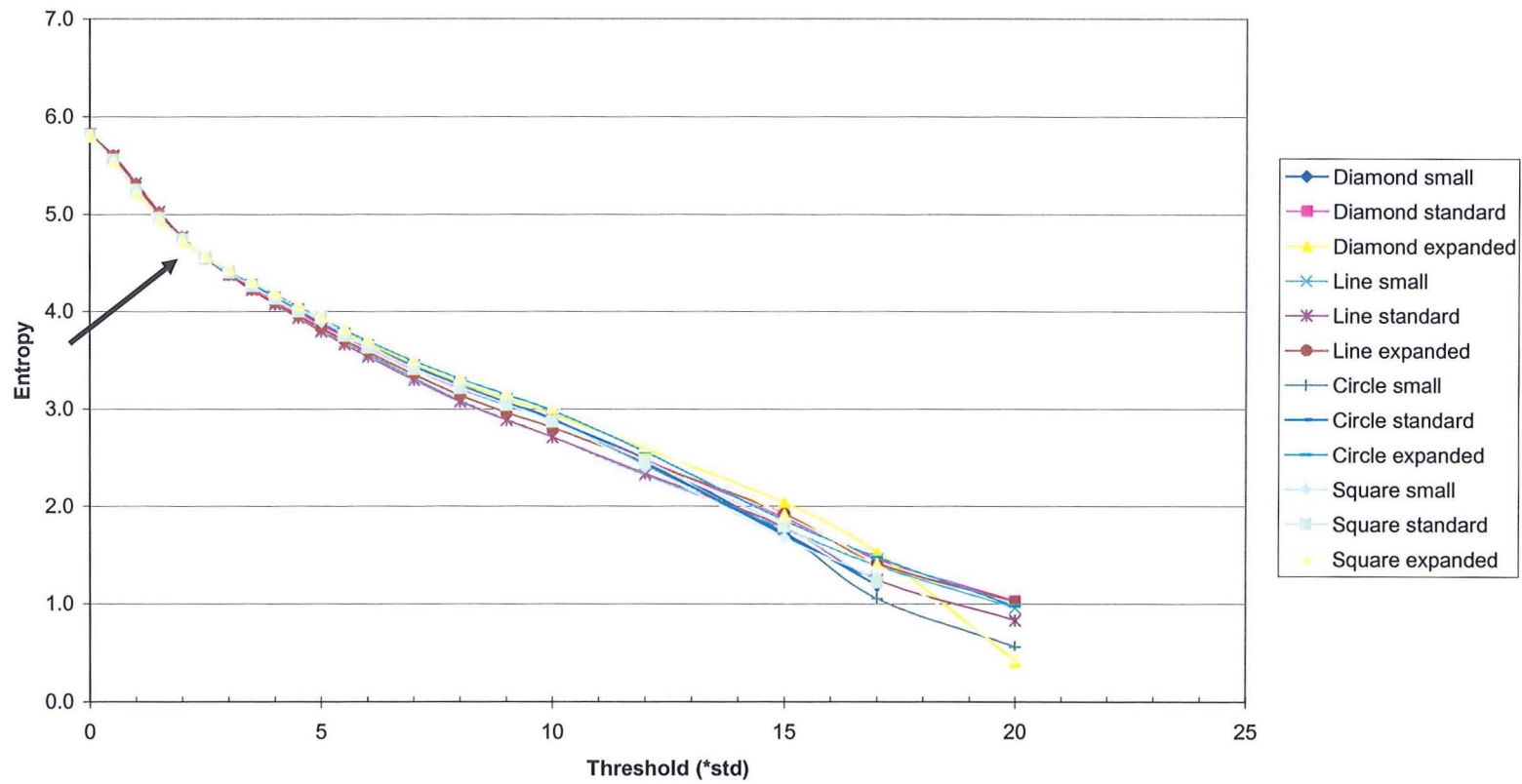
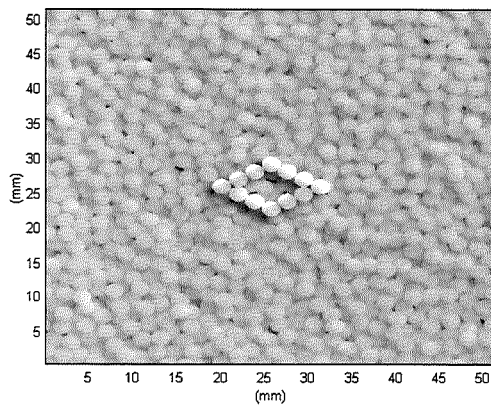
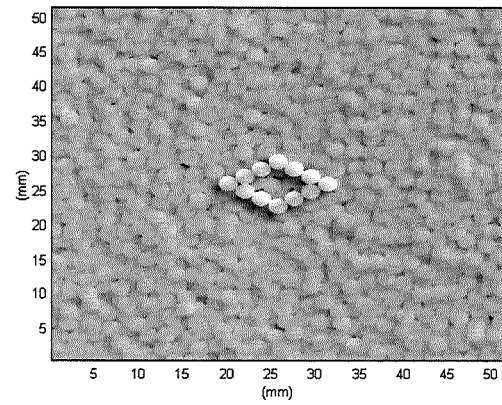


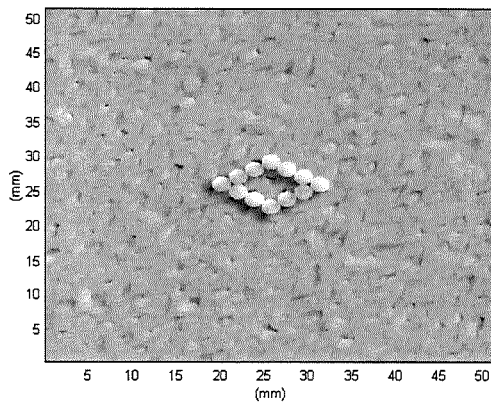
Figure 5.9 Plot of entropy for different surface features (soft threshold).



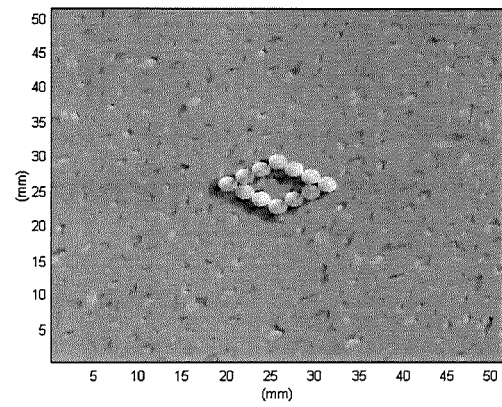
(a) 0



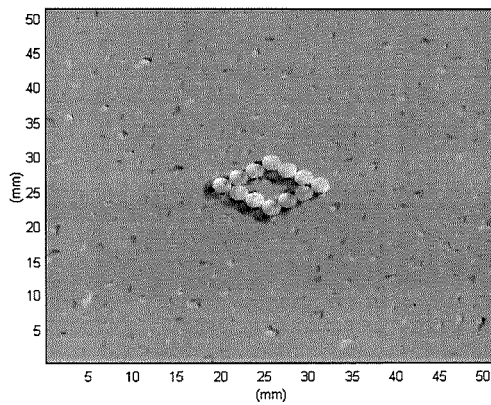
(b) 0.5



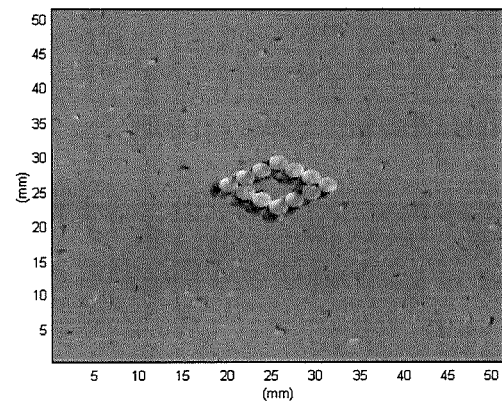
(c) 1.0



(d) 1.5



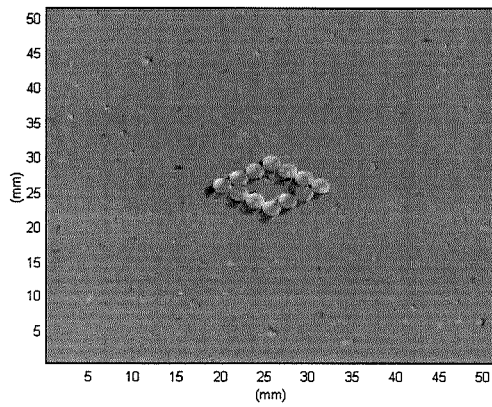
(e) 2.0



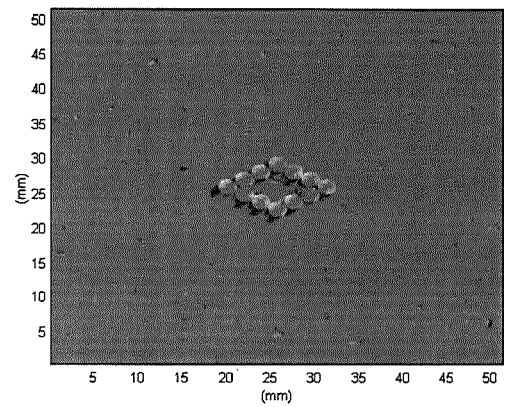
(f) 2.5

**Figure 5.10** Reconstruction of a hard thresholded surface.

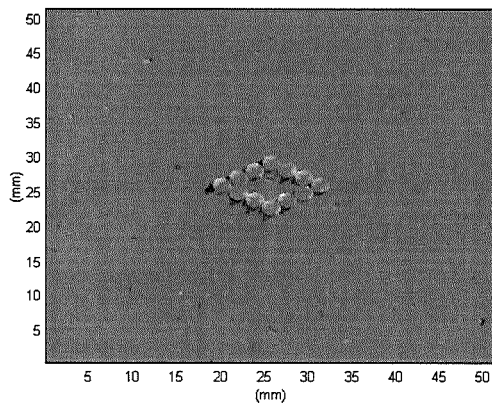




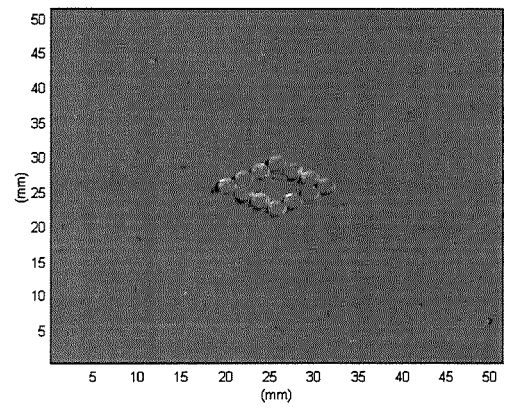
(g) 3.0



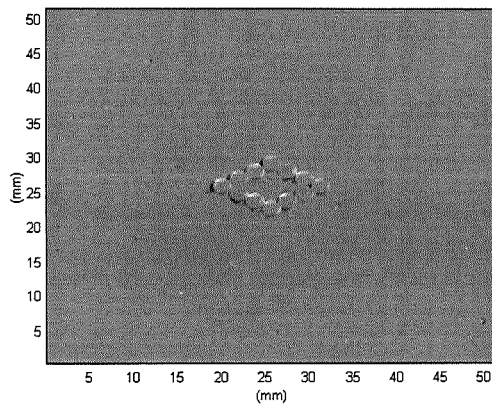
(h) 3.5



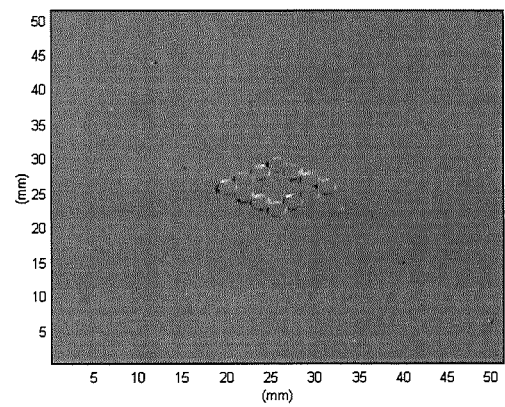
(i) 4.0



(j) 4.5

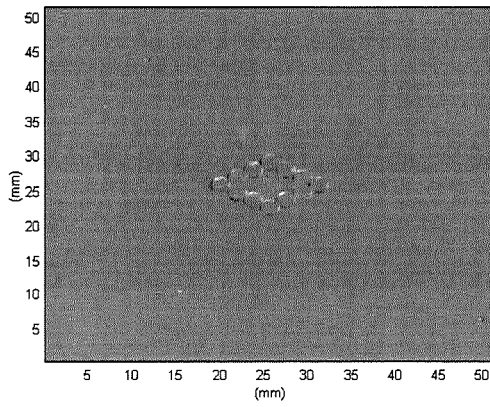


(k) 5.0

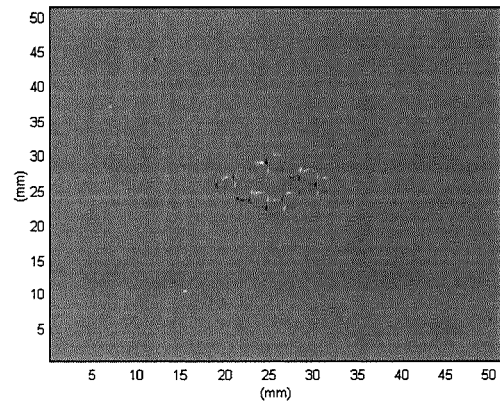


(l) 5.5

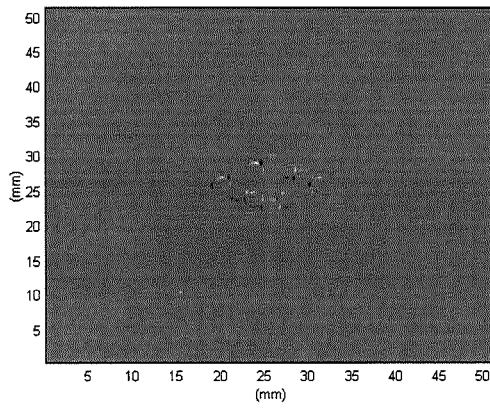
**Figure 5.10 (continued)** Reconstruction of a hard thresholded surface.



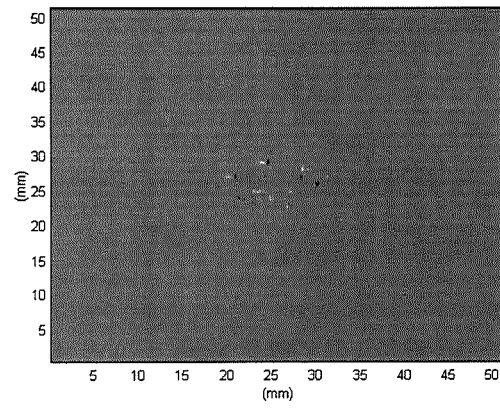
(m) 6.0



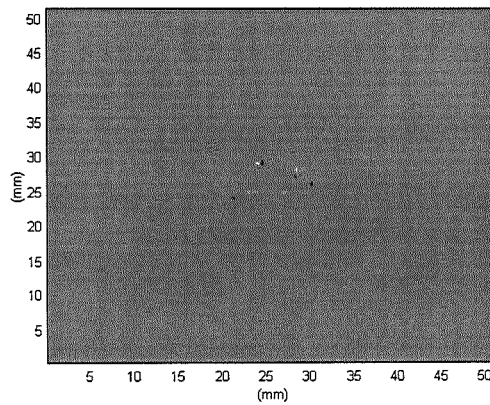
(n) 7.0



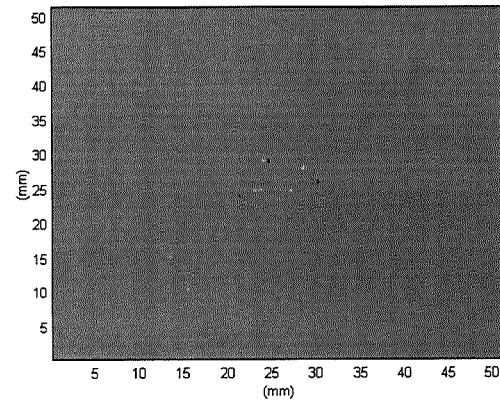
(o) 8.0



(p) 9.0

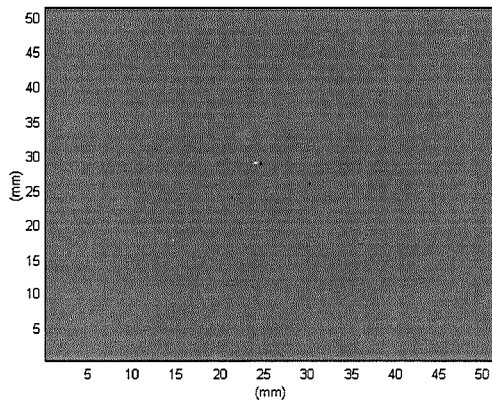


(q) 10.0

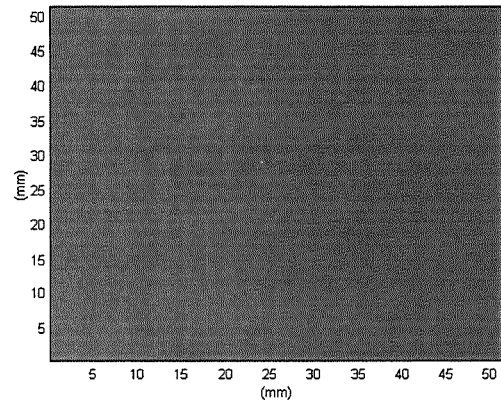


(r) 11.0

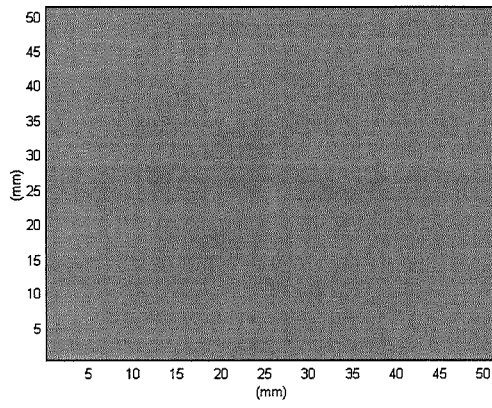
**Figure 5.10 (continued)** Reconstruction of a hard thresholded surface.



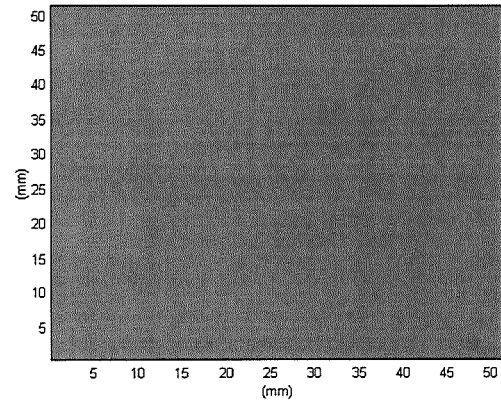
(s) 13.0



(t) 15.0

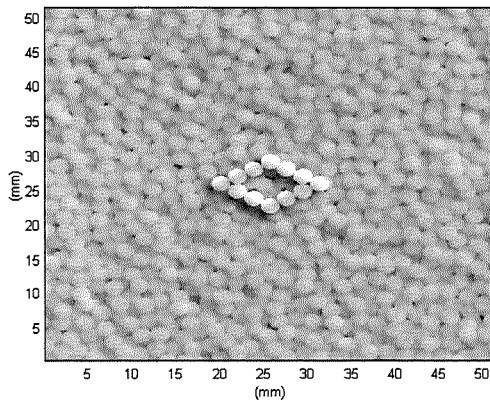


(u) 17.0

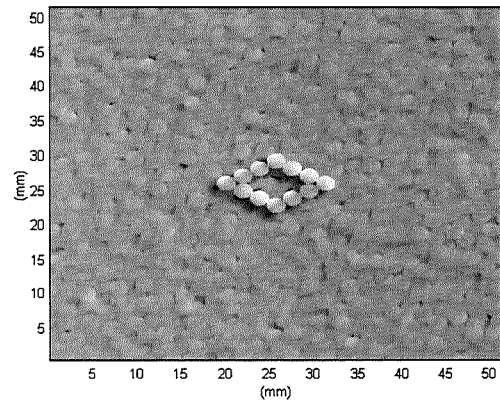


(v) 20.0

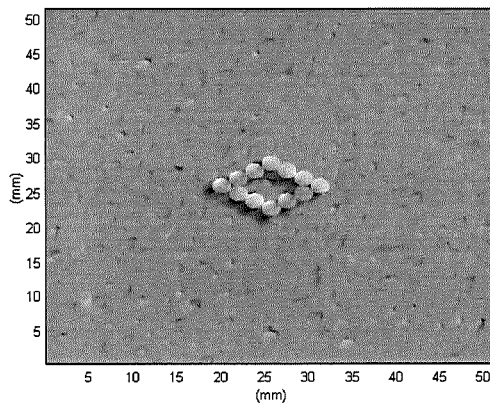
**Figure 5.10 (continued)** Reconstruction of a hard thresholded surface.



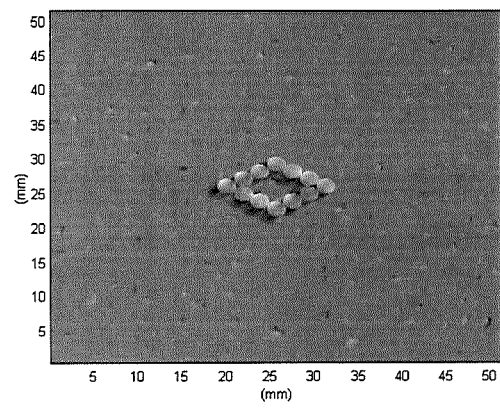
(a) 0



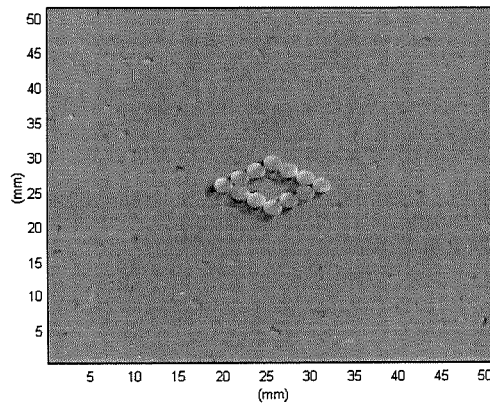
(b) 0.5



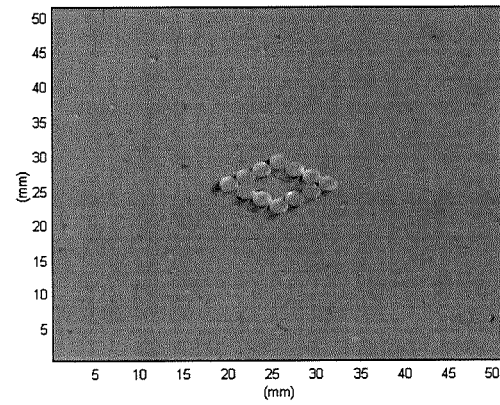
(c) 1.0



(d) 1.5

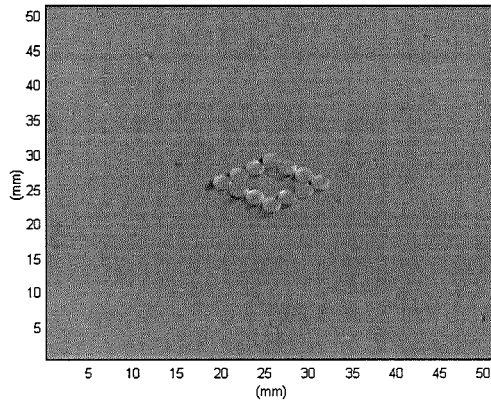


(e) 2.0

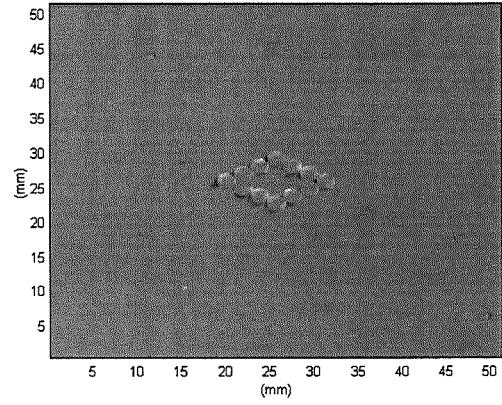


(f) 2.5

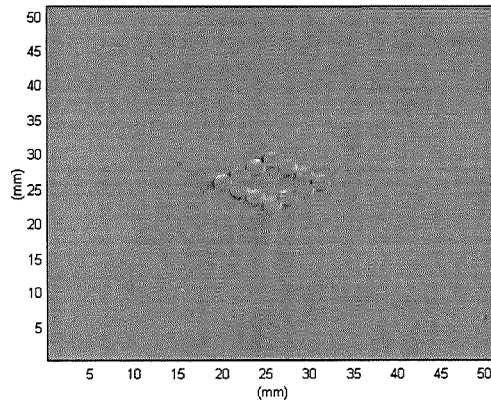
**Figure 5.11** Reconstruction of a soft thresholded surface.



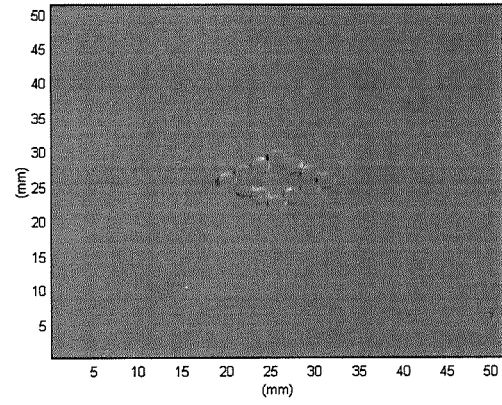
(g) 3.0



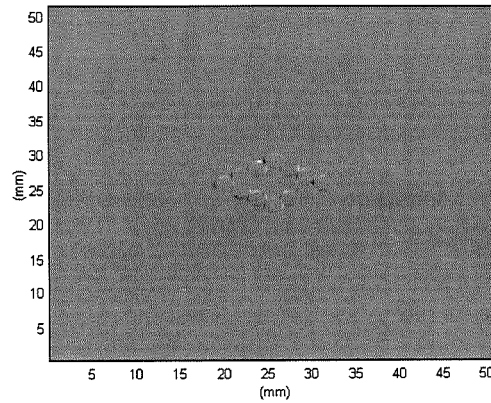
(h) 3.5



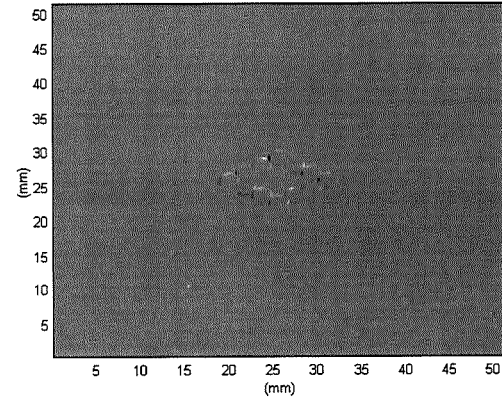
(i) 4.0



(j) 4.5

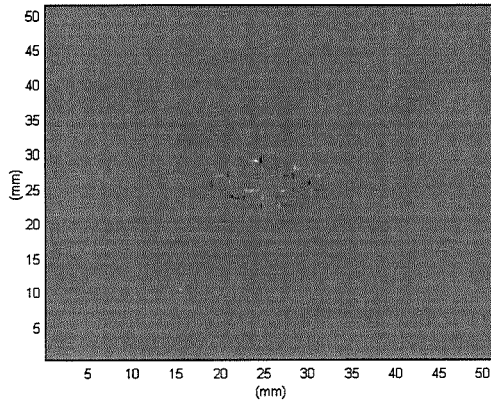


(k) 5.0

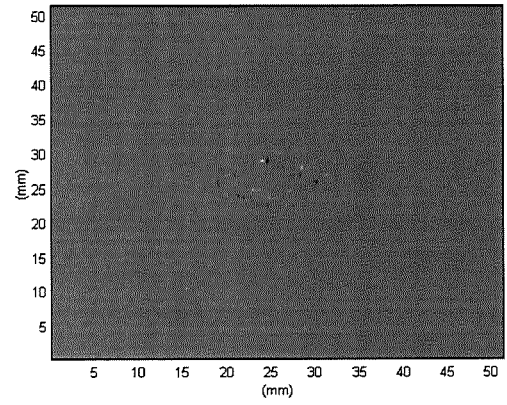


(l) 5.5

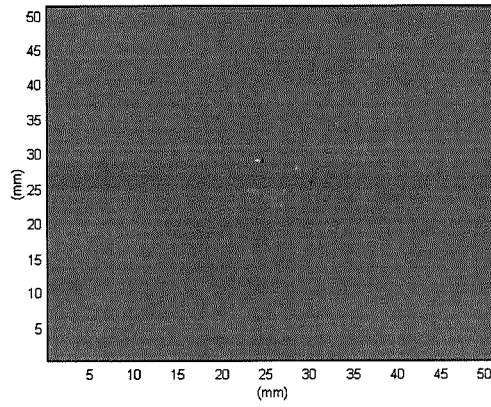
**Figure 5.11 (continued)** Reconstruction of a soft thresholded surface.



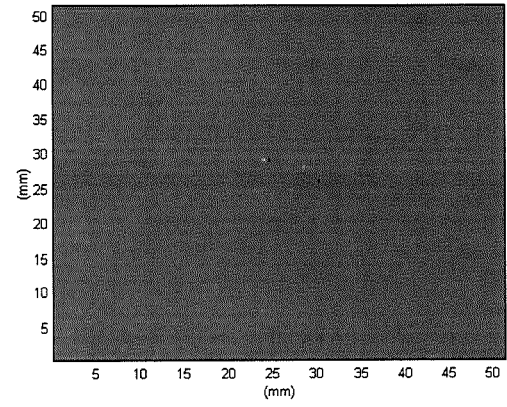
(m) 6.0



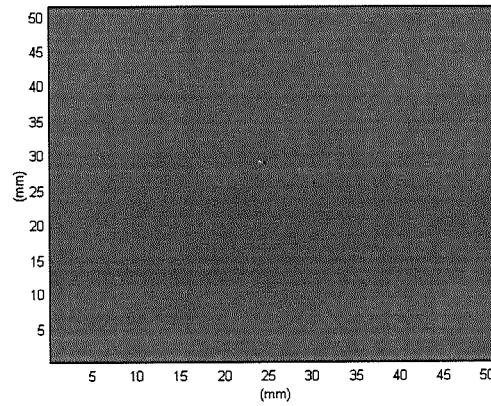
(n) 7.0



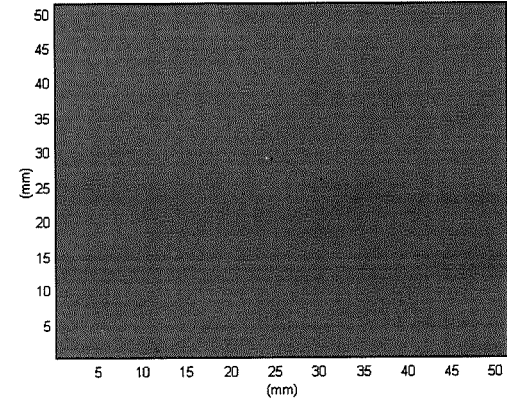
(o) 8.0



(p) 9.0

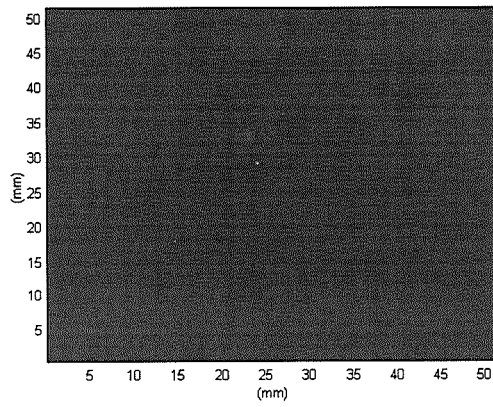


(q) 10.0

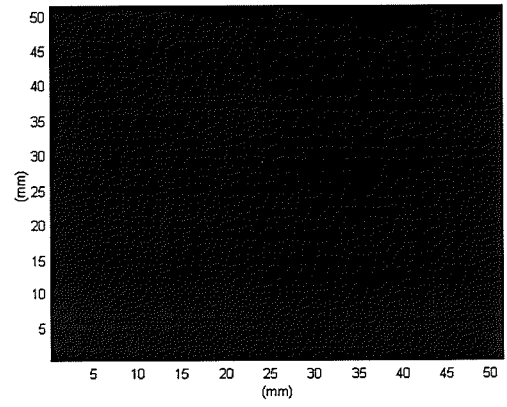


(r) 11.0

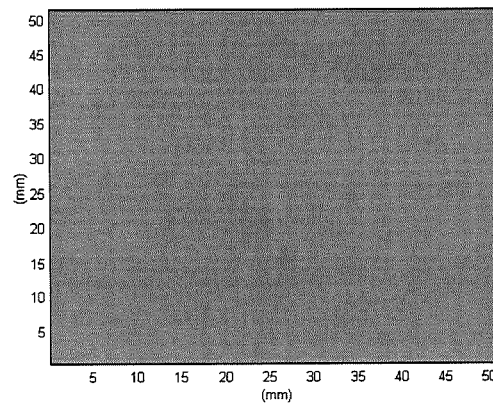
**Figure 5.11 (continued)** Reconstruction of a soft thresholded surface.



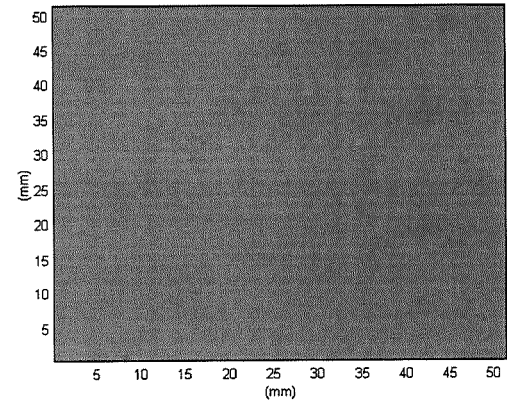
(s) 13.0



(t) 15.0



(u) 17.0



(v) 20.0

**Figure 5.11 (continued)** Reconstruction of a soft thresholded surface.

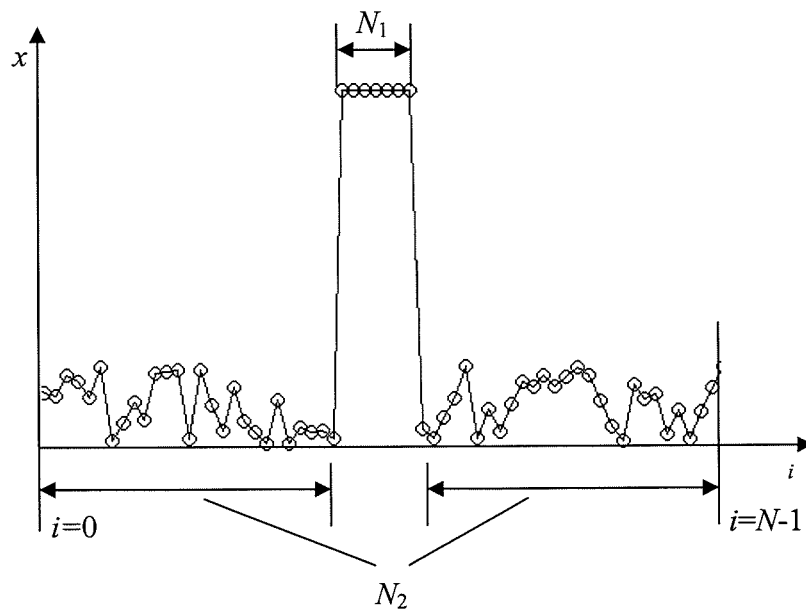
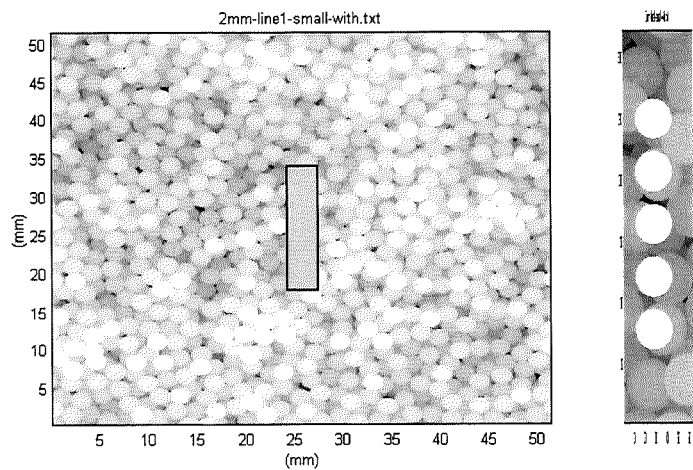
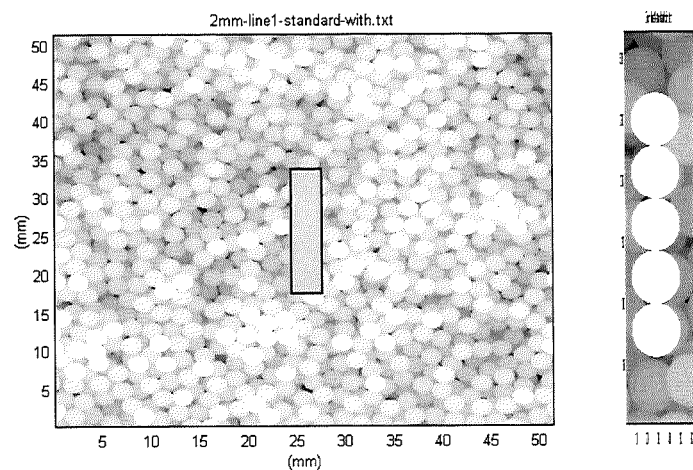


**Figure 5.12** Dividing the coefficients of a profile into two parts; feature part  $N_1$  and background part  $N_2$  ( $N=N_1+N_2$ ).

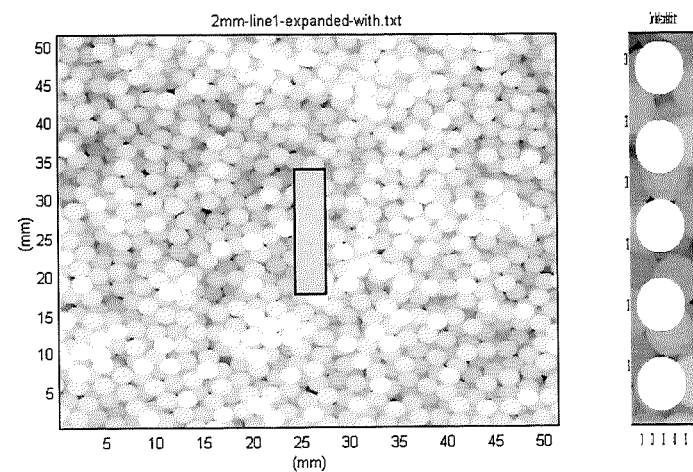




(a) Small line.

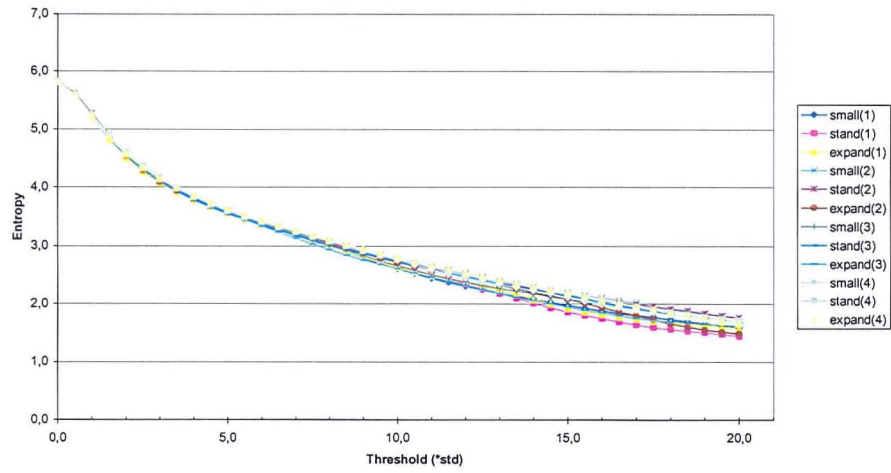


(b) Standard line.

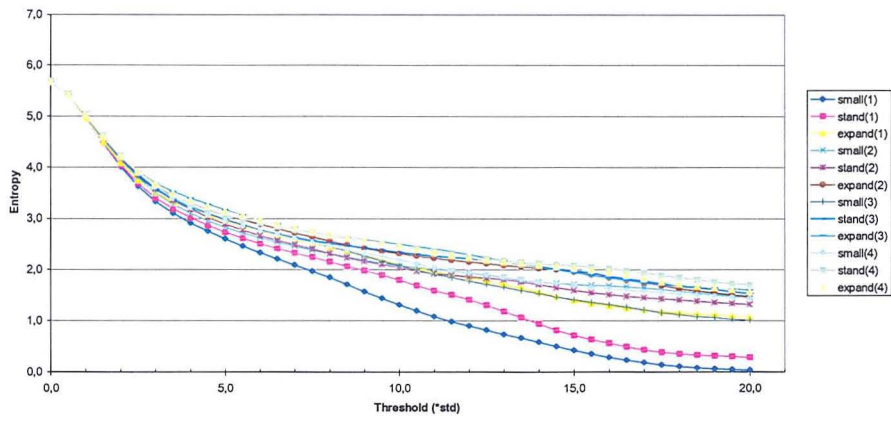


(c) Expanded line.

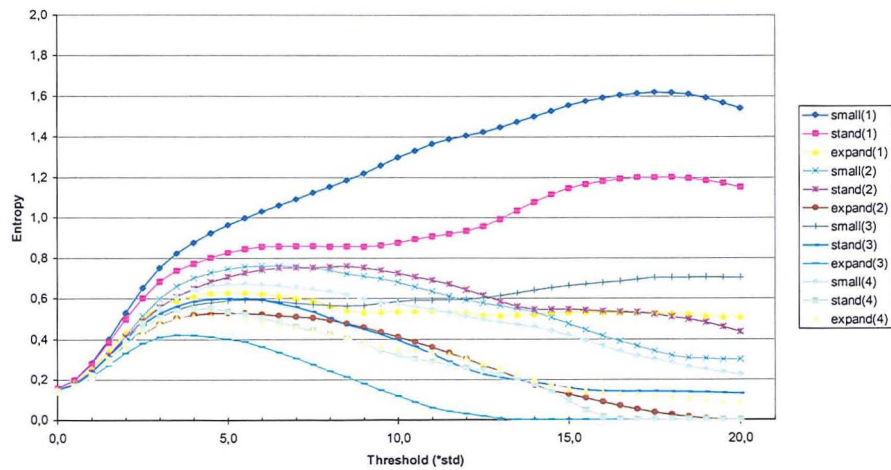
**Figure 5.13** Separation of surface into two areas, background area (left) and feature area (right). (Note that the feature area is shown enlarged.)



(a) Total entropy.

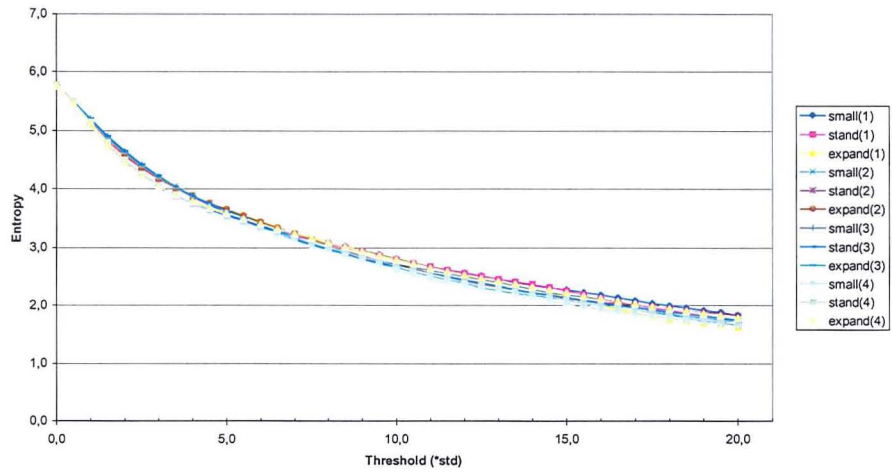


(b) Background entropy.

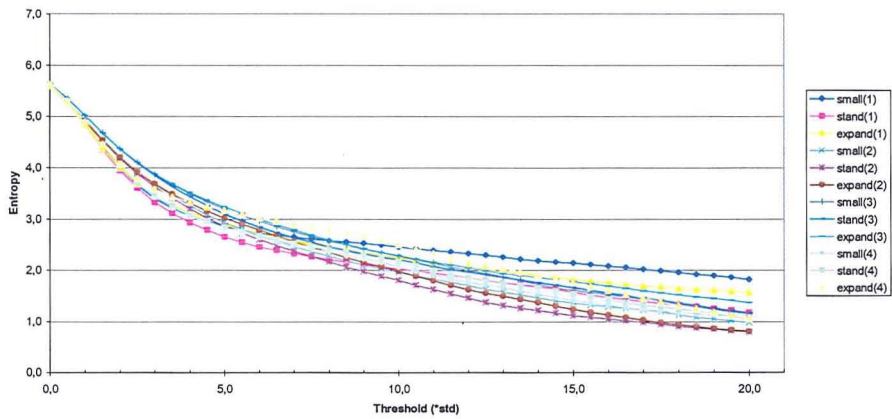


(c) Feature entropy (note exaggerated vertical scale used for clarity).

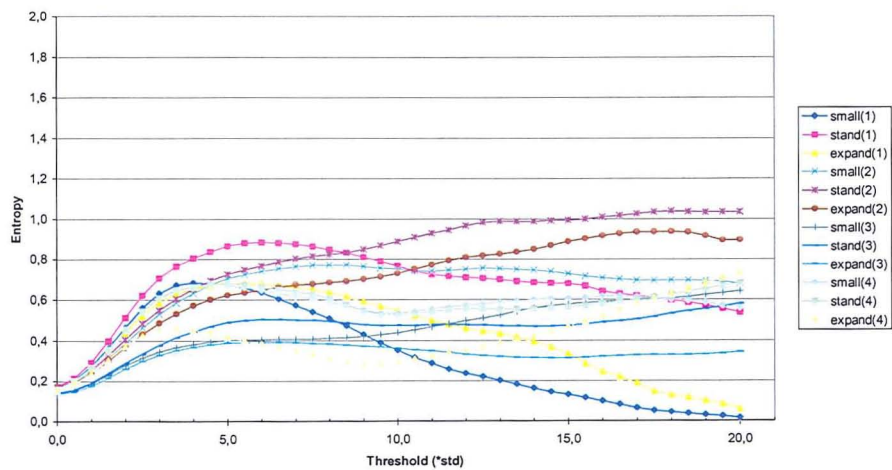
**Figure 5.14** Entropy measure through the thresholding process, underlying surface of grain size 2mm.



(a) Total entropy.

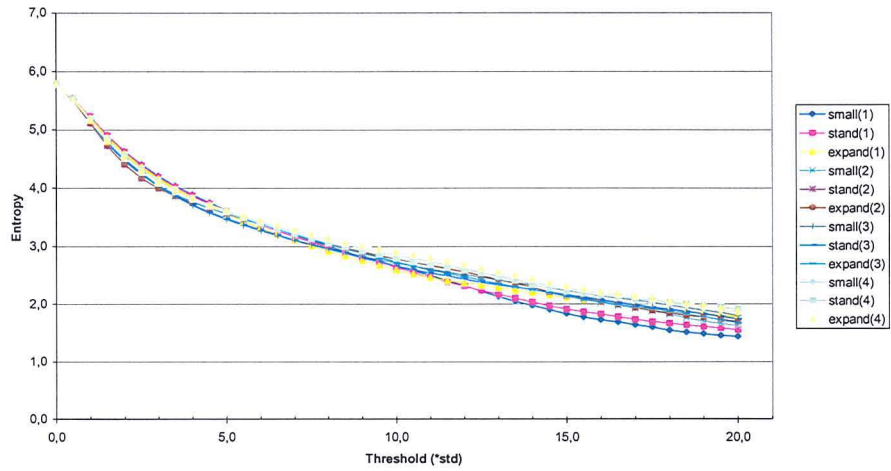


(b) Background entropy.

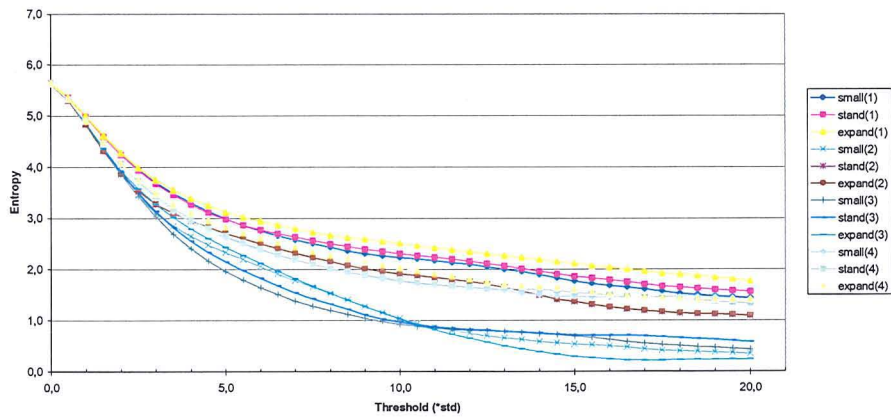


(c) Feature entropy (note exaggerated vertical scale used for clarity).

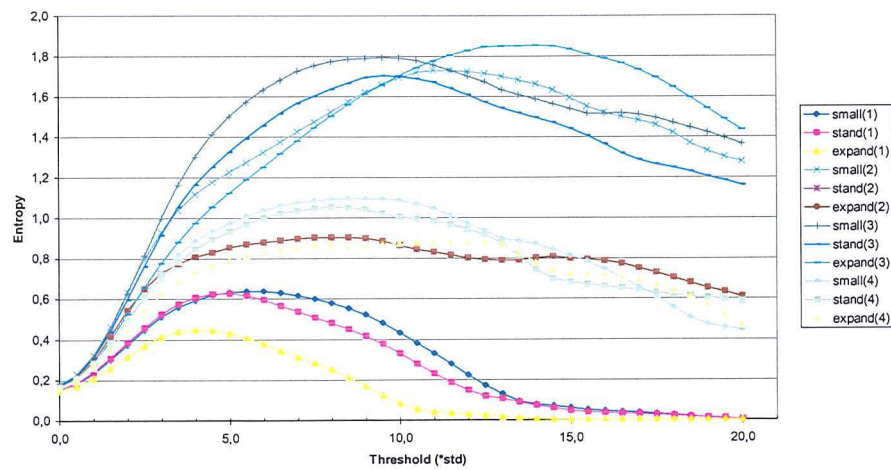
**Figure 5.15** Entropy measure through the thresholding process, underlying surface of grain size 3mm.



(a) Total entropy.

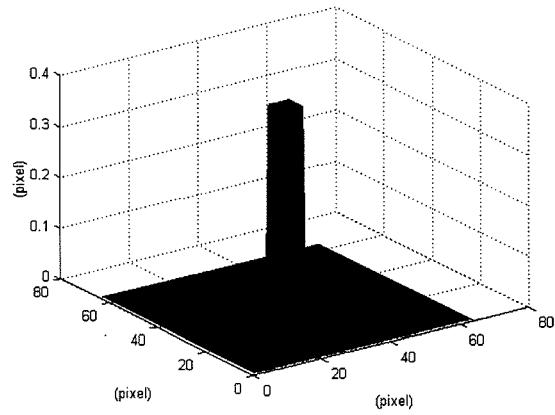


(b) Background entropy.

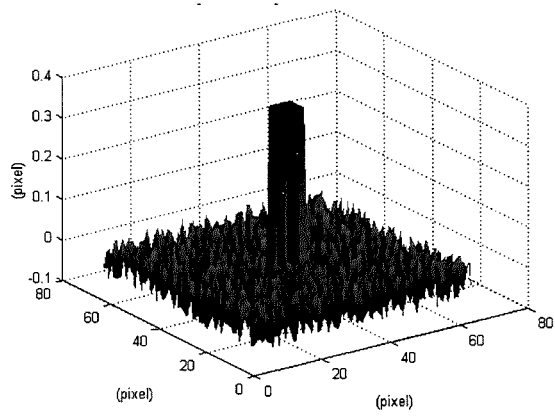


(c) Feature entropy (note exaggerated vertical scale used for clarity).

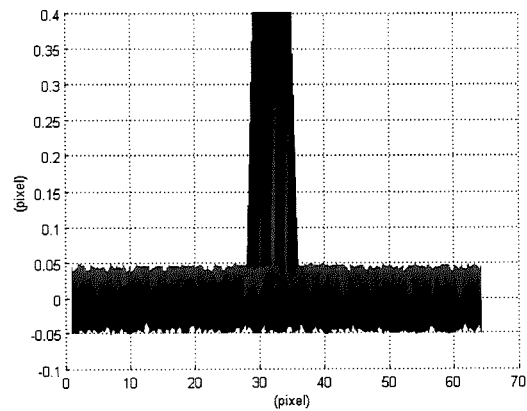
**Figure 5.16** Entropy measure through the thresholding process, underlying surface of mixture of grain sizes 2mm and 3mm.



(a) Flat background surface.

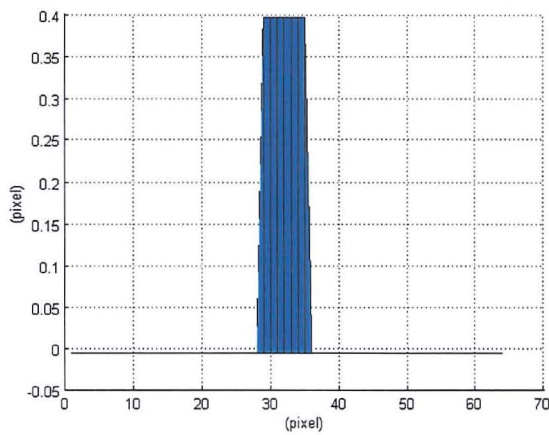


(b) Random background surface.

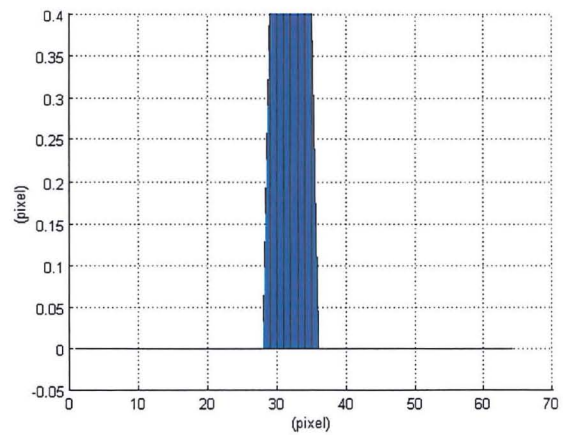


(c) Horizontal view of (b) showing the background surface normalised to have a mean of 0.

**Figure 5.17** Examples of two synthetically generated test surfaces.



(a) Last approximation was not added to reconstruction.



(b) Last approximation was added to the reconstruction.

**Figure 5.18** Present the difference between (a) not adding the approximation and (b) adding the approximation in the reconstruction.

This difference between the original background (set at zero) and the reconstructed background surface will generate a false high entropy value.

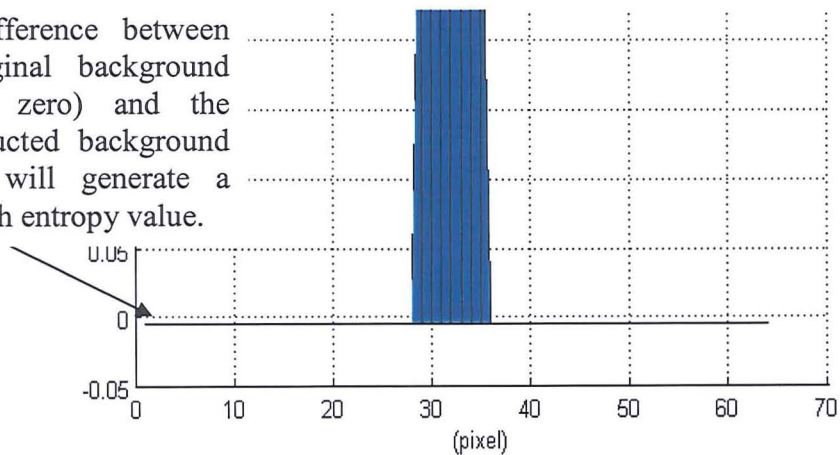
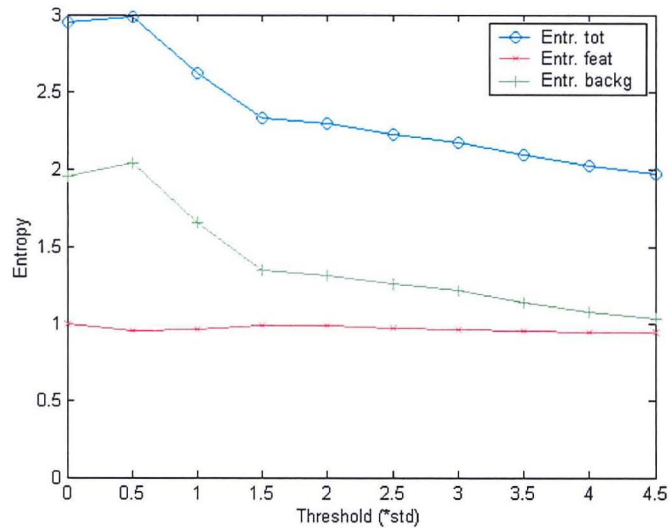
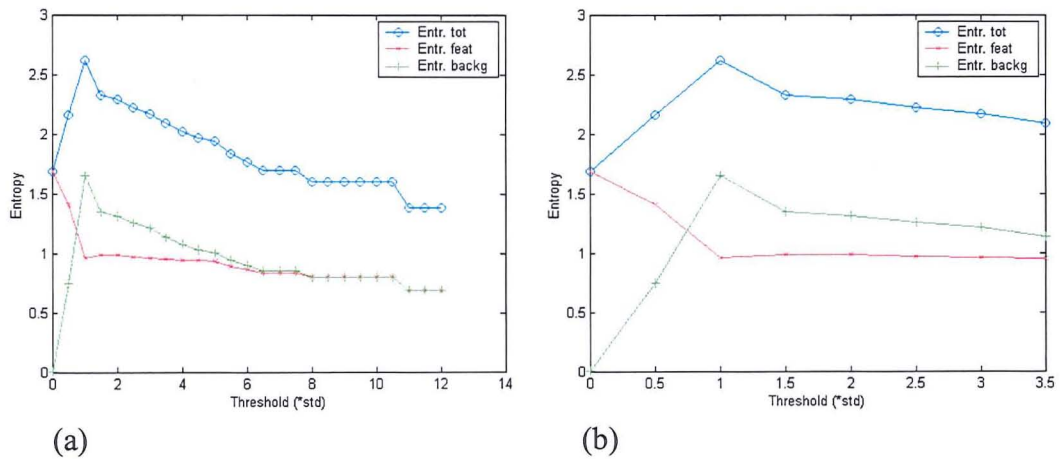


**Figure 5.19** The difference between zero and the reconstructed background surface will be picked up as information by the entropy measure.



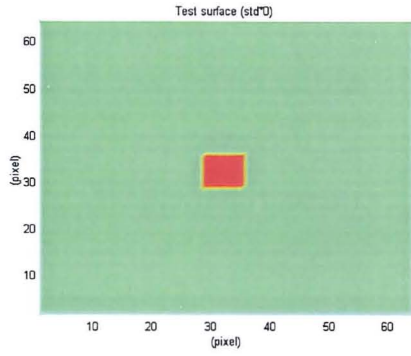
This example show the hard thresholding where the approximation has been excluded from the reconstruction. The entropy measure for the reconstructed background has picked up information in the background surface at  $0 \times \sigma$ . This is because the reconstructed background surface does not have a mean of zero, as can be seen in figure 5.18(a).

**Figure 5.20** Entropy values against hard threshold when the approximation at the largest scale has been excluded from the reconstruction.

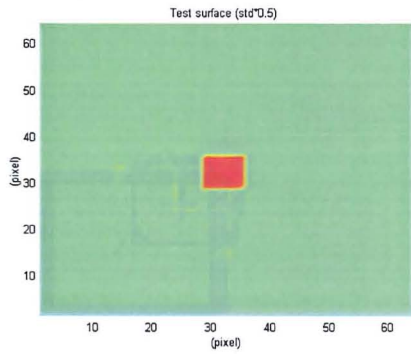
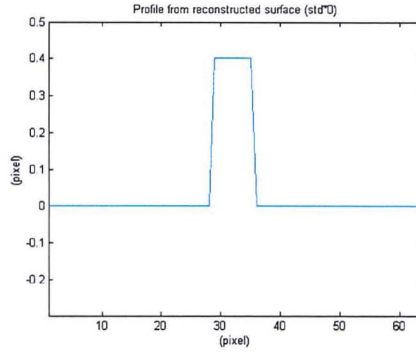


Total entropy, feature entropy and background entropy respectively applying a hard threshold. (a) The complete entropy curves and (b) entropy curves for the first threshold values between  $0 \times \sigma$  and  $3.5 \times \sigma$ .

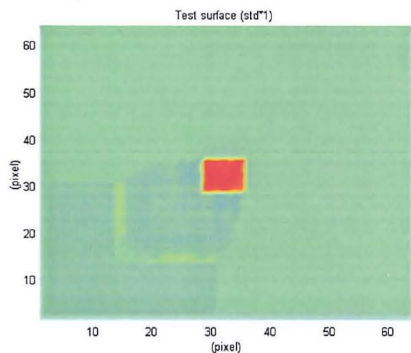
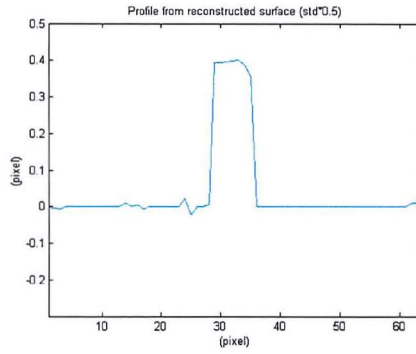
**Figure 5.21** Entropy against hard threshold for the reconstructed surface with a flat background surface (i.e. background values set to zero).



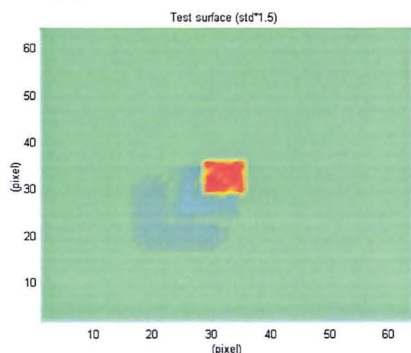
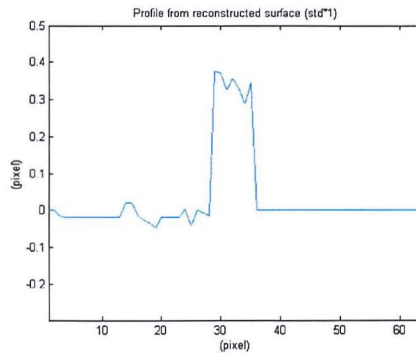
(a)  $\sigma = 0$



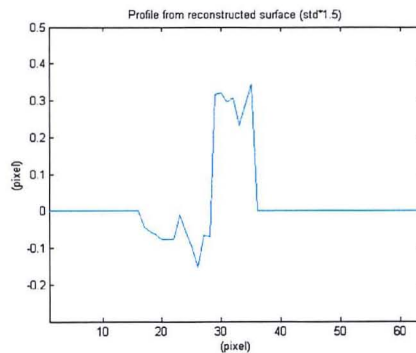
(b)  $\sigma = 0.5$



(c)  $\sigma = 1.0$



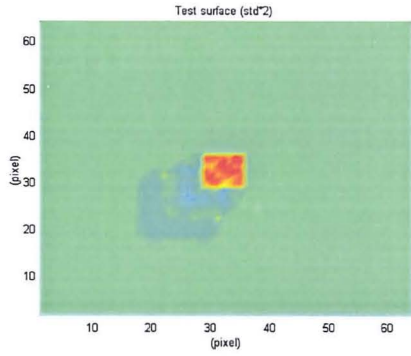
(d)  $\sigma = 1.5$



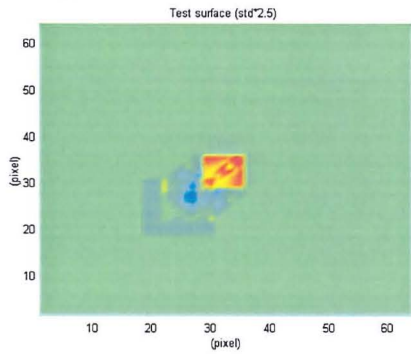
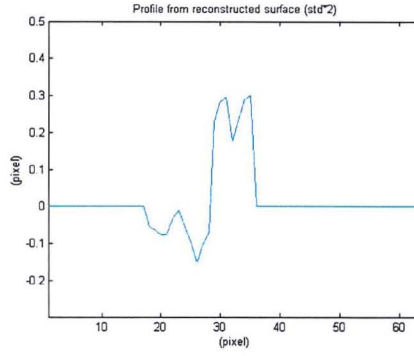
Surface plot (left) and a profile plot from the surface (right).

**Figure 5.22** Hard thresholded and reconstructed surface for different threshold values.

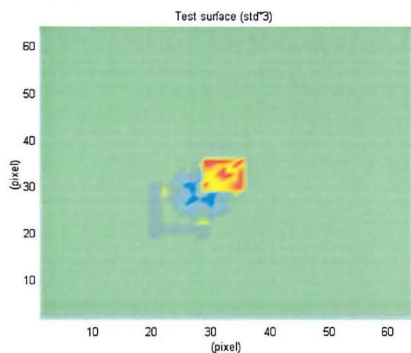
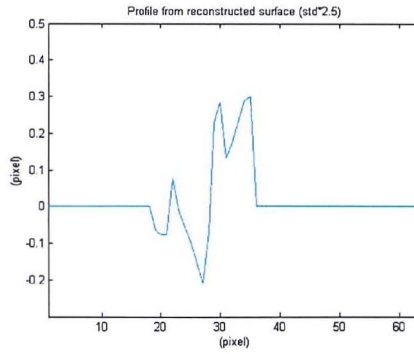




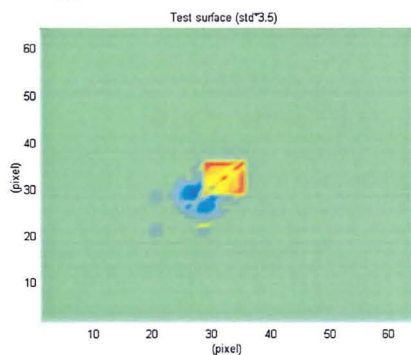
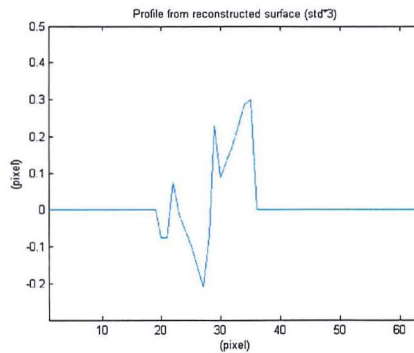
(e)  $\sigma = 2.0$



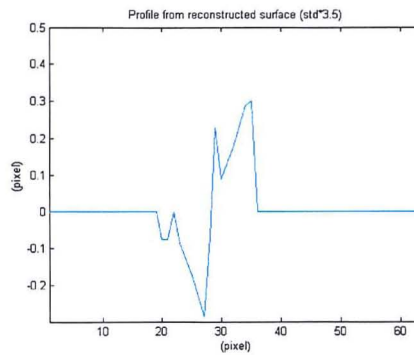
(f)  $\sigma = 2.5$



(g)  $\sigma = 3.0$

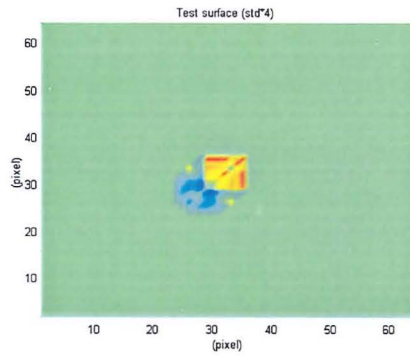


(h)  $\sigma = 3.5$

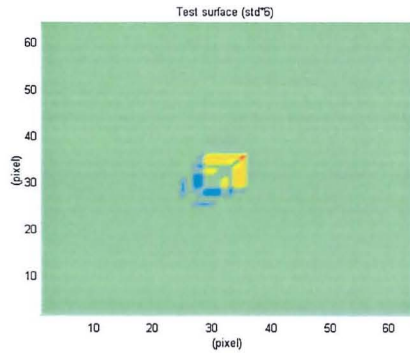
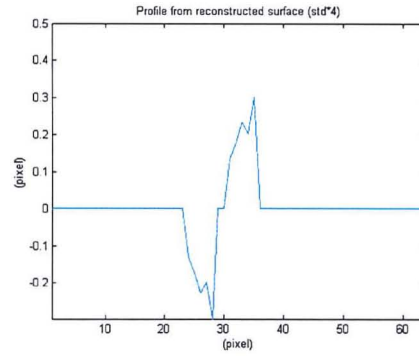


Surface plot (left) and a profile plot from the surface (right).

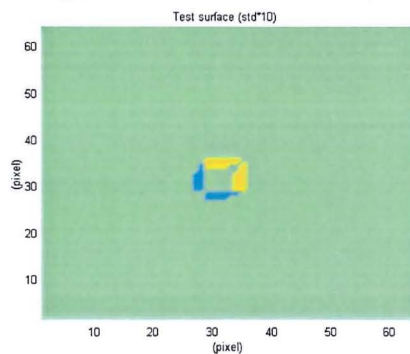
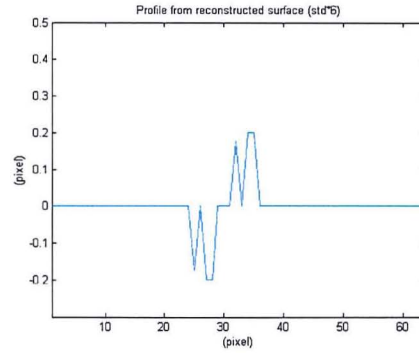
**Figure 5.22 (continued)** Hard thresholded and reconstructed surface for different threshold values.



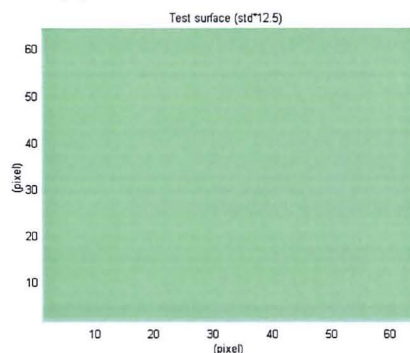
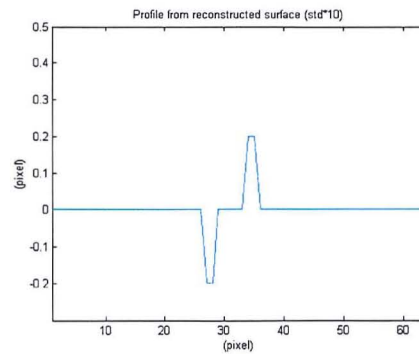
(i)  $\sigma = 4.0$



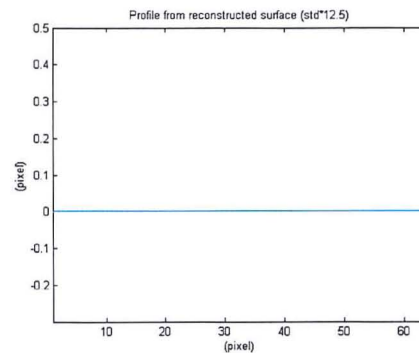
(j)  $\sigma = 6.0$



(k)  $\sigma = 10.0$

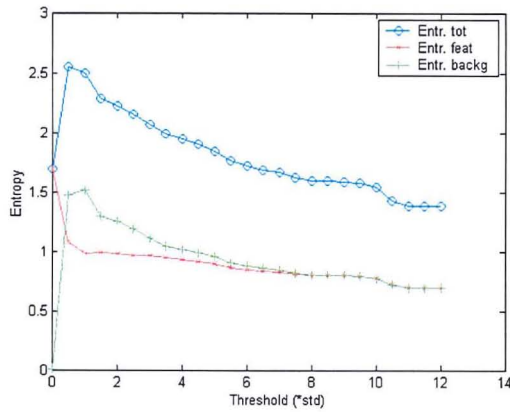


(l)  $\sigma = 12.5$

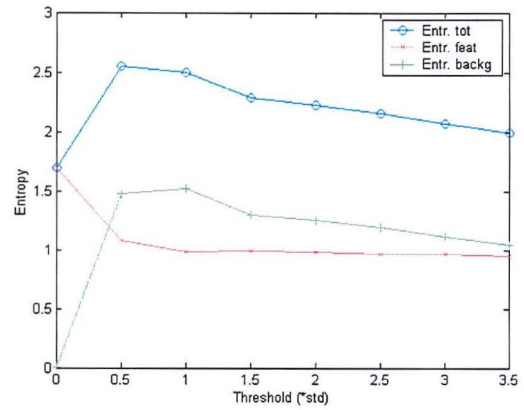


Surface plot (left) and a profile plot from the surface (right).

**Figure 5.22 (continued)** Hard thresholded and reconstructed surface for different threshold values.



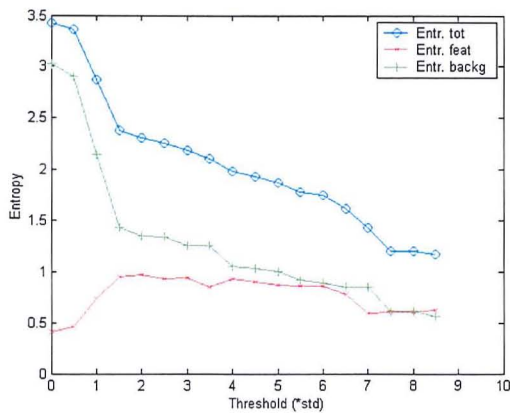
(a)



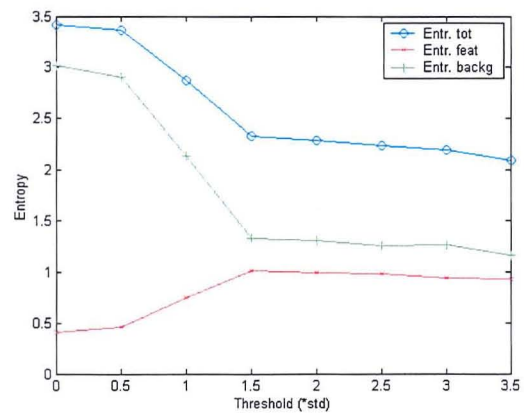
(b)

Total entropy, feature entropy and background entropy respectively applying a soft threshold. (a) The complete entropy curve and (b) the first threshold values between  $0 \times \sigma$  and  $3.5 \times \sigma$ .

**Figure 5.23** Soft threshold, entropy for the reconstructed surface with the background surface set to zero.



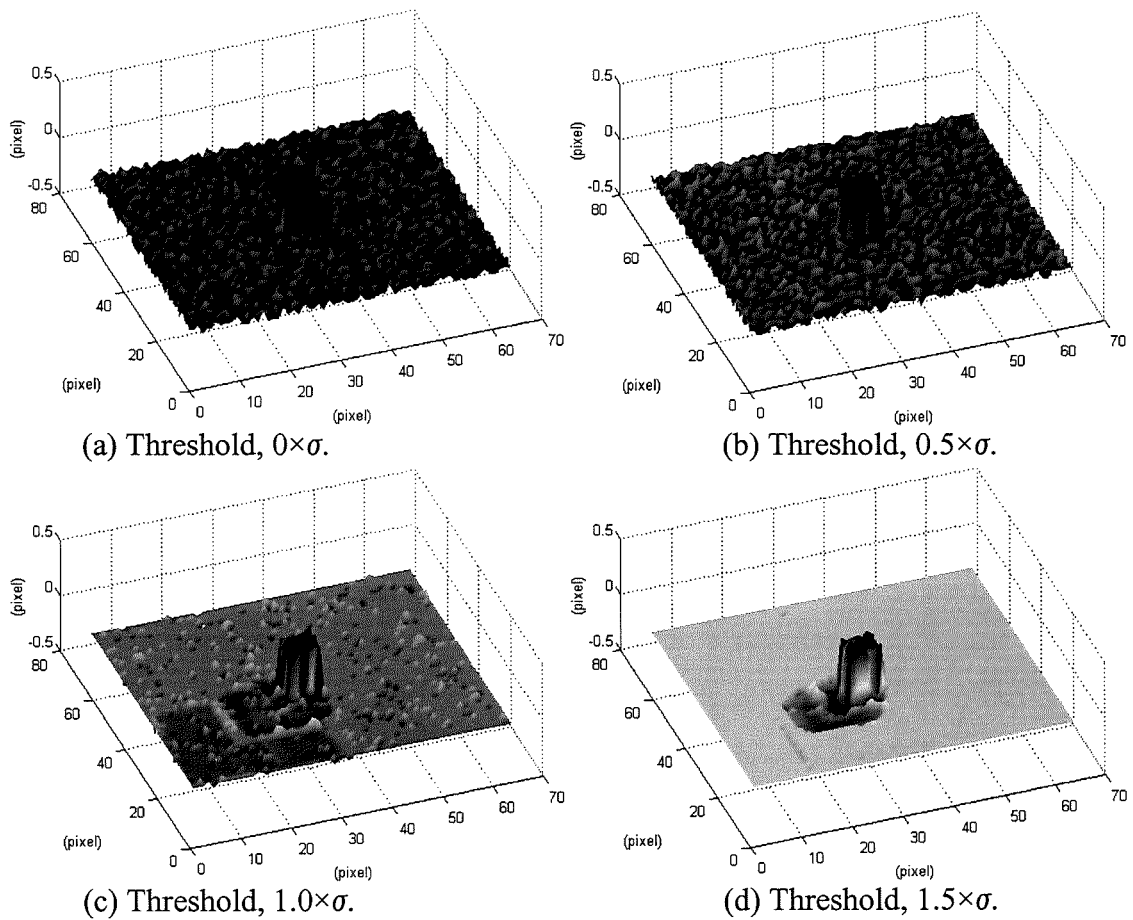
(a)



(b)

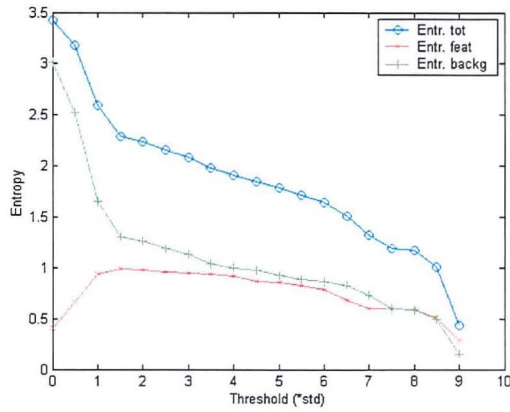
Total entropy, background entropy and feature entropy respectively applying a hard threshold. (a) The complete entropy curve and (b) the first 8 threshold values of the curve.

**Figure 5.24** Hard threshold, entropy for the reconstructed background surface generated from a uniformly distributing.

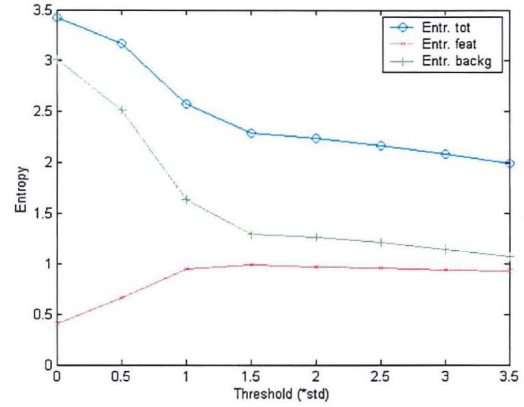


(a) Original surface (not thresholded), (b) for  $0.5 \times \sigma$  the background surface starts being removed by the thresholding process, (c) most of the background surface has now been removed at a threshold equal to  $1.0 \times \sigma$ , here the edge effects are also visible in the reconstructed surface and (d) for  $1.5 \times \sigma$  close to all of the original background surface has been removed leaving only the edge effect within the region of the background.

**Figure 5.25** Example of hard thresholding and reconstruction of test surface.



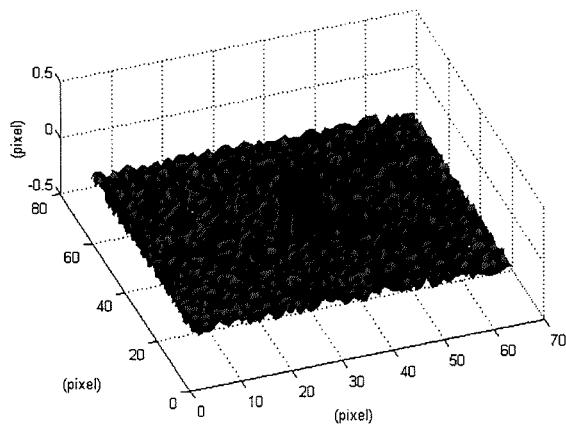
(a)



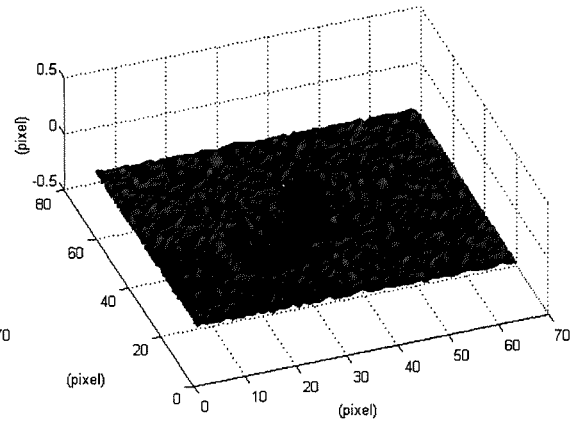
(b)

Total entropy, background entropy and feature entropy respectively applying a soft threshold. (a) The complete entropy curve and (b) the first 8 threshold values of the curve.

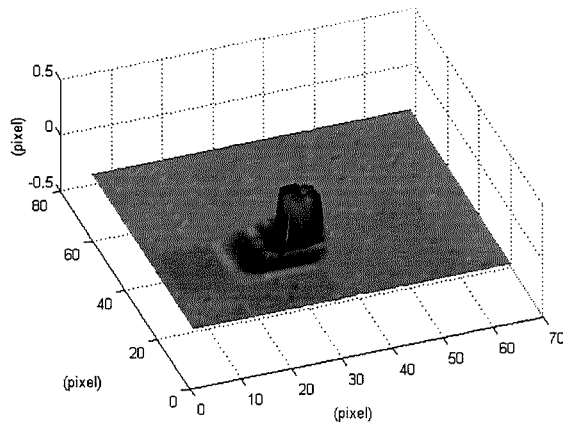
**Figure 5.26** Entropy for the reconstructed soft thresholded background surface generated from a uniformly distributing.



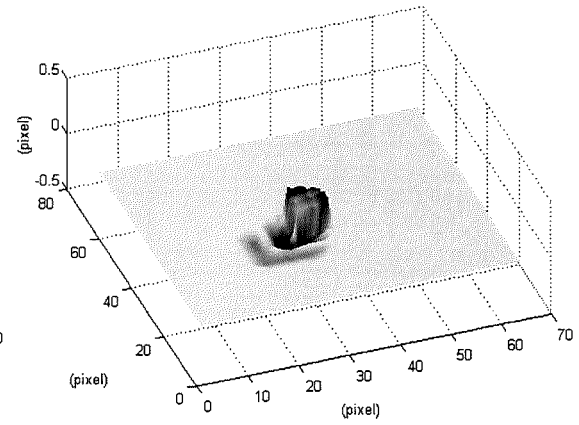
(a) Threshold,  $0 \times \sigma$ .



(b) Threshold,  $0.5 \times \sigma$ .



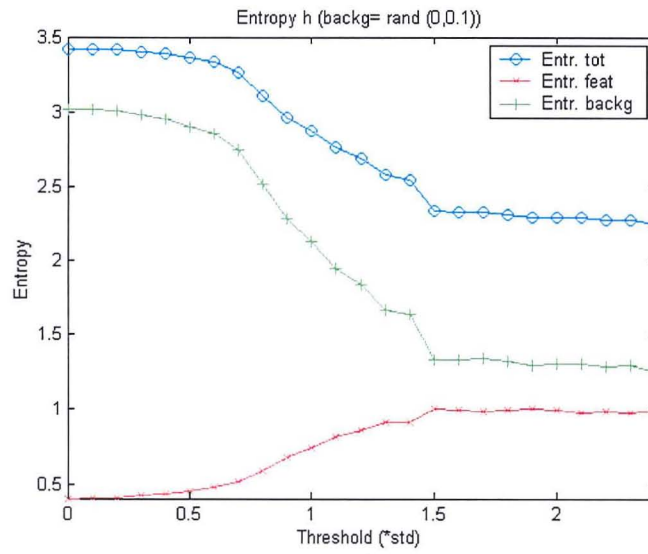
(c) Threshold,  $1.0 \times \sigma$ .



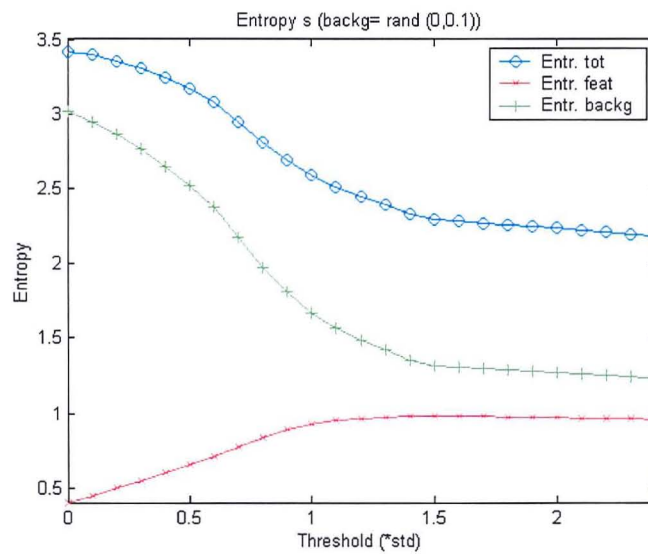
(d) Threshold,  $1.5 \times \sigma$ .

(a) Original not thresholded surface, (b) it is visible that part of the background surface have been removed in the thresholding process and how edge effects are appearing in the reconstruction, (c) near to the entire background surface has now been removed and (d) where the complete background surface have been taken away in the thresholding process left is only the feature and the edge effects.

**Figure 5.27** Example of soft thresholding and reconstruction of test surface.



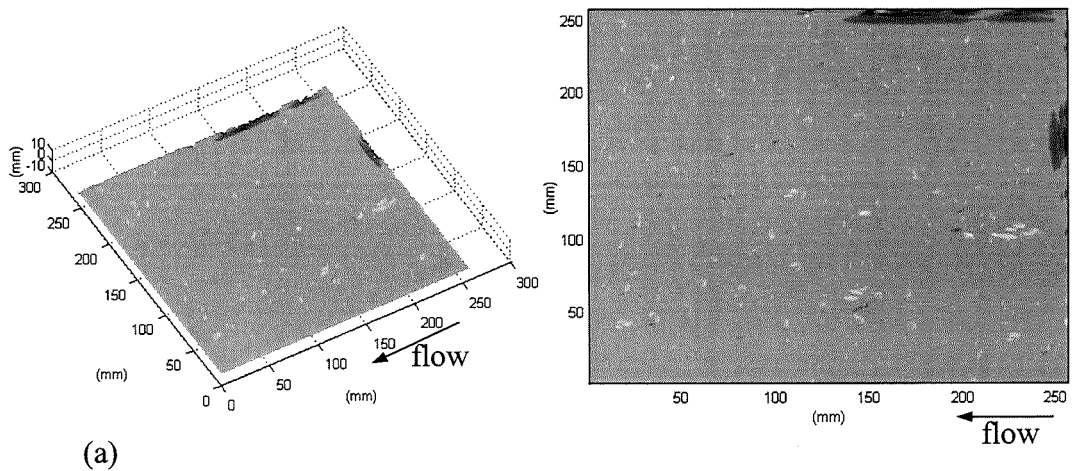
(a)



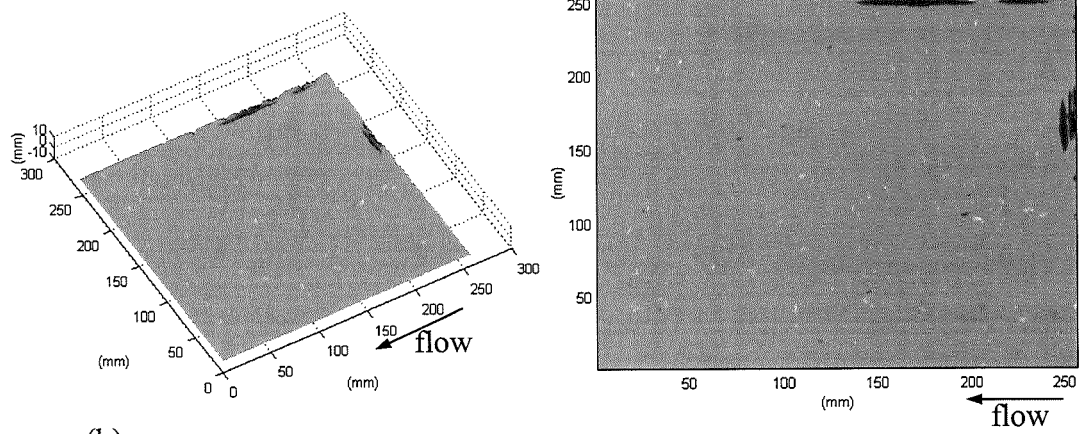
(b)

(a) Total entropy and entropies in the background and the feature regions applying hard thresholding and (b) total entropy and entropies in the background and the feature regions applying soft thresholding.

**Figure 5.28** Measuring the entropy in the thresholded and reconstructed test surface.



(a)

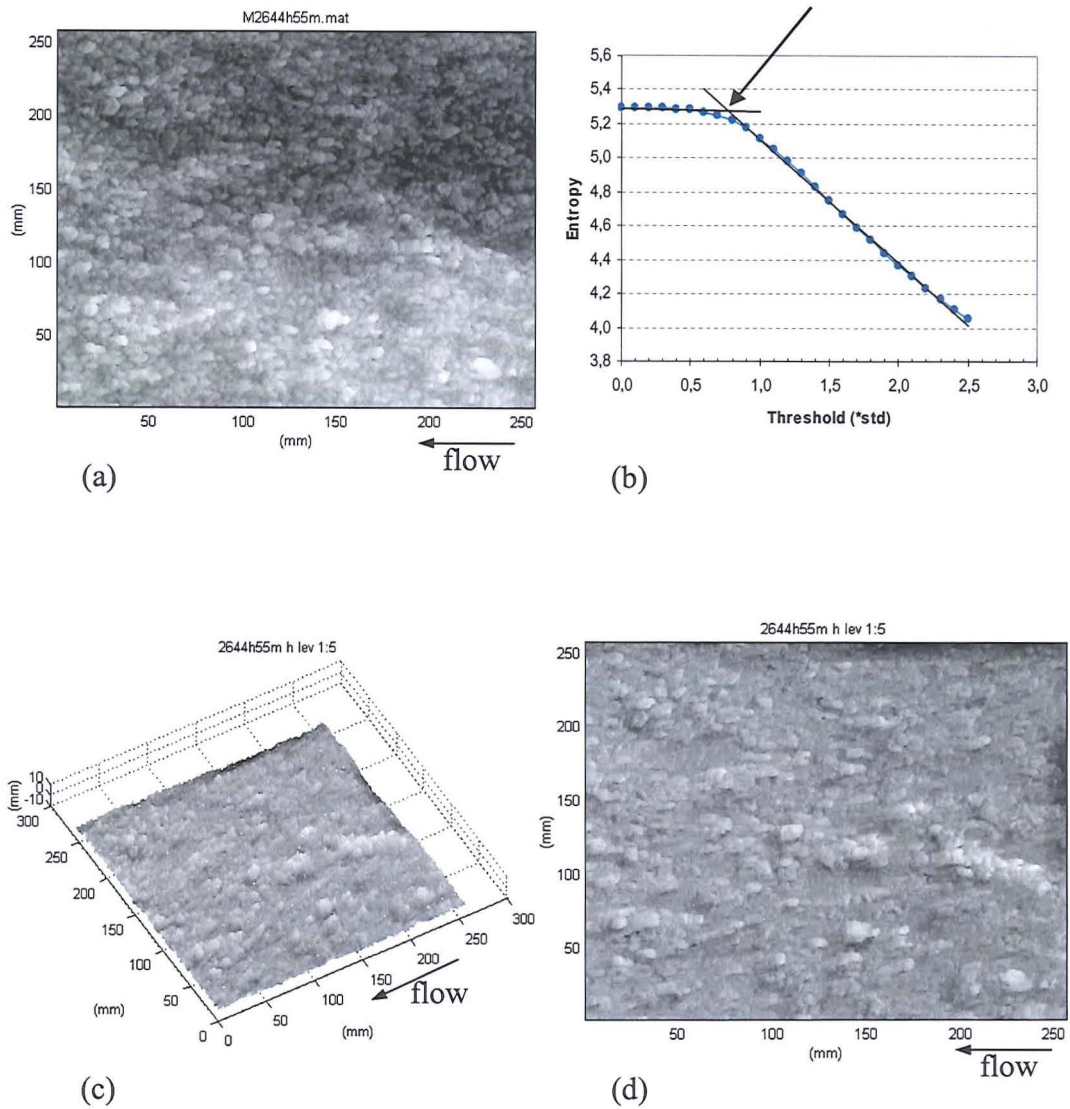


(b)

(a) Reconstructed experimental sediment surface applying a threshold value of  $2.5 \times \sigma$  and (b) the reconstruction of the same surface applying a threshold value of  $3.0 \times \sigma$

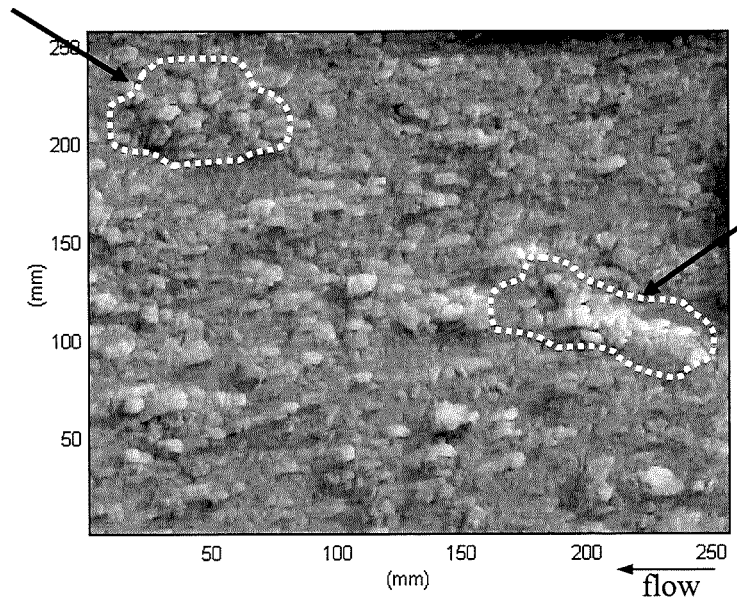
**Figure 5.29** Reconstruction of sediment surface (data-set '2644h55m') using threshold values  $2.5 \times \sigma$  and  $3.0 \times \sigma$ .



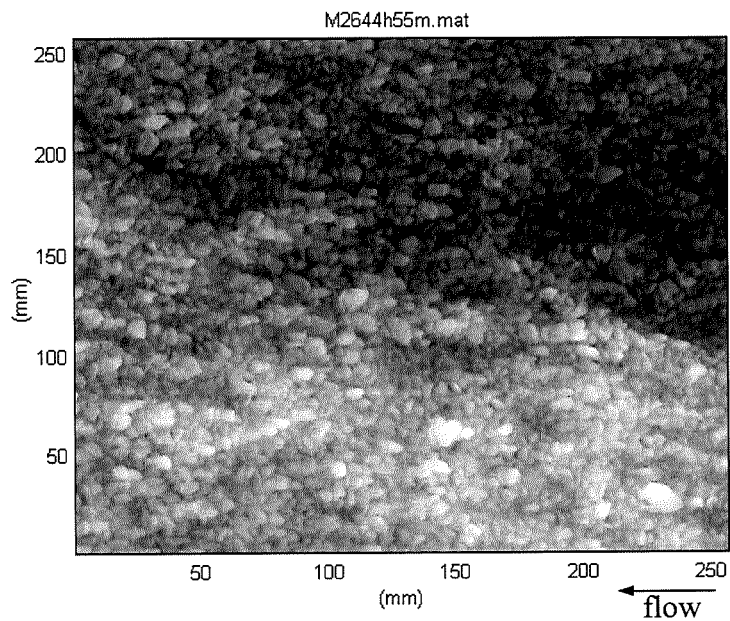


(a) The original river-bed sediment surface (data-set '2644h55m'), (b) the total entropy for the reconstructed surface in (a) for increasing threshold values and (c) and (d) the thresholded and reconstructed surface using a threshold value of  $0.75 \times \sigma$ .

**Figure 5.30** Thresholding of experimental river-bed sediment surface.



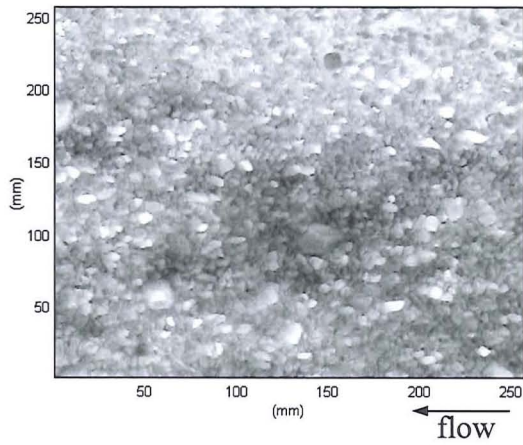
(a)



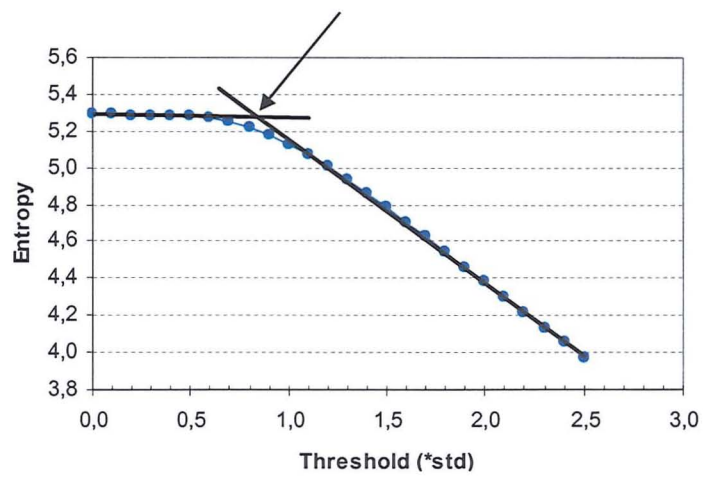
(b)

(a) The thresholded reconstructed surface where possible coherent structures have been marked with dotted lines and as a comparing (b) the original sediment surface.

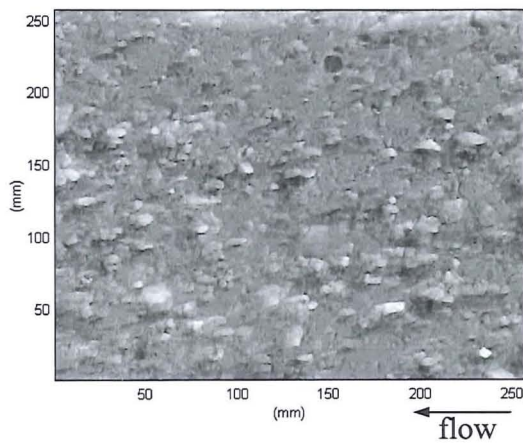
**Figure 5.31** Enhancement of possible coherent structure.



(a)



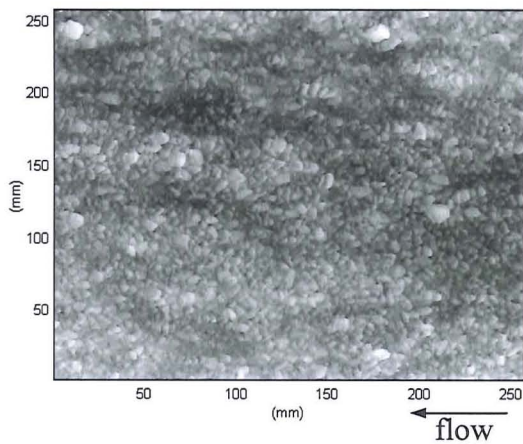
(b)



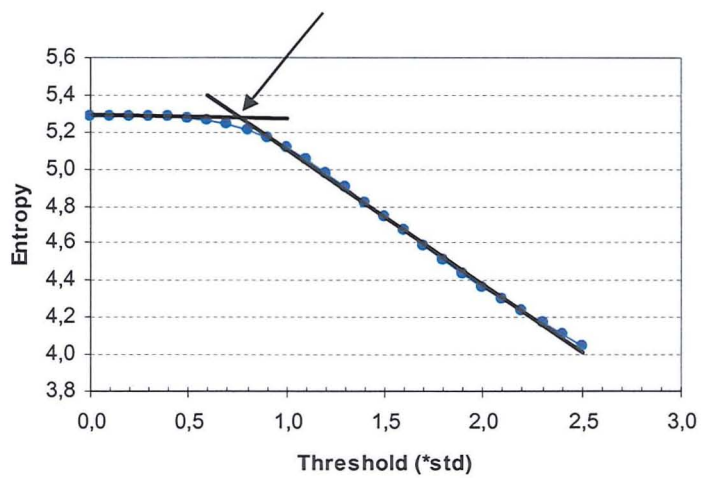
(c)

(a) The original data, (b) the entropy curve, cross section at approximately  $0.85 \times \sigma$  and (c) the reconstructed surface.

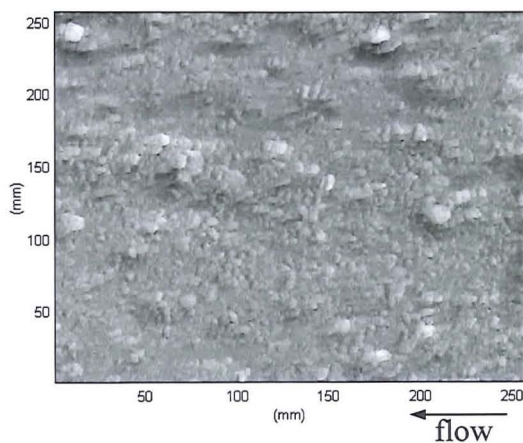
**Figure 5.32** Thresholding of experimental riverbed sediment surface, data-set '2631h00m'.



(a)



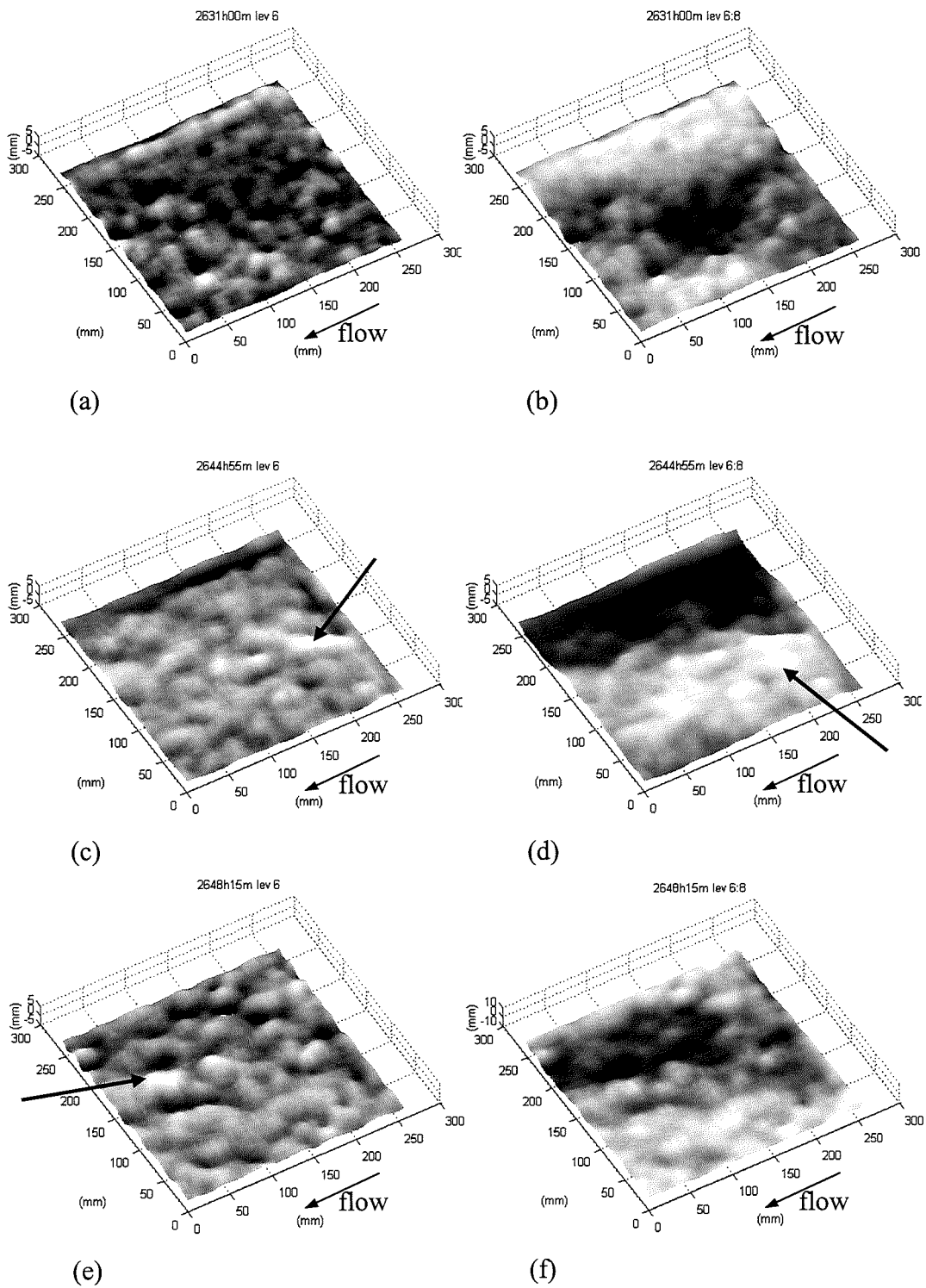
(b)



(c)

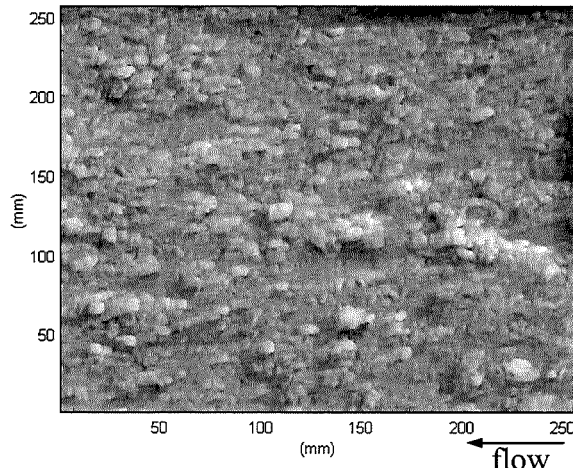
(a) The original data, (b) the entropy curve, cross section at approximately  $0.8 \times \sigma$  and (c) the reconstructed surface.

**Figure 5.33** Thresholding of experimental rived-bed sediment surface, data-set '2648h15m'.

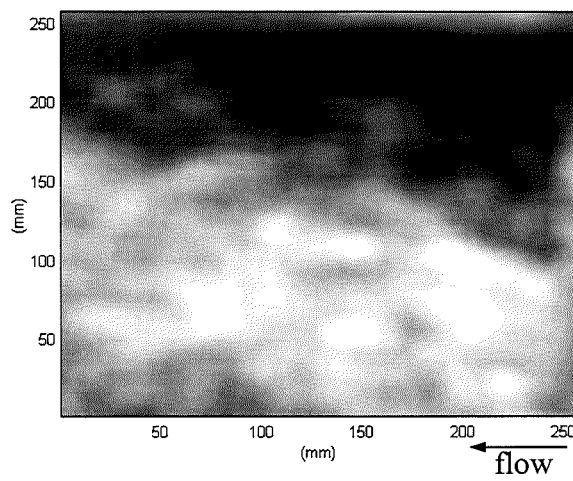


Reconstruction using detail 6 (left) and reconstruction using detail 6 to 8 (right).

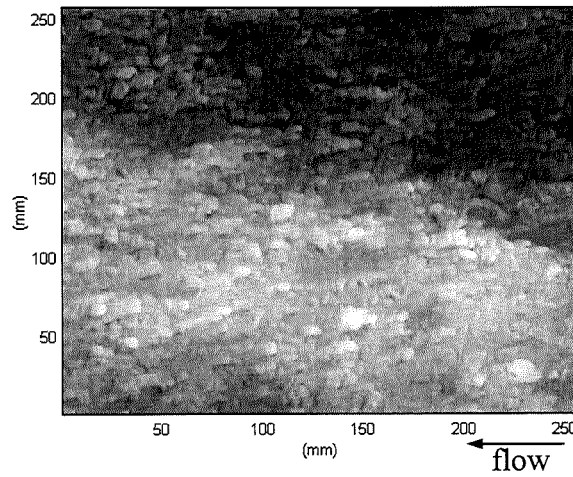
**Figure 5.34** Applying scale dependent thresholding to the sediment data.



(a)



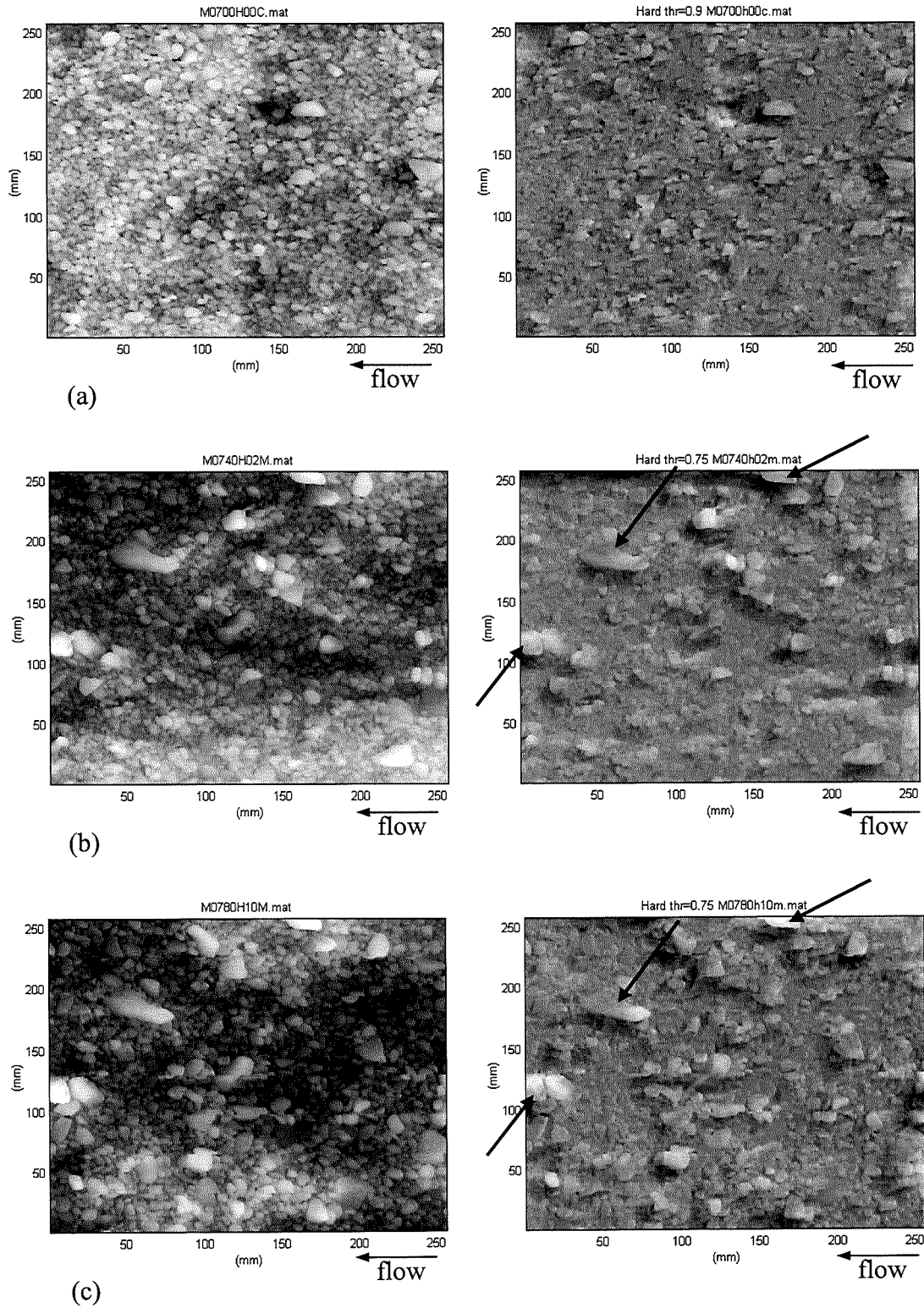
(b)



(c)

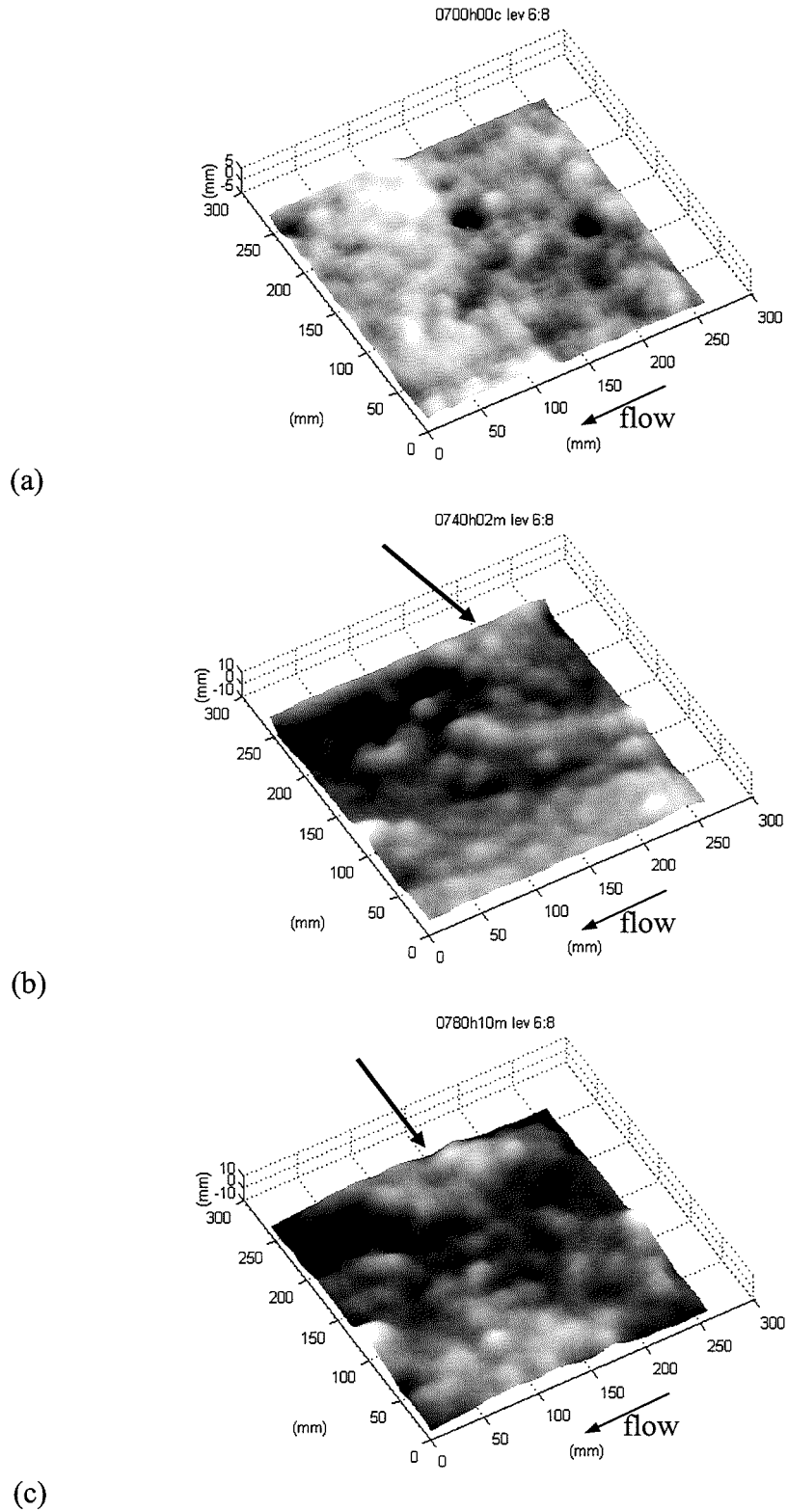
(a) Amplitude thresholded surface, (b) scale thresholded surface and (c) reconstruction combining (a) and (b).

**Figure 5.35** Reconstruction combining amplitude and scale threshold.



(a) Initial surface, data-set '0700h00c', (b) surface after 40hours running, data-set '0740h00m' and (c) the final surface scan, data-set '0780h00m'

**Figure 5.36** Applying amplitude thresholding to selected sediment surfaces in experiment 7 (right).



(a) Initial surface, data-set '0700h00c', (b) surface after 40hours running, data-set '0740h00m', and (c) the final surface scan, data-set '0780h00m'

**Figure 5.37** Applying scale dependent thresholding to selected sediment surfaces in experiment 7.



## **Chapter 6**

### **Summary of conclusions, discussion and recommendations**

- 6.1 Introduction**
- 6.2 Achievement of the aims**
- 6.3 Summary of completed work**
  - 6.3.1 Characterisation of profile traces**
  - 6.3.2 Global surface characterisation**
  - 6.3.3 Local feature recognition**
- 6.4 Conclusions from this thesis**
- 6.5 Recommendations for future research**

# CHAPTER 6

## SUMMARY OF CONCLUSIONS, DISCUSSION AND RECOMMENDATIONS

### 6.1. Introduction

This chapter summarises the work presented in this thesis. It is structured as follows: section 6.2 discusses the achievement of the aims detailed in chapter 1. Section 6.3 contains a summary of the main results from the analysis presented in previous chapters. Section 6.4 presents the main conclusions from the work carried out and, finally, section 6.5 provides recommendations for possible future investigations.

### 6.2. Achievement of the aims

The research was carried out to study the morphological changes occurring in river-bed sediment surfaces over time using wavelet transform-based analysis techniques. The aims, as stated in chapter 1, were:

1. to characterise the topographical structural behaviour of experimental river-bed sediment surfaces over time using wavelet transform-based tools,
2. to separate bed form features within the experimental river bed sediment surfaces using the wavelet thresholding technique.

To accomplish these aims the following objectives were established:

1. to undertake a literature review to appraise current applications of the wavelet transform as a method for surface analysis,
2. to develop computer algorithms for overall characterisation of the sediment surface data,
3. to develop computer algorithms for the enhancement of local surface features in the data,
4. to apply the developed algorithms to analyse both synthetic and experimental sediment surfaces data.

The work carried out attempted to meet all of these aims and objectives. However, a number of problems occurred which caused time delays to the project. The most significant difficulty was the relatively poor quality of the experimental rived-bed sediment surface data-sets used in the study. The data-sets contained a number of drop-out points which had to be dealt with prior to continuing the analysis and a significant amount of time was spent by the author in developing an algorithm to deal with these drop-out values prior to the main analysis work. Hence, less time was available to investigate the characteristics of the surfaces.

### **6.3. Summary of completed work**

This section contains a summary of the main results from this work.

#### **6.3.1. Characterisation of profile traces**

An initial investigation was undertaken using the 1-D wavelet transform to appraise its use as a profile characterisation tool.

A calibration study to test the method was carried out using synthetic fractional Brownian motion ( $fBm$ ) profile data with known scaling properties, characterised using the Hurst exponent ( $H$ ) scaling parameter. It was shown how the wavelet transform can be used effectively to characterise synthetic  $fBm$  profile data. The results showed small

differences between the known values of  $H$  and that determined using the wavelet transform-based method. Previous research by others has shown that for certain techniques  $H$  may only be determined with reliable accuracy for  $0.2 \leq H \leq 0.9$ . This was also found by the author for the results obtained using the wavelet transform method. These results are tabulated in table 3.3. For the cracked concrete profile data the mean value of  $H$  was found to be 0.84, 0.84 and 0.87 for the small, medium and large sized beams respectively using the DWT. Using the SWT the corresponding results were 0.83, 0.84 and 0.88 for the small, medium and large sized beams respectively. This is in agreement with previous studies by other authors who have shown that cracked concrete profiles have a scaling exponent close to  $H=0.8$ .

A brief study of medical signals (pulse oximeter waveforms) using the DWT indicated that the 1-D DWT can effectively remove both noise and signal drift from noisy pulse oximeter signals using a basic smoothing method. The DWT was also applied to determine the frequency content of two different types of ECG signals. The result showed a peak of 6.25 Hz for the ROSC signals and two peaks of 6.25 Hz and 3.13 Hz for the asystole signals. However, the technique was not able to determine shock outcome with the accuracy necessary for implementation within a medical device.

This preliminary work allowed the author to develop her skills by employing both 1-D discrete and 1-D stationary wavelet transform methods, prior to her main work concerning the analysis of surface data using 2-D wavelet transform techniques.

### **6.3.2. Global surface characterisation**

This study involved the development of a wavelet transform-based method to characterise the global topological characteristics of experimental river-bed sediment surfaces.

Prior to the analysis, drop-out values were removed from the surface data-sets. A number of methods were tried, of these Delaunay triangulation produced the best estimation of the true values at the locations of the drop-out points, especially at the edges of the data. The original experimental river-bed sediment surface data was therefore modified using this method prior to the main analysis.

Initial investigations showed that significant edge effects appear around the boundaries of the wavelet transform details. Algorithms were developed to remove these erroneous edge coefficients from the detail coefficients, whereby only the contribution to each scale detail from the surface components untainted by the edge remained in the analysis.

By plotting the cumulative scale dependent energy of the transform against scale, a distribution of the surface forms was generated: the *form size distribution (fsd)*. It was argued that this measure is more useful than the traditional *particle size distribution (psd)*, as it is the topographical form of the surface rather than the individual particle sizes that affect the near bed flow regime and hence bed friction characteristics. The analysis produced a number of *fsd* curves for each experiment. Studying the *fsd* curves it was shown that some data-sets exhibit a higher quantity of proportional energy at larger scale forms. It is suggested that this indicates larger topographical differences in the surface while a smaller amount of large scale energy represents a rather flat surface topography.

It was difficult to distinguish an obvious degradation pattern within each experiment. As sediment material is fed into the flume through the experiments (in all except one) a global equilibrium in the amount of sediment in the channel is soon reached. Further, the scanned area is relatively small, hence if particle structures form and/or break up in this region this leads to largely variable *fsds* over time (i.e. no local equilibrium in the sediment volume within the scanned area is achieved). Potential degradation can be seen in the results of the analysis for some of the experiments, which suggests that this method would be useful for detecting the coarsening of the sediment surface structure. However, verification of this would probably require a much larger scan size.

The research also showed that the DWT results in poorer reproducibility compared to the SWT. This is because the DWT downsamples the data at each level, hence at the larger scales only a few wavelet coefficients are produced. As the SWT does not involve downsampling it is more consistent over all scales and especially at larger scales. It was therefore recommended that computation of the *form size distribution* is performed using the SWT.

### **6.3.3. Local feature recognition**

This study investigated the use of wavelet thresholding techniques to identify local features on the sediment surfaces. An amplitude threshold was applied to extract dominant grains and a scale dependent threshold was applied to extract large-scale formations of grains within the surfaces.

The amplitude thresholding technique was tested using synthetic data. Evaluating the thresholding performance based on the energy content it was found that there is a much faster reduction in energy content for the background surface region compared to the feature region. In addition, there is an increase in the hard thresholded energies compared to the soft thresholded energies. However, no 'ideal' threshold value could be established and hence the Shannon entropy measure was applied.

The results showed that the entropy in the background decreases over the thresholding process, i.e. these surface components are reduced. However, the entropy for the feature increases indicating that the feature in fact gains components. It was concluded that the increase in feature entropy was due to the presence of edge effects in the reconstruction and the decrease of information within the whole surface. Further, the total entropy curve changes slopes through the thresholding process. Two distinct transition points between the slopes of the curve could be identified. The second of these transition points is located at the threshold value which was applied to extract the feature and completely remove the background. However, it was suggested that the initial transition point was related primarily to the reduction of smaller coefficients in the background surface and hence this would be an 'ideal' threshold value to apply to retain larger coefficients in the reconstruction and therefore enhance dominant features within the surface.

The results from the laboratory experimental sediment surface data analysis demonstrated that the proposed method could be used to enhance dominant grains within the surface for visual detection. The result showed that the later surface scans had more visible structures compared to the earlier surface scans. This is particularly evident in the unfed experiment shown in figure 5.36. Further, by applying a scale dependent wavelet threshold, the overall surface structure was obtained. The result

showed larger structural variations in the later surface scans compared to the initial surface scan, shown in figure 5.37. This would suggest that, for these experiments, the major degradation of the surface appears in the early stages of the sedimentation process. Evaluating the surface using these two thresholding methods allowed for structural changes over time to be detected.

#### **6.4. Conclusions from this thesis**

The following conclusions can be drawn from the work conducted in this thesis:

The discrete wavelet transform (DWT) has poorer reproducibility compared to the stationary wavelet transform (SWT). The DWT downsamples the data at each level, hence at the larger scales only a few wavelet coefficients are produced. In the study, conducted using synthetic sediment background surfaces, it was shown that the SWT is more consistent over all scales and especially at larger scales.

An amplitude wavelet threshold can be applied to highlight dominant grains within the surfaces. The study applied an amplitude threshold to extract dominant grains within the surfaces. The threshold value was determined in terms of total entropy measure. A transition point between the slopes of the entropy curve was identified as the ‘optimal’ threshold value to use to filter out less significant information and therefore enhance larger features (i.e. dominant grains) within the surface.

A scale threshold can be used for extract the general form of the surface. As the general overall form size of the surface is found within the large-scale details a scale threshold can be used to filter out these details.

The cumulative distribution of scale related wavelet detail energy provides a measure of the form sizes within the surfaces: the *form size distribution (fsd)*. As each wavelet scale detail can be related to a specific real physical size, this allows the prevalence of surface forms to be revealed.

The *fsd* measure could potentially be more useful than the traditional *particle size distribution (psd)*. It is argued that this is because the topographical form of the surface

rather than the individual particle sizes is likely to affect the near bed flow regime and hence bed friction characteristics.

The overall topography is related to the amount of large scale energy. Studying the results it is apparent that some of the *fsds* exhibit a higher quantity of proportional energy at larger scale forms. It is suggested that this shows larger topographical differences in the surface while a smaller amount of large-scale energy (often found in the initial *fsd*) is representative of a rather flat surface topography.

Because of the relatively small physical size of the scanned surfaces used in the analysis, highly variable *fsd* curves were produced over time. Local topographical changes in the scanned sediment surface area over time cause distinct changes in the *fsds*.

Erroneous edge effects coefficients may be taken account of in the analysis. The study showed that, due to misalignment between the edges of the data erroneous (usually large), edge effect coefficients are produced at the boundaries of the wavelet details. Algorithms were therefore developed which identified and removed the number of erroneous edge coefficients at each end of the transformed data where only the ‘valid’ coefficients were retained for further analysis.

## **6.5. Recommendations for future research**

This final section provides brief outline suggestions for future work stemming from this thesis. These are given below.

- This study has shown the potential of the wavelet transform as a sediment surface characterisation tool. However, to assess the use of the wavelet transform completely it is necessary to analyse further sediment surface data sets. The study described herein was limited because the scanned area of the sediment surface bed was relatively small and therefore largely variable *fsds* were produced over time. A more complete evaluation could be undertaken with further measurements of sediment surface beds using different sizes of arrays and space settings of the laser



profilometer. Further, from the results in experiment 7 (i.e. where no sediment material was fed into the flume) it appears that the major degradation occurred between the first and second data-sets. Therefore measuring the sediment surface at shorter time intervals at the beginning of the experiment may produce a clearer picture of the initial surface degradation of the sediment surface through wavelet analysis. These are pertinent issues to be investigated in future studies. The work carried out in this thesis should serve as a basis for such investigation.

- A preliminary study was carried out comparing the proposed wavelet based characterisation method, *fsd*, with the phases of mobility in the surface bed. However, from this study no obvious link between the changes in the *fsd* and the mobility data could be concluded. This could therefore be an interesting area for future research.
- This project aimed to investigate the use of the wavelet transform as a river-bed sediment surface characteristics tool, however the methods presented could be of potential use in other areas of civil engineering. One area that might benefit is the determination of the roughness inside pipes which are in use and may have changed over time. This is currently determined through visual inspection of the surface.
- Due to time limitations in the project, the work completed for the research was not able to fully scrutinise wavelet thresholding of the experimental sediment surface data. The current investigation highlighted the possibility of applying wavelet amplitude thresholding to extract dominant grains within sediment surfaces. An attempt was made to identify an 'ideal' threshold value for extracting these features based on the measurements of the total entropy. It was only possible to analyse limited number of experimental data-sets in this study. Future studies could therefore include complete sets of experimental sediment surface data-sets to fully evaluate the wavelet thresholding technique as a tool to detect movement of sediment material over time.

## **APPENDICES**

## Appendix A

<i>Program</i>	<i>page</i>
fBmgen.m.....	310
fBm_dwt.m.....	311
fBm_swt.m.....	312
prof_dwt.m.....	313
prof_swt.m.....	314
interp1.m .....	315
interp2.m .....	316
modcorn.m.....	317
fsddwt.m.....	318
fsdswt.m .....	320
file_energy.....	321
file_entr1.m .....	322
file_entr2.m .....	322

**Program: fBmgen.m**

**Generating fractional Brownian motion (fBm) traces**

```

M=10; % max level
N=2^M; % number of points in fBm signal
NT=100; % number of traces
MEM=6*N; % memory required to give fBm good statistics
Kf=10; % diffusion type coefficient, (spreading of the trace)

H=0.7; % scaling property
gam=1/gamma(H+0.5); % gamma function used in definition of fBm
r_1=randn(NT,MEM+N); % generating vector of normally distributed random numbers
r_1=r_1*((2*Kf)^0.5)*(1^H);

afbm=zeros(NT,N);
for k=1:NT;
    for i=1:N
        fbm1=0;
        fbm2=0;
        for j=i-MEM:-1
            fbm1 = (fbm1+(i-j)^(H-0.5) - (j)^(H-0.5) ) *r_1(k,j+MEM));
        end
        for j=0:i-1
            fbm2= (fbm2+(i-j)^(H-0.5) ) *r_1(k,j+MEM));
        end
        afbm(k,i)=fbm1+fbm2;
    end
end
afbm=afbm.*gam;
size(afbm)
save('c:\fbm\fbm\fbm07.dat','afbm','-ASCII');

```

*Program: fBm\_dwt.m*

**Determine scaling properties of fBm traces using the DWT**

```

                                % wavelet information
wname='db2';                    % wavelet used
dwtmode('per');                % wavelet mode
[Lo_D,Hi_D,Lo_R,Hi_R] = wfilters((wname));    % wavefilters
[F1,F2]=wfilters((wname),'d'); % d=decomposition filter, F1=low pass and F2=high pass

NF=length(F1);
NE=floor((NF/2)/2);
NT=100;                        % number of fBm profiles
M=10;                          % maximal level of decomposition

for k=1:NT;
    y=x(k,:);
    si=size(y);
    len=length(x);

                                % DWT - decomposition
    [A,L] = wavedec(y',M,F1,F2); % A = the wavelet decomposition vector,
                                % L = bookkeeping vector

                                % modifying the wavelet coefficients
    if NF>2;
        for m=1:M;
            coeflength=2^(M-m);
            leftedge(m)= NE;    % number of edge coefficients, left edge
            rightedge(m)= NE;  % number of edge coefficients, right edge

            a {m}=detcoef(A,L,m);
            a {m}=a {m}(NE+1:coeflength-NE,:); % excluding the edge coefficients
            alen=length(a {m});

            if alen>0;          % calculating the variance of the traces

                V(k,m)=(sum(sum(a {m}.^2)/(alen)));

            end
        end
    end
end
avevar=sum(V)/NT;             % calculating the mean variance

```

*Program: fBm\_swt.m*

**Determine scaling properties of fBm traces using the SWT**

```

                                % wavelet information
dwtmode('per')                % wavelet mode
wname='db2'                   % wavelet used
[Lo_D,Hi_D,Lo_R,Hi_R] = wfilters((wname))           % wavefilters
[F1,F2]=wfilters((wname),'d'); % d=decomposition filter, F1=low pass and F2=high pass
NF=length(F1)

NT=100;                        % number of traces
M=10;                          % maximal level of decomposition

for k=1:NT;
    y=x(k,:);
    storlek=size(y)
    len=length(y)

                                % SWT - decomposition
    [swa,swd] = swt(y,M,(wname));

                                % modifying the wavelet coefficients
    for lev = 1:M;
        lev;
        leftedge=[(2^lev-1)*(NF/2-1)];           % number of edge coefficients, left edge
        rightedge= [((2^lev-1)*(NF/2))];        % number of edge coefficients, right edge
        x=zeros(1,2^M);

        x=[swd(lev,(leftedge+1:len-rightedge))]; % excluding the edge coefficients
        xlen=length(x);

        if xlen>0;                    % calculating the variance of the traces

            var(k,lev)=(sum(sum(x.^2))/(xlen));
        end
    end
end

avevar=sum(var)/NT                % calculating the mean varaince

```

**Program: prof\_dwt.m**

**Determine scaling properties of concrete crack profiles using the DWT**

```

load c:\crack_data\m4r.dat -ASCII          % load the file
 profname = 'm4r';

                                % wavelet information
wname='db2'                        % wavelet used
dwtmode('per')                    % wavelet mode
[Lo_D,Hi_D,Lo_R,Hi_R] = wfilters((wname)) % wavefilters
[F1,F2]=wfilters((wname),'d');     % d=decomposition filters, F1=low pass and F2=high pass
Energy=sum(sum(y.^2))
M=11;                              % maximal level of decomposition

                                % DWT - decomposition
[A,L] = wavedec(y,M,F1,F2);       % A = the wavelet decomposition vector
                                % L = bookkeeping vector

                                % modifying the wavelet coefficients
NF=length(F1);
NE=floor((NF/2)/2);

if NF>2
  for m=1:M
    coeflength=2^(M-m);
    leftedge(m)= NE;              % number of edge coefficients, left edge
    rightedge(m)= NE;            % number of edge coefficients, right edge

    a{m}=detcoef(A,L,m);
    a{m}=a{m}(NE+1:coeflength-NE,1); % excluding the edge coefficients
    alen=length(a{m});

    if alen>0;                   % calculating the variance for the profile
      V(m)=(sum(sum(a{m}.^2)/(alen)));
    end
  end
end

                                % plotting the variance against the scale
figure; plot(log(V)/log(2), 'b-o');
title(['Variance ', (profname),', DWT, Daub4 (4 filtcoef), mod coef, per']);
xlabel('level'); ylabel('log(var)/log(2)');

varri=log(V)/log(2);
save variance varri -ascii;

```

**Program: prof\_swt.m**

**Determine scaling properties of concrete crack profiles using the SWT**

```

load c:\crack_data\m4r.dat -ASCII          % load the file
profname = 'm4r';
y=m4r(1:2^M,2);

                                % wavelet information
dwtmode('per')                    % wavelet mode
wname='db2'                        % wavelet used
[Lo_D,Hi_D,Lo_R,Hi_R] = wfilters((wname)) % wavefilters
[F1,F2]=wfilters((wname),'d');     % d=decomposition filters, F1=low pass and F2=high pass
NF=length(F1);                    % length of the wavelet filter
len=length(y);
M=11;                              % maximal level of decomposition

                                % SWT - decomposition
[swa,swd] = swt(y,M,(wname));

                                % modifying the wavelet coefficients
for lev = 1:M;
    lev;
    leftedge=[(2^lev-1)*(NF/2-1)]; % number of edge coef, left edge
    rightedge= [(2^lev-1)*(NF/2)]; % number of edge coef, right edge
    x=zeros(1,2^M);
    x=[swd(lev,(leftedge+1:len-rightedge))]; % excluding the edge coefficients
    xlen=length(x)
    if xlen>0;
                                % calculating the variance of the profile
        var(lev)=(sum((sum(x.^2))/xlen)) % divide by 2^lev for SWT energies!
    end
end

                                % plotting the variance against the scale

figure; plot(log(var)/log(2),'b-o');
title(['Variance ', (profname), ', SWT, Daub4 (4 filtcoef), mod coef, per']);
xlabel('level'); ylabel('log(variance)/log(2)');

```



**Program: interp1.m**

**Removing drop-out points, linear interpolation (row and columns)**

```

A = [file]; Z=A(:,3);
len=length(Z)/512

drop=find(matrix <-900);           % finding the number drop-out points in the data set, i.e.
ledrop=length(drop)               % ...values <-900
[i,j]=find(matrix <-900);

m=[ ];
x=(1:len);                        % the length of the row

for NN=1:512;

    y=matrix(NN,:);               % picking out the NN row and all the columns in that row.
                                % change to (:,NN) to pick out columns instead to produces...
                                % ... matrix2

    yy=[ ];
    xx=[ ];

    for i=1:len;                  % picking out the values to interpolate, less than -900
        if y(i) < -900;
            else

                yy=[yy,y(i)];      % putting the values into new vectors
                xx=[xx,x(i)];
            end
        end
        length(x);
        length(xx);
        if length(x) ~= length(xx);

            y = interp1(xx,yy,x,'linear', 'extrap'); % determine the new values of the vector using

        end
        matrix1(NN,:) = y;        % saving the values into matrix
    end

    drop=find(matrix <-100);     % checking the matrix for drop-out values.
    ledrop=length(drop)

matrix=(matrix1+matrix2)/2       % new matrix without drop-out points.

```

**Program: interp2.m**

**Removing drop-out points, interpolation using triangulation**

```

for j=1:5;
    file_name=filelist(j);
    filename = ['c:\matlabR12\work\Surface\1900\',dirdetails(j).name];
    load_file=load(filename,'-ASCII');
    AA=[load_file];
    size(AA);
    len=length(AA)

drop=find(A<-900);           % finding the number of drop-out points in the matrix
dropfi=length(drop)
si=length(load_file)

if si==262144;              % using only surface data with size 512x512, i.e. 262144 data
                             % ... points

    [rows cols]=size (A);
    x=[ ];
    y=[ ];
    z=[ ];

for i=1:rows;               % removal of drop-out points, the code keeps only values
                             %... greater then -900

    if(A(i,3)>-900);
        x=[x,A(i,1)];
        y=[y,A(i,2)];
        z=[z,A(i,3)];
    end
end

ti = 0:0.5:255.5;
tj = 128:-0.5:-127.5;
[XI,YI]=meshgrid(ti,ti);   % making up a new grid [XI,YI]
ZI = griddata(x,y,z,XI,YI); % the new values are interpolated on the grid [XI,YI]

ZI;
drop=find(ZI <-500);       % checking if all the drop-out points have been removed
droppoints=length(drop)
time=cputime-t

```

*Program: modcorn.m*

**Compensate for 'missing' bottom right corner**

```

load c:\Surface\Sediment\Griddata\FILE.mat -ASCII;
profname = 'FILE.m';
matrix=[FILE.m];

x2=matrix(1:100,(512-100):512));

drop=find(matrix==NaN);           % finding the NaN in the matrix
drop_out=length(drop);           % finding the number of NaN in the matrix
[i,j]=find(~isnan(matrix));      % returns 1 if not equal to NaN

before=matrix(1,:);
x=1:512;
for i=1:512;

    xx=[ ]; yy=[ ];

        y=matrix(i,:);           % going through each row of the matrix
        j=find(~isnan(y));       % locating NaN (if any) at each row
        y(j);

        yy=[yy,y(j)];
        xx=[xx,x(j)];

        if length(x) ~= length(xx);
            yi=interp1(xx,yy,x,'nearest','extrap');           % determine the new values of the vector
                                                                %...using extrapolate.

        xxstart=xx(1);
        xxend=xx(end);
        y(1:xxstart-1)=y(xxstart);
        y(xxend+1:(length(y)))=y(xxend);

    end
    matrix(i,:)=y;
end

```

*Program: fsddwt.m*

**fsd - edge effects 2-D DWT**

```

MM=13; % determine size edge coefficients
lenn = 2^MM; % make this level much greater than the size of the
% analysed data so the edge coefficients will be right.

i=1:lenn;

xx(i)=0; xx(lenn)=1; % length of edge coefficients
yy(i)=0; yy(1)=1; % putting last coefficient to a number (left)
% putting first coefficient to a number (right)

[Al,Ll] = wavedec(xx,MM,F1,F2);
[Ar,Lr] = wavedec(yy,MM,F1,F2);

edright=[ ]; edleft=[ ];

al=[ ];
ar=[ ];
for mm=1:MM;
    al{mm}=detcoef(Al,Ll,mm); % top and left edge
    edtop(mm)=length(find(al{mm}((1:(2^(MM-mm))/2))~=0)));
    edleft(mm)=length(find(al{mm}((1:(2^(MM-mm))/2))~=0)));

    ar{mm}=detcoef(Ar,Lr,mm); % bottom and right edge
    edbottom(mm)=length(find(ar{mm}(((2^(MM-mm))/2)+1:end)~=0)));
    edright(mm)=length(find(ar{mm}(((2^(MM-mm))/2)+1:end)~=0)));
end

% the discrete wavelet transform
[C,S] = wavedec2(x,M,wname);
exdata=512-len % compensate for extra data at beginning

for lev= 1:M;
    Nocoef_org(lev)=(2^(M-lev))^2; % number of original coefficients at...
    % ...each scale
    Nocoef(lev)=(2^(M-lev)-edtop(lev)-edbottom(lev))... % number of 'true' coefficients left at
    *(2^(M-lev)-edleft(lev)-edright(lev)); %...each scale after modifying the edges

    le(lev)=(2^(M-lev)-edleft(lev)-edright(lev));

    add{lev}(1:lev,1:lev)=0; % extracting wavelet coefficients from the transform
    h{lev} = detcoef2('h',C,S,(lev)); v{lev} = detcoef2('v',C,S,(lev));
    d{lev} = detcoef2('d',C,S,(lev)); a{lev} = detcoef2('a',C,S,(lev));

    add1 {lev}=h{lev}+v{lev}+d{lev};
    langd(lev)=length(add1 {lev});

    if langd > le;
        % removing edge coefficients from the transformed matrix
        add {lev}=add1 {lev}(((edtop(lev))+1):(2^(M-lev))-edbottom(lev)),...
        (((exdata-1)/2^(lev))+edleft(lev)+1):(2^(M-lev))-edright(lev));

        eng(lev)=(sum(sum(add{lev}.^2))); % energy of the details coefficients

    if eng(lev)>0; % mod. for area difference
        eng2(lev)=(eng(lev)*(Nocoef_org(lev)/Nocoef(lev)));
    end
end

```

Appendix A

```
end
end

                                % the form size distribution (fsd) based on the DWT
totaleng=sum(sum(eng2));

for lev=1:M;
  if eng(lev)>0;
    FSD1(lev)=((eng2(lev)/totaleng)*100);           % determine the % of energy at each
                                                    %...scale
    FSD2(lev)=sum(FSD1(1:lev));                   % adding the FSD1 together
  end
end

FSD2
```

*Program: fsdswt.m*

**fsd - edge effects 2-D SWT**

```

M=9; mm=2^M;
matrix=A(1:mm,1:mm);
x=matrix; % surface data

wname='db2'; % analysing wavelet information
[A,H,V,D] = swt2(x,M,wname);
[F1,F2]=wfilters((wname),'d'); % wavelet filter
N=length(F1)

for lev= 1:M; % determine the size of the edge coefficients

    edtop=((2^lev)-1)*(N/2-1); % number of edge coefficients at the top and left edges
    edleft=((2^lev)-1)*(N/2-1);
    edbottom=((2^lev)-1)*(N/2); % number of edge coefficients at the bottom and left edges
    edright=((2^lev)-1)*(N/2);

    Ncoef_org(lev)=(2^M)^2; % number of original coefficients at each level

    Ncoef(lev)=(2^M-edtop-edbottom)... % no. of 'true' coefficients left at each
        *(2^M-edleft-edright); % ... level after mod. the edges

    le=length(H(1,,:),lev) % length of the matrix
    le2=(le-edleft-edright) % minus size of edge effects if le2<0 all edge
        % effects i.e. no coe. left in matrix

        if le2 > 0;
            HH(:, :, lev)=H(:, :, lev)/4^(lev/2);
            VV(:, :, lev)=V(:, :, lev)/4^(lev/2);
            DD(:, :, lev)=D(:, :, lev)/4^(lev/2);

            add = HH(((edtop + 1):(2^M)-edbottom),((edleft+1):(2^M)-edright)),lev)...
                +VV(((edtop + 1):(2^M)- edbottom),((edleft+1):(2^M)-edright)),lev)...
                +DD(((edtop+1):(2^M)- edbottom),((edleft+1):(2^M)-edright)),lev);

            % detremine the energy
            energy(lev)=(sum(sum(add.^2)))*(Ncoef_org(lev)/Ncoef(lev))
            engtot=(energy(lev)+engtot)
        end
    end
end % the form size distribution (fsd) based on the SWT

for lev=1:(M-2);
    if le>0;
        dist(lev)=(energy(lev)/engtot)*100;
        dist2(lev)=sum(dist(1:lev));
    end
end

dist2
energy

```

*Program: file\_energy.m*

**Determine the energy content in the feature and the background part**

```

                                % setting the masks for the analysis
xmaskinside=zeros(m,n);
xmaskoutside=zeros(m,n);
xmaskinside(find(xdiffnorm>4))=1;           % feature mask
xmaskoutside(find(xdiffnorm<4))=1;         % background surface mask

                                % original energy in the surface
energy_org=sum(sum(x.^2))                 % total energy
energydiamond_org=sum(sum((x.*xmaskinside).^2)); % energy in feature part
energysurf_org=sum(sum((x.*xmaskoutside).^2)); % energy in feature part
ration_D_S = (energydiamond_org/energysurf_org);

                                % stationary wavelet transform
ETOTAL=sum(sum(x.^2))
wname='db1'
dwtmode('per');
M=4;
[A,H,V,D] = swt2(x,M,wname); si=size(A)

for lev=1:M;                          % standard deviation for the details

std=sqrt(( sum(sum(H(:, :, lev).^2+V(:, :, lev).^2+D(:, :, lev).^2))/(rows*columns));

                                % thresholding the transform coefficients
                                % threshold value for each scale
thres=std*(mults);
H(:, :, lev) = wthresh(H(:, :, lev),(thr),thres);
V(:, :, lev) = wthresh(V(:, :, lev),(thr),thres);
D(:, :, lev) = wthresh(D(:, :, lev),(thr),thres);
end

                                % reconstruction
XADD(1:m,1:n)=0;
for lev=1:M;
    HH=H(:, :, lev)/4^(lev/2);
    VV=V(:, :, lev)/4^(lev/2);
    DD=D(:, :, lev)/4^(lev/2);
X=iswt2(HH,wname)+iswt2(VV,wname)+iswt2(DD,wname);
size(X);
XADD=XADD+X;
end

                                % energy in the thresholded surface
energytotal=sum(sum(XADD.^2));           % total energy
energydiamond=sum(sum((XADD.*xmaskinside).^2)); % energy in feature part
energysurf=sum(sum((XADD.*xmaskoutside).^2)); % energy in feature part

```

**Program: file\_entr1.m**

**Measure of entropy**

```

                                % XADD is the thresholded and reconstructed surface
XMODADD=abs(XADD)^2;                                % absolute values of the XADD surface
XMODSUM=sum(sum(XMODADD));
XPROB=XMODADD./XMODSUM;

ENTROPYINC=zeros(m,n);
for ii=1:m;
    for jj=1:n;
        if(XPROB(ii,jj) ~= 0);
            ENTROPYINC(ii,jj)=XPROB(ii,jj)*log10(XPROB(ii,jj));
        end
    end
end
end

```

**Program: file\_entr2.m**

**Measure of entropy – feature and background area**

```

                                % XADD is the thresholded and reconstructed surface
XMODADD=abs(XADD)^2;                                % absolute values of the XADD surface
XMODSUM=sum(sum(XMODADD));
XPROB=XMODADD./XMODSUM;

ENTROPYINC=zeros(m,n);
entropyA=zeros(m,n);                                % feature area
entropyB=zeros(m,n);                                % background area
for ii=1:m;
    for jj=1:n;
        if(XPROB(ii,jj) ~= 0);
            ENTROPYINC(ii,jj)=XPROB(ii,jj)*log10(XPROB(ii,jj));

            if jj>=351 & jj<=670 & ii>=485 & ii<=548;
                entropyA(ii,jj)=XPROB(ii,jj)*log10(XPROB(ii,jj));
            else
                entropyB(ii,jj)=XPROB(ii,jj)*log10(XPROB(ii,jj));
            end
        end
    end
end

end
end

```



## **Appendix B**

### **Published papers**

1. Nyander A, Addison P S, McEwan I and Pender G (2002) "River bed surface roughness analysis using 2-D wavelet transform-based methods", The 15<sup>th</sup> ASCE Engineering Mechanics Conference, June 2-5, New York , USA.
2. Nyander A, Addison P S, McEwan I and Pender G (2003) "Wavelet decomposition of sediment surface to characterise scale dependent properties and reveal individual feature", 16<sup>th</sup> Scottish Fluid Mechanics Meeting, May 28, University of Dundee, Dundee, U.K.
3. Nyander A, Addison P S, McEwan I and Pender G (2003) "Analysis of river bed surface roughness using 2D wavelet transform-based method" The Arabian Journal for Science and Engineering, Vol.28(1C), June, pp.107-121.
4. Nyander A, Addison P S, McEwan I and Pender G (2004) "Wavelet thresholding of simulated sediment to highlight pertinent bedform features", 17<sup>th</sup> Scottish Fluid Mechanics Meeting, May 19, University of Strathclyde, Glasgow, U.K.



## RIVER BED SURFACE ROUGHNESS ANALYSIS USING 2-D WAVELET TRANSFORM-BASED METHODS

Annie Nyander<sup>1</sup>  
Paul S Addison<sup>2</sup>  
Ian McEwan<sup>3</sup>  
Gareth Pender<sup>4</sup>

### ABSTRACT

This paper describes the analysis of river bed sediment surface data using the two-dimensional discrete wavelet transform. When sedimentation occurs in a channel the topography of the bed surface will change which in turn will affect the flow characteristics. It is therefore important to be able to characterise the bed surface topography. In this study the sediment surface data was analysed using the wavelet transform - a relatively new mathematical tool for data analysis. Interest in this analysis method has increased during recent years, and today it can be found in a number of areas in both science and engineering. The sediment data set was decomposed into a range of scales using the Daubechies 12 wavelet for the analysis. By determining the energy in the scale ranges a novel distribution, the *form size distribution*, of the bed forms was computed.

**Keywords:** River Bed, Sediment Surface, Wavelet Analysis, Surface Forms.

### INTRODUCTION

The wavelet transform is a relatively new signal analysis technique and it has, during recent years, gained in importance as an analysis method. It was not until the beginning of the 1990 s that the technique started being used by scientists and engineers for data analysis. However, today the application of the wavelet transform can be found in a number of areas. It has been shown to have advantages over other signal analysis methods and has found many practical uses in science and engineering (Addison, 2002) including surface analysis (Dougan *et al*, 2000; Frantziskonis *et al*, 2000; Jiang *et al*, 1999; Lee *et al*, 1997; Moktadir and Sato, 2000; and Xiong *et al*, 2001).

In our study, the two-dimensional discrete wavelet transform (2-D DWT) was used to analyse sediment surface data sets collected during a study of the armouring of river beds (McEwan *et al*, 2002; Pender *et al*, 2001).

---

<sup>1</sup> Faculty of Engineering and Computing, Napier University, Edinburgh, U.K. E-mail: a.nyander@napier.ac.uk

<sup>2</sup> Faculty of Engineering and Computing, Napier University, Edinburgh, U.K.

<sup>3</sup> Dept. of Engineering, University of Aberdeen, Aberdeen, U.K.

<sup>4</sup> Dept. of Civil & Offshore Eng., Heriot-Watt University, Edinburgh, U.K.

## SEDIMENT TRANSPORT

When sedimentation occurs in an erodable channel the topography of the bed surface will change unavoidably. This change of the surface topography may significantly affect the flow in the channel as the new surface geometry affects the local disturbance of the flow. The main influence on the flow is the surface roughness (Julien, 1995). For the analysis of a flow in a channel it is therefore important to be able to characterise the bed surface topography.

## RIVER BED SURFACE SEDIMENT DATA

Graded sediment was placed in a trapezoidal concrete channel and subjected to a water flow which caused size selective sediment transport. An area of 256mm square was monitored over time with a 3-D laser displacement meter having a spacing of 0.5 mm between measurements. Each scan produced a 512 by 512 array of 3-D co-ordinates of the surface from which a model of the surface could be constructed (McEwan *et al*, 2002; Pender *et al*, 2001). One of the surface height data sets is used in the analysis described in this paper.

## THE WAVELET TRANSFORM

A wavelet is a small wave or pulse which can be compressed and stretched to different scales. The basic wavelet function is defined as  $\psi(t)$ . A family of wavelets are generated by *dilating* the function using the scaling parameter  $a$  and *translating* it using the location parameter  $b$ , i.e.

$$\Psi_{(a,b)}(t) = \frac{1}{\sqrt{a}} \psi\left(\frac{t-b}{a}\right) \quad (1)$$

### The continuous wavelet transform (CWT)

For a continuous signal  $x(t)$  the continuous wavelet transform is given by

$$T(a,b) = \int_{-\infty}^{\infty} \frac{1}{\sqrt{a}} \psi\left(\frac{t-b}{a}\right) x(t) dt \quad (2)$$

### The discrete wavelet transform (DWT)

The DWT is constructed by choosing discrete values for  $a$  and  $b$ , where the wavelet dilation and translation is controlled by integer indices  $m$  and  $n$  respectively e.g.  $a = a_0^m$  and  $b = nb_0 a_0^m$ . The DWT is useful for computing scale-dependent statistical measures from 1-D and 2-D data sets (Addison *et al*, 2001). The discretisation of the wavelet is given by

$$\Psi_{m,n}(t) = \frac{1}{\sqrt{a_0^m}} \psi\left(\frac{t - nb_0 a_0^m}{a_0^m}\right) \quad (3)$$

The DWT of the  $x(t)$  will then have the form

$$T_{m,n} = \int_{-\infty}^{\infty} \frac{1}{\sqrt{a_0^{m/2}}} \psi\left(a_0^{-m} t - nb_0\right) x(t) dt \quad (4)$$

where the values of  $T_{m,n}$ , known as the wavelet coefficients, are given on a grid with index  $m,n$ .

#### *The scaling function*

Associated with the orthonormal wavelets is the scaling function  $\phi(t)$  (or the father wavelet) defined as

$$\phi_{m,n}(t) = 2^{-m/2} \phi(2^{-m}t - n) \quad (5)$$

The scaling function is used to smooth a signal by separating the approximations ( $S$ ), low frequency components, from the details ( $D$ ), high frequency components. The equation for approximation coefficients ( $S_{m,n}$ ) given as

$$S_{m,n} = \int_{-\infty}^{\infty} x(t) \phi_{m,n}(t) dt \quad (6)$$

This separation into details and approximations using the wavelet and the scaling function is known as the multiresolution analysis. Multiresolution makes it possible to decompose a signal into component parts at different resolutions. The signal is studied at a coarse resolution to give the overall picture while the finer resolutions capture the details in the signal.

#### **Wavelet energy**

After full decomposition of a signal is performed the energy contained within the wavelet coefficients at each scale is defined as

$$E_m = \sum_{n=0}^{2^M - m - 1} (T_{m,n})^2 \quad (7)$$

### **THE 2-D DISCRETE WAVELET TRANSFORM**

For the analysis of 2-D signals  $f(t_1, t_2)$  i.e. plane, surfaces, one need to use two-dimensional wavelets, where  $t_1$  and  $t_2$  are the two spatial co-ordinates. The simplest way to construct 2-D wavelet bases is by using three wavelets functions defined as

$$\begin{aligned} \Psi^H(t_1, t_2) &= \phi(t_1)\psi(t_2) \\ \Psi^V(t_1, t_2) &= \psi(t_1)\phi(t_2) \\ \Psi^D(t_1, t_2) &= \psi(t_1)\psi(t_2) \end{aligned} \quad (8)$$

where  $H$ ,  $V$  and  $D$  stand for *horizontal*, *vertical* and *diagonal*. The scaling functions for the 2-D wavelet transform is given by

$$\Phi(t_1, t_2) = \phi(t_1)\phi(t_2) \quad (9)$$

#### **Energy in the 2-D wavelet transform**

The energy of the 2-D data set is given by

$$E = \sum_{i=0}^{2^M-1} \sum_{j=0}^{2^M-1} (X_{o,i,j})^2 = \sum_{i=0}^{2^M-1} \sum_{j=0}^{2^M-1} (W_{i,j}^{(m)})^2 \quad (10)$$

where  $X_{o,i,j}$  and  $W_{i,j}^{(m)}$  are the elements on the matrices located on row  $i$  and column  $j$ . The energy in the original surface is equal to the energy in the transform, (Daubechies, 1992).

## ANALYSIS

An example of a river bed sediment surface data set is shown in FIG. 1. Where the surface was scanned after 76 hours and 50 minutes from the start of the experimental run.

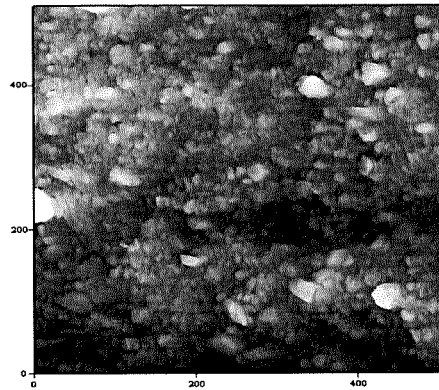


**FIG. 1. Original surface**

Performing the 2-D DWT using the Daubechies 12 wavelet illustrated in FIG. 2., the original surface can be subdivided into a number of details (scale ranges).

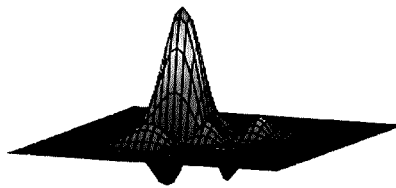


**FIG. 2. Daubechies 12 wavelet**

The details for the sediment bed surface are shown in FIG. 3., where Detail 1 represents the smallest scale and Detail 9 represents the largest scale. Each detail in the transform can be linked to a specific physical size. The data were collected every 0.5 mm and the scale has the power of two giving the relationship  $0.5 \times 2^m$ , where  $m$  is the scale which ranges between  $m = 1$  K 9.

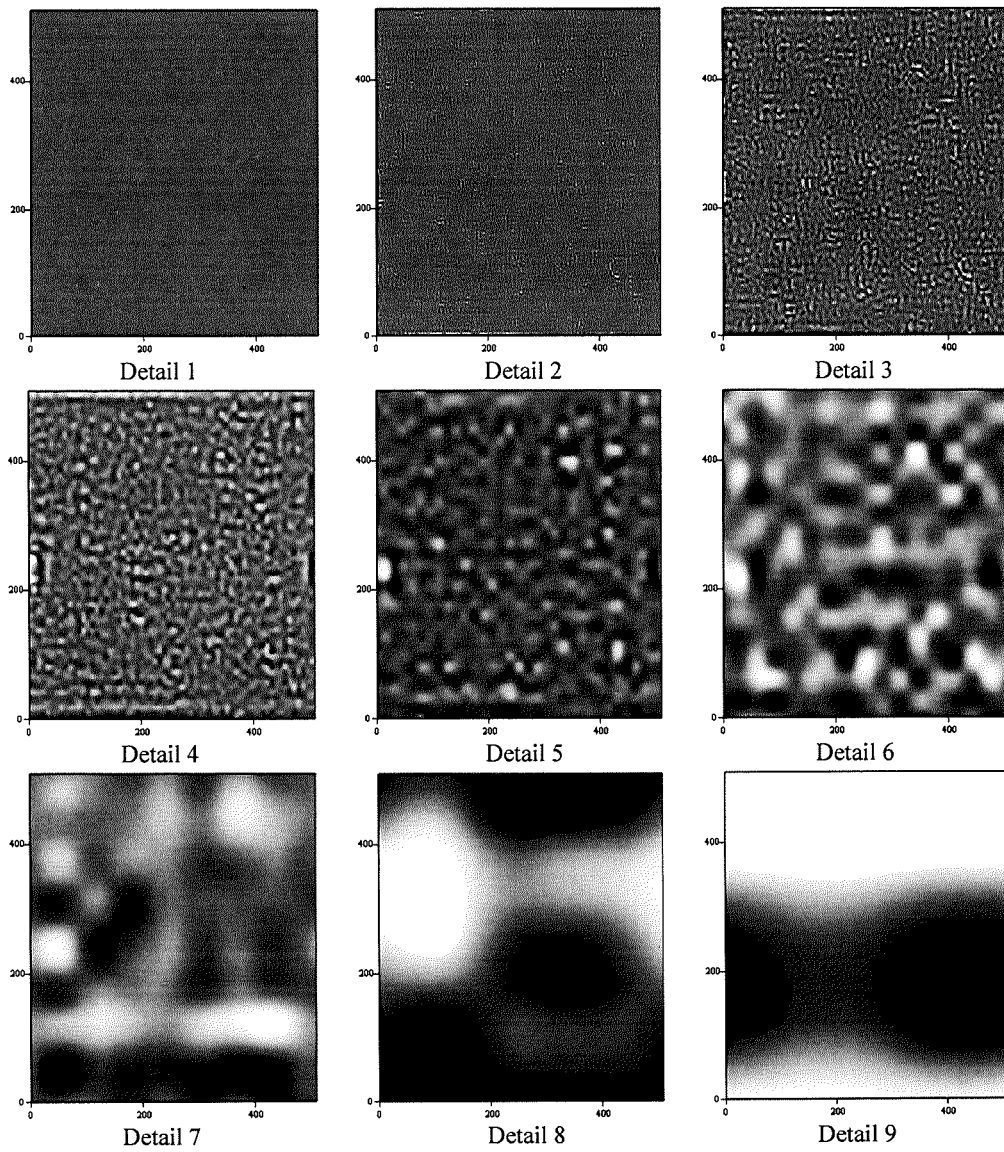


**FIG. 3. Wavelet details**

## RESULT

The energy in each detail can be linked to the occurrence of physical forms within each scale range. The total of each scale dependent wavelet-based energy is equal to the energy of the original surface. Hence the wavelet based energy at each scale provides information on how much of the surface can be attributed to each particular form 'size'. From this energy distribution it is possible

to generated a *form size distribution* (rather than a *particle size distribution*). This is shown in FIG. 4., where the contribution of each feature range at each scale is determined with the wavelet transform.

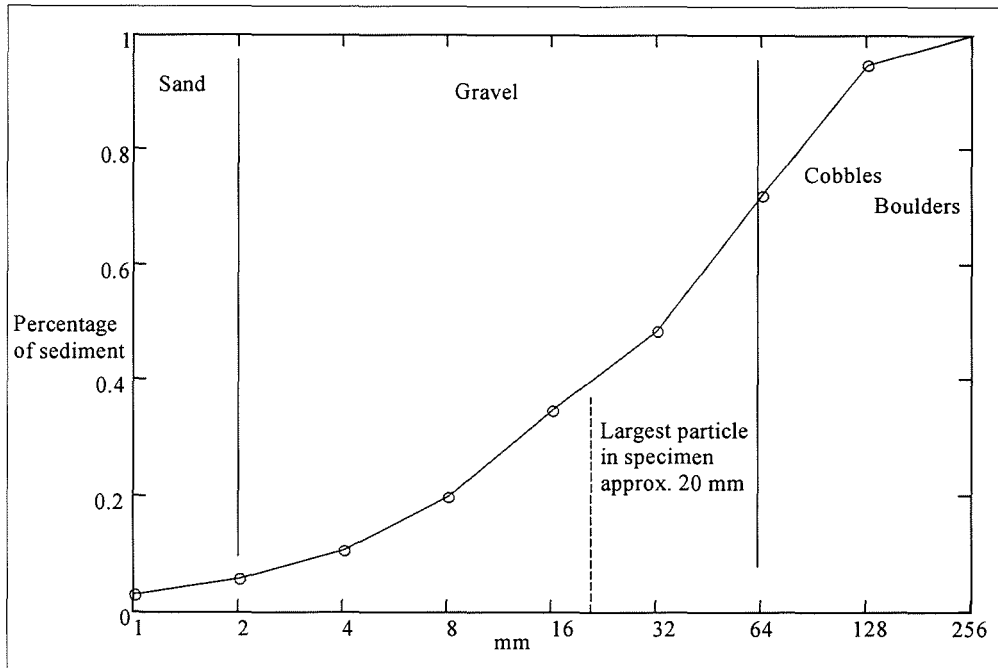


**FIG. 4. Form size distribution**

## CONCLUSION

From the plot of FIG. 4 it can be seen that scales corresponding to the largest form sizes do not correspond to individual sediment grain sizes, since no grains were used which were larger than approximately 20 mm in size - i.e. between scale 5 and 6. At scales larger than these the wavelet decomposition is picking up the distribution of surface formations, or “forms”, rather than specific particles sizes.

In fact, scales less than scale 6 are also related to the overall structure, as many small particles can be picked up as one large form at a larger scale. This is shown schematically in FIG. 5. Hence, instead of actually determining the *particle size distribution* of the sediment surface, our method determines the *form size distribution* of the sediment surface. We believe that the *form size distribution* of a surface will be more useful for characterising river bed surfaces than the *particle size distribution*, as it is the overall form distribution of the surface which affects the flow characteristics.

Future work will analyse complete sediment data sets over time to determine the changes in the surface topographies that occur during the bed armouring process. It is also intended to investigate the generation of the form size distribution using the coefficient modulus values rather than the energies. Finally, it is proposed to use non-decimated or stationary wavelet transforms (Morris and Peravali, 1999, Ngan *et al*, 1999 and Lee *et al*, 2000) in future work. These employ a

pseudo-continuous translation parameter ( $b$ ) which, although they destroy the orthogonality condition of the DWT and are computationally more expensive to use, are translation invariant and provide better resolution in the transform space.

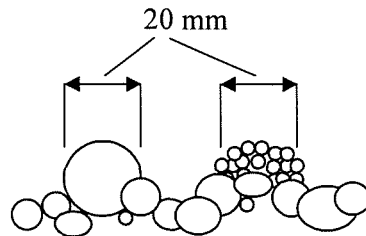


**FIG. 5. Groups of smaller particles can form a larger feature or form (i.e. at a larger scale).**

## REFERENCES

- Addison, P.S. (2002), *The Illustrated Wavelet Handbook: Applications in Science, Engineering, Medicine and Finance*, Institute of Physics Publishing, London, U.K.
- Addison P.S., K.B. Murray and J.N. Watson, (2001), "Wavelet transform analysis of open channel wake flows," *ASCE J. Engineering Mechanics*, 58-70.
- Daubechies, I. (1992), *Ten lectures on wavelets*, SIAM, Philadelphia, USA.
- Frantziskonis, G.N., L.B. Simon, J. Woo and T.E. Matikas (2000), "Multiscale Characterization of pitting corrosion and application to an aluminum alloy," *European Journal of Mechanics A-Solids*, **19**, 309-318.
- Jiang, X.Q., L. Blunt and K.J. Stout (1999), "Three-dimensional surface characterization for orthopaedic joint prostheses," *Proceedings of the Institutions of Mechanical Engineers part-H*, **213**(11), 49-68.
- Julien, P.Y., (1995), *Erosion and sedimentation*, Cambridge University press, New York, USA.
- Lee, S-H., H. Zahouani, R. Caterini and T.G. Mathia, (1998), "Morphological characterisation of engineered surfaces by wavelet transform," *International Journal of Machine Tools & Manufacture*, **38**(5-6), 581-589.
- Lee, S.L., C.K. Lee and K.Y. Yoo (2000) "New lifting based structure for undecimated wavelet transform," *Electronics Letters*, **36**(22), 1894-1895.
- McEwan, I.K., T.M. Sheen, G.J. Cunningham and A.R. Allen (2000), "Estimating the size composition of sediment surfaces through image analysis," *Proceeding of the Institution of Civil Engineers-Water Maritime and Energy*, **142**, 189-195.
- Moktadir, Z. and K. Sato (2000), "Wavelet characterization of the submicron surface roughness of anisotropically etched silicon," *Surface Science*, **470**, L75-L62.
- Morris, J.M. and R. Peravali (1999), "Minimum-bandwidth discrete-time wavelets," *Signal Processing*, **76**, 181-193.
- Ngan, S-C, S.M. LaCorte and X. Hu (1999), "Temporal Filtering of Event-Related fMRI Data Using Cross-Validation," *NeuroImage*, **11**, 797-804.
- Pender, G., T.B. Hoey, C. Fuller and I.K. McEwan, (2001) "Selective bedload transport during the degradation of well sorted graded sediment bed," *Journal of Hydraulic Research*, **39**(3), 269-277.



Xiong, F., X.Q. Jiang, Y. Gao and Z. Li, (2001), "Evaluation of engineering surfaces using a combined fractal modeling and wavelet analysis method," *International Journal of Machine Tools & Manufacture*, **41**, 2187-2193.

**Title:**

Wavelet decomposition of sediment surfaces to characterise scale dependent properties and reveal individual features.

**Authors:**

Annie Nyander<sup>1</sup>, Paul S. Addison<sup>2,3</sup>, Ian McEwan<sup>4</sup> and Gareth Pender<sup>5</sup>.

1. School of the Built Environment, Napier University, Edinburgh.
2. School of the Built Environment, Napier University, Edinburgh
3. CardioDigital Ltd, Elvingston Science Park, Gladsmuir, East Lothian.
4. Department of Engineering, University of Aberdeen, Aberdeen.
5. School of the Built Environment, Heriot-Watt University, Edinburgh.

**Abstract:**

When sedimentation occurs in a river channel, the topography of the bed surface changes which in turn affects the flow characteristics. It is therefore important to be able to characterise the bed-surface topography during and after the sedimentation process. This study applies the wavelet transform; a relatively new mathematical tool for data analysis. Interest in this analysis method has increased during recent years, and today it can be found in a number of areas in both science and engineering.

Here the preliminary results applying the 2D discrete wavelet transform to analyse river bed sediment surface data are presented. The original river-bed sediment surface in Figure 1 was decomposed into a number of wavelet scales using the Daubechies 12 wavelet. Determining the energy for each scale the global bed surface topography may be characterised in terms of a novel parameter, the *form size distribution*, shown in Figure 2. In addition that pertinent local bedform features may be highlighted using a wavelet thresholding-based technique, as shown in Figure 3.

**Keywords:** River Bed, Sediment Surface, Wavelet Analysis, Surface Forms.

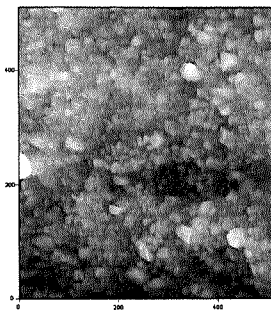


Figure 1 Original surface.

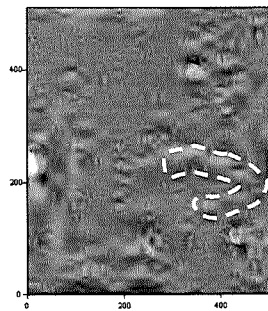


Figure 3 Finding pertinent features through thresholding of the wavelet coefficients.

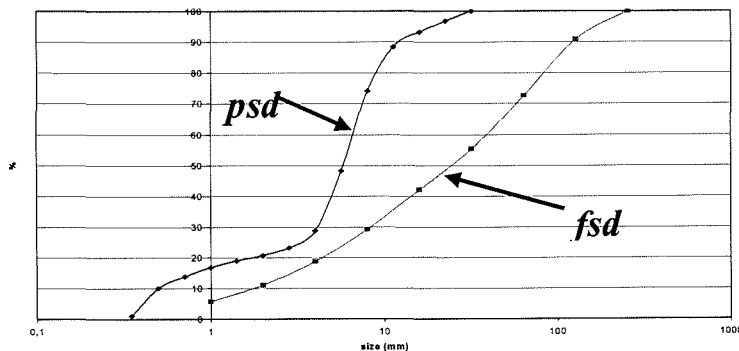


Figure 2 Comparing the particle size distributions (*psd*) and the novel form size distribution (*fsd*) for a river bed sediment surface.

## ANALYSIS OF RIVER BED SURFACE ROUGHNESSES USING 2D WAVELET TRANSFORM-BASED METHODS

**Annie Nyander\***

*Research Student, School of the Built Environment  
Napier University, Edinburgh, U.K.*

**Paul S. Addison**

*Professor of Fluid Mechanics, School of the Built Environment  
Napier University, Edinburgh, U.K.*

**Ian McEwan**

*Reader, Department of Engineering, University of Aberdeen, Aberdeen, U.K.*

**Gareth Pender**

*Professor of Environmental Engineering, Department of Civil and Offshore  
Engineering, Heriot-Watt University, Edinburgh, U.K.*

### مَصْلَحًا

عندما يحدث الترسب في قناة نهريّة تتغير طوبوغرافية سطح الطبقة الأرضية مما يؤثر في خصائص التدفق ، ولذلك فمن المهم القدرة على تمييز طوبوغرافية سطح الطبقة الأرضية في أثناء عملية الترسب وبعدها. ويصف هذا البحث نتائج دراسة تمهيدية تُخصّ تحليل بيانات الترسب على سطح الطبقة الأرضية لمجرى النهر باستعمال تحويلية الموجة الصغيرة الرقمية ذات البُعدين. كما نظهر كيف يمكن تمييز طوبوغرافية مساحه سطح الطبقة الأرضية الإجمالية بوساطة وسيط مُبتكر يكمن في توزيع حجم الشكل ، وأيضاً يُمكن إلقاء الضوء على تلك المميزات الوثيقة الصلة بشكل الطبقة الأرضية المحلية باستعمال أسلوب تعريب الموجة الصغيرة ، إضافة إلى ذلك نختبر تحويلية الموجة الصغيرة الثابتة كطريقة تعريب مُحسنة لانتزاع المميزات ، وكما نظهر الاختلاف السلوكي بين هندسة الطبقة الأرضية وهندسة سطح منحنى متكرر اصطناعي.

\*Address for Correspondence:  
Napier University  
School of the Built Environment  
10 Colinton Road  
Edinburgh EH10 5DT  
U.K.  
e-mail: a.nyander@napier.ac.uk

#### ABSTRACT

When sedimentation occurs in a river channel, the topography of the bed surface changes, which in turn affects the flow characteristics. It is therefore important to be able to characterize the bed surface topography during and after the sedimentation process. This paper describes results from a preliminary study conducted to analyze river bed sediment surface data using the two-dimensional discrete wavelet transform. We show how the global bed surface topography may be characterized in terms of a novel parameter, the *form size distribution*, and also that pertinent local bedform features may be highlighted using wavelet thresholding-based techniques. In addition, we test the stationary wavelet transform as an enhanced method of thresholding for feature extraction and we show the difference in behavior between the bed surface geometry and the geometry of a synthetic fractal surface.

*Key Words:* river bed, sediment surface, wavelet analysis, surface roughness.

## ANALYSIS OF RIVER BED SURFACE ROUGHNESSES USING 2D WAVELET TRANSFORM-BASED METHODS

### 1. INTRODUCTION

An investigation was conducted concerning the application of the discrete wavelet transform to the characterization of two-dimensional river bed sediment surface data. Of particular interest to the study was the characterization of the rearrangement of the bed surface during flood flow regimes and the associated sedimentation process. When sedimentation occurs in an erodable channel the topography of the bed surface will inevitably change. This change of the surface topography will significantly affect the flow in the channel as the new bed surface geometry affects the local disturbance of the flow. The main influence on the flow is the surface roughness [1]. For the analysis of a flow in a channel it is therefore important to be able to characterize the bed surface topography. In order to understand and predict the physical processes which regulate the transport of sediment, one needs to quantify the nature of the surface layers. A variety of methods have been proposed in the literature to determine the surface size composition. Kellerhals and Bray [2] concluded from their study of a number of current methods that the 'grid by number' technique produced results that were directly equivalent to grain size distribution originated from a volumetric sieve analysis. In this method, a sample is obtained by collecting particles (found under the nodes of a regular grid) and the number of particles in the various size classes is used to form the size distribution. McEwan *et al.* [3] used an adaptation of this method to obtain the grain sizes from the analysis of plan view images, including laser altimeter data, photogrammetric data, digital photographs, and scanned photographs.

The wavelet transform (WT) has been found to be particularly useful for analyzing signals which can best be described as aperiodic, noisy, intermittent, transient, and so on. Its ability to examine the signal simultaneously in both time and frequency in a distinctly different way from the traditional Short Time Fourier Transform (STFT) has spawned a number of sophisticated wavelet-based methods for signal manipulation and interrogation. Wavelet transform analysis has now been applied in the investigation of a multitude of diverse physical phenomena, from climate analysis to the analysis of financial indices, from heart monitoring to the condition monitoring of rotating machinery, from seismic signal denoising to the denoising of astronomical images, from crack surface characterization to the characterization of turbulent intermittency, from video image compression to the compression of medical signal records, and so on [4].

Recently, wavelet analysis has been employed in a variety of surface analysis tasks including the characterization of fractional Brownian motions surfaces and cracked concrete surfaces [5], pitting corrosions [6], and orthopedic joint prostheses [7]; general surface roughness analysis [8]; the characterization of surface roughness of silicon [9]; and the evaluation of engineering surfaces [10]. In the study we present herein, the two-dimensional discrete wavelet transform (2D DWT) was used to characterize sediment surface data sets collected during a study of the armoring of river beds [3, 11].

### 2. BACKGROUND: ANALYSIS METHODOLOGY AND DATA

#### 2.1. The Wavelet Transform

There is now an abundance of literature concerning the wavelet transform and its many applications. In this section, the wavelet transform will be outlined briefly. A wavelet is a small wave or pulse which can be compressed and stretched to different scales. The basic wavelet function, also known as the mother wavelet, is defined as  $\psi(t)$ . From this function a family of wavelets are generated by *dilating* the function using the scaling parameter  $a$  and *translating* it using the location parameter  $b$ , *i.e.*:

$$\Psi_{(a,b)}(t) = \frac{1}{\sqrt{a}} \psi\left(\frac{t-b}{a}\right). \quad (1)$$

The discrete wavelet transform (DWT) is constructed by choosing discrete values for  $a$  and  $b$ , where the wavelet dilation and translation is controlled by the integer indices  $m$  and  $n$  respectively, *e.g.*  $a = a_0^m$  and  $b = nb_0a_0^m$ . The DWT is

useful for computing scale-dependent statistical measures from 1D and 2D data sets [12]. The discretization of the wavelet is given by

$$\Psi_{m,n}(t) = \frac{1}{\sqrt{a_0^m}} \Psi\left(\frac{t - nb_0 a_0^m}{a_0^m}\right). \quad (2)$$

The DWT of a signal or function  $x(t)$  then becomes:

$$T_{m,n} = \int_{-\infty}^{\infty} x(t) \frac{1}{a_0^{m/2}} \Psi(a_0^{-m} t - nb_0) dt, \quad (3)$$

where the values of  $T_{m,n}$ , known as the wavelet coefficients, are given on a grid with index  $m,n$ . Associated with the orthonormal wavelet function is the scaling function  $\phi(t)$  (or the father wavelet) defined as:

$$\phi_{m,n}(t) = 2^{-m/2} \phi(2^{-m} t - n). \quad (4)$$

The scaling function is used to smooth a signal by separating the approximations ( $S$ ), low frequency components, from the details ( $D$ ), high frequency components. The equation for approximation coefficients ( $S_{m,n}$ ) is given as:

$$S_{m,n} = \int_{-\infty}^{\infty} x(t) \phi_{m,n}(t) dt. \quad (5)$$

This separation into details and approximations using the wavelet and the scaling function is known as multiresolution analysis. Multiresolution makes it possible to decompose a signal into component parts at different resolutions. The signal is studied at both fine and coarse resolutions with the coarse analysis giving the structure of the surface and the fine analysis presenting the small details. After full decomposition of a signal is performed, the energy contained within the wavelet coefficients at each scale is given by:

$$E_m = \sum_{n=0}^{2^{M-m}-1} (T_{m,n})^2. \quad (6)$$

### 2.1.1. The Two-Dimensional (2D) Discrete Wavelet Transform

For the analysis of 2D data sets,  $f(t_1, t_2)$ , i.e. planes and surfaces, one needs to use two-dimensional (2D) wavelets, where  $t_1$  and  $t_2$  are the two spatial co-ordinates. The simplest way to construct 2D wavelet bases is by using three wavelets functions defined as,

$$\begin{aligned} \Psi^H(t_1, t_2) &= \phi(t_1)\psi(t_2) \\ \Psi^V(t_1, t_2) &= \psi(t_1)\phi(t_2) \\ \Psi^D(t_1, t_2) &= \psi(t_1)\psi(t_2), \end{aligned} \quad (7)$$

where  $H$ ,  $V$ , and  $D$  represent the *horizontal*, *vertical*, and *diagonal* components. The scaling functions for the 2D wavelet transform is given by:

$$\Phi(t_1, t_2) = \phi(t_1)\phi(t_2). \quad (8)$$

The energy of the 2D data set is given by:

$$E = \sum_{i=0}^{2^M-1} \sum_{j=0}^{2^M-1} (X_{0,i,j})^2 = \sum_{i=0}^{2^M-1} \sum_{j=0}^{2^M-1} (W_{i,j}^{(m)})^2, \quad (9)$$

where  $X_{0,i,j}$  and  $W_{i,j}^{(m)}$  are the elements of the original surface (with the mean removed) and the wavelet coefficients at scale  $m$  respectively. As we can see the energy of the original surface is equal to the energy in the transform, [13].

## 2.2. River Bed Surface Sediment Data

Bed armoring takes place during flood flow conditions and comprises the rearrangement of the bed sediment grain sizes. Water currents progressively armor the surface layer by breaking weak inter-particle bonds and promoting stronger re-bonding arrangements. Armoring increases with time and renders the deposit more erosion resistant [14].

The sediment data sets interrogated in this study have previously been used to investigate the bed armoring process in rivers during flood flow [15]. The data comes from experiments that were carried out experimental facilities at HR Wallingford Ltd. in the UK. The financial support for these experiments was provided by the Engineering and Physical Science Research Council (EPSRC Grant Numbers GR/L22058 and GR/L22065) to the Universities of Aberdeen and Glasgow and also by the European Union through a Human Capital Mobility grant to HR Wallingford Ltd. The sediment transportation experiments were conducted in a trapezoidal concrete channel (flume) with a width of 2.46m, length of 18m, and a slope equal to 1:400 (0.25%). Graded sediment was placed in the flume and it was then subjected to a water flow which caused size selective sediment transport. The bed surface was monitored during the flood flow (photographs, longitudinal water surface profiles and water temperature were taken) and at the end of each working day (after 6–9 hours running) an area (256 mm sq.) was scanned with a 3D laser displacement meter. Each measurement in the scan had a spacing of 0.5 mm, which produced a 512 by 512 array of 3D co-ordinates of the surface. From this scan a model of the surface can be constructed. For more information regarding the data sets the reader is referred to references [3, 11, 15].

## 3. ANALYSIS

An example of a river bed sediment surface data set is shown in Figure 1, where the surface was scanned after 76 hours and 50 minutes from the start of the experimental run within a tilted hydraulic channel.

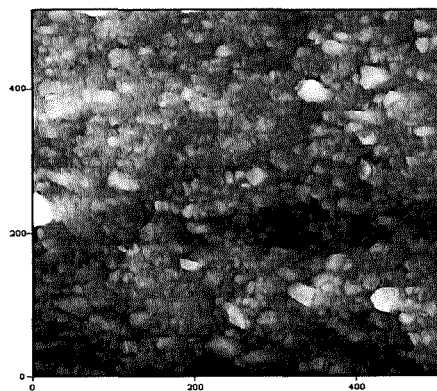


Figure 1. Original surface.

Performing the 2D DWT using, for example, the Daubechies 12 wavelet (illustrated in Figure 2), the original surface can be subdivided into a number of details (scale ranges). Examples of four consecutive details from the wavelet transform for the sediment bed surface are shown in Figure 3. Each detail in the transform can be linked to a specific physical size. The data were collected every 0.5 mm and the scale has the power of two giving the relationship  $0.5 \times 2^m$ , where  $m$  is the scale which ranges between  $m = 1 \dots 9$ .

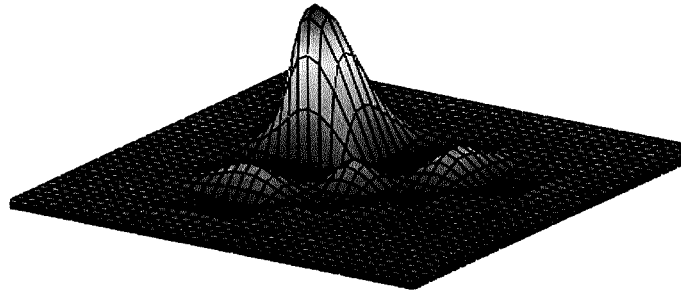


Figure 2. Daubechies D12 wavelet.

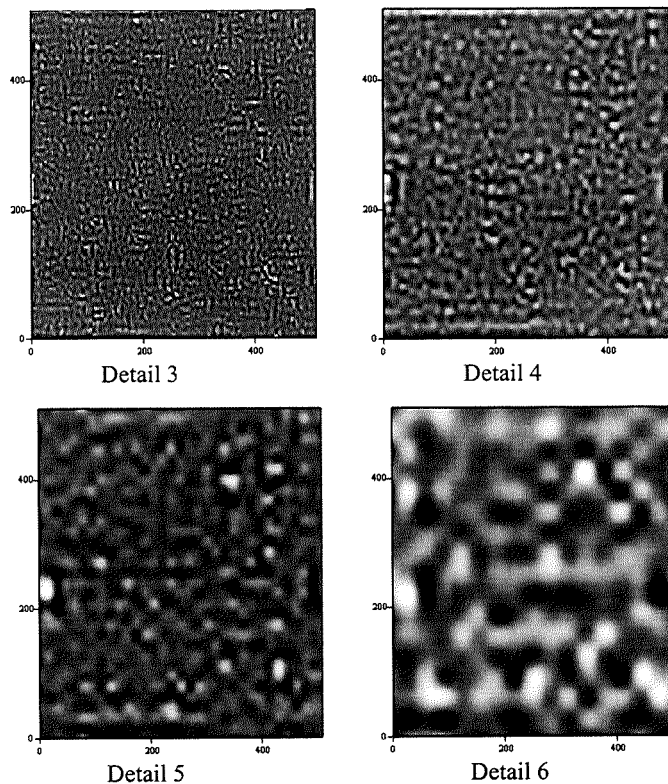


Figure 3. Example of wavelet details from the DWT of the surface in Figure 1 using a D12 wavelet.



### 3.1. Form Size Distribution: a New Surface Characteristic

The traditional measure of the characteristic ‘sizes’ of a sediment bed surface is the *particle size distribution (psd)*. This measures the cumulative percentage by weight of particles within different size ranges; where the distribution of weights is determined using a series of sieves of successively smaller mesh sizes [16]. The particle size distribution for the sediment surface given in Figure 1 is shown in Figure 4(a). We can see from the plot that this sediment has a maximum grain size of around 20 mm.

Each detail of the wavelet transformed surface can be associated with physical surface forms within a range of scales. Figure 4(a) shows the cumulative sum of the modulus of the coefficients at each scale expressed as a percentage of the total sum of all wavelet coefficient moduli at all scales. This curve is therefore representative of the distribution of surface form scales and hence we call it the *form size distribution (fsd)*. Figure 4(b) shows the results of four different experimental surfaces. The *fsd*'s of these surfaces are shown to be very similar and all differ markedly from the *psd* which was the same for each experimental surface. From the plots in Figure 4 it can be seen that scales corresponding to the largest form sizes (*i.e.* >100 mm) cannot correspond to individual sediment grain sizes because none of the grains

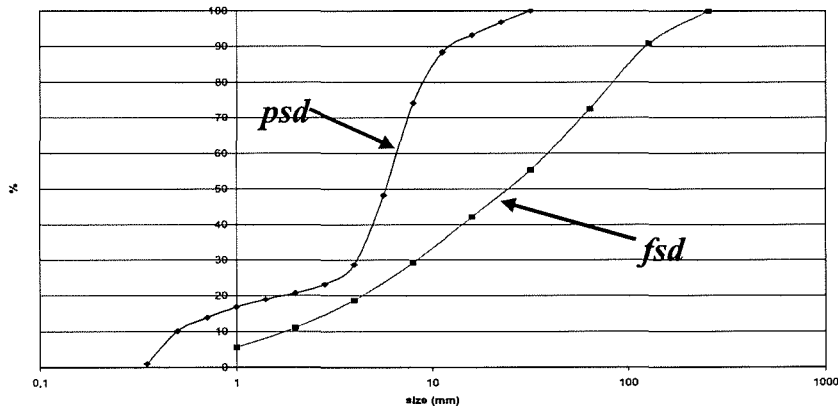


Figure 4(a). Particle and form size distributions for surface of Figure 1.

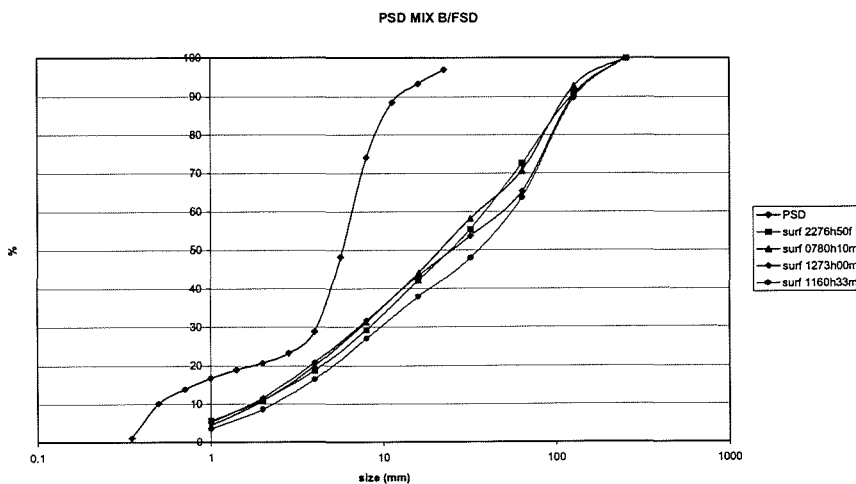


Figure 4(b). Particle and form size distributions for four experimental surfaces.

were larger than approximately 20 mm (*i.e.* between scales  $m=5$  and 6 — the maximum of the *psd*). At scales larger than these, the wavelet decomposition picks up specific surface formations, or “forms”, rather than individual particles. In fact, we can also conclude that *forms* at scales less than scale 5 are also related to the overall structure. This is because coherent masses of small particles can be picked up as larger forms at larger scales. This is shown schematically in Figure 5. We believe that the *form size distribution* of a surface will be a more useful measure for characterizing river bed surfaces than the *particle size distribution*, as it is the aggregate topographical nature of the surface which affects the flow characteristics and not the constituent bed surface grain size distribution. This point is shown schematically in Figures 6(a) and 6(b), which shows the flow over two surfaces with similar *particle size distribution* but different *form sizes distributions*. Figure 6(a) shows a surface with a higher degree of large scale forms than that of Figure 6(b), which is much flatter. The two surfaces will affect the flow differently depending on their surface topology. The rougher surface (Figure 6(a)) will cause a greater disturbance to the flow increasing its bed friction characteristics and altering flow depths and velocity distributions within the channel.

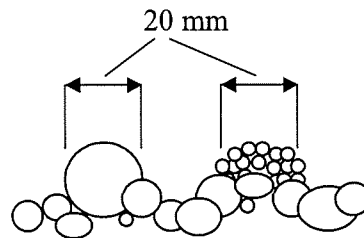
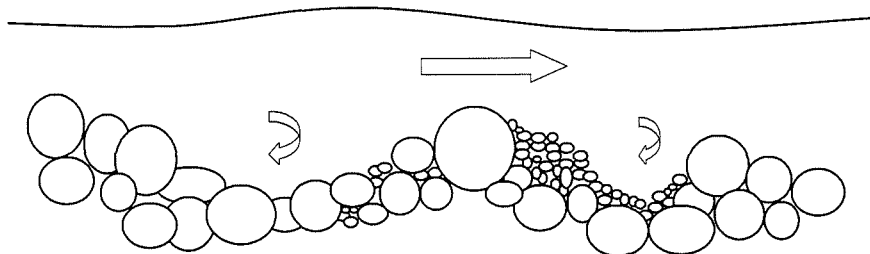
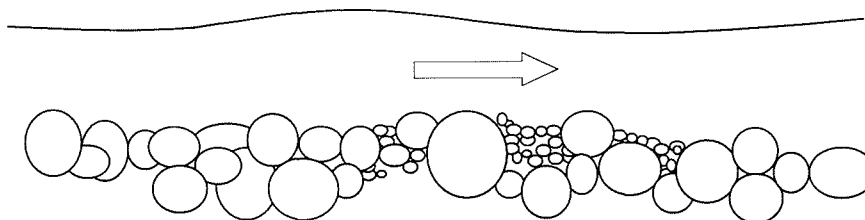


Figure 5. Groups of smaller particles can form a larger feature or form (*i.e.* at a larger scale).



(a) Flow over a rough surface.



(b) Flow over a flat surface.

Figure 6. River flow over two different sediment surface topographies.

Finally, we tested the fractal nature of the sediment surface of Figure 1. Previous work by our group has shown that both wavelet and Fourier spectral methods are superior to traditional fractal methods (*e.g.* the box counting and variable bandwidth methods) for analyzing engineering surfaces [5], in particular when a single data realization and not an ensemble average is analyzed. Figure 7 shows the energy plotted against scale for the sediment surface wavelet coefficients compared to a synthesized fractional Brownian motion (fBm) surface with Hurst exponent  $H=0.6$ . For the fBm we would expect to see a linear increase in coefficient energies with scale. (For more information on fBm's see Addison [17], ch. 4.) The relatively linear increase in coefficient energies with scale for the fBm surface contrasts with the drop off in coefficient energy for the sediment surface indicating that the sediment surface is not (mono)fractal in its behavior across scales. Similar results were obtained for other experimental surfaces.

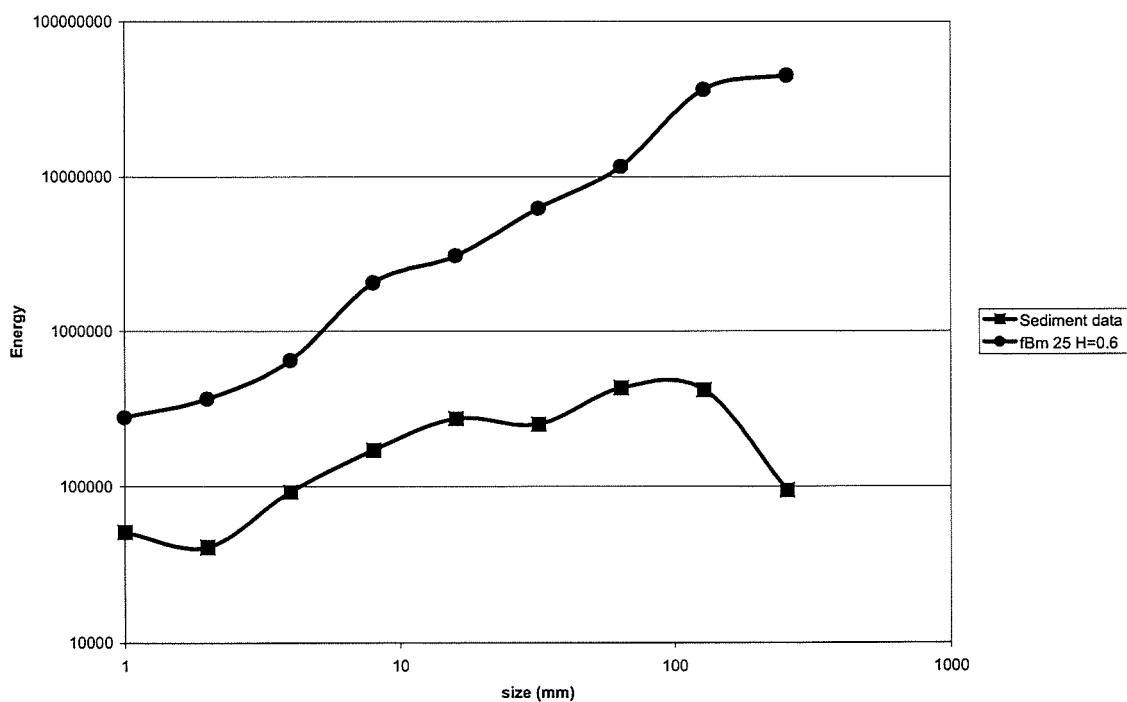


Figure 7. Logarithmic plot of wavelet coefficient energy against scale for the sediment surface of Figure 1 and a synthesised fBm (Hurst exponent  $H=0.6$ ).

### 3.2. Bed Surface Detection Using Wavelet Thresholding

It is known that distinct grain formations may appear during the armoring process of river beds [18]. In order to detect and extract these predominant formations or features in the surface, we applied thresholds to the wavelet coefficients prior to using them in the reconstruction of the surface details. We employed amplitude thresholding where small-amplitude wavelet coefficients are removed regardless of their position. Interesting work has been done by others in the area of wavelet thresholding. For example, Abramovich *et al.* [19] have conducted research into methods for the determination of suitable criteria for choosing the correct wavelet threshold; Barclay *et al.* [20] have compared threshold-based smoothing and denoising methods for test data signals; and Tikkanen [22] has removed simulated noise in ECG signals using both hard and soft thresholding. See also the texts by Odgen [21], ch. 8, and Addison [4], ch. 3, which present a variety of wavelet thresholding methods.

The two most common ways of thresholding data is by applying either a *soft* or a *hard* threshold, where the threshold ( $\lambda$ ) is related to the mean value of the wavelets coefficients. The two different thresholds are expressed as:

$$T_i^{soft} = \begin{cases} \text{sign}(T_i)(|T_i| - \lambda) & |T_i| > \lambda \\ 0 & |T_i| \leq \lambda \end{cases} \quad (10)$$

$$T_i^{hard} = \begin{cases} T_i & |T_i| > \lambda \\ 0 & |T_i| \leq \lambda. \end{cases} \quad (11)$$

The main problem associated with denoising is in the determination of the criteria with which to choose the threshold ( $\lambda$ ). Too large a value of  $\lambda$  will cut out information of the true signal while too small a value of  $\lambda$  will retain unwanted noise in the reconstructed signal.

Using the thresholding method detailed above, the original experimental bed surface in Figure 8(a) is reconstructed, with the detail coefficients obtained by applying three thresholds individually. In addition, only the thresholded details

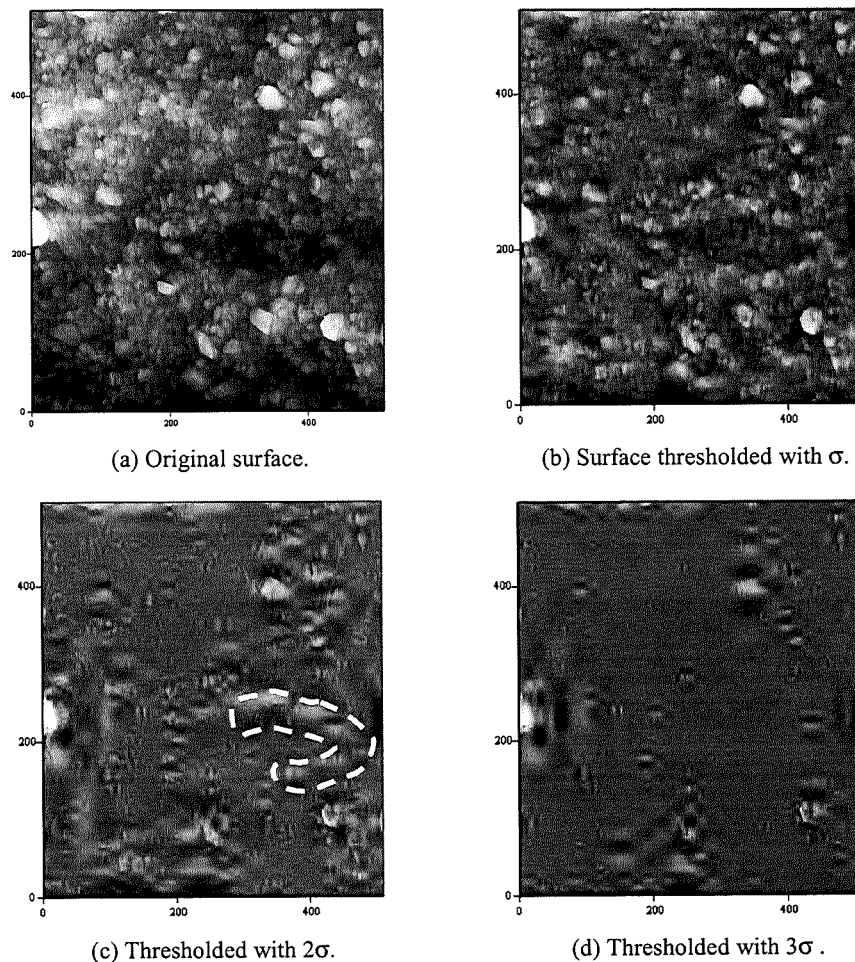


Figure 8. Finding features through thresholding the wavelet coefficients.

D1 to D6 are used for the reconstruction. In Figure 8(b) the threshold is set to  $\sigma$ , where  $\sigma$  is the standard deviation of the wavelet coefficients at each scale, *i.e.* all coefficients larger than  $\sigma$  are kept and coefficients less than  $\sigma$  are set to zero. There is a considerable resemblance to the original surface. Figure 8(c) shows the thresholded surface using  $2\sigma$ . Here much of the smaller features are taken away and coherent structures can be clearly seen in the surface. The last figure, Figure 8(d), is the surface thresholded with  $3\sigma$ . Only the largest features in the original data are retained in the reconstruction. From these three reconstructions, the one thresholded with  $2\sigma$  appears to provide the most interesting information. Here dominant larger features are clearly visible within the surface. One possible coherent feature (possibly a partial diamond feature) is enclosed by the dashed line shown in the plot. Features found by thresholding in this way prove useful in indicating where sediment has gathered on the surface in distinct formations. Applying an optimal threshold to the data sets over time will make it possible to compare the grain over time to detect bed form movements. Again, it should be noted that we have used a single surface here to illustrate the method; however, we find similar features for other experimental data sets (not shown herein).

### 3.3. Thresholding Using the Stationary Wavelet Transform

Although computationally more intensive, the stationary wavelet transform (SWT) will provide better resolution, especially at larger scales, and ensure translation invariance in the decomposition. We do not go into detail of the SWT herein but rather refer the reader to the papers by Morris and Peravali, Ngan *et al.*, and Lee *et al.* [23–25]. In this section we briefly describe some recent work which uses the SWT to analyze synthetic test surfaces to which synthetic diamond-shaped clusters of particles were added.

One of the original test surfaces together with the addition of the diamond feature is shown in Figure 9. In order to extract the diamond shape from the surface both hard and soft thresholding was used and here we employed the Daubechies D2 (Haar) wavelet. A range of threshold values were used from  $0.1\sigma$  to  $10\sigma$ , where  $\sigma$  is the *standard deviation* of the wavelet coefficients at each scale. Performing the 2D inverse wavelet transform and adding selected details together allowed features and patterns in the surface to be detected. Figure 10 shows the reconstruction for each individual detail from 1 to 4 for the coefficients thresholded at  $1.5\sigma$ . Figure 11 shows the combined reconstructions for levels 1 to 4 for both soft and hard thresholding at various threshold values. The reconstructions using scales 1 to 3 and for thresholds set to  $1\sigma$ ,  $2\sigma$ , and  $3\sigma$  are plotted in Figures 11(a) to (c) respectively for soft thresholding and Figures 11(d) to (f) respectively for hard thresholding. Performing the 2D inverse wavelet transform and adding selected details together in this way allows features and patterns in the surface to be detected. Tables 1 and 2 show the

**Table 1. Proportion of Energies within the Synthetic Feature and Background Regions Remaining after Thresholding at Various Threshold Values for Soft Thresholding.**

Threshold Value in Terms of Coefficient Standard Deviation	Proportion of Reconstructed Energy for Synthetic Feature	Proportion of Reconstructed Energy for Background Surface
0.0	1.000	1.000
0.1	0.862	0.766
0.2	0.739	0.580
0.3	0.631	0.436
0.4	0.537	0.325
0.5	0.455	0.241
1.0	0.187	0.053
1.5	0.070	0.012
2.0	0.025	0.003
2.5	0.009	0.001
3.0	0.003	0.000
3.5	0.001	0.000
5.0	0.000	0.000
5.2	0.000	0.000
6.0	0.000	0.000
10.0	0.000	0.000

proportion of energies left in the regions where the added feature lies and the background surface region after thresholding for each of the thresholds employed. For example for a soft threshold of  $1\sigma$ , 18.7% of the original energy remains in the feature region whereas only 5.3% of the background surface energy remains. As the threshold value increases the energies in both the feature and background regions reduce, but the background reduces much more rapidly. However, there is a trade off between the enhanced feature signal as compared with the background and the accuracy of reconstruction due to reduction in coefficients used at the higher thresholds. The question of what is a good measure of the reconstruction's ability to highlight pertinent features is still open (and is perhaps both user and problem dependent). Also noticeable from the tables is the increase in the hard thresholded energies as compared to the soft thresholded energies as we would expect as the remaining coefficients in the soft thresholded method are reduced by the value of the threshold, hence reduce in energy.

**Table 2. Proportion of Energies within the Synthetic Feature and Background Region Remaining after Thresholding at Various Threshold values for *Hard Thresholding*.**

Threshold Value in Terms of Coefficient Standard Deviation	Proportion of Reconstructed Energy for Synthetic Feature	Proportion of Reconstructed Energy for Background Surface
0.0	1.000	1.000
0.1	0.999	0.998
0.2	0.994	0.987
0.3	0.983	0.958
0.4	0.964	0.915
0.5	0.947	0.857
1.0	0.773	0.450
1.5	0.556	0.182
2.0	0.311	0.070
2.5	0.174	0.025
3.0	0.083	0.007
3.5	0.036	0.001
5.0	0.008	0.000
5.2	0.008	0.000
6.0	0.000	0.000
10.0	0.000	0.000

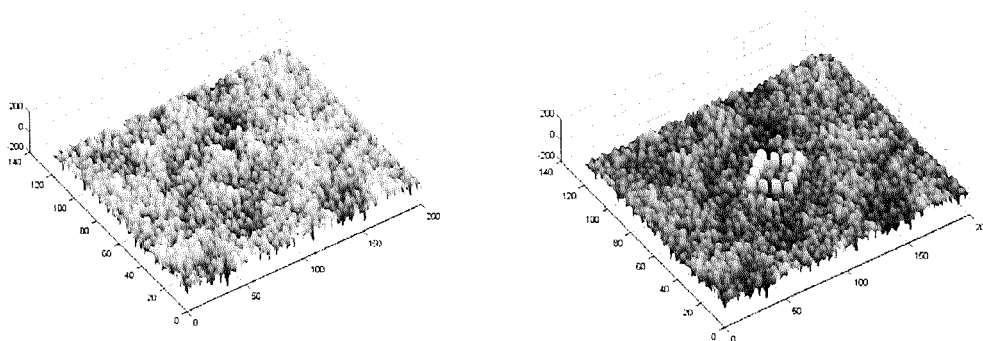


Figure 9. Original Surface (left) and Surface with Synthetic Diamond Feature added (right).

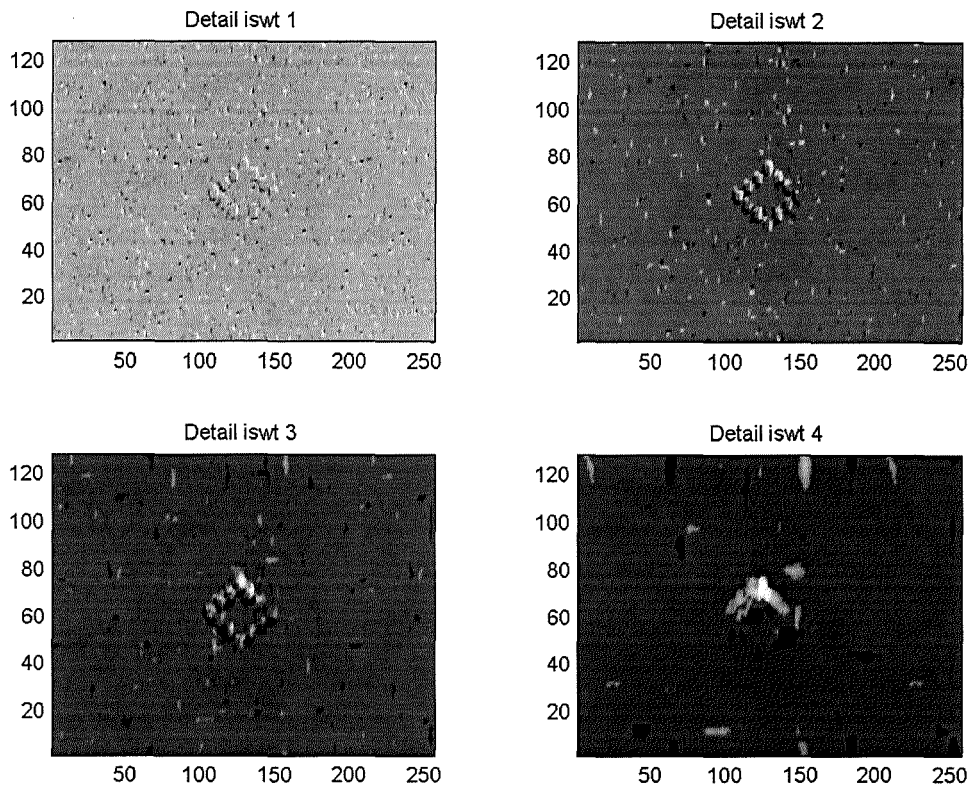
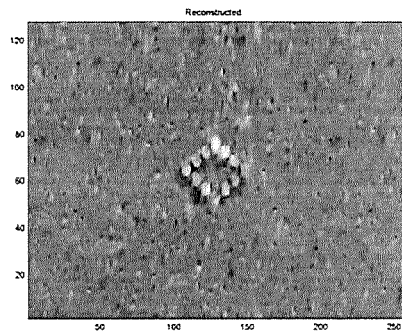


Figure 10. Reconstruction of details hard thresholded at  $1.5\sigma$  at scales 1 to 4.

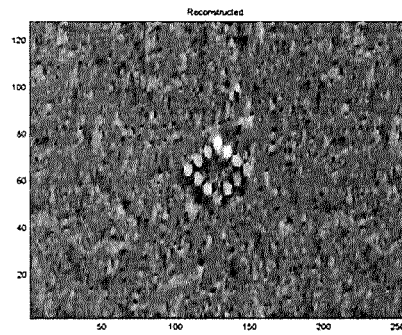
#### 4. RESULTS AND DISCUSSION

The work described in this paper demonstrates how the wavelet transform may prove to be a very useful analyzing tool for studying the characteristics of river bed sediment surfaces. The research shows how the 2D Discrete Wavelet Transform (DWT) can be used to separate the forms of the surface into different details or size ranges. The cumulative transform modulus plotted against the associated length scale or 'size' gives a *form size distribution (fsd)*. The authors believe that this measure will be more useful than the traditional *particle size distribution*, as it is the topographical form of the surface rather than the individual particle sizes that affects the near bed flow regime and hence bed friction characteristics. The research also illustrates how the wavelet transform may prove to be a useful tool for the identification of coherent structures appearing on the bed surface. This can be achieved by thresholding the wavelet transform coefficients for each of the details respectively. Features elucidated by the thresholding process in this way may indicate where sediment has gathered on the surface in distinct formations. It is known that bed forms move during the sedimentation process and this method of feature identification could prove useful in locating and following the spatio-temporal behavior of such features.

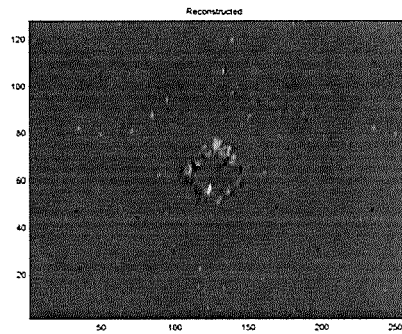
Future work will concentrate on the analysis of a series of sediment data sets recorded over a period of time during flood flows to study the dynamics of the surface topographies that occur during the bed armoring process. In addition, the non-decimated or stationary wavelet transform (SWT) will be further employed in the analysis of the experimental surfaces.



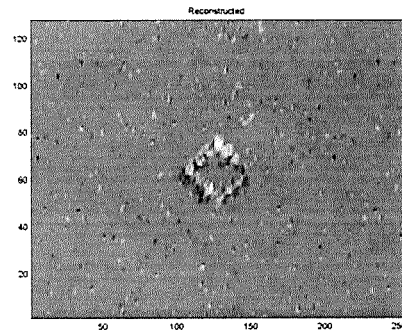
(a) Soft Threshold =  $1\sigma$



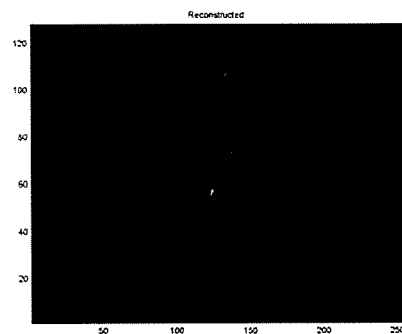
(d) Hard Threshold =  $1\sigma$



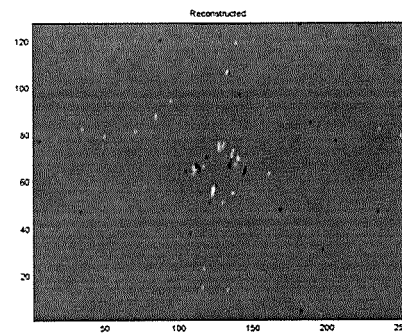
(b) Soft Threshold =  $2\sigma$



(e) Hard Threshold =  $2\sigma$



(c) Soft Threshold =  $3\sigma$



(f) Hard Threshold =  $3\sigma$

Figure 11. Synthetic diamond feature extraction through wavelet thresholding.



## REFERENCES

- [1] P.Y. Julien, *Erosion and Sedimentation*, New York: Cambridge University Press, 1995.
- [2] R. Kellerhals and D.I. Bray, "Sampling Procedures for Coarse Fluvial Sediments", *Journal of the Hydraulic Engineering Division, ASCE*, **97(8)** (1971), p. 1165.
- [3] I.K. McEwan, T.M. Sheen, G.J. Cunningham, and A.R. Allen, "Estimating the Size Composition of Sediment Surfaces Through Image Analysis", *Proceeding of the Institution of Civil Engineers — Water Maritime and Energy*, **142** (2000), p. 189.
- [4] P.S. Addison, *The Illustrated Wavelet Handbook: Applications in Science, Engineering, Medicine and Finance*. London: Institute of Physics Publishing, 2002.
- [5] L.T. Dougan, P.S. Addison, and W.M.C. McKenzie, "Fractal Analysis of Fracture: a Comparison of Dimension Estimates", *Mechanics Research Communications*, **27(4)** (2000), p. 383.
- [6] G.N. Frantziskonis, L.B. Simon, J. Woo, and T.E. Matikas, "Multiscale Characterization of Pitting Corrosion and Application to an Aluminum Alloy", *European Journal of Mechanics A — Solids*, **19** (2000), p. 309.
- [7] X.Q. Jiang, L. Blunt, and K.J. Stout, "Three-Dimensional Surface Characterization for Orthopaedic Joint Prostheses", *Proceedings of the Institutions of Mechanical Engineers Part-H*, **213(11)** (1999), p. 49.
- [8] S-H. Lee, H. Zahouani, R. Caterini, and T.G. Mathia, "Morphological Characterisation of Engineered Surfaces by Wavelet Transform", *International Journal of Machine Tools & Manufacture*, **38(5-6)** (1998), p. 581.
- [9] Z. Moktadir and K. Sato, "Wavelet Characterization of the Submicron Surface Roughness of Anisotropically Etched Silicon", *Surface Science*, **470** (2000), p. L75.
- [10] F. Xiong, X.Q. Jiang, Y. Gao, and Z. Li, "Evaluation of Engineering Surfaces Using a Combined Fractal Modeling and Wavelet Analysis Method", *International Journal of Machine Tools & Manufacture*, **41** (2001), p. 2187.
- [11] G. Pender, T.B. Hoey, C. Fuller, and I.K. McEwan, "Selective Bedload Transport During the Degradation of Well Sorted Graded Sediment Bed", *Journal of Hydraulic Research*, **39(3)** (2001), p. 269.
- [12] P.S. Addison, K.B. Murray, and J.N. Watson, "Wavelet Transform Analysis of Open Channel Wake Flows", *ASCE J. Engineering Mechanics*, 2001, p. 58.
- [13] I. Daubechies, *Ten Lectures on Wavelets*. Philadelphia: SIAM, 1992.
- [14] T.E. Lisle and M.A. Madej, "Spatial Variation in Armouring in a Channel with High Sediment Supply", Ch. 13 in *Dynamics of Gravel-bed Rivers*. ed. P. Billie, R.D. Hey, R. Thorne, and P. Tacconi. Chichester: John Wiley & Sons Ltd, 1992.
- [15] B.B. Willetts, G. Pender, and I.K. McEwan, "Experiments on the Transport of Graded Sediment", *Proceeding of the Institution of Civil Engineers — Water Maritime and Energy*, **130** (1998), p. 217.
- [16] R.F. Craig, *Soil Mechanics*, 4th edn. Wokingham, Berkshire: Van Nostrand Reinhold (UK) Co Ltd, 1987.
- [17] P.S. Addison, *Fractals and Chaos, an Illustrated Course*. London: Institute of Physics Publishing, 1997.
- [18] S.J. Tait, B.B. Willetts, and J.K. Maizels, "Laboratory Observations of Bed Armouring and Changes in Bedload Composition", Ch. 10 in *Dynamics of Gravel-bed Rivers*. ed. P. Billie, R. D. Hey, R. Thorne, and P. Tacconi. Chichester: John Wiley & Sons Ltd, 1992.
- [19] F. Abramovich, T.C. Bailey, and T. Sapatinas, "Wavelet Analysis and its Statistical Applications" *The Statistician*, **49(1)** (2000), p. 1.
- [20] V.J. Barclay, R.F. Bonner, and I.P. Hamilton, "Applications of Wavelet Transforms to Experimental Spectra: Smoothing, Denoising and Data Set Compression", *Analytical Chemistry*, **69(1)** (1997), p. 78.
- [21] R.T. Ogden, *Essential Wavelets for Statistical Applications and Data Analysis*. Boston: Birkhäuser, 1997.
- [22] P.E. Tikkanen, "Nonlinear Wavelet and Wavelet Packet Denoising of Electrocardiogram Signal", *Biological Cybernetics*, **80** (1999), p. 259.
- [23] J.M. Morris and R. Peravali, "Minimum-Bandwidth Discrete-Time Wavelets", *Signal Processing*, **76** (1999), p. 181.
- [24] S-C Ngan, S.M. LaCorte, and X. Hu "Temporal Filtering of Event-Related fMRI Data Using Cross- Validation", *NeuroImage*, **11** (1999), p. 797.
- [25] S.L. Lee, C.K. Lee, and K.Y. Yoo "New Lifting Based Structure for Undecimated Wavelet Transform", *Electronics Letters*, **36(22)** (2000), p. 1894.

Paper Received 27 September 2002; Revised 26 January 2003; Accepted 19 March 2003.

**Title:**

Wavelet thresholding of simulated sediment surfaces to highlight pertinent bedform features

**Authors:**

Annie Nyander<sup>1</sup>, Paul S. Addison<sup>2,3</sup>, Ian McEwan<sup>4</sup> and Gareth Pender<sup>5</sup>.

1. School of the Built Environment, Napier University, Edinburgh.
2. School of the Built Environment, Napier University, Edinburgh
3. CardioDigital Ltd, Elvingston Science Park, Gladsmuir, East Lothian.
4. Department of Engineering, University of Aberdeen, Aberdeen.
5. School of the Built Environment, Heriot-Watt University, Edinburgh.

**Abstract:**

When sedimentation occurs in a river channel, the topography of the bed surface changes which in turn affects the flow characteristics. This study applies the wavelet transform; a relatively new mathematical tool for data analysis. Interest in this analysis method has increased during recent years, and today it can be found in a number of areas in both science and engineering.

In this investigation a wavelet thresholding-based technique have been applied to highlight pertinent bedform features in simulated sediment surfaces with superimposed bed-features. One of the sediment surfaces is shown in figure 1. Using the wavelet transform the surface was transformed into scale details (or scale related wavelet coefficients). A threshold was then applied to the wavelet coefficients where coefficient larger then the threshold value were kept and coefficient smaller then the threshold value were removed, as illustrated in figure 2. Here the threshold values are set to equal multiples of the standard deviation ( $\sigma$ ) of the wavelet coefficients at each scale. Figure 3 show the thresholded and reconstructed surfaces for three different threshold values,  $1 \times \sigma$ ,  $2 \times \sigma$  and  $3 \times \sigma$ . Thus, this show that using a wavelet thresholding technique the background surface can be removed and the feature part of the surface extracted.

**Keywords:** River Bed, Sediment Surface, Wavelet Analysis, Surface Forms, Thresholding.

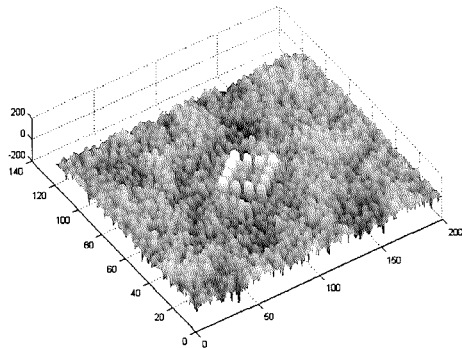


Figure 1 Simulated sediment surface

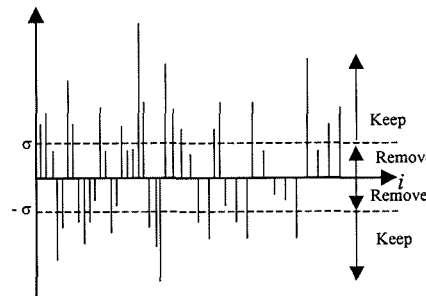
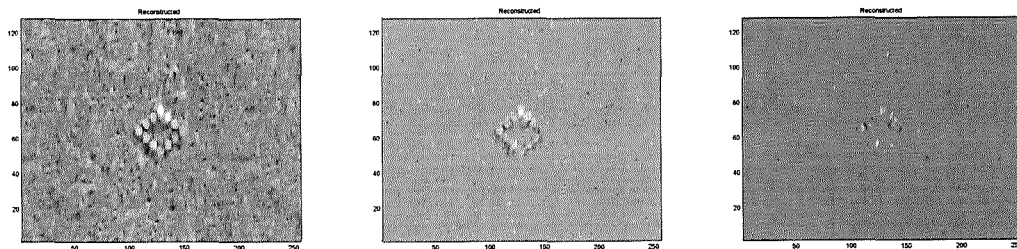


Figure 2 Thresholding the wavelet coefficient



(a)  $1 \times \sigma$

(b)  $2 \times \sigma$

(c)  $3 \times \sigma$

Figure 3 Thresholded and reconstructed surfaces

## **REFERENCES**

- Abramovich F, Bailey T C and Sapatinas T (2000) "Wavelet analysis and its statistical applications", *The Statistician*, Vol.49(1), pp.1-29.
- Abramovich F, Sapatinas T and Silverman B W (1998) "Wavelet thresholding via Bayesian approach", *Journal of the Royal Statistical Society. Series B*, Vol.60(4), pp.725-749.
- Adams J (1979) "Gravel size analysis from photographs" *Journal of Hydraulic Engineering Division*, Vol.105, pp.1247-1255.
- Addison P S (1997) *Fractals and chaos: An illustrated course*, Institute of Physics Publishing, Bristol.
- Addison P S (1999) "Wavelet analysis of the breakdown of a pulsed vortex flow", *Proceedings of the institution of Mechanical Engineering part C – Journal of Mechanical Engineering Science*, Vol.213, pp.217-229.
- Addison P S (2002) *The Illustrated Wavelet Transform Handbook*, Institute of Physics Publishing, London.
- Addison P S, McKenzie W M C, Ndumu A S, Dougan L T and Hunter R (1999) "Fractal cracking of concrete: Parameterization of spatial diffusion", *Journal of Engineering Mechanics*, June, pp.622-629.
- Addison P S, Murray K B and Watson J N (2001a) "Wavelet transform analysis of open channel wake flows", *ASCE Journal of Engineering Mechanics*, Vol.127, pp.58-70.
- Addison P S and Ndumu A S (1999) "Engineering applications of fractional Brownian motion: self-affine and self-similar random processes", *Fractals*, Vol.7(2), pp.622-629.
- Addison P S, Sibbald A and Watson J N (1997) "Wavelet analysis: A mathematical microscope with civil engineering applications", *Insight*, Vol.39(7), pp.493-497.
- Addison P S, Uchipichat N, Watson J N, Clegg G R, Robertson C E and Steen P A (2001b) "Wavelet power spectrum-based prediction of successful defibrillation from ventricular fibrillation", 23<sup>rd</sup> Annual International Conference of the IEEE Engineering and Medicine and Biology Society, Istanbul, Turkey.
- Addison P S and Watson J N (1997) "The wavelet transform as a tool for the analysis of surface roughness", *SiF News*, The Paint Research Association, Issue9, pp.5-7.
- Addison P S, Watson J N, Clegg G R, Holzer M, Sterz F and Robertson C E (2000) "Evaluating arrhythmias in ECG signals using wavelet transforms", *IEEE Engineering in Medicine and Biology*, Vol.19(5), pp.104-109.
- Alsberg B K, Woodward A M and Kell D B (1997) "An introduction to wavelet transforms for chemometricians: a time-frequency approach", *Chemometrics and intelligent laboratory systems*, Vol.37, pp.215-239.

- Barclay V J, Bonner R F and Hamilton I P (1997) "Applications of wavelet transforms to experimental spectra: smoothing, denoising and data set compression", *Analytical Chemistry*, Vol.69(1), pp.78-90.
- Barndroff-Nielsen O E (1989) "Sorting, texture and structure", *Proceedings of the Royal Society Edinburgh*, Vol.96B, pp.167-179.
- Bergh J, Ekstedt F and Lindberg M (1999) *Wavelets*, Studentlitteratur, Lund.
- Berkner K and Wells R O (2002) "Smoothness estimates for soft-threshold denoising via translation-invariant wavelet transforms", *Applied and computational harmonic analysis*, Vol.12(1), pp.1-24.
- Best J, Buffin-Berlanger T, Kirkbride A and Reid I (2001) "Visualization of coherent flow structures associated with particle clusters: temporal and spatial characterization revealed using ultrasonic Doppler velocity profiling", *IAHR Conference New Zealand Hydraulic Society*, Canterbury, New Zealand.
- Bitzer K and Salas R (2002) "SIMSAFADIM: three-dimensional simulation of stratigraphic architecture and facies distribution modelling of carbonate sediments", *Computer and Geosciences*, Vol.28(10), pp.1177-1192.
- Boniforti M A, Magini R and Sciortino G (1997) "Background noise effects on modelling transitional shear flows", *JSME International Journal Series B-Fluids and Thermal Engineering*, Vol.40(3), pp.386-394.
- Bracic M and Stefanovska A (1998) "Wavelet-based analysis of human blood flow dynamics", *Bulletin of Mathematical Biology*, Vol.60(5), pp.919-935.
- Brayshaw A C, Frostick L E and Reid I (1983) "The hydrodynamics of particle clusters and sediment entrainment in coarse alluvial channels", *Sedimentology*, Vol.30, pp.137-143.
- Brislawn C M (1995) "Fingerprints go digital", *Notices of the AMS*, Vol.42(11), pp.1278-1283.
- British Standards Institution BS EN 197-1: (2000), *Cement, Composition, specifications and conformity criteria for common cements*.
- British Standards Institution BS 882: (1983), *Aggregates from natural sources for concrete*.
- British Standards Institution BS 1377: (1990) *British Standard methods of soil test for soils for civil engineering purposes*.
- Bushuyev S D and Sochnev S V (1999) "Entropy measurement as a project control tool", *International Journal of Project Management*, Vol.17(6), pp.343-350.
- Butler J B, Lane S N and Chandler J H (2001a) "Automated extraction of grain-size data from gravel surfaces using digital image processing", *Journal of Hydraulic Research*, Vol.39(5), pp.519-529.

- Butler J B, Lane S N and Chandler J H (2001b) "Characterization of the structures of river-bed gravels using two-dimensional fractal analysis", *Mathematical Geology*, Vol.33(3), pp.301-329.
- Carling P A, Gözl E, Orr H G and Radecki-Pawlik A (2000a) "The morphodynamics of fluvial sand dunes in the River Rhine near Mainz, Germany. I. Sedimentology and morphology", *Sedimentology*, Vol.47(1), pp.227-252.
- Carling P A, Gözl E, Orr H G and Radecki-Pawlik A (2000b) "The morphodynamics of fluvial sand dunes in the River Rhine near Mainz, Germany. II. Hydrodynamics and sediment transport", *Sedimentology*, Vol.47(1), pp.253-278.
- Chadwick A and Morfett J (1986) *Hydraulics in Civil Engineering*, Allen & Unwin Ltd, London.
- Chen J, Itoh S and Hashimoto T (1993) "ECG data compression by using wavelet transform", *IEICE Transactions on Information and Systems*, Vol.E76D(12), pp.1454-1461.
- Chen Q, Yang S and Li Z (1999) "Surface roughness evaluation by using wavelet analysis", *Precision Engineering*, Vol.23, pp.209-212.
- Chen X, Raja J and Simanapalli S (1995) "Multi-scale analysis of engineering surfaces", *International Journal of Machine Tool and Manufacture*, Vol.35(2), pp.231-238.
- Chiaia B, van Mier J G M and Vervuurt A (1998) "Crack growth mechanisms in four different concretes: microscopic observations and fractal analysis", *Cement and Concrete Research*, Vol.28(1), pp.103-114.
- Chow V T (1959) *Open-channel hydraulics*, McGraw-Hill, Singapore.
- Church M, Hassan M A and Wolcott J F (1998) "Stabilizing self-organized structures in gravel-bed stream channels: Field and experimental observations", *Water Resources Research*, Vol.34, pp.3169-3179.
- Coifman R R and Donoho D L (1995) "Translation invariant de-noising", *Lecture Notes in Statistics*, Vol.103, pp.125-150.
- Corbin M, Hera A and Hou Z (2000) "Locating damage regions using wavelet approach", The 14<sup>th</sup> ASCE Engineering Mechanics Conference, May 21-24, Austin, Texas, USA.
- Craig R F (1987) *Soil Mechanics, 4<sup>th</sup> edition*, Van Nostrand Reinhold Co Ltd, Wokingham, Berkshire.
- Daubechies I (1988) "Orthonormal bases of compact supported wavelets", *Communications on Pure and Applied Mathematics*, Vol.41, pp.909-996.
- Daubechies I (1992) *Ten lectures on wavelets*, SIAM, Philadelphia.

- Davidson R, Labys W C and Lesourd J-B (1998) "Wavelet analysis of commodity price behaviour", *Computational Economics*, Vol.11, pp.103-128.
- Dietrich W E, Kirchner J W, Ikeda H and Iseya F (1989) "Sediment supply and the development of the coarse surface layer in gravel-bedded rivers", *Nature*, 340, pp.215-216.
- Donoho D L (1993) "Nonlinear wavelet methods for recovery of signals, densities, and spectra from indirect and noisy data", *Proceedings of Symposia in Applied Mathematics*, Vol.00, pp.173-205.
- Donoho D L and Johnstone I M (1994) "Ideal spatial adaptation by wavelet shrinkage", *Biometrika*, Vol.81, pp.425-455.
- Donoho D L and Johnstone I M (1995) "Adapting to unknown smoothness via wavelet shrinkage", *Journal of the American Statistical Association*, Vol.90(432), pp.1200-1224.
- Donoho D L and Johnstone I M (1998) "Minimax estimation via wavelet shrinkage", *The Annals of Statistics*, Vol.26(3), pp.879-921.
- Donoho D L, Johnstone I M, Kerkyacharian G and Picard D (1995) "Wavelet shrinkage: Asymptopia?", *Journal of the Royal Statistical Society, Series B*, Vol.57, pp.301-369.
- Dougan L T (2002) "Fractal geometric analysis of spatially self-affine stochastic fracture", Ph.D. Thesis, Napier University, Edinburgh.
- Dougan L T, Addison P S and McKenzie W M C (2000) "Fractal analysis of fracture: a comparison of dimension estimates", *Mechanics Research Communications*, Vol.27(4), pp383-392.
- Einstein A (1905) "Über die von der molekularkinetischen Theorie der Wärme geforderte Bewegung von in ruhenden Flüssigkeiten suspendierten Teilchen", *Annalen der Physik und Chemie*, IV, Vol.17, pp.549-560.
- EPSRC Grant Reference: GR/J67567, Pender G, Ervine D A, Hoey T B and Herbertson J G, "Transport of graded sediment in bankfull and overbank flow".
- EPSRC Grant Reference: GR/L22058, McEwan I K, Willetts B B and Pender G, "The response of graded sediment systems to change in flow regime and sediment supply".
- EPSRC Grant Reference: GR/L22065, McEwan I K, Willetts B B and Pender G, "The response of graded sediment systems to change in flow regime and sediment supply".
- EPSRC Grant Reference: GR/L54448/01, McEwan I K and Willetts B B, "The role of coherent flow structures in the sediment over flat beds at high Reynolds number".

- Fedorenko Y V and Husebye E S (1999) "First breaks - automatic phase picking of P- and P-onsets in seismic records", *Geophysical Research Letters*, Vol.26(21), pp.3249-3252.
- Ferreira C B R and Borges D L (2003) "Analysis of mammogram classification using a wavelet transform decomposition", *Pattern Recognition Letters*, Vol.24, pp.973-982.
- Fischer R and Akay M (1996) "A comparison of analytical methods for the study of fractional Brownian motion", *Annals of Biomedical Engineering*, Vol.22, pp.537-543.
- Flandrin P (1992) "Wavelet analysis and synthesis of fractional Brownian motion", *IEEE Transactions on Information Theory*, Vol.38(2), pp.910-917.
- Frantziskonis G (2002) "Multiscale characterization of materials with distributed pores and inclusions and application to crack formation in an aluminium alloy", *Probabilistic engineering mechanics*, Vol.17, pp.359-367.
- Frantziskonis G and Deymier P A (2000a) "Wavelet methods for analysing and bridging simulations at complementary scales – the compound wavelet matrix and application to microstructure evolution", *Modelling and simulation in material science and engineering*, Vol.8, pp.649-664.
- Frantziskonis G and Deymier P A (2000b) "Compound wavelet matrix for bridging simulations at complementary scales-application to microstructure evolution", 14<sup>th</sup> ASCE Engineering Mechanics Conference, Texas.
- Frantziskonis G and Hansen A (2000) "Wavelet-based multiscaling in self-affine random media", *Fractals*, Vol.8(4), pp.403-411.
- Frantziskonis G N, Simon L B, Woo J and Matikas T E (2000) "Multiscale characterization of pitting corrosion and application to an aluminium alloy", *European Journal of Mechanics. A*, Vol.19, pp.309-318.
- French R H (1994) *Open-channel Hydraulics*, McGraw-Hill, International Editions, Civil Engineering Series.
- Gessler J (1990) "Friction factor of armoured river beds", *Journal of Hydraulic Engineering*, Vol.116(4), pp.531-543.
- Goupillaud P, Grossmann A and Morlet J (1984) "Cycle-octave and related transforms in seismic signal analysis", *Geoplotation*, Vol.23, pp.85-102.
- Grossmann A and Morlet J (1984) "Decomposition Hardy functions into square integral wavelets of constant shape", *SIAM Journal on Mathematical Analysis*, Vol.15, pp.723-736.
- Grossmann A and Morlet J (1985) "Decomposition of functions into wavelets of constant shape, and related transforms, in Mathematics and Physics", *Lectures on Recent Results*, L. Streit, ed., World Scientific Publishing, Singapore.



- Grossmann A, Kronland-Martinet R and Morlet J (1987) "Reading and understanding continuous wavelet transforms", *Wavelet: Time-Frequency Methods and Phase Space*, Proceedings of the International Conference, Marseille, Springer-Verlag.
- Grubb H J and Walden A T (1997) "Characterizing seismic time series using the discrete wavelet transform", *Geophysical Prospecting*, Vol.45, pp.183-205.
- Haar A (1910) "Zur Theorie der orthogonalen Functionen-Systeme", *Mathematische Annalen*, Vol.69, pp.331-371.
- Hajj M R, Jordan D A and Teileman H W (1998) "Analysis of atmospheric wind and pressure on a low-rise building", *Journal of Fluids and Structures*, Vol.12, pp.537-547.
- Hajj M R, Tieleman H W and Tian L (2000) "Wind tunnel simulation of time variations of turbulence and effects on pressure on surface-mounted prisms", *Journal of Wind Engineering and Industrial Aerodynamics*, Vol.88, pp.197-212.
- Hale M T and Adhami R (1998), "Operational vibration specification of helicopter stores using wavelet analysis", *J.IEST*, Vol.41(5), pp.17-30.
- Haynie A and Frantziskonis G (2001) "Multiscale material characterization and application to artificially created microstructures", pp.529-532, in *Computer Methods and Advances in Geomechanics: Proceedings of the Tenth International Conference*, ed Tuscon, Arizona,.
- Heald J (2001) "Development of probabilistic prediction methods for graded sediment from discrete particle simulations", Ph.D. Thesis, University of Aberdeen, Aberdeen.
- Hilton M L and Ogden R T (1997) "Data analytic wavelet threshold selection in 2-D signal denoising", *IEEE Transactions on signal processing*, Vol.45(2), pp.496-500.
- Hubbard B B (1996) *The world according to wavelets*, A K Peters, Wellesley, MA.
- Hunziker R P and Jaeggi M N R (2002) "Grain sorting processes", *Journal of Hydraulic Engineering*, Vol.128(12), pp.1060-1068.
- Issa M A and Hammad A M (1993) "Fractal characterization of fracture surface in mortar", *Cement and Concrete Research*, Vol.23, pp.7-12.
- Issa. M A and Hammad A M (1994) "Assessment and evaluation of fractal dimensions of fractal fracture surface digitized images", *Cement and Concrete Research*, Vol.24(2), pp.325-334.
- Jansen M, Malfait M and Bultheel A (1997) "Generalised wavelet cross validation for wavelet thresholding", *Signal processing*, Vol.56, pp.33-44.
- Jasper W J, Garnier S J and Potlapalli H (1996) "Texture characterization and defect detection using adaptive wavelets", *Optical Engineering*, Vol.35(11), pp.3140-3149.

- Jiang X Q and Blunt L (2001) "Morphological assessment of *in vivo* wear of orthopaedic implants using multiscalar wavelets", *Wear*, Vol.250, pp.217-221.
- Jiang X Q, Blunt L and Stout K J (2000) "Development of a lifting wavelet representation for surface characterization", *Proceedings of the Royal Society of London. Series A*, Vol.456, pp.2283-2313.
- Jiang X Q, Blunt L and Stout K J (1999) "Three-dimensional surface characterization for orthopaedic joint prostheses", *Proceedings of the Institution of Medical Engineering Part H – Journal of Engineering in Medicine*, Vol.213(H1), pp.49-68.
- Jiang X Q, Blunt L and Stout K J (2001a) "Application of the lifting wavelet to rough surfaces", *Journal of the International Societies for Precision Engineering and Nanotechnology*, Vol.25, pp.83-89.
- Jiang X Q, Blunt L and Stout K J (2001b) "Lifting wavelet for three-dimensional surface analysis", *International Journal of Machine Tool and Manufacture*, Vol.41, pp.2163-2169.
- Josso B, Burton D R and Lalor M J (2001) "Wavelet strategy for surface roughness analysis and characterisation", *Computer methods in applied mechanics and engineering*, Vol.191, pp.829-842.
- Josso B, Burton D R and Lalor M J (2002) "Frequency normalised wavelet transform for surface roughness analysis and characterisation", *Wear*, Vol.252, pp.491-500.
- Jung C R and Scharacanski J (2003) "Adaptive image denoising and edge enhancement in scale-space using the wavelet transform", *Pattern Recognition Letters*, Vol.24, pp.965-971.
- Kalayci T and Özdamar O (1995) "Wavelet preprocessing for automated neural network detection of EEG spikes", *IEEE Engineering in Medicine and Biology Magazine*, Vol.14(2), pp.160-166.
- Katul G and Vidakovic B (1996) "The partitioning of attached and detached eddy motion in the atmospheric surface layer using Lorentz wavelet filtering", *Boundary Layer Meteorology*, Vol.77(2), pp.153-172.
- Kellerhals and Bray (1971) "Sampling procedures for coarse fluvial sediment", *Journal of the Hydraulic Engineering Division*, Vol.97(8), pp.1165-1180
- Kim C H and Aggarwal R (2000) "Wavelet transforms in power system, Part 1 General introduction to the wavelet transforms", *Power Engineering Journal*, April, pp.81-87.
- Kneller B and Buckee C (2000) "The structure and fluid mechanics of turbidity currents: a review of some recent studies and their geological implications", *Sedimentology*, Vol.47(1), pp.62-94.
- Kondolf G M (1994) "Geomorphic and environmental effects of instream gravel mining", *Landscape and Urban Planning*, Vol.28(2-3), pp.225-243.

- Krim H, Tucker D, Mallat S and Donoho D L (1999) "On denoising and best signal representation", IEEE Transactions on Information Theory, Vol.45(7), pp.2225-2238.
- Laine A F, Schuler S, Fan J and Hudu W (1994) "Mammographic features enhancement by multiscale analysis", IEEE Transactions on Medical Imaging, Vol.13(4), pp.725-740.
- Lalonde P and Fournier A (1997) "A wavelet representation of reflectance function", IEEE Transactions on Visualization and Computer Graphics, Vol.3(4), pp.329-336.
- Lane E W and Carlson E J (1953) "Some factors affecting the stability of canals constructed in coarse granular materials", Proceedings of the Minnesota International Hydraulics Convention, Sep.
- Lark R M and Webster R (2001) "Changes in variance and correlation of soil properties with scale and location: analysis using an adapted maximal overlap discrete wavelet transform", European Journal of Soil Science, Vol.52, pp.547-562.
- Lau K-M and Weng H-Y (1995) "Climate signal detection using wavelet transform: How to make a time series sing", Bulletin of the American Meteorological Society, Vol.76, pp.2391-2402.
- Lázaro J C, San Emeterio J L, Ramos A and Fernández-Marrón (2002) "Influence of thresholding procedures in ultrasonic grain noise reduction using wavelets", Ultrasonics, Vol.40, pp.263-267.
- Lee B Y and Tarng Y S (2000) "Drill fracture detection by the discrete wavelet transform" Journal of Materials Processing Technology, Vol.99, pp.250-254.
- Lee S-H, Zahouani H, Caterini R and Mathia T G (1998) "Morphological characterisation of engineered surfaces by wavelet transform", International Journal of Machine Tool and Manufacture, Vol.38, pp.581-589.
- Lemarié P-G and Meyer Y (1986) "Ondelettes et bases hilbertiennes" Revista Matemática Iberoamericana, Vol.2, pp.1-18.
- Li S, Kwok J T, Zhu H and Wang Y (2003) "Texture classification using the support vector machines", Pattern Recognition, Vol.36, pp.2883-2893.
- Lisle T E and Madej M A (1992) "Spatial variation in armouring in a channel with high sediment supply", Chapter 13 in *Dynamics of Gravel-bed Rivers*, Ed. Billie P, Hey R D, Thorne R and Tacconi P, John Wiley & Sons Ltd.
- Liu P C (2000) "Wave grouping characteristics in nearshore Great Lakes", Ocean Engineering, Vol.27, pp.1221-1230.
- Maktadir Z and Sato K (2000) "Wavelet characterization of the submicron surface roughness an anisotropically etched silicon", Surface Science, Vol.470, pp.L57-L62.
- Mallat S G (1986) "Multiresolution approximation and wavelets", Preprint GRASP Lab. Department of Computing and Information Science, University of Pennsylvania.

- Mallat S G (1989a) "A theory of multiresolution signal decomposition: the wavelet representation", IEEE Transactions on Pattern Analysis and Machine Intelligence, Vol.11, pp.674-693.
- Mallat S G (1989b) "Multiresolution approximation and wavelet orthonormal bases of  $L^2$ ", Transaction of the American Mathematical Society, Vol.315, Sept, pp.69-87.
- Mallat S G (1989c) "Multifrequency channel decompositions of images and wavelet models", IEEE Transaction in Acoustic Speech and Signal Processing, Vol.37, pp.2091-2110.
- Mallat S G (1999) *A wavelet tour of signal processing*", Academic Press, San Diego.
- Mandelbrot B B and Van Ness J W (1968) "Fractional Brownian motions. fractional noises and applications" Siam Review, Vol.10(4), pp.422-437.
- Mandelbrot B B and Wallis J R (1969) "Computer experiments with fractional Gaussian noises, Part 2, Rescaled Ranges and Spectra", Water Resources Research, Vol.5(1), pp.242-259.
- Mandelbrot B B, Possoja D E and Pully A J (1984) "Fractal character of fracture surfaces of metals", Nature, Vol.208, pp.721-722.
- Manian V and Vasquez R (1998) "Scaled and rotated texture classification using a class of bases functions", Pattern Recognition, Vol.31(12), pp.1937-1948.
- Marion A (1996) "Equilibrium bed material composition for well-graded sediment mixtures in a compound channel", Research Report SR474, HR Wallinford.
- Marion A, Tait S J and McEwan I (2003) "Analysis of small-scale gravel bed topography during armouring", Water Resources Research, Vol.39(12), pp.1334-1344.
- McEwan I K (2002) "Discussion of "Flow turbulence over fixed and weakly mobile gravel beds" by Vladimir Nikora and Derek Goring", Journal of Hydraulic Engineering, A.S.C.E., Vol.128(3), pp.359-360.
- McEwan I K, Heald J and Goring (1999) "Discrete particle modelling of entrainment from a mixed grain size sediment bed", Proceedings I.A.H.R. Symposium on River, Coastal and Estuarine Morphodynamics, Geneva, Italy, Vol.I.
- McEwan I K, Jefcoate B J and Willetts B B (1999) "The grain-fluid interaction as a self-stabilizing mechanism in fluvial bed load transport", Sedimentology, Vol.46(3), pp.407-416.
- McEwan I K, Sheen T M, Cunningham G J and Allen A R (2000) "Estimating the size composition of sediment surfaces through image analysis", Proceedings- Institution of Civil Engineers: water, maritime and energy, Vol.142, pp.189-195.
- McEwan I K, Sørensen M, Heald J, Tait S, Cunningham G, Goring D and Willetts B (2004) "Probabilistic modelling of bed-load composition", Journal of Hydraulic Engineering, A.S.C.E., Vol.130(2), pp.129-139.

- McKay, D J S (2002) "Analysis of river-erosion control geosynthetics", Ph.D. Thesis, Glasgow Caledonian University, Glasgow.
- Meyer Y (1986a) "Ondettes et fonctions splines", Lectures given at the University of Torino, Italy.
- Meyer Y (1986b) "Ondettes, fonctions splines at analyses graduees" Seminaire EDP, Ecole Polytechnique, Paris, France.
- Meyer Y (1990) "Ondelettes et operatures, I: Ondelettes, II: Operatures de Calderon-Zygmund, III Operatures multilineaires", Hermann, Paris.
- Meyer-Peter E and Muller R (1948) "Formulas for bed-load transport", Proceedings of the 3<sup>rd</sup> meeting of IAHR, Stockholm pp.39-64.
- Meyers S D, Kelly B G and O'Brien J J (1993) "An introduction to wavelet analysis in oceanography and meteorology: With application to the dispersion of Yanai waves", Monthly Weather Review, Vol.121, pp.2858-1866.
- Moktadir Z and Sato K (2000) "Wavelet characterization of the submicron surface roughness of anisotopically etched silicon", Surface Science, Vol.470, pp.L57-L62.
- Moreau F, Fibert D and Saracco G (1995) "Filtering non-stationary geophysical data with orthogonal wavelets", Geophysical Research Letters, Vol.23(4), pp.40-410.
- Morris J M and Peravali R (1999) "Minimum-bandwidth discrete-time wavelets", Signal Processing, Vol.76(2), pp.181-193.
- Moulin P (1994) "Wavelet thresholding techniques for power spectrum estimation", IEEE Transactions on Signal Processing, Vol.42(11), pp.3126-3136.
- Murray K (2000) "Wavelet transform analysis of turbulent wake flow", Ph.D. Thesis, Napier University, Edinburgh
- Murtagh F and Starck J L (2003) "Quantization from Bayes factors with application to multilevel thresholding", Pattern Recognition Letters, Vol.24(12), pp.2001-2007.
- Nason G P (1996) "Wavelet shrinkage using cross-validation", Journal of the Royal Statistical Society. Series B, Vol.58, pp.463-479.
- Nason G P and Silverman B W (1995) "The Stationary Wavelet Transform and some Statistical Applications", Lecture Notes, Vol.103, pp.281-300. In *Wavelets and Statistics* (A Antoniadis and G Oppenheim, Eds) Springer-Verlag, New York.
- Ndumu A S (2000) "Fractal-based stochastic simulation and analysis of subsurface flow and scale-dependent solute transport", Ph.D. Thesis, Napier University, Edinburgh.
- Ngan S-C, LaConte S M and Hu X (2000) "Temporal filtering of event-related fMRI data using cross-validation", NeuroImage, Vol.11, pp.797-804.

- Nikora V, Goring D, McEwan I, Griffiths G (2001) "Spatially averaged open-channel flow over rough bed", *Journal of Hydraulic Engineering, A.S.C.E.*, Vol.127(2), pp.123-133.
- Nikora V, Heald J, Goring D and McEwan I (2001) "Diffusion of saltating particles in unidirectional water flow over a rough granular bed", *Journal of Physics A: Mathematical and General*, Vol.34, pp.L743-L749.
- NiÑo Y, Lopez F and Garcia M (2003) "Threshold for particle entrainment into suspension" *Sedimentology*, Vol.50(2), pp.247-263.
- Nyander A, Addison P S, McEwan I and Pender G (2002) "River bed surface roughness analysis using 2-D wavelet transform-based methods", *The 15<sup>th</sup> ASCE Engineering Mechanics Conference*, June 2-5, New York , USA.
- Nygaard J O and Grue J (2000) "Wavelet methods for the solution of wave-body problems", *Journal of Engineering Mathematics*, Vol.38, pp.323-354.
- Ogden R T, (1997) *Essential wavelets for statistical applications and data analysis*, Birkhäuser, Boston
- Pan Q, Zhang L, Dai G and Zhang H (1999) "Two denoising methods by wavelet transform", *IEEE Transactions on Signal Processing*, Vol.47(21), pp.3401-3406.
- Papanicolaou A N, Strom K, Schuyler A and Talebbeydokhti N (2003) "The role of sediment specific gravity and availability on cluster evolution", Vol.28, pp.69-86, *Earth Surface Processes and Landforms*, John Wiley & Sons Ltd, Chichester, UK
- Pender G, Hoey T B, Fuller C and McEwan I K (2001) "Selective bedload transport during the degradation of a well sorted graded sediment bed", *Journal of Hydraulic Research*, Vol.39(3), pp.269-277.
- Percival D B and Mofjeld H O (1997) "Analysis of subtidal coastal sea level fluctuations using wavelets", *Journal of the American Statistical Association*, Vol.92(439), pp.868-880.
- Pesquet J C, Krim H and Carfantan H (1996), "Time-invariant orthonormal wavelet representations" *IEEE Transactions on Signal Processing*, Vol.44(8), pp.1964-1970.
- Pettit C L, Jones N P and Ghanem R (2000), "Wavelet-based detection and classification of roof-corner pressure transients", *Wind and Structures*, Vol.3(3), pp.159-175.
- Pettit C L, Jones N P and Ghanem R (2002), "Detection and simulation of roof-corner pressure transients", *Journal of Wind Engineering and Industrial Aerodynamics*, Vol.90, pp.171-200.
- Pincus S M (1990) "Approximate entropy as a measure of system complexity", *Proceedings of the National Academy of Science of the United States of America*. Vol.88, March, pp.2297-2301.

- Pincus S M and Goldberger A L (1994), "Physiological time-series analysis: what does regularity quantify?", *American Journal of Physiology*, Vol.266(4Pt2), pp.H1643-1656.
- Pislaru C, Freeman J M and Ford D G (2003) "Modal parameter identification for CNC machine tools using wavelet transform", *International Journal of Machine Tools and Manufacture: Design, research and application*, Vol.43, pp.987-993.
- Qu B (1999) "The use of fractional Brownian motion in the modelling of the dispersion of contaminants in Fluids", Ph.D. Thesis, Napier University, Edinburgh
- Qui J, Paw U K, Shaw R (1995) "The leakage problem of the orthonormal wavelet transform when applied to atmospheric turbulence", *Journal of Geophysical Research*, Vol.100(D12), pp.25769-25779.
- Raja J, Muralikrishnan B and Fu S (2002) "Recent advances in separation of roughness, waviness and form", *Journal of the International Societies for Precision Engineering and Nanotechnology*, Vol.26, pp.222-235.
- Reid I, Frostick L E and Brayshaw A C (1992) "Microform roughness elements and the selective entrainment and entrapment of particles in gravel-bed rivers", in *Dynamics of Gravel-bed Rivers*, Ed. Billie P, Hey R D, Thorne R and Tacconi P, John Wiley & Sons Ltd.
- Richman J S and Moorman J R (2000) "Physiological time-series analysis using approximate entropy and sample entropy", *American Journal of Physiology - Heart and Circulatory Physiology*, Vol.278, pp.H2039-H2049.
- Rioul O and Vetterli M (1991) "Wavelet and signal processing", *IEEE Signal Processing Magazine*, Vol8(4), October, pp.14-38.
- Raudkivi A J (1976) *Loose boundary hydraulics*, 2<sup>nd</sup> ed, Pergamon Press, New York.
- Rivenæs J C (1997) "Impact of sediment transport efficiency on large-scale sequence architecture: results from stratigraphic computer simulation", *Basin Research*, Vol.9(2), pp.91-105.
- Rott N (1990) "Note on the history of the Reynolds number", *Annual Review Fluid Mechanics*, Vol.22, pp.1-11.
- Ryan S (2001) "The influence of sediment supply on rates of bedload transport: a case study of three streams on the San Juan national forest", *Proceedings of the Seventh Federal Interagency Sedimentation Conference*, March 25-29, Reno, Nevada, USA.
- Salyer J W (2003) "Neonatal and pediatric pulse oximetry", *Respiratory Care*, Vol.48(4), pp.386-398.
- Sanz J L, Argüeso F, Cayón L, Martínez-González E, Barreiro R B, and Toffolatti L (1999a) "Wavelet applied to cosmic microwave background maps: a multiresolution analysis for denoising", *Monthly Notice of the Royal Astronomical Society*, Vol.309, pp.672-680.

- Sanz J L, Barreiro R B, Cayón L, Martínez-González E, Ruiz G A, Díaz F J, Argüeso F, Silk J and Toffolatti L (1999b) "Analysis of CMB maps with 2D wavelets" *Astronomy & Astrophysics Supplement Series*, Vol.140, pp.99-105.
- Schiff S J, Aldroubi A, Unser M and Sato S (1994) "Fast wavelet transformation of EEG", *Electroencephalograph and clinical Neurophysiology*, Vol.91, pp.442-455.
- Shin T and Han I (2000) "Optimal signal multi-resolution by genetic algorithms to support artificial neural networks for exchange-rate forecasting", *Expert Systems with Applications*, Vol.18, pp.257-269.
- Silva M Z, Gouyon R and Lepoutre F (2003) "Hidden corrosion detection in aircraft aluminium structures using laser ultrasonics and wavelet transform signal analysis", *Ultrasonics*, Vol.41, pp.301-305.
- Simonsen I, Hansen A and Nes O M (1998) "Determination of Hurst exponent by use of wavelet transform", *Physical Review E*, Vol.58(3), pp.2779-2787.
- Smith G N and Smith I G N (1998) *Elements of Soil Mechanics*, 7<sup>th</sup> edition, Blackwell Science, Cambridge.
- Solbø S and Eltoft T (2002) "T-WMAP: A wavelet based statistical speckle filter for SAR images", 5<sup>th</sup> Nordic Signal Processing Symposium, October 4-7, Trollfjord, Norway
- Srinivasan R S and Wood K L (1997) "A form tolerancing theory using fractals and wavelets", *Journal of Mechanical Design*, Vol.119, pp.185-193.
- Stachowiak G W and Podsiadlo P (2004) "Classification of tribological surfaces", *Tribology International*, Vol.37, pp.211-217.
- Starck J-L, Murtagh F and Gstaad R (1998) "A new entropy measure based on the wavelet transform and noise", *IEEE Transactions on Circuits and Systems II-Analog and Digital Signal Processing*, Vol.45(8), pp.1118-1124.
- Staszewski W J (1998) "Wavelet based compression and feature selection for vibration analysis", *Journal of Sound and Vibration*, Vol.211(5), pp.735-760.
- Staszewski W J, Pierce S G, Worden K, Philp W R, Tomlinson G R and Culshaw B (1997) "Wavelet signal processing for enhanced Lamb-wave defect detection in composite plates using optical fiber detection", *Optical Engineering*, Vol.36(7), pp.1877-1888.
- Strang G and Nguyen T (1996) *Wavelet and Filter Banks*, Wellesley-Cambridge Press, Wellesley, MA, USA.
- Strom K, Papanicolaou A N, Evangelopoulos M and Odeh M (2004) "Microforms in gravel bed rivers: Formation, disintegration and effects on bedload transport", *Journal of Hydraulic Engineering*, A.S.C.E, Vol.130(6), pp.554-567.
- Strömberg J O (1982) "A modified Fransklin system and higher order spline systems on  $R_n$  as unconditional bases for Hardy spaces", in *Conference in Harmonic Analysis*



- in Honour of Antoni Zygmund., Wadsworth Mathematics Series. Vol.II, pp.475-493.
- Struzik Z R (2001) "Wavelet methods in (financial) time-series processing", *Physica A*, Vol.296, pp.307-319.
- Szilagyi J, Parlange M B, Katul G G and Albertson J D (2003) "An objective method for determining principal time scales of coherent eddy structures using orthonormal wavelets", *Advances in Water Resources*, Vol.22(6), pp.561-566.
- Tait S J and Willetts B B (1991) "Characterisation of armoured bed surfaces", *Proceeding of International Grain Sorting Seminar, Zurich, Germany*.
- Tait S J, Willetts B B and Maizels J K (1992) "Laboratory observations of bed armouring and changes in bedload composition", Chapter 10 in *Dynamics of Gravel-bed Rivers*, Ed. Billie P, Hey R D, Thorne R and Tacconi P, John Wiley & Sons Ltd.
- Tanaka M, Sakawa M and Kato K (1997) "Application of the wavelet transform to compression of mechanical vibration data", *Cybernetics Systems*, Vol.28, pp.225-244.
- Teit J G Jr and Kritikos H H (1992) "SAR ocean representation using wavelets", *IEEE Transactions on Geoscience and Remote Sensing*, Vol.30(5), pp.1089-1094.
- Teng H and Qi Y (2003) "Application of wavelet technique to freeway incident detection", *Transport Research Part C*, Vol.11, pp.289-308.
- Turner S, Feurstein M C and Teich M C (1998) "Multiresolution wavelet analysis of heartbeat intervals discriminates healthy patients from those with cardiac pathology", *Physical Review Letters*, Vol.80(7), pp1544-1547.
- Tikkanen P E (1999) "Nonlinear wavelet and wavelet packet denoising of electrocardiogram signal", *Biological Cybernetics*, Vol.80, pp.259-267.
- Toh S (1995) "Time correlation between entropy and/or energy distribution into scales by 2D wavelet in 2D free-convective turbulence", *Journal of Physical Society of Japan*, Vol.64(3), March, pp.685-689.
- Torrence C and Compo G P (1997) "A practical guide to wavelet analysis", *Bulletin of the American Meteorological Society*, Vol.79(1), January, pp.61-78.
- Tsai D-M and Hsiao B (2001) "Automatic surface inspection using wavelet reconstruction", *Pattern Recognition*, Vol.24, pp.1285-1305.
- Tsai M C, Tseng E C and Cheng M Y (2000) "Design of a torque observer for detecting abnormal load", *Control Engineering Practice*, Vol.8, pp.259-269.
- Tyler C W and Kontsevich L L (2001) "Stereoprocessing of cyclopean depth images: horizontally elongated summation fields", *Vision Research*, Vol.41, pp.2235-2243.

- Visser M (2003) "Physical wavelets: Lorentz covariant, singularity-free, finite energy, zero action, localized solutions to the wave equation" *Physics Letters A*, Vol.315, pp.219-224.
- Wang A L, Yang C X and Yuan X G (2003a) "Evaluation of the wavelet transform method for machined surface topography 1: methodology validation", *Tribology International*, Vol.36, pp.512-526.
- Wang A L, Yang C X and Yuan X G (2003b) "Evaluation of the wavelet transform method for machined surface topography 2: fractal characteristic analysis", *Tribology International*, Vol.36, pp.527-535.
- Wang K and Huang H K (1996) "Medical image compression by using three-dimensional wavelet transformation", *IEEE Transaction on Medical Imaging*, Vol.15(4), pp.547-554.
- Wang W J and McFadden P D (1995) "Application of orthogonal wavelets to early gear damage detection", *Mechanical Systems and Signal Processing*, Vol.9(5), pp.497-507.
- Wang Y (1995) "Jump and sharp cusp detection by wavelet", *Biometrika*, Vol.82, pp.385-397.
- Wang Y (1999) "Change-points via wavelets for indirect data", *Statistica Sinica*, Vol.9, pp.103-118.
- Wang Y and Moon K S (1997) "Methodology for the multi-resolution simulation of grinding wheel surface", *Wear*, Vol.211, pp.218-225.
- Watson J N, Addison P S, Clegg G R, Holzer M, Sterz F and Robertson C E (1999a) "A novel wavelet transform based analysis reveals hidden structures in ventricular fibrillation", *Resuscitation*, Vol.43(2), pp.121-127.
- Watson J N, Addison P S and Sibbald A (1999b) "The de-noising of sonic echo test data through wavelet transform reconstruction", *Shock and Vibrations*, Vol.6, pp.267-271.
- Watson J N, Addison P S, Feng T and Sibbald A (2002) "Wavelet transform-based methods for use in the analysis of non-destructive testing (NDT) signals", *Recent Research Development in Sounds and Vibration*, Vol.1, pp.647-657.
- Weiss L G and Dixon T L (1997) "Wavelet-based denoising of underwater acoustic signals", *Journal of the Acoustical Society of America*, Vol.101(1), pp.377-383.
- Weyrich N and Warhola G T (1995) "De-noising using wavelet and cross-validation", *NATO adv. Study. Inst. C*, Vol.454, pp.523-532.
- Whitlow R (1995) *Basic Soil Mechanics*, 3<sup>rd</sup> edition, Longman Scientific & Technical, Harlow, England.
- Wickerhauser M V (1994) *Adapted Wavelet Analysis: from Theory to Soft-Ware*, Wellesley, MA, Boston.

- Willetts B B, Pender G and McEwan I K (1998) "Experiments on the transport of graded sediment", Proceedings - Institution of Civil Engineers: water, maritime and energy, Vol.130, Dec, pp.217-225.
- Williams J R and Amaratunga K (1994) "Introduction to wavelet in engineering", International Journal for Numerical Methods in Engineering, Vol.37, pp.2365-2388.
- Xiao S J, Jiang X Q, Blunt L and Scott P J (2001) "Comparison study of the biorthogonal spline wavelet filtering for areal rough surfaces", International Journal of Machine Tool and Manufacture, Vol.41, pp.2103-2111.
- Xiong F, Jiang X J, Gao Y and Li Z (2001) "Evaluation of engineering surfaces using a combined fractal modeling and wavelet analysis method", International Journal of Machine Tool and Manufacture, Vol.41, pp.2187-2193.
- Xu Y, Weaver J B, Healy D M and Lu J (1994) "Wavelet transform domain filters: a spatially selective noise filtration technique", IEEE Transactions on Image Processing, Vol.3(6), pp.747-758.
- Zahn D, Sarabandi K, Sabet K F and Harvey J F (2000) "Numerical simulation of scattering from rough surfaces: A wavelet-based approach", IEEE Transactions on Antennas and Propagation", Vol.48(2), pp.246-253.
- Zunino L, Pérez D, Garavaglia M and Rosso O A (2004) "Characterization of laser propagation through turbulent media by quantifiers based on the wavelet transform", Fractals (in publishing process at time of submission).